
Semaine de l'astrophysique
Besançon, Kursaal
29 juin - 3 juillet 2009
http://sf2a.obs-besancon.fr
Journées SF2A 2009
Journées communes avec la Société Suisse d'Astrophysique et d'Astronomie :
• PNCG « High-resolution numerical simulations »
• PNPS/PNP « Connecting our understanding of star and planet formation and physics »
Conférences grand public dans le cadre de l'AMA09
Comité d'organisation
France ALLARD
Stéphane BASA
Jonathan BRAINE
Denis BURGARELLA
Corinne CHARBONNEL
Mohammad HEYDARI-MALAYERI
Jürgen KNÖDLSEDER
Bertrand LEFLOCH
Joël PETETIN
Martine PIDANCIER
Céline REYLE
Daniel ROUAN
Réza SAMADI
David VALLS-GABAUD
Hervé WOZNIAK
Réalisation : Edith Burgey, Institut UTINAM. Crédit photographique : Serge Brunier
SF2A SOCIÉTÉ FRANÇAISE D'ASTRONOMIE & D'ASTROPHYSIQUE
Ville de Besançon
Le Doubs
cnrs INSU
UFC
Observatoire de Besançon
microalpha
cnes
Franche-Comté Conseil régional
l'Observatoire de Paris
cea
hp
EDP SCIENCES
2009 ANNÉE MONDIALE DE L'ASTRONOMIE

Contents

Participant list

Imen Al Samarai (samarai@cppm.in2p3.fr)
Danielle Alloin (danielle.alloin@cea.fr)
Nicolas André (nicolas.andre@cesr.fr)
Frédéric Arenou (frederic.arenou@obspm.fr)
Bérengère Argence (argence@apc.univ-paris7.fr)
Monique Arnaud (monique.Arnaud@cea.fr)
Julien Aublin (aublin@lpnhe.in2p3.fr)
Marc Audard (Marc.Audard@unige.ch)
Jean-Charles Augereau (augereau@obs.ujf-grenoble.fr)
Carine Babusiaux (carine.babusiaux@obspm.fr)
Carla Baldovin-Saavedra (carla.baldovin@unige.ch)
Jean Ballet (jballet@cea.fr)
Christophe Barache (christophe.barache@obspm.fr)
Matteo Barsuglia (barsuglia@apc.univ-paris7.fr)
Stéphane Basa (stephane.basa@oamp.fr)
Laurène Beauvalet (beauvalet@imcce.fr)
Bruno Bézard (bruno.Bezard@obspm.fr)
Samuel Boissier (samuel.boissier@oamp.fr)
Xavier Bonfils (xavier.bonfils@obs.ujf-grenoble.fr)
Carla Bonifazi (bonifazi@lpnhe.in2p3.fr)
Mickaël Bonnefoy (mbonnefo@obs.ujf-grenoble.fr)
Sylvain Bontemps (bontemps@obs.u-bordeaux1.fr)
Alessandro Boselli (Alessandro.Boselli@oamp.fr)
Jean-baptiste Bossa (bossa.jb@gmail.com)
Caroline Bot (bot@astro.u-strasbg.fr)
Géraldine Bourda (Geraldine.Bourda@obs.u-bordeaux1.fr)
Jonathan Braine (braine@obs.u-bordeaux1.fr)
Richard Britto (britto@tifr.res.in)
Pierre Brun (pierre.brun@cea.fr)
Denis Burgarella (denis.burgarella@oamp.fr)
Clotilde Busschaert (mrskloo@hotmail.com)
Clément Buton (cbuton@ipnl.in2p3.fr)
Nahuel Cabral (nahuelcabral@yahoo.fr)
Jean-noel Capdevielle (capdev@apc.univ-paris7.fr)
Nicole Capitaine (nicole.capitaine@obspm.fr)
Yvain Carpentier (yvain.carpentier@u-psud.fr)
Cécile Cavet (cecile.cavet@obspm.fr)
Alberto Cellino (cellino@oato.inaf.it)
Benoît Cerutti (benoit.cerutti@obs.ujf-grenoble.fr)
Gilles Chabrier (chabrier@ens-lyon.fr)
Corinne Charbonnel (Corinne.Charbonnel@unige.ch)
Patrick Charlot (charlot@obs.u-bordeaux1.fr)
Sebastien Charnoz (charnoz@cea.fr)
Eric Chassefière (eric.chassefiere@latmos.ipsl.fr)
Nicolas Chotard (n.chotard@ipnl.in2p3.fr)
Bruno Christophe (bruno.christophe@onera.fr)
Suzy Collin-Zahn (suzy.collin@obspm.fr)
Stéphane Colombi (colombi@iap.fr)
Anne Coupeaud (anne.coupeaud@cesr.fr)
Jean-michel Courty (courty@spectro.jussieu.fr)
Aurélien Crida (A.Crida@damtp.cam.ac.uk)
Françoise Crifo (francoise.crifo@obspm.fr)

Timea Csengeri (timea.csengeri@cea.fr)
Frédéric Daigne (daigne@iap.fr)
Sarah Dandy (sarah.dandy@onera.fr)
Jos De Bruijne (jdbruijn@rssd.esa.int)
Bernard Debray (bernard.debray@obs-besancon.fr)
Thibaut Decressin (decress1@astro.uni-bonn.de)
Omar Delaa (omar.delaa@obs-azur.fr)
Florent Deleflie (Florent.Deleflie@obs-azur.fr)
Xavier Delfosse (Xavier.Delfosse@obs.ujf-grenoble.fr)
Philippe Delorme (pd10@st-andrews.ac.uk)
Karine Demyk (demyk@cesr.fr)
Michel Dennefeld (dennefel@iap.fr)
Jean-Michel Desert (desert@iap.fr)
Vincent Desjacques (dvince@physik.uzh.ch)
Michel Devel (michel.devel@ens2m.fr)
Paola Di Matteo (paola.dimatteo@obspm.fr)
Noël Dimarcq (noel.dimarcq@obspm.fr)
Boris Dintrans (dintrans@ast.obs-mip.fr)
Alain Doressoundiram (alain.doressoundiram@obspm.fr)
Catherine Dougados (Catherine.Dougados@obs.ujf-grenoble.fr)
Sylvain Douté (sylvain.doute@obs.ujf-grenoble.fr)
Pascal Dubois (dubois@astro.u-strasbg.fr)
Yohan Dubois (dubois.yohan@gmail.com)
Fabrice Duvernay (fabrice.duvernay@univ-provence.fr)
Nicolas Epchtein (epchtein@unice.fr)
Pierre Exertier (Pierre.Exertier@obs-azur.fr)
Laurent Eyer (laurent.eyer@unige.ch)
Nicolas Fabas (fabas@graal.univ-montp2.fr)
Emeric Falize (Emeric.Falize@obspm.fr)
Benoit Famaey (bfamaey@ulb.ac.be)
Philippe Feautrier (Philippe.Feautrier@obs.ujf-grenoble.fr)
Agnès Fienga (agnes@obs-besancon.fr)
Thierry Foglizzo (foglizzo@cea.fr)
Bernard Foing (Bernard.Foing@esa.int)
Francesco Fontani (Francesco.Fontani@unige.ch)
Laure Fouchet (laure.fouchet@space.unibe.ch)
Thibault Garçon (thibault.garcon@subatech.in2p3.fr)
Maryvonne Gerin (gerin@lra.ens.fr)
Berrie Giebels (berrie@llr.in2p3.fr)
Marie Godard (marie.godard@ias.u-psud.fr)
René Goosmann (goosmann@astro.u-strasbg.fr)
Cyril Grima (cyril.grima@obs.ujf-grenoble.fr)
Alain Grosjean (alain.grosjean-dom@obs-besancon.fr)
Jérôme Guilet (jerome.guilet@cea.fr)
Pierre Guillard (pierre.guillard@ias.u-psud.fr)
Thomas Guillet (thomas.guillet@cea.fr)
Jean-louis Halbwachs (halbwachs@astro.u-strasbg.fr)
Garabed Halladjian (halladjian@cppm.in2p3.fr)
Guillaume Hébrard (hebrard@iap.fr)
Sebastien Heinis (sebastien@pha.jhu.edu)
Daniel Hestroffer (hestro@imcce.fr)
Mohammad Heydari-malayeri (m.heydari@obspm.fr)
Mathieu Hirtzig (mathieu.hirtzig@obspm.fr)
Béatrice Honvault (bhonvaul@univ-fcomte.fr)

Pascal Honvault (pascal.honvault@univ-fcomte.fr)
Agnieszka Jacholkowska (Agnieszka.Jacholkowska@cern.ch)
Christine Joblin (christine.joblin@cesr.fr)
Mohamed Jorfi (mohamed.jorfi@univ-fcomte.fr)
Samer Kanaan (samer.kanaan@obs-azur.fr)
David Katz (david.katz@obspm.fr)
Pierre Kervella (pierre.kervella@obspm.fr)
Jürgen KnÖdlseder (knodlseder@cesr.fr)
Nadège Lagarde (Nadege.Lagarde@unige.ch)
Azzedine Lakhlifi (azzedine.lakhlifi@obs-besancon.fr)
Eric Lantz (eric.lantz@univ-fcomte.fr)
Francois Leblanc (francois.leblanc@latmos.ipsl.fr)
Sébastien Lebonnois (sllmd@lmd.jussieu.fr)
Sandrine Lefebvre (sandrine.lefebvre@latmos.ipsl.fr)
Anica Lekic (anica.lekic@gmail.com)
Jean Louis Lemaire (jean-louis.lemaire@obspm.fr)
Arturo Lopez Ariste (arturo@themis.iac.es)
Benoit Lott (lott@cenbg.in2p3.fr)
Julien Lozi (julien.lozi@onera.fr)
André Maeder (andre.maeder@obs.unige.ch)
Ulysse Marboeuf (marboeuf@obs-besancon.fr)
Marie Martig (marie.martig@cea.fr)
Jean-michel Martin (Jean-Michel.Martin@obspm.fr)
Lilian Martin (lilian.martin@subatech.in2p3.fr)
Claire Martin-Zaidi (claire.martin-zaidi@obs.ujf-grenoble.fr)
Annaëlle Maury (anaelle.maury@cea.fr)
Héloise Méheut (hmeheut@apc.univ-paris7.fr)
Simona Mei (simona.mei@obspm.fr)
Anthony Meilland (meilland@mpifr-bonn.mpg.de)
Hélène Menager (helene.menager@obs.ujf-grenoble.fr)
Gilles Metris (gilles.Metris@obs-azur.fr)
François Mignard (francois.mignard@oca.eu)
Florentin Millour (fmillour@mpifr.de)
Hakima Mokrane (hakima.mokrane@obspm.fr)
Guy Moreels (guy.moreels@obs-besancon.fr)
Audrey Moudens (audrey.moudens@univ-rennes1.fr)
Olivier Mousis (olivier.mousis@obs-besancon.fr)
Nicolas Muller (nicolas.muller@onera.fr)
Sébastien Muller (mullers@chalmers.se)
Quang Nguyen-luong (quang.nguyen-luong@cea.fr)
William O'mullane (womullan@sciops.esa.int)
Pierre Ocvirk (ocvirk@astro.u-strasbg.fr)
Laurent Pagani (laurent.pagani@obspm.fr)
Sebastien Peirani (peirani@iap.fr)
Guy Perrin (guy.perrin@obspm.fr)
Jean-marc Petit (petit@obs-besancon.fr)
Jérôme Pety (pety@iram.fr)
Daniel Pfenniger (daniel.pfenniger@unige.ch)
Sylvain Picaud (sylvain.picaud@univ-fcomte.fr)
Bernard Pichon (Bernard.Pichon@oca.eu)
Nicolas Picot Clemente (picot@cppm.in2p3.fr)
Cedric Plantard (plantard@obs-besancon.fr)
Etienne Pointecouteau (pointeco@cesr.fr)
Nicolas Pradel (pradel@astron.nl)

Thierry Pradier (pradier@in2p3.fr)
Nicolas Rambaux (nicolas.rambaux@imcce.fr)
Alejandra Recio-blanco (arecio@oca.eu)
Yves Revaz (yves.revaz@epfl.ch)
Céline Reylé (celine@obs-besancon.fr)
Jean-yves Richard (jean-yves.richard@obspm.fr)
Annie Robin (annie.robin@obs-besancon.fr)
Florent Robinet (robinet@lal.in2p3.fr)
Nemesio Rodriguez Fernandez (rodriguez@iram.fr)
Françoise Roques (francoise.roques@obspm.fr)
Daniel Rouan (daniel.rouan@obspm.fr)
Evelyne Roueff (evelyne.roueff@obspm.fr)
Philippe Rousselot (phil@obs-besancon.fr)
Jean-pierre Rozelot (rozelot@obs-azur.fr)
Julien Salmon (julien.salmon@cea.fr)
Réza Samadi (reza.samadi@obspm.fr)
David Sanchez (dsanchez@poly.in2p3.fr)
Alexandre Santerne (Alexandre.Santerne@oamp.fr)
Jun'ichi Sato (junichi.sato@cea.fr)
Jean-françois Sauvage (jean-francois.sauvage@onera.fr)
Daniel Schaerer (daniel.schaerer@unige.ch)
Nicola Schneider-Bontemps (nschneid@cea.fr)
Mathias Schultheis (mathias@obs-besancon.fr)
Ella Sciamma O'brien (ella.sciamma.obrien@gmail.com)
Thierry Semaan (thierry.semaan@obspm.fr)
Benoit Semelin (benoit.semelin@obspm.fr)
David Sing (sing@iap.fr)
Chantal Stehle (chantal.stehle@obspm.fr)
Romain Teyssier (romain.teyssier@gmail.com)
Patrice Theule (patrice.theule@univ-provence.fr)
Caroline Thomas (caroline.thomas@univ-fcomte.fr)
William Thuillot (thuillot@imcce.fr)
Gabriel Tobie (gabriel.tobie@univ-nantes.fr)
Céline Toubin (celine.toubin@univ-lille1.fr)
Philip Tuckey (philip.tuckey@obspm.fr)
Catherine Turon (Catherine.Turon@obspm.fr)
Stephane Udry (stephane.udry@unige.ch)
Kevin Van Keulen (kevin@obs-besancon.fr)
Elisabeth Vangioni (vangioni@iap.fr)
Peggy Varnière (varniere@apc.univ-paris7.fr)
Isabelle Vauglin (vauglin@obs.univ-lyon1.fr)
Christian Veillet (veillet@cfht.hawaii.edu)
Anne Verhamme (a.verhamme1@physics.ox.ac.uk / anne.verhamme@unige.ch)
Francois Vernotte (francois.vernotte@obs-besancon.fr)
Alain Vienne (alain.vienne@univ-lille1.fr)
Nicolas Vilchez (vilchez@cesr.fr)
Michal Was (mwas@lal.in2p3.fr)
Jean-paul Zahn (Jean-Paul.Zahn@obspm.fr)
Philippe Zarka (Philippe.Zarka@obspm.fr)
Andreas Zech (Andreas.Zech@obspm.fr)

SF2A

Common session

SF2A 2009
M. Heydari-Malayeri, C. Reylé and R. Samadi (eds)

MAGNETIC JETS FROM YOUNG STARS: HIGH-ANGULAR RESOLUTION OBSERVATIONS

Dougados, C.[1]

Abstract. Supersonic jets are one of the most spectacular manifestation of the formation of a young star. Although their connection with magnetic processes is well established, the exact origin of jets is still a major open issue in star formation. I review in this contribution constraints on magnetic jet launching models derived from high-angular resolution observations of the inner 100 AUs in T Tauri winds. I then discuss open questions and future directions in jet studies, in particular the expected contributions of near-infrared and radio interferometry (with the second generation VLTI instrumentation and ALMA/NOEMA).

1 Introduction

Jets are observed at all phases of stellar formation where active accretion occurs (i.e. for ages less than a few Myrs). The physical mechanism by which mass is ejected from young stars and collimated into jets still remains a fundamental open issue. In addition to injecting mechanical energy at large scales, jets may play a crucial role in the regulation of the angular momentum and the final mass of the forming protostar. Moreover, as I will detail below, proto-stellar jets provide indirect constraints on the central Astronomical Units (AU) of the young star-disc system, still largely unaccessible to direct observations, which are critical regions for planet formation models. Jets from young stars, because of their proximity, offer a unique opportunity to investigate the accretion/ejection mechanisms at unprecedented angular resolution.

The supersonic ejection velocities (Mach number $V_j/C_s \simeq 30$), the cylindrical collimation achieved very close to the central source ($z < 30-50AU$) and the large ejection efficiencies observed (mass ejection to accretion rate ratios $\simeq 0.1$) can all be accounted for by accretion driven magneto-hydrodynamic wind models. A large scale magnetic field, anchored in a central rotating object, provides natural auto-collimation through the Lorentz force generated by the azimutal B_ϕ. Three classes of steady MHD wind models have been extensively studied. They differ by their launching region: either the magnetic field lines are anchored at the stellar surface (see for e.g. Sauty et al. 2002), in the inner regions of the accretion disc (Ferreira 1997), or at the interface between the stellar magnetosphere and the accretion disc (X-wind, Shu et al. 1994). These different origins have distinct implications for the magnetic structure and angular momentum regulation of the inner star-disc system. Steady disc wind solutions require in particular an equipartition magnetic field (with magnetic pressure comparable to thermal pressure) in the inner regions of the disc (r < a few AUs). This required magnetisation of the inner disc would then have strong implications on planetary formation models. The star-disc interaction is also the probable source of sporadic mass-loss, including coronal mass ejections. However, this mass-loss would require an external collimation agent. See Ferreira et al. (2006) for a thorough discussion of the different possible sources of mass-loss in young stars.

I first summarize in this contribution major results from high-angular resolution studies of the launching regions of proto-stellar jets, obtained my myself and collaborators, especially within the context of the Research and Training Network JETSET. I then discuss most recent developments and future directions.

2 Microjets from T Tauri stars: optical and near-infrared high-angular resolution studies

T Tauri stars are optically revealed pre-main sequence stars with ages of $\simeq 10^6$ yrs that have already emerged from their native environment. They are however still actively accreting matter from circumstellar discs and

[1] Laboratoire d'Astrophysique de Grenoble, UMR 5571, BP 53X, F-38041 Grenoble Cédex 9

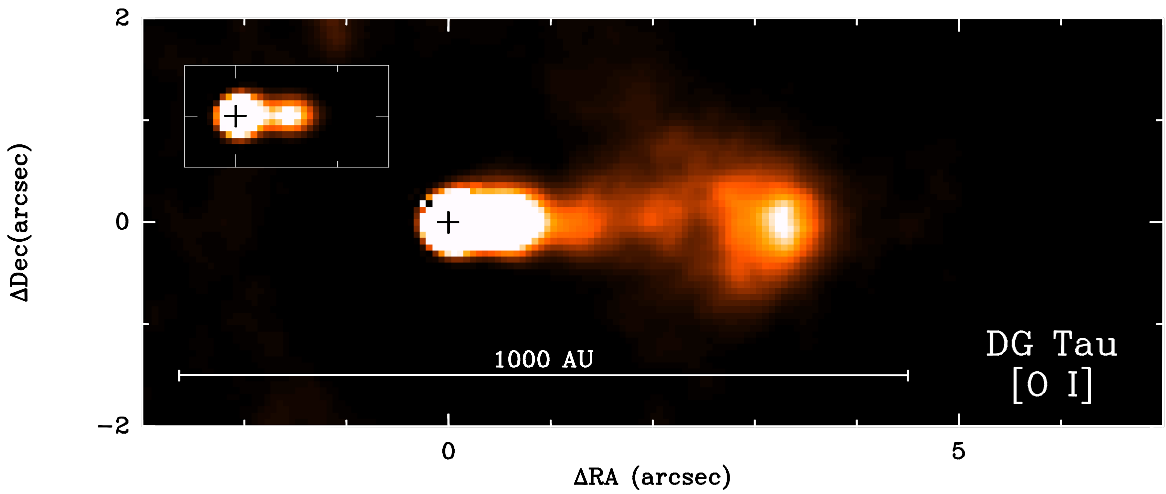

Fig. 1. Deconvolved [O I]λ6300Å+ continuum narrow band image of the DG Tauri jet obtained with the PUEO Adaptive optics system on the Canada-France-Hawaii telescope. The spatial resolution achieved is $0.1''$. Insert (*top left*) is a high-contrast image near the source. Figure adapted from Dougados et al. (2000).

driving small-scale jets (see Fig. 1). Although less powerful than the HH flows driven by the younger embedded protostars, T Tauri jets give direct observational access to the innermost collimation and acceleration regions of the wind ($z \leq$ a few 100 AUs), allowing to derive meaningful constraints to launching models.

Protostellar jets radiate a wealth of emission lines in the optical and near-infrared domains, tracing a partially ionized plasma at temperatures T $\simeq 5{\times}10^3$-10^4 K, characteristic of post-shock cooling regions. Both HST and adaptive optics on ground-based telescopes allow to reach angular resolutions of $\simeq 0.1''$, corresponding to 14 AU at the distance of the Taurus star forming cloud. High-angular resolution techniques have been recently combined with spectro-imaging instruments allowing to reach spectral resolutions ranging between 3000 and 10000 (velocity resolution between 30 and 100 km s^{-1}). To date, $\simeq$ 15 jets from T Tauri stars have been mapped in the optical and near-infrared domains with such instrumentation (see Ray et al. 2007 for a review). I review below the observed excitation conditions, morphological and kinematical properties of the atomic component in the central regions of the jets.

• Jet widths and collimation: In Ray et al. (2007) we compile all available jet widths measurements derived on scales less than 200 AU from the driving source. Beyond $z \simeq 50$ AU, close to cylindrical collimation is achieved with semi-opening angles consistent with thermal radial expansion ($tan(\theta) = C_s/V_j$). Current constraints on the launching region of the atomic component is r < 3 AU.

• Kinematics: Terminal velocities of 200-400 km s^{-1}, 2-3 times the escape velocity of the central star, are reached within 20 AU from the central source. Some jets, like the one from DG Tauri, present a shell of material at intermediate velocities (30-200 km s^{-1}) which surrounds the more collimated high velocity flow (see e.g. Lavalley-Fouquet et al. 2000). A recent important advance came from the detection in 6 T Tauri jets of velocity gradients across the jet body, indicative of rotation velocities $V_\phi = 5 - 15$ km s^{-1}(Bacciotti et al. 2002; Coffey et al. 2004, 2007). These observations put strong constraints on the launching region (Ferreira et al. 2006, see below). However the observed transverse velocity asymetries may trace other effects than rotation in the jet body. We have launched a program with the Plateau de Bure interferometer to study the connexion between disc and jet rotation. In one case, out of the 3 investigated so far, the sense of rotation in the disc inferred from millimetric observations is opposite to the jet sense of rotation deduced from HST observations (Cabrit et al. 2006). In addition, our near-infrared study of the DG Tauri microjet with SINFONI shows evidence for jet axis precession which could generate velocity asymetries similar to the ones observed (Agra-Amboage et al. in prep).

• Excitation conditions: Estimates of electronic densities, ionisation fractions and temperatures are derived from observed optical and near-infrared line ratios. The onion-like structure of the flow seen in the kinematics is also observed: ionisation fractions and total densities increase with flow velocity (see Ray et al. 2007). Estimates of mass-loss rates give ejection to accretion rate ratios $\simeq 10$ % . Optical and near-infrared line ratios are well reproduced by J-type shock models, with shock velocities $\simeq 20$ % of the flow velocity (see e.g. Lavalley-Fouquet et al. 2000). Internal working surfaces produced by flow ejection veriability on timescales of a few yrs are the most likely source for the observed structures of the flow.

2.1 *Implication for jet launching models*

Ejection mechanism appear steady on the characteristic dynamical timescales of the inner disc regions. Ferreira et al. (2006) and Cabrit (2007) discuss the implications of the derived atomic jet properties for steady ejection models. In particular in Ferreira et al. (2006), we compute the specific angular momentum in the jet predicted by steady wind solutions. In summary:

1) Stellar wind models predict a very small specific angular momentum in the jet, 2 orders fo magnitude smaller than current observational estimates/upper limits. However, they can account for the observed terminal velocities and for mass-loss rates ≤ 10 % of the accretion rate, provided significant extra energy is deposited at the base of the outflow. Indeed, since T Tauri stars rotate at only 10 % of break-up, centrifugal launching is not very effective and strong pressure gradients are needed to accelerate a wind from the stellar surface. This energy could be extracted from the accretion process but requires a very efficient conversion mechanism.

2) Wide-angle wind originating from the disc co-rotation radius ("X-winds") predict a moderate specific angular momentum, roughly 10 times lower than current observational estimates /upper limits. These models predict a very narrow range of observed terminal velocities and fail to account for the intermediate flow velocities (10-100 km s^{-1}) sometimes observed. It is also not clear how this model would brake down the central protostar and explain its slow rotation rate.

3) Disc winds with moderate magnetic lever arms (Casse & Ferreira 2000) originating from the inner AUs of the accretion disc, succeed in reproducing observed collimation and kinematical properties, including reported rotation signatures as well as observed mass-loss rates. However, these disc wind solutions require heat input at the upper disc surface layers, which origin is still unknwon. In addition, disc winds will not help in braking down the central protostar.

In conclusion, disc winds originating from the inner AUs of the accretion disc seem to reproduce best the ensemble of observational properties of atomic jets. These models require a strong magnetisation of the inner disc ($B = B_{eq} \simeq 0.2G$ at $r_0 = 1AU$), which has a strong implication for the structure of the inner disc (Combet & Ferreira 2008) as well as on planetary formation and migration models in these regions (see e.g Terquem et al. 2003). However disc winds do not solve all current issues, in particular the critical one related to the angular momentum of the central protostar. A stellar wind component may be required to explain the low rotation rates observed for the central object and the hot ($T > 10^5$ K) outflowing plasma traced by UV lines and X-ray emission (see below). Different components of mass-loss may be present, and contribute in various proportion at different stages of the protostellar evolution.

3 Recent developments and open questions

3.1 *Different components of the ejection?*

3.1.1 Micro-molecular flows

One recent development has been the detection of micro-molecular flows probed in the near-infrared with the H_2 2.121μm line or in the millimetric domain through the ^{12}CO line. In the two cases studied in details, DG Tauri (Agra-Amboage et al. in prep) and HH 30 (Pety et al. 2006), a slowly expanding ($V < 20$ km s^{-1}) small-scale molecular cavity is detected around the high-velocity atomic jet (Fig. 2). This molecular flow can be naturally explained in the context of the disc wind models. Indeed, Panoglou et al. (2009) have recently shown that streamlines originating from launching radii $r_0 \geq 1$ AU in the disc will remain mostly molecular. The observed properties of these small scale molecular flows (collimation, kinematics) appear compatible with the predictions of a disc wind originating from $r_0 = 1 - 10$ AU, i.e. extending the atomic flow probed with

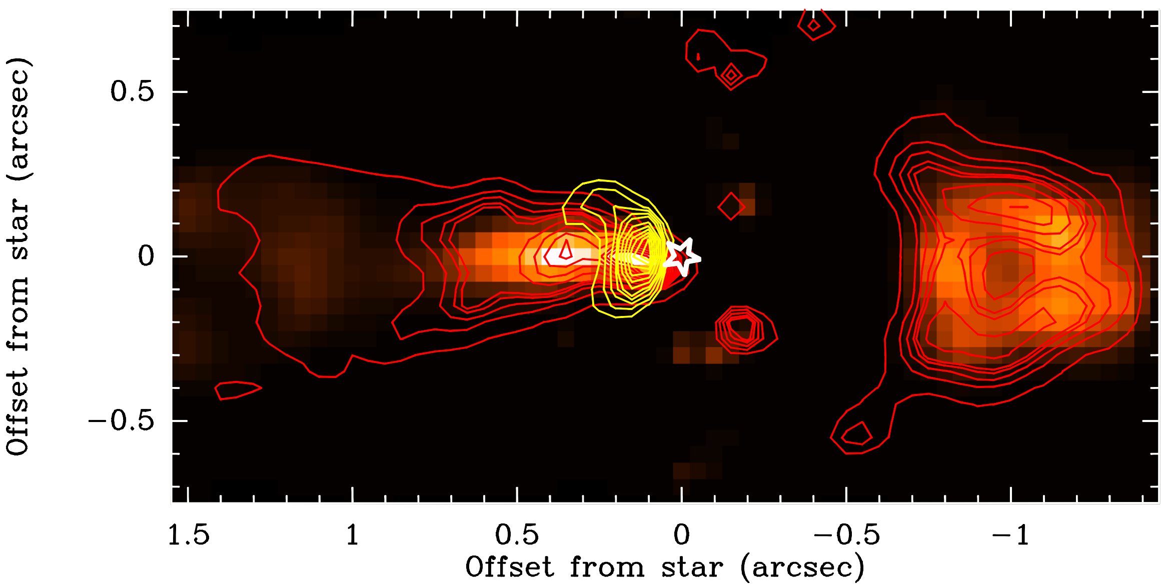

Fig. 2. Composite image of the [Fe II]1.644μm and $H_2$2.212μm emissions in the DG Tau microjet illustrating the nested structure of the flow. . High-velocity [Fe II]1.644μm emission ($V > 150$km s^{-1}) is shown as the background image. Red contours trace the medium-velocity [Fe II] emission ($V < 150$km s^{-1}) and yellow contours the H_2 emission ($V < 50$km s^{-1}). The white cross locates the stellar continuum position. Figure adapted from Agra-Amboage (2009).

optical lines. However, an alternative origin in a photo-evaporated wind cannot be excluded. In that latter scenario, FUV and X-ray radiation from the accretion shock creates a photo-dissociation region on the surface of the disc from which a photo-evaporated wind can originate. This component of mass-loss may play a role in the dispersal of outer disc material.

3.1.2 X-ray emission from jets

Gudel et al. (2007) reported the detection of soft X-ray emission in a few T Tauri stars in addition to the usual absorbed hard X-ray component associated with chromospheric activity. In one case, this emission is spatially resolved and clearly associated with the jet (Gudel et al. 2008). The origin of this high temperature plasma (T = 3.7 10^6 K) in the jet is unclear: it could trace either the high velocity innermost streamlines of a disc wind, or an inner hot and diffuse stellar wind component. Coordinated observing campaigns of the DG Tauri microjet will be conducted this winter combining a deep Chandra imaging and ground-based multi-wavelength spectroscopic studies that will allow to study the relationship between the different mass-loss tracers and hopefully clarify the origin of this MK plasma.

3.2 The influence of the stellar magnetosphere ?

One critical component in our understanding of the star-disc interaction and its role in jet launching and stellar angular momentum regulation is the strength and topology of the stellar magnetic field. As part of the MAPP collaboration led by J.F. Donati a large observing campaign is conducted with the spectro-polarimeter ESPADONS/CFHT aimed at characterizing the topology of the magnetic field in 20 pre-main sequence stars. To date, magnetic topologies for 4 T Tauri stars have been investigated with this method (Donati et al 2007, 2008; Hussain et al. 2009). The inferred magnetic topologies appear strongly correlated with the internal structure of the star (fully convective stars appear to host more simple fields, predominantly dipolar, than partly convective ones). Clearly the sample needs to be increased and the relationship with the jets studied. In parallel to these observational studies, 2D MHD numerical simulations of the star-disc interaction have been conducted in the framework of the JETSET collaboration (Bessolaz et al. 2008; Zanni et al. in press). 3D simulations, necessary to take into account the complexity of the recovered magnetospheres, are currently under development in collaboration between J. Ferreira (LAOG) and C. Zanni (Turin university). In coming years, the combination of these two approaches is expected to lead to significant advances in our understanding of the role of the stellar magnetic field in jet launching and stellar angular momentum regulation.

3.3 Jets across the stellar mass spectrum

Jets have been now identified across the stellar mass spectrum from massive Herbig Ae/Be stars (2-8 $M_\odot$) to brown dwarfs (Whelan et al. 2005, 2007). A detailed study of the microjet from the intermediate-mass star RY Tau (Agra-Amboage et al. 2009) shows properties quantitatively similar to the jets from lower mass T Tauri stars, suggesting a common origin.

4 A Bright Jet future

High-angular resolution studies of jets conducted on spatial scales 10-100 AUs brought significant new constraints to jet launching models. Clearly increasing the sample of sources observed with such techniques is critical to consolidate the conclusions reached so far. Indeed, some critical questions remain open:

1. Do different components of mass-loss contribute (stellar, disc wind, photo-evaporated wind) ? This question can be addressed with a detailed study of the relationship between different mass-loss tracers such as the one conducted in DG Tau.
2. Do all accreting protostars launch a jet and with the same mechanism ? To answer this question a statistical study is critically needed to correlate quantitatively the jet properties (terminal velocity, mass-loss rate, collimation) with the source properties (stellar mass, rotation, magnetic field, disc accretion rate...).
3. What is the evolution of mass-loss through all phases of star formation ?

Clearly, to definitely identify the origin of jets in young stars requires significantly increasing the angular resolution. In this respect, two major facilities are expected to yield significant advance in coming years:

4.1 Probing the central AU: spectrally resolved near-IR interferometry

Near-infrared interferometric instruments such as AMBER on the VLTI now allow to probe milli-arcsecond spatial scales corresponding to 0.1-1 AU at the Taurus distance. With the spectral resolution offered by AMBER (R=1000 and 10000), it now becomes possible to probe the hot gaseous component traced by the HI Brγ line in the very inner regions of young star disc systems. The formation of the HI emission lines in young stars, the most prominent tracer of hot gas, is still unknown: accretion flows, winds, disc atmosphere or a combination of these processes. Preliminary observations of a sample of young massive stars (Herbig Ae/Be stars) showed that the Brγ line emitting region is located between the stellar magnetosphere and the dust sublimation radius (Tatulli et al. 2007; Kraus et al. 2008). In collaboration with M. Benisty & F. Bacciotti (Arcetri Obs., Italy), we have launched observing programs with AMBER/VLTI of a selection of young stars, associated with large scale jets, aimed at: 1) spectrally resolved interferometric observations at R=10000 resolution and 2) imaging interferometry with large UV coverage of the Brγ line emitting region. These observations will provide the first direct constraints on the gaseous component on scales < 1 AU, ie the launching regions of jets.

4.2 Jets from younger protostars: NOEMA and ALMA contributions

Another major contribution to jet studies is expected from NOEMA and ALMA. With ALMA it will be possible to conduct detailed morphological and kinematical studies of the collimation and acceleration regions of the youngest jets (ages $\leq 10^5$ yr), similar to what is conducted in the optical/near-infrared for T Tauri jets. This will allow to study for the first time the secular evolution of jet properties, in particular collimation, as illustrated by the pioneering study with IRAM/PdBI of the very young HH212 jet (age $\simeq 10^4$ yr) by Cabrit et al. (2007). This study showed that the collimation properties of this very young jet are similar to the ones of the more evolved T Tauri jets, suggesting both that the environment does not play a significant role in jet collimation and that the same mechanism is at play throughout all stages of star formation. With ALMA we will conduct detailed studies of a few selected jets. With NOEMA it will be possible to conduct for the first time a statistical study of embedded young jets allowing to correlate their properties with the properties of their parent molecular cores (angular momentum, magnetic field, core mass).

In conclusion, I believe we stand now at a crossroads in jet studies from the observational as well as from the modelling point of view. On one hand, a wealth of new cutting-edge observations will soon become available: from stellar magnetic field mapping (with ESPADONS and SPIROU), to constraints on the jet launching zone (especially from 2d generation VLTI imaging instruments such as PIONEER, GRAVITY, VSI), and out to the scales of jet collimation and acceleration (with ALMA and NOEMA in the millimetric domain and existing and planned spectro-imaging instruments like MUSE/VLT and JWST/NIRSPEC in the optical/NIR). On the other hand, MHD modelling works have now matured to the point that a direct comparison to observations is conceivable. Indeed, 3D MHD numerical simulations of the star-disc interaction become possible (Romanova et al. 2008; Zanni et al. in prep.) as well as MHD numerical simulations of jet propagation reaching scales of 100 AU (Murphy et al. in prep). Therefore we have now the prospect to gather in the coming years a coherent vision of the accretion-ejection connexion in young stars.

This contribution would not have been possible without the fruitful collaborations generated by the JETSET network as well as the input/inspiration from many collaborators, especially: V. Agra-Amboage, S. Cabrit, J. Ferreira, M. Benisty, F. Bacciotti, T. Ray, M. Gudel, J.F. Donati, J. Pety.

References

Agra-Amboage, V., Dougados, C., Cabrit, S., Ferruit, P., Garcia, P. 2009, A&A, 493, 1029

Agra-Amboage, V. 2009, PhD thesis.

Bacciotti, F., Ray, T. P., Mundt, R., Eislöffel, J., & Solf, J. 2002, ApJ, 576, 222

Bessolaz, N., Zanni, C., Ferreira, J., Keppens, R., Bouvier, J. 2008, A&A, 478, 155

Blandford, R. D. & Payne, D. G. 1982, MNRAS, 199, 883

Cabrit, S., Pety, J., Pesenti, N., Dougados, C. 2006, A&A, 452, 897

Cabrit, S., Codella, C., Gueth, F., et al. 2007, A&A, 468, L29

Casse, F. & Ferreira, J. 2000, A&A, 361, 1178

Coffey, D., Bacciotti, F., Woitas, J., Ray, T. P., & Eislöffel, J. 2004, ApJ, 604, 758

Coffey, D., Bacciotti, F., Ray, T. P., Eislöffel, J., Woitas, J. 2007, ApJ, 663, 350

Combet, C., & Ferreira, J. 2008, A&A, 479, 481

Donati, J.F., et al. 2007, MNRAS, 380, 1297

Donati, J.F., et al. 2008, MNRAS, 386, 1234

Dougados, C., Cabrit, S., Lavalley, C., & Ménard, F. 2000, A&A, 357, L61

Ferreira, J. 1997, A&A, 319, 340

Ferreira, J., Dougados, C., Cabrit, S. 2006, A&A, 453, 785

Gudel, M., Telleschi, A., Audard, M., et al. 2007, A&A, 468, 515

Gudel, M., Skinner, S. L., Audard, M., Briggs, K. R., Cabrit, S. 2008, A&A, 478, 797

Hussain, G,. et al. 2009, MNRAS, 398, 189

Kraus, S., Hofmann, K.-H., Benisty, M., et al. 2008, A&A, 489, 1157

Lavalley-Fouquet, C., Cabrit, S., Dougados, C. 2000, A&A, 356, L41

Pety, J., Gueth, F., Guilloteau, S., Dutrey, A. 2006, A&A, 458, 841

Panoglou, D., et al. A&A in press A. C., 1996, ApJ, 468, L103

Ray, T., Dougados, C., Bacciotti, F., Eislffel, J., Chrysostomou, A. 2007, in Protostars and Planets V, B. Reipurth, D. Jewitt, and K. Keil (eds.), University of Arizona Press, Tucson, p.231-244

Romanova, M. M., Kulkarni, A. K., Lovelace, R.V.E. 2008, ApJ, 673, L171

Sauty, C. & Tsinganos, K. 1994, A&A, 287, 893

Sauty, C., Trussoni, E., Tsinganos, K. 2002, A&A, 389, 1068

Shu, F., Najita, J., Ostriker, E., et al. 1994, ApJ, 429, 781

Tatulli, E., et al. 2007, A&A, 464, 55

Terquem, C. 2003, MNRAS, 341, 1157

Zanni, C., Ferreira, J., Bessolaz, N., A&A, in press

Whelan, E. T., Ray, T. P., Bacciotti, F., et al. 2005, Nature, 435, 652

Whelan, E., T., et al. 2007, ApJ, 659, L45

SF2A 2009
M. Heydari-Malayeri, C. Reylé and R. Samadi (eds)

INFLUENCE OF THE SOLAR RADIATION ON EARTH'S CLIMATE USING THE LMDZ-REPROBUS MODEL

Lefebvre, S.[1], Marchand, M.[1], Bekki, S.[1], Keckhut, P.[2], Claud, C.[3], Cugnet, D.[1] and Thuillier, G.[2]

Abstract. The atmospheric response to the 11-year solar cycle is studied using the fully interactive 3-D coupled chemistry-climate model LMDz-REPROBUS (CCM). We show a comparison between two series of 20-year runs, one in maximum of activity and the other in minimum. The stratosphere-troposphere system indicates partly significant response to a solar cycle enhancement of UV radiation. We show how the changes in stratospheric ozone, temperature and zonal wind are connected.

1 Introduction

The impact of solar irradiance variations on the terrestrial atmosphere has long been seen as an important issue. Despite the fact that it is one of the main drivers for Earth's climate, the mechanism by which its short-term variation influences atmospheric parameters is controversial and difficult to prove. During the 11-year solar cycle, the Total Solar Irradiance varies from less than 0.1%. However, about 30% of the radiation changes over a solar cycle occur below 250 nm (Lean 1989). Moreover, photodissociation is an essential component of ozone formationand the stratospheric ozone modulated by the solar cycle could be at the origin of changes in the Brewer-Dobson circulation (Shindell et al. 1999 and references herein). The polar night jet could also be affected as shown by Kodera & Kuroda (2002), Matthes et al. (2006) and Haigh & Blackburn (2006).

2 Stratospheric response to solar forcing

LMDz-REPROBUS is a CCM including full representations of dynamical, radiative, and chemical processes in the atmosphere and their interactions, specially feedbacks of the chemical tendencies on the dynamics : in particular, ozone is strongly affected by dynamics and transport. Details are included in Jourdain et al. (2008) and references herein. Solar variability is forced explicity in the model through changes in the photolysis rates: two 20-year runs, one in maximum of activity and the other in minimum, are computed and we show here results concerning a comparison between these two series by computing the mean difference between them.

Preliminary results for the temperature, the zonal wind and the ozone concentration are shown in Figure 1. We only plotted graphes for the Northern winter months where the solar signal is strongly zonally asymmetric. The stratosphere is generally warmer of about 0.5 to 1 K at maximum, accompanied by a slight cooling at low latitude in the troposphere, suggesting a dynamical origin. At higher latitudes, the response is well marked with a reversal of the temperature difference. The temperature anomalies are associated to zonal wind ones with a positive anomaly of u in January. A clear ozone increase is visible in the stratosphere at solar maximum, with a peak at 10 hPa in the equatorial band.

3 Discussion and conclusions

These results correspond to a reinforcement of the polar vortex in January with a destabilization in February, under solar maximum conditions (SMC). The temperature response is consistent with the observations in the

[1] UVSQ; UPMC Univ. Paris 06; CNRS/INSU, LATMOS-IPSL, Tour 45-46, 4 place Jussieu, 75252 PARIS cedex 05, France
[2] UVSQ; UPMC Univ. Paris 06; CNRS/INSU, LATMOS-IPSL, Route des Gatines, BP 3, 91371 Verrières Le Buisson, France
[3] LMD/IPSL, Ecole Polytechnique, 91128 Palaiseau Cedex, France

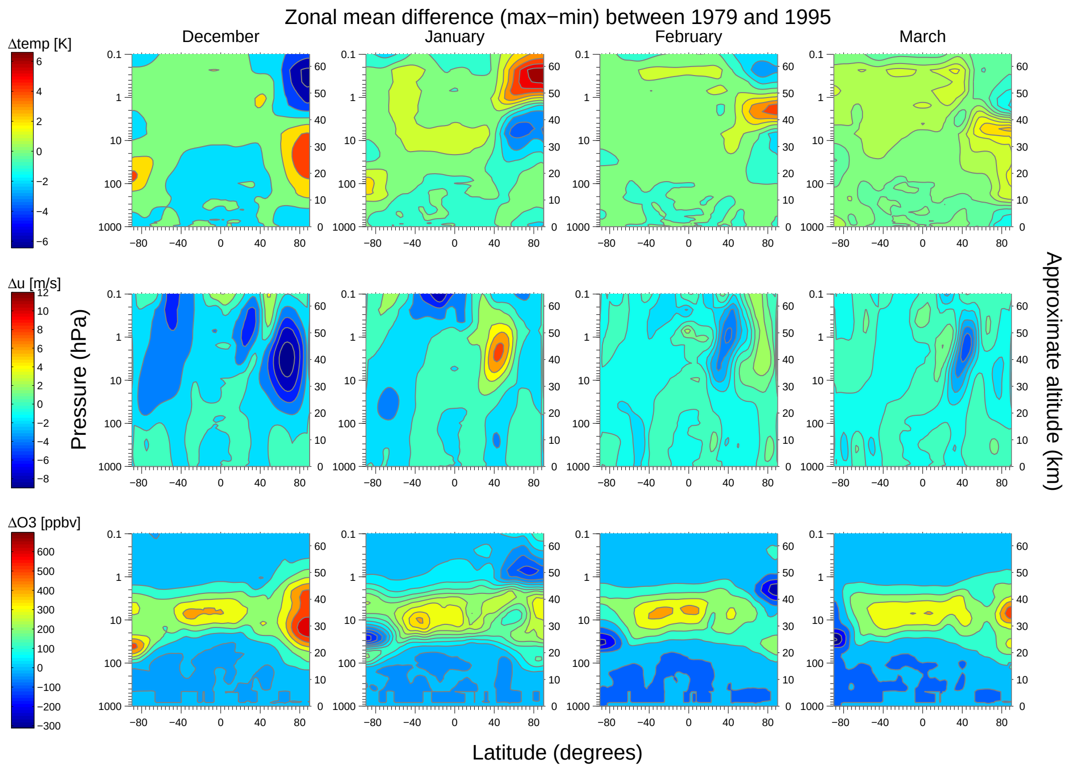

Fig. 1. Zonal mean difference (max-min) for the temperature *temp* (top), the zonal wind u and the ozone concentration O_3, in the atmosphere for the Northern winter months (December to March).

upper stratosphere-lower mesosphere (direct effect on ozone) as shown by Keckhut et al. (2005). By a study concerning SSU temperature measurements and ERA-40 zonal wind response to solar cycle, Claud et al. (2008) also demonstrated that in the lower stratosphere, temperatures are generally warmer for low- and mid-latitudes under SMC, and that, at high latitude, the polar vortex is stronger with the exception of February and to a lesser extent March in the northern hemisphere. main circulation. In particular, Kodera & Kuroda (2002) has argued that changes in the winter polar stratosphere brought about by anomalous solar heating may influence the passage of upward propagating planetary waves and thus their deposition of momentum that will influence the strength of the mean overtuning of the stratosphere. Gray et al. (2001) also demonstrated that zonal wind anomalies in the sub-tropical upper stratosphere can influence the timing and amplitude of sudden stratospheric warmings, events during the polar winter in which enhanced planetary wave activity disturbs the cold polar vortex. which will permit to investigate the interaction of the planetary waves. Moreover, In a next future is planned the analysis of a run with a real solar signal as input for the irradiance.

S. Lefebvre is supported by a CNES post-doctoral grant.

References

Claud, C., Cagnazzo, C., & Keckhut, P. 2008, JASTP, 70, 2031

Gray, L. J., Phipps, S. J., Dunkerton, T. J., et al. 2001, Quart. J. R. Meteo. Soc., 127, 1985

Haigh, J. D., & Blackburn, M. 2006, Space Sci. Rev., 125, 331

Jourdain, L., Bekki, S., Lott, F., & Lefèvre, F. 2008, Ann. Geophys., 26, 1391

Keckhut, P., Cagnazzo, C., Chanin, M.-L., Claud, C., & Hauchecorne, A. 2005, JASTP, 67, 940

Kodera, K., & Kuroda, Y. 2002, JGR, 107(D24), 4749

Lean, J. L. 1989, Science, 244, 197 2425 109, D06101

Matthes, K., Kuroda, Y., Kodera, K., & Langematz, U. 2006, JGR, 111, D06108

Shindell, D., Rind, D., Balachandran, N., Lean, J., & Lonergan, P. 1999, Science, 284, 305

SF2A 2009
M. Heydari-Malayeri, C. Reylé and R. Samadi (eds)

THE NEXT GENERATION VIRGO CLUSTER SURVEY

Mei, S.[1], Ferrarese, L.[2], Balkowski, C.[3], Boissier, S.[4], Boselli, A.[5], Bournaud, F.[6], Duc, P.A.[7], Emsellem, E.[8], Gavazzi, R.[9], Hudelot, P.[10], Ilbert, O.[11], Lancon, A.[12], Mellier, Y.[13], van Driel, W.[14], Vollmer, B.[15] and & the NGVS collaboration

Abstract. The Next Generation Virgo Cluster Survey (NGVS) is a large program on the Canada France Hawaii Telescope to survey the Virgo Cluster (PI: Laura Ferrarese, http://astrowww.phys.uvic.ca/ lff/NGVS.html). The survey will perform deep imaging of the central region of the cluster up to its virial radius and in five band–passes (u*,g',r',i',z'). The total exposure time will be 771 hours over 4 semesters from Spring 2009 to Spring 2012, with a French exposure time contribution of 325 hours. Because of its depth and extension, the survey will be the main optical reference for all future studies of the Virgo cluster in the coming decades. The program's main scientific objectives are: the characterization of the faint-end shape of the luminosity function, galaxy scaling relations, globular cluster populations, the role of environmental effects in galaxy evolution, the role of nuclear star clusters and black holes in galaxy evolution, star formation and chemical enrichment in the cluster environment.

1 Introduction

The Next Generation Virgo Cluster Survey (NGVS) is a large program on the Canada France Hawaii Telescope to survey the Virgo Cluster (PI: Laura Ferrarese). The survey will perform deep imaging in five band-passes (u*,g',r',i',z') of the region inside the virial radius of the cluster, for a total area of 104 deg^2. The total exposure time will be 771 hours over 4 semesters, from Spring 2009 to Spring 2012, with a French exposure time contribution of 325 hours. The program is an international collaboration of mainly French, Canadian, and Hawaiian scientists.

2 Scientific objectives

The main objectives of the program are: the characterization of the faint-end shape of the luminosity function, galaxy scaling relations, globular cluster populations, the role of environmental effects in galaxy evolution, the role of nuclear star clusters and black holes in galaxy evolution, star formation and chemical enrichment in the cluster environment.

[1] GEPI-Observatoire de Paris, University of Paris D. Diderot
[2] NRC/HIA
[3] GEPI-Observatoire de Paris
[4] LAM
[5] LAM
[6] AIM/CEA
[7] AIM/CEA
[8] ESO
[9] IAP
[10] IAP
[11] LAM
[12] Observatoire de Strasbourg
[13] IAP
[14] GEPI-Observatoire de Paris
[15] Observatoire de Strasbourg

In Spring 2008, we started collecting our first data from a Pilot Project that includes the central 4 deg^2 of the Virgo Cluster, centered on M87 (Canadian PI: Laura Ferrarese, French PI: Simona Mei).

Fig. 1 and 2 show our first images. The two figures are composite color images of the spectacular galaxy NGC 4438 and of the region around M87, respectively. Our images were reduced with TERAPIX.

The excellent quality of these images confirms that, with respect to previous optical surveys (e.g., the Virgo Cluster Catalogue (VCC); Binggeli et al. 1985, 1987), the NGVS will yield improvements in depth (100x in luminosity for point sources), surface brightness (40x), angular resolution (6x in encircled energy), completeness, wavelength coverage (five bands versus one for the VCC), and synergistic opportunities with the many planned or ongoing Virgo surveys at other wavelengths.

Our first large–program observations taken in 2009 are being reduced and analyzed by the collaboration.

Fig. 1. On the left, the central region of the Virgo cluster from our pilot project. On the right, NGC 4438, composite image from our pilot project. These images were reduced with TERAPIX. Credit : NGVS/CNRS/CEA

References

Binggeli, B. et al. 1985, AJ, 90, 1681

Binggeli, B. et al. 1987, AJ, 94, 251

SF2A 2009
M. Heydari-Malayeri, C. Reylé and R. Samadi (eds)

CLUSTERS OF GALAXIES AT THE PLANCK TIME

Pointecouteau, E.[1]

Abstract. Nodes of the filaments forming the cosmic web traced by the dark and baryonic matter, galaxy clusters are the place of many physical processes that shape a complex interaction between the formation and the evolution of galaxies, their environment and large scale structures. Their various components can be observed from X-ray to radio wavelengths. The ESA space mission Planck surveyor, lauched on May 14^{th} this year, is currently surveying the whole sky from sub-millimeter to centimeter wavelengths. Hundreds of new clusters are expected to be detected from the this survey. I review here various axis of research in the field of galaxy clusters studies, and I investigate the prospect of the detection of new distant clusters with the Planck satellite, which is expected to shed new light in the field of the formation and evoltution of large scale structures, and to provide cosmological constraints complementary to those derived from the CMB measurements.

1 Introduction

With the launch of the Planck Surveyor satellite this spring, a new window is opening for the study of galaxy clusters. Hundreds of new massive halos are expected to be detected by the Planck satellite via their Sunyaev-Zeldovich effect (SZE – Sunyaev & Zeldovich 1972). Their studies at the Planck frequencies and their follow-up at other wavelengths (such as in X-rays) will shed new light on our understanding of the formation and evolution of these large scale structures, and on their tight link to the overall matter and energy content of the Universe.

In the standard model of hierarchical structure formation, clusters form through gravitational collapse of dark matter (DM) around primordial over-densities (Bertschinger 1985). They are the largest auto-gravitating bound structures observed to date. They are located at the connecting nodes of the filamentary structures of the Universe. Clusters of galaxies form an homogeneous population of objects mainly constituted by DM (80% of their total mass), hot ionized gas (15% of their total mass) and galaxies (5% of their total mass). The population of clusters is a powerful tool in cosmology as well as in the study of the formation and evolution of structures. Their mass function, $N(M, z)$, their spatial distribution, their content in gas, are directly correlated with the (dark and baryonic) matter and energy content of the Universe, thus to the power spectrum of primordial density fluctuations, $P(k)$. Cosmological constraints from clusters are complementary to constraints from the Cosmic Microwave Background (CMB) or from supernovae. Also, clusters are especially fitted to probe the Universe bellow $z = 2$, where the effect of dark energy is predominant (Allen et al. 2004; Mantz et al. 2009). In the standard model, the collapse of structure is mainly driven by gravitation. However, we know that non-gravitational processes play an important role in the formation and in the evolution of structures: pre-heating of the gas by AGNs or supernovae, galactic winds, radiative cooling, metal enrichment... (e.g. Borgani et al. 2004; Voit 2005; Schindler & Diaferio 2008). The respective roles of all these processes have still to be understood and disentangled. They can be studied through their impact on the overall structural and scaling properties of clusters. (e.g. Croston et al. 2008; Pratt et al. 2009b,a; Arnaud et al. 2009). The inaccurate knowledge we currently have of these statistical properties limits our ability to properly understand the history of clusters formation, its coupling with the galaxy formation and evolution.

In the following I review three particular axis in clusters studies: (i) the importance of the measurement and use of clusters mass in halos studies (next section). (ii) the role of non-gravitational processes (Sec. 3) and the importance of mergers and dynamical activity in the formation of clusters (Sec. 4). I then briefly present the Planck cluster survey together with basics on the Sunyeav-Zel'dovich effect (Sec. 5). Finally I discuss the expectations for the Planck surveys in terms of cluster detection and follow-up plans (Sec. 6).

[1] Universitè de Toulouse, CNRS, CESR, 9 av. du colonel Roche, BP 44346, 31028 Toulouse Cedex 04, France
E-mail: pointeco@cesr.fr

2 The mass of clusters and cosmology

In the hierarchical model of structure formation, the population of clusters is homogeneous and self-similar, and characterised by structural and scaling properties: the matter distribution in clusters is universal, and well defined scaling laws link all the physical properties of clusters together (e.g. the X-ray luminosity-temperature relation is expected to be $L_X \propto T^2$) making the cluster population a two parameters population describe by its redshift z and its mass M: $Q(z, M) = A(z) \times M^{\alpha}$.

Cosmological numerical simulations in a standard framework have demonstrated these predictions (Navarro et al. 1997). XMM-Newton and Chandra have brought strong observational evidences for this universality in shape of the DM profile. Indeed, the study of local samples of relaxed objects have led to the precise measurements of their density and temperature profiles, thus to the determination of their dynamical mass profiles from the early type galaxy to the cluster scale (Pointecouteau et al. 2005; Vikhlinin 2006; Humphrey et al. 2006). Moreover, the scaling relations such as the mass-temperature relation, $M - T$ (Arnaud et al. 2005; Vikhlinin 2006), or the mass-integrated Comptonisation paramterer relation, $M - Y_X$ (i.e. derived from X-rays – Nagai et al. 2007; Arnaud et al. 2007, 2009), are now well calibrated for nearby relaxed clusters. Furthermore, together with the current constraints on the concentration-masse relation, $c - M$ (Pointecouteau et al. 2005; Vikhlinin 2006; Buote et al. 2007), these recent results demonstrate our qualitative and quantitative understanding of the physics of the DM collapse in the framework of the standard model down to the group regime in the local Universe. Henceforth, clusters (measurements in X-rays) have also been used for cosmological studies making use of the cluster (cosmic) baryonic fraction (Allen et al. 2004) and the cluster mass function (Vikhlinin et al. 2009). The same X-ray data have also helped to test MOND theories at the scale of groups and clusters (Pointecouteau et al. 2005; Angus et al. 2008).

However, problematic such as the mass distribution in the outskirts of clusters where virialisation is ongoing; the instrinsic dispersion of the $c - M$ relation (that links to epoch of cluster formation); the link between the dynamical state of clusters and their mass distribution and mass measurements; the proper quantification of the evoltution; detail of the non-gravtationnal physics... are still under deep investigation. In these studies the mass is a key ingredient in our understanding of the cluster population as it directly links to the matter and energy content of the Universe. However it is an "end-of-the-line" indirect observable for most observationnal methods (i.e. X-ray, velocity dispersion of galaxies, gravitationnal lensing, SZ), and its measurement (beside the gravitationnal lensing) relies on the observables of the baryonic components of clusters (i.e. galaxies and the intra-cluster medium (ICM) hot gas). Therefore, the characterisation of the properties of the baryonic content of clusters and of the physics driving its evoltution is a prerequisite to further use the cluster population as a cosmological probe.

3 Impact of non-gravitationnal physics in clusters

We know that non-gravitational processes at play in the ICM medium (e.g. radiative cooling, (pre)heating, feedback of galaxy formation on the ICM,...) play a fundamental role during the formation history of galaxy clusters (see reviews by Voit 2005; Arnaud et al. 2005). Their effect is deeply linked to the process involved in the formation history of member galaxies (galactic winds, ram-pressure stripping, AGN jets, SN rate...), thus to the star formation history within. This connection links physical processes spawning from scales of a few parsec to a few mega-parsecs. In the ICM, the baryons properties bear the signature of all these different processes. During the past decade, the high spatially resolved sectroscopy capabilities of the XMM-Newton and Chandra X-ray observatories have greatly help to improve our understanding of the formation and the evolution of halos, and thus the physics of the hot gas hosted by these halos from galactic to cluster scales. However, the observed departures to the predicted statistical properties for the hot gas component are important (see for instanc Pratt et al. 2009b,a) and reflect the impact of physical non-gravitational processes at play in IGM/ICM on the baryonic component of halos.

Current numerical simulations now implement most of these processes (Borgani et al. 2004; Kay et al. 2004) however they still fail to model them properly and to correctly explain the observed departures to similarity. From the observationnal side, huge progress has been made, especially via the systematic study of unbiased complete representative sample such as the REXCESS sample (Böhringer et al. 2007; Croston et al. 2008; Pratt et al. 2009b,a; Arnaud et al. 2009). We now have a quite clear picture of the structural and scaling properties of clusters and of the overall role of non-gravitationnal processes for local clusters. Quantifying the evolution

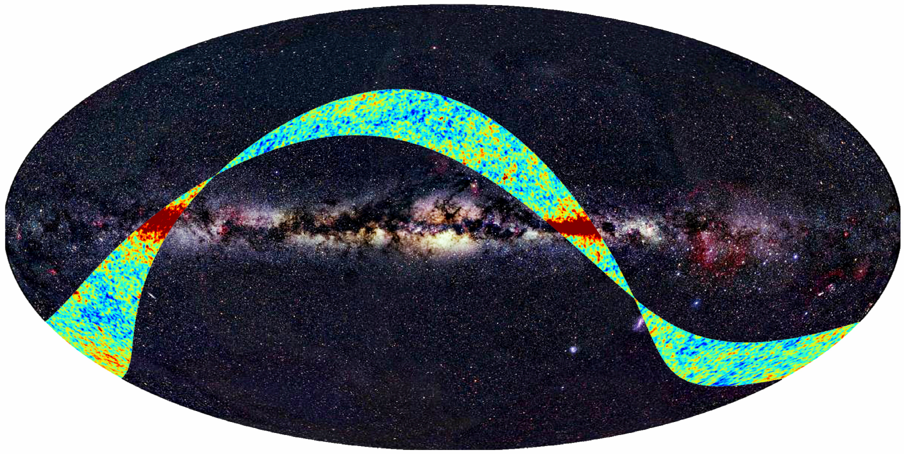

Fig. 1. The Planck first light survey overlaid on the digitalize sky survey (Credits: A. Mellinger) as published in the ESA press release of 17/09/2009 (see http://sci.esa.int/).

of the impact of these processed on the properties of clusters remains an observational challenge. Indeed the departure to purely gravitation driven self-similar evolution is small. Tentative works have tried to quantify these deviation (e.g. O'Hara et al. 2007), but systematic studies on well defined sample at high redshifts need to be carries out and compared with the local reference.

4 Hierarchical structure formation

In the past 10 years, a handful of new distant clusters have been detected up to very high redshift either via the X-ray emission of their hot ICM gas, e.g. RX J0848.9+4452 ($z = 1.26$, Rosati et al. 1999), XMMU J2235.3-2557 at ($z = 1.39$, Mullis et al. 2005), XMMXCS J2215.9-1738 ($z = 1.45$, Stanford et al. 2006); or via the study of their their near-infrared emitting members galaxies, e.g. ISCS J143809+341419 ($z = 1.41$, Stanford et al. 2005). Beyond this range of redshifts, overdensities of galaxies have been significantly detected and associated with proto-clusters candidates, e.g. Ly-α and Lyman break galaxies clustered near radio galaxies (Miley et al. 2004; Overzier et al. 2008).

From the first stage of galaxy clustering to the almost virialised massive halos, merger processes are the key of cluster assembly. The zoology of morphologies observed up to high z, as well as the increasing amount with redshift of sub-structures and dynamical activity in groups and clusters (Jeltema et al. 2005; Maughan et al. 2008), denotes the many dynamical states existing within massive halos, and are the signature of their merging history. Observed density and temperature rims and discontinuities, cold fronts and other shocks in hot gas halos are also the signature of the dynamical state of clusters and groups (Durret et al. 2005; Sauvageot et al. 2005; Markevitch & Vikhlinin 2007). XMM-Newton and Chandra data have been crucial to link the merger and accretion history of halos, as well as processes such as galaxy mergers and interactions, or ram pressure stripping to the evolution of member galaxies in dense environements (Rasmussen et al. 2008; Jeltema et al. 2008), and to the process of chemical enrichment traced via the observation of X-ray lines (Leccardi & Molendi 2008; Werner et al. 2008).

In this context, the interplay between the cluster dynamical activity, the mass accretion onto the SMBH hosted by the brightest cluster galaxies, the member galaxies SFR activities, the AGNs feedback energy injected within the ICM, the absence of cool gas in large amount at the groups and clusters centre is rather complex and emphasizes the difficulty to understand the physics of cluster mergers and massive halo assembly, which beyond the purely gravitational approach, remains probably one of the more delicate and complex problem in the study of large scale structures.

In this overall scientific framework the now ongoing Planck Surveyor survey if probably the best current way to look for and investigate this population of objects.

5 The Planck satellite and the SZ effect

The Planck Surveyor satellite was lauch on May 14^{th} 2009. This ESA space mission is designed to survey the whole sky in the frequency range 30-857 GHz with the primary scientific objective of mapping the temperature fluctuations of the Cosmic Microwave Background (CMB – Planck Collaboration 2006).

Beside this primary goal Planck will allow for the first time, thanks to its full sky coverage, to observe and sample the population of massive clusters of galaxies up to high redshift. Indeed the inverse Compton scattering of CMB photons by the hot ICM electrons shifts the energy distribution of CMB photons towards higher temperature. This effect therefore produces a characteristic distortion of the CMB spectrum in the direction of galaxy clusters. The intensity of this so called thermal Sunyaev-Zel'dovich effect (SZE – Sunyaev & Zeldovich 1972) is directly proportional to the electron thermal pressure integrated along the line of sight (i.e. the ICM pressure). A companion effect is due to the intrinsic cluster velocity in a comobile volume. This Doppler effect, or kinetic SZE, is at least an order of magnitude smaller than the thermal SZE. The following equations gives the basics of SZ quantities.

The SZ monochromatic brightness is expressed as:

$$\left.\frac{\Delta I_\nu}{I_\nu}\right|_{th} = y\; f(x) \tag{5.1}$$

where $f(\nu, T_e)$ depicts the spectral shape of the SZE which has a second-order dependance to the hot gas temperature due to weakly relativistic electrons (Pointecouteau et al. 1998). e subscript refers to electron intra-cluster quantities. y is the Comptonisation parameter, which reads as:

$$y = \frac{k}{m_e c^2}\,\sigma_T \int_l T_g(r)\, n_e(r)\, dl' \tag{5.2}$$

The measure SZE flux can be expressed as:

$$F_{SZ} = \int_\Omega y' d\Omega' \int_\nu f(\nu', kT) d\nu' \tag{5.3}$$

where Y is the integrated Comptonisation parameter:

$$Y = \int_\Omega y(\Omega') d\Omega' = \frac{kT}{m_e c^2}\frac{\sigma_T}{d_A^2} N_e \propto f_{gas} kT \frac{M_{tot}}{d_A^2} \tag{5.4}$$

As shown by the equation above, the SZ flux is directly proportional to the ICM thermal pressure, i.e. $P_{gas} = M_{gas} \times T_{gas}$, thus to the cluster total mass (through the gas fraction, f_{gas}). If the SZE brightness is independant from redshift, the SZE flux sufers a classical $1/(1+z)^4$ diming due to its dependance in d_A^2.

6 Expectations from the Planck all sky survey

Assuming a ΛCDM comology, the current predictions for the Planck survey gives a range of ∼1500-2000 clusters to be detected (see Fig. 2 right). To date we know about 1000-1200 X-ray clusters, mainly from the ROSAT all sky survey cluster catalogues (NORAS and REFLEX, Böhringer et al. 2000, 2004) and from ROSAT serendipitous catalogues. Taking into account the Planck sensitivity, only massive hot clusters (i.e. $M > 3-6\times10^14$ M$_\odot$, $kT > 5-7$ keV) are expected to be detected. Due to the all sky nature of the Planck survey, this will provide us with a unique, all sky, mass limited, complete cluster sample that should be efficient up to high redshifts. It is worth to stress that massive and distant clusters are rare objects, thus the most constraining for cosmology and formation of structures in a Universe where evolution is driven by gravitation.

To date, we know only a handful of clusters above $z = 0.5$ and with $kT > 7$ keV (see Fig. 2 left). Above this redshift and temperature, we expect from 50 to 200 new detected clusters in the Planck survey. A considerable increase in number that will allow us to investigate in details the statistical properties of the high mass end of the distant cluster population. More specifically we will look at the ICM X-ray properties of this new SZ clusters (i.e. L_X, kT, M_{gas}); derive their (distributions in) dynamical mass (under the hypothesis of the HE and sphericity) and entropy; look at their content in gas (i.e. f_{gas}); calibrate the $Y_{SZ} - M$ relation and its evolution, mandatory to proceed with the full scientific exploitation of an catalogue of SZ clusters.

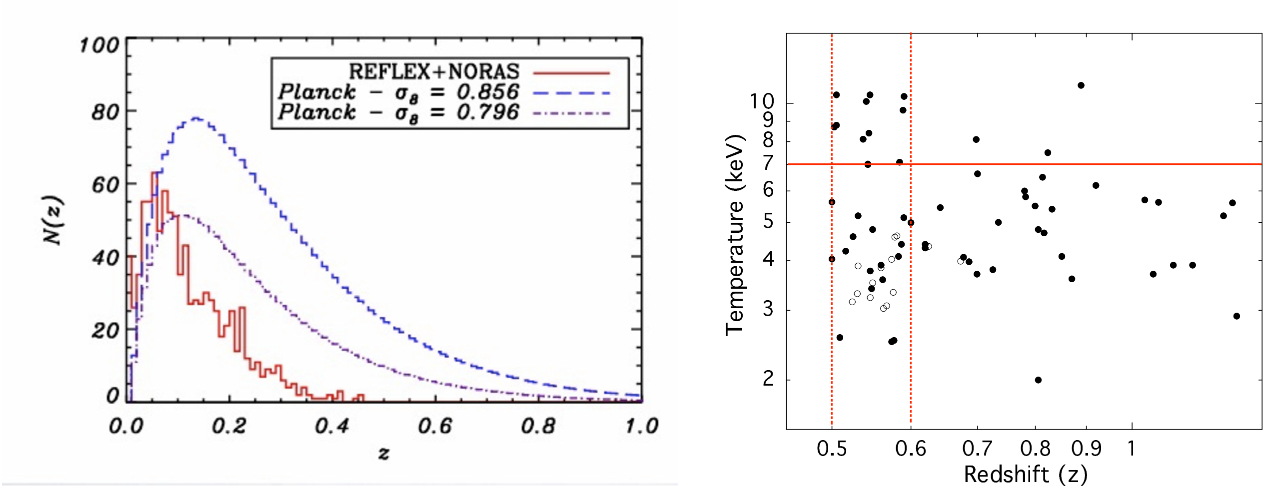

Fig. 2. Left : Comparison between the redshift number counts of the NORAS+REFLEX RASS catalogues and the expectation for the Planck all sky survey (courtesy of A. Chamballu, Chamballu et al 2009, in prep). **Right**: Known clusters above $z = 0.5$ (Courtesy of M. Arnaud).

These objectives obviously require for each cluster candidate: (i) an optical identification and redshift estimation, (ii) a cross-combination of Planck SZ data with X-ray observations of these clusters. Therefore, we will undertake an systematic optical and X-ray follow-ups of a well defined and selected sampe of new detected Planck clusters. If the fisrt and primary goal of an optical follow-up will be the identification of the Planck cluster candidates and the estimation of their photometric redshift, the scientification implications of an X-ray follow-up are deeper. As these clusters are massive, they are expected to be X-ray luminous even at hight redshift (i.e. $0.8 < z < 1.0$): $f_X[0.5\text{–}2\text{ keV}] > 10^{13}$ erg/s/cm^2). Such fluxes are encouraging for the perspective of an X-ray follow-up program with XMM-Newton. We can compare to similar existing X-ray observation of high redshift clusters. For instance, the temperature of MS 1054-0321 ($z = 0.83$, $f_X[0.5\text{-}2\text{ keV}] = 2.5 \times 10^{13}$ erg/s/cm^2) was derived with a 10% precision with an exposure time of 25ks (Gioia et al. 2004). So based on the aforementioned expected number of high redshift clusters and considering an exposure time of 25-50ks per target, as an indication of what could be done with XMM-Newton, we would need a very large program of 5-10Ms to follow-up 100-200 Planck clusters candidates (see also Bartlett et al. 2008).

7 Conclusion

The Planck satellite is currently surveying the sky and is expected to provide us with the detection of about 2000 clusters. From this unique all sky survey, we will draw a sub-sample of SZ selected distant clusters. From the Planck SZ measurements together with multi-wavelength follow-ups of this sample we will scrutinize their physical properties. In the framework of the study of galaxy clusters, Planck should allow us to derive constraints to address questions among which: (i) How do non-gravitatinnal processes produce departure from the simplest gravitational model. (ii) How does the ICM history depends on each of these physical individual processes. (iii) How do cluster of galaxies evolve. (iv) How do the first large scale structures form. (iv) What comsmological constraints can we draw from Planck clusters study.

I would like to thanks to the organisers of the *Journées de la SF2A* 2009. I am grateful to the PNCG “bureau” which entrusted me with the PNCG review for 2009. I would like to thank M. Arnaud, S. Maurogordato, A. Chamballu and C. Ferrari for providing me with useful inputs and material used for my presentation. This work was supported by grant ANR-06-JCJC-0141.

References

Allen, S. W., Schmidt, R. W., Ebeling, H., Fabian, A. C., & van Speybroeck, L. 2004, MNRAS, 353, 457
Angus, G. W., Famaey, B., & Buote, D. A. 2008, MNRAS, 387, 1470
Arnaud, M., Pratt, G. W., Piffaretti, R., et al. 2009, eprint arXiv:0910.1234

Arnaud, M., Pointecouteau, E., & Pratt, G. W. 2005, A&A, 441, 893

Arnaud, M., Pointecouteau, E., & Pratt, G. W. 2007, A&A, 474, L37

Bartlett, J. G., Chamballu, A., Melin, J.-B., Arnaud, M., & of the Planck Working Group 5, M. 2008, Astronomische Nachrichten, 329, 147

Bertschinger, E. 1985, ApJ Suppl., 58, 39

Böhringer, H., Schuecker, P., Guzzo, L., et al. 2004, A&A, 425, 367

Böhringer, H., Schuecker, P., Pratt, G. W., et al. 2007, A&A, 469, 363

Böhringer, H., Voges, W., Huchra, J. P., et al. 2000, ApJ Suppl., 129, 435

Borgani, S., Murante, G., Springel, V., et al. 2004, MNRAS, 348, 1078

Buote, D. A., Gastaldello, F., Humphrey, P. J., et al. 2007, ApJ, 664, 123

Croston, J. H., Pratt, G. W., Böhringer, H., et al. 2008, A&A, 487, 431

Durret, F., Neto, G. B. L., & Forman, W. 2005, A&A, 432, 809

Gioia, I. M., Braito, V., Branchesi, M., et al. 2004, A&A, 419, 517

Humphrey, P. J., Buote, D. A., Gastaldello, F., et al. 2006, ApJ, 646, 899

Jeltema, T. E., Binder, B., & Mulchaey, J. S. 2008, ApJ, 679, 1162

Jeltema, T. E., Canizares, C. R., Bautz, M. W., & Buote, D. A. 2005, ApJ, 624, 606

Kay, S. T., Thomas, P. A., Jenkins, A., & Pearce, F. R. 2004, MNRAS, 355, 1091

Leccardi, A. & Molendi, S. 2008, A&A, 487, 461

Mantz, A., Allen, S. W., Rapetti, D., & Ebeling, H. 2009, eprint arXiv:0909.3098

Markevitch, M. & Vikhlinin, A. 2007, Physics Reports, 443, 1

Maughan, B. J., Jones, C., Forman, W., & Speybroeck, L. V. 2008, ApJ Suppl., 174, 117

Miley, G., Overzier, R., Tsvetanov, Z., et al. 2004, Nature, 427, 47

Mullis, C. R., Rosati, P., Lamer, G., et al. 2005, ApJ, 623, L85

Nagai, D., Kravtsov, A. V., & Vikhlinin, A. 2007, ApJ, 668, 1

Navarro, J. F., Frenk, C. S., & White, S. D. M. 1997, ApJ, 490, 493

O'Hara, T. B., Mohr, J. J., & Sanderson, A. J. R. 2007, eprint arXiv:0710.5782; Submitted to ApJ

Overzier, R. A., Bouwens, R. J., Cross, N. J. G., et al. 2008, ApJ, 673, 143

The Planck Collaboration, 2006, "The Scientific Programme of Planck",eprint arXiv:astro-ph/0604069

Pointecouteau, E., Arnaud, M., & Pratt, G. W. 2005, A&A, 435, 1

Pointecouteau, E., Giard, M., & Barret, D. 1998, A&A, 336, 44

Pratt, G. W., Arnaud, M., Piffaretti, R., et al. 2009a, eprint arXiv:0909.3776, submitted to A&A

Pratt, G. W., Croston, J. H., Arnaud, M., & Böhringer, H. 2009b, A&A, 498, 361

Rasmussen, J., Ponman, T. J., Verdes-Montenegro, L., Yun, M. S., & Borthakur, S. 2008, MNRAS, 388, 1245

Rosati, P., Stanford, S. A., Eisenhardt, P. R., et al. 1999, Astron. J., 118, 76

Sauvageot, J. L., Belsole, E., & Pratt, G. W. 2005, A&A, 444, 673

Schindler, S. & Diaferio, A. 2008, Space Science Reviews, 134, 363

Stanford, S. A., Eisenhardt, P. R., Brodwin, M., et al. 2005, ApJ, 634, L129

Stanford, S. A., Romer, A. K., Sabirli, K., et al. 2006, ApJ, 646, L13

Sunyaev, R. A. & Zeldovich, Y. B. 1972, Comments on Astrophysics and Space Physics, 4, 173

Vikhlinin, A. 2006, ApJ, 640, 710

Vikhlinin, A., Kravtsov, A. V., Burenin, R. A., et al. 2009, ApJ, 692, 1060

Voit, G. M. 2005, Reviews of Modern Physics, 77, 207

Werner, N., Durret, F., Ohashi, T., Schindler, S., & Wiersma, R. P. C. 2008, Space Science Reviews, 134, 337

SF2A 2009
M. Heydari-Malayeri, C. Reylé and R. Samadi (eds)

PRESENTATION OF THE LOW FREQUENCY ARRAY (LOFAR)

Pradel, N.[1]

Abstract. The Low Frequency Array (LOFAR) is a multi-purpose, low frequency (10-250 MHz) sensor array. LOFAR is a radio-interferometer with most stations inside a 100 km disk and with longest baseline around 1500 km. It is based on relatively cheap and numerous stations across the Europe centred in the Netherlands and use real-time software correlation. Its main purposes are to study radio sky sources at these frequencies (including pulsar), transient phenomena, magnetism in the universe and to create an accurate sky model at these frequencies. Technical description of the array, as well as a description of its astronomical possibilities, are presented.

1 Introduction

Lofar (Falker et al. 2007) is a new generation radio telescope. It is an array of numerous (25000) and cheap antennas, connected directly through internet to a software correlator : LOFAR can be referred to a software telescope.

2 Description of the array

Each station is composed of tenths of Low Band Antennas (LBA) and of tenths of High Band Antennas (HBA). LBA are sensitive to the 10-90 MHz band and HBA are sensitive to the 110-240 MHz band.

LOFAR is composed from a core in the north part of the Netherlands, of some remote stations across the Netherlands and of some stations in the nearby countries (Germany, France, Sweden, United Kingdom).

Various baseline lengths start from several meters in the inner core to $\sim$ 1500 km between international stations. The angular resolution with only the Dutch array is between a few arc-seconds to a few tenths of arc-seconds depending of the frequency. Expected sensibilities will be around 10 mJy for the LBA and below 1 mJy for the HBA for 1 hour integration time.

3 Key science projects

LOFAR is mainly designed for 6 key science projects.

- Deep extragalactic surveys : LOFAR sensitivity and its possibility to observe many sources in the sky at the same time (through software created multi-beams) will create an accurate model of the sky at these frequencies, as well as it will bring insights in stars and galaxies formation at $z > 6$, intercluster magnetic fields, etc...
- Epoch of reionisation : The H1 line at 21 cm is in the frequency range of LOFAR at z between 6 and 11.5. As the reionisation epoch is known to start at $z \sim$ 15-20 and end at $z \sim 6$ (WMAP experiment, Hinshaw et al. 2009), LOFAR will be an excellent tool to explore this almost unknown period.
- Pulsars/transients : with the LOFAR μ-second time resolution, it is possible to observe pulsars and even to detect single pulses. As more and more stations will be available, sensitivity will increase and more pulsars and transient phenomenas (such as extrasolar planet bursts) will be detected and studied.

[1] ASTRON, Oude Hoogeveensedijk 4, 7991 PD Dwingeloo, Netherlands

- Solar physic and space weather : the study of the Sun will imply routine imaging, Solar burst mode triggering observations, joint observation campaigns of LOFAR with other ground- and space-based instruments and single stations used as spectrometers to monitor the Sun. As well, angular resolution of LOFAR will permit direct observations of the corona radio emission.
- Cosmic Magnetism : Faraday screens and rotation measure synthesis/Faraday tomography will be used to investigate the 3-D structure of local magnetic fields in the Milky Way and probe the magneto-ionic structure of the very local ISM surrounding the Sun. Spectro-polarimetry with LOFAR will allow the study of the so far unexplored domain of very small Faraday rotation measures and weak magnetic field strengths.
- Cosmic Rays : using self-triggered data acquisition boards, LOFAR offers a unique possibility for studying the origin of high-energy cosmic rays through the detection of air showers of secondary particles caused by interaction of cosmic rays with the Earth's atmosphere.

4 A French station

A French LOFAR station will be built at the radio observatory of Nancay. Beside the standard international LOFAR station (composed by an electronic back-end, 96 LBA and 96 HBA antennas), a non-standard equipment is under study.

This new equipment is made of 96 modules connected to the already existing back-end. Each module is composed by a ten antennas array, and is designed to observe frequencies below 85 MHz and especially below 30 MHz (where LOFAR stations are less sensitive).

5 Telescope time

A call for proposal was released with a deadline in September 2009. This call was mainly designed for the key science projects during the commissioning phase. During that time, any experiment useful for the commissioning of LOFAR can also be selected.

The commissioning phase will last until the release of a Global Sky Model which might be obtained later this year or early next year (beginning or spring of 2010). Other calls for proposal will be released afterwards for open time experiments.

To have more informations about LOFAR and the proposal submission, please contact lofarproposal@astron.nl or sciencesupport@astron.nl. The LOFAR project is still in commissioning phase so any technical, software, or science insight is welcome.

6 Conclusion

LOFAR is a new generation radio-telescope : its adaptability is provided by software created beams, buffer boards and real-time correlation and pre-processing. LOFAR is the first SKA precursor in the field.

It will give us new insights in galaxies formation ($z > 6$), cosmic magnetism, cosmic rays, transient phenomena and pulsars,... It will also give us a better understanding of radio-objects at its observing frequencies, widely unknown for now.

LOFAR is now in building and commissioning phase. All projects relative (or not) to the Key Science Projects are welcome.

I would like to thank the French Society of Astronomy and Astrophysics for its financial support to help me to attend to the meeting. I would like to thank my home laboratory, ASTRON, to allow me to join this meeting as well as its support to attend to it.

References

Falcke H. D., et al. 2007, HiA, 14, 386

Hinshaw G., et al. 2009, ApJS, 180, 225

SF2A 2009
M. Heydari-Malayeri, C. Reylé and R. Samadi (eds)

FOLLOW-UP OF COROT TRANSITING EXOPLANETS WITH HARPS AND SOPHIE SPECTROGRAPHS

Santerne, A.[1], Moutou, C.[1], Bouchy, F.[3,2], Hébrard, G.[3] and Deleuil, M.[1]

Abstract. The CoRoT space mission is detecting every semesters several tens of exoplanets transiting candidates. Among this candidates, there are several background eclipsing binairies. The radial velocity follow-up, performed with the high-resolution spectrographs HARPS (3.6m ESO) and SOPHIE (1.93m OHP), consists to measure the mass of companions and allows to characterize the nature of transiting object. For the faintest target (14<mv<16) observed at low S/N, the moon background light may affect the spectra and introduce systematic errors in the Radial Velocity measurements. We studied the influence of this effect and optimized the data reduction pipeline in order to minimize it.

1 Introduction

The CoRoT mission is the first space mission dedicated to search extrasolar planets by the transit method. Transiting exoplanets are crutial for the global comprehension of planetary systems and compared planetology because they are the only ones were the density can be computed by measuring their radius and mass with two complementary methods. CoRoT planetary candidates radius is determined with CoRoT light curve. Their nature and their mass are established and measured with SOPHIE (1.93m - OHP) and HARPS (3.6m - La Silla) spectrographs. CoRoT detects every semester about 50 planetary candidates with a V-magnitude between 11.5 and 16. CoRoT already discovered the first transiting telluric planet (CoRoT-7b : Leger et al. 2009 and Queloz et al. 2009), the first transiting brown darf (CoRoT-3b : Deleuil et al. 2008) and the first planets around active stars (CoRoT-2b : Alonso et al. 2008 and Bouchy et al. 2008).

2 Radial velocity follow-up

SOPHIE is a high-resolution spectrograph installed on the 1.93m telescope of Haute Provence Observatory in France. All CoRoT planetary candidates with V-magnitude less than 15 are followed by SOPHIE with a radial velocity precision in the range 10-50 m.s^{-1}. In 2.5 years of CoRoT follow-up, we followed and solved more than 80 candidates.
HARPS is a high-resolution spectrograph installed on the 3.6m telescope of La Silla Observatory in Chili. HARPS can follow CoRoT planetary candidates until a V-magnitude of 16 with a precision better than 30 m.s^{-1}. In 2.5 years, we followed and solved more than 60 candidates.

3 The Moon background light

During observation in presence of the Moon, the Sun spectrum, reflected by the Moon and diffused by the atmosphere, is additionned with the star spectrum. For faint target, this additionnal spectrum could affect the measurement of their radial velocity. Indeed, the radial velocity is measured by calculating the Cross-Correlation Function (CCF) between an observed spectrum and a numeric mask. This CCF represents the average line of

[1] Laboratoire d'Astrophysique de Marseille, OAMP, Université Aix-Marseille & CNRS,38 rue Frédéric Joliot Curie,13388 Marseille cedex 13, France
[2] Observatoire de Haute-Provence, OAMP, Université Aix-Marseille & CNRS,F-04870 St.Michel l'Observatoire, France
[3] Institut d'Astrophysique de Paris, Université Pierre & Marie Curie & CNRS, 98bis Bd Arago, 75014 Paris, France

the spectrum. However, if the relative radial velocity of the Moon is close to the radial velocity of the star, the additionnal Sun spectrum lines could deform the spectrum lines of the star and affect the measurement of their radial velocity and bissector. This effect can be corrected only if the instrument is able to observe simultaneously the sky and the target in differents channel. The correction consist to substract the sky CCF from the star CCF.

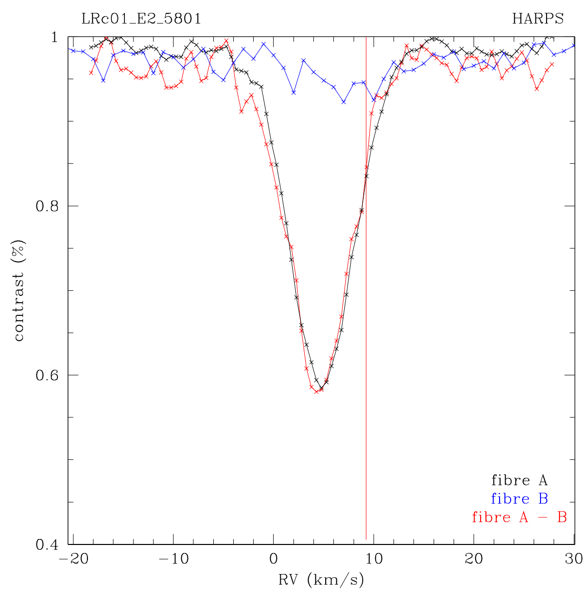

Fig. 1. Results of one observation of the CoRoT target LRc01_E2_5801 (V-magnitude = 16.2). Black curve shows CCF on the A fiber from HARPS (CoRoT target + sky), blue curve shows the CCF on the B fiber (only sky) and the red line indicate the theorical relative radial velocity of the Moon. Finally, the red curve is the result of the correction of the Moon background light. Amplitude of correction is -270 m.s^{-1}.

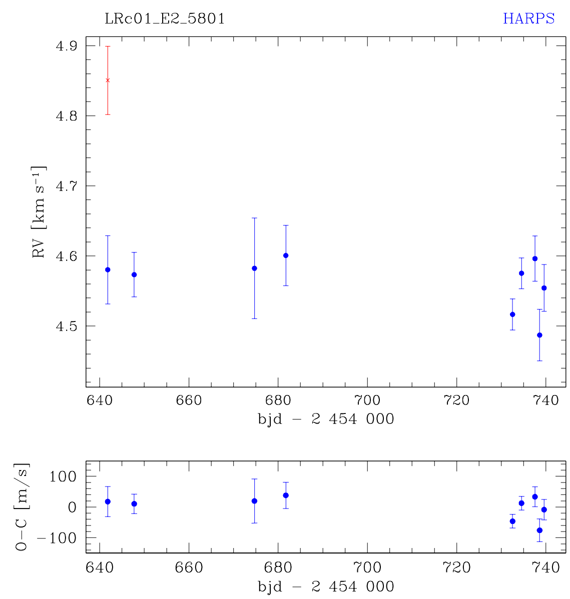

Fig. 2. Radial velocity measurements realised with HARPS of the CoRoT target LRc01_E2_5801 (V-magnitude = 16.2). The Moon background light affected observation showed in Fig. 1 is represented in red. Blue points are corrected or non-affected by the Moon background light.

On HARPS spectrograph, this effect appears for target fainter than 13th V-magnitude and may affect the radial velocity measurement with an amplitude of several hundred of m.s^{-1}.

References

Alonso, R., Auvergne, M., Baglin, A., et al. 2008, A&A, 482, L21

Bouchy, F., Queloz, D., Deleuil, M., et al. 2008, A&A, 482, L25

Bouchy, F. and The Sophie team, 2006, SOPHIE: the successor of the spectrograph ELODIE for extrasolar planet search and characterization

Cabrera, J., Fridlund, M., Ollivier, M., 2009, A&A

Deleuil, M., Deeg, HJ., Alonso, R., et al. 2008, 491, 889

Leger, A., Rouan, D., Schneider, J., al. 2009, ArXiV e-prints, 0908

Mayor, M., Pepe, F., Queloz, D., et al. 2003, Messenger, 114, 2003

Queloz, D., Bouchy, F., Moutou, C., et al. 2009, A&A

SF2A 2009
M. Heydari-Malayeri, C. Reylé and R. Samadi (eds)

INVOLVEMENT OF HYPERLEDA IN A WIDE FIELD IR IMAGER AT CONCORDIA

Vauglin, I.[1], Prugniel, P.[1] and Koleva, M.[2]

Abstract. French and Australian members of the ARENA consortium propose a 2 meter-class telescope at Dôme C, called PLT, dedicated to wide field infra-red imaging and driven by major astrophysical key projects. We present the foreseen contribution of the Observatoire de Lyon to handling, processing and distribution of the data products.

1 A large telescope at Concordia

The numerous results of site testing campains at Concordia, Dôme C, over the past years have convinced that the outstanding seeing conditions, transparency, background level and stability of this site represent an unique opportunity for ground-based astronomy. The most important gain is in K_{dark} (2.4 μm) and L-band (3.8 μm) but still very interesting in M and N-bands. To take the best advantage of this opportunity, we propose to place there a wide-field, high angular resolution 2.5 m telescope optimized for the near-infrared, called PLT (Polar Large Telescope, see Epchtein, N., this conference). It's the result of two projects: WHITE, a french project proposed by Burgarella et al. 2008, and PILOT, australian project leaded by Storey (Storey et al. 2007). The first light of PLT is planned for the Antarctic winter 2017.
In such a project, to guarantee an optimal scientific return and the widest visibility, processing, archiving and distributing the data play a major role. The team of the Observatoire de Lyon proposes to use its expertise in this field (HyperLeda database, DENIS survey, Virtual Observatory) to contribute to the design and deployment of the data processing. Our team developed the HyperLeda database, widely used for extragalactic physics. It can be found at the adress: http://leda.univ-lyon1.fr.
It contains compilations of measurements published in the litterature and in the large surveys. These data are used to produce an uniform and homogeneous catalogue with multi-wavelength informations on galaxies (Paturel et al. 2005).
The main scientific interest of our team is to trace the cosmic history of the star formation and of the metal enrichment of dwarf galaxies in order to improve the interpretation of stellar content and mass assembly at low and intermediate redshifts.

2 Data processing and distribution of the data products

Our goal is to provide homogeneous and high quality data in the shortest delay to the users community.
Several astronomical experiments produce large flux of data, from Terabytes to Petabytes each year (SDSS, VISTA, GAIA). Because it combines a high angular resolution with a large field of view and a fine time resolution, PLT will be one of the great data producers (around 0.5 to 1TB/day). For a robust data handling system, these figures require a storage and processing on the telescope site, at Concordia. Because of the restrictions in the data transfert volume, only the derived data-products, catalogues of extracted sources and light curves, will be transferred immediately to the remote operation center in Lyon for release to the astronomers.

[1] Université de Lyon, F-69000, Université Lyon 1, Observatoire de Lyon, F-69230 Saint-Genis-Laval, CRAL, UMR 5574
[2] Instituto de Astrofisica de Canarias, Tenerife, Spain

2.1 Data processing

The data processing has to be performed on the site and in quasi-real time. Each individual frame has to be corrected for instrumental effects and all the frames of a given observing block are combined to form a data-cube whose first two axes are position (or wavelength in case of spectroscopy) and third axis is the time.

The raw and reduced data are stored in the telescope database and transferred off-line to the remote operation center. This transfers will be possible during summer season. The meta-data of each observation are transferred on-the-fly to the remote operation center.

The sources' detection and extraction will proceed as usual (determination of the precise astrometry and of the PSF). The choice of algorithm for source detection will depend on the astrophysical programs. The standard processing pipeline will use classical source extraction method.

For some observations, and in particular for the legacy surveys, we will produce added-value data-products. All the observations of deep fields or multi-epoch programs will be co-added to achieve the deepest detection. The catalogues will be cross-identified with the HyperLeda database in order to construct multi-wavelength spectral energy distributions, and the results will be distributed through HyperLeda.

2.2 Distribution of the data-products

The catalogues of extracted sources and the meta-data of the observations will be immediately available to the astronomers from the remote operation center in Lyon, through HyperLeda. The access during the proprietary period will be made through a secured web site. The data access will then be publicly released after this delay, through the Virtual Observatory.

3 Instrument simulator

In order to test and validate the complete observational process, including the data-processing and analysis, we will simulate astrophysical fields, observe them with a virtual telescope and process them as real observations. The two steps of (i) simulating astrophysical fields and (ii) constructing the virtual telescope are needed in an early stage of the instrument design to assess to performances and to prepare the observations and their exploitation.

3.1 simulations of fields

Realistic fields, including source confusion (crowded fields), will be provided using various physical hypotheses. For the extragalactic sources, we will use cosmological simulations (like, for example, GalICS). The Galactic foreground will be added using the Modèle de Besançon. The simulated 2D images will be observed with a virtual telescope. That is, we will simulate the effects of the atmosphere, of the telescope and of the detectors in order to produce mock individual frames that will be processed exactly as real observations.

3.2 performance assessment and observation preparation

The simulations and the virtual telescope will be made available at an early phase of the instrument design in order to assess the performance. Because of the constraint on the simulations and construction of the virtual telescope, successive versions of these elements will be made during the development phase of the project. They will integrate the updated knowledge of the instrument model and the best available astrophysical models.

References

Burgarella, D., Le Roux, B., Langlois, M., et al. 2008, Proceedings of the SPIE, SPIE.7012E..82B

Paturel, G., Vauglin, I., Petit, C., Borsenberger, J., Epchtein, N., Fouqué, P; Mamon, G, 2005, A&A, 430, 751

Paturel, G., Petit, C., Rousseau, J., Vauglin, I., 2003, A&A, 405, 1

Storey, J., Ashley, M., Burton, M., Lawrence, J., 2007, EAS Publications Series, Volume 25, 255

ASGAIA

Preparation to GAIA

GAIA AND ULTRA HIGH PRECISION SPACE PHOTOMETRY

Baglin, A.[1] and Catala, C.[1]

Abstract. The era of ultra high precision stellar photometry from space on long and continuous duration has started with the launch of CoRoT. It is followed by Kepler (NASA) and will continue hopefully in the next decade by PLATO (ESA). All these missions need precise determinations of the fundamental parameters of their targets through other means. GAIA will be the mission to provide these data and then to increase significantly their scientific return.

1 Introduction

With the launch of CoRoT, starts a very rich period for high precision relative stellar photometry.

The major scientific objectives to be accessed by this technique are of essentially two kinds:

- detection of candidate exoplanets through their transit in front of their parent star
- stellar flux variability as an indicator of the physics of the stellar body, through asteroseismology but also through direct time indicators like modulation due to rotation.

Both fields need a good knowledge of the stellar fundamental parameters (temperature, mass, luminosity, chemical composition......) as illustrated with some CoRoT results. GAIA, with the determination of distance, temperature, chemical composition and in some cases mass, will be the best complementary mission to fulfill this need.

Table 1. The 3 major ultra high stellar photometry missions

Mission	CoRoT	Kepler	PLATO(n)
Period of operation	2007-2012	2009-2014+	2017- 2023
Duration: 1 obs	150 d	5 y	3y + 2y +nx(3-5 months)
Sampling	32s	15 to 1min	50s
Continuity	97%	?	$\geq$ 95%
Diameter (cm)	27	90	76
Targets Nb	150 000	100 000	250 000 (500000)
Magnitude range	10-16	9-14	4-13
Distance range	500-1000	400-800	10-500

2 Preparation and Interpretation

The need for stellar fundamental parameters is important for both the preparatory phase, and the interpretation of the data, but is treated in a different way.

During the preparatory phase, one has to optimise the selection of the targets among the different candidates in a given field. The interpretation needs the best knowledge of the properties of the observed stars, obtained by all possible means.

[1] LESIA, Observatoire de Paris.

As CoRoT and Kepler have been launched before GAIA, the complementarity will concern only the intepretation phase. Their preparations have used specific ground based observations to determine luminosity class and spectral types. For PLATO, the situation is more favorable, as GAIA will be able to contribute to both phases.

3 Stellar variability as seen from CoRoT

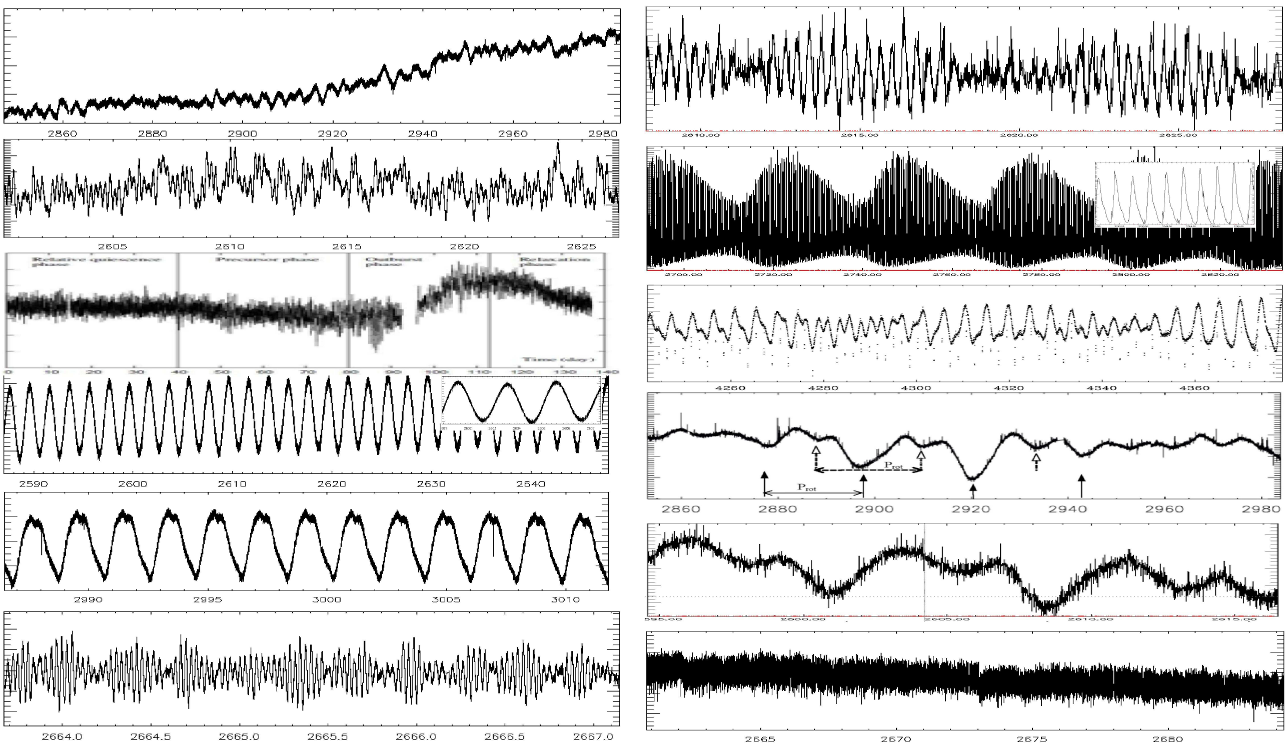

Fig. 1. Lights curves of several CoRoT targets on different durations. The left part correponds to the seismology channel, and the right one to the exoplanet channel. The accuracy on each measurement is approximately 10^{-4}

At the level of CoRoT photometric accuracy, more than 45 % of stars have detectable periodic variations. Many more vary but with no detected periodicity, and more work is needed to interpret all these data. What does this infomation tell us about stellar physics? Let's cite just a few early examples.

3.1 Rotation

The generally spotted nature of the surface of stars is seen in very accurate photometry as modulations at the rotation frequency. So true surface rotation is a direct product of CoRoT. Combined to other fundamental parameters it becomes possible to trace its variations during the evolution of stars using a large sample of targets if their parameters (T_{eff}, M, L) are well known (Fig. 2,a).

3.2 Seismology

Results are numerous in seismology as already 100 stars have been observed with a sufficient quality for such studies. Interpretation take more time than expected because Nature is always more complex than we foresee! The discovery of solar like oscillations in solar like stars, which was the major goal fo CoRoT has been achieved (fig 2b). But, in the already observed targets, which are slightly hotter than the Sun, the data analysis and mode identification is difficult due to small life times of the modes, the larger rotation, and a quite strong surface activity. The first interpretation leads to a determination of the convective core larger than expected. In B stars, the low frequency modes discovered by CoRoT can be interpreted only with an analogous structure.

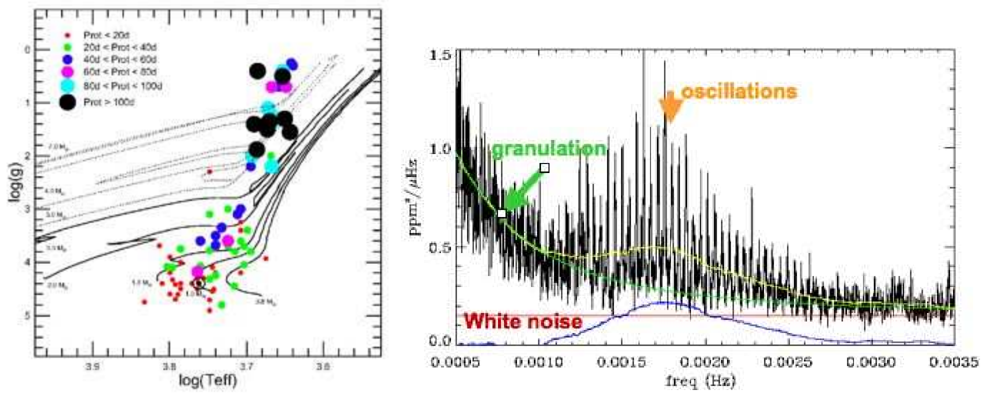

Fig. 2. *a, left*: Evolution of the rotation along the evolutionnary track of the Sun derived from CoRoT observations. *b, right* : Power spectrum of a 6th magnitude solar-like star, observed during 60 days, showing the different components : white instrumental noise, granulation and oscillations, in the frequency domain (0.5, 3.5) mHz.

3.3 Seismology and galactic structure

CoRoT has discovered solar like oscillations in a large sample of red giants, as a additional programme of the exoplanet field. They are identified as red-clump stars. The distribution of the maximum amplitude and of an average large separation give access to the distribution of the stellar radius and mass, and thus represent a most promising probe of the age and star formation rate of the disk, and of the mass-loss rate during the red-giant branch.

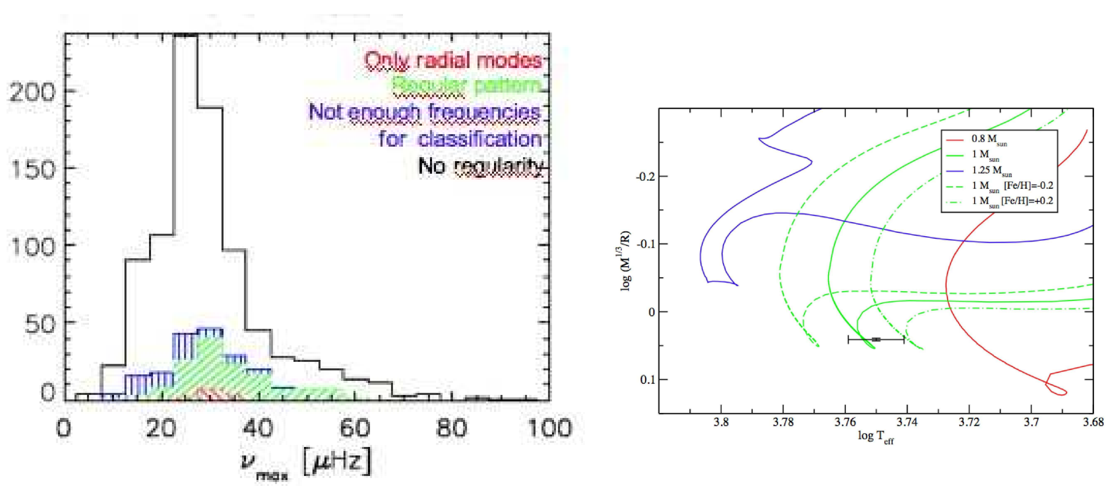

Fig. 3. *a, left:* Histogram of the frequency of the maximum amplitude of the solar like osclations in red giants. *b, right*: Evolutionnary tracks in the $logT_{eff}$, $\frac{M_{star}^{1/3}}{R_{star}}$ plane illustrating the uncertainties in the mass determination.

3.4 Granulation

Superimposed on the oscillations in the domain of frequencies around one mHz, a continuum component, already known in the Sun is easily measured in most solar type stars with CoRoT (Fig. 2,b). These stars (slightly hotter than the Sun) have higher energy in the granulation. More targets will confirm this result (or not!).

4 Planets ans stellar parameters

Transits give access to $\frac{R_{pl}}{R_{star}}$ and $\frac{M_{star}^{1/3}}{R_{star}}$ with a very high precision (10^{-3}). Radial velocities measure the amplitude of the orbital variations and determine $\frac{M}{M_{star}}\ \sin i$. If the planet transits, i is known from the light curve, so the mass ratio is determined with a high precision. But, as illustrated by Figure 3b, uncertainties on the stellar parameters remain quite large. For instance, an uncertainty of 50K on the effective temperature (which is preently not reachable) leads to an uncertainty on the mass of 0.06 solar mass. Even more important is the determination of the chemical composition. An uncertainty of 20% translates into an uncertainty on the mass of 10% (assuming that the surface composition is the initial composition of all the material).

The very poor knowledge of the mixing proceses in the stellar interiors lead to estimate the corresponding uncertainties to at least 13% in Mass, 5% in Radius. But the situation will certainly be improved by the seismology results. Only the knowledge of the size of the convective cores of intermediate stars will help improving the ages determintations close to the main sequence.

5 The PLATO(n) mission

Selecting targets for the PLATO input catalogue:
The observation strategy is to have two long (2 to 3 year) sequences of monitoring of two distinct fields, followed by a one-year step-and-stare phase during which several additional fields will be observed for a few months each.

A first major task in preparation of the mission will be to identify the cool dwarfs/subgiants in the very wide field of view of the instrument. A most efficient way of achieving this target selection will be to rely on stellar radii determined from early GAIA results. With stellar luminosities known to better than 30-40% and effective temperatures determined to within about 10% (500 K accuracy), which is well achievable using astrometry and multiband photometry in the first two years of GAIA exploitation, stellar radii will be known to within 15-20%, which is amply sufficient to distinguish dwarfs and subgiants from giants and supergiants.

This information is needed at least 18 months before launch, i.e. in mid-2016 for a launch at the end of 2017, in order to allow enough time to set up completely the PLATO input catalogue, and prepare all parameters of the data treatment software. This is more than four years after GAIA launch, and more than two years after the expected first partial release of GAIA results. Access to the needed data should therefore present no difficulty, even in the hypothesis of a GAIA delay, either of the launch, or of the first data release.

Characterizing the neighbourhood of PLATO selected targets:
PLATO photometry will be sensitive to the presence of nearby polluting sources, which can either be intrinsically variable, or simply create spurious signal in the photometric algorithm due to satellite jitter. Methods have been developed to correct for these perturbations, but a precise knowledge of the vicinity of each PLATO target is needed for these corrections to be applied.

What is needed is a full catalogue of faint neighbouring sources, including their positions, magnitudes and colours, down to approximately 19th magnitude, in sub-fields of at least 1 arcmin around each PLATO target. This information will be used to optimize the photometric algorithm for each target, and therefore will impact on the fine tuning of the onboard data treatment software. It is therefore also needed by mid-2016. The information that could be contained in GAIA first release (positions, G band magnitudes, and colours from the red and blue spectrophotometry) will be sufficient for this purpose.

Interpretation of the PLATO(n) data:
A more precise measurement of the radii of all stars observed by PLATO, and more particularly of the host stars of the detected exoplanets, will be necessary at the time the first results from PLATO will become available. This will happen about 2 to 3 years after the launch, i.e. not earlier than 2019. The final release of GAIA may be available by then (in the case that the observational phase is five years and the final catalogue is produced two years after that). In that case the access to the needed data should be straightforward. However, if GAIA is extended to six years, it is probable that the intermediate GAIA data releases will suffice.

More precisely, stellar radii to within 2-3% will be necessary, both to measure the planet radii to the same kind of accuracy, and second to place tight constraints of stellar interior structure models of the exoplanet host stars, coming in addition to the seismic observations of PLATO. This implies a knowledge of the stellar luminosities to within 5%, which will be easily achieved by GAIA for cool dwarfs as bright as 11th or 13th magnitude, and therefore closer than 200 (resp 500) pc. Effective temperatures will also need to be determined to within 1% (50 K). This will be achieved with the help of dedicated high resolution, high signal-to-noise spectroscopic observations obtained as part of the groundbased follow-up programme.

Hopefully, new generations of ultra high recision velocimeters as EXPRESSO will be available at that time beng able to measure the masses of planets as small as 1 earth mass and even smaller.

6 Conclusions

The ESA cosmic vision programme, if it selects PLATO will provide a unique combination of stellar parameters measurements which will improve considerably our physical knowledge of the stars, of their role in the galactic evolution, and of their planetary systems.

SF2A 2009
M. Heydari-Malayeri, C. Reylé and R. Samadi (eds)

CELESTIAL REFERENCE FRAMES IN THE GAIA ERA

Bourda, G.[2,1] and Charlot, P.[2]

Abstract. A working meeting about Gaia and celestial reference frames, funded by the French AS-Gaia, took place in Bordeaux in October 2008. Researchers from Paris, Nice and Bordeaux observatories met in order to lay the foundations of future studies and collaborations in this field. The fundamental celestial reference system is materialized by the International Celestial Reference Frame (ICRF), based on the VLBI (Very Long Baseline Interferometry) position of extragalactic radio sources with sub-milliarcsecond accuracy. On the basis of at least 10 000 Quasi Stellar Objects (QSOs), Gaia will permit to create its own celestial reference frame by 2015–2020, with an unprecedented positional accuracy (ranging from a few tens of microarcseconds (μas) at magnitude 15–18 to about 200 μas at magnitude 20). For consistency between optical and radio positions, it will be important in the future to align these two frames (the Gaia reference frame and the ICRF) with the highest accuracy. This alignment will be important not only for guaranteeing the proper transition if moving from the radio domain to the optical domain, but also for registering the radio and optical images of any celestial target with the highest accuracy. In this paper, we present the context and the goals of this meeting, review the work carried out in each of the three observatories, and present the outcome of the meeting as well as prospects for the future.

1 Introduction

The French "Action Spécifique Gaia" (AS-Gaia) allocated in 2008 a financial support for organizing a working meeting about the International Celestial Reference Frame (ICRF) and the future extragalactic celestial reference frame from Gaia, as proposed by Patrick Charlot. This workshop took place in Bordeaux Observatory, on 24 October 2008, with 13 participants from three different institutes in France: Laboratoire d'Astrophysique de Bordeaux (LAB – Bordeaux), Observatoire de la Côte d'Azur (OCA – Nice), and SYstèmes de Référence Temps-Espace (SYRTE – Paris). The goal of this meeting was to present the work carried out in each laboratory in the framework of the celestial reference frame for Gaia, in order to coordinate the activities at the national level and generate potential collaborations. Accordingly, several relevant scientific topics were examined in the light of the most recent studies (e.g. the celestial reference frame in the optical and radio domains, the astrometric observations of quasars, or the determination and simulation of catalogs of QSOs). In this paper, we report about this meeting and introduce briefly the research activities presented and discussions that took place during this workshop (for more details see http://www.obs.u-bordeaux1.fr/m2a/meeting/meeting_gaiasrqso).

2 Context

The ICRF is the realization at radio wavelengths of the International Celestial Reference System (ICRS; Arias et al. 1995), through Very Long Baseline Interferometry (VLBI) measurements of extragalactic radio source positions (Ma et al. 1998; Fey et al. 2004). During the International Astronomical Union (IAU) 27$^{\rm th}$ General Assembly at Rio de Janeiro (Brazil), in August 2009, the ICRF2 was adopted as the new fundamental celestial reference frame (see http://www.iers.org/documents/publications/tn/tn35/tn35.pdf). The ICRF2 currently consists of a catalog with the VLBI coordinates of 3414 extragalactic radio sources (from which 295 are defining sources), including the VLBA Calibrator Survey (VCS; see Petrov et al. 2008 and references therein), with sub-milliarcsecond accuracy. It has a noise floor of only 40 μas and an axis stability of 10 μas.

[1] Observatoire de Paris, CNRS, SYRTE, UMR 8630, 75014 Paris, France
[2] Université de Bordeaux, CNRS, Laboratoire d'Astrophysique de Bordeaux, UMR 5804, 33271 Floirac Cedex, France

The ESA space astrometric mission Gaia, to be launched beginning 2012, will survey all stars and QSOs brighter than the apparent optical magnitude 20 (Perryman et al. 2001). Optical positions with Gaia will be determined with an unprecedented accuracy, ranging from a few tens of μas at magnitude 15–18 to several hundreds of μas at magnitude 20 (Lindegren et al. 2008). Based on current estimates from local surveys, it is anticipated that 500 000 such QSOs should be detected. Of these, only the objects with the most accurate positions (e.g. with magnitude brighter than 18) will be used to define the frame. Simulations show that the residual spin of the Gaia frame could be determined to 0.5 μas/yr with a "clean sample" of about 10 000 sources (Mignard 2002). A preliminary Gaia catalog is expected to be available by 2015 with the final version released by 2020.

In the future, aligning the ICRF and the Gaia frame will be crucial for ensuring consistency between the measured radio and optical positions. This alignment, to be determined with the highest accuracy, requires several hundreds of common sources, with a uniform sky coverage and very accurate radio and optical positions. Obtaining such accurate positions implies that the link sources must have an apparent optical magnitude brighter than 18 (for the highest Gaia astrometric accuracy), and no extended VLBI structures (for the highest VLBI astrometric accuracy). This work is identified as the Gaia work package GWP-S-335-15000 "Alignment to ICRF source list" within the Gaia Data Processing and Analysis Consortium (DPAC).

3 Scientific domains involved

3.1 The celestial reference frame with Gaia

François Mignard (OCA) reviewed the process for determining the Gaia celestial reference frame, which eventually may be based on the optical positions of about 20 000 QSOs (if the criterion "magnitude brighter than 18" is kept). This frame will be at first entirely independent from the ICRF (i.e. with an arbitrary origin and rotating with respect to ICRF), and various steps will have to be completed in order to obtain a frame with no global rotation. The CU8 (Coordination Unit 8: "Catalogue Access") procedure to recognize quasar emission based on photometric information was presented. This will lead to the separation of QSOs from stars or galaxies within the Gaia data. Additional activities relevant to the determination of the Gaia frame will be necessary in the future and have already begun (e.g. simulation of catalogs of QSOs, construction of initial catalog of QSOs for Gaia, alignment with the ICRF). Furthermore, the various possible transverse motions the QSOs may suffer from have been identified (e.g. microlensing, matter ejection, superluminous motion, variable galactic aberration, macrolensing, accelerated motion in the local group), hence leading to an estimate of the accuracy that the Gaia frame should achieve of the order of 0.5–0.3 μas/yr for the residual spin, based on a sample of 50 000–20 000 QSOs.

Jean-Christophe Mauduit (OCA) presented the simulations carried out to create a realistic photometric and spectroscopic catalog of QSOs (i.e. good position distribution, fully representative of photometric and redshift distributions, and synthetic spectra) in the framework of CU2 (Coordination Unit 2: "Data Simulations"), on the basis of a complete Universe model and previous photometric investigations (Slezak & Mignard 2007). A primary spectro-photometric catalog considering the AGN variability has been completed, but discriminating between the various types of quasars (i.e. AGN, QSOs, Seyfert, BL Lac) from spectro-photometric information seems highly challenging for the future.

Jean Souchay (SYRTE) presented the Large Quasar Astrometric Catalog (LQAC; Souchay et al. 2008), which is a compiled catalog of QSOs based on the most reliable optical and radio information available in the literature (e.g. optimized positions, u b v g r i z photometry, redshift, flux densities in several radio bands, and absolute magnitude). This catalog is meant to improve over the catalog of Véron & Véron (2006), where several heterogeneities remain. It is also the basis for constructing the Initial Catalog of QSOs for Gaia (the Large Quasar Reference Frame, LQRF), which is a specific task Alexandre Andrei (Brazil – SYRTE) is responsible for within the DPAC of Gaia (CU3; Coordination Unit 3: "Core Processing"). This catalog should help classifying the Gaia data (Andrei et al. 2009).

3.2 Ground-based optical observations of QSOs, prior to the launch of Gaia

Sébastien Bouquillon (SYRTE–Paris Observatory) presented the current optical astrometric projects, relevant to the Gaia mission, for which observations are planned in the near future. Their purpose is to study: (1) the link between the variations of the magnitude and the photocentre of a quasar, (2) the relation between radio and optical positions of quasars, and (3) the influence of the host galaxy on the photocentre of a quasar. Apart from observing the WMAP satellite (which has similar characteristics as the future Gaia satellite) in preparation of the Gaia mission, thinking of supplementing the observations of Gaia, they plan to observe QSOs down to magnitude 25.

Patrick Charlot presented the optical observations carried out with the meridian instrument at Bordeaux Observatory, which contribute to studying the AGN short and long-term variability. About 50 objects are regularly monitored and for some of them the data base is more than 10 years long.

3.3 Aligning Gaia and VLBI celestial reference frames

François Mignard presented the theoretical basis to establish an accurate alignment within the next 10 years between the two extragalactic celestial reference frames, Gaia (optical) and ICRF (VLBI), in order to ensure continuity between these frames. To establish this alignment, one must define the pole and the origin of the Gaia frame, and then on the basis of a sample of common sources, the best fit between the two frames has to be determined by estimating three rotations. Typically, the accuracy of $\sim$80 μas could be achieved with $\sim$100 sources brighter than magnitude 20. A problem still remains unresolved with the optical-radio core shift (i.e. physically different optical and radio positions), which should induce an additional random noise. On one hand, one can think of solving this issue by averaging and finally removing this effect with the use of several link sources, but on the other hand, this information can be of high interest for astrophysical purposes. As mentioned by Patrick Charlot, a recent study by Kovalev et al. (2008) showed that on average the optical-radio core shift between VLBI and Gaia positions might be of the order of 100 μas (on the basis of a sample of 29 sources, from which they extracted the core-shift between S and X radio bands), which is not negligible at all regarding the anticipated accuracy of the Gaia and VLBI frames by 2015-2020.

Finally, it was shown that only 10% of the current ICRF sources (70 sources) are suitable for the alignment with the future Gaia frame (Bourda et al. 2008), which highlights the need to identify further link sources. We are now extending this study to the ICRF2, which also comprises the VCS surveys (as mentioned above). From the 2197 VCS sources within ICRF2, we found that 2108 have an identified optical counterpart, but only 208 sources are brighter than magnitude 18. We expect to identify another 50–100 sources suitable for the Gaia link. From these studies, it is already clear, however, that one will have to go to weaker flux level to come up ultimately with several hundreds of appropriate Gaia-ICRF link sources. This is the reason why we initiated a multi-step VLBI observational project to observe a sample of 447 sources selected from the NVSS catalog (NRAO VLA Sky Survey; Condon et al. 1998). This project, aimed at finding new VLBI sources suitable for the alignment with the future Gaia frame, will be carried out in three steps, in collaboration with the Max Planck Institute for Radio Astronomy (Bonn, Germany) and the Jodrell Bank Observatory (Manchester, UK). About 90% of the sources (398 sources) were detected in the initial step, conducted during two 48-hours experiments with the EVN (European VLBI Network) in June and October 2007, showing promising results for the future stages of this project (i.e. the mapping of the sources detected and the determination of the astrometric positions for the most point-like of these). The second stage of this project began in March 2008, with global VLBI observations (EVN+VLBA; Very Long Baseline Array) of 105 sources from those detected in step 1. About half of these were found to be point-like (Figure 1), hence indicating that they are suitable for the Gaia alignment. A proposal for observing the rest of the sources detected (293 sources) was submitted to complete the imaging of all the sample. Subsequent astrometric observations are expected to be completed within the next two years.

4 Conclusion

Several actions are conducted within the Gaia community in France in order to prepare for the determination of the Gaia frame as well as to align it with the ICRF or its successor by 2015–2020. The working meeting reported in this paper, financed by the French "Action Spécifique Gaia", was found to be very fruitful, generating many discussions. It was suggested that another such meeting be organized again (in 2010 ?). The idea of an international meeting in the framework of the Gaia DPAC astrometric community (CU3/CU8) was also mentioned as a possibility.

The authors would like to thank the French "Action Spécifique Gaia" (AS-Gaia) for the financial support that was allocated, which

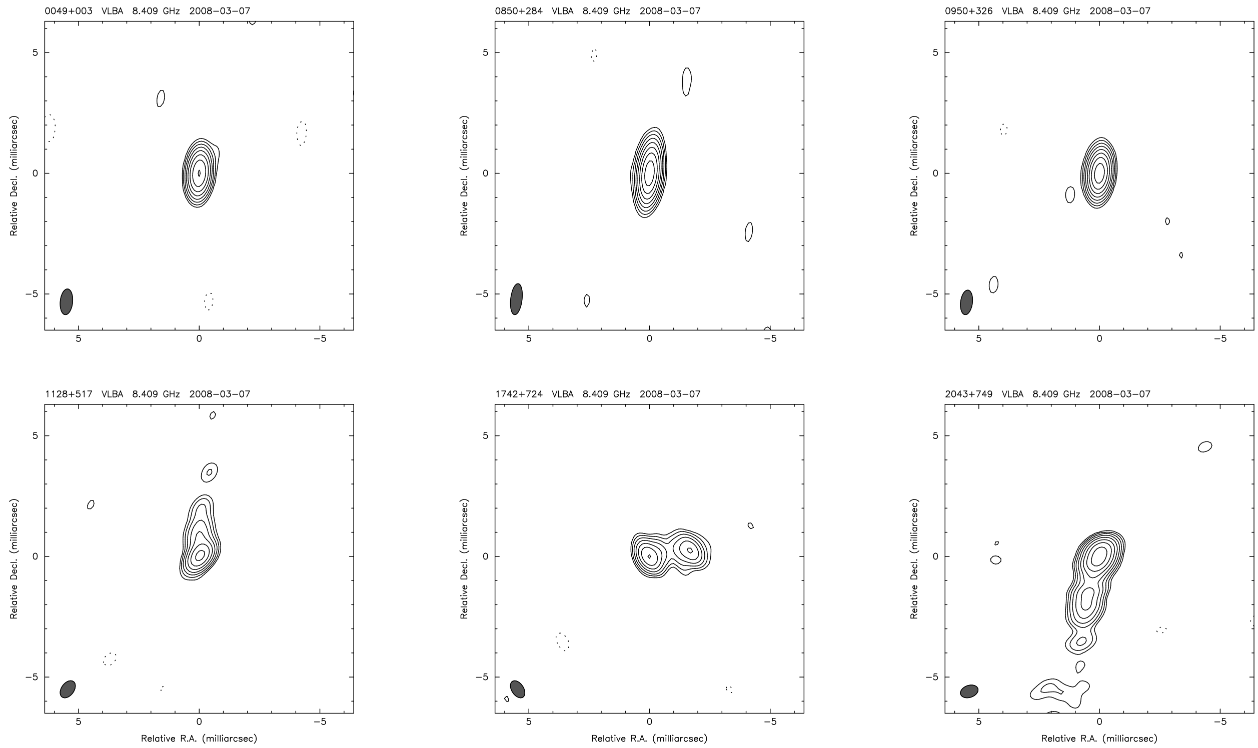

Fig. 1. Examples of VLBI maps (at X band), produced at Bordeaux Observatory, for sources observed during the first global experiment mentioned above (in March 2008). Upper panel: Sources suitable for the ICRF-Gaia alignment (i.e. point-like sources). Lower panel: Sources that are not suitable for the ICRF-Gaia alignment (i.e. sources with extended VLBI structures).

allowed us to organize this working meeting.

References

Andrei, A. H., Souchay, J., Zacharias, N., Smart, R. L., Vieira Martins, R., et al. 2009, A&A, 505, 385

Arias, E. F., Charlot, P., Feissel, M., & Lestrade, J.-F. 1995, A&A, 303, 604

Bourda, G., Charlot, P., & Le Campion, J.-F. 2008, A&A, 490, 403

Condon, J. J., Cotton, W. D., Greisen, E. W., Yin, Q. F., Perley, R., et al. 1998, AJ, 115, 1693

Fey, A. L., Ma, C., Arias, E. F., Charlot, P., Feissel-Vernier, M., et al. 2004, AJ, 127, 3587

Kovalev, Y. Y., Lobanov, A. P., Pushkarev, A. B., & Zensus, J. A. 2008, A&A, 483, 759

Lindegren, L., Babusiaux, C., Bailer-Jones, C., Bastian, U., Brown, A. G. A., et al. 2008, In: A Giant Step: from Milli- to Micro-arcsecond Astrometry, IAU Symposium No. 248 Proceedings, ed. W. J. Wenji, I. Platais, & M. A. C. Perryman (Cambridge University Press), 217

Ma, C., Arias, E. F., Eubanks, T. M., Fey, A. L., Gontier, A.-M., et al. 1998, AJ, 116, 516

Mignard, F. 2002, In: Gaia: A European space project, ed. O. Bienaymé, & C. Turon (EAS Publications series 2), 327

Perryman, M. A. C., de Boer, K. S., Gilmore, G., Hog, E., Lattanzi, M. G., et al. 2001, A&A, 369, 339

Petrov, L., Kovalev, Y., Fomalont, E., & Gordon, D. 2008, AJ, 136, 580

Slezak, E., & Mignard, F. 2007, GAIA-C2-TNOCA-ES-001

Souchay, J., Andrei, A. H., Barache, C., Bouquillon, S., Gontier, A.-M., et al. 2009, A&A, 494, 799

Véron-Cetty, M.-P., & Véron, P. 2006, A&A, 455, 773

SF2A 2009
M. Heydari-Malayeri, C. Reylé and R. Samadi (eds)

THE DETERMINATION OF ASTEROID PHYSICAL PROPERTIES FROM GAIA OBSERVATIONS. GENERAL STRATEGY AND A FEW PROBLEMS

Cellino, A.[1], Hestroffer, D.[2], Tanga, P.[3] and Dell'Oro, A.[1]

Abstract. Gaia observations are expected to produce a real revolution in asteroid science. Apart from major improvements in the determination of orbital elements, Gaia data will make it possible to derive for large numbers of objects a determination of the most important physical properties, including mass, size, average density, rotational period, spin axis direction, overall shape, and geometric albedo. Here, we focus mainly on the determination of sizes, rotational properties and shapes, and show some of the main problems that are encountered in the data analysis procedures.

1 Introduction

In spite of the tremendous progress that has been made in recent years in the field of the determination of physical properties of the minor bodies of our Solar System, our knowledge of these bodies is still not satisfactory due to the difficulty in getting detailed physical information about them, due to their intrinsic faintness, and also due to the fact that both asteroids and comets are extremely heterogeneous, and include bodies characterized by great diversity in many respects. Fundamental physical parameters including masses and sizes are mostly unknown for the vast majority of the objects, since they are extremely difficult or impossible to obtain by means of remote observations. For instance, only for a handful of objects which are either among the biggest members of the asteroid population, or have been visited *in situ* by space probes, we have reasonable measurements of the mass. As a consequence, also the average density is largely unknown for the vast majority of the population. What is done usually is only some tentative estimate based on extrapolations of the values found for a handful of objects observed *in situ* by space probes. Since the asteroid population exhibits a heterogeneity of spectral reflectance properties, likely related to differences in overall composition and thermal histories, such extrapolations are mostly tentative and quite uncertain in most cases. Needless to say, it is very frustrating to carry out astrophysical studies of objects for which even the average density is essentially not known. Unfortunately, even in this new era of development of increasingly large telescopes and increasingly sensitive detectors at different wavelengths, it is very difficult to expect that ground-based remote observations can produce in the near future a big wealth of new accurate measurements of the fundamental physical parameters of a large sample of asteroids and comets. In this respect, this branch of Planetary Sciences is still waiting for a revolution.

In this paper, we show that the forthcoming Gaia mission can be this much expected revolution, especially for what concerns the studies of the physical properties of the asteroids. This is a consequence of the fact that Gaia will be in many respects a major step forward in the history of the tools available for remote observations of bodies as the asteroids. Due to its unprecedented performances in terms of astrometric accuracy, Gaia will produce a huge improvement in the determination of the orbits of the minor bodies, eventually leading to the measurement of the mass for a significant number of large asteroids, and to the direct measurement of non-gravitational effects affecting the orbital motion of several small near-Earth objects. Moreover, the direct measurement of the size for a big sample of main-belt objects is also expected to be possible. Combined estimates of mass and size will lead to reliable estimates of the average density for a sizeable sample of objects belonging to different taxonomic classes. In addition, the excellent photometric and spectroscopic performances of Gaia

[1] INAF - Observatoire de Turin (Italie)
[2] IMCCE, Observatoire de Paris
[3] OCA, Observatoire de Nice

are expected to produce a wealth of data including the determination of the rotational properties, the overall shapes (useful to improve the reliability of density estimates), the reflectance spectra at visible wavelengths and a taxonomic classification for a significant sample of the asteroid population.

In the following sections we present more in detail some of the results we expect to obtain from Gaia observations of asteroids, and we point out some technical problems that are relevant for a thorough exploitation of the future Gaia data.

2 Asteroid signals in the GAIA astrometric field

In this Section, we assume that the reader is familiar with the overall design of the Gaia scientific payload, in particular the optical design, the scanning law of the satellite, the design of the CCD matrix in the focal plane, and the TDI (transfer delay integration) mode of data acquisition. This general information is given in several papers, including Mignard et al. 2007.

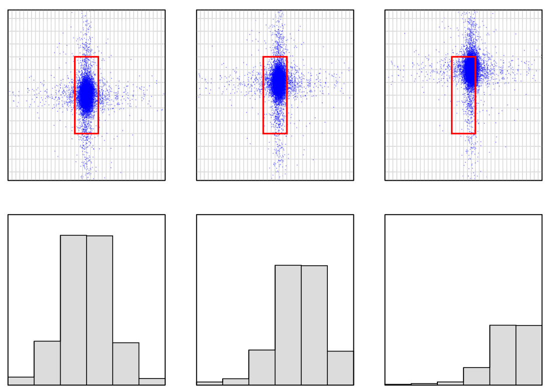

Fig. 1. Signal collected in the observing window of three consecutive CCDs in the astrometric field of view, for an asteroid moving 15 mas/sec in the along-scan direction, and 45 mas/sec in the across-scan direction. The corresponding recorded signals are shown at the bottom.

Figure 1 shows the simulated signal of an asteroid moving across the field of view of Gaia, as it transits in the observing window in different CCDs. The Figure summarizes some important problems related to the observation of moving objects. In particular, the collected photons tend to shift outside the observing window during a single transit in the Gaia field of view, and the corresponding signal recorded by different CCDs progressively changes as the object tends to exit the window. Since the position and size of the observing window in each different CCD in the focal plane is fixed at the beginning of the object's transit, a moving object tends to move progressively off-center in the observing windows of adjacent CCDs, and may in principle even exit the window if the apparent motion is sufficiently fast. Note that the recorded signal is the sum of all the photoelectrons integrated over each column of the observing window. In Figure 1 an observing window consisting of 6 columns is shown as an example. This corresponds to the most general case, wider windows being automatically selected on the basis of increasing apparent brightness of the source when it is first detected at the beginning of its transit across the Gaia field of view. The analysis of the signal is carried out by the routines of CCD processing, which are based on a standard signal model, solving simultaneously for the apparent angular size of the asteroid, and for its apparent motion, generally only in the along-scan direction.

The signal of an asteroid is fit by a model which takes into account the object's motion and apparent angular size. In particular, at a preliminary stage, the signal is fit to a very simple and not very realistic model of a spherical object seen at zero phase angle, i.e., at perfect sun opposition. In a second step, when the result of the inversion of disk-integrated photometry is available (see below), a more realistic model of a triaxial ellipsoid object with semi-axes $a > b > c$, seen at the correct phase angle is applied. If the number of collected photo-electrons is sufficiently large, i.e., when the object is sufficiently bright, and at the same time the angular size of the object is not negligible, it is possible to solve for the largest semi-axis of the triaxial ellipsoid shape (the b/a and c/a axial ratios being already known from photometric inversion). The measurement of the size gives reliable results whenever favorable conditions are met in terms of the apparent angular size of the object, and its apparent brightness. For a given object, these conditions can be met or not in different transits, depending on its absolute size and on the observing circumstances. In cases in which it turns out that the signal analysis can produce an estimate of the size with an uncertainty better than 10%, we speak of an actual size measurement. Based on an extensive simulations of five years of Gaia observations, Figure 2 shows, as a function of the diameter in km, how many times the size of different asteroids will be measured with an accuracy better than 10%. As it can be seen, the results are very encouraging, and show that direct measurements of the sizes of asteroids will be possible for all objects down to sizes a little above 20 km. This corresponds to a number of objects of the order of 1,000 for which Gaia is expected to provide direct size measurements, a very impressive result.

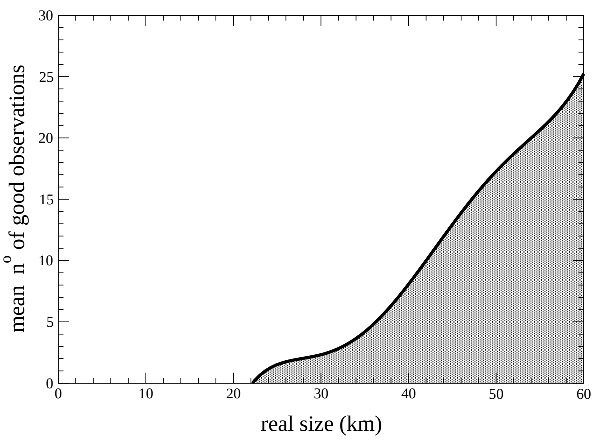

Fig. 2. Number of "good observations", namely transits for which the size can be measured with an accuracy better than 10%, for objects of different sizes. Based on an overall simulation of the Gaia detections of known main belt asteroids.

When the apparent angular size of an object will be measurable, the signal being different with respect to that of a point-like source, another very important parameter will be derived, mainly the amount of the difference between the apparent position of the photocenter of the signal, and that of the sky-projected barycenter of the object, taking into account its apparent projected shape and defect of illumination. The amount of this so-called "photocenter shift" will be important, since it will be used to correct the astrometric measurement of the object resulting from the photocenter position. When applicable, this correction will be used to improve the accuracy of the astrometric measurement, and will lead to a more accurate computation of the object's orbit.

3 Masses, densities and Yarkovsky effect

Every main-belt asteroid will be observed on the average about 70 times during the five-years operational lifetime of Gaia. While the usual astrometric accuracy of ground-based asteroid observations ranges between 0.05 and 1.0 arcsec, the astrometric accuracy of Gaia measurements for each single transit will range between 0.1 and 1.0 milli-arcsec (mas). As a consequence, the uncertainties in the orbital elements of the asteroids observed by Gaia will decrease by a factor of about 100. This will make it possible to measure tiny dynamical effects that are usually beyond the limit of ground-based observations. In particular, the deflections experienced by small asteroids when having close encounters with the largest objects in the main belt will be measurable, leading to the derivation of the masses of the perturbers. According to simulations, in this way the masses of about 100 among the largest asteroids will be measured. The accuracy of each single mass measurement is expected to be of the order of 10^{-12} solar masses, but combining different mass measurements for a single asteroid, corresponding to close approaches with different smaller objects, the accuracy should sensibly improve, possibly reaching values of the order of 10^{-14} solar masses. In the case of (1) Ceres, this would correspond to an accuracy of 0.01% in the mass determination, a very impressive result.

Having at disposal masses, sizes and overall shapes for about 100 asteroids, the average densities of these objects will be also determined with good accuracy. This will be another tremendous improvement in our knowledge of the physical properties of asteroids, taking also into account that among these 100 objects there will be asteroids belonging to a wide variety of taxonomic classes. For the first time, we will have the possibility to assess whether different taxonomic classes correspond also on the average to different densities, determined by differences in overall composition and/or internal macro-porosity.

Another consequence of the excellent astrometric accuracy of Gaia measurements will be the direct measurement of the effect of non-gravitational mechanisms on the orbital motion of small asteroids. In particular, the Yarkovsky effect is known to produce a small, steady drift in semi-major axis of small asteroids. This will produce a measurable effect on the recorded positions in some cases. According to simulations by Delbò et al. 2008, a measurement of the Yarkovsky drift should be possible for a number of about 35 near-Earth asteroids that will be observed by Gaia. Since the Yarkovsky effect depends on many physical parameters of an object, including size, spin axis orientation, rotation period and thermal inertia, the direct measurement of the effect for these objects will be a very important achievement for the physical studies of the asteroid population.

4 Spin, shape, taxonomy

Gaia will have remarkable photometric and spectrophotometric capabilities. For thousands of asteroids, disk-integrated photometric data, corresponding to different transits in the Gaia field of view, will be recorded. For each object, this will be a series of photometric snapshots taken over a five-years time span. As explained by Cellino et al. (2007, 2009) these data will be used to obtain information on the rotational properties of the objects (spin period, spin axis direction) and on their overall shapes. As explained in the above papers, the procedure developed to perform the photometric inversion of Gaia data is based on a genetic algorithm, and will use a simple triaxial ellipsoid model to fit asteroid shapes. According to the tests carried out so far, the spin properties are expected to be derived with good accuracy, of the order of fractions of a second for the rotation period, and a few degrees in the coordinates of the spin pole. As for the shapes, the results should be more qualitative, due to the simple shape model adopted to minimize CPU time. The number of objects for which we can expect to derive an accurate photometric inversion should be of the order of $10,000$. This will be another major result of Gaia, and will make it possible to carry out studies of the distributions of spin properties among dynamical family members, with important consequences on our overall understanding of asteroid collisional evolution. The determination of overall shapes will also be very useful to improve the accuracy of volume computations, needed to compute average estimates of density for the largest asteroid in the main belt (see previous Section).

Spectrophotometric data will range between 0.33 and about 1 μm, and will be used to derive a new taxonomic classification based on Gaia data. The sample should include several tens of thousands objects. Interestingly, the blue region of the visible spectrum, that has been largely lost in recent taxonomic classifications, will be included in Gaia data. This will be very important to identify distinct sub-classes of objects having a generally primitive composition, including the very interesting F class. Objects of this class have been found to be interesting in many respects, and might share asteroidal and cometary properties (Cellino et al., 2001). In addition to being *per se* an important resource, the taxonomy obtained by Gaia will be also an excellent tool to discriminate among membership of asteroids to mutually overlapping dynamical families.

A.C. gave a presentation on this subject at the SF2A 2009 conference in Besançon, while being Invited Researcher at the IMCCE in Paris (June - July 2009). This article summarizes the results obtained by an international team of scientists working in the Coordination Unit 4 of the Data Processing and Analysis Consortium (DPAC) of Gaia. We thank in particular F. Mignard, K. Muinonen, T. Pauwels, J. Berthier, W. Thuillot, J.-M. Petit, M. Delbò, S. Mouret, Ph. Bendjoya.

References

Cellino, A., Zappalà, V., Doressoundiram, A., Di Martino, M., Bendjoya, Ph., Dotto, E., Migliorini, F. 2001, Icarus, 152, 225

Cellino, A., Tanga, P., Dell'Oro, A., & Hestroffer, D. 2007. ASR, 40, 202

Cellino, A., Hestroffer, D., Tanga, P., Mottola, S., & Del l'Oro, A. 2009, A&A, in press

Delbò, M., Tanga, P., & Mignard, F. 2008. P&SS, 56, 1823

Mignard, F., Cellino, A., Muinonen, K., Tanga, P., Delbò, M., Dell'Oro, A., Granvik, M., Hestroffer, D., Mouret, S., Thuillot, W., & Virtanen, J. 2007, EMP, 101, 97

SF2A 2009
M. Heydari-Malayeri, C. Reylé and R. Samadi (eds)

STATUS OF THE GAIA SPACECRAFT DEVELOPMENT

de Bruijne, J.H.J.[1], Escolar, D.[2] and Erdmann, M.[2]

Abstract.
Gaia, ESA's ambitious astrometric mission due for launch in spring 2012, will provide multi-epoch, micro-arcsecond astrometric and milli-magnitude photometric data for the brightest one billion objects in the sky, down to at least magnitude 20. Spectroscopic data will simultaneously be collected for the subset of the brightest 100 million stars, down to about magnitude 17. This massive data volume will allow astronomers to reconstruct the structure, evolution, and formation history of our galaxy, the Milky Way. It will also revolutionise studies of the solar system and stellar physics and will contribute to diverse research areas, from extra-solar planets to general relativity.

Underlying Gaia's scientific harvest will lie a catalogue, built on the space-based measurements. During the 5-year nominal operational lifetime, Gaia's payload, with at its heart a CCD mosaic containing nearly 1 billion pixels, will autonomously detect all objects of interest and observe them throughout their passage of the focal plane. This contribution addresses the summer-2009 development status of the Gaia spacecraft, with particular emphasis on the torus and the deployable sunshield assembly. These two sub-systems reached important milestones on the day this presentation was orally delivered to the SF2A, namely 29 June 2009. On this day, the qualification model of the sunshield arrived at the ESTEC test facilities for thermal tests inside the Large Space Simulator. On the same day, the torus brazing was successfully concluded.

1 The Deployable Sunshield Assembly

Gaia will perform micro-arcsecond astrometry of over 1 billion objects in our Galaxy and beyond. In order to achieve the required measurement precision, the spacecraft and payload must be shielded from direct sunlight and maintained at a stable, low temperature: any thermal instability at the level of a few tens of micro-Kelvins or more can affect the final accuracy of the measurements that will be made.

The thermal stability of the Gaia spacecraft will be largely determined by a sunshield, with a diameter of 10.2 m when fully deployed and covering a surface of $\sim$75 m^2, the sun-facing area of which has to remain flat within a few millimeters deviation over the entire spacecraft lifetime. The sunshield assembly is composed of 12 rigid, rectangular panels and 12 foldable, triangular sections. In order to fit inside the launcher fairing, the assembly must be folded against the sides of the Gaia spacecraft during launch. After launch, the sunshield will deploy to form a flat structure at the base of the spacecraft, supporting two parallel blankets of multi-layer insulation (MLI) which will act as thermal shields so that the solar flux is damped by a factor of $\sim$280. In addition, the sunshield has to provide structural support for 8 deployable solar panels. All this has to be achieved with a mass of 125 kg. The large size and foldable MLI sections make this a unique sunshield design.

The qualification model (QM) of Gaia's deployable sunshield assembly (DSA) is functionally representative of the flight model and comprises three rigid panels plus the two sections of foldable MLI between them. Thermal vacuum and thermal balance (TV/TB) testing of this model is part of a comprehensive qualification test campaign designed to verify the compliance of the sunshield with design and operational specifications. The qualification test campaign includes functional testing (deployment), vibrational testing (launch conditions), environmental testing (including the TV/TB test), and life-cycle testing (ensuring its endurance with multiple deployment tests).

[1] Research and Scientific Support Department of the European Space Agency, European Space Research and Technology Centre, Keplerlaan 1, 2201 AZ, Noordwijk, The Netherlands
[2] Gaia Project of the European Space Agency, European Space Research and Technology Centre, Keplerlaan 1, 2201 AZ, Noordwijk, The Netherlands

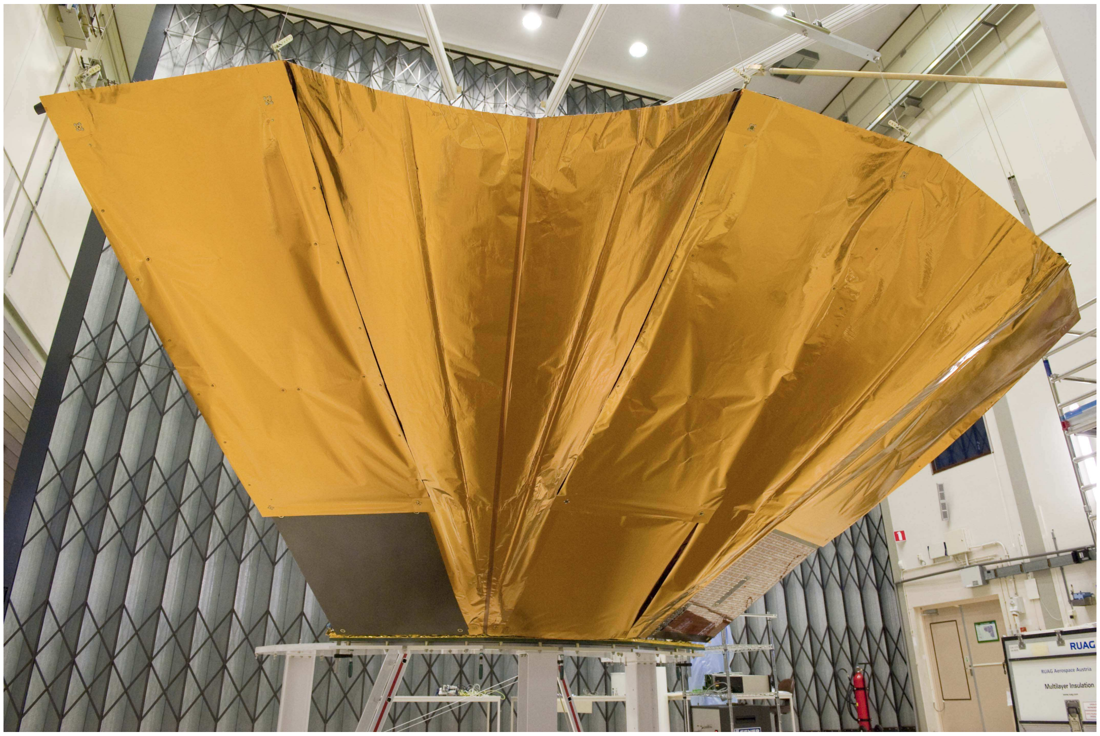

Fig. 1. This picture shows the Gaia deployable sunshield assembly (DSA) qualification model (QM) during deployment tests in the cleanroom at ESTEC, Noordwijk, The Netherlands. This model arrived at the ESTEC test facilities on 29 June 2009 for thermal tests inside the Large Space Simulator (LSS). Before the tests inside the LSS, several deployment tests of the sunshield were performed in the cleanroom at ambient conditions. This view shows the qualification-model sunshield during this deployment. The gold-coloured blanket of multi-layer insulation (MLI) is the sun-side blanket of the sunshield. Like the parallel-installed, shadow-side blanket behind it, it is made up of fixed sections attached to the three rectangular frames, and two foldable sections between the frames which are rolled in stowed configuration and unroll during deployment. The dark-coloured squares at the left and right bottom of the sunshield are solar panels. Copyright: ESA.

On 29 June 2009, the qualification-model sunshield arrived at ESA's ESTEC space centre in Noordwijk, the Netherlands, after transport from the SENER[1] premises in Spain. After arrival, the sunshield was unpacked and prepared for a deployment test at ambient conditions inside the ESTEC cleanroom. The MLI blankets were attached to the sunshield, and a zero-gravity kit – three masts with pulleys and counterweights used to simulate weightlessness – was installed. The deployment test involved the sunshield opening from its stowed configuration to its fully deployed configuration and was successfully completed on 3 July 2009 (Figure 1).

On 11 July 2009, the sunshield was transfered to the Large Space Simulator (LSS) for the TV/TB test. The LSS, with its 9.5-metre-diameter main chamber, is the only facility in Europe where tests of the Gaia sunshield can be performed in deployed configuration under simulated space conditions. The rectangular panels of the sunshield each measure about 0.8 m $\times$ 3.2 m and, once deployed, the qualification-model sunshield measures roughly 6.0 m $\times$ 4.0 m.

The main objective of the TV/TB test is to verify the deployment performance in simulated orbit conditions, the alignment and planarity (flatness) of the sunshield once it is deployed and exposed to the Sun, and the thermal performance of the sunshield. Inside the LSS chamber, the environmental conditions are regulated to simulate conditions encountered during operations in space. Shrouds with liquid nitrogen flowing through them cool the chamber to below 100 K. The chamber is vacuum pumped to a pressure of less than 10^{-8} bar.

During the tests, the planarity of the deployed sunshield was tested with videogrammetry measurements.

[1]SENER is developing the Gaia sunshield. The company is subcontractor to EADS Astrium, responsible for the overall design and development of the spacecraft. The frames and the blankets of the sunshield are supplied to SENER by RUAG, Austria.

Fig. 2. This picture shows the Gaia flight-model torus at the BOOSTEC premises at Bazet, near Tarbes, France. Pictured are members of the BOOSTEC and EADS Astrium SAS team just after the torus removal from the brazing furnace. The 3-metre-diameter, quasi-octagonal torus, which will support the two Gaia telescopes and the focal-plane assembly (FPA), is composed of 17 individual, custom-built, Silicon-Carbide (SiC) segments, all of which were constructed by BOOSTEC under contract to the Gaia prime contractor, EADS Astrium SAS. Starting on 28 April 2009, the 17 elements were assembled and aligned into the form of the torus. The torus brazing took place from 24–29 June 2009. Following the successful completion of the brazing, the torus has been delivered to EADS Astrium SAS in Toulouse for assembly of the bipod and release mechanisms (BRMs). Copyright: ESA.

This technique uses video observations of reflectors placed at specific points on the sunshield to accurately determine the relative positions of these points during the test. Deviations from the desired flat shape of the sunshield in its deployed configuration can be identified this way.

The thermal performance was monitored by 150+ temperature sensors attached to the sunshield and by temperature-map measurements of the sun-exposed surface of the deployed sunshield using an infrared camera. During the TB/TV test, the solar illumination was simulated at different intensity levels with special lamps generating up to 1400 W m^{-2} (just over 1 solar constant). The collimated light beam from these lamps was horizontal so the sunshield was deployed from horizontal to vertical position while inside the LSS. A mask in the form of a large foil shield, with a window exactly matching the shape of the deployed sunshield, stood in front of the opening where the collimated beam entered the main chamber. This mask allowed light to impinge directly only onto the sun-exposed side of the sunshield and blocked light that would otherwise pass the sunshield and reflect inside the vacuum chamber back onto the shadow side of the sunshield. Weightlessness conditions were simulated using the zero-gravity kit.

On 11 July 2009, the sunshield was lowered into the LSS chamber using an overhead crane. In the following days leading up to the TV/TB test, the set-up and the sunshield were prepared inside the LSS chamber. A dry run of the deployment inside the LSS was performed on 17 July 2009 under normal cleanroom conditions with the chamber still open. After bringing the sunshield back to its stowed configuration, the chamber door was closed on 20 July 2009, signalling the start of the TV/TB test in simulated space conditions. This test lasted 7 days. After completion of the TV/TB test, the sunshield was removed from the LSS and moved back to the cleanroom, where the life cycle deployment testing in ambient conditions was completed.

At the time of writing, the sunshield is waiting for a second slot of LSS tests to be performed in October

2009. After these tests, the qualification model will be delivered to the Gaia prime contractor, EADS Astrium SAS. Upon successful completion of this test campaign, the manufacturing of Gaia's flight-model sunshield will commence, incorporating all results from the qualification-model test campaign in the definitive design and assembly of the flight-model sunshield.

2 The torus

On 29 June 2009, the Gaia spacecraft development passed an important milestone when the 17 individual segments of the torus, a key structural element of the payload, were brazed into one coherent structure at the BOOSTEC premises at Bazet near Tarbes, France. The results of this process were successfully concluded after a mandatory inspection point (MIP) of the torus on Monday 20 July 2009.

The 3-metre-diameter, quasi-octagonal torus, which will support the two Gaia telescopes as well as the focal-plane assembly (FPA), is composed of 17 individual, custom-built segments. The scientific requirements of the mission translate to a requirement for a payload that is mechanically and thermally ultra stable, reaching micro-Kelvin and pico-meter levels. For these reasons, all elements of the torus are constructed from Silicon Carbide (SiC), a ceramic material with very special physical characteristics: it is very light-weight and the low thermal expansion coefficient and high thermal conductivity of SiC mean that it is a very stable material which can quickly dissipate thermal gradients. In addition, SiC is twice as stiff as steel.

Construction of the individual torus segments began more than one year ago at BOOSTEC. The process started with a 'green body' SiC powder and an organic binder material that was compressed with hydrostatic forces in a high-pressure facility. The resulting chalk-like material is easy to mill, although very abrasive in nature. Each of the 17 segments of the torus was milled from a green body. The segments were then sintered in a furnace to produce a solid, hard body. The segment interface surfaces were subsequently lapped to create an extremely flat surface so that there was a tight interface between segments during the brazing process. After lapping, the individual segments were subject to static-proof tests in which forces exceeding the range and magnitude of those experienced during launch were applied. Silicon Carbide, like most ceramics, is a hard material which is subject to fracturing due to microscopic flaws in the structure. The likelihood of fracturing is statistical in nature. The best way to ensure that the segments that are used in the construction of the flight model of the torus will not crack when in space is to verify their integrity by means of static-proof tests. Segments which passed these tests were validated for launch conditions and have been used to construct the torus.

Starting on 28 April 2009, the torus began to take shape as the individual elements were assembled together and precision-aligned using laser trackers and reference points on the torus segments. A special braze paste was applied to the interface points between each of the segments. When heated above 1000 degrees, this paste melts and seals the joints by capillary action: the torus then becomes one complete unit.

The completed torus was placed in the brazing furnace[2] at BOOSTEC on Wednesday 24 June 2009 and remained there until the morning of Monday 29 June 2009. After a cooling-down period, the torus was removed from the furnace and moved to the laboratories for post-brazing quality control (Figure 2). This included a thorough visual inspection of external and internal surfaces – the latter by means of borescopes – and ultrasonic inspection to confirm the integrity of the structure. On 20 July 2009, the torus was formally declared flight ready, marking a major milestone of the spacecraft development.

In August 2009, the torus was delivered to EADS Astrium SAS, the Gaia prime contractor, in Toulouse, France. At the time of writing, the assembly of the payload module, including the torus and mirrors, is being prepared. The first elements in line to be integrated are the folding optics structure (FOS) – supporting the M4/M'4 mirrors and the RVS optics module – and the bipod and release mechanisms (BRMs).

The oral presentation associated to this contribution was delivered on 29 June 2009, the day that the torus brazing cycle ended and the qualification model of the sunshield arrived at the ESTEC test centre. This proceedings contribution is heavily based on web articles which appeared on ESA's Science and Technology Gaia webpages. We gratefully acknowledge the contribution of Karen O'Flaherty and Guido Kosters of the Programme Management Support Office of the European Space Agency in the preparation of these web articles. High-quality versions of Figures 1 and 2, as well as other images, can be downloaded from http://sci.esa.int/gaia.

[2]The furnace at BOOSTEC was built for brazing the Herschel 3.5-metre-diameter primary mirror, and has also been used for the optical bench of the JWST NIRSPEC instrument.

SF2A 2009
M. Heydari-Malayeri, C. Reylé and R. Samadi (eds)

THE GAIA MISSION AND VARIABLE STARS

Eyer, L.[1], Mowlavi, N.[2], Varadi, M.[1], Spano, M.[1], Lecoeur-Taibi, I.[2] and Clementini, G.[3]

Abstract. The Gaia satellite, to be launched in 2012, will offer an unprecedented survey of the whole sky down to magnitude 20. The multi-epoch nature of the mission provides a unique opportunity to study variable sources with their astrometric, photometric, spectro-photometric and radial velocity measurements. Many tens of millions of classical variable objects are expected to be detected, mostly stars but also QSOs and asteroids. The high number of objects observed by Gaia will enable statistical studies of populations of variable sources and of their properties. But Gaia will also allow the study of individual objects to some depth depending on their variability types, and the identification of potentially interesting candidates that would benefit from further ground based observations by the scientific community. Within the Gaia Data Processing and Analysis Consortium (DPAC), which is subdivided into 9 Coordination Units (CU), one (CU7) is dedicated to the variability analysis. Its goal is to provide information on variable sources for the Gaia intermediate and final catalogue releases.

1 Introduction

Each object will be observed by Gaia a mean of 70 times during the 5 year mission. For each transit, Gaia will have quasi-simultaneous broad-band (G) photometry, blue (BP) and red (RP) spectro-photometry, and radial velocity spectrometer (RVS) measurements (in half of the cases for this latter instrument). As the shortest integration time is 4.4 seconds, variable sources can be detected on time scales from tens of seconds to years. The photometric precision should reach the milli-magnitude level at the bright end, and about 20 mmag at a magnitude of 20. In addition, the highly accurate astrometry will provide parallaxes and proper motions that will complement the photometric and RVS data. Most of the known variability types will benefit from the Gaia mission, thanks to its multi-epoch observations. In order to give to the scientific community the opportunity to perform follow-up ground based observations, the Gaia consortium puts in place a system of alerts and intermediate releases. For some events that occur uniquely and on a short time scale, a flux-based alert will be issued by the DAPC Coordination Unit 5 dedicated to the Photometric reduction. Variability announcements that are less time critical, for example those providing a list of candidates of interesting variable sources such as RR Lyrae stars, will be prepared by the Coordination Unit 7 (CU7) responsible of the analysis of all types of variables outside the solar system.

2 The Gaia scanning law

Gaia is a survey mission and is scanning the whole sky according to a prescribed law, designed to optimise the astrometric results. The Gaia sampling has been previously described in Eyer & Mignard (2005). Since that study, some modifications have been brought to the satellite design and to the scanning law. However, the general conclusions for the sampling properties do not change for the astrometric field.

The general behaviour of the time sampling pattern results from the design and operating mode of the satellite: Gaia has two fields of view separated by 106.5 degrees, and rotates around itself with a period of 6 hours. As a result, a sequence of measurements consists of several transits separated successively by 1h46m

[1] Geneva Observatory, University of Geneva, 1290 Sauverny, Switzerland
[2] ISDC, Geneva Observatory, University of Geneva, 1290 Versoix, Switzerland
[3] INAF Osservatorio Astronomico di Bologna, 40127 Bologna, Italy

and 4h14m, which correspond to the times elapsed from one field to the other. The next sequence of transits appears about 1 month later, due to the rotation axis precession and the satellite orbital motion. Between 40 and 250 per transit measurements will thus be collected for each star during the five year mission, depending on its ecliptic latitude, with a predicted mean number of 80 measurements. If we take into account "dead times", a recent study shows that the expected mean number of measurements lowers to 70 (de Bruijne 2009).

The Gaia time sampling is very similar to the time sampling of Hipparcos since their scanning laws were built on the same principle, but it significantly differs from the time sampling of ground based photometric surveys. In Fig. 1, we present the sampling properties of different missions and projects for a randomly chosen star. The spectral window of Gaia varies quite a lot from one region of the sky to another. We also remark that the high amplitude peaks in the spectral window, which are causing aliases in the Fourier space, are located at high frequencies for Gaia, as it is for Hipparcos.

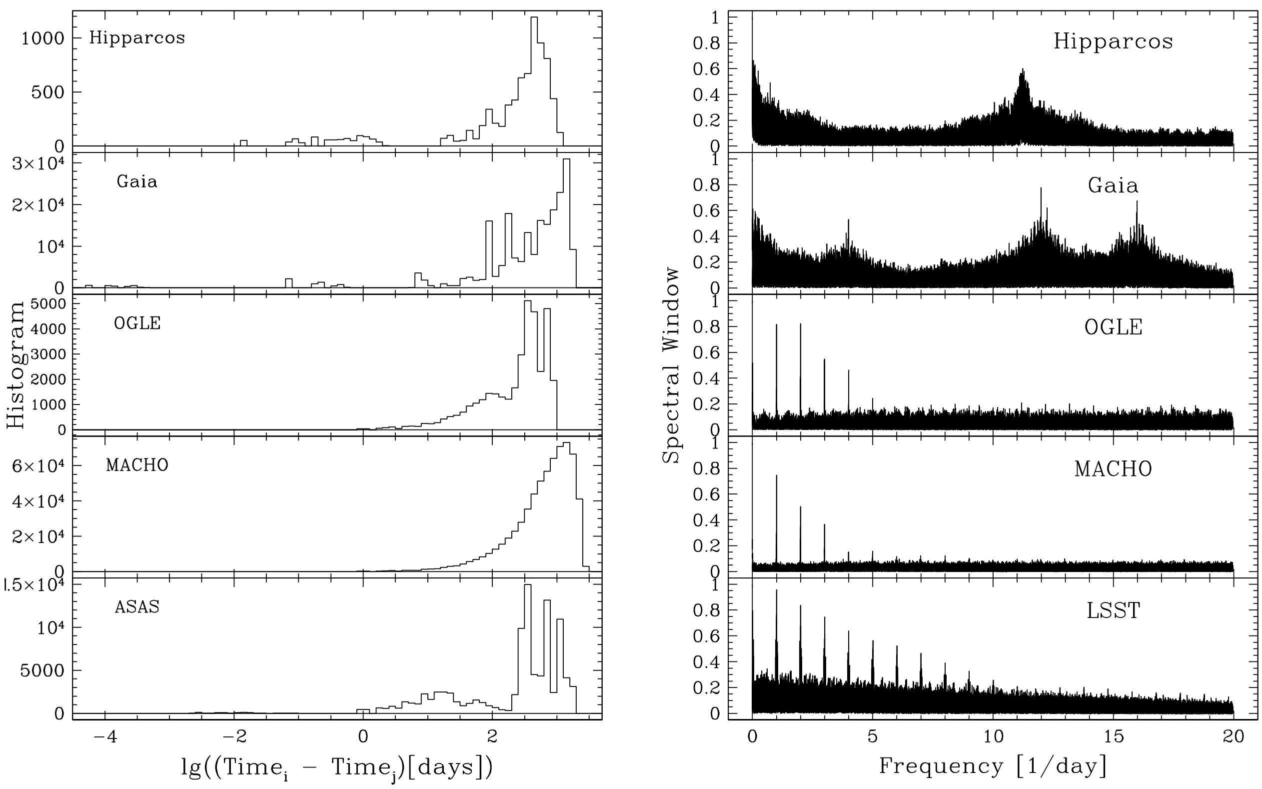

Fig. 1. Sampling properties of different missions and projects. Left: Histograms of the time differences between two successive measurements for a randomly chosen star, per mission or project. Right: Spectral windows of different surveys. The predicted time lags for Gaia are given based on per CCD photometry.

3 Periodic and short periods variable stars

The detection rate of mono-periodic signals observed by Gaia is expected to be quite good for a wide range of periods. Eyer & Mignard (2005) showed that this period recovery for regular variable stars depends on the ecliptic latitude, reaching more than 95% over more than 40 degrees of ecliptic latitudes and for S/N ratios as low as 1.3.

The Gaia time sampling and the CCD data acquisition scheme allow in principle to probe stellar variability also on time scales as short as several tens of seconds, thereby giving potential access to the study of short-period (less than a few hours) variable stars in a large and homogenous sample of stars. In order to explore that time scale regime, Varadi et al. (2009), in a first step, extended the work of Eyer & Mignard (2005) to periods shorter than two hours, and showed that the period recovery of a sinusoidal signal with a Gaia time sampling is above 90% for S/N ratios as low as 1.0, provided that per-CCD photometry is used. A second step has been initiated by Mary et al. (2006) to introduce multi-periodic sinusoidal signal, simulating the case of the roAp star HR 3831. Simulating 16 frequencies for that star, they were able to recover three frequencies from a noiseless curve. The third step consists in testing the recovery capability of non-linear multi-periodic light curves. The study is performed on simulated light curves of ZZ Ceti stars (Varadi et al. 2009) and takes into account the flux transfer of a sinusoidal signal from the base of the convective envelope of those stars to their surface. The results of those simulations show that the non-linear effect introduced by the flux transfer through the envelope degrades by only a few percents the performance of the recovery rate of the main period for multi-periodic ZZ Ceti stars. The next step should consider the case of non-stationarity of variability that characterises several classes of short pulsators. In these cases, the stellar pulsation periods and amplitudes can change on time scales from weeks to years. Further studies are under way to analyse the impact of those effects on the Gaia detection capability of those stars.

4 Pseudo-periodic and irregular variable objects

Due to the nature of the Gaia sampling, the behaviour of irregular and pseudo-periodic variable objects poses many challenges. First, their irregular nature makes their characterisation particularly difficult. Some methods such as the structure function/variogram (Eyer & Genton 1999) can help characterising the variability time-scales present in the source. This technique was applied for example by Eyer (2002) to search QSOs in OGLE-II database. Second, they may "contaminate" the sample of periodic variable stars. The analysis of the pseudo-periodic stars can indeed identify spurious frequencies from their Fourier spectrum and wrongly classify them as periodic variables. This lowers the quality of the catalogue of periodic variable objects.

The analysis of irregular or pseudo-periodic variable objects is however interesting, as it can lead to the detection of rare cases of variable objects. An example is given by the secular variable stars such as post-Asymptotic Giant Branch stars.These stars are evolving so fast that the photometric variations due to their stellar evolution can become detectable on human time scales. Few such stars have been seen to cross the entire colour-magnitude diagram in some decades. In Gaia, a work package is dedicated to the detection and characterisation of such stars based on the search of global changes in their magnitude or colour. Preliminary studies are carried out in existing surveys such as OGLE (Spano et al. 2009) and EROS.

5 Transients

The detection of transient events is also challenging. About 6,000 supernovae, for example, are expected to be detected by Gaia down to magnitude 19 (Gilmore 2009), with one third of them being detected before maximum light. While they are not likely to be a source of contamination for the catalogue of periodic stars, their possible confusion with other types of non-periodic stars remains to be addressed, and an adequate procedure should be put in place for their detection.

Microlensing events are other transient phenomena that are of potential interest for Gaia. Over the 1988 microlensing events detected in OGLE-III, 66% (1324 events) have at least one measurement within the lensing event (Wyrzykowski 2009). For events with time-scales longer than 30 days the statistics improves to 93%. The automatic detection and fast identification of microlensing events are not obvious though, despite the fact that they have clear signatures with a smooth and achromatic rise and fall. An algorithm is being set up to detect such events (Eyer et al. 2009). A preliminary comparison of our microlensing event candidates with those of Wozniak (2001) indicates a high recovery rate on OGLE-II data. The application of our algorithm to the Hipparcos catalogue resulted in only few false detections, showing that the robustness of the identification procedure.

6 Variable stars simulations

In order to test the algorithms that are set up in CU7 to detect and characterise the variable objects observed by Gaia, simulated light curves are produced for an increasing number of types of variable stars (Mowlavi 2009).

Currently, Cepheids, RR Lyrae of types ab and c, delta Scuti stars, ACVn stars, Miras, roAp stars, semi-regular variables, ZZ Ceti stars, dwarf novae, active galactic nuclei and microlensing events are simulated.

The simulated light curves, together with the properties of each type of variable stars (their location in the HR diagram and the probability of their occurrence), are provided to Coordination Unit 2 (CU2) in order to feed their Gaia simulation code. Simulated Gaia time series of variable stars, as realistic as possible, are thus aimed to test the CU7 software.

7 Ground based Observations

The Gaia DPAC may need some ground based data to help the preparation of its data processing. A Working Group, Ground-Based Observations for Gaia (GBOG), has been formed and is establishing the need of such observations and is also coordinating the proposals to ESO. For the variability analysis, it has been felt that there is a wealth of data which are already available, e.g. Hipparcos, MACHO, EROS, OGLE, CoRoT, HAT, SDSS data and therefore there is no need to gather additional data for the moment.

A network of 12 telescopes of 1-2 m size is currently in place within CU7. It is worth mentioning that the use of such 1-2 m class telescopes is particularly adequate also for the photometric follow-up studies of variable stars. Within DPAC, such follow-up should be only done for validation purpose. However these telescopes could be used for the scientific exploitation, once the data is public. Spectroscopic studies of bright variables such as Cepheids, Long Period variables or RR Lyrae stars will also benefit from those small size telescopes.

We would like to thank the whole Gaia team in Geneva: M. Beck, P. Dubath, L. Guy, A. Jan, K.Nienartowicz, L. Rimoldini, as well as the CU7 members who are contributing to the work on the CU7 Variability Processing and Analysis. We also want to thank J. de Bruijne for discussions on the scanning law.

References

de Bruijne 2009, private communication

Eyer L., & Mignard F. 2005, MNRAS 361, 1136

Eyer L., Evans D.W., & Lecoeur-Taibi I. 2009, Gaia document: GAIA-C7-SP-GEN-LE-008

Eyer L., & Genton M.G. 1999, A&AS 136, 421

Eyer L. 2002, AcA 52, 241

Gilmore G. 2009, March Kick-off GREAT meeting, Cambridge, UK

Holl B., Hobbs D., & Lindegren L. 2009, IAU 261, 1703

Mary D. et al. 2006, Gaia document: GAIA-C7-TN-ARI-DM-003-1

Mowlavi N. 2009, Gaia document: GAIA-C7-UG-GEN-NM-006

Spano M., Mowlavi N., Eyer L., & Burki G. 2009, in Stellar Pulsation, Challenges for Theory and Observation, AIP, in press

Varadi M., Eyer L., Jordan S., Mowlavi N., & Koester D. 2009, in Stellar Pulsation, Challenges for Theory and Observation, AIP, in press

Wozniak P.R., Udalski A., Szymanski M., et al. 2001, Acta Astronomica, 51, 175

Wyrzykowski L. 2009, Gaia document: GAIA-C5-TN-IOA-LW-001

SF2A 2009
M. Heydari-Malayeri, C. Reylé and R. Samadi (eds)

TESTING GRAVITY IN THE MILKY WAY WITH GAIA

Famaey, B.[1] and Bienaymé, O.[1]

Abstract. With the advent of Gaia, it will be possible to design tests of gravity on the scale of the Galaxy. Observations of external galaxies indeed suggest a one-to-one analytic relation between gravity at any radius and the enclosed baryonic mass, a relation summarized by Milgrom's law of modified Newtonian dynamics (MOND). Within its modified gravity interpretation, MOND makes very specific predictions allowing to differentiate it from a spherical halo of dark matter. Here, we show that MOND can be tested with Gaia by measuring dynamically the disk surface density at the solar radius, the radial mass gradient within the disk, or the velocity ellipsoid tilt angle above the Galactic plane at various heights and various Galactocentric radii. However, these tests require an extremely accurate baryonic mass model for the Milky Way.

1 Introduction

The long-term goal of the Gaia mission is to get an accurate estimate of the Galactic gravitational potential by analyzing the motion of several hundreds millions stars up to ~ 15 kpc: the full dataset should be available around 2020. However, when the first releases of data will be available around 2015, it will already be possible to answer crucial questions about the dynamics of our Galaxy. Among them, a currently harshly debated question is whether the missing mass problem is due to the existence of dark matter or to a modification of the gravitational law on galaxy scales. Here, following the work of Bienaymé et al. (2009), we show how large-scale spectroscopic and astrometric surveys in general, and Gaia in particular, could help answer this question.

2 Cold Dark Matter or Modified Newtonian Dynamics?

The concordance cosmological model based on the existence of Cold Dark Matter (CDM) is very successful on large scales. However, the predictions of the model are in contrast with a number of observational facts on galaxy scales. A non-exhaustive list of issues is (i) the predicted overabundance of satellite galaxies; (ii) the prediction of cuspy dark matter halos, whereas observations point toward dark halos with a central constant density core; (iii) the problems to form large enough baryonic disks due to their predicted low angular momentum within simulations; and (iv) the departures from the CDM scenario recently found in tidal dwarf galaxies (e.g., Gentile et al. 2007). In addition to these discrepancies with observations, galaxies also follow tight scaling relations that are hard to explain without much fine-tuning of CDM. For instance, (i) the baryonic Tully-Fisher relation (relating the baryonic mass of a disk galaxy to the fourth power of its circular velocity), whic! h is valid for all disk galaxies with negligible scatter; (ii) the Faber-Jackson relation (relating the luminosity of an elliptical galaxy to the fourth power of its velocity dispersion), valid for elliptical galaxies, and more generally, the fundamental plane for elliptical galaxies; (iii) the universality of the dark and baryonic surface densities of galaxies within one scale-length of the dark halo (Gentile et al. 2009); and (iv) the mass discrepancy-acceleration relation (relating the dark-to-baryonic mass ratio to the gravitational acceleration), which holds for all disk galaxies at any galactocentric radius (McGaugh 2004). This last relation notably involves an acceleration scale $a_0 \sim 10^{-10}$ ms^{-2} whose significance is far from clear. Below this gravitational acceleration, the enclosed dark mass starts to dominate over baryons in galaxies, and this acceleration scale also fixes the slope and zero-point of the Tully-Fisher and Faber-Jackson relations. Final! ly, galactic rotation curves often display obvious features (bumps or wiggles) that are also clearly visible in the stellar or gas distribution ("Renzo's rule"), which is difficult to understand in galaxies dominated by collisionless dark matter.

[1] Observatoire Astronomique, Université de Strasbourg, CNRS UMR 7550, F-67000 Strasbourg, France

Table 1. Values predicted from the Besançon MOND model as seen by a Newtonist compared to observations, for the local surface density and the tilt of the velocity ellipsoid.

	Besançon MOND	Observations
$\Sigma_\odot(z = 1.1\,\mathrm{kpc})$	78 $M_\odot/\mathrm{pc}^2$	74 ± 6 $M_\odot/\mathrm{pc}^2$ (Holmberg & Flynn 2004)
Tilt at $z = 1$ kpc	6 degrees	7.3 ± 1.8 degrees (Siebert et al. 2008)

This could thus all point towards a modification of the gravitational law on galaxy scales: for instance, Milgrom (1983) postulated that for gravitational accelerations below a_0, the true gravitational attraction g approaches $(g_N a_0)^{1/2}$ where g_N is the usual Newtonian gravitational field (as calculated from the observed distribution of visible matter). This alternative paradigm is known as modified Newtonian dynamics (MOND), and uncannily explains all the scaling relations mentioned above (but it does not work for galaxy clusters). Such a modification of Newtonian dynamics could come at the classical (non-covariant) level from a modification of either the kinetic part or the gravitational part of the Newtonian action (with usual notations; ϕ_N being the Newtonian gravitational potential):

$$S = \int \frac{1}{2}\rho v^2 d^3x\, dt - \int \left(\rho\phi_N + \frac{|\nabla\phi_N|^2}{8\pi G}\right) d^3x\, dt, \tag{2.1}$$

where modifying the first term is referred to as "modified inertia" and modifying the second term as "modified gravity". Bekenstein & Milgrom (1984) have devised a modified gravity framework in which $|\nabla\phi_N|^2$ is replaced by $a_0^2 F(|\nabla\phi|^2/a_0^2)$ in Eq. 2.1, where $F(y)$ is a free function with defined asymptotic properties reproducing $g = (g_N a_0)^{1/2}$ in the spherically symmetric weak-field limit.

Within this Bekenstein & Milgrom modified gravity interpretation, MOND makes very specific predictions allowing to differentiate it from a spherical halo of dark matter. Here, we outline these predictions, that Gaia and other large-scale surveys could help to test.

3 How Gaia can help

We build these predictions using the free function $F(y)$ of Famaey & Binney (2005) and the MOND Milky Way model of Wu et al. (2008)[1]. This model is based on one of the most realistic possible baryonic mass models of the Milky Way, the Besançon model (Robin et al. 2003).

Once the MOND gravitational potential of the model is known, one can apply the Newtonian Poisson equation to it, in order to find back the density distribution that would have yielded this potential within Newtonian dynamics. In this context, as shown in Bienaymé et al. (2009), MOND predicts a disk of "phantom" dark matter allowing to differentiate it from a Newtonian model with a dark halo

(i) By measuring the force perpendicular to the Galactic plane: at the solar radius, MOND predicts a 60 percent enhancement of the dynamical surface density at 1.1 kpc compared to the baryonic surface density, a value not excluded by current data. The enhancement would become more apparent at large galactic radii where the stellar disk mass density becomes negligible.

(ii) By determining dynamically the scale length of the disk mass density distribution. This scale length is a factor $\sim$1.25 larger than the scale length of the visible stellar disk if MOND applies. Such test could be applied with existing RAVE data (Zwitter et al. 2008), but the accuracy of available proper motions still limits the possibility to explore the gravitational forces too far from the solar neighbourhood.

(iii) By measuring the velocity ellipsoid tilt angle within the meridional galactic plane. This tilt is different within the two dynamics in the inner part of the Galactic disk. However the tilt of about 6 degrees at z=1 kpc at the solar radius is in agreement with the recent determination of 7.3 ± 1.8 degrees obtained by Siebert et al. (2008). The difference between MOND and a Newtonian model with a spherical halo becomes significant at z=2 kpc.

[1]We use the model labelled "MOND $g_{\rm ext} = 0.1a_0$" in Wu et al (2008), meaning that the modulus of the external gravitational field acting on the Milky Way is chosen to be $a_0/100$

Such easy and quick tests of gravity could be applied with the first releases of future Gaia data. To fix the ideas on the *current* local constraints, the predictions of the Besançon MOND model are compared with the relevant observations in Table 1. Let us however note that these predictions are *extremely* dependent on the baryonic content of the model, so that testing gravity at the scale of the Galaxy heavily relies on star counts, stellar population synthesis, census of the gaseous content (including molecular gas), and inhomogeneities in the baryonic distribution (clusters, gas clouds).

We thank HongSheng Zhao, Xufen Wu, and Dominique Aubert for their contribution to Bienaymé et al. (2009).

References

Bekenstein, J., Milgrom, M., 1984, ApJ, 286, 7

Bienaymé, O., Famaey, B., Wu, X., et al., 2009, A&A, 500, 801

Famaey, B., Binney, J., 2005 MNRAS, 363, 603

Gentile, G., Famaey, B., Combes, F., et al., 2007, A&A, 472, L25

Gentile, G., Famaey, B., Zhao, H.S., Salucci, P., Nature, 461, 627

Holmberg, J., Flynn, C., 2004, MNRAS, 352, 440

McGaugh, S.S., 2004, ApJ, 609, 652

Milgrom, M., 1983, ApJ, 270, 365

Robin, A. C., Reylé, C., Derrière, S., Picaud, S., 2003, A&A, 409, 523

Siebert, A., Bienaymé, O., Binney, J., et al., 2008, MNRAS, 391, 793

Wu, X., Famaey, B., Gentile, G., et al., 2008, MNRAS, 386, 2199

Zwitter, T., Siebert, A., Munari, U., et al., 2008, AJ, 136, 421

SF2A 2009
M. Heydari-Malayeri, C. Reylé and R. Samadi (eds)

A SELECTION OF SB WHICH COULD GET ACCURATE MASSES FROM GAIA ASTROMETRY

Halbwachs, J.-L.[1] and Arenou, F.[2]

Abstract. Gaia will provide astrometric measurements accurate enough for deriving the masses of spectroscopic binary (SB) components with uncertainties around 1 %. A list of a bit less than 100 SB is set up for that purpose. However, the spectroscopic elements of these systems need to be derived again from accurate radial velocity measurements in order to achieve a 1 % accuracy on the masses.

1 Introduction

Several progresses in our knowledge of double stars are expected from the forthcoming Gaia mission. The statistical properties of binaries, which are clues for the understanding of their formation process, will be derived from samples larger from the present ones by several orders of magnitude (Halbwachs et al. 2003a). Ten years ago, Halbwachs & Arenou (1999) pointed out that the astrometric Gaia measurements could lead to the masses of a lot of components of double-lined spectroscopic binaries (SB2). The elements of the SB2 orbit lead to the products $\mathcal{M}_1 \sin^3 i$ and $\mathcal{M}_2 \sin^3 i$, where $\mathcal{M}$ refers to component masses and i to the inclination of the orbital plane. Up to the present time, accurate stellar masses have been obtained from SB2 which are also eclipsing binaries. The inclinations of these systems are then derived from the analysis of the light curve. This method is quite reliable, but it may be applied only to few SB2, since it requires inclinations very close to $\pi/2$. Moreover, eclipsing binaries have usually short periods and close components, and are therefore not representative of single stars since they often suffer from mass exchange between the components. At the opposite, an astrometric orbit is easier to derive when the period is close to the time span of the observations (5 years with Gaia) than when the components are close. For these reasons, masses derived from SB orbits and inclinations coming from the astrometric observations of the forthcoming Gaia satellite would be quite relevant, if their uncertainties would be sufficiently small. In practice, it is considered that errors around 1 % or less are required for improving the models of stellar physics.

2 A method for selecting SB that could provide accurate masses

Let us consider a binary for which we have a list of radial velocity (RV) measurements and a list of astrometric measurements. In practice, the most efficient method for deriving the orbital elements of such system consists in using together the measurements of all kinds in a sole computation. However, our purpose hereafter is to select known SB for which Gaia could provide an important missing information, that is the sinus of the inclination. The SB elements of these binaries were usually obtained from RV measurements with moderate uncertainties, i.e. a few hundreds of m/s, or even around 1 km/s. Therefore, we have estimations of $\mathcal{M}_1 \sin^3 i$ and $\mathcal{M}_2 \sin^3 i$ which are not very accurate, but may be greatly improved by measuring again the RV of these stars with a CCD-spectrovelocimeter. The RV errors are then around 1 m/s for stars with small RV amplitudes, and it should be a few tens of m/s for a typical SB. For selecting the SB which could receive accurate masses, it is assumed hereafter that the spectroscopic elements of the binaries may be derived with negligible errors. Then, the elements period P, eccentricity e, periastron epoch T_0, periastron argument ω, and projected semi-major axis of the photocenter $a_0 \sin i$ are fixed in the derivation of the astrometric orbit, and the errors of the

[1] Observatoire Astronomique de Strasbourg, 11 rue de l'université, F-67000 Strasbourg, France
[2] Observatoire de Paris-Meudon, 5 place Jules Janssen, F-92190 Meudon, France

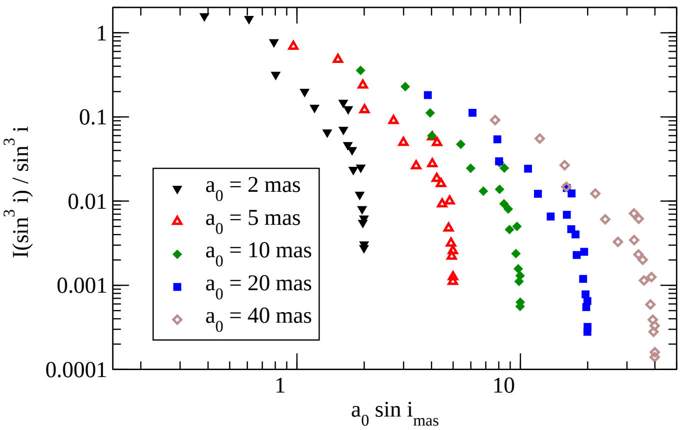

Fig. 1. Uncertainties of $sin^3 i$ derived from Gaia astrometric observations for simulated SB with various semi-major axes.

masses will come only from the errors of the astrometric measurements. The selection problem consists then in evaluating the uncertainty of $\sin^3 i$ (i.e., of i) that may be expected on the basis of the SB elements. It is not difficult to calculate $a_0 \sin i$ from the elements of the SB orbit and from the distance of the system, assuming a mass-luminosity relation: For the wavelengths used by Gaia astrometry, the difference of magnitudes between main sequence components is simply $\Delta G = -7.3 \log q$, where q is the mass ratio.

It comes from simulations that, for periods shorter than 5 years, Gaia could provide inclinations with uncertainties $I(i)$ which roughly obey the equation:

$$I(i) = \frac{3}{a_0 \sin i} \tag{2.1}$$

where $a_0 \sin i$ is in mas and $I(i)$ is in degrees. This relation is only approximate (by a factor of about 2), since the actual error will depend on parameters like the eccentricity of the orbit and the position angle of the periastron, and on the observation epochs. A consequence of Eq. 2.1 is that the relative error of $\sin^3 i$ is then related to both $a_0 \sin i$ and $\sin^3 i$, since it is:

$$\frac{I(\sin^3 i)}{\sin^3 i} = 3\, \frac{I(i)}{\tan i} \times \frac{\pi}{180} \tag{2.2}$$

Therefore, it is impossible to predict the uncertainties of the masses which may be obtained from Gaia astrometric measurements for a given SB2. This is illustrated by Fig. 1, where the relative errors of $\sin^3 i$ are plotted as a function of $a_0 \sin i$ for a few simulated SB2 with different a_0. It appears that the relative error of $\sin^3 i$ is dramatically rising when the inclination decreases.

In a rough approximation, it comes from Eq. 2.1 and 2.2 that we will get masses with errors smaller than 1 % when the actual inclinations are larger than the limit:

$$i_{min} = \arctan \frac{5\pi}{a_0 \sin i} \tag{2.3}$$

where $a_0 \sin i$ is again in mas. As a consequence, it is only possible to derive a probability to obtain masses with an error better than 1 %, assuming a statistical distribution for the inclinations. Since it is reasonable to assume that the orientations of the orbits with respect to the plane of the sky are isotropic, we assume hereafter that the distribution of i is $f(i) = \sin i$. This relation applies to all binaries in space, and we assume it hereafter for any known SB, except for those for which the inclinations are already known thanks to Hipparcos astrometry.

It is worth noticing that a priori estimations of the inclinations could be obtained from $\mathcal{M}_1 sin^3 i$ by evaluating the masses of the primary components from their spectral types. However, this method would be hazardous, since it would introduce a bias in favour of the systems with primaries less massive than expected from the mass – spectral type relation. It is safer to discard it for that reason.

3 A list of stars which could get masses with a 1 %–accuracy

Our purpose is to search masses better than 1 %. Since it is not possible to compute a priori the expected accuracy of a component mass, we select the SB for which the probability to get such accurate masses is larger than 50 %. We consider SB2, but also SB1 when the minimum mass ratio is larger than 0.3. The secondary spectra could then be visible on high-resolution CCD observations.

In order to obtain accurate RV measurements, only the stars brighter than 12.5 mag and with declinations above -5 degrees are considered hereafter; moreover, the stars brighter than 6 mag are discarded from the selection, since they will not receive accurate astrometric measurements from Gaia. Three lists of known SB were thus prepared:

1. The nearby G-K dwarf binaries with astrometric orbits derived from Hipparcos (Halbwachs et al. 2003b). This list contains 25 SB with inclination errors less than 15 degrees. The mass ratios of these systems are coming from SB2 orbits or from the astrometric solution.

2. The SB9 catalogue (Pourbaix et al. 2009). This up-to date catalogue contains 776 SB with F to M spectral types and periods between 30 days and 10 years.

3. A list of SB members of common proper motion (CPM) systems (Halbwachs, Mayor & Udry, 2007). This list contains 34 SB with unpublished orbits and periods longer than 30 days.

The distances of the stars were derived from various methods. The trigonometric parallaxes were used when their uncertainties are better than 20 %. Otherwise, a spectroscopic parallax was derived. When the luminosity class of the star was not known, it was inferred from the reduced proper motion, $H = V + 5 \log \mu + 5$, where μ is the proper motion in arcsec. When $H > 0$, the star was assumed to be a dwarf, otherwise it is a giant. For the stars of the SB9 list, the spectroscopic parallaxes were corrected for extinction, using the coordinates of the stars and a galactic extinction model (Arenou et al., 1992).

For each SB, thousands of simulated binaries were generated, assuming known the actual elements and generating the unknown parameters like i and Ω, the position angle of the periastron. For each virtual binary, Gaia astrometric measurements were produced with a simple model (Halbwachs 2009), and the inclination of the orbit was derived from these observations, assuming the elements of the SB orbit. The proportion of virtual systems with inclination errors better than 1 % was thus obtained. The SB was selected when this rate was larger than 50 %. At the end, 96 SB were retained: 10 nearby G-K dwarfs with Hipparcos astrometric orbits, 78 SB9 stars, and 8 CPM stars. The faintest is a 10.17 mag star. Seven stars are earlier than F5 and 2 are of M-type, but the vast majority are G-K stars.

4 On the accuracy of $\mathcal{M} \sin^3 i$

We have selected SB for which $\sin^3 i$ may be found at the 1 % level of accuracy, assuming that the SB orbital elements are perfectly known. In this section, we want to be sure that $\mathcal{M} \sin^3 i$ may be accurately derived with a few high-precision RV measurements. For that purpose, RV measurements were generated with the following hypotheses: (a) The observation epochs obey a Poisson distribution, with an average number of 14 RV measurements within 7 years, starting from 2011; (b) the standard error of the epoch measurements is 50 m/s. Again, thousands of virtual SB were generated for each of the 96 SB of the list, and the standard deviation of the errors of $\mathcal{M}_1 \sin^3 i$ and $\mathcal{M}_2 \sin^3 i$ are computed. Figure 2 shows the selected SB plotted in a eccentricity vs relative error of $\mathcal{M}_1 sin^3 i$ diagram. About 50 SB in our selection should get $\mathcal{M}_1 \sin^3 i$ with errors less than 1 %. This is rather encouraging, since, for simplicity, the measurements already available were not taken into account in the computations above. In reality, they will be considered and the periods of the binaries – and therefore the $\mathcal{M} \sin^3 i$ terms – will be much more accurate than in the simulations. This concerns especially the periods larger than 7 years, and which were not covered with the simulated RV. Moreover, it is visible on Fig. 2 that the accuracy of $\mathcal{M}_1 sin^3 i$ is falling when the eccentricity increases, especially when it is larger than 0.6. Again, the accuracy should be much better in reality, if the observation epochs are not taken at random but chosen in order to observe near the periastron, each time this would be feasible.

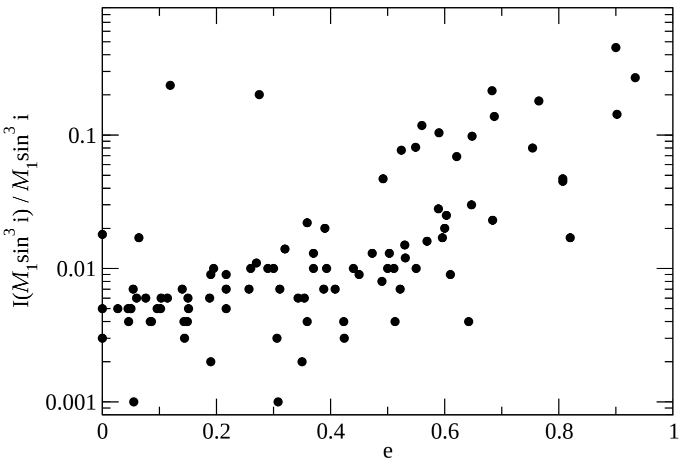

Fig. 2. Uncertainties of $\mathcal{M}_1 sin^3 i$ derived from high-precision RV measurements as a function of eccentricity.

5 Conclusion

We have prepared a list of 96 SB which could get masses with a 1 % accuracy if the elements of their spectroscopic orbits are derived again from high precision RV measurements. An accuracy of 50 m/s, which is quite feasible now, should be sufficient for that purpose. Would the RV observations begin in 2011, more than one hundred stars (2 per SB) could get accurate masses as soon as the Gaia astrometric measurements will be delivered.

This research has made use of the VizieR catalogue access tool and of the SIMBAD database, operated at CDS, Strasbourg, France

References

Arenou, F., Grenon, M., Gómez, A. E., 1992, A&A 258, 104

Halbwachs, J.-L., 2009, MNRAS 394, 1075

Halbwachs, J.-L., Arenou, F., 1999, Baltic Astronomy 8, 301

Halbwachs, J.-L., Arenou, F., Eggenberger, A., Mayor, M. & Udry, S., 2003a, in Gaia Spectroscopy, Science and Technology, ed. U. Munari, ASP Conf. Ser. 298, 339

Halbwachs, J. L., Mayor, M., Udry, S. & Arenou, F., 2003b, A&A 397, 159

Halbwachs, J. L., Mayor, M. & Udry, S., 2007, in Binary Stars as Critical Tools and Tests in Contemporary Astrophysics, IAU Symposium no. 240, ed. W.I. Hartkopf, E.F. Guinan & P. Harmanec, p. 427, Cambridge U. Press

Pourbaix, D., Tokovinin, A. A., Batten, A. H., Fekel, F. C., Hartkopf, W. I., Levato, H., Morell, N. I., Torres, G. & Udry, S., 2009, SB9: 9th Catalogue of Spectroscopic Binary Orbits, VizieR On-line Data Catalog: B/sb9. Originally published in: 2004, A&A 424, 727

SF2A 2009
M. Heydari-Malayeri, C. Reylé and R. Samadi (eds)

GAIA SPECTROSCOPY: OVERVIEW AND SYNERGIES WITH GROUND-BASED SURVEYS

Katz, D.[1]

Abstract. This talk reviews the current status of the Gaia-RVS design and performance. It examines the synergies between Gaia and ground-based spectroscopic surveys. It concludes on the possible additional spectroscopic surveys that could complement Gaia in the quest for understanding the Milky-way.

1 Introduction

The first science driver of Gaia is the understanding of the structure, formation and history of our Galaxy. To fulfil this objective, Gaia will continuously scan the celestial sphere during 5 years with its 3 instruments: the astrometric instrument (providing the positions, parallaxes and proper motions), a low resolution spectro-photometer made of 2 "arms", i.e. blue and red (providing the atmospheric parameters, interstellar reddening and mean alpha elements to iron ratio) and a middle resolution spectrograph, the Radial Velocity Spectrometer - RVS (for the derivation of the radial velocities, but also for the "brightest" stars: rotational velocities, atmospheric parameters, some individual abundances and interstellar reddening). This talk reviews the current status of the RVS design (Sect. 2) and performance (Sect. 3). It examines the synergies with the current ground-based spectroscopic surveys (Sect. 4). It concludes on the possible additional spectroscopic surveys that could complement Gaia in the quest for understanding the Milky-way (Sect. 5).

2 RVS design

The Radial Velocity Spectrometer (RVS) is an integral field spectrograph, i.e. it disperses all the light that enters its 0.22×0.39 square degree field of view. It is a medium resolving power spectrograph, $R = \lambda/\Delta\lambda = 11\ 500$, with a 27 nm wavelength range in the near-infrared: [847,874] nm. The RVS focal plane is located on the edge of the Gaia focal plane (all the instruments share the same focal plane) and, as the other instruments, it is illuminated by the 2 Gaia telescopes. The RVS focal plane is paved with 12 red-enhanced CCDs (3 in the direction of the scan times four in the perpendicular direction). Over the 5 years of the mission, the RVS will observe on average 40 times each source (times 3 CCDs along the scan direction, for an average number of 120 spectra over the mission). The exposure time per CCD is 4.42 s, leading to an average total exposure time of $\sim$530 s.

In late type stars, the strongest features in the RVS wavelength range is the ionised Calcium triplet. Several weak lines of e.g. Iron, Titanium or Magnesium are also present. In early type stars, the dominant lines are Hydrogen lines from the end of the Paschen series. The domain also contains weak lines, e.g. the Calcium triplet that has strongly decreased in intensity, ionised Iron, Nitrogen or Neon. The RVS domain also contains a Diffuse Interstellar Band, DIB, located at 862 nm, which unlike many DIBs seems to correlate reliably with the $B - V$ excess (Munari et al. 2008) and therefore can be used to map the interstellar reddening. Figure 1 presents 2 examples of synthetic spectra, convolved to the RVS resolving power, for a G5 (left) and a B5 (right) main sequence stars.

The full Gaia focal plane is made of 102 "science-CCDs" (of 8.847 mega-pixels each) for a total of about 902 mega-pixels. The CCDs are operated in Time Delay Integration (TDI) mode, i.e. the charges are continuously

[1] Observatory of Paris, GEPI, UMR8111

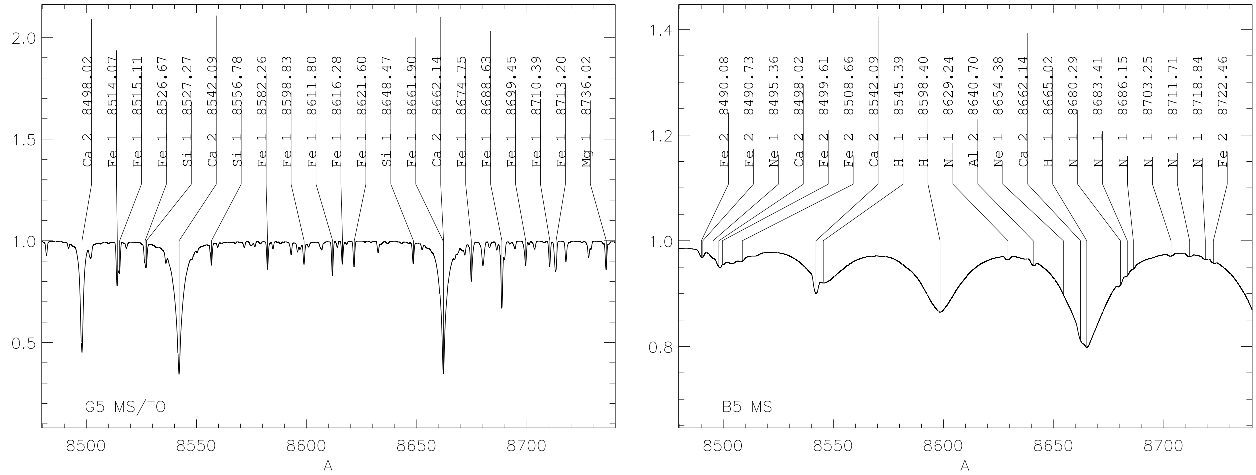

Fig. 1. Synthetic spectra of a G5 (left) and B5 (right) main sequence stars in the RVS wavelength range. The two spectra have been convolved to the RVS resolving power. The main lines are identified.

transferred through CCD columns in order to follow the sources as they cross the field of view. The antenna bandwidth is too restricted to allow for continuously transmitting the full focal plane (almost 1 billion pixels) from the second Lagrange point (at 1.5 millions kilo-meters from the Earth), where the satellite will be located. Instead, astrophysical sources are detected by the on-board software in real-time and "windows" are allocated around the objects that should be transmitted to the ground. The RVS windows are 1260 pixels long (in the spectral dispersion direction, which is also the scan direction) and 10 pixels high (in the direction perpendicular to the dispersion). Inside a window, different samplings are used depending on the magnitude of the target: the brightest sources $6 \leq V \leq 8$ are transmitted in 2D full resolution, the intermediate brightness sources $8 \leq V \leq 11$ are collapsed to 1D (i.e. summed over the spatial dimension) before reading and the faintest sources $11 \leq V \leq 17$-18 are both collapsed in the spatial dimension and binned by group of 3 pixels in the spectral direction, in order to limit both the telemetry load and the readout noise.

There is a maximum number of windows that can be allocated at any given time. As a consequence, in dense areas, the RVS will be limited to observe the 36 000 brightest sources per square degrees. In the case of, e.g. the Baade's window, this surface density translates into a limiting magnitude for the RVS of V$\sim$13-14.

3 RVS performances

Table 1 summarises the RVS performance. The left part presents the signal to noise ratio expected for a G2V star as a function of V magnitude for (i) a single transit and (ii) at the end of the mission when all the observations will be combined. At the faint end, even the total signal collected is small and it will be possible to extract the radial velocities only from the combined information and not from a single spectrum.
The central part shows the limiting magnitude of the RVS for the different parameters that will be extracted from its spectra. The cumulative numbers of stars down to the respective limiting magnitudes are provided in the next column. It should be noted that for the atmospheric parameters and interstellar reddening, the limiting magnitudes provided in the table correspond to the limits where spectro-photometry and RVS data can be jointly used to constrain these parameters. At fainter magnitude, the spectro-photometer will still provide estimates of the atmospheric parameters and mean metallicity (with a precision of 0.2 to 0.4 dex for stars brighter than V=16 and 0.5 to 0.7 dex around V=18).
The right part recalls the specifications for the radial velocity precisions as defined in the "Gaia Mission Requirement Document - MRD" (ESA, 2006), which contains all the scientific specifications for the Gaia mission. The acronym MP stands for metal-poor and corresponds here to $[Fe/H] = -1.5$ dex.

Table 1. Summary of the RVS performance. Left: Signal to noise ratio for a G2V star as a function of magnitude, for 1 transit and for the total mission. Centre: Limiting magnitudes (and the corresponding cumulative numbers of sources) for the different parameters that will be derived from RVS spectra. Right: Radial velocity performance specifications (MP stands for metal-poor, i.e. here $[Fe/H] = -1.5$ dex).

V	S/N (per transit)	S/N (full mission)
6	150	1000
10	20	150
12	8	50
14	2	10
16		2

Parameters	V_{lim}	N stars
Vr	17-18	150-300 10^6
v sin i	13	5 10^6
Teff logg	13	5 10^6
$[Fe/H]$	13	5 10^6
$[X/Fe]$	12	2 10^6
E(B-V)	13	5 10^6

Spectral type	V	Vr (km/s)
B1V	7	1
B1V	12	15
G2V	13	1
G2V	16.5	15
K1IIIMP	13.5	1
K1IIIMP	17	15

4 Synergies with ground-based spectroscopic surveys

4.1 *Gaia and RVS boundaries*

The modern multiplex spectrograph technology allows ground-based surveys to complement Gaia and the RVS in the areas were they show limitations:

- In dense areas (such as the Galactic disk and bulge), the RVS will be limited to the 36 000 brightest stars per square degrees.
- The radial velocity precision in the magnitude range [15,17] is modest, e.g. ≥ 5 km.s^{-1} for a G5V star.
- In the faint Gaia magnitude range, i.e. about [17,20], the RVS will provide no radial velocities.
- For stars fainter than about 12-13, the mean metallicities provided by Gaia will have a relatively modest precision, i.e. 0.2 to 0.4 dex down to V=16 and about 0.5 to 0.7 dex at V=18.
- Individual abundances will be available only for the 2 millions brightest stars down to V=12.

4.2 *Kinematical synergies*

The ground based spectroscopic surveys will complement Gaia kinematics in several ways:

- The LAMOST-LEGUE (Cui, 2009) survey (2.5 millions stars over the magnitude range $17 < g < 20$ in the northern hemisphere) and SEGUE (Yanny et al. 2009) survey (240 000 stars in the magnitude range $14 < g < 20$) will provide radial velocities for stars that are too faint to be observed by the RVS and down to the Gaia limiting magnitude.
- RAVE (Zwitter et al. 2008 - several fields in the Galactic plane), APOGEE (Allende-Prieto et al. 2008 - 100 000 stars in the disk and bulge) or WINERED (Tsujimoto et al. 2008 - 1 million stars) will observe in dense areas of the sky, where the RVS observations will be affected by the overlapping with neighbouring sources and by the limitation to the 36 000 brightest stars per square degrees.

4.3 *Chemical synergies*

Ground-based spectroscopic surveys will also complement Gaia in the study of the chemistry of the Galaxy:

- With higher resolving powers, WINERED ($R = \lambda/\Delta\lambda = 100\ 000$), HERMES (R=30 000) and APOGEE (R=20 000) will provide finer spectroscopic information.
- With larger and/or complementary wavelength range, ground based surveys will allow to both refine the precisions on the measured abundances and to measure additional species. This is the case for WINERED ([0.9,1.35] μm), APOGEE ([1.52,1.69] μm) or HERMES ([370,950] nm).

- HERMES (1.2 millions stars in the southern hemisphere down to $V < 14 - 15$) and APOGEE ($H < 13.5$) will provide abundances 2 to 3 magnitudes fainter than the RVS.
- WINERED (bulge) and APOGEE (disk/bulge) will provide abundances in dense areas (where the RVS will be affected by the crowding and restricted to the 36 000 brightest stars per square degrees).

5 A need for additional complementary surveys

With several surveys showing clear synergies with Gaia (in particular LAMOST and SEGUE for the kinematic and HERMES for the chemistry), one can wonder whether additional complementary surveys are needed to support Gaia? A lot of activity, meetings, thinking, studies have taken place over the last two years, to answer this question: e.g. ESO-ESA working group on Galactic populations, chemistry and dynamics (Turon et al. 2008), the Nice (http://www.oca.eu/rousset/GaiaSpectro) and ESO (http://www.eso.org/sci/meetings/ssw2009/index.html) meetings.

From these reflexions, it appears that (at least) two additional instruments would be extremely valuable in support to Gaia:

- For the radial velocities, a LAMOST-like instrument, but located in the southern hemisphere: a low resolving power (R∼5 000), a large field of view (1 or several square degrees) a high multiplexing (1000 or more fibbers). A wavelength range in the infra-red would help observing in absorbded areas. This instrument would aim to observe stars in the magnitude range $16 < V < 20$ with a precision of 1 to a few (i.e. better than 5) km.s^{-1}.
- For the chemistry, an HERMES-like instrument, but located in the northern hemisphere: a high resolving power ($20\ 000 < R < 40\ 000$), a field of view of the order of 1 square degree, a high multiplexing (about 500 fibbers). The wavelength range should allow for the full characterisation of the targets (i.e. derivation of effective temperature, surface gravity, micro-turbulence and mean metallicity) and for the derivation of the abundances of the key chemical species for the study of the Milk-Way chemical history. The aim of this instrument would be to observe about 1 million stars down to magnitude V∼ 16.

Over the last 2 years, a lot of people have worked on defining the best ground-based strategy to support Gaia's science case. This presentation incorporates many of their ideas presented in documents, meetings or e-mail discussions. I would like to thanks the actors of these discussions, in particular F. Arenou, C. Babusiaux, O. Bienaymé, P. Bonifacio, A. Gómez, M. Haywood, V. Hill, A. Recio-Blanco, A. Robin, F. Royer, A. Siebert, C. Soubiran, F. Thévenin and C. Turon.

References

Allende-Prieto, C., Majewski, S.R., Schiavon, R., Cunha, K., Frinchaboy, P. et al. 2008, AN, 329, 1018

Cui, X., 2009, AAS, 21322601

ESA, 2006, GAIA-EST-RD-00553

Munari, U., Tomasella, L., Fiorucci, M., Bienaym, O., Binney, J. et al. 2008, A&A, 488, 969

Tsujimoto, T., Kobayashi, N., Yasui, C., Kondo, S., Minami, A. et al. 2008, IAUS, 248, 510

Turon, C., Primas, F., Binney, J., Chiappini, C., Drew, J. et al. 2008, ESA-ESO Working group report n°4

Yanny, B., Rockosi, C., Newberg, H.J., Knapp, G.R., Adelman-McCarthy, J.K. et al. 2009, AJ, 137, 4377

Zwitter, T., Siebert, A., Munari, U., Freeman, K.C., Siviero, A. et al. 2008, AJ, 136, 421

SF2A 2009
M. Heydari-Malayeri, C. Reylé and R. Samadi (eds)

SOME ASPECTS OF STELLAR MODELLING IN THE GAIA TEAM AT THE OBSERVATOIRE DE LA CÔTE D'AZUR

Merle, T.[1], Santoro, L.[1], Pichon, B.[1], Bigot, L.[1], Thévenin, F.[1] and Morel, P.[1]

Abstract. The objective of the Gaia mission (2012) is to provide the largest and most accurate astrometric survey of our Galaxy. From Gaia measurements, information will be derived about the history of our Galaxy, its early formation and its chemical composition. It is therefore of crucial importance to develop and test the methods and tools that will be used in the processing and analysis of the data. The derivation of the chemical abundances will impact on the formulation of the galactic evolutionary models. We present our investigations on –1– NLTE effects on atomic line profiles, the use of 1D or 3D modelling of the atmospheres and –2– radiative diffusion and rotation on stellar evolution models.

1 3D NLTE line formation

We are currently building new accurate and up-to-date atomic models that will be used with different model atmospheres to produce reliable line data to perform the chemical abundance determinations. Tests are performed in the framework of the SAM group which involves different institutes, namely Uppsala, Nice, Meudon, Oslo (Stellar Atmosphere Modelling : `http://www.astro.uu.se/~ulrike/GaiaSAM`).

The atomic models in progress are Ca I, Ca II, Mg I and II. They are important for the chemical evolution of the Galaxy because they are good α–elements tracers. Several studies modelizing Ca lines exist (one of the most recent is Mashonkina et al. 2007), demonstrating the importance of NLTE effects on Ca II IR triplet lines. These lines are essential for the Gaia RVS (Radial Velocity Spectrometer). In this respect, we are performing a very realistic and complete atomic model of Ca I & II. We will use these atomic models together with 3D models of stellar atmospheres to perform full 3D NLTE line synthesis with the code MULTI (Carlsson 1986).

We show on Fig. 1 a comparison between LTE (code MOOG) and NLTE (code MULTI) 1D line synthesis with a MARCS atmospheric model (Gustafsson et al. 2008) of Sun for the 8498 Å line of the CaII IR triplet. The synthetic profiles are compared with the integrated solar flux called FTS (Brault & Neckel 1987). The NLTE treatment fits better the line core of the observed flux than the LTE treatment. The line core cannot be fitted perfectly because of the absence of chromosphere in the MARCS atmospheric model. Indeed, the line core of Ca II triplet is formed in the upper layers of the atmosphere. Moreover, we can note the asymmetry in FTS data due to the convection that can be impossible to reproduce with 1D static atmospheric model.

We are also currently working on 3D models of the Sun and stars to get better fits (asymmetry, line shifts). The 3D approach gives a more realistic interpretation and prediction of the velocity fields in the atmosphere, something that 1D hydrostatic models are incapable of. Indeed, because of their hydrodynamical approach, the 3D models do not need any free parameters such as the macro-, micro- turbulence and mixing-length. The use of these time-dependent, 3D, hydrodynamical atmospheric models to compute stellar abundances has already proven to give significative differences compared with 1D modelling in particular for metal-poor stars and has already led to a significant revision of the solar abundances (Asplund et al. 2005), even if it is still debated (see, for instance, the last review of Aspund et al. 2009).

2 Improvements of stellar evolution models

We are testing the contribution of the rotation on the theoretical evolutionary tracks in the HR diagram for 1D models of stars. As a first application, we follow the work of Lebreton et al. (2001), using the Hyades

[1] Université de Nice Sophia-antipolis, Laboratoire Cassiopée (UMR 6202 du CNRS), Observatoire de la Côte d'Azur, B.P. 4229, 06304 Nice Cedex 4, France

cluster because there are 5 binary stars with estimated masses and the metallicity is well known. Moreover, the projected rotational velocities for the binary systems and for several single stars have been measured by several authors (Glebocki et al. 2000 and Nordstroem et al. 2004). For the binary systems we have an estimate of the rotational velocity V_{rot} and for the other stars we proceed with a statistical inversion approach (Chandrasekhar et al. 1950). The V_{rot} estimate will be used in the code Cesam2k (see `http://www.oca.eu/cesam`) with implemented theory of rotation described in Mathis & Zahn (2004) and the chemical element diffusion. In this manner, we investigate the contribution of these processes for the stellar evolution and their effect on chemical abundances concerning the determination of masses and ages. Now, we can build new theoretical isochrones of the Hyades cluster and determine its age. Several other clusters will be investigated with the same procedure to test the influences of the rotation on stellar age determination with the future Gaia data.

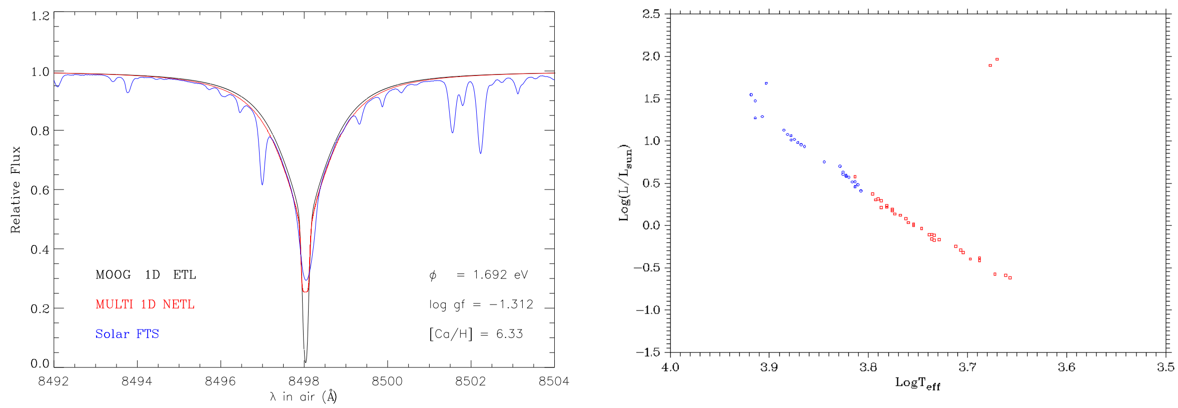

Fig.1. Left: comparison LTE / NLTE of a flux profile of the Ca II line at 8498 Å. Right: HR diagram of Hyades cluster. Red dots represent stars with $V_{rot} \leq 20$ km s^{-1} and blue dots stars with $V_{rot} \geq 20$ km s^{-1}.

3 Conclusion

The use of realistic stellar atmospheres (3D hydrodynamic LTE atmosphere + NLTE radiative transfer with accurate atoms) and stellar evolutions (evolution with radiative diffusion with/without rotation) would provide astrophysical analysis tools for a better determination of stellar parameters which will be of crucial importance for the interpretation of results of the Gaia mission. In particular, it will lead to:
- More realistic stellar abundances which will provide better Galactic abundances;
- Better constraints on ages and masses for the open clusters like the Hyades;
- Calculation of convective lineshifts for Zero-Point Radial velocities with applications to Gaia;
- New limb darkening calculations for stellar interferometry diagnostics providing more accurate stellar diameters using VLTI (Bigot et al. 2006) or the CHARA instruments;

which are the recent works in progress in our group.

References

Asplund, M., Grevesse, N., & Sauval, A.J. 2005, ASP Conference Series, 336, 25

Asplund, M., Grevesse, N., Sauval, A.J., & Scott, P. 2009, ARAA, 47, 481

Bigot, L., Kervella P., Thévenin, F., & Ségransan, D. 2006, A&A, 446, 635

Brault, J., & Neckel, H. 1987, Spectral atlas of solar absolute disc-averaged and disc-center intensity from 3290 to 12510Å, unpublished, available at: `ftp://ftp.hs.uni-hamburg.de/pub/outgoing/FTS-Atlas/`

Carlsson, M. 1986, Uppsala Astronomical Observatory Report, 33

Chandrasekhar, S., & Munch, G. 1950, ApJ, 111, 142

Glebocki, R., Gnacinski, P., & Stawikowski, A. 2000, Acta Astron., 50, 509

Gustafsson, B., Edvardsson, B., Eriksson, K., Jørgensen, U.G., Nordlund, Å, & Plez, B. 2008, A&A, 486, 951

Lebreton, Y., Fernandes, J., & Lejeune, T. 2001, A&A, 374, 540

Mashonkina, L., Korn, A.J., & Przybilla, N. 2007, A&A, 461, 261

Mathis, S., & Zahn, J.P. 2004, A&A, 425, 229

Nordstroem, B., Mayor, M., Andersen, J. et al. 2004, A&A, 418, 989

SF2A 2009
M. Heydari-Malayeri, C. Reylé and R. Samadi (eds)

GAIA RVS DATA REDUCTION : THE 6^{TH} DIMENSION

Meynadier, F.[1], Crifo, F.[1], Katz, D.[1], Thévenin, F.[2], Berthier, J.[5], Bigot, L.[2], Delle Luche, C.[1], Doressoundiram, A.[3], Gomez, A.[1], Guerrier, A.[4], Hestroffer, D.[5], Hubert, A.-M..[1], Jasniewicz, G.[6], Jean-Antoine, A.[4], Ludwig, H.[1], Martayan, C.[1], Nguyen, A.-T.[4], Ocvirk, P.[7], Pichon, B.[2], Royer, F.[1], Sartoretti, P.[1], Siebert, A.[8], Soubiran, C.[9], Turon, C.[1], Veltz, L.[7] and Viala, Y.[1]

Abstract. This poster describes the current organisation of RVS data processing among the Gaia-DPAC (Data Processing & Analysis Consortium), with a particular focus on the French community's contribution.

1 Introduction

The Radial Velocity Spectrometer (RVS) is a slitless spectrometer which will operate in the Gaia satellite. As its name suggests it will, amongst other tasks, determine the radial velocity of a large number of sources (100 to 200 million) : this will give us access to the only component of the star's velocity which can not be determined by astrometry. It has to be noted that measuring radial velocity simultaneously with astrometric and photometric parameters measurements is a significant improvement over Gaia's precursor, the Hipparcos mission.

2 RVS Data reduction within the global GAIA data reduction scheme

The Gaia Data Processing & Analysis Consortium (DPAC) is organised into several coordination units which cover the whole data processing chain. One of these coordination units, CU6, is devoted to the RVS data processing, taking almost raw instrumental data as input. Its output is then directed to the Main Database (which will feed the catalogue) and to other scientific chains for further analysis.

In practice, the CU6 algorithms will be run at the CNES Data Processing Center which will also host CU4 (Object processing) and CU8 (Astrophysical Parameters) software. The CNES is responsible for integrating the software modules written by scientists in Java, and running them on dedicated hardware.

3 Processing chain

The processing chain is divided into 5 packages : Extraction, calibration, radial velocity zero-point, single transit analysis and multiple transits analysis.

The first step is to retrieve pixel blocks, disentangle overlapping objects, remove contaminants and perform appropriate geometric transformations in order to output a cleaned 1D spectrum.

The calibration step is indeed a self-calibration, as there is no internal calibration source. This self-calibration relies on redundant observations throughout the mission.

[1] GEPI–Observatoire de Paris UMR 8111, 5, place Jules Janssen 92195 Meudon cedex
[2] Cassiopée–Observatoire de la Côte d'Azur UMR6202, BP 4229 06304 NICE Cedex 4
[3] LESIA–Observatoire de Paris UMR 8109, 5, place Jules Janssen 92195 Meudon cedex
[4] CNES, 18 avenue Edouard Belin, 31 401 TOULOUSE CEDEX 9
[5] IMCCE–Observatoire de Paris UMR 8028, 77 avenue Denfert-Rochereau, 75014 Paris
[6] GRAAL–UMR5024, Université de Montpellier II, Place Eugène Bataillon - CC 72, 34095 Montpellier Cédex 05 FRANCE
[7] Astrophysikalisches Institut Potsdam, An der Sternwarte 16, D-14482 Potsdam
[8] Observatoire Astronomique de Strasbourg UMR 7550, 11 rue de l'Université 67000 Strasbourg
[9] Laboratoire d'Astrophysique de Bordeaux UMR 5804, 2, rue de l'Observatoire - BP 89 -33270 Floirac

Zero-point determination for radial velocities supposes a wide search for RV standard stars with homogeneous coverage of the sky. This is currently performed by several ground-based observation programmes, which data will be compared to RVS measurements in order to settle the RV zero-point (see poster by Crifo et al., this meeting).

“Single Transit Analysis” (STA) consists in fitting template spectra to the measured spectra, thus determining the source’s radial velocity for each “transit” (meaning “each time the source passes across the focal plane”).

“Multiple Transit Analysis” (MTA) gathers data from STA every 6 months and performs additional analysis (such as variability detection and basic modelling).

4 Scientific objectives

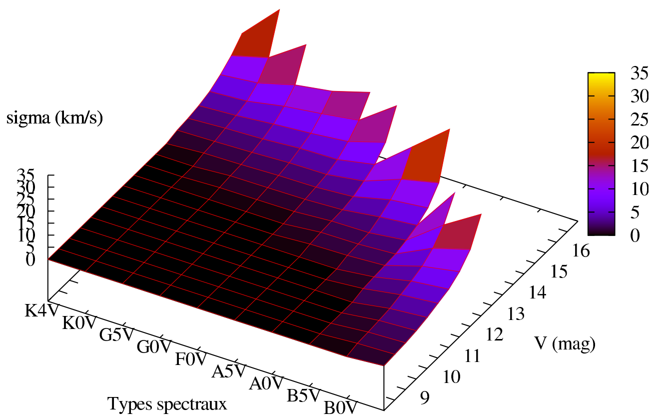

Fig. 1. Uncertainty on RV determination as a function of spectral type and V magnitudes, as derived from RVS performance simulations. This radial velocity survey will cover the whole sky up to 17th magnitude for late type stars, which show the strongest lines in the RVS spectral range. For a given magnitude, RV will therefore be more accurately determined for solar-type stars.

This survey will contribute to our knowledge of the Galaxy’s kinematics and dynamics, but the spectra will also bring some information about effective temperature and surface gravity. Some emission lines will also be detected and will help characterizing B[e] stars or stars with envelopes or accretion discs. Other goals are reachable when analysing RVS data together with photometric data collected by the BP/RP instrument : chemical abundances will be determined for a large number of sources, which will allow to study their distribution and therefore bring insights about the dynamical and chemical of the galaxy, origin of the halo, the search for extremely metal-poor objects, studies of the thick disk. Open questions like the existence of a vertical chemical gradient in the disk may be addressed, and the chemical aspects of stellar associations and streams that Gaia will find will be studied.

5 French involvement

The French astrophysical community is strongly represented in the RVS data processing preparation, in collaboration with (mainly) UK (Mullard Space Science Laboratory) and Belgium (Observatoire Royal, Institut d’Astrophysique et de Géophysique).

David Katz (GEPI–Observatoire de Paris) is the coordinator of this unit, assisted by Mark Cropper (MSSL, UK) and Frédéric Meynadier (GEPI). The first two steps of the processing chain (extraction and calibration) as well as MTA are under MSSL responsibility; zero-point determination is led by Gérard Jasniewicz (GRAAL, Université de Montpellier) and STA is led by Yves Viala (GEPI). Specific CU6 simulations are realised by Paola Sartoretti (GEPI). On CNES side, technical coordinator Anne Jean-Antoine Piccolo and quality insurance manager Anne-Thérèse Nguyen are responsible for integrating and running the software for CU6.

Overall, the 26 persons whose names appear on this poster account for approximatively half of the people working for CU6 across Europe.

SF2A 2009
M. Heydari-Malayeri, C. Reylé and R. Samadi (eds)

GAIA CATALOGUE AND ARCHIVE, PLANS AND STATUS

O'Mullane, W.[1]

Abstract. The Gaia Data Processing and Analysis Consortium (DPAC) has been, and continues to, work on the software for processing the Gaia data. The result will be an unprecedented celestial catalogue of about one thousand million objects with astrometric accuracies far exceeding anything currently available. But little has been heard about the catalogue itself, its availability, content etc. Some work has been done in this area and the status is explained in this short article.

1 Introduction

The Gaia Satellite and its capabilities are covered by de Bruijne (2009). ESA will build, under contract to EADS Astrium, the satellite and launch it from French Guiana aboard a Soyuz in 2012. The Data processing is a community task and the DPAC was officially put in place in 2006 to perform this task. Currently over 300 DPAC members (a DPAC member must work a minimum of 10% on Gaia) are working on the data processing systems. There is also some ESA involvement in DPAC with ESAC contributing to many tasks an leading some. In particular CU1 concerning the overall architecture of the system is led and heavily supported by ESAC. There will also be ESAC involvement in the archive.

When DPAC was made official via an Announcement of Opportunity from ESA in 2006 the catalogue/archive was explicitly excluded. DPAC as agreed in 2006 consists of nine coordination units, the ninth of which was to deal with the archive and to be activated at a later stage. This may entail a further announcement of opportunity but it is a matter for the DPAC Executive and Gaia Science Teams to agree with the Project Scientist.

Hence what we are really discussing here is Coordination Unit 9 (CU9). A first set of requirements (O'Mullane 2009) regarding the Archive has been agreed with DPACE and GST and are discussed below. Some tentative agreements on data releases are included in the document and will be outlined below.

2 Architecture of the archive

Within the DPAC architecture the Gaia Main Database (MDB) will contain all processed data from the satellite. This will be versioned at regular intervals and is the logical starting point for creating the Gaia catalogue as depicted in Figure 1. The catalogue is not however a simple copy of the MDB, it must be more refined and must present a single coherent dataset to the community (no longer divided by coordination unit). Furthermore the MDB is not designed for the type of arbitrary querying or data mining which will be required of the archive.

Figure 1 also shows multiple archives, ESA must have a copy of the archive as ESAC has been designated repository of all space science data for the agency. This does not preclude other copies for institutes who seriously want a copy. The system should be fairly portable.

In general CU9 will be an integral part of DPAC - it could function in no other way. Indeed, as for CU1, some CU9 members will have to come from the existing CUs, of course in many cases this will mean finding additional effort within the CU. For the purposes of discussion the archive is seen as comprising several components as depicted in Figure 2. Some of these are discussed further below. The components are :

- **Ingestor (ING)** to populate the archive.

[1] European Space Astronomy Centre, Madrid, Spain

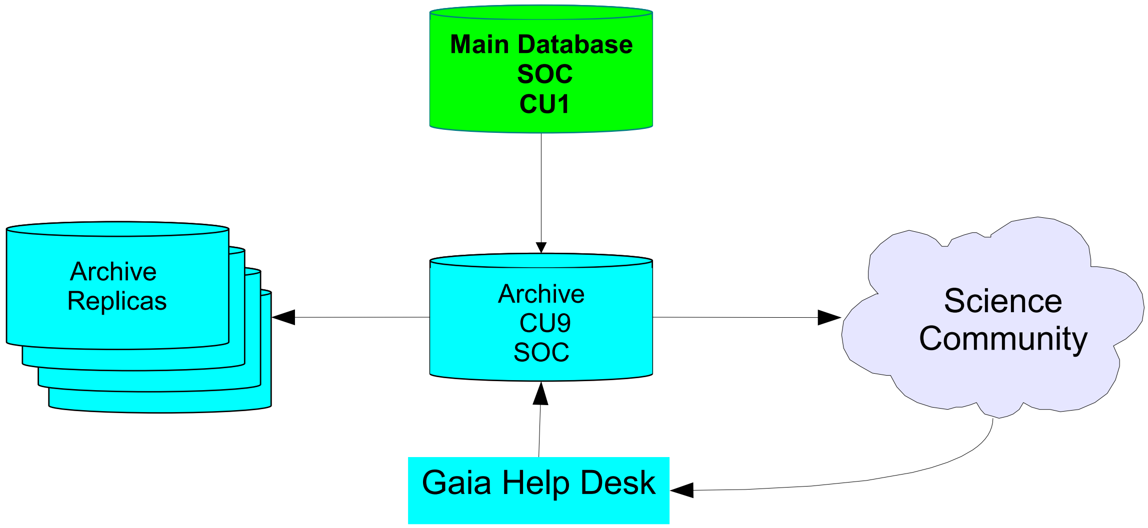

Fig. 1. Context of the Gaia archive. Derived from the Main Database the archive provides an interface to the general community. The possibility for multiple archive copies is also considered.

- **Storage System** Physical disk, machines and DBMS.
- **Interrogation System (ITG)** to effectively query the archive.
- **Advanced Applications (ADV)** for value added access.
- **Documentation (DOC)** to allow users understand the archive.
- **Science Alerts (SAA)** Anomaly based Science Alerting.
- **Public Outreach (PBO)** to engage general public.
- **Help desk (HLP)** to answer users' questions.
- **Community Interface (CIF)** to provide a consolidated portal.

2.1 Community Interface

The general idea is that the archive should have a public oriented feel - no special "professional" site should exist. Rather all come to the same starting point but the professional obviously will dig deeper to a more extensive set of tools and information. Some form of no-login access should be provided with advanced features available with fairly easy self-registration. Many tools should be included in the archive for example; some sort of sky browser - perhaps a customisation of the SDSS Sky Browser (Szalay 2002) or Google Sky. Availability, of at least higher level information, in multiple language of course goes without saying.

2.2 Documentation

Documenting the catalogue will be CU9's most important task. Again much information exists in the document repository of DPAC and the MDB Dictionary Tool but it will need to be made presentable to a general audience and brought up to date. Knowledge of the algorithms will need to be extracted from the various CUs. There should be extensive pre-calculated statistics e.g. source and observation maps, histograms of sources per magnitude bin, spectral type, etc . Additionally some informational plots should be provided e.g. Hertzsprung-Russell diagrams, Hess diagrams, galactic-kinematics diagrams etc. A project history should be provided.

Although undoubtedly too large to print in its entirety some printed volume or volumes would be interesting. Perhaps the source catalogue, without transits and spectra, could be provided on some form of media.

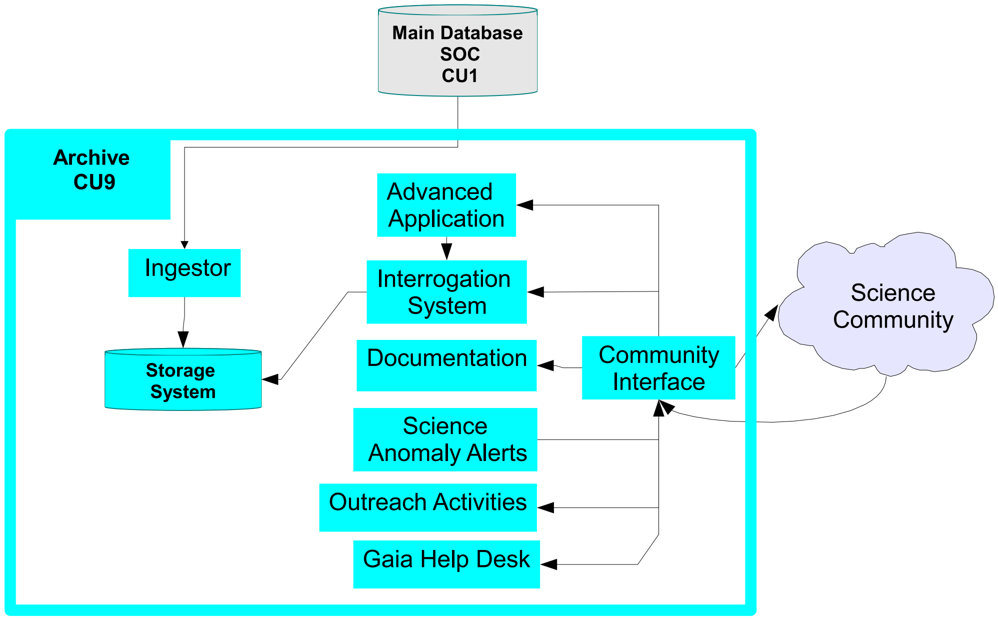

Fig. 2. Gaia archive components. This decomposition was done only to facilitate thinking about the archive, it does not mean CU9 will end up with this exact set of components.

2.3 *Interrogator*

There will be both graphical and programmatic interfaces to the archive. Virtual observatory protocols such as TAP and SIAP shall be implemented. Users will have access to a SQL equivalent and/or ADQL. All of these interfaces require a fast engine to answer queries. Simply putting the data in a Database will not work - it will need to be tuned and will need to make use of spatial indexing techniques such as HTM and HEALPix (O'Mullane 2001). Whatever it is, it needs to be fast !

2.4 *Science Alerts*

From early in the mission, flux based alerts will come from CU5 - these should be VOEvent based. Additionally CU4 are in direct contact with IMCCE to provide NEO orbits as they become available. The archive should contain at least a record of the alerts and possibly a publishing mechanism for alerts coming from other CUs. Currently DPAC is concentrating on data processing - possibly other alerts will arise later. In any case first results coming from Gaia should be available not too long after the nominal mission starts.

3 Schedule

A definitive release schedule has not yet been finalised between GST, DPACE and ESA and depends very much on the data quality from the satellite and the processing systems. The intention is certainly not to wait until 2020 and the *final* catalogue before getting data to the community. It should be possible to provide some form of astrometry and possibly photometry about two years in to the mission. This could be followed in the fifth year by an update, with the final release after eight years as planned. Only the final date is definitive of course but there is agreement to do several other intermediate releases, the Science Management Plan (Gaia Project Scientist 2006) calls for at least one intermediate catalogue release.

Mignard also considers a special release after possibly six months of nominal mission. With the first full sky from Gaia it would be possible to pick out the hundred thousand Hipparcos stars and provide new proper motions for them spanning 21 years and with accuracies of 50 to 100 $\mu as/year$. This is generally seen as desirable.

Technically it is not feasible to have a data release until about eighteen months of nominal mission data have been collected. Allowing for processing time it would be about two years of nominal mission before a reasonable release could be made. One must remember that most of Gaia's calibration involves the data taken by Gaia itself during the mission. Hence CU9 could start after launch which would reduce risk for CU9 of launch delays. It is acknowledged that some work does need to start before that time. GST and DPACE are considering how best to achieve this, (O'Mullane 2009) is a start.

4 Open Areas

There are several open areas which require far more investigation in CU9. The final archive is so far in the future that we should not be bound by our current thinking as to what constitutes an archive.

Brown suggests an attempt at a *living archive* in which new ground based observations could be coupled with Gaia data to improve the source catalogue. This, for example, would allow improved solutions for binaries. The question of allowing additions to the released catalogue is quite tricky, there are issues of quality, security and maintenance. But since a complete printed catalogue is impossible why not a completely new type of archive?

Modelling is also very popular and sophisticated these days. Binney asks how we will be able to compare a model to the Gaia catalogue. Should such a facility be provided ? How would it work? Hogg (Hogg 2008) goes further and suggests archives should be encoded in a model to answer other questions, not just to compare models.

Although virtual observatory protocols will be implemented and the VO provides dynamic cross matching it is felt that perhaps a few major catalogues should be matched. The VO can do no more than give the lowest common denominator - a focused match could provide better results. It may merit including some match tables in the archive.

Szalay has said for many years that with the new surveys we need to bring the processing to the data not the data to the processing. Virtualisation could be an excellent way to do this - one could make a range of virtual machines available *in the archive* for users to install and run their programs on. Then just let them download the result. The local storage provided by CasJobs and VO Space partially does this but the complexity of code which can be sent is limited i.e. for CasJobs one can only send SQL programs. Virtualisation with appropriate access libraries would allow almost any code to be run. This may be the only way to bring fully general models to the data. This obviously has very serious security implications.

5 Conclusion

Coordination Unit 9 (CU9) will be tasked with setting up the Gaia archive. Since most data will not be suitable for public consumption before about two years into the mission, CU9 could start in earnest after launch. Initial ground work would need to be laid in the coming years however. The Gaia archive will be an excellent resource challenging us to rethink our concept of an archive. With Science alerts indeed the first Gaia data will be available before any catalogue is released.

The Gaia Data Processing Consortium Executive and the Science Team Members have provided valuable insights in the production of (O'Mullane 2009) upon which this short article is based.

References

de Bruijne, J., 2009, These Proceedings

Gaia Project Scientist, (ESA/SPC(2006)45).

Hogg, D. W., Lang D., 2008, arXiv:0810.3851v1. Classification and Discovery in Large Astronomical Surveys proceedings.

O'Mullane, W., DPACE, 2009, DPAC Document WOM-033

O'Mullane, W., Banday, A. J., Górski, K. M., Kunszt, P., Szalay, A. S, 2001, Mining the Sky Proceedings

Szalay, A., et al., 2002, ACM SIGMOD 2002 proceedings.

PERSPECTIVES TO SIMULATE GALAXY DYNAMICS

Pfenniger, D.[1]

Abstract. The current practices of modeling the dynamics of galaxies can be projected for the next decade. The exponential growth of computer capabilities has reached a threshold where the particle representation is a superior way to capture subtleties of galactic dynamics than Boltzmann's perfect phase-space fluid representation. The up-to-now often neglected departures of strict symmetries and time invariance of the actual Milky-Way, and the impact on dynamics of stellar physics will need to be modeled in more detail in order to match the observational data and extract more information of it . This will be possible with the coming generation of computers which will allow to represent each individual star of a galaxy. Modeling the interstellar medium will remain a difficult problem for more time though.

1 Introduction

The continuous advances in observational techniques require sometimes to set back and re-examine whether current theoretical methods and assumptions need to be readjusted. The joined exponential growths of the amount of observational data and of the computer capabilities mean that some threshold may be reached beyond which radical changes must be made: this is a typical sign of a scientific "revolution", although this word sounds exaggerated when applied to a specialized field like Galactic astronomy. Indeed, the real major revolution impacting all the society comes from the continuous advances over 60 years of the technologies associated with semi-conductor electronics.

The question we want to address here is whether Galactic astronomy is close to such a threshold. The answer is clearly yes for the period 2010-2020 as argued below.

2 Moore's law

The growth of computing power is a historically unprecedented technological jump, where we have seen about a 30 times performance growth every 10 years over 60 years for electronic components based on semi-conductors. This is commonly called the Moore law, after Gordon E. Moore pointed out (1965) that the transistor density in integrated circuits doubled every year. This growth leads to technological and economical pressure on other technologies like data storage which are incited to follow a similar exponential growth. Almost all the sectors of the society are progressively transformed, including sciences. Most of the progress achieved for example in medicine, or astronomy, follows actually for a substantial part from this technological revolution, which allows pervasive computing.

The other essential aspect of Moore's law is economic. The growth of performance occurs not only in an absolute way, but also on the proportionate decrease of cost for a given performance. This means that a given computational capability is accessible to a larger and larger proportion of laboratories, scientists and people. The performance of the present top super-computers will become easy to afford for average scientists after about 5 to 15 years, and for the general public after 20 to 30 years. For example, a present-day laptop computer is comparable in power to a top high-performance computer of the 80's.

[1] Geneva Observatory, University of Geneva, CH-1290 Versoix, Switzerland

3 Purpose of computer simulations

For sciences dealing with complex problems, like biology, earth-sciences, or astronomy, high performance computing plays the role that mathematics has fulfilled over the last centuries for physics: to provide tools for modeling the studied objects in a controlled and abstracted way. Physics could profit more of the tools of mathematics than other fields because the studied systems are selected to be as simple as possible. In complex fields the simplest systems are already too complicated to be handled by a pen and paper approach. In astronomy, already an isolated star or an isolated galaxy as a whole are too complicated to be described without computers. This is the reason why the understanding of these objects really progressed since the availability of computers.

Modeling with mathematics or computers is invaluable to reduce the apparent complexity of the studied problems to a level which can be grasped with our finite brains. Indeed, understanding a process is reaching a level of mental representation sufficiently intuitive for not requiring any calculation. As an example, practitioners of galaxy simulations can eventually figure out the outcome of particular initial conditions before performing the computation, like "seeing" in advance how the collision of two galaxies will proceed.

Thus computational science plays an increasingly important role in sciences, complementing traditional mathematics with new tools with no earlier counterpart. Once a complex process is understood, i.e., represented in a way manageable by a human brain, it is possible to think about it, and either find applications for applied sciences, or how to progress along the quest of knowledge in fundamental sciences. In astronomy, typically a better understanding allows to steer observations or instrument development in a more efficient, intelligent way than practicing blind search.

4 Change of paradigm

For a long time the best representation of a collisionless stellar system was thought to be Boltzmann's equation without collision term,

$$\partial_t f + \vec{v} \cdot \partial_{\vec{x}} f - \partial_{\vec{x}} \Phi \cdot \partial_{\vec{v}} f = 0, \tag{4.1}$$

where $f(\vec{x}, \vec{v}, t)$ represents the phase space mass density, and $\Phi(\vec{x}, t) = -G \int d^3x' \rho(\vec{x}', t)/|\vec{x} - \vec{x}'|$ is the gravitational potential generated by the spatial density distribution $\rho(\vec{x}, t) = \int d^3v f(\vec{x}, \vec{v}, t)$. This continuous representation of, in reality, a granular mass distribution was made on the model of gas or plasma kinetic where the number of particles is typically of the order of 10^{26}, suggesting to take the limit of an infinite number of particles and to represent the flow of particles as a smooth differentiable flow in phase-space. Note that in gas kinetic the molecule collisions, even if rare, are the essential ingredient making the path of molecules chaotic, rapidly unpredictable, and leading to a smooth f. In stellar dynamics, without collisions the star trajectories may preserve correlations and memory of the past that should lead, a priori, to irregular, non-differentiable f. This point, how and why f should be differentiable, is an open question in stellar and galactic dynamics. A smoothing mechanism is required. A possible candidate is Miller's (1966) exponential N-body system instability, but this remains to be better documented.

In a galaxy made of N stars, N is however never very large as for molecules in a gas container. If we adopt $N = 10^{11}$ and want to discretize phase space in a number of bins, we can have at most N populated bins, that is, at most $N^{1/6} \approx 68$ divisions per phase space coordinate, which is not a very smooth representation of the, in principle, differentiable function f. Actually, with 1 cell per particle the representation is like a sum of delta functions, far from representing a differentiable function; using, say, 100 particles per cell to smooth fluctuations brings down the number of divisions per phase space coordinate to 32: the averaged function is smoother but the bin resolution is then lower.

So the collisionless Boltzmann equation when applied to galaxies has conceptual difficulties to match well the intended systems. In contrast, the N-body model is a much more faithful representation of an ensemble of stars in mutual gravitational interaction. The problem in the past was that the description of the N-body evolution was leading to a unaccessible amount of computations. Contrary to gas kinetics, classical thermodynamics is not applicable to stellar systems since gravitation is a long ranged force, making gravitational systems non-extensive. Extensivity is an essential assumption with usual statistical mechanics. As a result, astronomers have been forced to use numerical simulations to describe self-gravitating systems, which they did as soon as computers became available.

There are several observational constraints which also demand to abandon the idea that a differentiable f is a good way to represent the distribution of stars:

1. The local stellar kinematics obtained from from Hipparcos and other sources (e.g. Dehnen 1998) shows that the velocity distribution of local stars is non-smooth, made of clumps in phase-space. Here we obtain an observational local evidence that f is not well represented by a differentiable function resembling a Maxwellian distribution.

2. Infrared view of the spiral stellar content (e.g. Seigar & James 1998) shows that spiral arms are strong non-linear density perturbations, so that self-gravity is locally not negligible in stellar arms. This raises doubt that axisymmetric static Milky-Way models where spirals are at most weak perturbations in a smooth potential assumptions for describing the stellar motions inside the Milky-Way.

3. Milky-Way CO surveys, such as the one of Dame et al. (2001), show that cold gas distribution is very clumpy and irregular, unlike what would be expected using classical gas dynamics of non-self-gravitating gases. The clumpiness of molecular clouds actually shows the evidence that the gas distribution at least is highly time-dependent at small scale, introducing a "noise" in the global potential. Again molecular clouds are at least partly self-gravitating over a range of scales, which raises doubt about a straight use of thermodynamics in such systems.

4. The stellar halos of the Milky-Way and nearby galaxies has been progressively mapped in sufficient detail (e.g. Ibata et al. 2005) to show a highly intricate structure made of stellar streams and dissolving dwarf galaxies contradicting the classical representation of these halos as virialized, steady structures. If we include in the stellar halo the galaxies orbiting the Milky-Way and also perturbing it, we obtain again another source of time-dependence.

Otherwise there are theoretical evidences that typical galactic potentials must be time-dependent:

1. Sellwood & Sparke (1988) showed first that barred galaxies are surrounded by spiral arms that rotate at one or several pattern speeds, but slower than the bar one. This breaks the time invariance that can be kept in barred galaxies when describing the galaxy in the bar rotating frame of reference. There is no way to avoid therefore time-dependence in barred galaxies with surrounding spiral arms.

2. Fux (1997,1999) could match several of the inner Milky-Way characteristics and fine details in the stellar and gas distribution by running N-body simulations and finding the best location of the Sun in the disk and at a given time in the run. Each of the best fits found is only valid over a very short time, of order of a few 10^6 yr, which means that the model is highly time-dependent with respect to the level of detail of the Milky-Way that we can use for constraining models. It means that if we would observe the Milly Way a few 10^6 yr earlier or later, we would observe substantial differences, especially in the gas distribution.

All these works point to the need to consider the Milky-Way as a time-dependent and non-axisymmetric system. Only self-consistent N-body models can achieve the detail level required by future observational data.

5 Future simulations

Moore's law has brought us today to reach the level where $N \sim 10^{10} - 10^{11}$ particles can be followed in a super-computer. This has been achieved recently in cosmological simulations (Teyssier et al. 2009; Boylan-Kolchin et al. 2009), because cosmological simulations require less integration time steps than typical galaxy simulations. However with the growth of computer power it is clear that the threshold of representing every star, or every star more massive than the Sun, in a Milky-Way type galaxy model is within reach, less than 10 years. The sensible problem of softening then almost disappears. Only in this way can phase space correlations such as streams be studied and compared with observations. At this level star formation and evolution can be followed too, first in simplified ways. Energy and momentum transfer between stars and the interstellar gas is an important aspect of the global dynamics, but also it will be important to follow the stellar mass loss from AGB stars that over several Gyr must have also a dynamical effect on the global galactic structure.

The effects of the environment such as accretion will be more and more taken into account in galaxy models, because from the cosmological context the environment appears as having played an especially important factor in the past, but will continue to impact the evolution of the Milky-Way for the next billions years. For example our version of the Milky-Way/Andromeda merging, is forecast for taking place during the next $\sim 3 - 8$ Gyr. A snapshot of a movie of the whole sky appearance made for educational purpose is shown in Fig. 1.

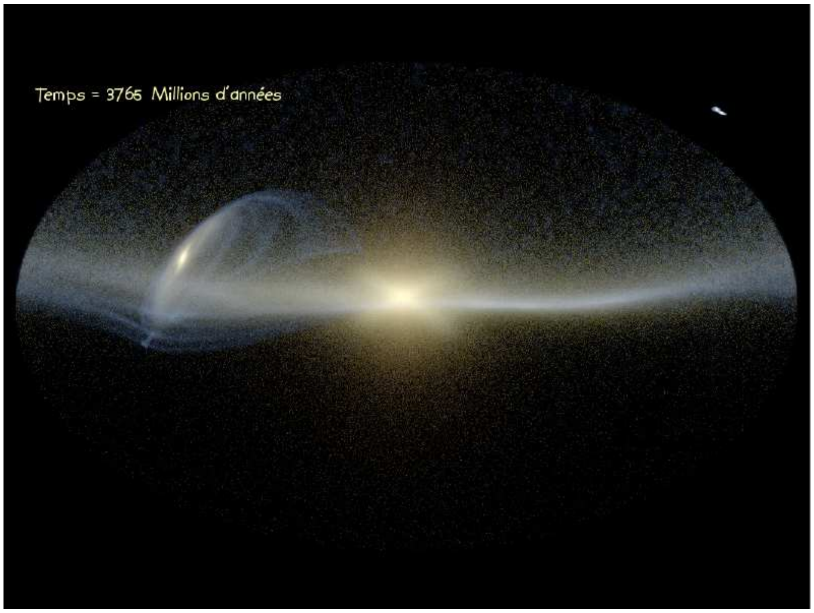

Fig. 1. The whole sky 3765 Myr from now as viewed from the Sun in a $30 \cdot 10^6$ particle simulation of the Milky-Way/Andromeda merging (Revaz & Pfenniger 2010). A drastic change of the Milky-Way appearance will occur illustrating how time-dependence then will still be a relevant property of the Milky-Way.

Interstellar gas dynamics will stay a very hard physical and computational problem though, due to the high dynamical and time ranges taking place in the interstellar medium. Springel (2009) using computational geometry methods (Voronoi cell spatial decomposition and finite volume scheme preserving flow invariants) has showed how to solve several pending problems in traditional Eulerian and Lagrangian hydrodynamical simulations. His scheme seems promising and removes in an elegant way shortcomings of both the Eulerian and Lagrangian approaches, at the expense of a larger software complexity.

In addition, the physics of the interstellar medium, and in particular of dust grains, is crucial for representing correctly cooling, chemistry and radiation transfer in the Galaxy. Presently the main barrier is more understanding the basic physics at play rather than modeling it on the computer. This is certainly an aspect that will need much more time than global dynamics for being mastered.

6 Conclusion

At the level of precision reached by present and future instruments, disk galaxies must be seen as time-dependent structures with multiple patterns rotating at different speeds. Modeling the optical part of the Milky-Way with N-body models containing as much particles as stars is feasible during the next decade. However gas and dust modeling will remain a difficult, not to underestimate problem for a longer time.

References

Boylan-Kolchin, M., Springel, V., White, S. D. M., Jenkins, A., Lemson, G. 2009, MNRAS 398, 1150

Dame, T. M., Hartmann, D., Thaddeus, P. 2001, ApJ, 547, 792

Dehnen, W. 1998, Astron. J., 115, 2384

Fux, R. 1997, Astron. Astrophys., 327, 983; 1999, Astron. Astrophys., 345, 787

Ibata, R., Chapman, S., Ferguson, A. M. N., Lewis, G., Irwin, M., Tanvir, N. 2005, ApJ, 634, 287

Miller, R.H. 1966, ApJ, 146, 123

Moore, G.E. 1965, Electronics, 38, 114

Revaz, Y., Pfenniger, D. 2010, in preparation

Seigar, M. S., James, P. A. 1998, MNRAS, 299, 685

Sellwood, J. A., Sparke, L. S. 1988, MNRAS, 231, 25S

Springel, V. 2009, submitted to MNRAS (arXiv:0901.4107)

Teyssier, R., Pires, S., Prunet, S., Aubert, D., Pichon, C., et al. 2009, Astron. Astrophys., 497, 335

SF2A 2009
M. Heydari-Malayeri, C. Reylé and R. Samadi (eds)

DETERMINATION OF PLANETARY SYSTEMS WITH GAIA

Rambaux, N.[1], Couedtic, J.[1], Laskar, J.[1] and Sozzetti, A.[2]

Abstract. The astrometric performance of Gaia will allow to discover thousands of extrasolar planets. This work especially focuses on the detection of multiple-planet systems subject to strong gravitational interactions, for which the assumption of independent Keplerian orbits breaks down. We present the first results obtained by using a Bayesian approach to fit the numerous parameters of the systems.

1 Introduction

The astrometric performance of Gaia (few μas) will allow to discover thousands of extrasolar planets (Sozzetti et al. 2007; Casertano etal 2008). Therefore, in these papers it is shown that Gaia might detect massive planets (Mp 2-3 MJupiter) at an orbital distance from 1 to 4 AU.

In this large sampling of extrasolar planets, Gaia will detect systems with multiple companions and some of them will present complex dynamics through strong gravitational interactions and/or resonant orbits. For these systems independent Keplerian orbits break down. This work focuses on the detection of multiple-planet systems subject to strong gravitational interactions. We present the first results obtained by using a Bayesian approach in order to fit the numerous parameters of the planetary systems.

2 Model and Bayesian approach

We study perturbations induced by planetary companions on the barycentric motion of the star in the astrometric data. Therefore the astrometric signature for one planet is

$$\alpha = \frac{a_p}{d}\frac{M_{pl}}{M_\star} \tag{2.1}$$

where, M_p, $M_\star$ are masses of the planet and star, a_p semi-major axis of the orbit and d distance Earth-Extrasolar system.

The number of parameters to fit in this problem is 7 times the number of planets, where the 7 variables are the semi-major axis (or log(Period)), eccentricity, inclination, ascending node, argument of periastron, mean anomaly, and planetary mass.

Ford (2005), Ford etal (2005), and Gregory (2007) applied successfully the Bayesian approach to radial velocity measurements. Following these works we develop a Bayesian model to fit multi-planetary systems to Gaia astrometic data. Indeed, the Bayesian method is well designed to explore efficiently the parameter space and to avoid local minima inherent to Levenberg-Marquardt method or high number of iteration as in Genetic Algorithms (see discussion in Ford 2005). We use a Markov Chain Monte Carlo (MCMC) technique in order to compute the probability functions that is well suited for high-dimensional parameter spaces. The orbital problem is solved by numerical integration of the N-body problem in order to take into account the mutual interactions. Figure 1(a) is a simulation that illustrates the behavior of one (very short) Markov Chain and Figure 1(b) shows the corresponding probability distribution for the eccentricity. In this optimistic case the MCMC method converges towards the expected orbital values.

---

[1] University Pierre et Marie Curie - Paris 6; IMCCE, Observatoire de Paris, CNRS UMR 8028
[2] INAF-Osservatorio Astronomioco di Torino, Pino Torinese, Italy

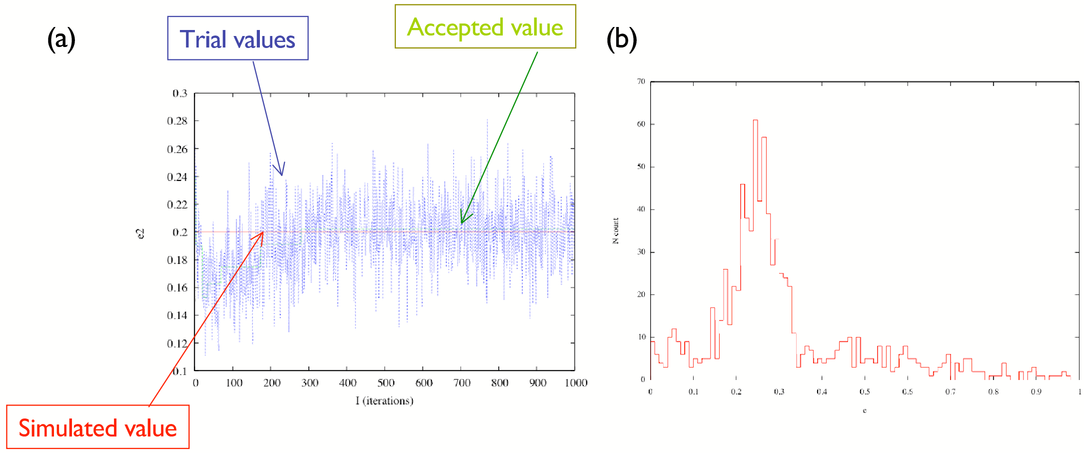

Fig. 1. (a) Example of Markov Chain (in practice the chain is around 10^5 iterations). (b) Probability distribution for the eccentricity.

We carry on to improve the model and to test the convergence process for various scenarios of orbital configuration. The first main difficulty in the Gaia framework is to develop an automatic scheme. Indeed, the efficiency of the Markov Chain depends on the correct ratio of rejected/accepted trial in order to sample well the parameter space (and to find the global minimum) in a relatively short computer-time. The second point is to introduce the Gelman-Rubin criteria in order to decide the convergence of the chain. The main challenge for the Gaia module is to obtain an automatic and efficient algorithm for measurements and at the same time an algorithm robust enough to avoid false detections.

3 Stability Criteria

In order to obtain realistic orbital parameters, we check the fit with stability criteria. One possibility is to use analytical (i.e. fast) stability criteria such as the Hill criterion (Marchall and Bozis 1982; Barnes and Greenberg 2007):

$$-\frac{2M}{G^2 M_*^3} c^2 h > 1 + 3^{4/3} \frac{m_1 m_2}{m_3^{2/3}(m_1+m_2)^{4/3}} - \frac{m_1 m_2 (11 m_1 + 7 m_2)}{3 m_3 (m_1+m_2)^2} \tag{3.1}$$

where M is the total mass of the system, m_1 is the mass of the more massive planet, m_2 is the mass of the less massive planet, m_3 is the mass of the star, G is the gravitational constant, $M_* = m_1 m_2 + m_1 m_3 + m_1 m_2$, c is the total angular momentum of the system, and h is the energy.

Nevertheless, this criteria is not efficient for resonant orbits or more than 3-body problem. Other criteria are studied as for example the chaotic diffusion of orbits.

This work inscribes in the module CU4-DU437 of Gaia. Its objective is dedicated to the search of the stability of the extrasolar planets and to characterize the existence of planetary companions (N2) with strong mutual interactions.

References

Casertano, S., et al. 2008, Astronomy & Astrophysics 482, 699
Sozzetti et al. 2007, in Exoplanets: Detection, Formation, and Dynamics, Proceedings IAU Symposium No. 249,
Gregory, P. C. 2007, MNRAS, 374, 1321
Ford, Lystad, & Rasio 2005, Nature, 434, 873;
Ford, E.B. 2005, The Astronomical Journal, 129, 1706
Marchall & Bozis 1982, Celestial Mechanics, 26, 311
Gladman 1993, Icarus, 106, 247.
Barnes & Greenberg 2007, The Astrophysical Journal, 665: L67L70

SF2A 2009
M. Heydari-Malayeri, C. Reylé and R. Samadi (eds)

MULTIOBJECT SPECTROSCOPY AS COMPLEMENT FOR GAIA

Recio-Blanco, A., Hill, V.[1] and Bienaymé, O.[2]

Abstract. The Gaia mission will have an unprecedent impact on our knowledge of the Milky Way by unveiling populations through the study of chemistry and dynamics. It will open new horizons that, nevertheless, will need to be completed with specific surveys of Galactic Archaeology. An analysis of those needs for the different Galactic stellar populations has recently been carried out during a workshop gathering the French community involved in Galactic Archeology and stellar physics. The outcome of this meeting regarding the needs for ground-based spectroscopic surveys as a complement to Gaia, placed in the context of present and future surveys, is presented here.

1 Introduction

Gaia is a pioneering ESA astronomy mission set to revolutionise our view of the Galaxy with a precise and detailed stereoscopic survey of the billion brightest celestial objects. High-accuracy astrometry will allow Gaia to exactly pinpoint the position of a star and to measure its movement across the sky, whilst spectroscopic measurements will allow the radial velocity to be determined. Gaia will also gather photometric data, measuring the brightness of a star in a few dozen colours. This array of data will reveal a moving, three-dimensional Milky Way map of unprecedented scope and precision, as well as providing profiles of the physical properties of each star, including luminosity, surface gravity, temperature and elemental composition. The Gaia satellite will be launched Spring 2012.

Gaia will provide accurate estimates of a range of key parameters, however, the Gaia Radial Velocity Spectrometer (RVS) indeed has a higher limiting magnitude than the astrometric instrument (g$\sim$ 14 to 16.5 vs. 20) and a very limited spectral coverage hampering the chemical analysis of the stars. During the Nice workshop, supported by the AS Gaia, (19-20 February 2009; http://www.oca.eu/rousset/GaiaSpectro/), the needs of complementary spectroscopic observations were examined at the light of the Gaia inpact on our knowledge of the different Galactic populations. The workshop gathered 23 participants, and was specifically timed to trigger thoughts about such complements in the french community, in time to participate the ESO Spectroscopic Survey Workshop (http://www.eso.org/sci/meetings/ssw2009), where we presented the conclusions[1] of our meeting. The context of other present and future surveys has also been taken into account.

2 The context of future surveys

On the observational front, the international scene is evolving fast. Very wide (or all-sky) multi-band photometric (SDSS, 2MASS), have flourished, allowing to probe the Milky-Way populations (especially the halo) to a depth (and homogeneity) that had never been reached before. One striking example concerns the recent tomography of the Milky Way halo from SDSS down to magnitudes of g$\sim$22 by Juric et al. (2008) or Ivezic et al. (2008), providing strong constraints on stellar densities associated with the discs and halo, as well as rough but very large scale metallicity maps that are challenging our views of the thick disc formation. Large spectroscopic surveys (SDSS including SEGUE; RAVE) are also on the way, promising to unravel the chemo-dynamics of Galactic stellar populations. Both these surveys are based on low-resolution spectra (R$\sim$2000 for

[1] Laboratoire Cassiopée, Univ. de Nice Sophia-Antipolis, CNRS, Observatoire de la Côte d'Azur, Nice, France
[2] Université de Strasbourg, CNRS, Observatoire Astronomique, France

[1]http://www.eso.org/sci/meetings/ssw2009/presentations/RecioBlanco.pdf

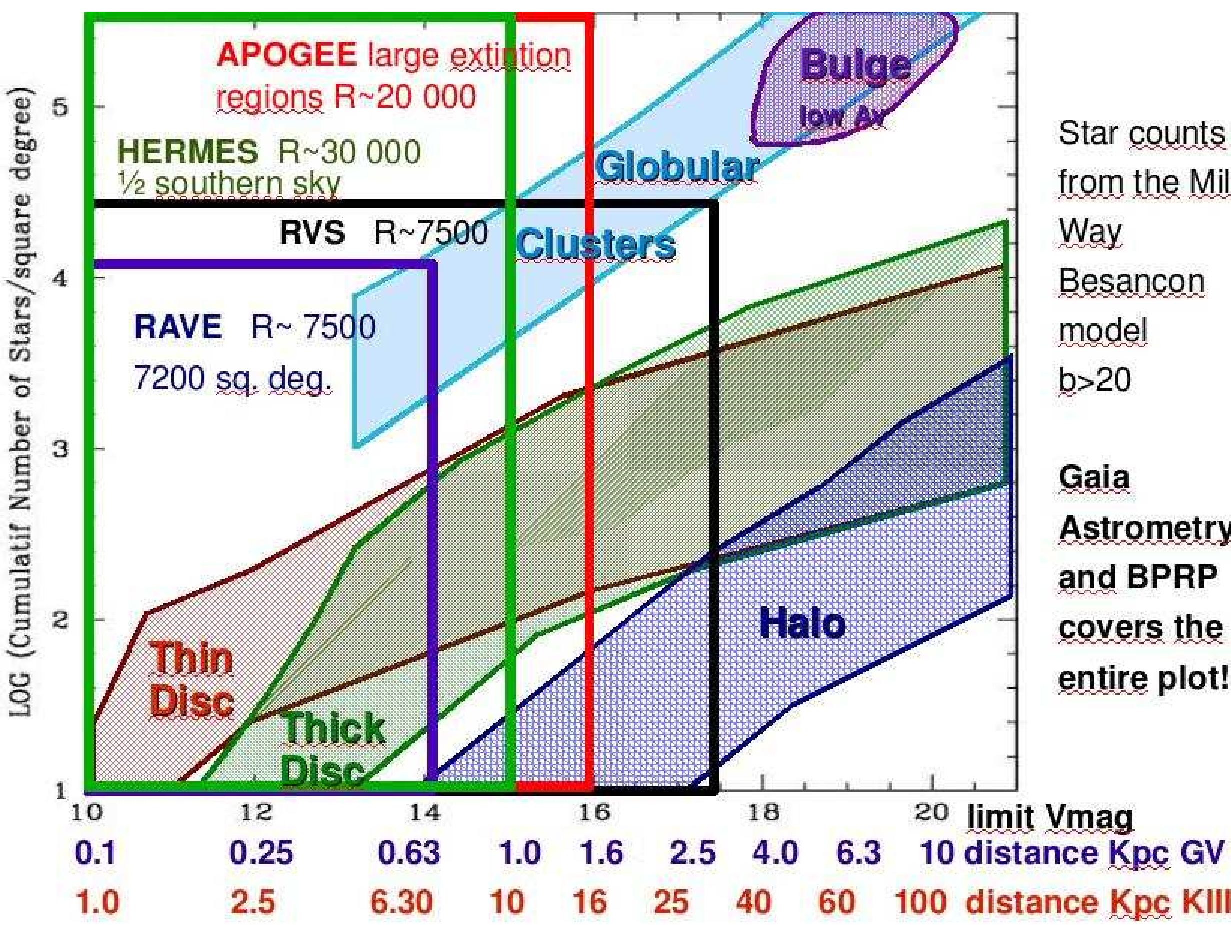

Fig. 1. Plot of the number density and locus of different components of the Milky Way v. V magnitude and equivalent distance for two spectral types as relevant to the follow-up of stars from Gaia. Stellar densities were computed using the Besancon model (Robin et al. 2003) for lattitudes of b>20. The magnitude limits of some other spectroscopic surveys are indicated for comparison, and their resolution and total area coverage are are noted. [note: the various y-axis location of these surveys are meerly for lisibility and do not correspond to any real stellar density.]

SDSS and 7500 for RAVE), and will provide radial velocities (to ∼5-10 km/s and 2km/s accuracy resp.) as well as stellar parameters and a global metallicity indicator for gigantic numbers of stars (around 240000 and ∼80000 respectively). These two major surveys are complementary in that the SDSS is much deeper (g∼20) and probes mostly the galactic halo and thick disc, while RAVE is restricted to a much smaller volume (limited to I=13) and therefore probes best the thin and thick discs. Future stellar surveys at the 2014 horizon include low-resolution surveys such as SEGUE II (part of SDSSIII), LAMOST, but also a new generation of surveys based on higher resolution spectra (R∼20000 or more) such as APOGEE (part of SDSSIII, dedicated to the Galactic plane in IR), WFMOS (GEMINI-Subaru project), or HERMES (R∼30000, V<14, covering one half of the southern sky).

Figure 1 is a plot of the stellar number density and locus of different components of the Milky Way vs. V magnitude and equivalent distance. Two spectral types as relevant to the follow-up of stars from Gaia are considered. The star counts have been taken from the Besancon model for a Galactic latitude b>20. The locus of most of the previously mentioned spectroscopic surveys is shown. The Gaia astrometry and spectrophotometric data will cover the entire plot. It can be seen that there is lack of a high resolution survey *in the north* for stars with V<16, that is, stars that will have good geometric distances and kinematics from the Gaia observations. On the other hand, no high or low resolution surveys are planed for the fainter stars, for which Gaia will furnish neither the radial velocity nor the precise chemical information. This opens two different pathways for the Gaia complementary observations.

3 Science cases

During the workshop, the science cases concerning the different Milky Way and dwarf galaxies populations were examined. The impact of the Gaia mission, but also the information that will not be provided by Gaia were taken into account.

Concerning the Milky Way Thin disc, Gaia will provide, for the first time, disc evolution constraints as a funtion of stellar absolute ages. In particular, the star formation rate over several kiloparsecs will test the inside-out formation scenario. In addition, the infall evolution will be constrained by the chemical abundances evolution with age. For all those purposes, an improvement of the Gaia atmospheric parameters for stars fainter than V=16 (with no RVS measurements) will be necessary to get good age estimations. Moreover, a spectroscopic survey allowing to refine the chemical abundance information for those faint stars (the Gaia spectrophotometry will only give an estimation of the star's global metallicity) would allow the identification of kinematic groups, the study of the Thin Disc structure and constrain the existence of a radial mixing.

Regarding the Thick Disc, Gaia will allow its characterization far from the solar neighbourhood and the detection of accretion events and inhomogeneities. Nevertheless, a complement of the Gaia radial velocity and chemical abundance measurements for faint stars will be necessary. This will permit, in particular, to constrain the radial and vertical chemical and velocity gradients, the scale-heigh variation with Galacticentric distance and che chemical evolution.

The view that Gaia will provide of the Galactic Bulge has been recently been analysed by Reylé et al. (2009), and turns out to be quite partial, owing to the combination of extinction on the line of sight and crowding. Complementary measurements of radial velocity and chemical abundances for faint stars and a larger (l,b) coverage are mandatory for a better constraint of the the Bulge formation scenario, the star formation history and the impact on disc chemical evolution and dynamics as well as for the search for matter accretion traces. Because the Bulge is heavily redened in most regions, spectroscopic measurements will be best suited in the infrared.

The external regions of Galactic globular clusters will be observed by Gaia, that will provide the parallaxes of several thousands to several tens of stars (depending on the distance and the cluster concentration). On the contrary, the RVS, due to its lowest density limit will only observe for a subsample of the clusters, several hundreds to some tens of stars. A complement of the Gaia radial velocity measurements is necessary to improve the impact of Gaia on the study of the Globular cluster's internal dynamics. On the other hand, possible new clusters will be identified by the Gaia survey, and follow up observations constraining radial velocitys and chemical abundances will be needed. Similar complementary data will be necessary to improve the scientific exploitation of Gaia measurements in the Halo, including the nearby satellites of the Milky-Way. In particular, the refinement of the Halo substructure, with an estimate of the fraction of accreted stars, and a comparison of the field Halo population and the Milky Way dwarf galaxies will require additional radial velocity and chemical abundance measurements for faint stars. In this case, a wide field of view (>1-2 square degrees) is necessary for dedicated Halo observations, due to the low stellar density.

4 Conclusions - Recommandations

Based on these science cases, two basic recommandations can be made for large public surveys to complement the Gaia database for studies of the Galactic structure, kinematics and stellar populations.

- **A high-resolution follow-up of the relatively bright objects in Gaia (V<16-17)** This survey would aim at characterizing in detail the chemical composition of the stars for which Gaia will provide exquisite 3D kinematics. This will in turn provide direct information to complement kinematics in identify stellar populations, to identify their origins and formation mode(s). The resolution needed to obtain detailed chemical information is of a minimum of R=20000-40000. The scientific cases that will mostly benefit from such a survey are the understanding of the thin and thick disk outside of the solar neighborhood (including their radial, azimuthal and vertical structures, aswell as origin), aswell as the identification of stellar streams in these components. This survey would overlap partly with the current HERMES project, although aiming at deeper observations (typically 1-2 magnitudes deeper). It would therefore be best suited for the northern hemisphere where it would then be complementary to HERMES.

The Galactic halo at these magnitudes is still rather scare (probed mostly by giants), and would benefit most from a deeper survey (down to V of 19), in selected sky regions (requiring a 10m-class telescope).

The Galactic Bulge is heavily reddened and therefore calls for a specific survey in the infrared. The currently planned APOGEE survey (part of the SDSS-III surveys) will partly cover this area (having ideal resolutions and wavelength coverage), but being located in the Northern hemisphere, its visibility of the Bulge will be rather poor, leaving space for a similar survey from a southern 4m-class telescope.

• **A medium-resolution survey of faint stars in Gaia (17<V<20):** This survey would aim at aquiring the third velocity vector (radial velocities), in the magnitude range where it is unreachable with the onboard Radial Velocity Spectrograph (RVS), thereby complementing the transverse motions of Gaia to obtain 3D kinematics for a large fraction of the Gaia catalogue in this magnitude range. Aiming at a minimum resolution of R=5000 insure simultaneously that the radial velocity accuracy is of the order of 2-3km/s, sufficient to resolve cool kinematical streams (including dissolving globular clusters), and a robust estimate of the stellar metallicity. This survey, one magnitude deeper than the SDSS & SEGUE and twice its resolution, is mainly aimed at unravelling the structure and assembly history of the galactic halo, in particular detecting streams and substructures in the halo (out to 100kpc).

• **Need for single-object high-resolution spectrographs:** In addition to these large surveys, Gaia will also call for high-spectral resolution (or even extremely high resolution R>80000-100000) follow up of a limited number of object (hence with extremely low densities on the sky). For example, among others, exquisite chemical abundances and rotationnal velocities, are needed for a whealth of fundamental stellar physics issues that Gaia will adress, ranging from non-standard mixing and diffusion in stars, angular momentum evolution, nucleosynthesis, etc... For these follow-up, the Gaia stellar community will need access to high-resolution echelle spectrographs on 2-30m telescopes.

Resolution	FOV deg^2	Multiplex fibers/deg^2	λ Coverage Å	$\Delta\lambda$ Å(in one shot)	V mag	Total area
20000−40000	0.25 (1 for Halo)	250-1000	3700-12000	> 500	<16-17	Wide
20000−40000	0.25 (1 for Halo)	250-1000	3700-12000	> 500	17-20	Selected regions
> 20000	0.25	1000	J-H bands	one full band		Bulge
5000−10000	>1	250-1000	3700-12000	> 500	17-20	Very wide

We thank the AS-Gaia for supporting the workshop that was held in Nice in February 2009. Thank-you also to Olivier Bienaymé who presented the conclusions of the workshop at the SF2A meeting on very short notice.

References

Ivezić et al. 2008, ApJ 684, 287

Juric et al. 2008, ApJ 673, 864

Reylé, C.; Marshall, M.; Schultheis, M.; Robin,A.C., 2008, in SF2A-2008: Proceedings of the Annual meeting of the French Society of Astronomy and Astrophysics, astro.ph, 08123743

Robin A., Reylé C., Derrière S., Picaud S., 2003, Astron. Astrophys., 409,523

SF2A 2009
M. Heydari-Malayeri, C. Reylé and R. Samadi (eds)

SIMULATING GAIA OBSERVATIONS USING A "UNIVERSE MODEL"

Robin, A.C.[1], Reylé, C.[1], Grux, E.[1] and the Gaia DPAC Consortium

Abstract.
Preparing the Gaia mission requires large efforts dedicated to simulations of the observations. Several simulators have been constructed, generating telemetry, images, or the final database. All these tools use a "Universe Model" containing essentially the astronomical objects seen by Gaia and their characteristics, as well as a Relativity model and a radiation model for estimating the potential dammage to the CCDs. The construction of the Universe Model will be described, together with the computation of the astronomical sources characteristics, and the applications and limitations of such a model.

1 Introduction

The Gaia DPAC (Data Processing and Analysis Consortium) has decided to put a big effort on the simulation of the mission in order that all softwares prepared for the mission be sufficiently and extensively tested prior to launch. The simulation effort consists in doing several simulators. The GIBIS simulates the images at the output of the CCDs, GASS simulates the telemetry sent to the ground from the satellite after selecting objects and windows around the objects on board. GOG is dedicated to generating intermediate and final data in the data base, including estimations of measuring errors. These 3 simulators make use of two models : the Instrument Model, and the Universe Model (hereafter UM).

This UM is a set of algorithms for computing the positions at any time, and observational properties of any objects expected to be observed by the Gaia instruments. The distributions of these objects and the statistics of observables have to be as realistic as possible for simulations to be usable for estimating telemetry, testing software, simulating images, etc. The algorithms have also to be optimised in order that the simulations can be performed in reasonable time and can be redone when necessary. The complexity of the model is expected to increase during the preparation of Gaia.

Objects which will be, in fine, simulated are: solar system objects (planets, satellites, asteroids, comets), galactic objects (stars, nebulae, stellar clusters, diffuse light), extragalactic objects (galaxies resolved in stars, unresolved but extended galaxies, quasars and active galactic nuclei, supernovae). On top of these objects, a relativity model has to be implemented. The interstellar extinction has to be taken into account. Backgrounds have to be simulated, like the zodiacal light, or extended nebulae. The radiation environment of the satellite and its variation with time is also an element of the UM. For each of these simulated objects one needs to have their full 3D spatial distribution together with their spectral characteristics (to be able to compute photometry and spectroscopy, stable or variable in time), and their motions (for astrometric computations and for spectral corrections). Gravitational lensing for stars and galaxies are also to be simulated.

We here describe the main UM assumptions, the characteristics of the simulated objects, the spectral libraries, and we present the global statistics of the objects as computed from the UM.

2 Astrosources

For each "astrosource", the UM defines its characteristics in order to compute the observables. This includes: the photometry and variability with time, the astrometry (position at a given time, 3D velocities to compute radial velocity and proper motion, distance to the observer to compute the trigonometric parallax) and the

[1] Institut Utinam, Observatoire de Besançon, BP1615, F-25010 Besançon cedex

physical parameters which define the spectrum (effective temperature, gravity and metallicity for stars, Hubble type for galaxies, equivalent width and slope of the spectrum for quasars, taxonomical type for asteroids, etc.). The spectra are taken from spectral libraries, interpolated for the astrophysical parameters of the astrosource, and corrected for interstellar extinction, rotation and radial velocity.

Exoplanets are simulated orbiting single stars and creating transits. Multiple stars are generated and eclipses simulated when necessary. The proportion of multiple stars and the distribution in mass ratio and semi-major axis and statistically generated according to Arenou and Soderhjelm (2005). Multiple star simulations are of course not static. Beyond the Galactic properties of multiple stars, the astrometric, spectroscopic (radial velocity) and photometric (eclipses) effects of these objects have to be taken into account: in the course of the simulations of Gaia transits, the orbits are thus computed, the positions of both components are modified, though crudely in the case of eclipse. For extended objects (comets, asteroids, nebulae, etc.) shapes have to be modelled to allow the computation of the image. Figure 1 shows the main classes which allow to describe an astrosource.

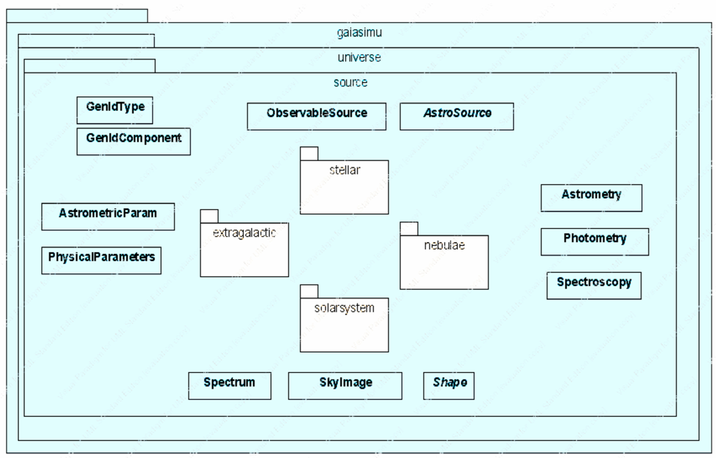

Fig. 1. Main classes describing an AstroSource.

3 Object generators

The "astrosources" have to be built from a set of generators which generate in any given direction of observations the objects which are present in the field of view of the instrument and their characteristics. Details on the various object generators can be found in Robin et al. (2009). The main aspects are described below.

Most of the objects in Gaia instruments are stars. To generate the stars in the Milky Way we use a version of the Besançon Galaxy Model which have been rewritten is Java. This version possess several improvements with regards to the standard model (Robin, et al, 2003). They are : full simulation of stellar multiplicity, inclusion of several stellar variability (delta Scuti, ACV, cepheids, RRab, RRc, roAp, semi-regular, dwarf novae), rare objects (Wolf Rayet, planetary nebulae). It also includes the computation of the microlensing towards the Galactic bulge, and uses the Drimmel & Spergel (2001) model as 3D extinction map for computing the extinction along any line of sight.

At present no stellar populations in local group galaxies have been implemented in the UM. Plans are done to simulate at least the stars in the Magellanic Clouds. Unresolved galaxies are generated using the Stuff (catalogue generation) and Skymaker (shape/image simulation) codes from E. Bertin, adapted in Java for the DPAC purpose. The galaxy simulator generates a mock catalog of galaxies with a 2D uniform distribution and a distribution in each Hubble type sampled from Schechter's luminosity function. Each galaxy is assembled as a sum of a disc and a spheroid and is put at its redshift and luminosity and K corrections are applied. The algorithm returns for each galaxy its position, magnitude, bulge to disc ratio, disk size, bulge size, bulge flatness, redshift, position angles, and V-I. A corresponding spectrum is extracted from a spectral library established from PEGASE2 software (www.iap.fr/pegase and Livanou et al, 2009). A shape image can be associated to the galaxy through library of images taken from the HST, rescaled and resampled at the correct distance.

Quasars are simulated from the scheme proposed in Slézak and Mignard (2007). To summarize, lists of sources have been generated with similar statistical properties as the SDSS, but extrapolated to G = 20.5 (the SDSS sample being complete to i = 19.1) and taking into account the flatter slope expected at the faint-end of the QSO luminosity distribution. Since bright quasars are saturated in the SDSS, the catalogue is complemented by the Véron-Cety & Veron (2006) catalogue of nearby QSOs.

The Solar System objects (SSOs) are only a little sample of the total number of objects expected to be observed by Gaia, but their peculiarities strongly condition the design of this part of the Universe Model. The semi-empirical statistical approach (constrained by observations) considered in the other parts of the Universe Model is no longer valid (in this first version of the Solar System Module) due to the high apparent motions of the SSOs. The reason is quite simple: it is not possible to generate a catalogue of objects (along with their physical information) for a certain (static) sky region, since the observed objects in that direction depends on time. Therefore, to generate a catalogue of SSOs we would need to specify both the sky region and observation time. However, if the simulations are required to be done in a reasonable computational time, the computation of the ephemerides along the mission of a set of ($\sim 10^5$) SSOs is not feasible in this first approach.

To solve this problem, the simulation must not be based on a reliable statistical model, but on catalogues containing orbital elements of SSOs, stored on disk. By computing SSOs ephemerides in time, and crossing the obtained positions with the Gaia Scanning Law, only the transiting ones (i.e. the SSOs inside one of the FoVs) at any time along the mission are selected. This transits list contains all the candidates expected to be observed, and obviously, it contains also the transit time in the corresponding FoV, the astrometric data and the apparent magnitude of these objects. This is the basic input for the simulation of the Solar System.

4 Universe Model output and tests

The Universe Model produces output catalogues of astrosources with their astrophysical parameters and all necessary parameters allowing to compute their contribution to Gaia observations (positions, velocities, rotation, light curve, shape, low and high resolution spectra, etc.) to be used by the simulators GASS, GIBIS and GOG. The output can be given either as an ascii file or directly ingested in the Main Data Base for processing.

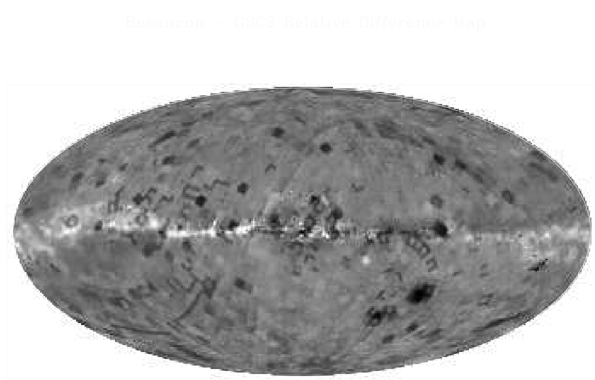

Fig. 2. Difference between GSC2 catalogue star counts at G=17 and galaxy model. Out of the Galactic plane the agreement is better than 10%. Significant excesses in the modelled star counts are found in the Galactic plane, that could be due to incompleteness in the data due to crowding, or to inappropriate model of extinction. Lack of counts in the model are found in the Magellanic cloud region (not included in the model) and in a few squared regions, most probably due to defects in the GSC2 photometric calibration.

In order to ensure that the model is reliable and realistic enough three level of tests are performed: unit tests on individual classes, integration tests on packages, and finally validation tests by comparison with real data. Concerning the third type, the validation of the stellar density has been done by comparing UM outputs with GSC-II catalogue over all sky (Drimmel et al, 2005). An example is given in fig 2. Moreover the Besançon Galaxy Model is extensively tested by comparison with many different data sets at various wavelengths (Robin et al, 2003). More tests are planned, for example on the number and separation of binaries, and by comparison of the model with the Hipparcos catalogue. We are also doing extensive kinematical tests by comparison of the simulations with Tycho-2 catalogue.

Figure 3 shows the predicted number of stars as a function of Galactic coordinates from the Gaia UM.

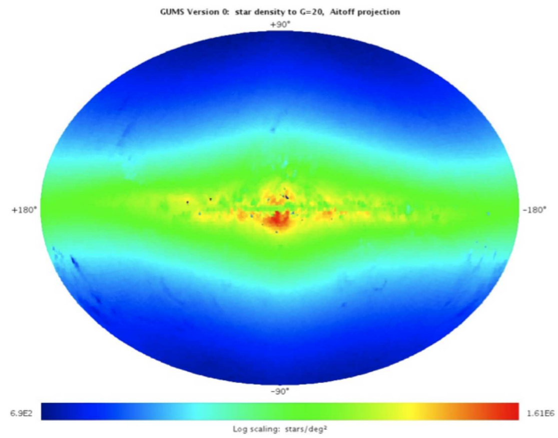

Fig. 3. Expected number of stars at magnitude G=20 from the Gaia DPAC Universe Model simulations GUMS.

5 Perspectives

The Gaia UM serves as providing simulations for testing purposes inside the DPAC. In the future and specially after launch the model will be maintained and will be further used for testing the analysis softwares. When waiting for real data, one will prepare the data interpretation using simulations in order to establish efficient methods for multivariate data analysis. Another application under study consists in doing a bayesian classifier based on prior probabilities computed from the simulations.

References

Arenou, F., Soderhjelm, S., 2005, ESASP.576..557

Drimmel, R., Spergel, D.N., 2001, ApJ 556, 181

Drimmel, R., Lattanzi, M.G., Spagna, A., Robin, A.C., Reylé, C., Luri, X., 2005, technical note SWG-RD-04.

Livanou E., Kontizas M., Karampelas, A., Kontizas E., Rocca-Volmerange, B., Tsalmantza P., Bellas-Velidis I. and Dapergolas A., 2009, Technical report GAIA-C8-TN-UOA-EL-001-1

Robin, A.C., Reylé, C., Derrière, S., & Picaud, S. 2003. A&A, 409, 523 -540

Robin, A.C., Reylé, C., Arenou, F., Babusiaux, C., Latorre i Musoll, A., Luri, X., Sartoretti, P., 2009, DPAC Technical note GAIA-C2-TN-LAOB-AR-004-7 "Universe Model Overview".

Slézak, E., Mignard, F., 2007, DPAC Technical note GAIA-C2-TN-OCA-ES-001-1 "A realistic QSO Catalogue for the Gaia Universe Model".

Véron-Cetty, M.-P. and Véron, P., 2006, A&A 455, 773.

SF2A 2009
M. Heydari-Malayeri, C. Reylé and R. Samadi (eds)

GAIA AND THE GROUND-BASED OBSERVATIONS OF THE SOLAR SYSTEM OBJECTS

Thuillot, W.[1], Tanga, P.[2] and Hestroffer, D.[1]

Abstract. An important part of the Gaia mission is devoted to the study of Solar System Objects. In this domain, ground-based observations can be favorably combined with the space observations and in some cases they appear as a unique support for completing the Gaia data. We have organized a workshop in Beaulieu/mer near Nice in October 2008 with the goal to discuss this topic. 26 participants attended this workshop, coming from several observatories in different countries. They have underlined different aspects of the ground-based observations related to the expected Gaia Solar System science. These aspects includes the determination of asteroid mass, shape and density, the measurement of Yarkorvsky effect, the astrometric follow-up of new objects, the improvement of astrometric measurements of ancient observations of natural satellites and those of the stellar occultation predictions.

1 Introduction

Among a huge amount of astrophysical objects, the Solar System bodies will be observed by the Gaia space probe during its five years mission. In the DPAC structure (Data Processing and Analysis Consortium) which deals with the data processing of this mission, the Coordination Unit 4 (CU4)is partly dedicated to prepare the data processing related to these objects. Beyond this data processing, several teams are thinking about the scientific impact of the mission which will certainly lead to an important update of our knowledge of the Solar System itself. Mignard et al. (2007), for example, describes the expected applications of the Gaia mission to the asteroid science. Therefore Gaia has the potential of changing our view of the asteroid population in particular. Furthermore, due to the peculiar characteristics of those bodies, and to their physical description, ground-based observations will be a fundamental mean to reinforce the scientific progress by complementing the Gaia data (Hestroffer et al. 2008). This situation is very different from that found, for example, in stellar physics where ground-based observations will essentially be used for calibration. In the Solar System domain, in fact, we deal with a possible concrete increase in the Gaia scientific impact. This is essentially due to the following:

- the mission duration (5 years) that could prevent extracting from Gaia data alone all the subtle dynamical effects;
- the geometry of observation, that could prevent obtaining precise orbits for dynamically peculiar objects discovered by Gaia itself (Inner-Earth and Earth-Crosser Asteroids);
- the possibility of opening new paths for future techniques, thanks to the availability of Gaia ultra-precise measurements;
- the contribution of other available techniques, namely adaptive optics and photometry.

In particular, it has been shown that an extension of the observation period to more than five years through ground-based instruments could improve the sample of masses measured by mutual perturbations; similar predictions can be formulated for non-gravitational forces such as the Yarkovsky effect. Also, the unprecedented precision of orbits and star positions could vastly improve predictions of star occultations by asteroids. Adaptive

[1] IMCCE, Paris Observatory, 77 av. Denfert-Rochereau, 75014 Paris (France)
[2] Cassiopée, OCA, Le Mont gros, 06300 Nice (France)

Optics and photometry could also contribute with shape and size measurements, especially valuable for determining the density of some key targets. Furthermore, a ground-based network is being structured for follow-up observations of possible discoveries.

The preparation and the optimization of ground-based complementary observations requires a good understanding of the expected Gaia results, and an international coordination effort. Dedicated and/or automated instruments could also be conceived and used for the future.

These are the reasons why we convened the interested people to discuss this subject at the workshop "Earth-based support to Gaia Solar System Science" which has been held in Beaulieu-sur-mer (near Nice, South of France) on 2008, October 27 and 28. 26 participants attended this workshop, coming from several observatories in different countries and addressed several questions involving mainly the small Solar System bodies.

2 Asteroids

Gaia will observe more than 250 000 asteroids down to magnitude 20 with an incomparable precision (0.1 to 1 mas for each single measurement). Near-Earth Asteroids (NEAs), Trojans and Centaurs will be concerned by these observations. Several contributions to the workshop have stressed the interest to organize ground-based campaign for some selected asteroids in order to improve the scientific return of these observations.

For example, the determination of around 100 asteroid masses by Gaia will be possible by measuring the gravitational deflection during close encounters (Mouret et al. 2007). But at the edge of the mission period, arcs of trajectories will be incomplete. In these cases, ground-based observations will allow to extend our knowledge of the orbital arcs and to add around 25 masses. This requires to organize campaigns of astrometric observations of these specific asteroids before the launch and after the end of the mission. This will be a valuable improvement of our knowledge, since at the present time only a small number of masses are known (only 40 masses are known with uncertainties better than 60 percent).

But other questions have also been addressed. High angular observations from the ground will allow to get a better understanding of the photocenter-barycenter offset and will give a mean to improve the determination of several orbits. It will allow to calibrate the sizes (Carry 2009) and in some case to reach the bulk density of several objects. On the other hand, such observations and also radar astrometry measurements, could lead to an important improvement of our knowledge of the Yarkovsky effect (Delbó et al. 2008)which is a main factor of uncertainties for NEAs in particular. Thus, the determination of size, shape, orientation and thermal properties could allow us to add more than 60 Yarkovsky effect detections to the 30-50 which will be detected by Gaia (detections for asteroids (6489) Golevka and 1992 BF are the only two direct detections known at this date).

The photometric measurements of asteroids by Gaia will give sparse measurements due to the scanning law, they will lead nevertheless to data very useful for the inversion problem. In some ambiguous cases, ground-based photometric observations of selected asteroids will allow us to get complementary data and to reach better results to model their shape.

The combination of Gaia astrometric observations with ground-based ones have been studied. The case of the orbits of newly detected NEAs appears to be drastically improved in some cases, when a too small number of Gaia measurements can be combined with ground-based astrometric measures. Nevertheless, due to the location of the probe at the Lagrange point L2, a strong parallax effect will affect the celestial coordinates of objects close to the Earth. This will require an accurate process for their detection from the ground after the discovery by Gaia and for the combination of the data. These problems have been discussed.

The figure 1 shows a global view of the asteroid science based on the Gaia data. It gives the number of asteroids involved in each of the six main fields of research: orbit improvement, shape and orientation, taxonomy, detection of binaries, estimate of the size, estimate of the mass. For three groups among these fields it gives the number of asteroids for which the following goals can be reached: estimate of the dynamical properties and composition and rotation parameters, estimate of the rotation parameters, composition, mass and albedo, estimate of all these parameters and of the non gravitational effects. For the two last groups, ground-based additional observations will bring an improvement for almost 2000 asteroids.

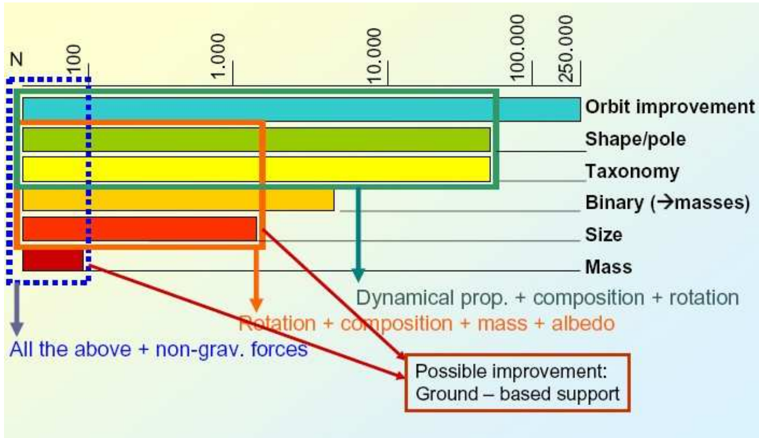

Fig. 1. A new global picture of the asteroids (courtesy P. Tanga)

3 Natural satellites

The Gaia astrometric measurements will be useful but not so efficient to improve the orbital models of the natural satellites. One main reason is that the duration of the mission is not long enough with respect to the periodic effects which have to be analyzed and which are generally much more long. The propagation of errors of the ephemerides of the main satellites of Saturn, in particular Mimas and Titan, has been studied (Desmars et al. 2009) by using the bootstrap method. One result is that in order to get a good accuracy of the models outside the period of observation, accurate observations on a short period is not necessarily better than average observations on a long timespan. The simulation of Gaia observations included in this analysis does not change significantly the global behavior.

In addition, ground-based observations remain necessary for the large satellites which will not be observed by Gaia. One major point is that a new reduction of many ancient astrometrical observations (photographic plates but also CCD frames) on the basis of the stellar astrometry using the Gaia catalogue will have an important impact on the dynamical models of the natural satellites, but also of the models of the planets (observed positions of its satellites lead to observed position of the planet itself). Therefore, the re-reduction using the Gaia catalog will be an important level to get accurate ephemerides useful for planetology, and for example for the detection of small secular effects induced by the tidal forces.

4 Comets

Gaia is not well suited for cometary science because of its limiting magnitude, of the lack of large field, of the slitless spectroscopy. Nevertheless around 50 cometary observations are awaited with the capacity to give access to astrometric measurements of the nucleus and to estimate the non gravitational forces. The modeling and simulation of the Gaia cometary observations are still in progress. Complementary observations from the ground could be interesting for a follow-up of possible cometary and unexpected activity of some Solar System bodies.

5 Stellar occultations

The observation of stellar occultations is a powerful method probing the Solar System Bodies and to estimate the size, the shape and the possible duplicity of the planetary objects. It allows also the probe of the atmosphere if any is present (see for example Widemann et al. 2009 or Sicardy 2006). Applying this method to investigate the transneptunian objects (TNO) is nowadays a big challenge, since the apparent diameters of the biggest ones (30 to 100 mas) is equivalent to the accuracy of the stellar catalogs (around 40 mas). Thus predictions are generally not accurate enough to ensure the success of these observations.

The Gaia stellar catalogue will then lead to a huge improvement of this kind of observations : predictions of the events will be more accurate, events by small objects will be more predictable (Tanga and Delbó 2007). One can foresee that in a few years of observations through a network, we could reach completeness of diameters measurements for asteroids down to 20 km .

6 Ground-based facilities

In some cases, complementary ground-based observations will required specific facilities. For example, transient events such as the detection of new fast moving objects by Gaia can be not reobserved by the probe due to the scanning law. The concerned objects (NEA, in particular Inner Earth Asteroid) may even be lost. A ground-based network of observing sites is then necessary and the setup of such a network is a task of the CU4 as well for observations on alert as for follow-up observations of specific objects.

In this context the robotic telescopes appear well adapted. A presentation of this facility, especially the TAROT system (Klotz 2008), has been presented at the workshop. The possibility to operate through a worldwide network of such telescopes (setted up with Tarot1 in France, Tarot2 in Chile, Zadko in Australia, Satino & Rosace in France) has been emphasized.

7 Conclusion

The Beaulieu workshop (Tanga 2008) was a nice opportunity to gather different teams interested by using the space data from Gaia and completing them with data from ground-based activities. Several physical and dynamical parameters of the Small solar System Bodies will be drastically improved. Asteroid astrometry will extend the number of the determined masses, will avoid the loss of some possible new objects, and help to get a better knowledge of some dynamical effects. Photometry will give help to determine the pole orientation. High Angular Resolution observations such as the adaptive optics, will give access to the bulk density of several asteroids, the mass of which will be estimated by Gaia. It will also permit the estimate of the Yarkovsky effect on several asteroids.

The observers that are running programs concerning physical properties of Minor Bodies have stressed the importance of having intermediate releases of Gaia astrometry. In particular, our knowledge of TNO possible atmospheres and asteroid sizes is strictly related to the capacity of providing predictions accurate enough for ensuring stellar occultation observations. The community has thus expressed a strong interest in the possibility of accessing intermediate releases (even degraded in quality or magnitude) of the Gaia star astrometry catalogue.

We are grateful to the following organizations which help us to organize and fund the workshop "Earth-based support to Gaia Solar System Science": Action spécifique Gaia, CNRS, Cassiopée-Côte d'Azur Observatory and especially the local staff, namely D. Kamm, S. Goletto, S. Rousset, IMCCE-Paris Observatory and especially the administrator I. Nicolas. The Scientific Organizing Committee was composed with P. Tanga (OCA), D. Hestroffer (IMCCE), M. Delbo (OCA), F. Mignard (OCA) and W. Thuillot (IMCCE).

References

Carry, B. et al. 2009, A&A, in press

Delbó, M. et al. 2008, PSS 56, 1823

Desmars, J. et al. 2009, A&A 499, 321

Hestroffer, D. et al. 2008, Proc.of the Annual meeting of the SF2A, C. Charbonnel, F. Combes and R. Samadi. Eds, 21

Klotz, A. et al. 2008, PASP 120, 1298

Mouret, S. et al., 2007, A&A 472, 1017

Mignard, F. et al. 2007, EMP 101, 97

Sicardy, B. et al. 2006, JGR 111, E11S91

Tanga, P. 2008, Workshop web site, www.oca.eu/tanga/GaiaEarthBased/

Tanga, P., & Delbó, M. 2007, A&A 474, 1015

Widemann, T. et al. 2009, Icarus 199, 458

SF2A 2009
M. Heydari-Malayeri, C. Reylé and R. Samadi (eds)

TWO YEARS OF CNRS-INSU 'ACTION SPÉCIFIQUE' GAIA

Turon, C.[1] and Arenou, F.[1]

Résumé. The 'Action Spécifique' Gaia (AS Gaia) has been created by the French National Institute for the Sciences of the Universe with the aim of enhancing the scientific return from the European Space Agency (ESA) Gaia mission, due to be launched during Spring 2012. The various actions taken during the last two years are presented here.

1 Introduction

Space Astrometry is a branch of space science where French scientists, Space Agency (CNES) and space industry have been deeply involved from the very beginning (ESA's Hipparcos was built from an original idea of Pierre Lacroute, the then Director of the Strasbourg Observatory). Building on the success of the Hipparcos mission, Gaia was proposed to ESA in 1993 (Lindegren & Perryman, 1996) within the frame of ESA's *Horizon 2000 Plus* long-term scientific programme. It was included in the ESA's Science Programme in 2000 and is due to be launched in Spring 2012. Many French astronomers contributed, in straight collaboration with other European colleagues, to establish the Gaia science case and to define the specifications of the astrometric, photometric and spectroscopic instruments of Gaia. The DPAC (Gaia Data Processing and Analysis Consortium) is chaired by François Mignard (Observatoire de la Côte d'Azur) and France is the first contributor to the Consortium (about 25 % of the members). Accordingly, the creation of an 'Action Spécifique' was proposed (Turon et al., 2007) to the CNRS National Institute for the Sciences of the Universe (INSU) and created in August 2007, for four years.

The challenge for AS Gaia is to prepare the French astronomers to be in a position to best exploit the Gaia scientific data in their quantity and diversity, and in their various domains of application. Its role is therefore to suggest and support actions in order to fulfil the needs in modelling and theoretical developments and on the complementary and follow-up observations that should be organised before, during and after Gaia operations. AS Gaia has also been requested by INSU to support the ground-based observations required by the Gaia data analysis and not otherwise funded.

Finally, AS Gaia is the voice of the French Gaia community towards our National funding authorities, and as such its chair attends CNES and INSU astronomy working meetings, contributes to the establishment of the INSU roadmap by producing documents and attending the various meetings, and supports the requests for funding or permanent positions.

2 Actions of the last two years

With a global funding of 30 k€ per year (15 k€ in 2007), AS Gaia opened three announcements of opportunity (end 2007, 2008 and 2009). The main broad lines of funding are the following :

– Ground-based observations required by the Gaia data analysis and not otherwise financed ;
– Organisation of topical workshops ;
– Modelling of the various objects which will be observed by Gaia : stars (interiors and atmospheres) ; the Galaxy ; Solar System objects ; galaxies ; compact objects (especially QSOs) ;
– Support to European and, more generally, international collaborations ;
– Support young astronomers attendance to international meetings ;
– Support to public outreach and conferences by the production of Gaia documentation in French.

[1] Observatoire de Paris, GEPI, CNRS UMR 8111, 92195 Meudon, France

2.1 Ground-based observations in support to Gaia data analysis

A number of ground-based observations are required to support the Gaia data analysis and a special group, GBOG, chaired by Caroline Soubiran, has been created within DPAC to co-ordinate these (Soubiran et al. 2008). AS Gaia contributed to the funding of various actions :

- Observation of radial velocity standard stars for the initial calibration of the spectrograph on board Gaia, the Radial Velocity Spectrograph (RVS) : observations performed with the Coralie spectrograph, operated by the Geneva Observatory in La Silla. The observations performed in France with the Sophie (Observatoire de Haute Provence) and Narval (Observatoire du Pic de Midi de Bigorre) spectrographs are funded by other national funding. See Crifo et al. (2009).
- Spectroscopic observations of minor planets to calibrate and test the performance of classification algorithms.
- Astrometric observations of WMAP, a test of the performance of such observations to accurately reconstruct the orbit of the satellite, as is planned to be done for Gaia.
- Support to the realisation of a pipeline for processing the Narval spectra.
- Support to the setting of a network of ground-based observations of Solar System minor bodies, especially near-Earth objects.

2.2 Meetings and workshops

After a kick-off meeting in December 2007, an annual meeting of AS Gaia is now hosted as a parallel session during the 'Journées de la SF2A', which is thanked here. All presentations and papers are available from the AS Gaia web site at wwwhip.obspm.fr/gaia/AS.

In addition to these annual plenary meetings, a number of topical workshops have been or are being organised :

- "**Reference systems and QSOs**", organised at Bordeaux Observatory by P. Charlot and G. Bourda, 24 October 2008. The main topics were : settling of the Gaia reference frame; study of the long-term and short-term variations of the photocentres of AGNs and of potential discrepancies between optical and VLBI positions; link of ICRF to the Gaia frame (Bourda & Charlot, this meeting).
- "**Earth-based support to Gaia Solar System science**", organised in Beaulieu sur Mer by P. Tanga and W. Thuillot, 27-28 October 2008. The main goals were to plan for ground-based observations which would complement Gaia observations (for example to enlarge the period of observation over the orbits of solar system objects, to plan for detailed spectroscopic observations, etc.); to identify new techniques which would become possible thanks to the unprecedented accuracy of Gaia positions and proper motions; to organise a network of ground-based observers (Thuillot & Tanga, this meeting).
- "**Multiplex spectroscopy in complement to Gaia**", organised at Nice Observatory by A. Recio-Blanco and V. Hill, 19-20 February 2009, in preparation to the March 2009 ESO workshop 'Spectroscopic Survey Workshop'. The goal was to anticipate the requirements in ground-based spectroscopy in complement to the Gaia data in the domain of Galactic Archeology : radial velocity and chemical abundances for stars not observed by the Gaia RVS or not observed in enough detail (Bienaymé et al., this meeting).
- "**The Milky Way**", organised at the Besançon Observatory by A. Robin, C. Reylé and M. Shulteis, 5-6 November 2009. The meeting will be devoted to the various methods used to test the models of formation and evolution of galaxies, in the context of Gaia.
- "**Gaia et la physique des AGNs**", organised at Nice Observatory by E. Slezak, is planned for early 2010. The AGNs Gaia catalogue will be much larger and much more homogeneous than ever obtained earlier. The aim of the meeting is to initiate the work on the impact of these data over the understanding of the physics of these objects.

These workshops have a high priority in the annual announcements of opportunity and proved to be very efficient to co-ordinate the work of various teams within France and to open the way to new national and international collaborations. We plan to organise other such workshops in the coming years.

2.3 Modelling for Gaia data analysis

Gaia will observe all objects down to magnitude $V = 20$, i.e. a very large variety of stars, Solar System bodies and compact extragalactic objects. To be able to identify, classify and characterise them, it is essential to have good models of these objects as seen by the Gaia instrument. With one billion objects observed, any category of objects will include a huge number of elements and the classification algorithms have to be carefully tested in advance. A number of such actions have been supported by AS Gaia these two last years :

- Improvement of the modelling of massive stars with emission lines. Test and improvement of the classification algorithms.
- Simulation of multiple stellar systems.
- Development of library of synthetic spectra of galaxies to be used for the automatic classification of galaxies unresolved by Gaia observations.
- Simulation of a catalogue of quasars and AGN, and test of its observation with Gaia.
- Simulation of the detection and observation of binary minor planets.
- Simulation of the observation of extended objects.

2.4 Modelling for Gaia data scientific exploitation

Gaia has the discovery potential of a survey which will provide data of unprecedented accuracy, of unprecedented quantity, and for high variety of objects, running from Solar System bodies to unresolved galaxies, through all spectral types and evolutionary stages, even the rarest or the fastest. As a result, the scientific exploitation of such data have to be carefully prepared in advance. In this respect, various works have been supported by AS Gaia :

- Kinematic and dynamical modelling of the galactic bulge ;
- 3D and NLTE modelling of stellar atmospheres, aiming at the improvement of the determination of atmospheric parameters and abundances ;
- Modelling of the various types of emission-line stars and search for criteria to identify each of them from the Gaia spectroscopic and photometric observations ;
- Development of an algorithm and software to predict close encounters between minor planets, with the aim of mass determination ;
- Development of criteria for the taxonomic classification and absolute magnitude determination of minor planets observed with Gaia ;
- Determination of the conditions of observation of comets with Gaia, modelling of the non-gravitational forces perturbing their orbits.

2.5 Communication

A few steps have been taken to help the development of communication in France about the project and produce documentation for conferences and exhibitions : edition of posters and folders, and translation of ESA’s documentation, about the various aspects of the Gaia mission and science, more generally about astrometry and its evolution across centuries ; funding of models of the satellite ; development of a section of the AS Gaia web site dedicated to documentation in French about astrometry, Hipparcos and Gaia.

3 Preparing for the future

AS Gaia, through its Scientific Committee, actively contributed to the preparation of the astronomy roadmap prepared by INSU during 2009 and produced several documents :

- a document about the permanent research positions that would be required to take full benefit of the French involvement in the Gaia data processing and analysis and its major contribution to the DPAC Consortium ;
- a document about ‘observation services’ (which constitute one part of the mandatory activities of scientists with a position of ‘astronomer’ in France).
- a document about ground-based observations, and relevant instrumentation and telescopes that would be needed to complement Gaia observations ;

- a special document dedicated to the complementary spectroscopic observations that would be essential in complement to Gaia measurements in the domain of Galactic astronomy, and to the relevant instrumentation (multiplex spectrograph on a wide field telescope), proposing several possible solutions ;
- a contribution to the document produced for the INSU roadmap by the 'Programme National de Cosmologie et Galaxies" ;
- a contribution to the document produced for the INSU roadmap for 'space-ground-based coordination'
- contributions to the ASTRONET forum about the use of 2-4 m telescopes.

All these actions have to be developed and enhanced in the coming years in straight co-operation both within France with the various 'Programmes Nationaux' and with the European colleagues and networks (ELSA, RTN on European Leadership in Space Astrometry ; GREAT, an ESF network ; and any further network proposal to the European Commission). In particular, the series of topical workshops should be continued, and initiatives related to modelling and ground-based observations will also be strongly supported. A special effort has still to be done about scientific communication and further preparation of documentation and of presentation material.

The Gaia data will give a major input to various fields of astronomy and astrophysics where the French scientists are involved, and it is essential that all steps are taken so that they are fully aware of the characteristics of these data, in accuracy, sky and magnitude coverage, and that they are fully prepared to fully exploit this unique opportunity.

The Scientific Committee of AS Gaia for the years 2007-2010 is composed of Catherine Turon (chair), Frédéric Arenou (substitute to C. Turon in national meetings), Olivier Bienaymé, Daniel Hestroffer, Vanessa Hill (link with Programme National Cosmologie et Galaxies, PNCG), François Mignard (Chair of DPAC), Bertrand Plez (link with Programme National de Physique Stellaire, PNPS), Annie Robin (link with PNCG), Caroline Soubiran (member of the Gaia Science Team), Frédéric Thévenin (link with PNPS). The AS Gaia may be contacted at AS.Gaia@obspm.fr or through its web site wwwhip.obspm.fr/gaia/AS.

Références

Bienaymé, O., et al., 2009, Multiobject spectroscopy as a complement for Gaia, this volume

Bourda, G., Charlot, P., 2009, Celestial Reference Frames in the Gaia era, this volume

Crifo, C., Jasniewicz, G., Soubiran, C., et al., 2009, The Gaia-RVS standards : a new full-sky list of 1420 stars with reliable radial velocities

Lindegren, L., & Perryman, M.A.C., 1996, A & A Suppl., 116, 579

Soubiran C., Allende Prieto, C. ; Altmann, M., et al., 2008, SF2A-2008 : Proceedings of the Annual meeting of the French Society of Astronomy and Astrophysics, C. Charbonnel, F. Combes and R. Samadi eds. Available on AS Gaia site

Thuillot, W., Tanga, P., 2009, this volume

Turon, C., Mignard, F., Arenou, F., 2007, Proposition pour une Action Spécifique Gaia

GRAAPH

Gravitation and Reference Systems

THE CONSTRUCTION OF THE LARGE QUASAR ASTROMETRIC CATALOGUE (LQAC)

Barache, C.[1], Bouquillon, S.[1], Souchay, J.[1], Andrei, A. H.[2], Taris, F.[1], Gontier, A.-M.[1], Lambert, S. B.[1], Arias, E. F.[3] and Le Poncin-Lafitte, C.[1]

Abstract. We gather the 12 largest quasar catalogues (4 from radio interferometry programs, 8 from optical survey) and we carry out systematic cross-identifications of the objects to obtain their best position estimates, and providing physical information at both optical and radio wavelenghts. This catalogue compilation designated LQAC, give equatorial coordinates of 113 666 quasars with 9 photometry magnitude, 5 radio fluxes, redshift and absolute magnitude.

1 Scientific and technical objectives

The main scientific objective was to build an astrometric and Multi-wavelength catalogue gathering all QSO's named Large Quasar Astrometric Catalogue (LQAC). This catalogue was also usefull to help for the construction of the optical catalogue reference frame (LQRF - Andrei et al., 2009), to complete optical data for radio sources from the Second Realization of the International Celestial Reference Frame (Alan L. Fey et al., 2009) and for the preparation of an input QSO catalogue for GAIA mission. The creation of this catalogue was also interesting for studies like the link between QSO's radio position and optical positions, the analysis of QSO neighbourhood, their distribution in space and their color magnitude diagrams.
The main technical objective was to compile the largest QSO catalogues following the astrometric precision of each catalogue in descending order. For each QSO, its catalogue origin was kept and a specific processing was done to detect the right or wrong double identifications. To our compiled set of catalogues we added only QSO from Véron and Véron (2006) catalogue which were not identified. We added also magnitude from large star survey catalogues (2MASS, GSC 2.3, B1.0) to complete magnitude information whenever it was necessary. To control our procedures we worked with two differents softwares (home fortran programs and virtual observatory tools) and two differents teams working on the same catalogues taken one by one and with the same compilation strategy.

2 Results

The final catalogue LQAC was constructed with the compilation of 12 large QSO catalogues (optical and radio) and included 113 666 quasars, 5 radio fluxes (1.4 Ghz, 2.3 Ghz, 5.0 Ghz, 8.4 Ghz, 24 Ghz), 7 photometric magnitude visible (u, b, v, g, r, i, z), 2 infrared magnitude (j, k) and the redshift value.
The accuracy of QSO sources was at the level of the milliarcsecond for sources from ICRF and not worse than 2 arc seconds for sources from Hewitt and Burbidge catalogue and Véron and Véron catalogue. In Fig. 1 (left) we show the accuracy of each catalogue and the radius choosen to make the cross-identification. In Fig. 1 (right) we show the accuracy of each catalogue after cross-identification. In Fig. 2 (left) we show the contribution in magnitude, fluxes and redshift of each individual catalogue (named from A to L letter) to the LQAC. After the construction of this catalogue, we have written an article on it in Astronomy and Astrophysics which has been published this year (Souchay, et al. 2009).

[1] Observatoire de Paris, SYRTE, France
[2] Observatorio Nacional and Observatorio do Valongo, MCT/UFRJ, Rio de Janeiro, Brasil
[3] Bureau International des Poids et Mesures, Sèvre, France

Catalogue	Flag	Wavelength	No. quasars	Accuracy ″	Search radius ″
ICRF-Ext2	A	radio	717	0.001	1
VLBA	B	radio	3 357	0.001	1
VLA-015	C	radio	1 701	0.015	1
JVAS	D	radio	2 118	0.2	1
SDSS	E	optical	74 868	0.2	1
2QZ	F	optical	22 971	0.2	1
FIRST	G	radio	969	0.5	2
VLA+015	H	radio	157	0.2	2
HB	I	optical+radio	7 245	1.5	2-5-30*
2MASS	J	infrared	–	0.2	1
GSC2.3	K	optical	–	0.2	1
B1.0	L	optical	–	0.2	1
VV06	M	optical+radio	85 189	1.0	2-5-10*

* Three different search radii have been considered for the cross-identification.

	Mean (mas)		σ (mas)			
	$\Delta\alpha\cos\delta$	$\Delta\delta$	$\Delta\alpha\cos\delta$	$\Delta\delta$	N_1	N_2
VLBA	−0.010	0.039	0.767	0.585	94	4
JVAS	−0.054	−0.009	1.025	1.391	63	10
VLA	−3.287	−0.081	9.793	12.629	90	5
SDSS	1.210	−12.203	52.022	51.728	96	4
2QZ	86.242	45.991	193.667	181.214	98	3
FIRST	−30.282	0.010	286.750	319.342	96	3
HB	97.800	100.152	726.512	785.789	85	5
VV06	30.393	286.513	582.571	586.322	97	3

N_1 stands for the number of quasars remaining after a 3σ rejection threshold algorithm, and N_2 for the number of necessary iteration.

Fig. 1. Left: Accuracy of individual catalogue. Right: Accuracy after cross-identification.

	A	B	C	D	E	F	G	H	I	J	K	L	Total
u	0	0	0	0	74 861	20 912	0	0	570	0	0	0	**96 343**
b	0	0	0	0	0	22 965	966	0	836	0	69 355	2 131	**96 253**
v	0	0	0	0	0	0	0	0	6 949	0	41 517	0	**48 466**
g	0	0	0	0	74 862	0	0	0	0	0	0	0	**74 862**
r	0	0	0	0	74 861	20 305	413	0	0	0	3 502	455	**99 537**
i	0	0	0	0	74 861	0	0	0	0	0	7 517	3 765	**86 143**
z	0	0	0	0	74 861	0	0	0	0	0	0	0	**74 861**
J	0	0	0	0	0	0	0	0	0	13 647	0	0	**13 647**
K	0	0	0	0	0	0	0	0	0	13 647	0	0	**13 647**
1.4 GHz	0	0	730	0	0	0	937	144	0	0	0	0	**1 811**
2.3 GHz	0	3 234	0	0	0	0	0	0	0	0	0	0	**3 234**
5.0 GHz	0	0	821	0	0	0	0	41	0	0	0	0	**862**
8.4 GHz	0	3 225	46	570	0	0	0	17	0	0	0	0	**3 858**
24 GHz	0	0	61	0	0	0	0	0	0	0	0	0	**61**
redshift	0	0	0	0	74 866	20 912	413	0	5 344	0	0	0	**101 535**

Fig. 2. Contribution of individual catalogue

3 OV Tools used

The Virtual Observatory Tools used to construct the LQAC were Aladin freeware (from CDS see http://aladin.u-strasbg.fr/aladin) to visualize the catalogues orign. We can see in Fig. 3 (left) the LQAC vizualised by Aladin freeware on the sky. We used VizieR tools from CDS (see http://vizier.u-strasbg.fr/viz-bin/VizieR) to get the differents catalogues files. At last we used Topcat and Stilts (see http://www.starlinl.ac.uk/stilts and http:/www.star.bris.ac.uk/ mbt/topcat) to make cross matching and to construct the LQAC Data Base. We can see in Fig. 3 (right) our complete LQAC xml file with Topcat. We have written in our A&A article a section about the OV tools used to show the power of these new tools and also to recognize the good work of the provider of these free tools (Fig. 4, left). The LQAC is now accessible on the CDS web with the reference J/A+A/494/799 this VizieR Web Service. We can see in Fig. 4 (right) the LQAC xml file in Vizier.

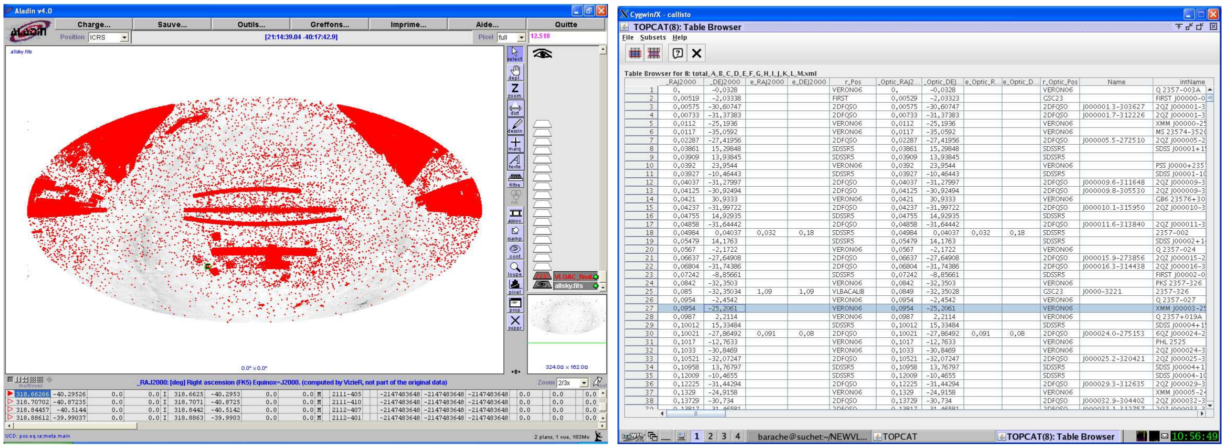

Fig. 3. Left: LQAC loaded with Aladin. Right: LQAC file loaded with topcat.

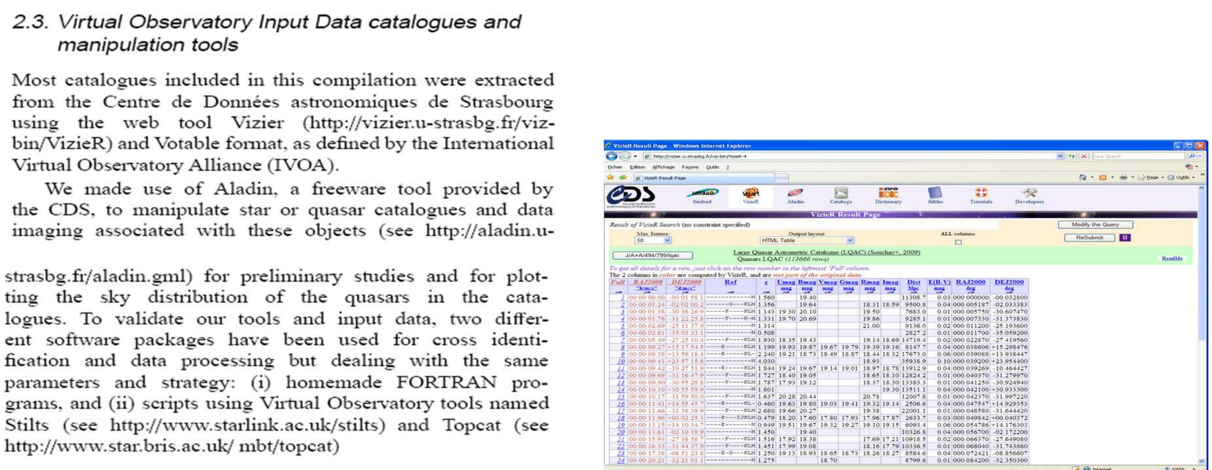

2.3. Virtual Observatory Input Data catalogues and manipulation tools

Most catalogues included in this compilation were extracted from the Centre de Données astronomiques de Strasbourg using the web tool Vizier (http://vizier.u-strasbg.fr/viz-bin/VizieR) and Votable format, as defined by the International Virtual Observatory Alliance (IVOA).

We made use of Aladin, a freeware tool provided by the CDS, to manipulate star or quasar catalogues and data imaging associated with these objects (see http://aladin.u-strasbg.fr/aladin.gml) for preliminary studies and for plotting the sky distribution of the quasars in the catalogues. To validate our tools and input data, two different software packages have been used for cross identification and data processing but dealing with the same parameters and strategy: (i) homemade FORTRAN programs, and (ii) scripts using Virtual Observatory tools named Stilts (see http://www.starlink.ac.uk/stilts) and Topcat (see http://www.star.bris.ac.uk/ mbt/topcat)

Fig. 4. Left: OV tools section of LQAC article. Right: LQAC file load by VizieR Web Service.

4 Conclusion

We are now preparing a new version of LQAC (LQAC 2.0) to improve the catalogue. We will resolve the wrong double QSO (300 pair of QSO's are in LQAC, their double status being doubtful). We will add some picture associated to each QSO and we will improve the homogeneity of magnitudes. We will also add a criterion of source geometry (for instance near star form than galaxy form).

The VO tools used for the LQAC were useful to get and study catalogue (Aladin, VizieR), to make cross-matching of sources (Topcat) and to manage, distribute the LQAC file catalogue easily (Topcat).
Howerver, theses tools are a little limited for instance to get the data from very large catalogues, to make some complex cross-matching. Moreover we have found difficulties to get the magnitude system photometric used in the magnitude of sources in VO tables.

References

Andrei, A. H., et al. A&A 2009 in press

Alan L. Fey, David Gordon, and Christopher S. Jacobs (eds.). (IERS Technical Note ; 35) 2009. 204 p., in print
Lambert, S. B., Gontier, A.-M. 2009, A&A 493, 317-323
Souchay, et al. 2009, A&A 494, 799-815
Véron-Cetty, M.-P.,&Véron. 2006, A&A,455,773

GRGS ILRS ANALYSIS CENTER CONTRIBUTION FOR THE ITRF2008 REALIZATION

Deleflie, F.[1] and Coulot, D.[2]

Abstract. The French Groupe de Recherche de Géodésie Spatiale (GRGS) became an official ILRS Analysis Centre (AC) in September 2007, and thus joined the ILRS Analysis Working Group (AWG) among other official analysis centres. It now delivers routinely products including Station Space Coordinates (SSC), Earth Orientation Parameters (EOP), and other ones, after being involved in SLR data processing since the early eighties. This paper aims to recall some recent research achievements carried out in the framework of the activities of this AC, and in particular ILRS contribution for ITRF2008. We also compare our results to those obtained by other ACs, in terms of SSC, EOP, translations, scale factors, and rotations.

1 Introduction

The Terrestrial Reference Frame (TRF) realizations are established and maintained with the global space geodetic networks. The network measurements must be precise, continuous, worlwide, and interconnected by co-location of different observing techniques. The requirements to be followed in the framework of the GGOS project are to perform a global TRF with an accuracy of 1.0 mm, and a stability of 0.1 mm/yr, ensuring a sea level rise measurement coherent with the altimetric data precision. It has to be noticed that for every 1 mm/yr Z-trend in the TRF origin, sea level rates are affected by 0.2 mm/yr (Beckley et al, 2007, Fig4).

The Satellite Laser Ranging (SLR) network is one of these geodetic networks, organized through the International Laser Ranging Service (ILRS) (Pearlman et al., 2002). Its Analysis Working Group (AWG) is producing, on a weekly basis, a 7-day arc combined solution with a minimum latency of 4 days, providing daily EOPs and weekly site coordinates, based on the contribution of up to 8 Analysis Centers (ACs). Each AC solution contains Space Station Coordinates (SSC) and daily EOPs, using Lageos and Etalon data, according to ILRS/AWG guidelines. As an official ILRS AC, GRGS (Groupe de Recherche de Géodésie Spatiale) provides such products, that are compared to each individual solution, and to the combined solution.

This work, performed over a long period of time, is the ILRS answer to the call for participation in ITRF2008, that was sent by the Combination Centers during the 2009 summer. We present here the work that was done by GRGS, and we analyse the comparison wrt the combined solution.

2 Post-fit analysis of Satellite Laser Ranging Data

Two geodetic satellites were used in this study to derive time series: Lageos-1 and Lageos-2. The network of tracking stations involves about 30 stations (most of them located in the northern hemisphere, due to a well-known inhomogeneity of the ILRS network), gathering up a total of 2000 to 3000 normal points per week. For the two satellites, over the 1993-2009 period, the averaged post-fit residual level is of the order of 1.4cm. The a priori force modelling accounts for the influence of the gravity field of the Earth, developed in spherical harmonics up to degree and order 30, and including a time-varying part due to oceanic and terrestrial tides,

[1] Géoazur - Terre Océan Espace - GRGS, Université Nice Sophia-Antipolis, Observatoire de la Côte d'Azur, CNRS, IRD, Université Pierre et Marie Curie ; Avenue Copernic, 06130 Grasse, France
[2] Institut Géographique National, LAREG - GRGS, ENSG, 6-8 Avenue Blaise Pascal, 77455 Champs-sur-Marne, France

third bodies effects. A set of six empirical coefficients is adjusted every week as well, to compensate the lackness of non gravitational force modelling acting on the trajectories: a factor for the solar radiation pressure (very close to 1, at the level of 10^{-6}), three coefficients towards the tangential direction (1 constant term, and two terms at the revolution period), two coefficients towards the normal direction (at the revolution period). Weekly normal matrices are derived relatively to the parameters to be kept in the combination: no range bias, except for a very limited number of stations (following the recommendations provided by the ILRS AWG), a set of SSC per week (relatively to the a priori TRF), daily EOPs.

Figure 1 and Figure 2 show the level of post-fit residuals analysis of weekly arcs. It is at the order of 1 cm.

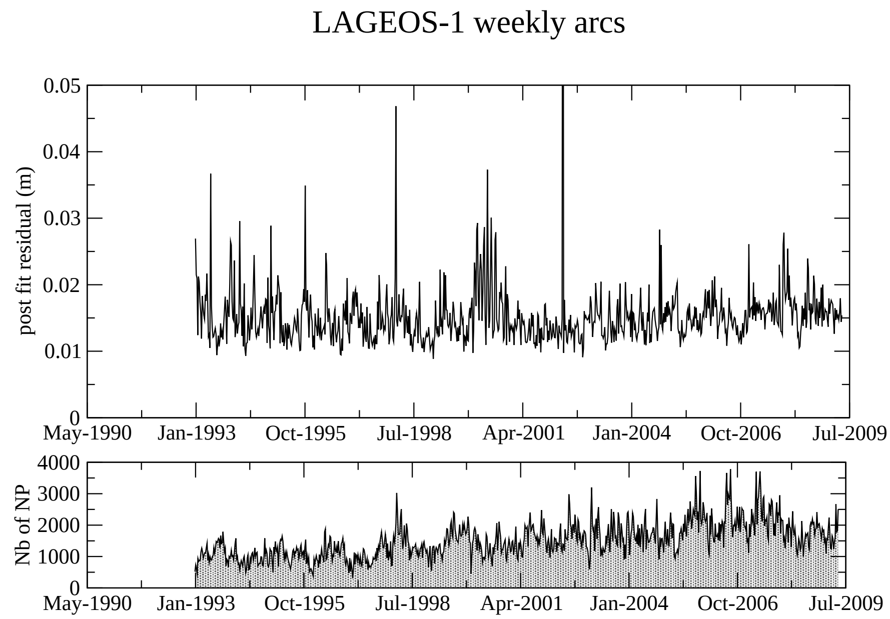

Fig. 1. Lageos-1 post-fit level of weekly residuals, over the period 1993-2009

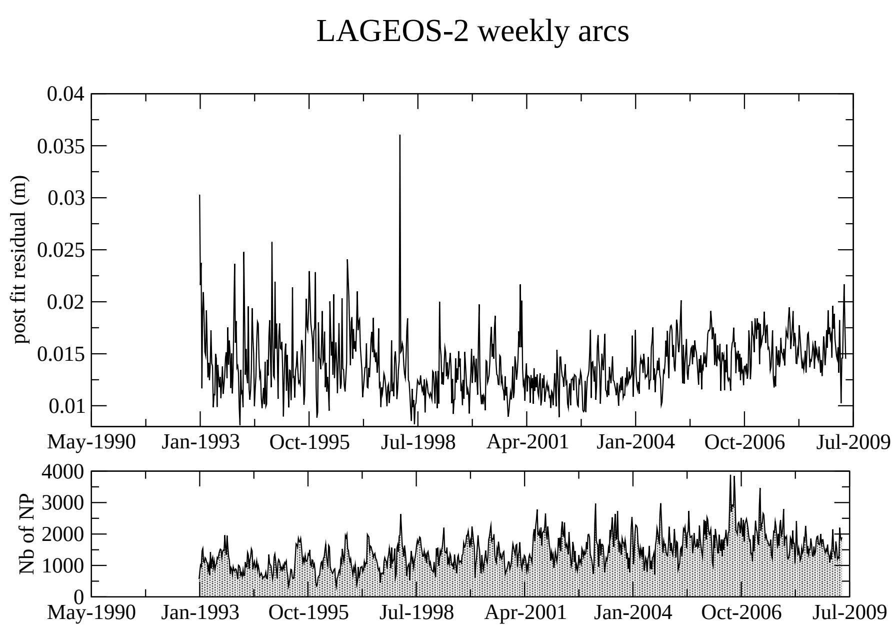

Fig. 2. Lageos-2 post-fit level of weekly residuals, over the period 1993-2009

3 Comparisons with the ILRS combined solution

Figure 3 and Figure 4 show the comparison, for the main parameters defining a TRF deduced from the orbit computations, between the ILRS combined solution and each AC contribution. It appears that, at least over that period of time, GRGS contribution is one of the closest to the combined solution.

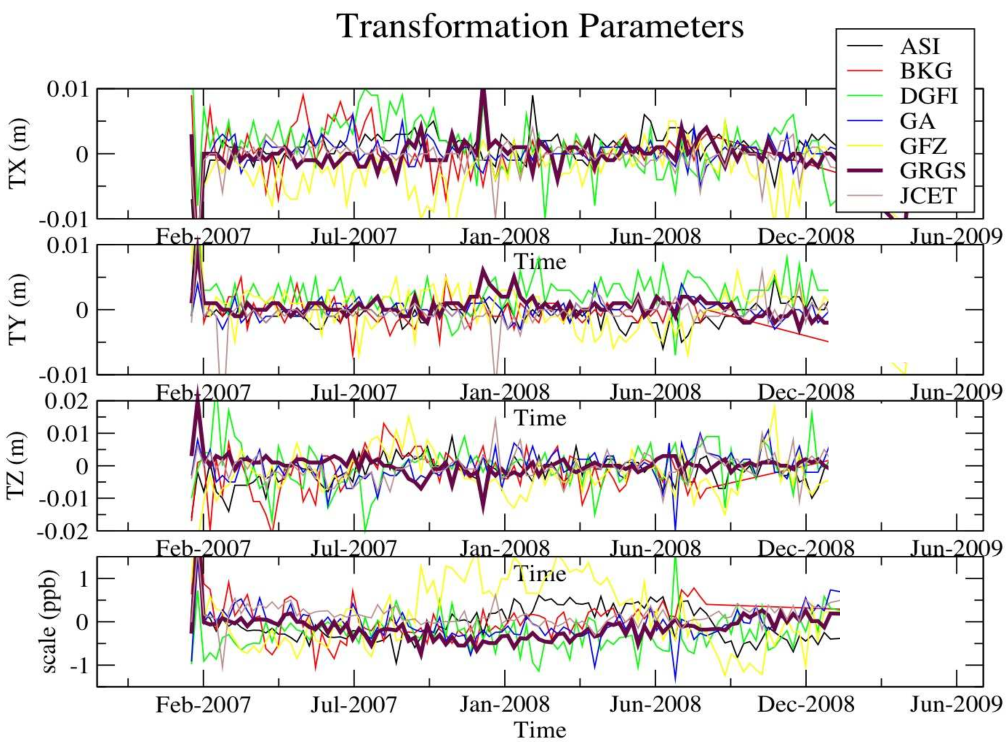

Fig. 3. Comparaison between Translation and Scale parameters provided by the different ACs, over 2007 and 2008, wrt the combined solution

Compared to the combined solution, the weekly mean residuals of the polar motion X and Y components of the solution provided by GRGS have a mean value at the level of 10 and 6 μas respectively, and a standard deviation of the order of 300 μas. The weekly mean residuals of the LOD values provided over 1992-2009 have a mean value at the level of 1 μs, and a standard deviation of the order of 60 μs. All these values are at the level of the solutions provided by the "best" ACs.

4 Impact of the a priori data corrections

ITRF retrieves coordinates and velocities from coordinate time series, under the asumption of linear station motion. But, unknown physical reasons or reasons due to technological evolution of a station equipment may induce a discontinuity within the corresponding coordinate time series. The AWG of the ILRS has identified part of these discontinuities, which have to be corrected by the insertion (and estimation) of biases to be applied before the computations. For the remaining cases, the time series is better fitted with a piece-wise linear function, estimating more than one set of coordinates and velocities. Figure 5 (Coulot et al., 2009) shows the impact of bias on the final products. It appears that the scale factor time series are more stable when station range biases are rigorously estimated and applied, and this rigorous estimation is one of the corner stones of the SLR technique, for which much work is still required by ACs, and GRGS in particular.

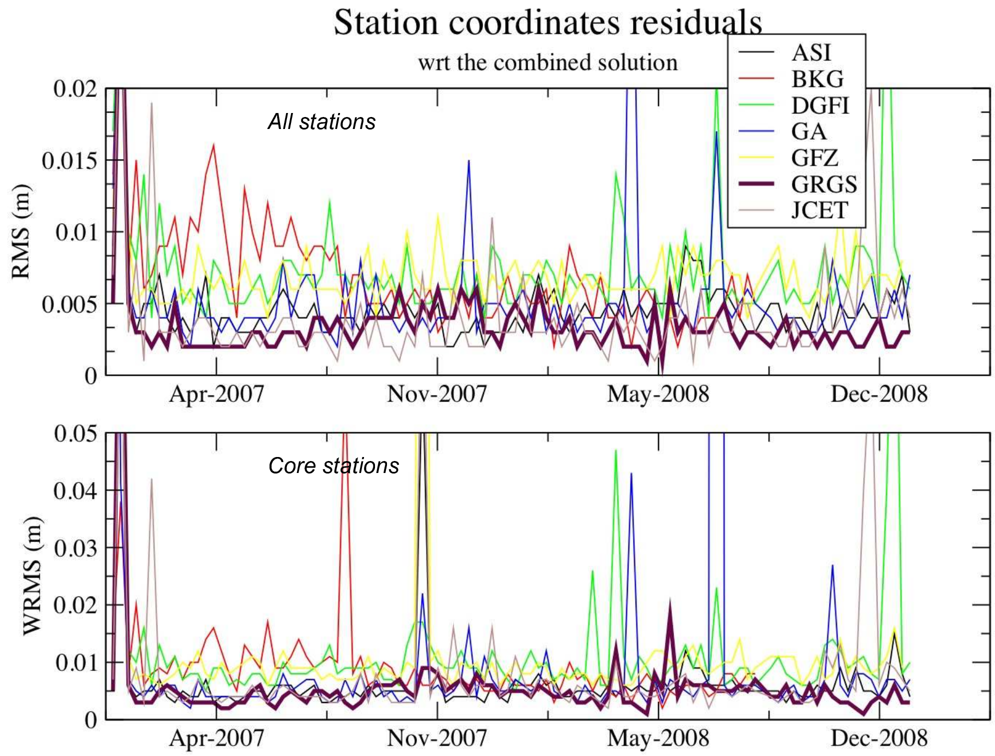

Fig. 4. Comparaison between Station Space Coordinate residuals provided by the different ACs, over 2007 and 2008, wrt the combined solution

5 Conclusion

GRGS, as an official Analysis Center of the ILRS, provides on a daily and weekly basis operational products that are available on ILRS website (http://ilrs.gsfc.nasa.gov), and on the OV-GAFF working group page (http://grg2.fr). These products are based on the recommendations provided by the AWG of the ILRS, and constitue the french SLR part of the realization of the new release of the International Terrestrial Reference Frame. Further investigation is still required to analyse precisely the accuracy and precision of the time series.

The authors thank the whole ILRS network and the staff working at the French Grasse station, and all the ones supporting french activities related to SLR data, CNES, GRGS, and Olivier Laurain, Bertrand de Saint-Jean, Pierre Exertier in particular.

References

Beckley B. D., F. G. Lemoine, S. B. Luthcke, R. D. Ray, N. P. Zelensky, 2007, Geophys. Res. Lett., 34, L14608, doi:10.1029/2007GL030002.

Coulot D., P. Berio, P. Bonnefond, P. Exertier, Dominique Feraudy, O. Laurain, F. Deleflie, Proceedings of the 2007 IAG General Assembly, Perugia, Italy, July 2 - 13, 2007, vol. 133, pages 39–46, Springer, IAG, 2009

Pearlman, M.R., Degnan, J.J., and Bosworth, J.M. 2002, The International Laser Ranging Service, Advances in Space Research, Vol. 30, No. 2, pp. 135-143, DOI:10.1016/S0273-1177(02)00277-6.

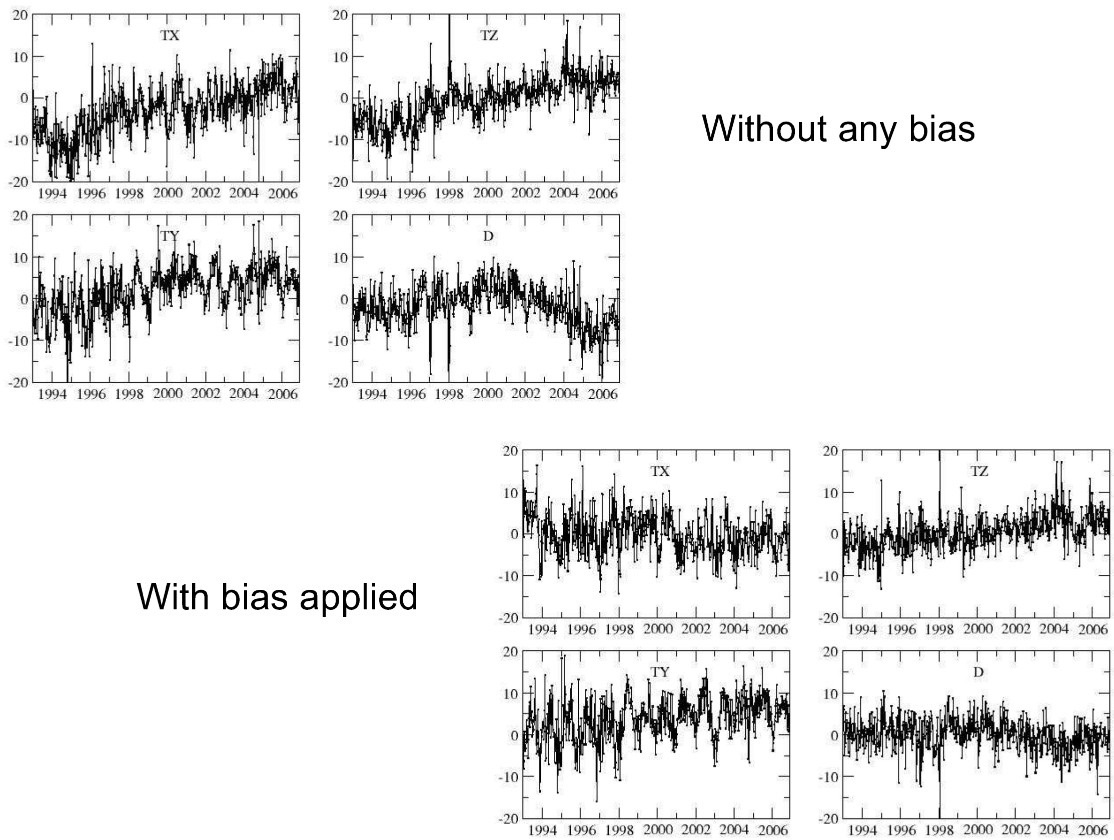

Fig. 5. Three translations and scale factor time series between weekly terrestrial frames and ITRF2000 in mm

SF2A 2009
M. Heydari-Malayeri, C. Reylé and R. Samadi (eds)

A LARGE CATALOGUE OF OBSERVATIONS OF SATURNIAN SATELLITES

Desmars, J.[1,2], Vienne, A.[1,3] and Arlot, J.-E.[1]

Abstract. COSS08 is a new catalogue of observations of the eight major Saturnian satellites which presents more than 130 000 observations (over 6 000 nights) from 1874 to 2007. The catalogue provides astrometric positions in a consistent format. The corrections applied for the reduction (refraction, aberration, phase effects) are indicated and when it was possible, the instrument and catalogue of reference star are also indicated.

1 Introduction

The eight major Saturnian satellites have been observed since their discovery during the 18th and the 19th. The first compilation of observations giving astrometric positions of Saturnian satellites is provided by Strugnell & Taylor (1990, ST90) with 51 000 observations from 1874 to 1989 in a consistent format. Harper & Taylor (1994, HT94) have extended this catalogue adding 15 000 observations from 1894 to 1922. Since 1989, many observations have been published in many different format. COSS08 (Catalogue of Observations of Saturnian Satellites) includes the observations of the previous catalogues and new ones published since 1989 and also old ones (before 1989) left out of the previous catalogues. All the observations are provided in a consistent format and the corrections (refraction, aberration, phase,...) applied for the reduction are indicated. The catalogue provides more than 130 000 observations (over 6 000 nights) of the eight major satellites of Saturn from 1874 to 2007 (Desmars et al., 2009).

2 The observations

The first observations of the catalogue are the micrometer measures from USNO made in 1874. The last observations of COSS08 are from Flagstaff in 2007. COSS08 is a compilation of four different sources:

- Observations from ST90 (reference 1-61): 51 000 observations (over 3500 nights) from 1874 to 1989. Some observations published in ST90 were reduced again and published in new articles. So these observations have been replaced by the new ones in COSS08.
- Observations from HT94 (reference 101-243): 15 000 observations from 1894 to 1922 most of them are micrometer measures.
- NSDC database (reference 420-552): The Natural Satellites Data Center provides data on natural satellites, published in different format (Arlot & Emelyanov, 2009).
- The recent observations (reference 600-608): 9 900 observations published recently and not included in NSDC.

3 Corrections of the reduction

To compare the positions given by a dynamical model with observations, we have to apply some correction like time scale, light time, aberration, refraction and phase effects. The time scale is uniform in COSS08. All the

[1] Institut de Mécanique Céleste et de Calcul des Éphémérides - Observatoire de Paris,UMR 8028 CNRS, 77 avenue Denfert-Rochereau, 75014 Paris, France
[2] Université Pierre et Marie Curie, 75005 Paris, France
[3] LAL - Université de Lille, 59000 Lille, France

observations are in UTC and TT (terrestrial time) is indicated for information. The light time is not corrected. The refraction, aberration phase effects are not necessary corrected by the observers. Sometimes, they have cleary indicated if these corrections were made. In that case, we have indicated 0 if the correction was made and 3 if the correction was not made. Most of time, the corrections are not indicated. In that case, we have adopted some rules. For example, if observations were made before 1950 (mostly micrometer observations) then we have assumed that no correction was made (we note 3 for the paramater). For observations after 1950 (mostly photographic plates), the corrections are assumed to be made. Nevertheless, many exceptions can be revealed. Finally, computing O-C with and without corrections allows to conclude.

4 The catalogue

The full catalogue is available on CDS (http://cdsweb.u-strasbg.fr/) or on web server of the IMCCE[1]. Each line provides many parameters such as the date of observation, the coordinates of the measure, the reference system and frame, the corrections of refraction, aberration and phase effects and the residuals of each observation (see Desmars et al., 2009, for details).

The O-C were computed with TASS1.7 model (Vienne & Duriez, 1995) according to the corrections. They are purely indicative. The distribution of the observations is not homogeneous (Fig1).

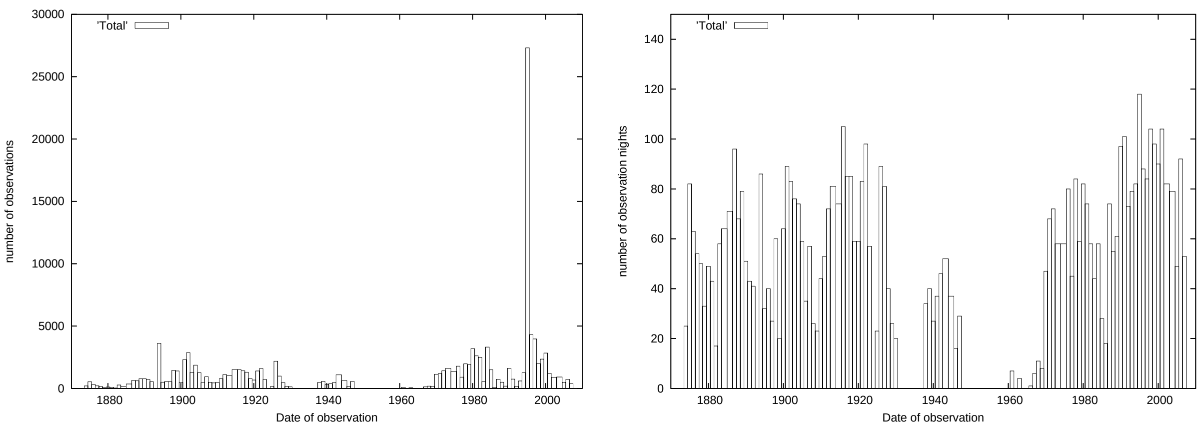

Fig. 1. Histogram of number of **Left:** observations **Right:** observation nights, at each opposition.

5 Conclusion

COSS08 is composed of more than 130 000 observations from 1874 to 2007. This catalogue can be used to fit dynamical model of the motion of Saturnian satellites. The large period covered allows also the detection of long-term perturbations in the satellite motion. Tidal effects may be detected by measuring an acceleration of the satellites (Lainey et al. 2007). Finally, we encourage observers to publish their data in the COSS08 format.

References

Arlot, J.-E., Emelyanov, N.V., 2009, A&A 503, 631

Desmars, J., Vienne, A., Arlot, J-E., 2009, A&A 493, 1183

Harper, D., Taylor, D.B., 1994, A&AS 284, 619

Lainey, V., Desmars, J., Arlot, J-E., et al., 2007, AGU Fall Meeting

Strugnell, P.R., Taylor, D.B., 1990, A&AS 83, 289

Vienne, A., Duriez, L., 1995, A&A 297, 588

[1]ftp://ftp.imcce.fr/pub/databases/NSDC/saturn/raw_data/position/1874-2007_S1-8_COSS08.data.txt

GRAVITY TESTS WITH INPOP PLANETARY EPHEMERIDES.

Fienga, A.[1], Laskar, J.[2], Kuchynka, P., Manche, H., Gastineau, M. and Leponcin-Lafitte, C.[3]

Abstract.
We present here several gravity tests made with the latest INPOP08 planetary ephemerides. We first propose two methods to estimate the PPN parameter β and its correlated value, the Sun J_2, and we discuss the correlation between the Sun J_2 and the mass of the asteroid ring. We estimate a possible advance in the planet perihelia. We also show that no constant acceleration larger than 1/4 of the Pioneer anomaly is compatible with the observed motion of the planets in our Solar System.

1 Introduction

Thanks to the high precision achieved with the observations deduced from spacecraft tracking, it becomes possible to estimate relativistic parameters γ and β of the Parametrized Post-Newtonian formalism of General Relativity (Will, 1993). Nevertheless, if γ plays a role in the equations of motion, it is worth noting that light propagation is only sensitive to that parameter. PPN γ can then be estimated with high accuracy by light deflection measurements by VLBI (Shapiro et al. 2004; Lambert & Le Poncin-Lafitte, 2009), by time delay during an interplanetary roundtrip, and by Doppler tracking data of a space mission (see for instance the Cassini experiment, Bertotti et al. 2003). This is also why, in the following, we assume $\gamma = 1$ in order to test only the sensitivity of PPN β on the perihelion's advance of planets. However, the Sun oblateness J_2 plays also a key role in this phenomena. Indeed, the usual expression of the advance of perihelion is given by (Will 2006)

$$\Delta\omega = \frac{2\varpi(2\gamma - \beta + 2)GM_{\text{sun}}}{a(1-e^2)c^2} + \frac{3\varpi J_2 R_{\text{sun}}^2}{a^2(1-e^2)^2} \tag{1.1}$$

where G and c are the newtonian gravitational constant and the speed of light in vacuum, respectively. J_2, M_{sun} and R_{sun} are the Sun oblateness, mass and equatorial radius, respectively, while a and e are the semi-major axis and the eccentricity of the precessing planet. The PPN β is, thus, correlated with the Sun oblateness J_2 through this linear relation. But, the β coefficient varies as $1/a$, while the J_2 coefficient is proportional to $1/a^2$. Using data from different planets will, thus, allow to decorrelate these two parameters. MEX and VEX tracking data have actually led to an important improvement of Mars and Venus orbits in INPOP08 (Fienga et al. 2009). Thanks to the information brought by the combination of very accurate tracking data of spacecraft orbiting different planets, the planetary ephemerides become thus an interesting tool for gravity testing. In the following, we give some examples of such tests.

2 Determination of PPN β and the Sun oblateness J_2

The advance of the perihelion induced by general relativity and the Sun J_2 has an impact very similar to the advance induced by the main-belt asteroids on the inner planet orbits. In INPOP08, a ring was added to average the perturbations induced by the main-belt asteroids which cannot be fitted individually by tracking observations. This ring has its physical characteristics (mass and distance to the Sun) estimated independently

[1] Observatoire de Besançon- CNRS UMR6213, 41bis Av. de l'Observatoire, 25000 Besançon
[2] Astronomie et Systèmes Dynamiques,IMCCE-CNRS UMR8028,77 Av. Denfert-Rochereau, 75014 Paris, France
[3] SYRTE-CNRS UMR8630, Observatoire de Paris, 77 Av. Denfert-Rochereau, France.

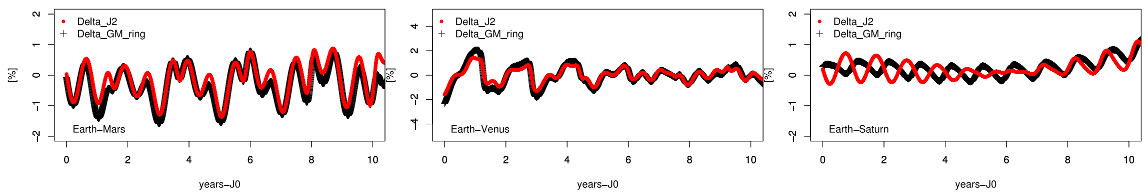

Fig. 1. Residuals obtained by comparisons between Mercury direct range, MGS/MO, MEX, VEX and Cassini range tracking data and ephemerides perturbed by a small change in the Sun J_2 (12%) and by a small change in the mass of the asteroid ring (17%).

Table 1. β intervals in which the residuals stay below the 5% limit. The values of β given here are estimated for $\gamma = 1$.

Data	β min	β max	Data	β min	β max	Data	β min	β max
MGS/MO+MEX	0.99995	1.0002	Jupiter VLBI	0.9996	1.0002	Viking	0.9995	1.0002
VEX	0.99990	1.0002	Saturn Cassini range	0.9998	1.0005	Mercury	0.9985	1.005

from the fit by considering the albedos and physical properties of 24635 asteroids (for more details see Kuchynka et al. 2008). As illustrated in figure 1, there is a correlation between the effect on the geocentric distance of the modeling of the ring as done in INPOP08, in one hand, and the effect of the Sun oblatness in the other hand. Indeed, on these plots, one may see how a small change in the value of the Sun J_2 (12%) induces, after the refit of the planet initial conditions a periodic effect very similar in amplitude and frequency as a change in the mass of the asteroid ring (17%). This effect is obvious on Mercury, Mars and Venus distances to the Earth, but not for Saturn. The Saturn-Earth distances are indeed not affected in the same way. We can also conclude that, when new accurate observations of outer planets will be obtained, they will be very useful to decorralate asteroid effects on planet orbits by combination with inner planet data. Finally, it stresses the crucial importance of having a model of the asteroid perturbations as a fixed ring, characterized independantly from the fit of planetary ephemerides. By fixing the ring, we limit then an overestimation of the value of the Sun J_2 merging in this value some effects induced by the asteroids.

In Fienga et al. (2009b), estimations of J_2 and β were done by least squares adjustements over different sets of data. The obtained results stress the correlations between J_2 and β. For more details, see Fienga et al. (2009b). An alternate strategy to study the sensitivity of the planetary ephemerides to J_2 and PPN β is to estimate how does an ephemeris built using different values for J_2 and PPN β and fitted on the same set of observations as INPOP08 differ from INPOP08. To estimate the sensitivity of the most accurate sets of data (Mercury direct range, VEX, MEX, MGS/MO, Cassini and Jupiter Galileo) used in the INPOP08 adjustment to the variations of values of J_2 and PPN β, we have estimated and plotted the S/N ratio defined as:

$$S/N = \frac{\sigma_{i,j} - \sigma_{0,0}}{\sigma_{0,0}}$$

where $\sigma_{i,j}$ is the 1-sigma dispersion of the postfit residuals of an ephemeris based on INPOP08 but with values of J_2 and PPN β different from the ones used in INPOP08 (which are $\beta = 1.0$ and $J_2 = 1.82 \times 10^{-7}$) and fitted to all the INPOP08 data sets, and $\sigma_{0,0}$ is the 1-sigma dispersion of the postfit INPOP08 residuals. Results presented as the S/N percentage, are plotted in figure 2 for MEX/MGS and VEX. For other plots see (Fienga et al. 2009b). As one can see in figure 2, the impact of the PPN β is not symmetric with respect to $\beta = 1$. In figure 2, one notices also the direct correlation between the S/N obtained with MGS/MO and MEX data and the one obtained for VEX. In table 1, we have gathered minimum and maximum values of PPN β defining the sensitivity interval of the different data sets. The sensitivity interval is the interval of PPN β for which the S/N remains below 5%. By considering figure 2 and table 1 it appears that MGS/MO and MEX data provide the most narrow interval of sensitivity with $0.99995 < \beta < 1.0002$. This interval is in agreement with the latest determinations done by Williams et al. (2009), Fienga et al. (2008) and Pitjeva (2006).

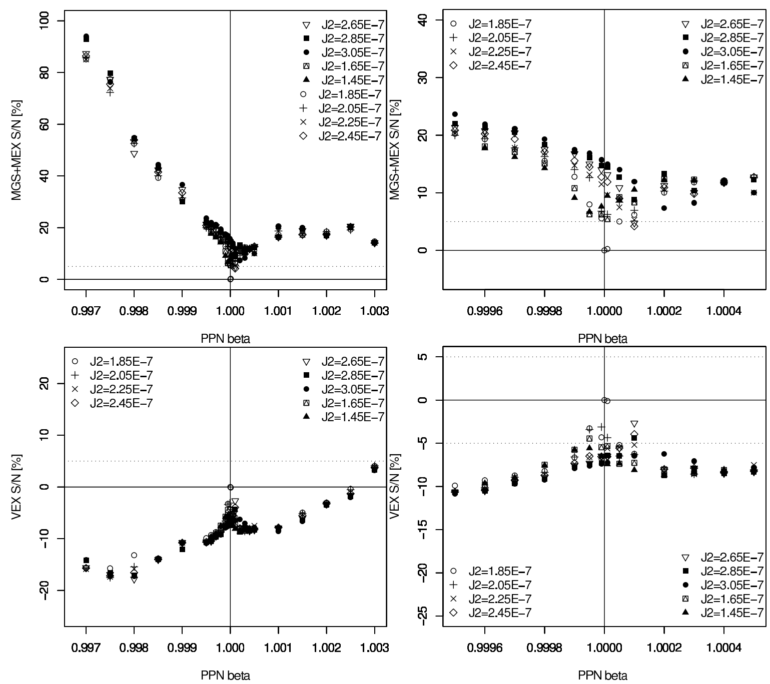

Fig. 2. Residuals obtained by comparisons between observations and ephemerides estimated with different values of PPN β (values given on x-axis of each subframes) and different values of the Sun J_2.

3 Secular advances of planetary perihelia

We are interested here in evaluating if the observations used to fit INPOP08 would be sensitive to supplementary precessions of the planet orbits. To estimate the sensitivity of the modern tracking data, we first fix J_2=1.8 $\times$ 10^{-7}, $\beta = 1$ and $\gamma = 1$. By fixing the value of the Sun J_2, we then isolated the impact of the secular advance of the perihelion, $\dot{\varpi}_{\text{sup}}$, for one given value of J_2. For each different value of $\dot{\varpi}_{\text{sup}}$, initial conditions of planets are fit to the INPOP08 observations and we compare the postfit residuals to the INPOP08 ones. The behaviour of the obtained S/N (as defined in section 2) is symmetrical to a minimum value, this minimal value being centered around $\dot{\varpi}_{\text{sup}} = 0$ or not. This symmetry explains why we give an interval of $\dot{\varpi}_{\text{sup}}$ for which the minimum of S/N is obtained. The best constraint on the Earth orbit is given by the Jupiter VLBI data set which gives the narrowest interval of $\dot{\varpi}_{\text{sup}}$. For Saturn, an offset in the minimum of the S/N is obtained for the Cassini tracking data set (-10 ± 8) and the VEX data set (200 ± 160). These estimations lead to determinations of a supplementary precession of the Saturn orbit that are only marginally statistically significant. By comparisons, (Pitjeva 2009) the value is very close to the one we obtain by considering only the S/N induced on the Cassini observations. This result shows how important the description of the method used for evaluating such quantities. The investigation about a statistically significant advance in the Saturn perihelion has to be continued in using more Cassini and VEX data. Indeed, a prolongation of the interval of time covered by these two data sets will improve the accuracy of the estimations. For more details see (Fienga et al. 2009b).

4 Does the Pioneer anomaly impact the ephemerides ?

We investigate the question of the Pioneer anomaly by using the INPOP08 planetary ephemerides as a test bed for some hypothesis describing the pioneer anomalies. A classic description of the pioneer anomalies (PA) is the appearance of a constant acceleration of about $8.75 \times 10^{-10}\mathrm{m\,s^{-2}}$, Sun-oriented after 20 AU (Anderson et al. 2002). We, thus, add this constant acceleration in the equations of motions of Uranus, Neptune and Pluto. We have then fit the modified ephemerides to observations usually used to built INPOP08. Residuals obtained after the fit are plotted in Figure 3. As it appears clearly in the residuals of Uranus right ascension, a constant acceleration of $8 \times 10^{-10}\mathrm{m\,s^{-2}}$ added to the classical Einstein-Hoffmann equations of motion can not be missed,

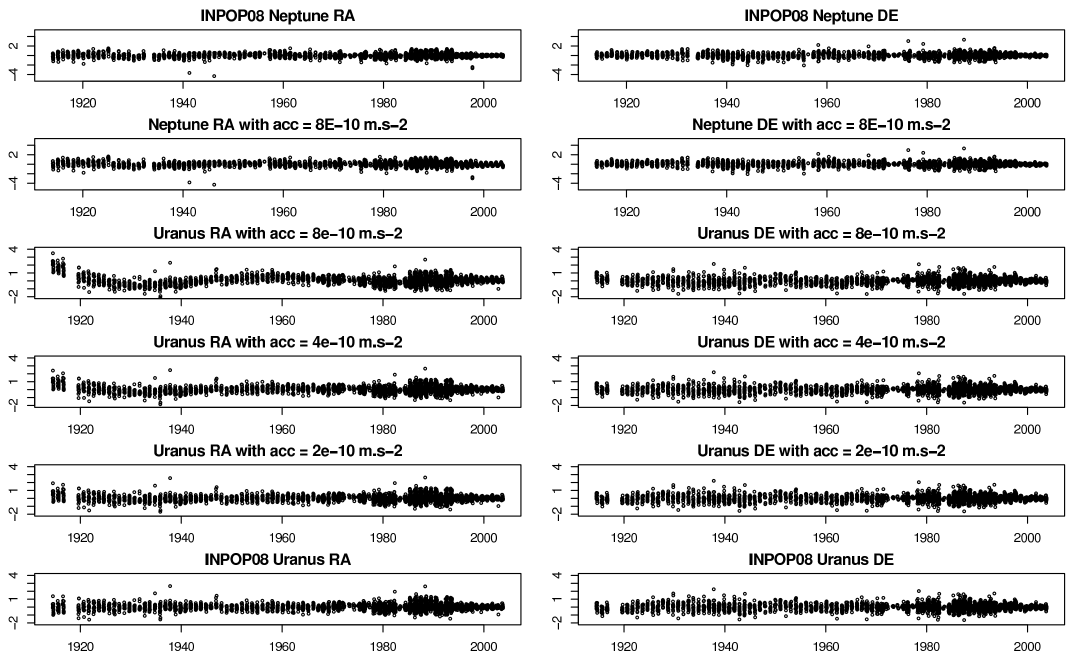

Fig. 3. Residuals in right ascension and declination of Neptune and Uranus obtained with INPOP08 (solution of reference) and fitted ephemerides including PA of different magnitudes: from 8 to 2 $\times 10^{-10}\mathrm{m\,s^{-2}}$. The x-axis are years and y-axis is in arcseconds.

even after the fit of the Uranus initial conditions. A systematic effect remains especially after 1930. This effect cannot be absorbed by the fit or by the noise of the old Uranus observations. By changing the value of the acceleration, one can see that the acceleration must be at least 4 times smaller than the one commonly adopted to be absorbed by the residuals. For Neptune and Pluto, the situation is different. For these planets, the effect of a constant acceleration is absorbed by the fit, as one can see on figure 3 with the postfit and prefit residuals of Neptune.

5 Conclusions

Concerning the determination of the PPN parameter β, an estimation of the sensitivity of planetary ephemerides to this parameter is done following two methods. Our results show that a global fit is needed in order to decorrelate parameters such as PPN β, the Sun J_2 and the asteroid pertubations. We have tested possible detection of an anomalous advance of perihelia of planets. More investigations are needed for the analysis of the perihelion rate of Saturn and more observations of Cassini and VEX data are necessary. Finally, the results obtained here for the Pioneer Anomaly conclude that no constant acceleration larger than 1/4 the PA can affect the planets of our solar system. If it was so, it would have been detected sooner. In the frame of the equivalence principle, this means that no constant acceleration larger than 1/4 the PA can be realistic.

References

Anderson, J. D., Laing, P. A., Lau, E. L., Liu, A. S., Nieto, M. M., Turyshev, S. G. 2002, *Phys. Rev. D*, 65, 082004

Bertotti, B., Iess, L., and Tortora, P. 2003, *Nature*, 425, 374

Fienga, A., Manche, H., Laskar, J.,Gastineau, M. 2009a, *A&A*, in press

Fienga, A., Laskar, J., Le Poncin-Laffite, C., Manche, H., Gastineau, M. 2009b, *IAU 261 Proceedings*, in press.

Fienga, A., Manche, H., Laskar, J.,Gastineau, M. 2008, *A&A*, 477, 315

Iorio, L., 2009, *AJ*, 137, 3615

Kopeikin, S., Makarov, V. 2008, *IAU Symposium*, 248, 391

Lambert, S., Le Poncin-Lafitte, C. 2009, *A&A*, 499, 331

Moyer, T.D.1981, *Cel. Mech.*, 23, 33.

Kuchynka, P., Laskar, J., Fienga, A., Manche, H., Somenzi, L. 2009, *JOURNEES-2008/ Astrometry, Geodynamics and Astronomical Reference Systems*

Pitjeva, E.V. 1986, *Byull. Inst. T. A., Ross. Akad. Nauk.*, 15, 538

Pitjeva, E.V. 2009, *JOURNEES-2008/ Astrometry, Geodynamics and Astronomical Reference Systems*

Shapiro, S.S., Davis, J.L., Lebach, D.E., and Gregory, J.S. 2004, *Phys. Rev. Lett.*, 92, 121101

Will, C. M. 2006, *Living Rev. Relativity*, 9, 3

Will, C.M. 1993, Cambridge University Press, New York, U.S.A.2nd edition

Will, C.M.1971, *Astrophys. J.*, 163, 611

Williams, J.G., Turyshev, S.G., Boggs, D.H. 2009, *Int. Jour. Mod. Phys. D*, arXiv, gr-qc0507083v2

T2L2/JASON-2, FIRST YEAR OF PROCESSING ACTIVITIES

Exertier, P.[1]

Abstract. The T2L2 (Time Transfer by Laser Link) project, developed by CNES and OCA will permit the synchronization of remote ultra stable clocks and the determination of their performances over intercontinental distances. The principle is derived from laser telemetry technology with a dedicated space equipment designed to record arrival time of laser pulses at the satellite. T2L2 was accepted in 2005 to be on board the Jason-2 altimetry satellite. It has been successfully launched from Vandenberg (CA, US) in June 2008. T2L2 acquired the first laser pulses a few days after the launch.

First analysis permitted to validate some important characteristics of the instrument such as sensitivity, noise, dynamic, event timer precision and ground to space time stability.

1 Introduction

T2L2 is a two way time transfer technique based on the timing of optical pulses together emitted by a Satellite Laser Ranging station (SLR) and detected by a dedicated space instrument (Fridelance et al., 1996); (Fridelance & Veillet, 1995). T2L2 was accepted as a passenger instrument on the altimetry Jason-2 satellite in 2005 (Samain et al., 2008). Jason-2 is a French-American follow-on mission to Jason-1 and Topex/Poseidon. Conducted by NASA and CNES, its goal is to study the internal structure and dynamics of ocean currents. The satellite was placed on a 1,336 Km orbit with 66 inclination by a Delta launcher the 20th of June, 2008.

The objectives of the T2L2 experiment on Jason-2 are threefold: *(i)* validation of optical time transfer (it should further allow to demonstrate one-way laser ranging), *(ii)* scientific applications concerning fundamental physics and time and frequency metrology allowing the calibration of radiofrequency techniques as GPS and Two-Way, and *(iii)* characterization of the on board DORIS oscillator (the space reference clock).

2 Experimental description

The ground segment of the experiment is based on the international laser ranging network. In addition, a given satellite laser ranging (SLR) station must be able to time both start and return times of laser pulses with a resolution of 1 ps. The laser station track the satellite as soon as it is in the right field of view, that is at a distance of less than 4000 Km. The whole duration of the satellite pass over the station is of 1000 s maximum.

The space instrument is based on a photo detector (in the 532 nm wavelength domain) and an event timer (resolution of 1 ps) linked to the space clock. A Laser Ranging Array (LRA) is also used to reflect the laser pulse toward the laser station. This LRA is provided by the JPL agency, basically as orbit determination system in addition to the GPS and DORIS orbitography space techniques. The space clock is an ultra-stable oscillator (USO, Quartz) which has been developed by CNES for the DORIS (Doppler Orbitography and Radiopositioning Integrated on Satellite) equipment. The GPS receiver of the PROTEUS plateform is connected to T2L2, in order to permanently date Pulse Per Second (PPS) coming from the GPS time in the on-board time scale; the row precision of these PPS is of $\pm 1\mu$sec. In addition to the photo detector used by the event timer, T2L2 is equipped with a second photo detector in order to measure the received energy of each optical event. Taking into account the electronic behaviour of the non-linear photo diode relatively to the number of photons, the measured energy is used to correct the time walk of the diode.

The mass of the T2L2 space equipment is 8 kg for the electronic module which is inside the satellite and 1.5 kg for the photo detection module located outside. Basically, T2L2 realizes a ground to space time transfer

[1] OCA, avenue Copernic, F-06130

between the ground clock linked to the laser station and the space clock of the satellite. The ground to ground time transfer between several remote clocks at ground is obtained through these individual space to ground time transfers. It can be obtained in a common view mode, when the distance between the laser stations is smaller than roughly 5000 Km, or in a non-common view mode when the distance is larger.

3 Data

3.1 T2L2 on board data

CNES is providing 1-day files of on board dates of optical events with a time delay of 1-2 days. Since the begining of the mission, T2L2 acquired roughly 150,000 to 250,000 events per day, consisting in solar noise, laser pulse, GPS PPS, or dedicated event for internal calibration.

A first data treatment has to be processed before all. The goal is to compute for each acquired event its aproximate GPS date (left part of Table 1); that permits to permanently establish a phase link between the GPS and DORIS time scales. Thanks to the GPS PPS, an absolute local frequency offset Δf is also estimated between the space clock and GPS along the time; after filtering the row data, the precisions of the phase link and of the local frequency offset have been estimated to 0.3 μsec and to 2-3.10^{-11} (in term of $\Delta f/f$ over 5000 s), respectively.

approximate date (via PPS-GPS)	code (and comment)	T2L2 count : (SEC)	(picoSEC)	energy
Julian date and secondes	1, 2, 4, 6	1-9999999	12 digits	0-32164
55000 12345.000001	4 (it's a PPS)	1000001	123456123456	-
55000 12346.000001	4 (id)	1000002	123456143456	-
55000 12347.000001	4 (id)	1000003	123456163456	-
55000 12347.123400	2 (it's an optical pulse)	1000003	246856165678	1234
55000 12347.223400	2 (id)	1000003	346856167890	678
55000 12348.000001	4 (it's a PPS)	1000004	123456183456	...
55000 ...	...	...	...	-

Table 1. Example of a T2L2 data file (right part) and of computed GPS date for each T2L2 event (left part). Code: 1 is an internal calibration event dedicated to the energy level, 2 is an optical event (laser pulse or noise coming from Earth's albedo), 4 is a GPS-PPS, 6 and 8 are internal calibration events

3.2 SLR full rate data

Since 1998, the International Laser Ranging Service (ILRS) is assuming a multi-satellite tracking for geosciences and Solar system applications from a network of 35 ground SLR stations. Among these stations, 17 are providing full rate ranging data for all Jason2 passes. A ranging data mainly consists in two quantities; *(i)* one date which is the start time (resolution of 1 ps) of a laser pulse, and *(ii)* the time of flight (tof) of this laser pulse between the station and the satellite LRA and return (which quantity is measured at the ps level).

As a system of time, a few SLR stations are using a standard Cesium but some of these have implemented an Hydrogen Maser. Thus, the precision of the start dates is of 1-5 ps, whereas the precision of the time of flight (the range) is of 25-35 ps for the best SLR systems (Exertier et al., 2006). In addition, the time stability over a satellite pass should be at 1-5 ps maximum.

From a quantitative point of view, the participating SLR stations provide betweeen 10 and 80 passes per month. In average, each pass is of 650 s duration and provides arround 1000 range measurements; SLR systems are using a 10Hz acquisition mode generally, but some of these have a 100Hz or a KiloHz mode. The SLR stations which contribute to the T2L2 tracking using all the technical requirements of the experiment are : Changchun (China), Koganei (Japan), Mt Stromlø(Aus), Herstmonceux (UK), Matera (I), Wettzell (G), and Grasse (F). But from month to month, there are new participating SLR systems.

4 Correlation between ground and on board dates

Because the T2L2 instrument is "on" permanently and is not able to identify the origin of each optical event (i.e., from which SLR station a laser pulse is coming), it is very important to make a correlation between the estimated arrival dates of laser pulses and the dates of T2L2 events that are recorded by the space clock. According to the T2L2 principle, the tof which is measured by an SLR station is used to compute the arrival date of a laser pulse at the satellite from the start date noted at ground. Obviously, this tof must be divided by 2 and, before all, must be corrected by the Sagnac effect (due to Earth's rotation) and by the on board position difference between the LRA and the T2L2 reference points which difference depends on the satellite attitude.

From this correlation, it emerges a time serie of what we call "triplet", consisting in three quantities: the ground and space times and the corresponding tof measured at ground (to be corrected). Obviously, considering the low energy level of the laser equipement serving as ranging systems (between 1 and 300 mJ), the divergence of the beam, the dispersion due to the atmosphere effect, the distance of the target, and finally the very small optical aperture of T2L2 opticalmodule, each emitted laser pulse from a ground station could have no equivalent on board. In that case, no "triplet" can be recorded. During the data processing, we effectively noted that higher energy level of SLR systems provides higher success of on-board events detection. The percentage of detected laser events by T2L2 relatively to the number of laser pulses emitted by a station varies from 1 to 100% with an average of 35%.

5 Stability of time transfer and conclusion

The ground to space time transfer represents the time offset between the space and the ground clocks. It is deduced from the following equation:

$$t_{start}^{UTC} + \frac{dt_{tof} + \delta t_{(Sagnac+attitude)}}{2} - t_{arrival}^{DORIS} + Instrumental\, corrections \tag{5.1}$$

The overall error budget of equation 5.1 should contain the precision of the laser ranging measurements (tof) which varies from an SLR station to another. But we can consider that the associated variance is decreasing with $\sqrt{N}$ where N is the number of row data. Thus, after averaging the tof over tens of seconds (typically 20-30 s) and properly filtering the data, the stability of ground to space time transfers (which is measured from a serie of "triplet") from Wettzell, Matera, Koganei or Grasse SLR stations ranges from 7 ps to 10 ps after 30 s of time integration using the TVAR estimator (Allan, 1983).

The fact that several SLR stations which time system is a Cesium (Grasse, Koganei) or better an Hydrogen Maser (Wettzell and Matera) , provide enough sets of "triplets" is extremely satisfactory in order to monitor the behaviour of the DORIS oscillator in space. For short time span, the stability of DORIS over 10 s and the very good results already obtained will permit to construct time transfers between two or several ground stations and the satellite if these stations are in common view. For longer time period (from 2 hours to few days), the monitoring of the DORIS oscillator sould be used to improve the technique as an orbitography and radio-positioning space technique available on board Jason2.

The author is very gratefull to colleagues of SLR stations. He adress many thanks to CNES and colleagues as E. Samain, Ph. Guillemot, I. Petitbon, Ch. Jayles, A. Auriol, for helpfull discussions and financial support.

References

Allan, D., 1983, Proc. of the 15th Annual Precise Time and Time Interval (PTTI) Meeting, 459-475

Fridelance, P., Samain, E. & Veillet, Ch., 1996, Experimental Astronomy, 91

Fridelance, P. & Veillet, Ch., 1995, Metrologia, 32(27)

Samain, E. et al., 2008, International Journal of Modern Physics D, 17(7), 1043-1054

Exertier, P. et al., 2006, Contribution of laser ranging to Earths sciences, C.R.A.S. - Geoscience Serie, 338, 958-967

SF2A 2009
M. Heydari-Malayeri, C. Reylé and R. Samadi (eds)

GRGS COMBINATION OF THE TERRESTRIAL FRAME AND EARTH ORIENTATION PARAMETERS AT THE OBSERVATION LEVEL. CONTRIBUTION TO ITRF2008 REALIZATION

Richard, J-Y.[1], Bizouard, C.[1], Bourda, G.[2], Deleflie, F.[3], Gambis, D.[1], Loyer, S.[4] and Soudarin, L.[4]

Abstract. A new version of ITRF (ITRF2008) is planned and requests combination of the various astro-geodetic techniques over a period of several years. In the framework of the " Groupe de Recherches de Godsie Spatiale ", GRGS, we are combining normal equations derived from the processing of four techniques on a regular weekly basis (GPS, VLBI, SLR and DORIS). Observations of these techniques are separately processed at different analysis centers of GRGS using the software package GINS-DYNAMO, developed and maintained by GRGS. The strength of the method is the use of a set of identical up-to-date models and standards in unique software. The datum-free normal equation matrices weekly derived from the analysis of each technique are stacked to derive solutions of Station Space Coordinates, and Earth Orientation Parameters (EOP). In this presentation, we explain the process to obtain weekly combined normal equations and validate the EOP global solutions with respect to C04 series and the SSC with respect to the ITRF2005.

1 Introduction

In this paper, we propose a combination process of geodetic observations to estimate both EOP and terrestrial frame (Coulot et al. 2007; Gambis et al. 2009). To have an overview of combination of geodetic techniques see Rothacher (2002). From 2007 until the end of 2008 normal equations (NEQ) concerning the four techniques VLBI, GPS, DORIS and SLR were processed to contribute to the new realization of the TRF, ITRF2008, whereas the former terrestrial frame ITRF2005 was published in 2007 (Altamimi et al. 2007). The process consists in using the NEQ produced by the Analysis Centers of VLBI (LAB Bordeaux Observatory), GPS and DORIS (CLS) and SLR (OCA Geoazur). Each Analysis Center produces weekly datum-free normal equations containing EOP and SSC, processed with the GINS/DYNAMO package. Other method of combination is presented in Pesek & Kostelecky (2006). The five EOP are pole coordinates (X,Y) and UT1-TAI (sampling 6 hours), nutation parameters ϵ and ψ (sampling 12 hours) and station coordinates (weekly measurement). Other parameters such as the gravity field coefficients, ocean tides, quasar coordinates, troposphere zenithal delay, orbital bias, satellite orbits, non gravitational forces, station shift coordinates are eliminated from stacked NEQ. The common geophysical models included within the GINS software, insure the consistency of observations, especially for EOP. In future, LLR observations could be included in these combinations, but the lack of LLR measurements between 2005 and 2009 disqualifies this technique.

The datum free normal equations generated by each analysis center are deposited on the ftp web site at the Paris Observatory (ftp://dynamo.obspm.fr/data/). Processes are then applied to construct the weekly combined normal equations. In the call for participation in ITRF2008, it was proposed to submit solutions resulting from a combination of various techniques at the observation level. The main requirements of ITRF2008 are to avoid any correction for geophysical fluid loading effects, except for tidal ocean loading, and to provide time series solutions in SINEX version 2.0 format in two classes: (1) Free singular normal equations (2) Solutions with TRF minimum/inner constraints.

[1] Observatoire de Paris SYRTE, 61 av. de l'Observatoire, 75014 Paris, France (jean-yves.richard@obspm.fr, +33 1 40 51 23 67)
[2] Université de Bordeaux LAB CNRS, Bordeaux, France
[3] Observatoire de la Côte d'Azur / Geoazur - GRGS, Grasse, France
[4] Collecte Localisation Satellite, Ramonville Saint Agne, France

2 Combination process

The working plan for constructing the ITRF2008 weekly normal equations is explicitly summarized in figure 1.

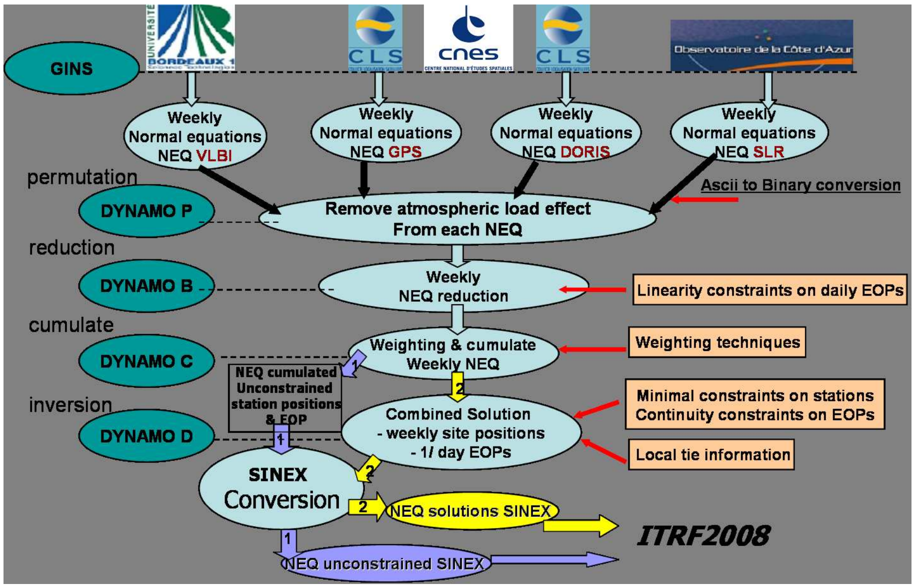

Fig. 1. Two steps are applied: 1- Production of NEQ solutions contributing to ITRF2008 and 2 -NEQ stacking using ITRF2005 and C04 as a priori for solution validation

2.1 Common process

EOP are sampled every 6h for X and Y pole coordinates and for UT and every 12h for nutation ϵ and ψ. To produce NEQ with daily EOP at 12pm as required, we introduce a linear piecewise constraint over each day and reduce the resulting EOP at 12pm. Equation system (1) express the linear constraint applied. P_j is the unknown parameter at the j date. $P_j(t)$ value (t=0,6,12,18) is forced to be on a line with an uncertainty $\sigma_P = 0.5$ for pole coordinates and for Universal Time. This linearity constraint is applied either on the corrections dP_j or on the solution plus corrections $P_j(t) + dP_j(t)$. In our case the linearity is applied on the EOP corrections with respect to the a priori EOP C04 series. These constraints on EOP are introduced while reducing all parameters not used and keeping the station coordinates as fixed to ITRF2005.

$$\begin{cases} P_j(6h) = \frac{3}{4}P_j(0h) + \frac{1}{4}P_{j+1}(0h) \\ P_j(12h) = \frac{1}{2}P_j(0h) + \frac{1}{2}P_{j+1}(0h) \\ P_j(18h) = \frac{1}{4}P_j(0h) + \frac{3}{4}P_{j+1}(0h) \end{cases}$$

Weekly resulting NEQ are weighted with a scaling factor depending on the techniques, and cumulated. The cumulated NEQ when reduced and unconstrained are produced on a weekly basis and available for steps 1 or 2.

2.2 Step 1: Unconstraint EQN in SINEX format

The non constraint normal equations are converted in SINEX format and sent to the ITRS Center (figure 1).

2.3 Step 2: Generating solutions in SINEX format

This second step consists in inverting the unconstrained weekly NEQ by introducing different constraints as explained by Sillard & Boucher (2001). First continuity constraints on daily EOP are applied with an uncertainty of 1.3mm for polar coordinates (X,Y) and for nutation (ϵ,ψ) and 1μs for Universal Time. Second systematic constraints are applied to stabilize the station positions. The station space coordinates corrections with respect to the a priori terrestrial frame ITRF2005 are limited to 1m for the three cartesian coordinates (X,Y,Z). The local ties information concerning 26 collocated stations are introduced and minimal constraints on transformation parameters are fixed to zero with a correction less than 10m. That forces the four technical networks to the a priori terrestrial frame ITRF2005 with a loose constraint. Earth orientation parameters and station space coordinates are estimated altogether in these weekly NEQ inversions. The daily EOP solutions and weekly station positions produced are deposited at the web site http://syrte.obspm.fr/~richard/ITRF2008/ (in ASCII format, SINEX format is now not available).

3 Earth Orientation Parameters solutions by combination at the observation level

Earth orientation parameters are determined throughout step 2. The combined NEQ solutions for pole coordinates are obtained by weighting GPS to 5.2, SLR to 1.7, VLBI to 1.9, and DORIS to 1.1 as obtained from the Helmert process (Sahin et al. 1992). The constraints mentioned in step 2 are applied. Since nutation and polar motion are correlated, retrograde polar motion corresponds to nutation, we choose as a first step to fix nutation to the a priori EOP C04 series. Station coordinates have been fixed to the a priori ITRF2005. The combined NEQ solutions for nutation (ϵ,ψ) are computed in cumulating the four techniques with the same weighting (GPS to 5.2, SLR to 1.7, VLBI to 1.9, and DORIS to 1.1) and by fixing the pole coordinates (X,Y) and UT to the a priori EOP C04 series. Although UT1 from VLBI is completed by GPS, DORIS and SLR UT1 measurements, their combinations do not improve UT1 estimation. This is due to the drift on UT1 issued from GPS measurements. Other approaches to combine GPS and VLBI were investigated by Thaller et al. (2006) and Gambis & Bizouard (2009). This approach is to be investigated to study the improvement of UT1 estimation by combination of VLBI UT1 and LOD from other geodetic techniques. The series of daily corrections for polar motion (X, Y) and solutions with their associated corrections for nutation (ϵ,ψ) are shown figure 2 as illustrations of the quality realized with respect to a priori EOP C04. To compare EOP solutions obtained for each geodetic technique to the combination series we have proceeded by cumulating the weekly NEQ separately for each technique with unit weighting. The estimation of EOP from cumulated NEQ of one technique consists to proceed in the same manner than step 2 mentioned above. The EOP solutions estimated by each technique are compared to EOP estimated by the multi-technique combination. RMS values weighted on inverse uncertainties are reported in Table 1. It appears that the combination leads to a small degradation of the pole component quality if we compare to GPS. This is probably due to the weighting of the different techniques for which the weight of GPS is under estimated in the combination. We can also note that nutation parameters have been better estimated by multi-technique combination in comparison with VLBI technique. It shows that nutation parameters are slightly improved by the multi-technique combination probably due to the density geodetic satellite for nutation measurements every 6h that contribute to stabilize these parameters.

EOP	VLBI	GPS	DORIS	SLR	Combination
X pole (μas)	352	72	435	271	90
Y pole (μas)	332	82	330	206	105
ϵ (μas)	388	X	504	548	291
ψ (μas)	341	276	359	690	281
UT1 (μs)	17.7	X	47	26.3	X

Table 1. Weighted RMS values on inverse uncertainties in μs (X: inconsistent)

4 Conclusions

The development of these processes allows computing simultaneously Earth Orientation Parameters and a terrestrial frame by combination at the normal equation level. The second aspect concerns the capability to compare our combination products (EOP and station positions) to others combination of intra techniques such as IVS, ILRS, IGS or IDS which contributes to the ITRF2008. The weekly weighting NEQ of each geodetic technique is worth being followed to optimize EOP measurements in order to benefit better from multi technique combination. Concerning analysis of transformation parameters and station space coordinates solutions, we invite to see Gambis Richard et al. (2009). For station positions it will be interesting to evaluate other sites

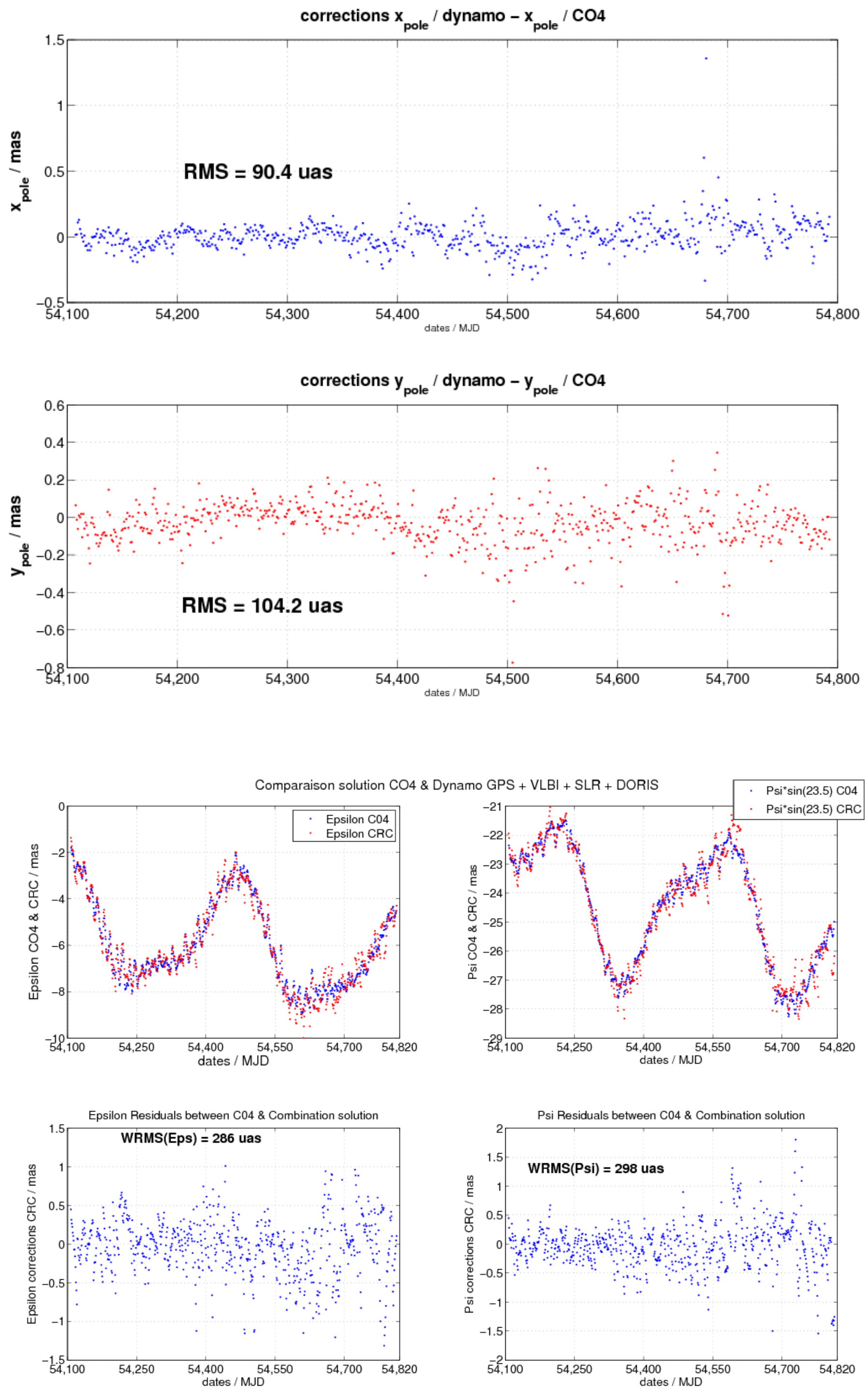

Fig. 2. Daily X and Y pole corrections, nutation solutions and corrections

with collocated stations to observe and compare the station motions with official ITRF2008. . Other method of combination is presented in Pesek & Kostelecky (2006) and should be compared to this one. Forthcoming papers will evaluate our combination products with others techniques over a longer period and to product solutions in order to participate to the future realization of ITRF.

The authors are grateful to H. Capdeville, J.M. Lemoine, T. Carlucci, for their assistance during this study. The authors express their thanks to CNES for making available GINS/DYNAMO package.

References

Altamimi, Z., Collilieux, X., Legrand, J., Garayt, B., Boucher, C. 2007, *ITRF2005, a new release of the International Terrestrial Reference Frame based on time series of station positions and Earth Orientation Parameters*. JGR, Vol. 112, B09401

Bizouard, Ch., Gambis, D., Becker, O., Richard, J.Y. 2009, *Combination of EOP from different techniques*. Proceedings of the "JSR spatio-temporels", 153

Coulot, D., Berio, P., Biancale, R., Loyer, S. et al 2007, *Toward a direct combination of space-geodetic techniques at the measurement level: Methodology and main issues*. JGR, Vol. 112, B05410

Gambis, D., Biancale, R., Carlucci, T. et al 2009, *Combination of Earth Orientation Parameters and terrestrial frame at the observation level*. Springer Verlag series, Series International Association of Geodesy Symposia, Vol. 134, Drewes (Ed), 3, DOI 10.1007/978-3-642-00860-3

Gambis, D., & Bizouard, C. 2009, *Monitoring UT1 using VLBI and GPS estimates*. Proceedings 19th European VLBI for Geodesy and Astrometry and EVGA Bourda, Charlot, Collioud (eds), 107

Pesek, I., & Kostelecky, J. 2006, *Simultaneous determination of earth orientation parameters and station coordinates from combination of results of different observation techniques*. Stud Geophys Geod 50, 537

Rothacher, M. 2002, *Towards a Rigorous Combination of Space Geodetic Techniques*. Proceedings of the IERS Workshop on Combination Research and Global Geophysical Fluids, IERS TN. No.30, Munich, Germany

Sahin M., Cross P. A., Sellers P. C. 1992, *Variance component estimation applied to Satellite Laser Ranging*. Bull. Geod., 66, 284

Sillard, P., & Boucher, C. 2001, *A review of algebraic constraints in terrestrial reference frame datum definition*. JGR, 75, 63

Thaller, D., Krgel, M., Rothacher, M., Tesmer, V., Schmid, R., Angermann, D. 2006, *Combined Earth orientation parameters based on homogeneous and continuous VLBI and GPS data*. JGR, Springer-Verlag, DOI 10.1007/s00190-006-0115-z

PCHE

High Energy Cosmic Phenomena

SF2A 2009
M. Heydari-Malayeri, C. Reylé and R. Samadi (eds)

SEARCH FOR NEUTRINOS FROM TRANSIENT SOURCES WITH THE ANTARES TELESCOPE AND OPTICAL FOLLOW-UP OBSERVATIONS

Al Samarai, I.[1], Dornic, D.[1], Basa, S.[2], Brunner, J.[1], Busto, J.[1], Boer, M.[3], Klotz, A.[3,4], Escoffier, S.[1], Gendre, B.[2], Le Van Suu, A.[3], Mazure, A.[2], Atteia, J.L.[5] and Vallage, B.[6]

Abstract. The ANTARES telescope has the opportunity to detect transient neutrino sources, such as gamma-ray bursts, core-collapse supernovae, flares of active galactic nuclei... To enhance the sensitivity to these sources, we have developed a new detection method based on the optical follow-up of golden neutrino events such as neutrino doublets coincident in time and space or single neutrinos of very high energy. The ANTARES Collaboration has therefore developed a very fast on-line reconstruction with a good angular resolution. These characteristics allow to trigger an optical telescope network; since February 2009, ANTARES is sending alert trigger one or two times per month to the two 25 cm robotic telescope of TAROT. This optical follow-up of such special events would not only give access to the nature of the sources but also improves the sensitivity for transient neutrino sources.

1 Introduction

The ANTARES neutrino telescope is located 40 km offshore Toulon in France at 2500 m depth in the Mediterranean sea. The Detector is a three dimensional net of 900 OMs (Optical Modules) distributed on 12 lines over 25 floors (storeys) per line. Each OM is a glass sphere housing the photomultiplier and its electronics. The goal of the experiment is to detect high energy muons induced by the interaction of cosmic neutrinos with the matter surrounding the detector. When the neutrino induced-muon goes through the detector or by its vicinity, a Cherenkov light cone is emitted along its track which is detected by the photomultipliers. The detection of such neutrinos would be the only direct proof of hadronic acceleration in cosmic rays and so, allows the identification of ultra high cosmic ray acceleration sources or even their discovery without ambiguity.

2 The Rolling Search

2.1 *Principle and advantages*

Originally proposed by Kowalski & Mohr, the principle is based on the detection of either a neutrino burst (doublet, triplet or more) coming from the same direction within a defined time window or the detection of a single high energy neutrino event by requiring that its energy is higher than a certain threshold (typically higher than few tens of TeV if a Waxman−Bahcall flux is considered). This should reduce significantly the atmospheric neutrino background (Dornic et al. 2008). In contrary to searches triggered by satellite detections which are limited by the satellites field of view (e.g. SWIFT field of view is 1.4 sr), this detection can cover instantaniously a whole hemisphere. More important, no assumption can be made on the nature of the source or on its mechanisms. Therefore, it is necessary to complement it by a follow up detection using other messengers than neutrinos. This follow up can be done by X-ray satellites, optical satellites or even radio for Gamma Ray Bursts.

[1] CPPM, Faculte des Sciences de Luminy, 163 avenue de Luminy, 13288 Marseille Cedex09, France
[2] LAM, BP8, Traverse du Siphon, 133376 Marseille Cedex 12, France
[3] OHP, 04870 Saint Michel L'Observatoire, France
[4] CESR, Observatoire Midi-Pyrénées, CNRS, Université de Toulouse, BP 4346, 31028 Toulouse Cedex 04, France
[5] LATT, Observatoire Midi-Pyrénées, CNRS, Université de Toulouse, 14 avenue E. Berlin, 31400 Toulouse, France
[6] CEA-IRFU, centre de Saclay, 91191 Gif-Sur-Yvette, France

2.2 Candidate sources

Gamma-Ray Bursts are probably the most energetic explosions in the Universe releasing more than $\sim 10^{51}$ ergs on time scales of seconds. These highly energetic jets make GRBs the most promising sources for cosmic rays acceleration. Being extremely relativistic ($\Gamma \sim 100$), protons are accelerated to high energies and interact with ambient prompt photons producing pions and kaons, which in their decay produce neutrinos (Guetta et al. 2003). Neutrinos are emitted with energies ranging from few tens of TeV to EeV and are expected to be contemporaneous with the gamma ray emission. After the gamma prompt emission and the expected neutrino signal emanating from GRBs, an afterglow at longer wavelengths can be detected ranging from X-rays to radio and lasting from seconds to few days after the explosion.

Long gamma-ray bursts have been found to be tightly connected with core-collapse supernovae (Hjorth et al. 2003) but few core-collapse SNe might have mildly relativistic jets (∼1%). In contrary to those expected to give birth to GRBs, these jets have a bulk Lorentz factor of a few ($\Gamma \sim 3$) which is insufficient for the jet to go through the progenitor outer layers. Nevertheless, neutrinos could be produced as protons can still be accelerated in such conditions. Hence, neutrinos are the only prompt emission which can be detected from these gamma-hidden sources (Ando & Beacom 2005). Using the mildly relativistic jet model from Paper I, the total expected neutrino flux from one core collapse supernova situated at 10 Mpc in ANTARES is presented in Fig. 1. The neutrino flux issued from pion decay and kaon decay are shown separately. A neutrino energy cut off at 20 TeV related to the cooling break energy of the parent meson and the parameters choice used in the model was applied as suggested in Paper I. ANTARES is sensitive to energies above 100 GeV. As a consequence, neutrinos from kaon decay are more likely to be detected by ANTARES.

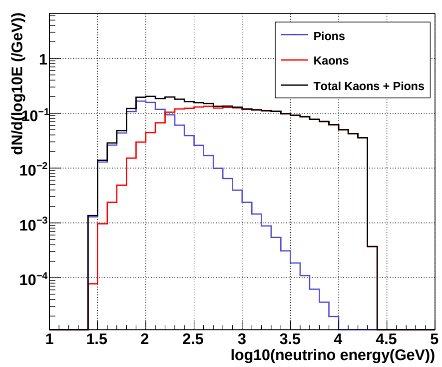

Fig. 1. Neutrino event spectrum in ANTARES from pion and kaon decay in the mildly relativistic jet model of Ando and Beacom for a core collapse supernova at 10 Mpc

3 ANTARES Neutrino alerts

Since the beginning of 2008, ANTARES has implemented an on-line event reconstruction. The trigger is based on local clusters of photomultiplier hits. Since this reconstruction was intended to work on-line, it takes 5 to 10 ms per event and has an acceptable angular resolution. The minimal condition for an event to be reconstructed is to contain a minimum of six storeys triggered on at least two lines. To select a background free sample of up-going neutrino candidates, a quality cut on χ^2 minimization based on the time and the charge of the muon track is applied. A key of success for the follow up procedure is a very fast event reconstruction so the dynamic reconstruction of the detector lines geometry is not used. As a consequence, the angular resolution is degraded comparing to the standard off-line reconstruction($0.2°$-$0.3°$) which includes the detector positioning. Hence, the off-line reconstruction will also be used afterwards to have the refined position of the emitted neutrino.

Two trigger types can actually induce an alert emission to the telescope. It could be a high energy event detection (around 10 TeV) or a detection of a burst of two or more neutrinos coming in $3° \times 3°$ angular window and 15 mn temporal window. The probability to have a high energy event in ANTARES is quite large since atmospheric neutrinos which might be very energetic account for an irreductable noise (around 1000 per year).

Doublets are expected to be detected around 5 10^{-3} per year, hence, their detection is almost significant. The detection of higher order multiplets are of course even more significant.

Currently, alerts sent to the telescope are caused mostly by highly energetic events selected with cuts on the number of touched floors and the amplitude of the hits. The selection is constrained by the fact that a reasonable number of one to two alerts per month should be sent to the telescope.

Fig. 2 represents the events distribution as a function of the touched floors used in the fit. With a cut on the number of touched floors greater than 19 and an amplitude greater than 150 photoelectrons, we are able to select 1.5 high energy events per month with a mean energy around 5 TeV calculated with the ANTARES 12 lines configuration. Furthermore, the angular resolution of the so selected events have to be lower than the telescope field of view ($\sim 1°$ radius). Fig. 3 points out the improvement of the angular resolution after cuts for high energy events selection. A mean angular resolution of 0.8° for 5 TeV events mean energy is found with the on-line reconstruction.

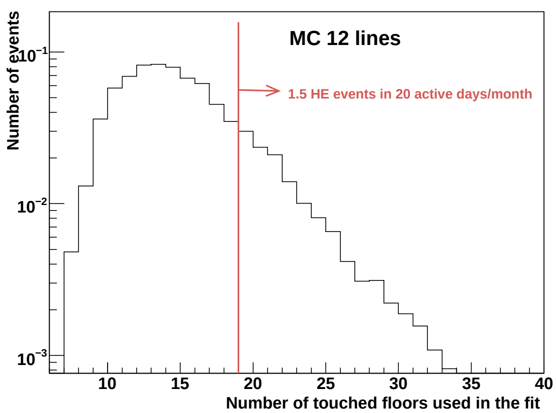

Fig. 2. Event distribution according to the number of touched floors used in the fit

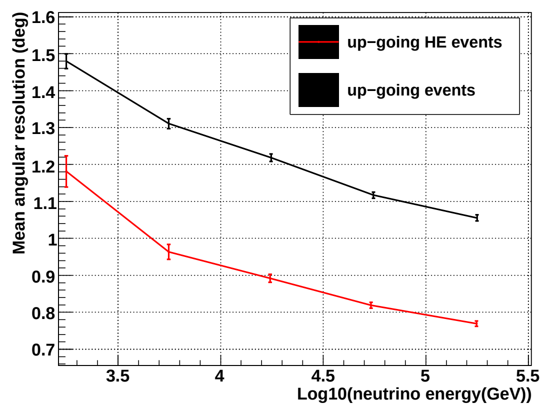

Fig. 3. Mean angular resolution as a function of the events mean energy

4 Optical Follow-up

TAToO is the project gathering ANTARES and TAROT telescopes for a follow up program. TAROT (*Télescope à Action Rapide pour les Objets Transitoires*, Rapid Action Telescope for Transient Objects; (Bringer, Boer et al. 1999)) is composed of two 25 cm robotic telescopes located at Calern in France and at La Silla in Chile. Its large field-of-view (1.86° × 1.86°) matches ideally the resolution of the ANTARES telescope. Moreover, its short repositionning time (around 10 seconds from the alert reception) is a great asset for the observation of the first moments after the neutrino signal.

The optical telescope observation strategy is of course specific to each detected object. While the optical afterglow from a GRB needs to be observed quite rapidly, core collapse supernovae can still be visible several days after the neutrino detection. For this reason, the observation strategy consists of a real time optical observation followed by others distributed over the month. Each observation involves six images of 3 minutes each.

5 Core collapse supernova detection in ANTARES

Considering the core collapse supernova jet model suggested in Paper I, we find that around 2 upward-going muon neutrino events coming from one core collapse supernova at 10 Mpc within 10 s should be expected. This rate is quite high, but for our particular triggers, this will be greatly reduced. In Fig. 4, one can see the distribution of the expected high energy neutrino events in ANTARES from one supernova as a function of its distance and the distribution of events with no conditions on energy which are multiplet candidates. Using a rate of core collapse supernovae of about 1 per year within a 10 Mpc sphere (Ando, Beacom, Yuksel 2005), one can calculate the number of detectable core collapse supernovae with our particular triggers.

The distance at which we obtain a maximal detection proability is around 4.5 Mpc for doublets comparing to 1.6 Mpc for high energy singlets. Poissonian fluctuations around the number of expected events was included leading to a large increase in the number of detectable supernovae, as one samples from a larger volume. The doublet trigger is more efficient for core collapse detection. In fact, when applying high energy conditions for singlets, the number of expected events is considerably reduced. Hence, high energy singlets are found to be less than doublets causing by this fact supernova-jet detection to be restricted within shorter distances. Furthermore, when using the model, a cut off energy around 20 TeV has been applied implying the rejection of highest energy events. The number of detectable supernovae within the distance of maximum detection probability is 2 10^{-3} per year for high energy singlets and 6 10^{-2} for doublets.

The rate of core collapse supernovae used is a lower limit. Indeed, the rate is expected to be 2 to 3 times higher as suggested in Paper II, especially for nearby galaxies (less than 4 Mpc) allowing a core collapse supernova detection within 5 years using the doublet trigger. This detection is not yet significant but the probability for a core collapse supernova detection with TAROT is not included. This should make the detection meaningful when considering the visibility volume and the efficiency of TAROT for supernova detection.

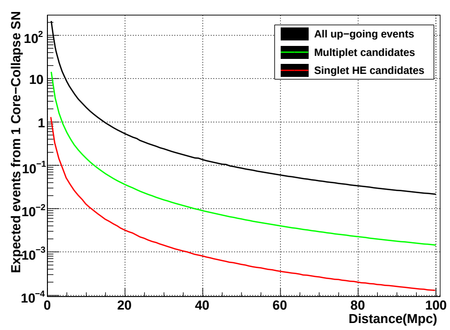

Fig. 4. Number of expected high energy events and candidate multiplet events in ANTARES from one core collapse supernova at 10 Mpc using Ando and Beacom supernova -jet model

6 Conclusion

TAToO is a transient sources search program using neutrino detection to trigger an optical telescope. At this time, two trigger types are used to send an alert to the telescope: the high energy singlets and the multiplet events. The angular resolution obtained with the on-line reconstruction can be reduced down to 0.2°-0.3° using the off-line reconstruction and hence the source direction can be refined after the alert sending. The on-line alert processing takes less than a minute for the direction to be sent to the telescope and can still be ameliorated. TAToO is now running efficiently and 8 alerts triggered by high energy events have already been sent successfully to the telescope. The image analysis is still in progress.

References

Kowalski, M. & Mohr, A. 2007, Astroparticle Physics, 27, 533-538

Dornic, D., et al, 2008, arXiv:astro-ph/0810.1452

Guetta, D., Hooper, D., et al. 2003, arXiv:astro-ph/0302524v2

Hjorth, J., et al. 2003, Nature 423, 847

Ando, S. & Beacom, J.F. 2005, arXiv:astro-ph/0502521v2 (Paper I)

Bringer M., Boer M., et al 1999, A&AS, 138 581

Ando, S., Beacom, J.F., Yuksel, H. 2005, Phys. Rev. Lett. 95 (2005) 171101 (paper II)

SF2A 2009
M. Heydari-Malayeri, C. Reylé and R. Samadi (eds)

OVERVIEW OF THE LISA MISSION AND R&D DEVELOPMENTS AT THE APC

Argence, B.[1], Halloin, H.[1], Jeannin, O.[1], Prat, P.[1], Turazza, O.[1], de Vismes, E.[1], Auger, G.[1] and Plagnol, E.[1]

Abstract. The study of the gravitational waves opens a new window for the observation of the universe. Completing the observations obtained from electro-magnetic waves, neutrinos and cosmic rays, the gravitational waves will provide informations on the most violent phenomena in the universe, as supernova explosions, collisions of binary systems or mergers of black holes. Their study will thus increase our knowledge in astrophysics, but also in cosmology and fundamental physics. This paper will make a short presentation of the future space interferometer LISA, aiming at detecting gravitational waves, and presents an overview of the R&D developments for LISA at the APC laboratory.

1 Introduction

The first idea of gravitational waves (GW) is attributed to Laplace in the early 19^{th} century. It took a hundred more years to get the first formalism of a gravitational wave. This was done by Einstein as a consequence of general relativity. A GW is described as a distortion of space-time resulting by the relative movement of massive objects. It leads to such small distance variations that only GW emitted by extremely massive objects can potentially be detected. Due to their very weak interaction with matter, GW offers an incomparable tool for the study of the early Universe. So, they are a unique way to access features of massive objects, as binary systems of black holes, neutron stars or white dwarfs, at different stages of evolution.

The existence of GW has been indirectly proven but there is still no direct detection. The first detectors to emerge in the 60s were resonant bars. Since the 90s, ground interferometers have been built and began collecting data in the last decade: VIRGO and GEO in Europe, LIGO in the United States and TAMA in Japan. The detection band of these detectors is between a few tens of Hz to several thousands. The lower limit is mainly fixed by the seismic noise. So the idea of a space interferometer emerged in the early 80s. The Laser Interferometer Space Antenna will be able to detect gravitational waves below 1 Hz and will thus complement ground interferometers observations.

2 Mission and Technology

2.1 LISA

The LISA mission is a joint ESA-NASA spaceborne project, aiming at detecting gravitational waves in the frequency range $10^{-4} - 1$ Hz (Danzmann K. 2000). It consists of 3 spacecraft in a nearly equilateral configuration orbiting around the sun, about 20 degrees behind the Earth. The spacecraft are separated by 5×10^6 km, constantly following free-flying masses located at their center.

On each spacecraft, two laser beams are emitted towards the other satellites, resulting in six laser links. These interferometric measurements are used to precisely monitor the distance between the inertial masses and, hence, to detect the tiny variation due to the passage of a gravitational wave. So, the expected performance of LISA relies on two main technical challenges: the ability for the spacecrafts to precisely follow the free-flying masses and an outstanding precision of the phase shift measurement.

[1] APC, Université Paris 7 Denis Diderot, 10, rue Alice Domon et Léonie Duquet, 75025 Paris Cedex 13, France
e-mail: `argence@apc.univ-paris7.fr`

The goal of LISA is to detect gravitational deformations as small as $\Delta L/L \approx 7 \times 10^{-21}/\sqrt{Hz}$ (i.e 7 pm per million of km) around 5 mHz. Contrary to a classical Michelson interferometer, the optical signal is obtained from two different laser sources. As a consequence the beam phase noise does not vanish and the relative frequency stability of the lasers must be at the same level as the expected sensitivity ($\Delta L/L = \Delta\nu/\nu$). This requirement is far beyond any standard stabilization technique developed on ground and foreseeable for a future space mission. Nevertheless, this stability can be achieved for LISA thanks to three successive stabilization stages :

Time Delay Interferometry : While each optical signal is the combination of two laser sources, the frequency noise of each source is also propagating on two laser links. Thus, by correctly combining the interferometric signals, taking into account the propagation delays (around 16 s between two spacecraft), it is possible to cancel the laser noises (and, so, recover a 'Michelson-like' signal). However, due to the finite precision of the time stamps (drifts of the ultra stable clocks), the application of this method is not perfect and the noise reduction factor is of the order of 10^8.

Arm-locking : In the interesting frequency range of LISA ($10^{-4} - 1$ Hz), the distance between the free-falling masses is very stable. Consequently, it can be used as a length (i.e. frequency) reference. This technique requires the frequency reference of the pre-stabilization to be slightly tunable.

Pre-stabilization : Even with TDI and arm-locking, the light emitted by the laser sources needs to be very stable, at the level of 10^{-13} in term of relative frequency change. Up to now, pre-stabilization on a Fabry-Perot cavity has been considered (Jedrich N. 2006). However, another pre-stabilisation technique often used in metrology (Hall et al. 1999 and references therein), based on the use of a hyperfine transition of the iodine molecule as frequency discriminator, may be an interesting way.

2.2 LISA Pathfinder

The LISA Pathfinder (LP) mission is a preliminary technological mission in order to test the numerous technologies that will be used by LISA. The launch is planned for the end of 2011. LISA Pathfinder consists of a single spacecraft including two inertial masses and an optical bench. These masses are nearly perfectly free-falling, the imperfection is caused by residual forces that create disturbances (electric fields, gravity gradients, solar wind, charged particules, etc). The main objective of this preliminary mission is to validate different experimental techniques related to the inertial masses. First, LP should help us to quantify the acceleration noise due to these residual forces that will perturbe the free-falling masses. Then, LP will test the capability of *drag free system* to correct the position of the satellite with respect to inertial masses. This involves testing the inertial sensors and the micro-propulsion system. The last main aim is to test the feasibility of laser interferometry at the level of accuracy envisaged for LISA (within one order of magnitude).

3 R&D developments at the APC

The R&D activities at the APC laboratory are focused on two main axes. The first one was to achieve a frequency stabilized laser system compatible with the pre-stabilization requirements of LISA. The second one is to design an optical simulator of LISA able to quantify the noise of the different instruments, to study the interactions of the different noises and to make the connection between physical measurements and reduction noise algorithms.

3.1 Laser Frequency Stabilization

The Fabry-Perot (FP) pre-stabilization technique, as planned for LISA, is based on a fixed-length, ultra stable optical resonator. It was proved to meet the LISA requirement in terms of intrinsic frequency stability (Jedrich N. 2006). Nevertheless, some limitations can be identified with this technique. First, the performance of the FP cavity is very sensitive to mechanical, but also to thermal disturbances. Additionally, they do not provide an absolute frequency reference. Finally, the performance of the arm-locking algorithm can be increased with the precise knowledge of the Doppler frequency shift (consequence of the relative drift of one spacecraft w.r.t another one). The pre-stabilization method presented here proposes an interesting alternate technique, based on molecular spectroscopy, that can circumvent these issues. It offers the required performance with very good long-term stability (fixed frequency reference). The knowledge of the Doppler shift is therefore directly measured from the beat frequency. The position of a molecular transition is also much less sensitive to thermal perturbations than a cavity, the constraints being typically relaxed by about 3 orders of magnitude.

These systems have to both meet the spatial constraints (simplicity, compactness, minimizing the consumption of energy) and achieve frequency stability performance comparable to those obtained in metrology. In order to perform a precise analyse of the frequency stability of our iodine stabilized laser, we decide to build two identical systems allowing frequency comparisons. Consequently, the stability of the systems is determined by the measurement of the joint performance.

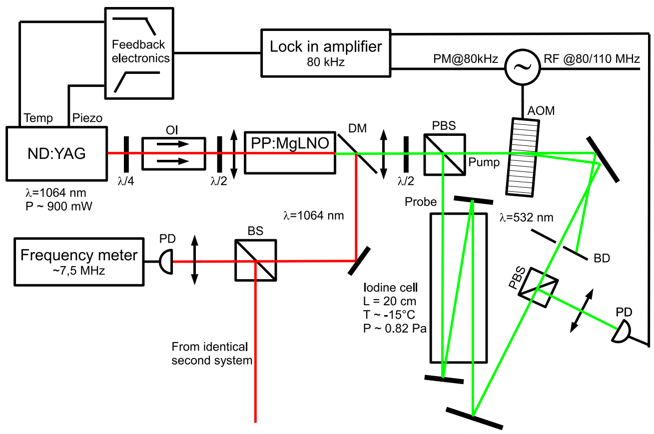

Fig. 1. Experimental layout of the iodine laser stabilization. OI: Optical Isolator, DM: Dichroic Mirror, BS: Beam Splitter, PBS: Polarization Beam Splitter, AOM: Acousto-Optic Modulator, PD: Photodiode, BD: Beam Dump, PM: Phase Modulation, RF: Radio Frequency

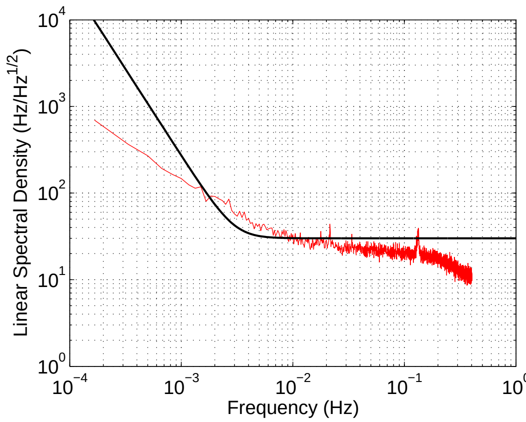

Fig. 2. Frequency stability of one system: in red, the linear spectral density corresponding to our data ; in black, our objective (see text for details).

The experimental setup of one of our system can be seen on figure 1. A complete description of the experience will be given in Argence et al. (in preparation). We use commercial NPRO Nd:YAG lasers that produce about 1W light power at 1064 nm, the wavelength chosen for LISA. Unfortunately, there is no known strong molecular resonance to lock the lasers around 1064 nm. However, iodine provides strong, narrow hyperfine transitions around 532 nm corresponding to the second harmonic of Nd:YAG laser. Thus, the frequency of the laser is doubled with a single pass through a non-linear crystal. A dichroic mirror is then used to separate the two wavelengths. The infrared parts of the two systems are then recombined with a beam splitter and sent to a fibred photodiode. The frequency noise of the beat is assumed to be the (quadratic) sum of the frequency noises of each of the systems.

The green beam is divided in two non-equivalent power parts: the pump beam and the probe beam. Both beams counter propagate within the iodine cell. This configuration allows to get rid of the Doppler broadening effect due to the thermal movements of the molecules. One of these beam (the pump) is strong enough to 'saturate' the line (i.e. a large part of the molecules on its path are in a excited state). The other beam (the probe), of much weaker intensity, is used to scan the absorption profile. The molecules that have already been excited by the pump beam cannot absorb the probe beam and then cause a dip in the absorption profile. With the two beams being of the same wavelength (or shifted by a constant value, see below), only molecules with a given velocity (projected on the light path) are simultaneously saturated by the pump and scanned by the probe beam.

The pump beam is frequency shifted and modulated by an acousto-optic modulator (AOM). The method used here is the modulation transfer spectroscopy (MTS), which already demonstrated very good results on similar experiments (Hall et al. 1999 and references therein). By four waves mixing, the modulation is transferred to the probe beam. The carrier side-bands interference produces a beat on the probe beam whose amplitude is roughly proportional to the derivative of the line profile and can then be used as an error signal for the feedback electronics. After demodulation with a lock-in amplifier, the error signal is fed through the feedback electronics, acting on the temperature and piezo-electric actuator of the laser crystal. The temperature is used for correction of large deviations on long timescales (below about 70 mHz), whereas the piezo-electric actuator handles higher frequencies, up to about 1 kHz.

The estimated linear spectral density for a single laser is plotted in figure 2. The solid line corresponds to the laser stability requirements fixed for the LISA mission and therefore our objectives of frequency stability (Jedrich N. 2006). Thus the frequency noise in terms of linear spectral density has to be below $30 \cdot \sqrt{1+\left(\frac{3mHz}{f}\right)^4} Hz/\sqrt{Hz}$ between 10^{-4} and 1 Hz. Above 10 mHz, the spectrum is roughly flat, below our objective of 30 $Hz/\sqrt{Hz}$, with a slight tendency to decrease toward 10 $Hz/\sqrt{Hz}$ at higher frequencies. Below 10 mHz, the frequency noise increases. This is probably due to thermal environnement fluctuations. The forthcoming move in a clean room, temperature-stabilized, should provide better results in this frequency range.

3.2 LISA On Table (LOT): Optical Simulator of LISA

Besides the technology of the inertial masses which will be tested with LISA Pathfinder, the success of the LISA mission depends on its capacity to measure very small displacements (i.e. for LISA, measuring phase difference variations). The measurement of this phase shift changes mainly relies on very good performance of the three stabilization stages: algorithms accuracy (TDI), precise feedback loops (arm-locking) and frequency pre-stabilization but also on extremely low noise of the different instruments (as phasemeters or photodiodes). Although the performance of these different key points can (at least partially) be tested in the lab, their interaction is difficult to simulate and predict. Especially, the travel time of the light from one spacecraft to another (16s) cannot be reproduced on ground. Nevertheless, in order to simulate the LISA signals, only the phase of the laser beams needs to be delayed, not the carrier (only the phase is carrying information). Given the low frequency range of phase variations, storing the phase information requires only moderate amount of memory.

Consequently, we are developing an optical simulator of LISA called LOT for LISA On Table. It will be able to test noises and interactions of different instruments and to apply on physical data the noise reduction algorithms as TDI. The LOT is divided into three parts corresponding to the three spacecraft. Each part contain one "local" beam and two "distant" ones. Initially, the same laser source will be used for the 9 beams, this allows to cancel the relative laser frequency noise. The phase (i.e. frequency) variations are introduced by acousto-optic modulators (AOM) with appropriate delays. A well-known configuration of the AOMs, called "cat's eye configuration", allows to change the frequency of the laser beam over a high range (>10MHz) with no angular deviation. The chosen configuration also allows the two "distant" beams to follow the same optical path on perpendicular polarisation. Then photodiodes connected to phasemeters (prototype developed at the AEI, Hanover) measure the beat between the "local" beam and the two "distant" ones. These beat signals can then be used for post-processing as TDI algorithm or frequency control (arm-locking).

4 Conclusion

The LISA mission is planned for launch in 2020. However, its future depends on the success of the LISA Pathfinder mission. Besides, the R&D developments at the APC are in progress, the laser pre-stabilisation on iodine shows results compatible to LISA requirements. With the help of others LISA teams, the APC is currently developing hardware simulator of LISA aiming at testing interaction between numerical algorithms and instruments.

The authors wish to thank A. Brillet (Observatoire de Nice) and O. Acef (Observatoire de Paris) for helpful discussions and involvement. We also acknowledge the French Space Agency (C.N.E.S.), especially J. Berthon and L. Mondin, for its technical and financial support of this work.

References

Danzmann K., 2000, Adv. Space Res., 25, 1129

Jedrich N., 2006, ESA - NASA LISA Technology Status Report.

Hall J.L. et al., 1999, IEEE Tran. on Instr. and Meas., 48, 583

SF2A 2009
M. Heydari-Malayeri, C. Reylé and R. Samadi (eds)

GAMMA-RAY SOURCE OBSERVATIONS WITH THE HAGAR TELESCOPE SYSTEM AT HANLE IN THE HIMALAYAS

Britto, R. J.[1], Acharya, B. S.[1], Chitnis, V. R.[1], Cowsik, R.[2], Dorji, N.[1], Duhan, S. K.[1], Gothe, K. S.[1], Kamath, P. U.[2], Mahesh, P. K.[2], Nagesh, B. K.[1], Naidu, A.[1], Parmar, N. K.[1], Prabhu, T. P.[2], Rao, S. K.[1], Saha, L.[3], Saleem, F., Saxena, A. K.[2], Sharma, S. K.[1], Shukla, A.[2], Singh, B. B.[1], Srinivasan, R.[2], Srinivasulu, G.[2], Sudersanan, P. V.[1], Tsewang, D.[2], Upadhya, S. S.[1] and Vishwanath, P. R.[2]

Abstract. We have observed Crab nebula using the recently commissioned wavefront sampling high altitude (4270 m) array, HAGAR, at Hanle in the Ladakh region of the Himalayas. Regular source observations have begun with the complete setup of 7 telescopes since Sept. 2008. HAGAR is the first array of atmospheric Cherenkov telescopes established at a so high altitude and was designed to reach a relatively low threshold with quite a low mirror area (31 m^2). Estimation of the sensitivity of the experiment is undergoing using several hours of data from the direction of Crab nebula, the standard candle source of TeV gamma-ray astronomy. Data were acquired using the On-source/Off-source mode and by comparing these sky regions the strength of the gamma-ray signal could be estimated. Gamma-ray events arrive close to telescope axis direction while the cosmic-ray background events arrive from the whole field of view. We discuss our analysis procedures for the estimate of arrival direction, estimate of gamma-ray flux from Crab nebula and the sensitivity of the HAGAR system etc in this paper. Also preliminary results on blazars 1es2344+514 and Mkn421 will be presented.

1 The HAGAR experiment

Located at 4270 m a.s.l., the HAGAR experiment (Latitude: 32°46'46" N, Longitude: 78°57'1"E) uses the Atmospheric Cherenkov Technique (A.C.T.). When a gamma-ray photon enters the Earth atmosphere, it causes a shower of relativistic particles. These particles initiate a spherical wavefront of blue-UV Cherenkov light which originates mostly from the shower maximum region (at about 10 km a.s.l. at 100 GeV). This wavefront has a width of few nanosecondes and forms on the ground a pool of light with a diameter of several tens of metres. Sampling the Cherenkov light using fast PMTs and recording precise relative arrival time between the detectors are the key for the detection of gamma rays at GeV energies, using wavefront sampling detectors.

Technical characteristics of the experiment are: 7 telescope array based on Wavefront Sampling Technique; 7 para-axially mounted parabolic mirrors of diameter 0.9 m in each telescope; f/D $\sim$ 1; fast Photonis UV sensitive PMT XP 2268B at the focus of each mirror and with a field of view of $3°17'$; data recorded for each event: relative arrival time of shower front at each mirror accurate to 0.25 ns using TDCs; total charge at each mirror recorded using 12 bit QDCs (ADCs); absolute event arrival time accurate to μs; for trigger generation, the 7 pulses of PMTs of a given telescope are linearly added to form telescope pulse, called *royal sum* pulse. A coincidence of any 4 telescope pulses above a preset threshold out of 7 royal sum pulses with in a resolving time of 150 to 300 ns generates a trigger pulse (Chitnis et al. 2009a).

At GeV energies, gamma-ray signal is strongly dominated by cosmic rays which also produce Cherenkov light. In order to remove all isotropic emission, source observation is done by pair, *i.e.*, by comparing the source region with a off-source region at same local coordinates on the sky.

[1] Tata Institute of Fundamental Research, Homi Bhabha Road, Mumbai 400 005, India
[2] Indian Institute of Astrophysics, Sarjapur Road, 2nd Block, Koramangala, Bangalore 560034, India
[3] Saha Institute of Nuclear Physics, 1/AF, Bidhannagar, Kolkata 700 064, India

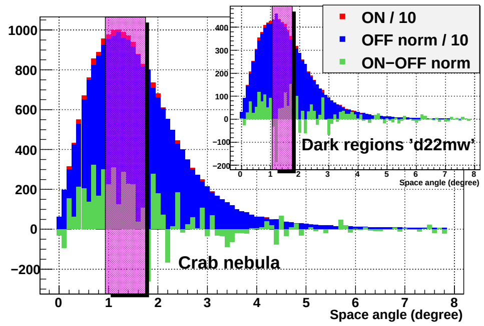

Fig. 1. Distribution of space angle of ON, OFF and ON-OFF events from the selected pairs on Crab nebula (in enclosed panel for the dark regions). For readability, ON and OFF distributions were respectively rescaled by a factor 10.

2 Signal extraction procedure

The HAGAR data analysis actually derived from the method used in the PACT experiment in Pachmarhi (Bose 2007). It is based on the arrival angle estimation of the incident atmospheric shower w.r.t. the source direction. This so-called space angle[1] is obtained for each event by measuring relative arrival times of the showers at each telescope. Precise time calibration of the optoelectronic chain is then required, as well as pointing accuracy (Chitnis et al. 2009a). Space angle is then computed by fitting the arriving spherical Cherenkov wavefront, using plane front approximation. For each event, the value of the χ^2 of the fit and other fit parameters are given, and the number of telescopes with valid TDC information, *i.e.* participating in the trigger, is written. Thus are defined 4 types of events, each type with a different number of degrees of freedom involved in our fitting procedure.

Atmospheric conditions change during observation time, reflected by variations on the trigger rate readings. This add systematics in our analysis. Normalization of background events of both the ON and OFF source data sets is done by comparing number of events at large space angles, where no signal is expected. This yield a ratio, called normalization constant, which allows to calculate the ON-OFF excess below one specific cut on the space angle distribution.

An important step in the validation of the analysis method is to analyse data pairs from fake sources (tracking dark regions), located at a similar declination as the observed gamma-ray source. Data were taken on a dark region located at the same declination as Crab nebula ($\simeq 22°$), and at the Milky Way border such as this standard source. Also, this dark region was associated in pair with other dark regions, shifted from the latter in right ascension, either towards the Galactic equator, or off the Milky Way. Because of source position constraint, the most recent pairs were formed from runs taken out off the Milky Way, but still at $\delta = 22°$. A statistical significance close to zero is then expected from this OFF-OFF analysis, if we are not dominated by systematic effects.

3 Data selection and preliminary results on dark regions and Crab nebula

Crab nebula is known as the standard candle of the gamma-ray astronomy. To get signal from this source is the priority of every new gamma-ray detector, in order to calibrate the instrument and optimize hadronic rejection. Now, we present preliminary selection of data as well as preliminary results so far obtained from observations carried out between September to December 2008 (Crab Nebula) and in April-May 2009 (dark regions).

Data selection is done using some parameters which characterize good quality data, in order to reduce systematics as much as possible. By run selection we reject acquisitions—or parts of them—where trigger rate is non stable and whose defaults in timing information are identified. Runs with high value of the trigger rate are laid aside for future analysis, as they were taken under different conditions. Then, the stability of the trigger rate of each run is quantified using one variable, called R_{stab}, defined as the RMS of the rate on the square root of its mean. For perfect poissonnian fluctuations, this variable is expected to be equal to 1. Run rejection is done for $R_{stab} \geq 1.25$.

Pair selection is then done by constraining several parameters. One of our selection parameter is related to the differences on the mean night sky backgroung rates. It was used for the Crab data, and for some of the dark regions. An other criterion is on the mean trigger rate values. Difference is imposed to be less than

[1]the angle between the direction of arrival of the shower and the direction of the source

Table 1. Result summary of the analysis of the selected pairs on the dark regions

Event type	No. selected pairs (initially 20)	duration (hour)	N_{ON}	N_{OFF}	excess	rate [2] (count(s) min^{-1})	significance (no. of σ)
All tel.	9	3.9	46643	47294	642.81 $\pm$ 302.52	3.18 $\pm$ 1.20	2.12
4 tel.	5	2.1	11732	12051	-62.78 $\pm$ 152.74	-0.55 $\pm$ 1.20	-0.46
5 tel.	7	3.1	12286	12635	-324.99 $\pm$ 157.80	-1.74 $\pm$ 0.85	-2.06
6 tel.	8	3.4	10123	10228	234.83 $\pm$ 140.45	1.14 $\pm$ 0.68	1.67
7 tel.	8	3.4	12502	12380	802.75 $\pm$ 153.59	3.91 $\pm$ 0.75	5.23

Table 2. Result summary of the analysis of the selected pairs on Crab nebula

Event type	No. selected pairs (initially 43)	duration (hour)	N_{ON}	N_{OFF}	excess	rate [2] (count(s) min^{-1})	significance (no. of σ)
All tel.	13	9.1	99000	100430	2604.47 $\pm$ 437.93	4.12 $\pm$ 0.70	5.95
4 tel.	9	6.5	31855	31587	1460.44 $\pm$ 247.22	5.91 $\pm$ 0.63	5.91
5 tel.	12	8.6	28486	29152	455.83 $\pm$ 235.66	1.93 $\pm$ 0.46	1.91
6 tel.	10	7.5	18517	18832	-237.96 $\pm$ 192.92	-1.93 $\pm$ 0.43	-1.23
7 tel.	12	8.5	20142	20859	926.16 $\pm$ 194.16	1.81 $\pm$ 0.38	4.76

2 Hz. These previous criteria are designed to control dramatic changes in atmospheric condition and acquisition within a pair. During the pair processing, ratio of events for each telescope are computed and constrained to be between 0.8 and 1.2. Events with $\chi^2 \geq$ (mean + 1 σ) are rejected, where χ^2 is the parameter of plane front fit. Further we reject events with space angle greater than 7°, as these are mostly due to bad fits. Space angle distribution is plotted for each pair and each event type. For a given space angle distribution, we call ψ_{85}, the edge containing 85 % of the remaining events. Then, constraint on the shape parameters of the space angle is applied: differences on the value of the ψ_{85} cuts, peak position, and FWHM are all three to be within 0°.15. At the last step of the selection, value of the normalization constant between ON and OFF events is computed and is constrained to be between 0.85 and 1.15. Due to this analysis procedure, some of our pairs are not fully selected or fully rejected, and only 1, 2 or 3 event types of some runs are selected.

After application of selection criteria and analysis cuts as defined above, dark region analysis can be performed from 9 selected pairs, and Crab signal can be estimated from 13 selected pairs. Normalization constant between ON and OFF event numbers is calculated considering the shape of the space angle distribution and between ψ_{85}(OFF) (typically found to lie between 1° to 1.75°) and 7°. The subtraction of the total number of normalized OFF events with total of ON events is perform below ψ_{85}(OFF), and shows an excess, as visible in figure 1, and reported in tables 1 and 2.

Rate excess from the pair analysis is now represented for each selected pair as a number of counts per minute, expected to contain a significant fraction of gamma rays, respectively for dark region and Crab nebula analysis (figure 2(a) and 2(b)). The global result of the analysis of 3.9 hours on dark regions shows a result compatible with zero, with a total significance of 2.12 σ. This indicates that systematic effects due to sky and time differences within one pair are not dominant in our analysis. However, a significance equal to 5.23 σ for events involving the 7 telescopes, requires more investigation. Also, additional data are to be added to this analysis.

From Crab nebula analysis, we report a rate of 4.12 ± 0.70 counts min^{-1}, corresponding to a significance of 5.95 σ, out of 9.1 hours of data. The expected values computed from simulation is 9.6 gamma rays per minute, and 5 σ for ~8 hours for this source, but without event rejection from analysis procedure. By rough extrapolation of simulations (Chitnis et al. 2009a), energy threshold of these analysis is expected to be around 200-220 GeV, for a collection area (effective surface) around $5 \times 10^4\ m^2$. This yield an integral flux of $\sim 8.2 \times 10^{-11} cm^{-2} s^{-1}$ from Crab nebula. Our result is consistent with the flux already calculated from other experiments (Fig. 2(c)).

4 Study of other sources and further improvements

In parallel with the development of our analysis on Crab nebula data, we performed preliminary analysis of the blazars 1es2344+514 and Markarian 421. The blazar 1es2344+514 was observed during Sept-Nov 2008. Out of 4.4 hrs of selected data, an upper limit was computed above a threshold expected to be $\sim$ 250 GeV (Shukla et

[2]Total mean rate is computed by applying a weight to each pair, corresponding of the number of event types selected

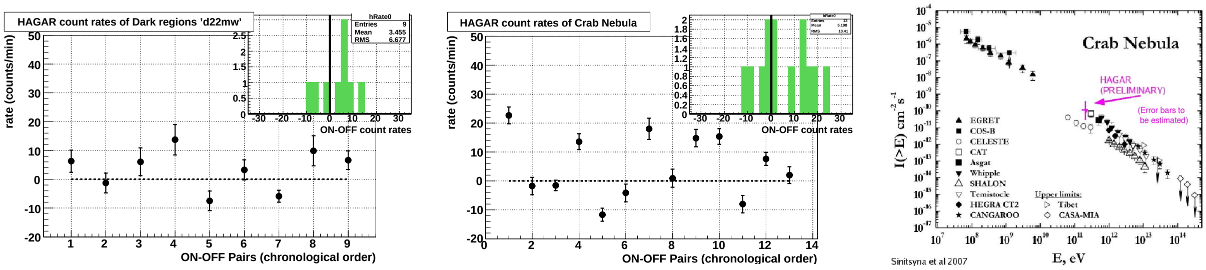

Fig. 2. Count rates of the selected pairs on the dark regions (left panel) and on Crab nebula (middle panel), in chronological order. Enclosed panels show the distributions of these counts. Right panel: integral spectrum of Crab nebula, as given by many experiments (Sinitsyna at al 2007). Preliminary flux estimation from HAGAR is added.

al 2009). Markarian 421 was observed during March-May 2009. No significant signal was found from the 6.6 hrs of selected data (Chitnis et al. 2009b). A preliminary study of pulsed emission from Crab and Geminga pulsars also led to upper limits on the fluxes (Acharya et al. 2009).

Improvement of the analysis procedure is currently going on. New modules are installed in the data acquisition system for additional informations. Till now, information from QDCs was not used, but first tests are conducted to implement discriminating variables based on the distribution of density of photons on the mirrors and telescopes. Also, spherical or parabolic fit of the Cherenkov wavefront is to be implemented, in order to reduce systematic error on the space angle estimation, and to take advantage of the angular resolution of HAGAR. Furthermore, newly installed Acqiris 1 Ghz flash ADC modules (model DC271A, using an 8-bit digitizer) are expected to improve many steps of our analysis, reduce systematics, and improve sensitivity of the experiment (Chitnis et al. 2009a). For example, software padding procedure used to balance night sky background between ON and OFF runs may replace the method of the normalization constant, as the latter is applied event by event and channel by channel.

5 Conclusions and Perspectives

Observation of the Crab nebula was carried out from September to December 2008 with the HAGAR telescope array at Hanle. Out of the 30 h of available data, a sample of 9.1 hours was selected. A preliminary analysis allowed us to report a 5.95 σ detection of $4.1 \pm 0.7\ \gamma\ min^{-1}$ above 200 GeV. Analysis of systematic uncertainties are under going. Further improvements in the pair selection, as well as development of hadronic rejection methods based on simulations and newly installed flash ADCs, are expected to improve this preliminary results, which are however consistent with previous measurements by other experiments operating at similar energies. This preliminary result gives encouraging persective for on-going observation on blazars and other gamma-ray sources.

Many persons from T.I.F.R. and I.I.A. have contributed towards the design, fabrication and testing of telescope and data acquisition systems of HAGAR. We thank them all.

References

Acharya B. S. et al, abstract # icrc0669, Proc. of the 31^{st} ICRC (2009)

Bose, D., Ph D thesis from T.I.F.R., Mumbai (2007)

Chitnis, V. R. et al, abstract # icrc0696, Proc. of the 31^{st} ICRC (2009a)

Chitnis, V. R. et al, abstract # icrc0697, Proc. of the 31^{st} ICRC (2009b)

Sinitsyna, V. G. et al, Proc. of the 30^{th} ICRC (2007)

Shukla, A. et al., Proc. of the 27^{th} meeting of the Astronomical Society of India (2009)

SF2A 2009
M. Heydari-Malayeri, C. Reylé and R. Samadi (eds)

.

THE COSMIC RAY LEPTONS PUZZLE

Brun, P.[1], Bertone, G.[2], Cirelli, M.[3] and Moulin, E.[1]

Abstract. Recent measurements of cosmic ray electrons and positrons by PAMELA, ATIC, Fermi and HESS have revealed interesting excesses and features in the GeV-TeV range. Many possible explanations have been suggested, invoking one or more nearby primary sources such as pulsars and supernova remnants, or dark matter. Based on the output of the TANGO in PARIS –Testing Astroparticle with the New GeV/TeV Observations in Positrons And electRons : Identifying the Sources– workshop held in Paris in May 2009, we review here the latest experimental results and we discuss some virtues and drawbacks of the many theoretical interpretations proposed so far.

1 Introduction

Cosmic ray leptons (electrons and positrons) are very interesting for the main reason that they probe our local Galactic environment as they propagate on a few kpc only. Their energy spectrum can encode lots of information about the source(s). In fact, because they loose energy very efficiently as they propagate, there are strong correlations between the spectral features and the distance to the source(s). For those reasons, and because the matter/antimatter ratio is higher than for other species such as protons, the leptonic channel has always been thought to be a good way to search for dark matter annihilation debris. In this paper we briefly review recent measurements of cosmic ray leptons as well as some possible interpretations. Note that this brief review cannot be all comprehensive by itself, for more details and discussions we invite the reader to consult the website of the TANGO in PARIS workshop.

2 The measurements

High energy leptons produce showers when passing through matter, they are observed with the help of calorimeters. For cosmic ray studies detectors can be magnetic spectrometers in which case they perform charge identification and separate electrons from positrons, or simple calorimeters in which case they measure the $e^- + e^+$ sum. Recent measurements are displayed in Fig. 1. PAMELA measured the positron fraction ($e^+/(e^- + e^+)$) between 1 GeV and $\sim$ 100 GeV (R. Sparvoli). An unambiguous rise of the fraction is observed above 10 GeV, as some previous experiments found some hints for. Other results are obtained without charge identification by the balloon experiment ATIC (J. Isbert), the Fermi satellite (J. Bregeon) and the ground-based HESS Čerenkov telescopes (K. Egberts). Data points are shown on the right panel of Fig. 1. The ATIC detector has 22 radiation lengths and a few % energy resolution, the ATIC collaboration claims the observation of a sharp peaked structure in the $e^- + e^+$ spectrum at $\sim$ 600 GeV. The same measurement as performed by Fermi (8.5 radiation length, $\sim$10% energy resolution) does not show such a prominent structure, but rather a smooth bump. The interesting region is at the edge of the HESS sensitivity, which observes a break in the spectrum. However, due to $\sim$15% energy scale uncertainty, HESS data points hardly contraint the precise shape of the excess. At the moment, the data seem inconsistent. Note however that large systematics (not displayed in Fig. 1) are present. Up to now it is still unclear which spectrum is closer to reality. However, whatever the real spectrum, these data probably indicate the presence of a nearby yet undetermined cosmic ray leptons source, as exposed below.

[1] CEA, Irfu, Service de Physique des Particules, Centre de Saclay, F-91191 Gif sur Yvette, France
[2] Institut d'Astrophysique de Paris, France. UMR7095-CNRS UPMC, 98bis Boulevard Arago, 75014 Paris, France
[3] Institut de Physique Théorique, CNRS URA 2306 & CEA/Saclay, F-91191 Gif-sur-Yvette, France

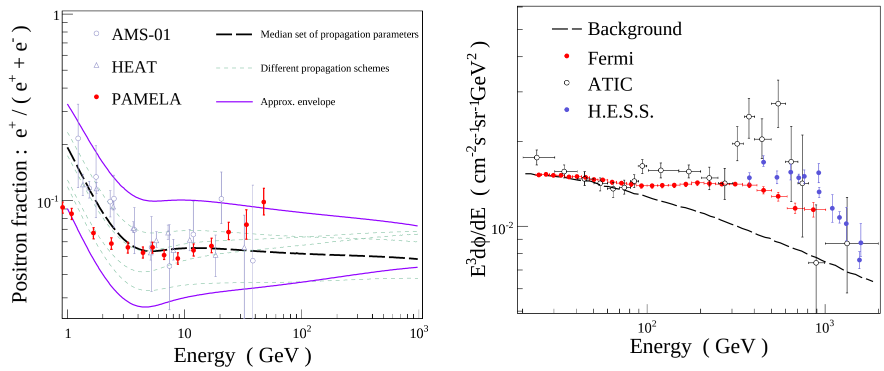

Fig. 1. Cosmic ray positron fraction (left) and electrons+positrons fluxes (right).

3 Models for cosmic ray transport

In the energy range which is considered here (GeV to TeV), it is thought that the bulk of cosmic rays comes from supernovae and their remnants. These sources are located in the Galactic disk, which is a few tenth of parsecs thick and whose radius is ∼30 kpc. Once produced and accelerated in the sources, they diffuse inside a flat ∼ 10 kpc cylinder in which they are deflected by the turbulences of magnetic fields. In addition, they can loose energy and get affected by the convective wind blowing from the disk outwards. The cosmic rays that are directly produced in the sources are called primaries. Some species found in cosmic rays (such as positrons, antiprotons, boron, etc.) do not originate from stars. These species are produced during the transport of primaries, by spallation reactions onto the interstellar medium.

Two approaches are used to compute cosmic ray fluxes at the Earth in order to compare with the measurements: semi-analytical (D. Maurin) and fully numerical (A. Strong). In the first case, mean values are used for the source properties (spatial distribution, intrinsic spectrum, etc.) and propagation parameters (diffusion coefficient, energy losse efficiencies, etc.), and simple boundary conditions are employed. The main advantage of this method is that it is much faster, thus allowing large scans of the propagation parameter space. This essential property permits to compute theoretical uncertainties on the flux as well as on any quantity derived from these parameters. In this framework, it is also easier to perform studies on the spatial origin of sources and local effects. The numerical approach is used in the Galprop code, which is a publicly available tool. In this framework, all type of data is used in a self-consistent way, including 3D gas model, cosmic ray sources, radiation fields, Galactic magnetic field model, etc. This allows in particular the computation of γ-ray diffuse fluxes, and the production of synchrotron skymaps, which the semi-analytical method still does not do.

This brief description of the computational tools is essential, because when a claim for a excess in some channel is made, those are the methods which are used to determine the expected background. An important point is that whatever the method to estimate the local cosmic ray lepton fluxes, conventional computations cannot account for the observed features. In other words, there is no allowed set of diffusion parameters which reproduces leptonic data with secondaries only. Indeed, these estimates lead to the mean secondary flux one can expect at the Earth location, but it is also shown that there should be large fluctuations in the spatial density of cosmic rays. This depends whether or not a primary source lies in the Earth neighborhood. Ordinary sources such as supernova remnants carry the same baryon number as the whole Universe so that antiparticles should be subdominant. The fact that the positron fraction is ∼10% might be already betraying their nature as secondary species; as most primaries are protons, charge conservation leads to a higher yield of positive charges within secondaries. As electrons and positrons only propagate on short distances of order 1 kpc, the observation of a rise of the positron fraction and a bump in the inclusive spectrum leads to the conclusion that there is a nearby source of high energy e^+/e^- pairs. In the following different possibilities for such a nearby source are reviewed, as well as possible constraints from multi-wavelength and other channels analyses.

4 Interpretations of the data

4.1 Conventional sources

As explained above, it is suspected that a nearby source of electrons and positrons significantly contributes to the measured flux. We first investigate standard sources which are known to exist, more exotic ideas are discussed in Sec. 4.2. As for conventional sources, one can mention two types : electromagnetic sources and non-electromagnetic ones. In the first case, pairs are produced via purely electromagnetic processes. These sources can be *e.g.* pulsars or γ-ray binaries. For these sources, counterparts in γ rays are expected. The second class of sources imply hadronic processes as well, it can be any type of astrophysical shock, like in supernova remnants. In that case, counterparts are expected in γ-rays and possibly in the antiproton channel as well.

Pulsars are good candidates for being the nearby source responsible for the excesses. They are rotating and strongly magnetized neutron star, within which $e^{\pm}$ pairs can be created in magnetic fields or by high energy photons collisions (B. Rudak). TeV-level leptons can be produced and accelerated in the environment of the neutron star and released in the interstellar medium provided the matter is diluted enough. For that last reason, mature pulsars such as Geminga, Loop I, Monogem (and others) are excellent candidates. All the data can be well fitted by adding pulsars to the conventional flux (I. Buesching, see Fig. 2). However, there is yet no obvious unique candidate as there are still free parameters in the models. In its first year of data taking, the Fermi satellite discovered plenty new pulsars showing that these objects seem to be ubiquitous in our Galactic environment. Unfortunately, a clear counterpart in γ-ray is not expected as the time scales for photons and charged particles are very different at all levels of the models (production, propagation).

Concerning supernova remnants, another possibility would be that secondary particles directly produced at the source had not been previously accounted for properly. In the standard picture, remnant material from the exploding star constitutes a shock in which particles are accelerated. It is now suggested that secondary particles produced in the shock itself could significantly increase the escaping positron fraction (P. Blasi). Decent fits of the data are obtained within this scenario, which turns out to be falsifiable. This model predicts a rise of the antiproton to proton ratio above 100 GeV. The PAMELA satellite has now precise results up to ~100 GeV and it is foreseen to measure higher energy antiprotons. Therefore it will be possible to test this scenario in the near future.

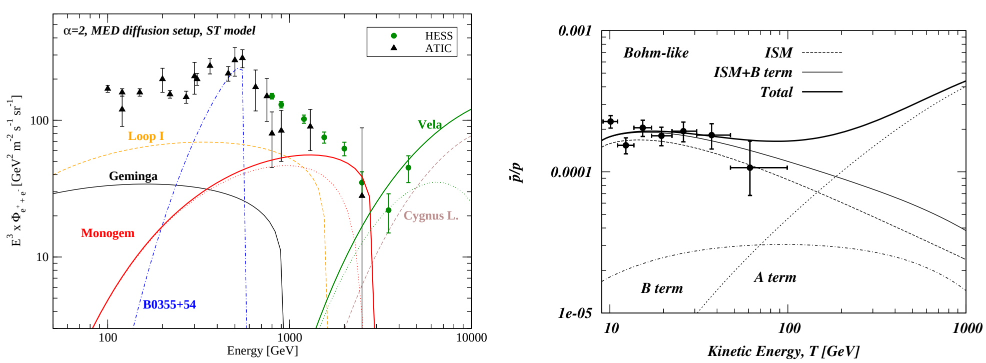

Fig. 2. Fit of the electron data with pulsars (plot from S. Profumo) and $\bar{p}$ predictions in case of secondary production within a supernovae remnant (P. Blasi).

4.2 Exotic ideas

Although it is definitely possible to reproduce the leptonic data with conventional sources, an extensively studied possibility would be that the features have a dark matter related origin. Observational data show that our Galaxy stars are dipped in a spherical dark halo whose extension is 10 times larger than the luminous disc. The dark matter appears to be non baryonic and could consist of massive yet undiscovered particles. It is believed that these particles were created in the early Universe and now haunt Galaxies. These particles must have very small interactions with conventional matter. It is possible however that they could decay or annihilate (A. Ibarra, M. Cirelli). The annihilation or decay product should carry no baryonic charge, thus producing standard particles and antiparticles in a 1:1 ratio. These process happen in the Galactic halo –possibly in the Earth neighborhood–, and the produced particles then diffuse just like conventionally produced cosmic rays, thus enlarging the antiparticle ratio.

Annihilating dark matter is particularly studied as the involved orders of magnitude nicely converge towards a canonical picture. Dark matter particles appear in Standard Model extensions which are often related to the breaking of the electroweak symmetry. In this framework, Weakly Interacting Massive Particles (WIMPs) have electroweak scale mass which is the same order of magnitude as the cosmic leptons features. Primordial self annihilations regulate the cosmological density, which defines a natural value for the annihilation cross section. As this value is close to the one inferred from electroweak scale interactions, this fact gives credit to the WIMP model. Unfortunately, when computing the related exotic cosmic ray production rate, canonical values gives lepton fluxes that are too low by 2-3 orders of magnitude. One needs then to invoke some mechanism for the enhancement of the annihilation rate. A possibility is an enhancements due to dense dark matter substructure, but this seems somehow unlikely (J. Lavalle). This can be achieved by assuming *e.g.* a non thermal production in the early Universe (then the annihilation cross section is not constrained from that). A more elegant solution appears for TeV scale WIMPs with the help of the Sommerfeld effect. This happens when masses and couplings have specific values which makes the annihilation cross section increase when parameters lead to WIMPs almost-bound states (J. Hisano). In that case, the colder the dark matter particles, the higher the annihilation cross section. It is essential though to compare exotic cosmic ray leptons with other messengers. For instance, PAMELA precisely measured the antiproton fluxes up to $\sim$100 GeV. Generic dark matter particles annihilations should produce antiprotons as well, so that antiproton measurement can constrain the production rate for exotic cosmic rays. It is shown that the enhancement factor for a conventional WIMP cannot exceed a factor of $\sim$10 not to overproduce antiprotons (F. Donato). To save the WIMP interpretation, it is therefore required to assume that hadronic annihilation channels are suppressed, leaving open only leptonic ones. This is the so-called leptophilic dark matter, for which a case can be made from the model-building point of view (either with supersymmetry (N. Fornengo) or within new classes of models (Y. Nomura)).

Links with other wavelength are also under investigation (how the electrons/positrons excesses can be linked to the 511 keV emission at the Galactic center (P. Jean) or the WMAP haze (G. Dobler)). The most conclusive results come from radio and γ ray data from the Galactic center and dwarf galaxies. Indeed if these leptons are from dark matter particle collisions, they should be produced in large quantity in other locations. For example, corresponding leptons should be produced at the Galactic center and generate radio waves while interacting with the magnetic field, which are above current observations. In general, even leptophlic dark matter is in conflict with other messengers/wavelength observations, at least within most straightforward models for dark matter distributions and magnetic fields.

5 Outlook

Most likely the lepton excesses observed by PAMELA, ATIC, Fermi and HESS are not caused by conventional secondary cosmic rays, meaning that a nearby source significantly contributes to the local flux. The main classes of candidate are astrophysical (*e.g.* a nearby pulsar or supernova remnant) or more exotic. The first case seems favored as one has to invoke non conventional scenarios for dark matter in order to avoid contraints from different observables. It is however very exciting to notice that we might be witnessing the direct effects of a TeV cosmic ray source for the first time. Further data analyses of current experiments will certainly provide important information, like whether one can detect a small anisotropy and its direction. Eventually, future experiments, both on the ground (K. Mannheim) or balloon borne and spatial detectors (L. Derome) will certainly offer the opportunity to have a deeper look into this problem.

We would like to warmly thank all the TANGO in PARIS speakers, as well as the members of the organizing committee : F. Aharonian, O. de Jager, J-F. Glicenstein, F. Iocco, R. Mohayaee, L. Pieri, P. Serpico and J. Silk. We acknowledge the Institut d'Astrophysique de Paris, ANR, IPhT/ CEA Saclay, Irfu/CEA Saclay, GdR Terascale and GdR PCHE for their support.

References

All citations refer to the TANGO in PARIS talk (and references therein) by the quoted author. Slides and videos of the talks are available at:
http://irfu.cea.fr/Meetings/TANGOinPARIS

SF2A 2009
M. Heydari-Malayeri, C. Reylé and R. Samadi (eds)

PAIR CASCADING IN GAMMA-RAY BINARIES

Cerutti, B.[1], Dubus, G.[1] and Henri, G.[1]

Abstract. In some gamma-ray binaries, pair production is strong and shapes the very high energy (VHE $>$ 100 GeV) radiation output. In LS 5039, a one-zone leptonic model reproduces the VHE gamma-ray modulation observed by HESS, but fails at orbital phases where gamma-gamma absorption is predominant. The development of pair cascading was proposed as an explanation for this discrepancy. We report on the formation of pair cascading radiation in a binary environment. One-dimensional and three-dimensional cascade radiation calculations are presented. The effect of the ambient magnetic field in the development of cascades is crucial and discussed.

1 Introduction

Gamma-ray binaries are well-established gamma-ray sources in the Galaxy. These systems are composed of a massive companion B*e*/O type star and a compact object. The three binaries discovered so far: LS 5039, LSI +61°303 and PSR B1259−63, present the same spectral and temporal characteristics throughout the electromagnetic domain from radio to TeV energies (see *e.g.* Dubus 2006b, and references therein). In the standard pulsar wind nebula scenario (Maraschi & Treves 1981; Dubus 2006b), the non-thermal radiation is emitted by a population of ultra-relativistic electron-positron pairs produced and accelerated at the vicinity of a young pulsar.

LS 5039 is composed of a O6.5V type star and an unknown compact object in a 3.9 day orbit. The orbital modulation of the VHE gamma-ray flux was observed by HESS (Aharonian et al. 2006). These observations enable to put strong contrains on models such as the particle distribution and the magnetic field (Dubus et al. 2008). LSI +61°303 and PSR B1259−63 contain a B*e* type star. The absence of a B*e* equatorial wind component in LS 5039 reduces the number of unknowns and makes this system an ideal object for modeling. In this tight binary, $\gamma\gamma$-absorption is strong and shapes the light-curve at VHE (Dubus 2006a). The combination of anisotropic inverse Compton scattering and pair production explains the observed modulation except close to superior conjunction where the flux is underestimated (Dubus et al. 2008). This mismatch occurs precisely at orbital phases where absorption is predominant. The produced pairs can reprocess a significant fraction of the absorbed radiation and initiate a cascade. The radiation emitted in the cascade decreases the global $\gamma\gamma$-opacity in the system, providing a viable explanation for this discrepancy. In this proceeding, we report on the formation of one-dimensional and three-dimensional pair cascading radiation in LS 5039.

2 The physics at work and the effect of the magnetic field on pair cascading

The absorption of the primary gamma-rays provides a large density of secondary pairs in the binary system. New generations of particles are produced as long as the photons radiated in the cascade stay close to the massive star and have enough energy for pair production. The escaping gamma-ray radiation is the result of a competition between emission and absorption. In addition to pair production, triplet pair production ($\gamma + e^{\pm} \rightarrow e^{\pm} + e^{+} + e^{-}$) provides also new pairs (Mastichiadis 1991), but these electrons may not contribute much to the cascade (see details in Cerutti et al. 2009a). The annihilation of pairs is ignored as well here since it occurs for pairs that are almost thermalized.

[1] Laboratoire d'Astrophysique de Grenoble, UMR 5571 CNRS, Université Joseph Fourier, BP 53, 38041 Grenoble, France

The ambient magnetic field has a dramatic influence on the development of the cascade. If the magnetic deviations of pairs trajectories are small ($B < 10^{-8}$ G in LS 5039), all the particles involved in the cascade are boosted in the direction of the primary gamma-ray because of relativistic effects. In this case, the cascade is one-dimensional and develops along the line of sight. From a distant observer, the system appears as a point-like and anisotropic gamma-ray source (see §3). For stronger magnetic field, pairs undergo sizeable deflections and radiate in other directions, the cascade becomes three-dimensional. If the Larmor radius of the electrons is smaller than the Compton interaction length $R_L < \lambda_{ic}$, pairs are confined and isotropized locally by the magnetic field. In the following, three-dimensional 'isotropic' cascade refers to this particular case. For LS 5039, the cascade can be considered as isotropic for $B > 10^{-2}$ G. The cascade radiation then originates from a spatially extended region and depends on the viewing angle (see §4). If the magnetic field strength exceeds a few Gauss, pairs cool down *via* synchrotron radiation rather than by inverse Compton scattering and the cascade is quenched (Bednarek 1997, Khangulyan et al. 2008).

3 One-dimensional cascade

In the one-dimensional case, the cascade dynamics can be explicitly and exactly described with a semi-analytical method. In LS 5039, the cascade radiation contribution is strong and highly variable along the orbit (see Fig. 1). The orbital parameters are taken from Casares et al. (2005) with an inclination of $i = 60^{\circ}$. The cascade does add more flux at superior conjunction as expected but overestimates HESS observations and the modulation cannot be accurately reproduced anymore. One-dimensional pair cascading can be ruled out but three-dimensional cascade cannot be excluded by this study. If magnetic deviations on pairs trajectories are large, the cascade radiation is redistributed at other orbital phases. This redistribution depletes the density of pairs at phases where many pairs are produced to the benefit of phases where only a few are created. Hence, one-dimensional pair cascading provides a theoretical upper-limit on the contribution of pair cascading radiation at superior conjunction (for more details see Cerutti et al. 2009a, submitted). In LSI +61°303 and PSR B1259−63, the cascade does not play any major role in the formation of the VHE γ-ray radiation, pair production remains small in these systems (Dubus 2006a). Note that such cascade is appropriate in an unshocked pulsar wind where the magnetic field is frozen into the plasma of pairs (Sierpowska-Bartosik & Torres 2008).

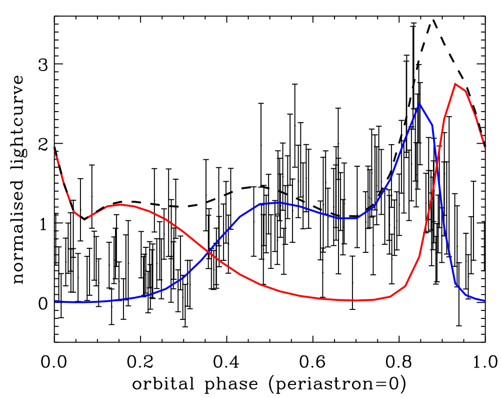

Fig. 1. Phase-resolved VHE light-curves in LS 5039. The one-dimensional cascade contribution (red line) is compared to the primary source (blue line) and to HESS measurements (black data-points, taken from Aharonian et al. 2006). The black dashed-line represents the sum of both components.

4 Three-dimensional isotropic cascade

The computation of three-dimensional pair cascading is not straightforward since no equations can be explicitly formulated in this case. Nevertheless, a semi-analytical approach is possible if the cascade is decomposed into discrete generations of pairs and gamma-rays. In the three-dimensional isotropic cascade model, pairs are locally isotropized and confined at their creation site by a disordered magnetic field. The binary system environment is surrounded by a plasma of secondary pairs radiating *via* inverse Compton scattering and synchrotron radiation. Figure 2 gives the spatial distribution of the first generation of VHE gamma-rays as observed by a distant observer at superior (*top*) and inferior (*bottom*) conjunctions in LS 5039. The first generation is extended and depends on the relative position of the observer compared with both stars. The anisotropic effects arise from the angular dependence in pair production and inverse Compton scattering. Synchrotron radiation is computed for a population of pairs with an isotropic distribution of pitch angles to the magnetic field. Even though the massive star is assumed point-like for spectral calculations, eclipses are taken into account (Fig. 2).

Figure 3 shows the VHE integrated γ-ray flux radiated by the first generation of pairs along the orbit in LS 5039. In this case, the cascade contribution is perfectly correlated with the primary source modulation. Phase-averaged spectra and modulation remain nearly unchanged. Interestingly, the cascade flux does not dominate except close to superior conjunction between phases $0.0 < \phi < 0.15$. At superior conjunction ($\phi \approx 0.06$), the flux is increased by a factor six thanks to the first generation of pairs, but more generations have to be considered to explain HESS observations (Cerutti et al., in preparation).

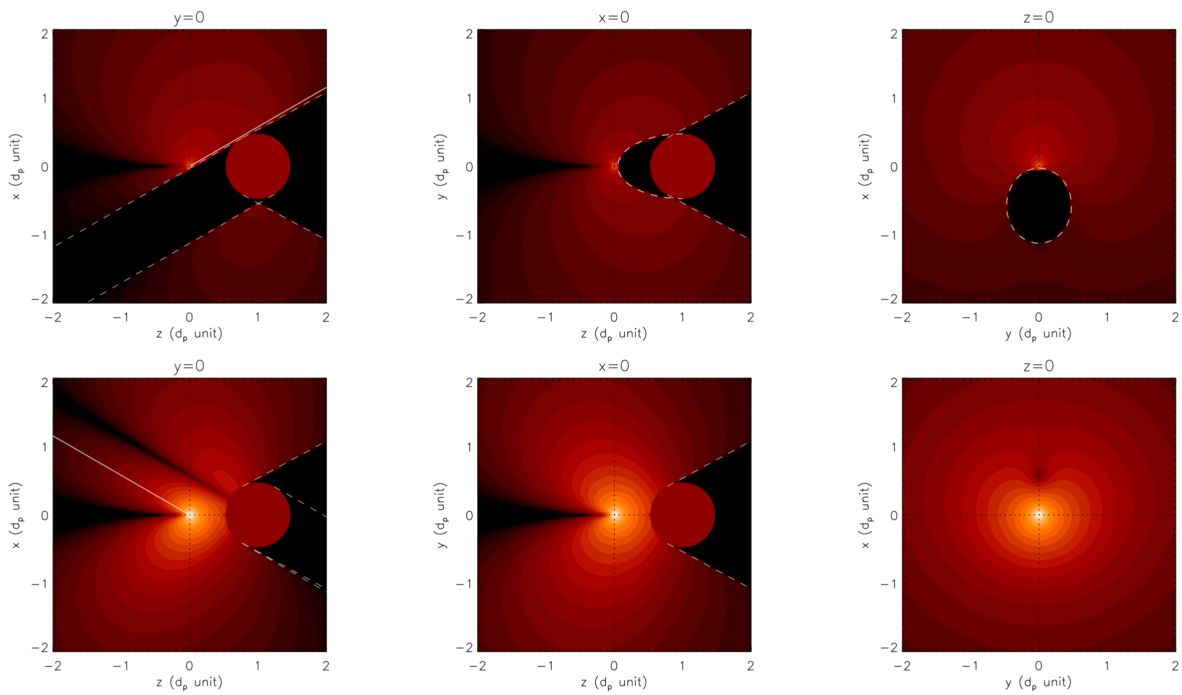

Fig. 2. These maps depict the spatial distribution and intensity of the VHE radiation produced by the first generation of pairs of the cascade in LS 5039 as observed by a distant observer (white solid line, left panels). Distances are normalized to the orbital separation d. The system is viewed at superior (*top*) and inferior conjunctions (*bottom*) in the three orthogonal planes: front view (*left*), top view (*middle*) and right view (*right*). The primary source lies at the origin. The eclipsed regions by the massive star (red disk) are delimited by white dashed lines.

5 Summary and conclusion

Pair production in gamma-ray binaries induces an addition complication in the modeling of the high energy gamma-ray emission. In some tight binaries such as LS 5039, pair production is strong and shapes the VHE gamma-ray output. Depending on the ambient magnetic field, a cascade of pairs can be initiated in the system. One-dimensional cascade arises if the magnetic field is unrealistically small ($B < 10^{-8}$ G) but provides a theoretical upper-limit to the cascade contribution at superior conjunction. HESS observations can rule out this kind of cascade. More realistic types of cascades such as three-dimensional isotropic cascade provide a viable explanation to understand HESS observations particularly at superior conjunction where the cascade radiation dominates over the primary source. Yet, the effect of the next generations of particles has to be

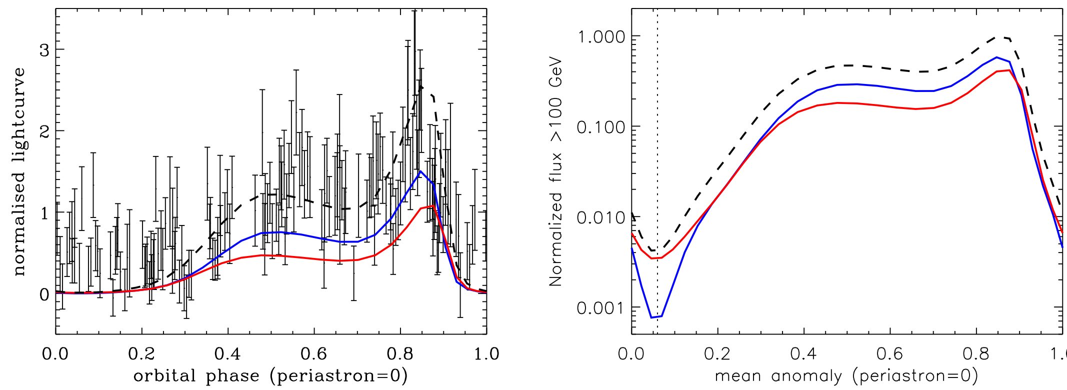

Fig. 3. *Left:* The same as in Fig. 1 for a three-dimensional cascade (first generation). *Right:* The same light-curves are shown in a semi-logarithmic scale. Superior conjunction is indicated by the black dotted line ($\phi \approx 0.06$).

studied. Complementary investigations using a Monte Carlo code are necessary to corroborate and confirm the implication of cascades in the formation of VHE radiation in gamma-ray binaries.

Acknowledgements: This work was supported by the *European Community* via contract ERC-StG-200911.

References

Aharonian, F.A., et al. (HESS collaboration), 2006, A&A, 460, 743
Bednarek, W., 1997, A&A, 322, 523
Casares, J., et al., 2005, MNRAS, 364, 899
Cerutti, B., Dubus, G., & Henri, G., 2009a, submitted
Dubus, G., 2006a, A&A, 451, 9
Dubus, G., 2006b, A&A, 456, 801
Dubus, G., Cerutti, B., & Henri, G., 2008, A&A, 477, 691
Khangulyan, D., Aharonian, F., & Bosch-Ramon, V., 2008, MNRAS, 383, 467
Maraschi, L., and Treves, A., 1981, MNRAS, 194, 1L
Mastichiadis, A., 1991, MNRAS, 253, 235
Sierpowska-Bartosik, A., & Torres, D.F., 2008, Astroparticle Physics, 30, 239

SF2A 2009
M. Heydari-Malayeri, C. Reylé and R. Samadi (eds)

ASYMMETRIC EXPLOSION OF CORE COLLAPSE SUPERNOVAE

Foglizzo, T.[1], Guilet, J.[1] and Sato, J.[1]

Abstract. The explosion of most massive stars depends on the revival of a stalled shock, a few hundred milliseconds after the birth of the central neutron star. Recent numerical simulations suggest that this revival is possible through an asymmetric explosion helped by a hydrodynamical instability named SASI. Its asymmetric character is also able to influence the kick and the spin of the resulting neutron star. We review the current status of these discoveries, and describe the advective-acoustic mechanism at work behind SASI.

1 Introduction

The explosion of massive stars is currently observed several hundred times per year as spectacular supernovae in external galaxies but yet, their explosion mechanism is still not satisfactorily understood. Numerical simulations have been able to reproduce a robust explosion only in the extreme cases where the progenitor is particularly light, or extremely magnetized, or rotates particularly fast. How does a standard massive star explode ? In the scenario proposed by Bethe & Wilson (1985), the success of the explosion depends on the efficiency of energy deposition by neutrinos below the stalled accretion shock, during the first second after core bounce. This mechanism is known to be inefficient in spherical symmetry (Liebendörfer et al. 2001). Hydrodynamical instabilities, however, may play an important role by breaking the symmetry and helping the revival of the stalled shock. Indeed, multidimensional simulations allowing for transverse motions, induced by neutrino-driven convection in the gain region, approached the explosion threshold (Burrows et al. 1995, Janka & Müller 1996), although this effect did not seem sufficient (Buras et al. 2003). The Standing Accretion Shock Instability (SASI) discovered by Blondin et al. (2003) has received considerable attention over the past 6 years, for its many unexpected consequences. SASI is distinct from neutrino-driven convection since it can even develop without neutrino-heating. It is characterized by large scale oscillations of the shock, dominated by the spherical harmonics l = 1, 2.

2 The unexpected -potential- consequences of SASI

(i) **Successful neutrino-driven explosion of a $15M_{\rm sun}$ progenitor.** The simulations of Marek & Janka (2009) showed the successful explosion of a $15M_{\rm sun}$ progenitor where neutrino energy deposition is efficient enough owing to the effect of SASI. A fraction of the postshock gas spends more time in the gain region in 2D than in 1D because of the convective motions. It is thus longer exposed to the neutrino flux (Murphy & Burrows 2008, Fernández & Thompson 2009b). The robustness of this scenario is still debated, more particularly its sensitivity to the softness of the equation of state inside the neutron star.

(ii) **A new mechanism of explosion driven by acoustic energy ?** SASI is the starting point of the acoustic explosion mechanism found by Burrows et al. (2006, 2007): SASI oscillations are able to excite g-modes inside the proto-neutron star, that generate in turn an acoustic flux which is powerful enough to revive the stalled shock. According to Weinberg & Quataert (2008) however, the energy of g-modes is likely to be dissipated locally by (unresolved) nonlinear coupling, instead of being redirected into an acoustic flux.

(iii) **Neutron star kick.** The asymmetric character of SASI can have important consequences on the birth conditions of the neutron star. Using 2D axisymmetric simulations, Scheck et al. (2004, 2006) estimated that

[1] CEA, Irfu, SAp, Centre de Saclay, F-91191 Gif-sur-Yvette, France and UMR AIM, CEA-CNRS-Univ. Paris VII, Centre de Saclay, F-91191 Gif-sur-Yvette, France

the kick received by the neutron star during the first seconds of the explosion can exceed 1000 km/s. The distribution of kick velocities inferred from their parametric study is compatible with the observed velocity distribution of pulsars.

(iv) **Neutron star spin.** The first 3D simulations of SASI revealed that a spiral mode is able to affect the spin of the neutron star, in a direction opposite to the rotation of the progenitor (Blondin & Mezzacappa 2007, Iwakami et al. 2009). This result was confirmed by Yamasaki & Foglizzo (2008) using a perturbative approach. Whether a spiral mode could dominate the evolution of SASI, in a non-rotating collapsing core, is not clear yet.

(v) **Gravitational waves signature.** The asymmetric motions induced by SASI are a source of gravitational waves which, if detected, could help characterize the explosion mechanism (Ott et al. 06, Kotake et al. 07, Marek et al. 09, Ott 09, Murphy et al. 09). The sensitivity of near-future detectors is sufficient to detect the SASI signature of individual events taking place inside our own Galaxy.

(vi) **Seed for subsequent mixing instabilities.** The asymmetric shape of the shock deformed by SASI is able to trigger mixing instabilities during its propagation through the envelope of the star (Kifonidis et al. 2006). The numerical simulations of Hammer et al. (2009) have revealed that the outward radial mixing of heavy elements and inward mixing of hydrogen is even more efficient in 3D than in 2D, leading to a better agreement with the observations of SN 1987A.

(vii) **Magnetic field amplification ?** According to the MHD simulations of Endeve et al. (2009), the development of SASI could amplify the magnetic field to 10^{15}G even in the absence of core rotation. This preliminary result obtained with adiabatic axisymmetric simulations has not been confirmed yet.

3 What do we really understand of SASI ?

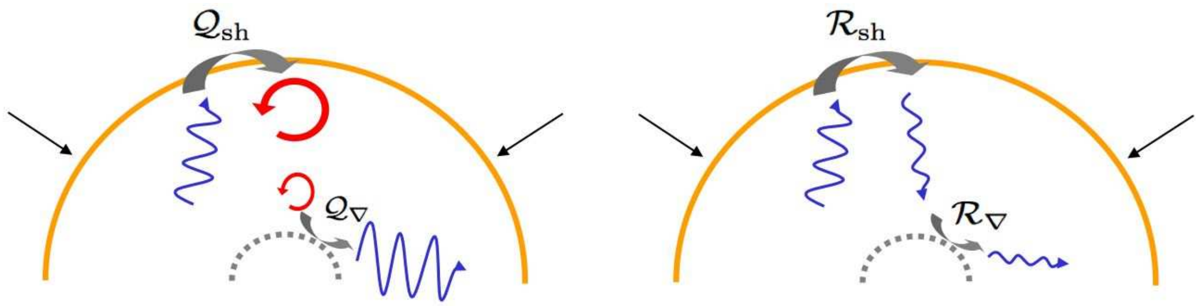

Fig. 1. Schematic views of the "advective-acoustic cycle" (left) and the "purely acoustic cycle" (right). Entropy/vorticity perturbations (circular arrows) are advected downward with the flow, and coupled to acoustic ones (wavy arrows) at the shock and in the decelerating flow. The linear coupling between these perturbations is described by coupling coefficients $\mathcal{Q}_{\rm sh}$, $\mathcal{Q}_\nabla$, $\mathcal{R}_{\rm sh}$, $\mathcal{R}_\nabla$. Growing evidence suggests that the advective-acoustic cycle can be unstable, while the purely acoustic cycle is stable.

In view of the spectacular possible consequences of SASI, a fundamental understanding of its mechanism is desired and has been a source of debate. In the subsonic flow between the shock and the neutron star, the interplay of advected and acoustic waves can be decomposed linearly onto two cycles illustrated by Fig. 1. Although the possibility of an unstable "purely acoustic cycle" has been invoked (Blondin & Mezzacappa 2006, Blondin & Shaw 2007), the only theoretical support for this explanation (Laming 2007) has been revised (Laming 2008). By contrast, the "advective-acoustic cycle" has been recognized as the driving mechanism by several authors who have gathered increasing evidence for this explanation (Blondin et al. 2003, Burrows et al. 2006, Ohnishi et al. 2006, Foglizzo et al. 2007, Scheck et al. 2008, Yamasaki & Foglizzo 2008, Fernández & Thompson 2009a). Part of the difficulty in recognizing the advective-acoustic mechanism in numerical simulations, even in the simplified set up proposed by Blondin et al. (2003), came from the lack of simple reference models where its properties would be fully understood.

The toy model illustrated by Fig. 2 is simple enough to be characterized analytically (Foglizzo 2009). The results of the linear analysis, confirmed by numerical simulations (Sato et al. 2009), can help us build our physical intuition about the advective-acoustic coupling responsible for an unstable cycle. In particular, the

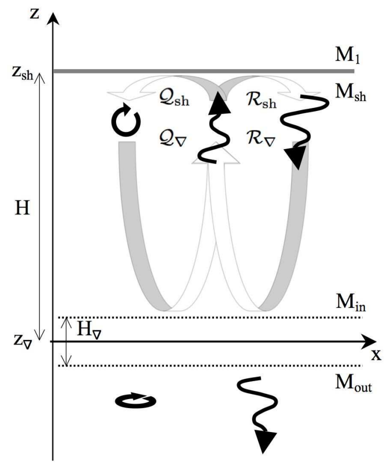

Fig. 2. Schematic view of the toy model. The unperturbed flow is planar, adiabatic, and decelerated through a stationary shock ($z_{\rm sh}$). The step-like external potential is uniform except in the deceleration region of size H_∇ around z_∇.

size H_∇ of the deceleration region is an important parameter responsible for a frequency cutoff $\omega_\nabla \sim v_\nabla/H_\nabla$ above which the advective-acoustic coupling is inefficient (Fig. 3a), due to incoherent acoustic emission (phase mixing). As a consequence, SASI is a low frequency, low-l instability.

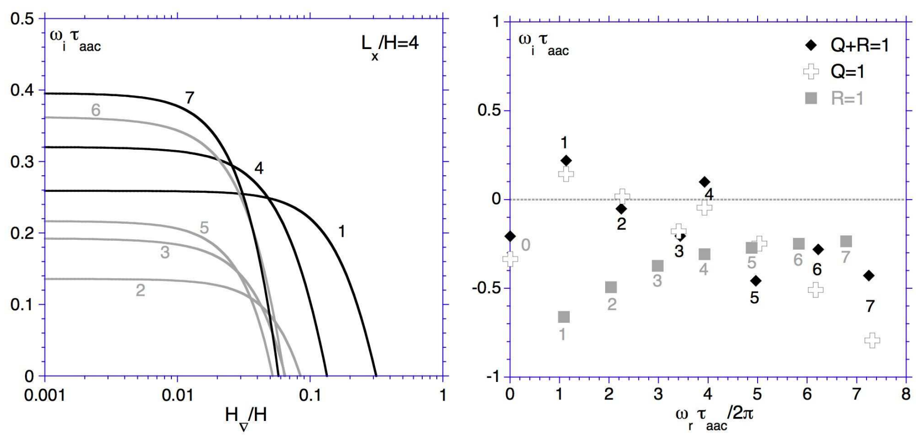

Fig. 3. Left (a): Dependence of the growth rate ω_i on the size H_∇ of the coupling region, when the amplitude $\Delta\Phi$ of the potential jump is kept constant. **Right (b):** For each value of the horizontal wavenumber $n_x = 0$ to 7, comparison of the most unstable modes associated to the advective-acoustic cycle alone (white crosses), the purely acoustic cycle alone (filled gray squares) and the full problem (filled black diamonds).

In this toy model, the efficiency $\mathcal{Q} \equiv \mathcal{Q}_\nabla \mathcal{Q}_{\rm sh}$ of the advective-acoustic cycle and the efficiency $\mathcal{R} \equiv \mathcal{R}_\nabla \mathcal{R}_{\rm sh}$ of the purely acoustic cycle can be calculated for all modes. The growth rate of the dominant mode is compared in Fig. 3b to the growth rates associated to each cycle considered separately: the growth rate associated to the advective-acoustic cycle alone is close to the growth rate of the toy model, while the purely acoustic cycle alone is always stable. As in Foglizzo & Tagger (2000), the influence of the purely acoustic cycle which can be either constructive (e.g. $n_x = 1, 4$) or destructive (e.g. $n_x = 2$).

The simple setup of this toy model can also be used to study the saturation mechanism of SASI: the acoustic feedback is decreased by the growth of parasitic instabilities on the advected wave of entropy/vorticity (Guilet et al. 2009).

4 Toward 3D simulations

The success of the neutrino-driven explosion, and its effect on the neutron star kick are among the most promising consequences of SASI. Yet these results still have to be confirmed by 3D simulations, whose computational cost preclude an accurate treatment of neutrino transport. Despite this difficulty, future parametric studies in 3D using a simplified transport should be able to elucidate the actual consequences of SASI on core-collapse supernovae. A detailed physical understanding of simple toy models can guide our interpretation of these complex simulations.

This work has been partially funded by the Vortexplosion project ANR-06-JCJC-0119.

References

Bethe, H.A. & Wilson, J.R. 1985, ApJ, 295, 14
Blondin, J.M, Mezzacappa, A., & DeMarino, C. 2003, ApJ, 584, 971
Blondin, J.M, & Mezzacappa, A. 2006, ApJ, 642, 401
Blondin, J.M, & Mezzacappa, A. 2007, Nature, 445, 58
Blondin, J.M, & Shaw, A. 2007, ApJ, 656, 366
Buras, R., Rampp, M., Janka, H.-T., & Kifonidis, K. 2003, Phys. Rev. Lett., 90, 241101
Burrows, A., Hayes, J., & Fryxell, B.A. 1995, ApJ, 450, 830
Burrows, A., Livne, E., Dessart, L., Ott, C. D., & Murphy, J. 2006, ApJ, 640, 878
Burrows, A., Livne, E., Dessart, L., Ott, C. D., & Murphy, J. 2007, ApJ, 655, 416
Endeve, E., Cardall, C.Y., Budiardja, R.D., Mezzacappa A. 2009, arXiv:0811.3385
Fernández, R. & Thompson, C. 2009, ApJ, 697, 1827
Fernández, R. & Thompson, C. 2009, ApJ, 703, 1464
Foglizzo, T. 2009, ApJ, 694, 820
Foglizzo, T., & Tagger, M. 2000, A& A, 363, 174
Foglizzo, T., Galletti, P., Scheck, L., & Janka, H.-Th. 2007, ApJ, 654, 1006
Guilet, J., Sato, J., & Foglizzo, T. 2009, ApJ submitted
Hammer, N.J., Janka, H.-Th., , & Müller, E. 2009, arXiv:0908.3474
Iwakami, W., Kotake, K., Ohnishi, N., Yamada, S., & Sawada, K. 2009, ApJ, 700, 232
Janka, H.-T. & Müller, E. 1996, A& A, 306, 167
Kifonidis, K., Plewa, T., Scheck, L., Janka, H.-Th., , & Müller, E. 2006, A&A 453, 661
Kotake, K., Ohnishi, N., & Yamada, S. 2007, ApJ, 655, 406
Laming, J. M. 2007, ApJ, 659, 1449
Laming, J. M. 2008, ApJ, 687, 1461
Liebendörfer M. et al. 2001, Phys. Rev. D, 63, 103004
Marek, A., & Janka, H.-Th. 2009, ApJ, 694, 664
Marek, A., Janka, H.-T., & Müller, E. 2009, A&A, 496, 475
Murphy, J.W., & Burrows, A. 2008, ApJ, 688, 1159
Murphy, J.W., Ott, C.D. & Burrows, A. 2009, arXiv:0907.4762
Ohnishi, N., Kotake, K., & Yamada, S. 2006, ApJ, 641, 1018
Ott, C. D., Burrows, A., Dessart, L., & Livne, E. 2006, Phys. Rev. Lett., 96, 201102
Ott, C.D. 2009, Class. Quant. Grav., 26, 063001
Sato, J., Foglizzo, T., & Fromang, S. 2009, ApJ, 694, 664
Scheck, L., Plewa, T., Janka, H.-Th., Kifonidis, K., & Müller, E. 2004, Phys. Rev. Lett., 92, 011103
Scheck, L., Kifonidis, K., Janka, H.T., & Müller, E. 2006, A& A, 457, 963
Scheck, L., Janka, H.-Th., Foglizzo, T., & Kifonidis, K. 2008, A& A, 477, 931
Weinberg, N.N., Quataert, E. 2008, MNRAS 387, L64
Yamasaki, T. & Foglizzo, T. 2008, ApJ, 679, 607

DETECTION AND CHARACTERIZATION OF THE COSMIC RAY AIR SHOWER RADIO EMISSION WITH THE CODALEMA EXPERIMENT

Garçon, T.[1] and the CODALEMA collaboration[1,2]

Abstract. The setup of the CODALEMA experiment installed at the Radio Observatory of Nançay, France, is described. The observed asymmetry, in the arrival direction distribution of radiodetected cosmic ray showers above 10^{17}eV, is interpreted as the signature of the geomagnetic origin of the air shower radio emission. In order to correlate the primary particle energy to the associated radioelectric field, the lateral distribution functions of the radio signals are carefully studied. In this aim, antenna's breakdowns or possible environmental effects modifiying these signals are currently analyzed and will be presented.

1 Introduction

The two major methods for the observation of extensive air showers (EAS) use surface detectors and fluorescence detectors, measuring respectively the charged particles at the ground level and the fluorescence light of the EAS. The advantage for the first one is its high duty cycle when the second one presents a large detection volume efficiency and a lower shower model dependence. The radiodetection technique could combine these advantages.

The idea of EAS radiodetection has been suggested for the first time in the 60's. The charge excess mechanism was first proposed as the origin of the induced radioelectric field (Askar'yan 1962). Today, the geomagnetic induced mechanism, which was suggested by Kahn et Lerche (Kahn 1965), are preferentially investigated (geosynchrotron radiations (Huege 2005), or transverse current induced emissions (Scholten 2008)). The first experiments in the 60's obtained promising but conflicting results, leading to the surrender of the giving up in the 70's. Today, with the improvement of fast electronics, EAS radiodetection becomes an operational technique. Several experiments, like CODALEMA in France (Ardouin 2005) or LOPES in Germany (Falcke 2005), have already observed evidence for a radio emission from EAS.

2 Setup of the CODALEMA experiment

The CODALEMA experiment uses three arrays of detectors : the particle detector array, the antenna dipole array and the Nançay decameter array. This later is dedicated to the study of the electric field with a high spatial resolution (Lecacheux 2009), but its results aren't discussed in the current analysis. The particle detector array is dedicated to the estimation of the shower characteristics (primary energy, arrival time, direction, size and core located of the EAS) using the particle density of the shower at the ground level. It consists in 17 scintillator stations on a grid of 340m × 340m (Fig. 1, left). The number of particles reaching the ground and the core position are calculated from the measured particle densities in these detectors. The lateral distribution is fitted with an analytical Nishimura-Kamata-Greisen lateral distribution using a minimization algorithm. Finally, the energy is computed by the CIC method with a resolution of 30%, from simulations of proton induced EAS run with AIRES (Sciutto 2005). This array produces also a logic signal to trigger the antenna signal acquisition. In order to detect the radio signals seen in coincidence with ground detectors a short active dipole (Fig. 1, right) was developed (Charrier 2007). It is made of two 0.6 m long and 0.1 m wide aluminium slats separated by a 10

[1] SUBATECH IN2P3-CNRS/Université de Nantes/Ecole des Mines de Nantes France

[2] LESIA, Observatoire de Paris-Meudon France - Station de Radioastronomie de Nançay France - LAL, IN2P3-CNRS/Université de Paris Sud Orsay France - LPSC, IN2P3-CNRS/UJF/INPG Grenoble France - ESEO, Angers France - LAOB, INSU-CNRS Besançon France - LPCE, SDU-CNRS Université d'Orléans France

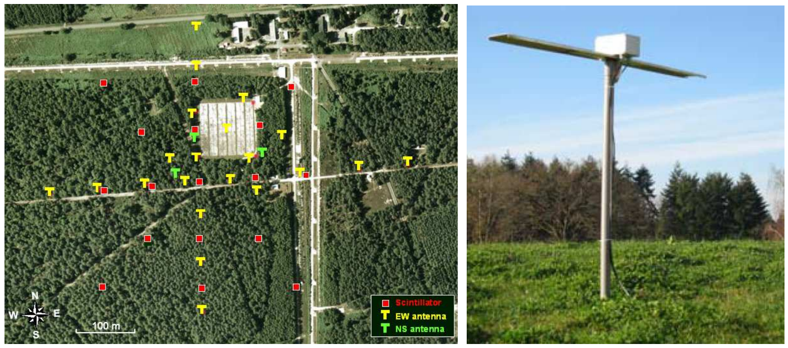

Fig. 1. Left : Schematic aeral view of the Codalema experiment. Plastic scintillators are depicted as squares, antennas as T, oriented in the NS and EW direction. **Right**: One dipole of the antenna array.

mm gap. This antenna, with smooth variations of lobe, is loaded by a dedicated high input impedance low noise amplifier providing a good sensibility and linearity at a high dynamics. The antenna array is made of a 600 $\times$ 450 m cross-shaped core of 14 antennas in East-West (EW) polarization, 7 antennas located between these arms and 3 other ones in North-South (NS) polarization (Fig. 1, left). A central shelter houses the acquisition sytem and power supplies and is connected to the detectors by cables. So-called Matacq ADC boards perform a 12-bits digitalization of signals, at a sampling rate of 1 GS/s and with a memory depth of 2560 points (i.e. 2.5 μs of signal). If the 5 central scintillator stations detect a signal in coincidence within a 600 ns gate width, a trigger is produced to record all signals of the two arrays. This trigger condition leads to an event rate of about 7 events per hour. The antenna signals are digitally filtered offline (23-83MHz), to eliminate FM and AM contributions, and corrected for the cable frequency response. Transient radio pulses are searched independently in each antenna waveform using a linear prediction method which eliminates also the emitters whose frequencies lie in the range used for the experiment. When pulses are detected, an absolute time is associated to each of them and corrected for the cable and electronics delays. From this information, the time and the arrival direction of the shower plane can be obtained by simple triangulation. Finally, the radio and particle events are folded into one single event. We limit the angular difference between both to 20 degrees and the time difference to $\pm$ 100 ns in order to keep only well reconstructed events and eliminate random radio events. A last criterion is applied if the larger particle density belongs to a scintillator in the middle of the array. For these so-called internal events, the energy and the shower core location can be estimated with a good accuracy. For details, see (Ardouin 2005, 2006, 2009).

3 Results

The energy distribution measured by the ground particle array for internal events is displayed Fig. 2, left, and compared with the same energy distribution of events measured in coincidence by the antenna array. The threshold of the radio detector is clearly visible below 10^{17}eV. Both distributions converge at 10^{18}eV. This reflects the increase of the radio detection efficiency at high energies. Fig. 2, center, represents the arrival directions of the radio events, in local coordinates, detected in the EW polarization. In the azimuthal distribution, a large asymmetry is visible in the observed event density between the North and the South sectors. This South side deficit is not observed on an antenna background (self-trigger) or for the internal scintillator events. This observation is thus not associated to a detector failure or a statistical fluctuation but requires an investigation of the electric field generation mechanism of the EAS. An obvious candidate for symmetry breaking effect in the electric field generation is the geomagnetic field, via the Lorentz force. The electric field magnitude of this contribution should depend on the values of the vector cross product $v \wedge B$ where v is the direction of the primary particle. The predicted event sky map computed with this hypothesis (Fig. 2, right) is very similar to the observed sky map. Especially, simulated zenithal and azimutal distributions are compared to the data and show both good agreement. The polarity (ie. the sign) of the signals and the preliminary results obtained for the antennas detecting in the NS polarization are also in good agreement with simulations. This result confirms the importance of geomagnetic mechanism in the radioelectric field creation process (Ardouin 2009).

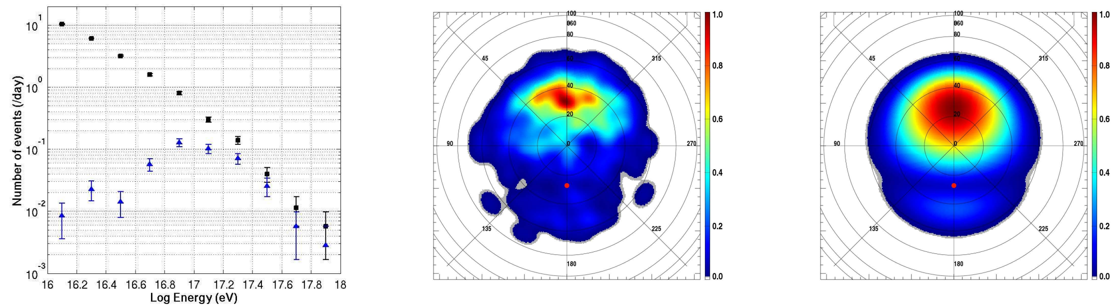

Fig. 2. Left : Energy distributions for internal events measured by the particle detectors (squares) and seen in coincidence by the antennas (triangles). **Center** : Sky map of observed radio events, detected in the EW polarization, using a 10° gaussian smooth (Zenith is at the center, North at the top, West at the left). The direction of the geomagnetic field is indicated by the red dot. **Right**: Sky map calculated by considering the EW component of the Lorentz force convolved by the trigger coverage map, and the antenna lobe. The color scale is normalized to 1 in the direction of the maximum.

4 Monitoring and effects of the environnement

The experimental setup of CODALEMA allows an independent measurement of the radioelectric field for each antenna. The electric field lateral distribution, which is simply the signal amplitude as a function of the distance to the shower axis is computed event by event and has been fitted with an exponential function, $E_0 e^{-\frac{d}{d_0}}$ (Allan's parameterization (Allan 1971)). The fit uses 4 free parameters, E_0, d_0, and the core position (X_0 and Y_0), and d is the distance to the shower axis. The event profiles are well fitted by such an exponential function and permit to study the correlation in energy, but for some of them ($\approx 20\%$), profiles are flat and an exponential fit doesn't make sense. Several detection effects could explain these unexpected profiles. To understand them, monitoring of the antenna array, on the one hand, and study of environnemental effects on the other hand are currently realized. For one year, a monitoring method has been setup to detect with accuracy breakdowns in the antenna array. The monitoring of the noise measured by each antenna during long data taking sequences is especially powerfull to underline breakdowns for one antenna, or an emergence of transmitter close to the array. The detection, the analysis, and the repair of these breakdowns become fast and easy. For several unexpected profiles, the removal from the fit of antennas showing breakdowns allows to increase the quality of the lateral distribution reconstruction (Fig. 3). Independently, it is possible to use an algorithm to ignore, in the analysis, the antenna signals which degrade strongly the profile. Both methods give similar results on profile corrections. A quantitative study is under way to compute the ratio of improved profiles with these methods.

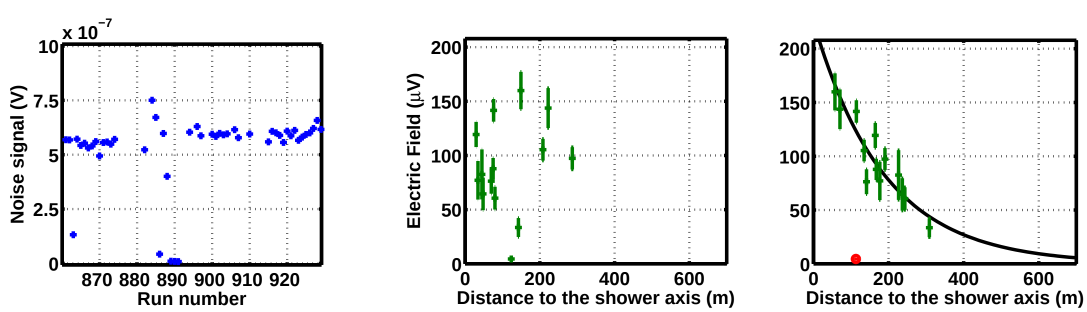

Fig. 3. Left : The monitoring shows a breakdown, between the 875th and 895th run (one month) for one antenna. **Center** The result of the lateral distribution fit for one unexpected profile, during the antenna breakdown. **Right** : Result after the removing of the dysfunctional antenna (red dot at the bottom) during the minimization process of the χ^2. An exponential profile is recovered. Consequently, the location of the shower core can change.

One additionnal correction has been obtained by analyzing the environnements of the antennas, which vary from one to the other. This is found to have an impact on the measured electric field (and consequently on the quality of the lateral distribution). For some arrival directions of events, frequency spectra of few antennas show oscillating features, which seem to be due to interference. One of these typical events showing oscillating patterns in the spectrum is presented Fig. 4. A complete simulation of the environnement of the antenna, with a signal coming from the direction of the shower, was done by the simulation software 4nec2X suggesting that the interference were due to the modification of the antenna lobe by a metallic shelter close to the antenna. The interference effect is well reproduced by the simulation. A personalized antenna lobe for this antenna can especially be used for all analysis processes (under investigation).

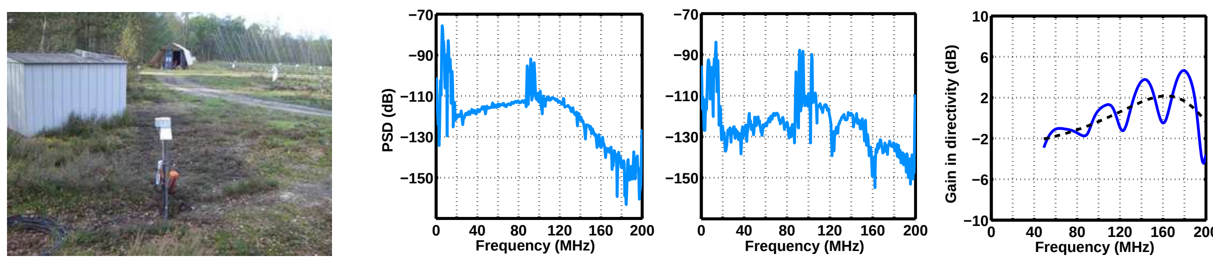

Fig. 4. From left to right **A** : Antenna close to the metallic shelter. **B** : Raw spectrum of a powerful event seen by one normal antenna. **C**: Raw spectrum of the same event seen by the antenna close to the metallic shelter. **D**: Simulated gain vs frequency for two antennas, for a white noise in the arrival direction of the cosmic ray (without considering the amplifier response). Doted lines : without shelter. Solid line : with the metallic shelter.

5 Conclusion

The CODALEMA experiment shows very promising results both in the physical interpretation of the results and in the developpement of the radiodetection method. Improvements in the simulations, and study of fine detection effects are currently under way. Moreover, radio detection with autonomous stations presently in developpement in the CODALEMA collaboration will allow to detect EAS at higher energies (10^{19}eV) and larger impact parameters (1000-2000m vs 400m today), and larger zenith angles. To reach this goal, the first stations are deployed at the same time on the CODALEMA site, and on the Pierre Auger Observatory for the AERA project.

References

Allan, H. R., 1971 , Progress In Elementary Particle And Cosmic Rays Physics, 10, 171

Ardouin, D., & al., 2005, Nucl. Instrum. Meth. A, 555, 148

Ardouin, D., & al., 2006, Astro. Phys., 26, 341

Ardouin, D., & al., 2009, Astro. Phys., 31, 192

Askar'yan, G. A., 1962, Soviet Physics, J.E.T.P., 14, 441

Charrier, D., 2007, & al., Nucl. Instrum. Meth. A, 572, 481

Falcke,H., & al., 2005, Nature, 435, 313

Huege, T., & Falcke, H., 2005, Astro. Phys., 24, 116

Kahn, F. D., & Lerche, I., 1965, *Radiation from cosmic ray showers*, Astronomy Department, University of Manchester

Lecacheux, A., & al., 2009, Proceedings of the 31st ICRC, Lodz

Scholten, O., Werner, K., & Rusydi, F., 2008, Astro. Phys., 19, 477

Sciutto, S.J., 2005, AIRES, version 2.8.0, 2005, http://www.fisica.unlp.edu.ar/auger/aires/

SF2A 2009
M. Heydari-Malayeri, C. Reylé and R. Samadi (eds)

MULTI-WAVELENGTH POLARIMETRY: A POWERFUL TOOL TO STUDY THE PHYSICS OF ACTIVE GALACTIC NUCLEI

Goosmann, R. W.[1]

Abstract. Accreting supermassive black holes reside in a very complex environment and the inner structure and dynamics of active galactic nuclei (AGN) are not well understood yet. In this note, I point out the important role that multi-wavelength polarimetry can play in understanding AGN. In addition to spectroscopy, the measurement of the polarization percentage and position angle provides two more observables that are sensitive to the geometry and kinematics of emission and scattering regions. Furthermore, time-dependent polarimetry allows to measure spatial distances between emission regions and scattering mirrors by applying a reverberation technique. For radiation coming from the direct vicinity of the black hole, the polarization also contains information about the space-time metric. Spectropolarimetry observations of AGN are obtained in the radio, the infrared, the optical, and the ultraviolet wave bands and in the future they are going be available also in the X-ray range. To interpret these observations in a coherent way, it is necessary to study models that do not only reproduce the broad-band spectroscopy properties of AGN but also their multi-wavelength polarization signature. I present a first step towards such models for the case of radio-quiet AGN. The modeling reveals the optical/UV and X-ray polarization properties of the reprocessed radiation coming from the obscuring torus. The discussion about the implications of such models includes prospects for the up-coming technique of X-ray (spectro-)polarimetry.

1 Observing and modeling the optical/UV and X-ray polarization of active galactic nuclei

Polarimetry and spectropolarimetry are powerful techniques to disentangle the complex structure and dynamics of the various media close to accreting supermassive black holes. In the optical waveband, polarimetry provided major support for the standard unification model of active galactic nuclei (AGN), when Antonucci & Miller (1984) found the first hidden type-1 nucleus in the Seyfert-2 galaxy NGC 1068 by revealing broad optical emission lines in the polarized flux spectrum. Many more hidden type-1 nuclei were then found by polarimetry. The technique enables a periscope view around the obscuring torus revealing the central ionizing source and the broad line region of a type-2 AGN. This periscope view is possible due to the scattering-induced polarization that originates mostly in the polar ionization cones of the AGN scheme. The analysis and modeling of large samples of Seyfert galaxies has further constrained the geometry and dynamics of the various scattering components that are relevant to the polarization of the continuum and the broad emission lines (see Smith et al. 2005 and references therein). A new dimension was added to the polarimetry technique when Gaskell et al. (2007) presented a reverberation of the optical polarization coming from the Seyfert galaxy NGC 4151. The reverberation time scale allowed to constrain the spatial distance between the illuminating source region and the polarizing mirrors. For NGC 4151 it was found that the size of the polarizing mirror should be comparable to the size of the low-ionization broad line region, while it was ruled out that the polarization arises from dust scattering by the inner surface of the much larger obscuring torus.

To correctly interpret the results of polarization measurements, it is important to conduct detailed and coherent modeling. Almost any interaction between radiation and matter leaves an imprint in the polarization signal coding information about the composition, dynamics and the geometry of the scattering mirror(s). In the complex environment of accreting black holes one therefore expects a strong impact of multiple scattering on the observed polarization spectrum. All these aspects should be considered in a polarization model, which is why the Monte-Carlo STOKES was written (Goosmann & Gaskell 2007) and continues to be developed.

[1] Observatoire Astronomique de Strasbourg, France

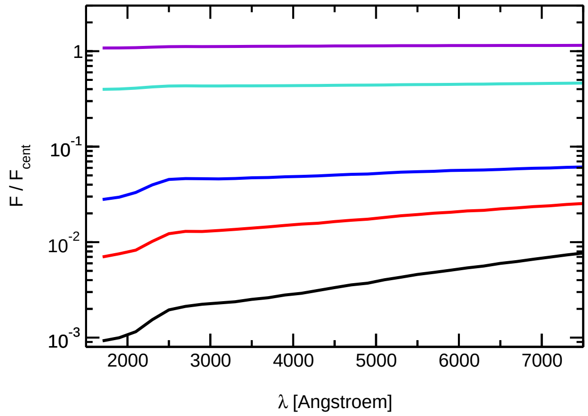

Fig. 1. Modeling the optical/UV dust extinction by a centrally illuminated large torus with an elliptical cross-section and half-opening angle $\theta_0 = 30°$. The fraction, F/F_*, of the central flux, F_*, seen at different viewing angles, i, and wavelengths, λ, is shown. From top to bottom i takes the values $i = 18°$ (purple, face-on view), $i = 32°$ (cyan), $i = 41°$ (blue), $i = 49°$ (red), and $i = 57°$ (black, intermediate viewing angle).

A first release of the code working in the optical/UV spectral range is publicly available and featured on the world wide web[1]. Recently, the code has been extended into the X-ray range by implementing a prescription of Compton scattering, X-ray photo-absorption and the production of iron Kα and Kβ lines. Now, it is thus possible to compute the polarization properties of a given AGN model simultaneously in the optical/UV and the X-ray band. This should give important constraints as several components of an active nucleus, such as the polar ionized outflows or the obscuring torus, reprocess both the optical/UV and the X-ray radiation.

2 Modeling the reprocessed optical/UV and X-ray spectra of the dusty torus

As a first step, I am going to focus on modeling the polarization properties of the reprocessed radiation emerging from the optically thick, dusty torus only. In the optical/UV range, the reprocessing has been extensively modeled with STOKES before (Goosmann & Gaskell 2007). Model setups for various torus geometries, half-opening angles, and dust compositions where examined. Here I apply again the model of a centrally irradiated torus with a large elliptical cross-section and a half-opening angle of $\theta_0 = 30°$. The size of the optical/UV emitting parts of the accretion disk is very small when compared to the size of the inner torus radius. Therefore, the central source is defined to be point-like. The incident radiation is supposed to be unpolarized and constant with wavelength λ. The dust composition follows a prescription for standard Galactic dust. The resulting scattering spectra as a function of the viewing angle i are recalled in Fig. 1. Note that the dust temperature must be below 1500 K for the dust being able to exist. Therefore, one does not expect any thermal re-emission in the optical/UV range considered here. The peak of the dust re-emission actually lies in the infrared waveband.

Next, I compute the X-ray reprocessing of the irradiated torus using the latest version of the STOKES code. In the X-ray range the sub-structure of the irradiating source should not be treated as simply as for the optical/UV band. The X-ray spectrum of AGN shows significant variability on very fast time-scales. It is therefore necessary to conclude that the X-ray emission comes from very compact regions close to the central black hole. One further assumes that a significant fraction of this primary radiation is being reprocessed by the accreting disk. Such a reflection from the disk polarizes the radiation, so that the X-ray spectrum impinging on the torus is no longer unpolarized. We take this fact into account by modeling self-consistently the multiple-reprocessing by the disk and the torus. For both regions we assume neutral reprocessing by an optically thick medium with solar elemental abundances. The disk is located at the symmetry center of the torus and being irradiated by a slightly elevated primary X-ray source (so-called lamp-post geometry). The size of the

[1] http://www.stokes-program.info/

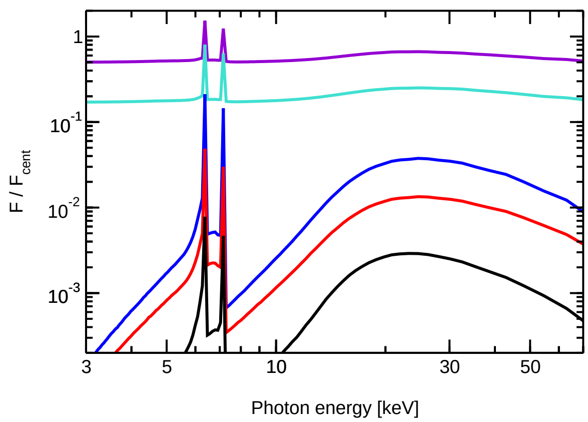

Fig. 2. Modeling the X-ray reprocessing from a system of a centrally illuminated disk situated inside the funnel of a large torus with an elliptical cross-section and half-opening angle $\theta_0 = 30°$. The denotations are as in Fig. 1.

reprocessing disk is small with respect to the inner radius of the torus. The height of the primary source above the disk is small against the disk size. The source isotropically emits a constant spectrum in photon energy.

The spectral results for the X-ray modeling are shown in Fig. 2. The reprocessed spectrum shows standard features, such as photo-absorption in the soft X-ray range, fluorescent Kα and Kβ lines at 6.4 keV and 7.1 keV and the characteristic reflection hump due to Compton down-scattering around 20—30 keV. At low inclination angles, when the observer can directly see the central source, the spectrum is dominated by the primary contribution. The reprocessing features are much more pronounced at higher inclinations when the primary source disappears below the torus horizon.

In Fig. 3, I show the spectrum of the resulting polarization degree for the X-ray and the optical/UV range. The X-ray data is now converted to photon wavelength. In both bands the polarization is positive and thus the polarization position angle is oriented perpendicularly to the symmetry axis of the system. For the X-ray range this is not necessarily obvious, as for a small irradiated X-ray region the position angle of the resulting polarization can also be aligned to the (projected) symmetry axis (Goosmann 2009). In this case, however, we assume the disk to be large with respect to the height of the primary source. A scattering torus with a half-opening angle of 30° can only produce perpendicular polarization in both wavebands considered.

It it interesting to compare the polarization degree P in both bands: the polarization is always weak at low inclinations when the spectrum is dominated by the unpolarized primary radiation. The situation is very different at higher inclinations. The highest polarization percentages appear in the soft X-ray range. Comparison with Fig. 2 shows that the strong polarization corresponds to fluxes decreasing toward low X-ray energies (longer wavelengths). The fluxes are more significant closer to the iron line complex, i.e. at 5—6 keV. Across the iron line, the polarization drops due to dilution by the unpolarized line emission. The Compton hump is significantly polarized. Across the hump maximum, P is slightly reduced due to the multiple Compton scattering that has a depolarizing effect. But the hard X-ray polarization always remains above ~ 10 %. In the optical/UV band the wavelength dependence of the polarization degree is influenced by the dust composition but the dominating effect is the torus half-opening angle (Goosmann & Gaskell 2007).

3 Future prospects for multi-wavelength polarimetry

The results presented in this note are first steps on the way to provide consistent and simultaneous polarization models for AGN in the optical/UV and the X-ray band. The advantage of using a flexible Monte-Carlo method like in STOKES lies in the possibility to coherently combine various reprocessing regions. For X-ray polarization emerging from close to the last stable orbit of the accretion disk, relativistic effects play an important role and the STOKES results have to be combined with a relativistic ray-tracing method - which then allows to probe the space-time structure in the direct vicinity of the black hole (Dovčiak et al. 2008).

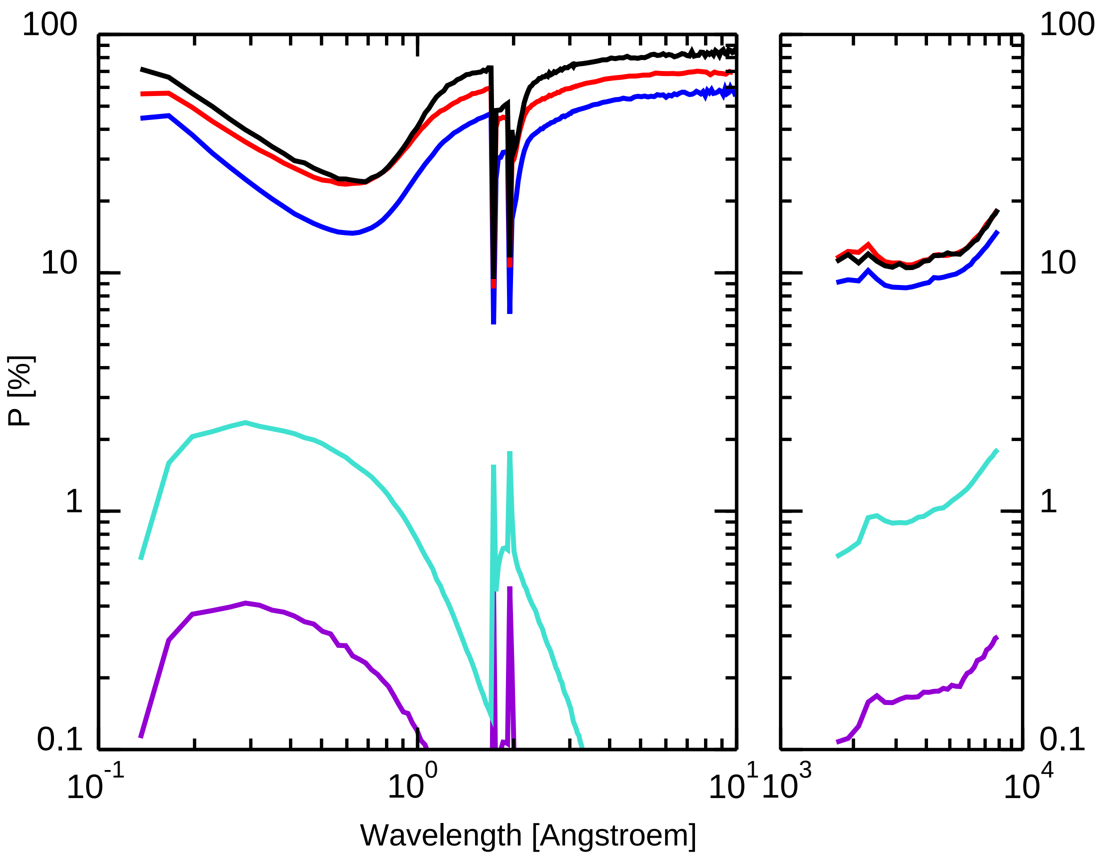

Fig. 3. Polarization degree, P, induced by the irradiated torus (see text) for the X-ray and the optical/UV band as a function of the photon wavelength, λ, and the viewing angle, i. From top to bottom i takes the values $i = 57°$ (black, intermediate viewing angle), $i = 49°$ (red), $i = 41°$ (blue), $i = 32°$ (cyan), and $i = 18°$ (purple, face-on view).

While polarimetry is an established technique in the optical waveband, we are still at the edge of the X-ray polarimetry era. The coming age of satellite-based X-ray polarimeters like the NASA GEM SMEX satellite (Swank et al. 2008) or the Italian mission project POLARIX (Costa et al. 2006) will enable us to test the type of modeling of which only a beginning is laid out here. In the future it is necessary to further explore the available parameter space by considering multiple reprocessing components and by varying their geometry and dynamics. Of course the number of model parameter increases - but so does the number of (polarimetry) observables as well as the spectral coverage of both, models and observations. Therefore, multi-wavelength polarimetry is a promising tool to further disentangle the complexity around accreting supermassive black holes.

References

Antonucci, R. R. J., & Miller, J. S. 1985, ApJ, 297, 621

Costa, E., et al. 2006, in "POLARIX: a small mission of X-ray polarimetry" in "Space Telescopes and Instrumentation II: Ultraviolet to Gamma Ray. Edited by Turner, Martin J. L.; Hasinger, Gnther. Proceedings of the SPIE, Volume 6266, pp. 62660R

Dovčiak, M., Muleri, F., Goosmann, R. W., Karas, V., & Matt, G. 2008, MNRAS, 391, 32

Gaskell, C. M., Goosmann, R. W., Merkulova, N. I., Shakhovskoy, N. M., & Shoji, M. 2007, arXiv:0711.1019

Goosmann, R. W. 2009 in "The polarization of complex X-ray sources", proceedings of the international conference "The coming age of X-ray polarimetry", 27-30 Arpil 2009, Rome, Italy. To appear in Cambridge University Press

Goosmann, R. W., & Gaskell, C. M. 2007, A&A, 465, 129

Smith, J. E., Robinson, A., Young, S., Axon, D. J., & Corbett, E. A. 2005, MNRAS, 359, 846

Swank, J., Kallman, T., & Jahoda, K. 2008, 37th COSPAR Scientific Assembly, 37, 3102

SF2A 2009
M. Heydari-Malayeri, C. Reylé and R. Samadi (eds)

THERMAL INSTABILITIES IN THE WIND OF NGC 3783

Goosmann, R. W.[1], Goncalves, A. C.[2], Holczer, T.[3], Mouchet, M.[4], Behar, E.[5], Collin, S.[6], Dumont, A.-M.[7], Godet, O.[8] and Kaspi, S.[9]

Abstract. Outflows in Active Galactic Nuclei play an important role for galaxy evolution and the enrichment of the intergalactic medium. In the X-ray range they appear as warm absorbers (WA). Thanks to the recently introduced Absorption Measure Distribution (AMD) method, the column densities of individual ionic species of the wind can be derived from observed X-ray spectra, which gives a new handle on constraining the physics of the WA. We report first results on the theoretical interpretation of an AMD analysis for the Seyfert galaxy NGC 3783. The AMD results based on the known 900-ksec Chandra observation suggest that the WA is in pressure equilibrium as was indicated before by spectral analysis. Conducting radiative transfer simulations for such a case we reproduce the measured ionic column-densities by adjusting several crucial parameters of the medium: the ionization parameter, the total column density, and the amount of micro-turbulence. We use the code TITAN that is particularly adequate to the radiative transfer in X-ray photoionized gases at constant total pressure. It turns out that the WA plasma is probably a clumpy, two-phase medium where cold, dense clumps are embedded in a hotter, diffuse gas.

1 Thermal instabilities in photoionized gases

A photoionized gas in thermal equilibrium such as in the warm absorber (WA) of active galactic nuclei can display thermal instabilities. The phenomenon can be illustrated when plotting the temperature versus the ratio of radiation to gas pressure (Krolik et al. 1981). The S-shape of the plot indicates the possible co-existence of several gas temperature phases at the same pressure ratio. At a given pressure, the gas can be in three (or more) thermal equilibrium states, which depend on the ionizing spectral energy distribution and other physical parameters related to the heating and cooling function of the gas. Some of these equilibrium states are thermally unstable, others are not.

The TITAN code for radiative transfer in X-ray irradiated plasma gas (Dumont et al. 2000, 2003) allows to choose between the hot and the cold stable solutions; it also provides an intermediate solution which can be understood as a mixture of the WA cold and hot phases (Gonçalves et al. 2007). In the work presented in this note we explore the intermediate solution of a WA gas in total pressure equilibrium.

2 Model comparison to the measured ionic column densities in the warm absorber of NGC 3783

Using a long Chandra observation, Holczer et al. (2007) apply the so-called AMD method to constrain the elemental abundances and the column densities $N_{\rm i}$ of various ionic species in the WA gas of the Seyfert galaxy NGC 3783. Gonçalves et al. (2006) have shown that the absorption spectrum of this object can be explained

[1] Observatoire Astronomique de Strasbourg, France; Observatoire de Paris, LUTh, Meudon, France
[2] Observatoire de Paris, LUTh, Meudon, France
[3] Technion, Israel Institute of Technology, Haifa, Israel
[4] Laboratoire Astroparticule et Cosmologie, Paris; Observatoire de Paris, LUTh, Meudon, France
[5] Technion, Israel Institute of Technology, Haifa, Israel
[6] Observatoire de Paris, LUTh, Meudon, France
[7] Observatoire de Paris, LUTh, Meudon, France
[8] Centre d'Etudes Spatiale des Rayonnements, Toulouse, France
[9] Technion, Israel Institute of Technology, Haifa, Israel

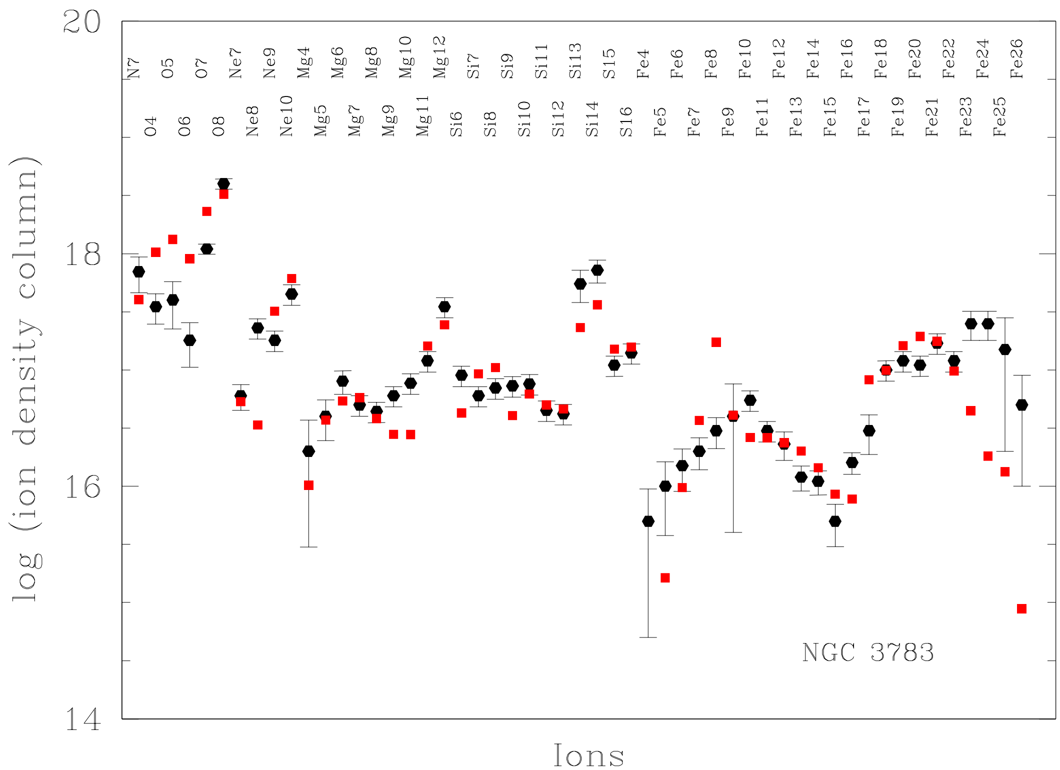

Fig. 1. Ionic column densities derived from the observed data by the AMD method (black circles with error bars; Holczer et al. 2007) and from the best TITAN model (red squares).

by a photoionized gas in constant total (i.e. gas + radiation) pressure. Here, we attempt to reproduce also the measured distribution of $N_{\rm i}$ computing various TITAN models. We vary the ionization parameter ξ, the total column density $N_{\rm H}$ of the gas, and its turbulent velocity $v_{\rm turb}$. The result for the best fitting model is shown in Fig. 1. The data is taken from the analysis by Holczer et al. (2007) and the model corresponds to the parameters $\xi = 2500$ cm ergs/s, $N_{\rm H} = 4 \times 10^{22}$ cm^{-2} and $v_{\rm turb} = 150$ km/s. There are striking similarities between the observed ionic column densities and the results from modeling the warm absorber in total pressure equilibrium. A discrepancy remains for the highest ionization species of iron where the model underestimates the observed column densities. This difference may be explained by the current limits on the measurements and/or theoretical computations of dielectronic recombination coefficients for highly ionized iron.

In addition to the best model shown in Fig. 1, other couples $(\xi, N_{\rm H})$ in the adjacent parameter region also provide a reasonable estimate of both the observed spectrum and the measured individual ionic column densities. We have examined the temperature and ionization profiles of our different models and compared them to the results of the AMD method. It turns out the model can reproduce the characteristic temperature gap revealed by the AMD analysis. This “forbidden” temperature zone seems to point out the existence of the thermal instability in the warm absorber gas. More details of this analysis will be published elsewhere.

References

Dumont et al. 2000, A&A 357, 223

Dumont et al. 2003, A&A 407, 13

Gonçalves et al. 2006, A&A 451, L23

Gonçalves et al. 2007, A&A 465, 9

Holczer et al. 2007, ApJ 663, 799

Krolik et al. 1981, ApJ 249, 422

SF2A 2009
M. Heydari-Malayeri, C. Reylé and R. Samadi (eds)

THE SATURATION OF THE STANDING ACCRETION SHOCK INSTABILITY BY PARASITIC INSTABILITIES

Guilet, J.[1], Sato, J.[1] and Foglizzo, T.[1]

Abstract. The Standing Accretion Shock Instability (SASI) is commonly believed to be the cause of large amplitude dipolar shock oscillations observed in numerical simulations of the stalled shock phase of core collapse supernovae. We investigate the role of parasitic instabilities as a possible cause of nonlinear SASI saturation. As the shock oscillations create both vorticity and entropy gradients, we show that both Kelvin-Helmholtz and Rayleigh-Taylor types of instabilities are able to grow on a SASI mode if its amplitude is large enough. We obtain approximate formulae for their growth rates, taking into account the effects of advection and entropy stratification, and use them to estimate the saturation amplitude of SASI. When applied to the set up of Fernández & Thompson (2009), this saturation mechanism is able to explain the dramatic decrease of the SASI power when both the nuclear dissociation energy and the cooling rate are varied. Our results open new perspectives for anticipating the effects, on the SASI amplitude, of the physical ingredients involved in the model of the collapsing star.

1 Introduction

The Standing Accretion Shock Instability (SASI) (Blondin et al. 2003; Scheck et al. 2008) takes place during the first second of the collapse of a massive star, causing the stalled shock to oscillate about the center of the star. 2D simulations suggest that the complex fluid motions triggered by this instability could be a crucial agent of explosion, either by helping the classical neutrino driven mechanism (Marek & Janka 2009; Murphy & Burrows 2008), or by a new mechanism based on the emission of acoustic waves from the proto-neutron star (Burrows et al. (2006), see however Weinberg & Quataert (2008)). The large scale ($l = 1 - 2$) induced asymmetry could also explain the high kick velocities of newly formed neutron stars (Scheck et al. 2006) and may affect their spin (Blondin & Mezzacappa 2007). The degree of asymmetry, however, directly depends on the saturation amplitude of SASI which is not well understood yet. The purpose of this work is to elucidate the saturation mechanism of SASI.

2 Method

We propose that the saturation of SASI takes place when a parasitic instability is able to grow on the SASI mode, and hence feeds upon its energy and destroys its coherence. A parasitic mode can affect the dynamics of SASI if its growth rate $\sigma_{\rm parasite}$ exceeds the growth rate $\sigma_{\rm SASI}$ of SASI. Pessah & Goodman (2009) used a similar criterion to estimate the saturation amplitude of the MRI due to parasitic instabilities. We first determine the local growth rate $\sigma_{\rm parasite}(r, \Delta A)$ of the parasitic instabilities, which is an increasing function of the SASI amplitude ΔA. We then use the criterion $\sigma_{\rm parasite}(r, \Delta A) = \sigma_{\rm SASI}$ to define the minimum amplitude $\Delta A_{\rm min}(r)$ of SASI above which parasites can compete with SASI at a given radius r, despite advection and cooling. The parasitic instabilities can alter the growth of SASI only if their growth takes place in a region which is vital to the mechanism of SASI. For example, if the mechanism of SASI is interpreted as an advective-acoustic cycle (Foglizzo et al. 2007; Foglizzo 2009), this cycle is most sensitive to the region between the shock and the deceleration region where most of the acoustic feedback is produced. Fortunately, as will be shown in Sect. 4,

[1] CEA, Irfu, SAp, Centre de Saclay, F-91191 Gif-sur-Yvette, France and UMR AIM, CEA-CNRS-Univ. Paris VII, Centre de Saclay, F-91191 Gif-sur-Yvette, France.

the local saturation amplitude displays a broad minimum around the radius $(r_* + r_{\rm sh})/2$, which defines a global saturation amplitude without much sensitivity on the details of the SASI mechanism.

We also performed non linear simulations measuring the acoustic feedback in the toy model of Sato et al. (2009). These simulations confirmed that the acoustic feedback is decreased when parasitic instabilities are able to grow. The details of the calculations can be found in Guilet et al. (2009).

3 Approximate description of the parasitic instabilities

We estimate the stability of the SASI mode in three steps. First, we study the simplest form of parasitic instability growing on a sinusoidal profile (a velocity profile for the Kelvin-Helmholtz instability, an entropy profile in a gravity field for the Rayleigh-Taylor instability). Second, we assess the stabilizing effect of a positive entropy gradient ∇S_0 in the stationary flow: the restoring force associated to buoyancy can weaken the growth of parasites. In a third step, advection is taken into account: if the fluid is advected fast enough, the instability may be able to grow in a lagrangian way but would actually decay at a fixed radius as the perturbations are advected away. We use numerical simulations to measure the propagation speed of the parasitic instability, by perturbing the SASI mode over a limited region of space (Fig. 1).

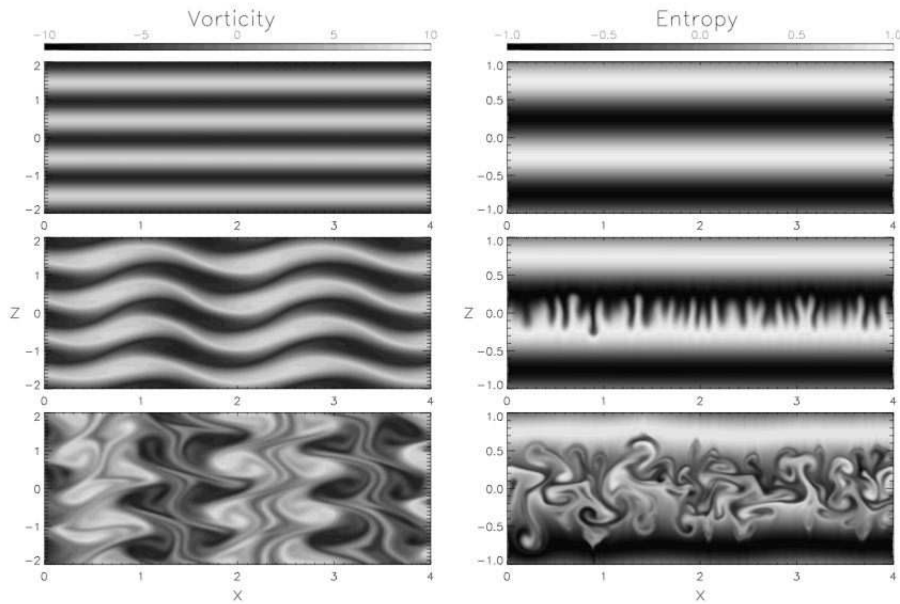

Fig. 1. Different stages in the evolution of the Kelvin-Helmholtz instability (*left*) and the Rayleigh-Taylor instability (*right*). The *upper panel* is the initial condition: a sinusoidal profile of transverse velocity (KH) or entropy (RT) with random perturbations localized around $z = 0$. The *middle panel* shows the time when KH just reached a nonlinear amplitude, and the mode structure can still be recognized. The *bottom panel* shows a more developed nonlinear stage of the instability.

3.1 The Kelvin-Helmholtz Instability

The Kelvin-Helmholtz instability feeds on the kinetic energy available in shear flows. Its growth rate scales like the maximum vorticity Δw, which is here created by SASI. When the stabilizing effects of stratification and advection are taken into account, the maximum KH growth rate can be approximated as :

$$\sigma_{\rm KH} \simeq \sigma_{\rm 0KH} \left(1 - \frac{\rm Ri}{\rm Ri_0} - \frac{v_z}{v_{\rm eff}}\right), \tag{3.1}$$

where $\sigma_{\rm 0KH} \sim 0.25\Delta w$. The Richardson number Ri is the squared ratio of vorticity to the Brunt-Väisälä frequency and $\rm Ri_0 \sim 0.24$ is the critical value for the stabilization by stratification. Finally $v_{\rm eff} \sim 1.5\Delta w/K$ is an effective propagation velocity of KH along the vertical direction.

3.2 The Rayleigh-Taylor Instability

The Rayleigh-Taylor instability feeds on the potential energy available when a low entropy fluid is sitting on top of a higher entropy one, in a gravitational acceleration g. We estimate the RT growth rate in the presence of advection and stratification as:

$$\sigma_{\rm RT} = 0.75\sqrt{\frac{\gamma-1}{\gamma} g\nabla\left(\Delta S + S_0\right)} - 0.6Kv_z, \tag{3.2}$$

where ΔS is the entropy amplitude of the SASI mode, S_0 is the dimensionless entropy of the stationary flow, K is the SASI wave number and v_z is the advection speed.

4 Comparison with the simulations of Fernandez & Thompson (2009)

In order to test this scenario, we have applied the above estimates to the setup of Fernández & Thompson (2009). Their simulations studied the effect of iron dissociation by removing a fixed energy per nucleon at the shock. This dissociation energy ϵ is varied in a parametric manner from zero to $\epsilon = 0.25v_{\rm ff}^2$ ($v_{\rm ff}$ is the free fall velocity at the shock), while the cooling function is adjusted in order to keep constant the stationary shock radius. These simulations are a very good test for any saturation mechanism because the saturation amplitude of SASI was found to be sensitive to the parameter ϵ.

The local saturation amplitude is minimum at an intermediate radius between the proto-neutron star and the shock (roughly at $r_{\rm mini} \sim (r_{\rm sh}+r_*)/2$). The reason is that just below the shock parasites are efficiently stabilized by advection, while close to the proto-neutron star they are strongly stabilized by the entropy stratification (Fig. 2, left). The most efficient growth of the parasites therefore takes place where neither advection nor stratification is strong. If the amplitude is larger than this quite flat minimum, the parasite can grow in a large region of the flow around the radius $r_{\rm mini}$. This minimum is thus a meaningful estimate of the amplitude at which the saturation by the parasites occurs (whether it be RT or KH).

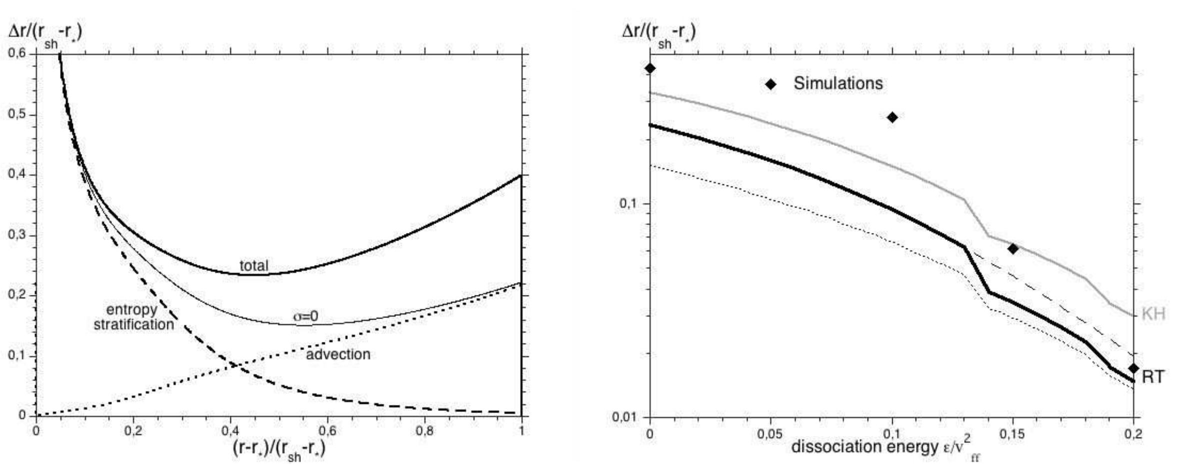

Fig. 2. *Left:* Effect of advection, entropy stratification, and SASI growth rate, on the "local saturation amplitude" of the shock displacement $\Delta r(r)$. This plot describes the saturation of the fundamental mode of SASI by the growth of the RT instability, when $\epsilon = 0$. The "local saturation amplitude" (thick line) is also shown when the growth rate of SASI is neglected (thin line). The dotted and the dashed lines show the contributions of advection and entropy stratification. The results are qualitatively the same if one considers the KH instability, or higher harmonics of SASI, or $\epsilon > 0$. *Right:* As a function of the dissociation energy ϵ, comparison of the saturation amplitude measured in the simulations by Fernández & Thompson (2009) (diamonds) with those deduced from RT (black thick line) and KH (gray thick line) instabilities growing on the most unstable SASI mode. The effect of neglecting the growth rate of SASI (dotted line), or considering only the fundamental mode of SASI (dashed line), is also shown.

The saturation amplitude predicted by our analysis of KH and RT instabilities is compared with the results of the simulations by Fernández & Thompson (2009) in the right panel of Fig. 2. The RT instability appears to grow at smaller SASI amplitudes than KH, and is thus expected to be the dominant parasitic mode. We note that the movies published online by Fernández & Thompson (2009) show mushroom-like structures, consistent with our conclusion that RT is the dominant secondary instability.

The trend of a strong amplitude decrease with increasing dissociation is reproduced by the parasitic instability saturation mechanism. Furthermore our estimate of the saturation amplitude is consistently $15-50\%$ below the simulated value at all ϵ. Given the uncertainties due to our approximate description of the parasites and the many other non linear effects we neglected, and given that we expected to underestimate the saturation amplitude, the agreement is very encouraging.

We can take advantage of the analytic nature of our description to understand the causes of this decrease. The dissociation energy loss at the shock leads to more compression, hence a slower advection speed and a faster propagation of parasitic instabilities against the flow. The saturation amplitude is decreased by a factor 4.5 between $\epsilon = 0$ and $\epsilon = 0.2$, due to the faster growth of RT. A change in the flow profile due in particular to the decrease of the entropy stratification is also responsible for a factor 2 decrease. Two other effects are responsible for a moderate 25% decrease : the decrease of the SASI growth rate, and the fact that the dominant SASI mode becomes dominated by higher harmonics (which are more sensitive to parasites).

5 Conclusion

We have developed the first predictive mechanism for the saturation of SASI, in which a parasitic instability growing on the SASI mode causes the saturation. The two potentially important instabilities, Rayleigh-Taylor and Kelvin-Hemhotz, have been characterized taking into account the effect of entropy stratification and advection. The saturation amplitude of a SASI mode has been estimated by comparing its growth rate with that of the parasitic modes. This estimate reproduces the decrease of the SASI power with dissociation energy observed in the simulations of Fernández & Thompson (2009).

If confirmed, our results would open new perspectives for anticipating the effect on the SASI amplitude of other physical ingredients ignored here such as a realistic equation of state, the neutrino-heating rate, and the rotation and magnetic field of the progenitor star. They could also be useful as an input for analytical models studying the possible consequences of SASI, such as the model for gravitational wave emission proposed by Murphy et al. (2009).

The authors are thankful to S.Fromang for stimulating discussions and his help with the code RAMSES, and R. Fernandez for sharing data from his simulations. This work has been partially funded by the Vortexplosion project ANR-06-JCJC-0119.

References

Blondin, J. M. & Mezzacappa, A. 2007, Nature, 445, 58

Blondin, J. M., Mezzacappa, A., & DeMarino, C. 2003, ApJ, 584, 971

Burrows, A., Livne, E., Dessart, L., Ott, C. D., & Murphy, J. 2006, ApJ, 640, 878

Fernández, R. & Thompson, C. 2009, ApJ, 697, 1827

Foglizzo, T. 2009, ApJ, 694, 820

Foglizzo, T., Galletti, P., Scheck, L., & Janka, H.-T. 2007, ApJ, 654, 1006

Guilet, J., Sato, J., & Foglizzo, T. 2009, submitted to ApJ

Marek, A. & Janka, H.-T. 2009, ApJ, 694, 664

Murphy, J. W. & Burrows, A. 2008, ApJ, 688, 1159

Murphy, J. W., Ott, C. D., & Burrows, A. 2009, ArXiv e-prints

Pessah, M. E. & Goodman, J. 2009, ApJ, 698, L72

Sato, J., Foglizzo, T., & Fromang, S. 2009, ApJ, 694, 833

Scheck, L., Janka, H.-T., Foglizzo, T., & Kifonidis, K. 2008, A&A, 477, 931

Scheck, L., Kifonidis, K., Janka, H.-T., & Müller, E. 2006, A&A, 457, 963

Weinberg, N. N. & Quataert, E. 2008, MNRAS, 387, L64

SF2A 2009
M. Heydari-Malayeri, C. Reylé and R. Samadi (eds)

FIRST POINT SOURCE SEARCHES WITH THE ANTARES NEUTRINO TELESCOPE

Halladjian, G. on behalf of the ANTARES collaboration[1]

Abstract. In the heart of the Mediterranean, at a depth of about 2500 m, the eyes of ANTARES monitor the Universe seeking high energy cosmic neutrinos in order to reveal the secrets of the cosmic rays which their origin remains unknown since the discovery of their existence in the early twentieth century. With its 12 lines, carrying 885 photomultipliers, ANTARES is the largest under water neutrino detector in the world since May 2008. In 2007, ANTARES was taking data with a smaller configuration (5 lines). The analysis of this data for point source will be discussed. The result is a new upper limit on the flux of high energetic cosmic neutrinos in the Southerm Hemisphere.

1 Introduction

To study high energy astrophysical sources such as active galactic nuclei, the gamma-ray bursters, supernovae remnants and microquasars, neutrinos are the ideal messenger. Indeed, they are stable, electrically neutral and they have low cross section of interaction with matter. The importance of neutrino astronomy is to study the origin of cosmic rays and their acceleration mechanism. The detection of high energy neutrinos and the measurement of their flux will constrain the hadronic-leptonic production rate of cosmic rays.

In order to study this sources and to solve these engimas, the ANTARES collaboration has installed a telescope in the Mediterranean sea 40 km off the southern coast of France. The neutrinos are detected, after charged current interactions, through the Cherenkov photons emitted in water by the secondary muons. The muon direction is reconstructed using the positions of touched photomultipliers and the arrival time of Cherenkov light. Above 10 TeV the angular difference between the incoming neutrino and the reconstructed muon is $< 0.3°$, the muon direction will point to the neutrino source.

In this proceeding, the analysis of data with a 5 lines detector (i.e. 375 photomultipliers) for point sources will be presented. These data were taken in 2007 (from February 2nd to December 8th) with effective live-time of 140 days.

2 Data sample used in point source analyses

The main background is the atmospheric muons produced during the interaction of cosmic rays with the atmosphere and the secondary muons produced when the atmospheric neutrinos interact with the matter. In order to reduce this background, several cuts are applied on the data after their optimization with the Monte-Carlo simulation study under the assumption of E^{-2} for the source. Only the up-going muons are considered to reject the very high flux of atmospheric muons. To eliminate the mis-reconstructed atmospheric muons (down-going muons), several quality cuts are used based on the number of hits and the quality of track reconstruction. Thus 94 events are obtained.

[1] Centre de Physique des Particules de Marseille - 163, avenue de Luminy - Case 902 - 13288 Marseille cedex 09
E-mail : halladjian@cppm.in2p3.fr

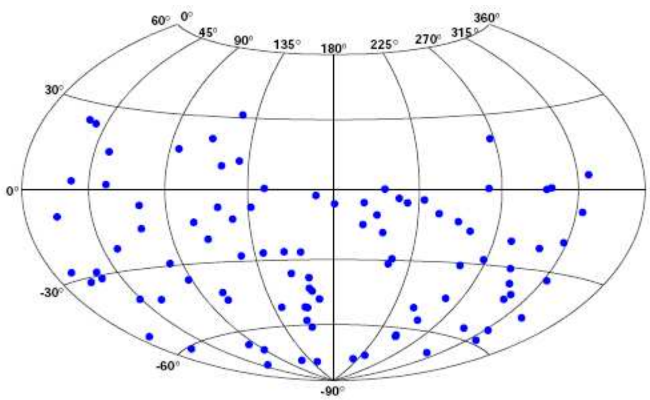

Fig. 1. The selected 94 neutrino candidates presented in equatorial coordinates skymap.

3 Point source search algorithms

For point source search, two statistical methods have been used, unbinned and binned algorithms. The simulations have shown that the sensitivity of the unbinned method, for a given number of signal and background, is 40% better than the binned method because the first one uses the information of the events distribution. This is why the second one is used as a cross-check to the first.

3.1 Unbinned method

The unbinned method, called Expectation-Maximization (EM) algorithm, is an iterative algorithm to maximize the likelihood estimation for finite mixture model problems, in this case mixture of signal and background events. As the name suggests, this method is constituted of two steps (per iteration). The expectation step evaluates the data in order to associate to each event the probability to be signal or background, and the maximization step use the output of E-step to find the set of parameters that maximize the likelihood.

The probability density function (PDF) of the signal is assumed to be a 2-dimensional Gaussian over a non-Gaussian PDF of the background which is a function of declination. This last one can be calculated after the scrambling of the right ascension of the data events.

Once the final set of parameter values is found, a criterion is needed to find the probability of the signal existence. The Bayesian Information Criterion (BIC) was used in this object. Contrary of its name suggestion, it can be used in a purely frequentist manner.

A large number of skymaps are simulated in order to define the BIC distribution for background-only and background+signal models. These distributions are used to calculate the p-value defined as the probability that the background produces a BIC value greater than the data one (BIC_{data}). For a given number of signal events model, if the 90% of the sky map simulations yield a BIC value bigger than BIC_{data}, this model is excluded.

3.2 Binned method

This method is a standard binned method whose goal is to find an excess of events inside a given cone assuming Poissonian statistics. To optimize the radus of the cone, the approach of minimization of the Model Rejection Factor (MRF) is used. This approach produces cone size of 3° to 4.5° (depends on the declination).

4 Results

To evaluate the 94 selected events presented in figure 1, two search strategies have been considered, the candidate source list search and the all-sky search.

For the first one, a list of candidate sources, shown in table 1, are selected in order to decrease the number of degrees of freedom (the right ascension and the declination of the source). No significant event excess was found. The lowest p-value calculated is 0.004 for HESS J1023-575 which corresponds to a 1.6σ post-trial significance.

For the all-sky search strategy, a pre-clustering algorithm selects at least two events separated by less than 5°. Then the p-value of the most significant cluster is given by the EM algorithm. The largest significant excess is found at ($\delta = -63.7°$, $RA = 243.9°$), with $\sigma = 1$. With the binned method, two events are found at this location.

Source name	δ (°)	RA (°)	$n_{\text{bin.}}$	p-value	Φ_{90}
PSR B1259-63	-63.83	195.70	0	-	3.1
RCW 86	-62.48	220.68	0	-	3.3
HESS J1023-575	-57.76	155.83	1	0.004	7.6
CIR X-1	-57.17	230.17	0	-	3.3
HESS J1614-518	-51.82	243.58	1	0.088	5.6
GX 339	-48.79	255.70	0	-	3.8
RX J0852.0-4622	-46.37	133.00	0	-	4.0
RX J1713.7-3946	-39.75	258.25	0	-	4.3
Galactic Centre	-29.01	266.42	1	0.055	6.8
W28	-23.34	270.43	0	-	4.8
LS 5039	-14.83	276.56	0	-	5.0
HESS J1837-069	-6.95	279.41	0	-	5.9
SS 433	4.98	287.96	0	-	7.3
HESS J0632+057	5.81	98.24	0	-	7.4
ESO 139-G12	-59.94	264.41	0	-	3.4
PKS 2005-489	-48.82	302.37	0	-	3.7
Centaurus A	-43.02	201.36	0	-	3.9
PKS 0548-322	-32.27	87.67	0	-	4.3
H 2356-309	-30.63	359.78	0	-	4.2
PKS 2155-304	-30.22	329.72	0	-	4.2
1ES 1101-232	-23.49	165.91	0	-	4.6
1ES 0347-121	-11.99	57.35	0	-	5.0
3C 279	-5.79	194.05	1	0.030	9.2
RGB J0152+017	1.79	28.17	0	-	7.0
IC22 hotspot	11.4	153.40	0	-	9.1

Table 1. Results of the search for cosmic neutrinos correlated with potential neutrino sources. The sources are divided into three groups: galactic (top), extra-galactic (middle) and the hotspot from IceCube with 22 lines (bottom). The source name and location in equatorial coordinates are shown together with the number of events within the optimum cone for the binned search, the p-value of the unbinned method (when different from 1) and the corresponding upper limit at 90% C.L. Φ_{90} is the value of the normalization constant of the differential muon-neutrino flux assuming an E^{-2} spectrum (i.e. $E^2 d\Phi_{\nu_\mu}/dE \leq \Phi_{90} \times 10^{-10}$TeV cm^{-2}s^{-1}). The integration energy range is 10 GeV - 1 PeV.

4.1 Systemtic uncertainties

The p-value is not affected by systematic uncertainties since the PDF of the background is calculated using the data. For the cosmic neutrino flux limits, the main systematic errors are the effective area and the angular resolution. The first one is estimated to be 15% in the energy range of 3 to 400 TeV. The main contribution is coming from the uncertainty of the optical modules efficiency and the absorption length of the light in the water. Above 10 TeV, the intrinsic angular resolution is better than 0.5° resulting from the reconstruction algorithm (0.3° for 12 lines detector). The absolute pointing precision is estimated to be about 0.2°. This one is calculated using the boat GPS position and analyzing the ANTARES acoustic positioning data.

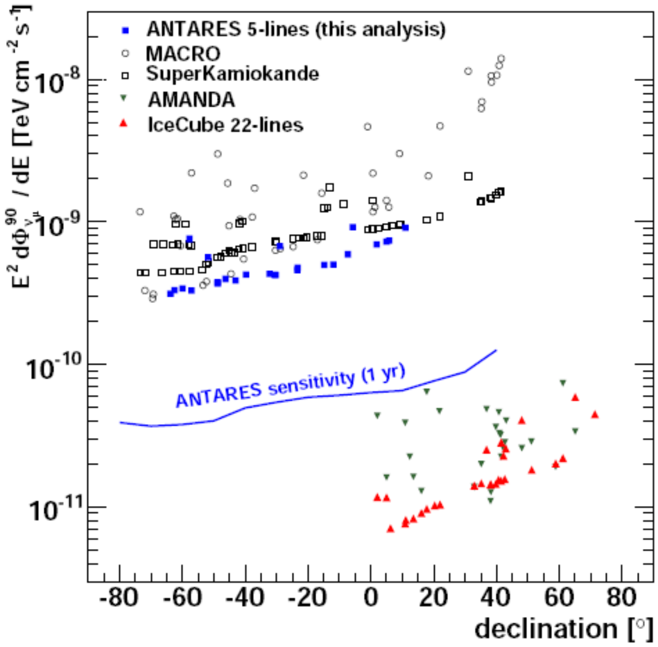

Fig. 2. Neutrino flux upper limits at 90% C.L. obtained by this analysis (solid squares), compared with the results from other experiments (IceCube , AMANDA , SuperKamiokande and MACRO). The sensitivity of ANTARES for one year with twelve lines is also shown (solid line). The source spectrum assumed in these results is E^{-2}, except for MACRO, for which an $E^{-2.1}$ spectrum was used.

5 Conclusion

The ANTARES telescope is complete since May 2008 and takes data. No evidence of neutrino sources has been found in the 5-line data taken in 2007. The analysis for point source (with binned and unbinned methods) provide a maximum excess of 1.6σ post-trial significance. The most restrictive upper limits on the flux of high energetic cosmic neutrinos in the Southerm Hemisphere have been set at the range $E^2 d\Phi_{\nu_\mu}/dE \sim 3 - 10 \times 10^{-10} TeV cm^{-2} s^{-1}$.

I would like to thank the ANTARES collaboration members and the SF2A organisation committee.

References

Dempster A P, Laird N M and Rubin D B, J.R. Statist. Soc. Series B **39** (1977) 1.
Aguilar J A and Hernandez-Rey J J, Astrop. Phys. **29** 2 (2008), 117.
Haughton D M A, Ann. Stat. **16** (1988) 342.
Hill G C and Rawlins K, Astrop. Phys. **19** 3 (2003) 393, astro-ph/0209350.
Abbasi R *et al.*, IceCube collaboration, Astrop. J. Lett. **701** (2009) 47, arXiv:0905.2253.
Abbasi R *et al.*, IceCube collaboration, Phys. Rev. D **79** (2009) 062001, arXiv:0809.1646.
Desai S *et al.*, SuperKamiokande collaboration, Astrop. Phys. **29** (2008) 42.
Thrane E *et al.*, SuperKamiokande collaboration, arXiv:0907.1594v1.
Ambrosio M *et al.*, MACRO collaboration, Astrophys. J. **546** (2001) 1038.

SF2A 2009
M. Heydari-Malayeri, C. Reylé and R. Samadi (eds)

SUMMARY OF THE 2008-2009 PCHE WORKSHOPS ON THE GALACTIC DIFFUSE GAMMA-RAY EMISSION

Lavalle, J.[1], Marcowith, A.[2] and Maurin, D.[3]

Abstract. We report on the two PCHE workshops on the *Galactic diffuse gamma-ray emission* held at LPTA-Montpellier in November 2008 and at LAPTH-Annecy in May 2009.

1 Introduction

The Galactic diffuse gamma-ray emission (DGRE) is a powerful tool to study cosmic ray (CR) physics in the MeV-TeV energy range on the one hand, and the interstellar medium (ISM) on the other hand, since it results from the interaction between both. It could also contain information on exotic physics, *e.g.* traces of dark matter (DM) annihilation, which could, however, only be interpreted so if the standard astrophysical processes are under control. Although the global understanding of the overall standard astrophysical processes at stake was considerably improved those last two decades, large theoretical and observational uncertainties still remain in the characterization of the different ingredients. Because the related expertnesses belong to rather separated scientific communities, it is worth trying to elevate the current understanding by means of an interdisciplinary framework. It is fortunate that French laboratories host experts in all of the relevant domains, and it is likely useful to federate an interdisciplinary network on this topic. This was precisely the aim of the two workshops that we recently organized at LPTA-Montpellier in November 2008, and at LAPTH-Annecy in May 2009, thanks to GDR PCHE fundings. These workshops gathered experts in the ISM, Galaxy dynamics and formation, CR sources and propagation, magneto-hydrodynamics (MHD), experimentalists as well as theorists. This offered a nice pedagogical platform to discuss the state-of-the-art in those different fields, during which students were fully involved, and allowed to settle down some specific issues and potential perspectives in the refinement of the techniques currently used in both theoretical and experimental analyses. Here, we summarize the most discussed points[1].

2 The ISM

A review on the ISM can be found in Ferrière (2001). The ISM constitutes the target "material" for interactions with CRs, which are at the origin of the DGRE. It is featured by a gas component, and a radiation component, the latter including (but not conventionally) the magnetic field. The interstellar gas (ISG) is involved (i) in nuclear interactions with CR nuclei that generate pions whose neutral component decays in gamma-rays of energies above $m_{\pi^0}/2$, and (ii) in electromagnetic interactions, mostly with the CR electrons through Bremsstrahlung processes that can also produce gamma-ray emission in the MeV-GeV energy range. The interstellar radiation field (ISRF) is due to the UV and optical starlight and to the IR dust emission concentrated in the Galactic disk, and seeds the inverse Compton (IC) interactions with CR electrons that also generate gamma rays; there is an additional contribution from the cosmic microwave background (CMB), which acts as an homogeneous target field for IC interactions. As observed from the Earth, the DGRE is the integral over the line of sight

[1] Università di Torino & INFN, Via Giuria 1, 10125 Torino — Italia
[2] LPTA, Université Montpellier II & CNRS-IN2P3, place Eugène Bataillon, 34095 Montpellier Cedex 5 — France
[3] LPNHE, Universités Paris VI - Paris VII & CNRS-IN2P3, 4, place Jussieu, 75005 Paris — France

[1]All presentations are available at the following websites: http://indico.in2p3.fr/conferenceDisplay.py?confId=1259 (password: GDRlpta), and http://indico.in2p3.fr/conferenceDisplay.py?confId=1910.

of all of these processes, and can be considered as a *partial* tracer of the ISM — since degenerate with the distribution of CRs. Therefore, in order to model, predict or understand the DGRE properly, it is important to characterize the ISM as precisely as possible, by describing its components in detail, in particular their density and their spatial distribution. The ISG exhibits different phases, and is mainly composed of hydrogen ($\sim 90\%$) in the form of neutral (HI), ionized (HII) and molecular gas (H_2), of helium ($\sim 10\%$) and of metals (gas or dust). Dust releases IR radiation that can feed the DGRE and affect the transport of CR electrons through IC scattering. The study of the different phases of the ISG unveils natural connections between them and the important role of turbulence to drive its structure evolution or to trigger phase transitions (Falgarone et al. 2007; Hennebelle et al. 2007). Very roughly, the gas distribution tracks the light distribution in the Galaxy, being concentrated in the bulge and the disk, and having its density decreasing rather quickly away from the disk or going towards the radial outskirts beyond the solar circle. A closer look involves spiral arms, which are more difficult to characterize observationally and to model (Pohl et al. 2008). Anyway, an accurate modeling of the ISG is necessary to derive consistent predictions of the DGRE, and is still to be investigated more deeply in the future. Viewed slightly differently, a good knowledge of CR physics could allow to infer interesting information on the interstellar gas from observations of the DGRE (*e.g.* Grenier et al. 2005). As radiative counterparts, the ISRF components mainly include the standard radiation generated by stars and dust, the CMB and the magnetic field. The former ones are responsible for IC processes with CR electrons. Aside from CMB, the ISRF components are spatially connected to the distribution of the ISM. As for the ISM, a good knowledge of the spatial features of the ISRF is important to control the IC processes and thereby the transport of CR electrons. The spatial distribution of the magnetic field is also an essential information regarding CR diffusion and synchrotron processes. It can be constrained from polarization measurements, but also from radio observations, which signs the synchrotron emission of CR electrons. As implicit above, emerges the need of a global picture of the Galaxy, wherein all components evolve in an intricate manner. There are already some promising studies on the way, relying on powerful numerical simulations, addressing *e.g.* the ISM phases (Fromang et al. 2006) or even the gaseous disk formation in the cosmological context (Agertz et al. 2009). CRs, which are described below, would be an additional component to consider within such frameworks. Observations of the DGRE provide a suited mean to test this global picture, complementary to other wavelengths.

3 CR sources and propagation

The understanding of the DGRE also implies that of CRs. CR physics involves the modeling of CR sources as well as CR transport in the ISM. Technically, the purpose is to predict the CR density and spectral features at any point $\vec{x}$ given an injection at any other source point $\vec{x}_s$. The propagation of Galactic CRs is well described phenomenologically since the early 1960's, though further important developments have followed (Ginzburg & Syrovatskii 1964; Berezinkii et al. 1990; Strong et al. 2007). It is mainly characterized by spatial diffusion due to scattering processes on moving magnetic turbulences that make the trajectories erratic, contrary to gamma rays that travel along geodesics. It is formally difficult to connect the spatial diffusion of CRs to the magnetic properties of the ISM because the latter are still not well understood. Instead, spatial diffusion is very often described by an isotropic and rigidity-dependent diffusion coefficient that one can constrain from both theoretical arguments and observational constraints; yet, it is still unclear whether or not diffusion proceeds isotropically (*e.g.* Marcowith et al. 2006). The spatial current of CRs is also characterized by convection that can be connected to galactic winds which drives flows of matter away from the disk in the vertical direction. Other important ingredients arising in the description of CR transport are the energy losses and reacceleration, which characterize diffusion in momentum space. The latter is related to spatial diffusion because also due to interactions with the moving magnetic scatterers. It depends on the diffusion coefficient and on the typical velocity of the scatterers, the Alfèn velocity in the frame of MHD; reacceleration is negligible above a few GV, typically. Energy losses turn out to play a major role for CR electrons, but have impact only on the low energy part of the spectrum for CR nuclei. These losses are due to convection, because of the adiabaticity of this phenomenon, to interactions with the ISG and to interactions with the ISRF (for CR electrons). A good description of the energy losses is therefore intimately related to that of the ISM. Finally, CR nuclei can also experience destructive nuclear interactions with the ISG, called spallation, or decay if instable (*e.g.* radioactive species). The full transport equation can be solved semi-analytically or numerically (for nuclei see *e.g.* Strong & Moskalenko 1998; Maurin et al. 2001; for electrons *e.g.* Moskalenko & Strong 1998; Delahaye et al. 2009) depending on the considered situations and on the assumptions. Except energy losses and spallations which are fixed by the description of the ISM and the interaction cross sections, the other transport parameters are usually constrained from observational data on CR nuclei. The characterization of CR sources remains an important challenge for the future, though significant progress has been achieved in the last two decades. Indeed, whereas it has been well established for a long time that Galactic sources are connected with supernova explosions, many uncertainties makes it difficult to feature these sources in details. Not only are the sources important as injecting CRs in the ISM, but also as contributing directly to the DGRE whenever unresolved. Basic principles of CR acceleration from shock waves in sources are understood (Malkov & O'C Drury 2001; Ellison et al. 2007), but being highly non-linear, this topic is still subject to intense research: the precise features of the CRs injected in the ISM are still lacking, from their relative composition and absolute density (*e.g.* electrons versus protons) to their spectral shape (*e.g.* acceleration efficiency, time evolution). It is obviously a complicated task since the source environment is likely to play an important role. Fortunately, considerable improvements in the observational devices, especially in X-ray and gamma-ray telescopes, have allowed very detailed multiwavelength analyses in the last decade, and to extract better constraints on source modeling. Nevertheless, there is still a crucial need of theoretical efforts in this domain. Again, numerical simulations can play an important role there, and some efforts are already made in that way (Ferrand et al. 2008). As said above, a global picture up to the Galactic scale would be very interesting because CR sources are expected to play an important role in the evolution of the ISM itself. This would permit many consistency tests, such as the spatial distribution of sources, its potential correlation with molecular clouds or other ISM phases, etc. Connected to this latter point, the study of interactions of CRs with molecular clouds at the vicinity of active sources offers an alternative way to survey both transport and acceleration processes (Gabici et al. 2009).

4 Experiments

The experimental landscape associated with the DGRE has undergone important improvements in the last decade, and is one of the main pillar for future theoretical developments. We have already emphasized the importance of multiwalength observations to better understand the ISM, the CR sources and propagation. Here we deliberately bias our review towards experiments in which French groups are involved. Since its launch in June 2008, the most efficient telescope to date to measure the gamma-ray sky in the energy range 10 MeV - 200 GeV, the LAT instrument onboard the Fermi satellite (Atwood et al. 2009), has already allowed the data analysis of the DGRE from a mid-latitude region (Abdo et al. 2009b). Aside from the obvious breakthrough that Fermi is about to offer thanks to the huge number of sources it will observe compared to its ancestor EGRET, Fermi is also able to measure the local CR electron flux with unprecedented statistics (Abdo et al. 2009a), and might even provide some information on CR nuclei (Lavalley & Piron 2008). Nevertheless, it will take years before a very detailed sky map is available, and many efforts in terms of gathering complementary information from other wavelengths, or in terms of theoretical model developments may be done in the meantime. At lower energy, the INTEGRAL satellite, which was devised to observe in the range $\sim$ 15 keV - 10 MeV, *i.e.* down to the hard X-rays, has already been used to feature the corresponding Galactic diffuse emission. The separation of the diffuse emission from point-sources was part of the challenges achieved from noteworthy upturns in the data analysis techniques (Bouchet et al. 2008). Among the broad information released from INTEGRAL data, the intense diffuse emission in gamma-ray around 511 keV detected in the Galactic bulge, involving the annihilation of electron-positron pairs at rest, is still unsolved, and is a nice example of the connection of the diffuse emission with CR propagation (Weidenspointner et al. 2008). At MeV energies and low latitudes, the DGRE is likely dominated by IC scattered photons, but predictions still hardly reach the measured intensities, though in better agreement with the latest INTEGRAL data than before, likely due to a better subtraction of point-sources. As regards the CR source studies, it is useful to recall that the INTEGRAL catalog is now rich of more than 400 objects (Krivonos et al. 2007). The data taking is programed until 2012. At ground, improvements in the detection and analysis techniques have made Cerenkov telescopes reach very good sensitivities and angular resolutions, allowing detailed studies of CR sources (Horns 2008). Among these experiments, HESS has been performing a survey of the Galactic plane for few years, leading to the detection of many (some extended, some even new) sources (Aharonian et al. 2005). In particular, this permitted to scrutinize astrophysical sites of CR interactions with molecular clouds (Aharonian et al. 2008b). HESS was also used recently to measure the CR electron flux on Earth (Aharonian et al. 2008a), unveiling a spectral cut-off around a few TeV. This demonstrates the potential of Cerenkov astronomy to deliver crucial information either for the understanding of CR sources, for the study of CR interactions with the ISM, and for that of very high energy CR electrons.

The analysis of the DGRE is still challenging because of the high level of systematic errors to control, but future developments in the analysis techniques as well as of Cerenkov arrays themselves, like the CTA project, will hopefully lead to interesting steps forwards in this domain (de Naurois & Rolland 2009). Coming now to CRs themselves, key measurements that provide powerful constraints on transport, whatever the model, are those of nuclei, more precisely of the ratio of secondaries to primaries. In particular sub-carbon to carbon, or sub-iron to iron ratios, are rather good tracers of the diffusion process, while radioactive species provide complementary information on different spatial scales. Most of experiments taking data on CR nuclei are balloon-borne experiments, like the CREAM experiment. The CREAM project corresponds to a series of flights using an apparatus designed to measure and identify CR nuclei with Z =1-26 and for energies in the range 1-1000 GeV/n. The data release of the Dec. 2008 flight is expected by the end of 2009, which will help reducing the experimental error bars compared to previous flights (Ahn et al. 2008). The measures can also be performed in space. The PAMELA satellite can measure the B/C ratio, but was more designed to observe light CR particles. Interestingly, since PAMELA data on the positron fraction were published (Adriani et al. 2009), it has become clear that the electron and positron component of CRs is still far from being understood accurately. Those CR electrons precisely provide an important contribution to the sub-GeV DGRE, and it could even help better understanding diffusion itself from its synchrotron emission at intermediate latitudes, as observed in radio — for instance, a lot can be learnt from the PLANCK satellite, which observes in the $\sim$ 10-850 GHz frequency band, in particular on the synchrotron Galactic foreground. While Fermi is also relevant in the observation of CR electrons, major improvements are expected with the installation of AMS02 onboard the ISS, foreseen in 2010. AMS02 offers a much better sensitivity compared to PAMELA, and was also designed to collect and identify CR nuclei up to $Z = 26$ in space with much better precision and statistics (Battiston 2007).

5 Conclusion

These workshops made emerge among the participants the will to maintain and even increase the efforts towards not only sharing knowledges between the different communities interested in the information DGRE may deliver, but also starting some new collaborations. We wish that this will be the case in the future, and that this dynamics will be fruitful. We thank all the participants and local organizers in Montpellier and Annecy, for the nice spirit they conveyed to the scientific (and other) discussions. Last but not least, we are indebted to the PCHE scientific committee for having supported our project.

References

Abdo, A. A., Ackermann, M., Ajello, M., et al. 2009a, Physical Review Letters, 102, 181101

Abdo, A. A., Ackermann, M., Ajello, M., et al. 2009b, Astrophys. J., 703, 1249

Adriani, O., Barbarino, G. C., Bazilevskaya, G. A., et al. 2009, Nature, 458, 607

Agertz, O., Teyssier, R., & Moore, B. 2009, MNRAS, 397, L64

Aharonian, F., Akhperjanian, A. G., Aye, K., et al. 2005, Science, 307, 1938

Aharonian, F., Akhperjanian, A. G., Barres de Almeida, U., et al. 2008a, Physical Review Letters, 101, 261104

Aharonian, F., Akhperjanian, A. G., Barres de Almeida, U., et al. 2008b, Astron. Astrophys., 483, 509

Ahn, H. S., Allison, P. S., Bagliesi, M. G., et al. 2008, Astroparticle Physics, 30, 133

Atwood, W. B., Abdo, A. A., Ackermann, M., et al. 2009, Astrophys. J., 697, 1071

Battiston, R. & The AMS-02 Collaboration. 2007, Nuclear Physics B Proceedings Supplements, 166, 19

Berezinskii, V. S., Bulanov, S. V., Dogiel, V. A. & Ptuskin, V. S. 1990, Astrophysics of cosmic rays (Amsterdam: North-Holland, 1990)

Bouchet, L., Jourdain, E., Roques, J., et al. 2008, Astrophys. J., 679, 1315

de Naurois, M. & Rolland, L. 2009, arXiv:0907.2610

Delahaye, T., Donato, F., Fornengo, N., et al. 2009, Astron. Astrophys., 501, 821

Ellison, D. C., Patnaude, D. J., Slane, P., Blasi, P., & Gabici, S. 2007, Astrophys. J., 661, 879

Falgarone, E., Levrier, F., & Hily-Blant, P. 2007, in EAS Publications Series, Vol. 23, EAS Publications Series, ed. M.-A. Miville-Deschênes & F. Boulanger, 73–86

Ferrand, G., Downes, T., & Marcowith, A. 2008, MNRAS, 383, 41

Ferrière, K. M. 2001, Reviews of Modern Physics, 73, 1031

Fromang, S., Hennebelle, P., & Teyssier, R. 2006, Astron. Astrophys., 457, 371
Gabici, S., Aharonian, F. A., & Casanova, S. 2009, MNRAS, 396, 1629
Ginzburg, V. L. & Syrovatskii, S. I. 1964, The Origin of Cosmic Rays (New York: Macmillan, 1964)
Grenier, I. A., Casandjian, J., & Terrier, R. 2005, Science, 307, 1292
Hennebelle, P., Audit, E., & Miville-Deschênes, M. 2007, Astron. Astrophys., 465, 445
Horns, D. 2008, arXiv:0808.3744
Krivonos, R., Revnivtsev, M., Lutovinov, A., et al. 2007, Astron. Astrophys., 475, 775
Lavalley, C. & Piron, F. 2008, in International Cosmic Ray Conference, Vol. 3, 1531–1534
Malkov, M. A. & O'C Drury, L. 2001, Reports on Progress in Physics, 64, 429
Marcowith, A., Lemoine, M., & Pelletier, G. 2006, Astron. Astrophys., 453, 193
Maurin, D., Donato, F., Taillet, R., & Salati, P. 2001, Astrophys. J., 555, 585
Moskalenko, I. V. & Strong, A. W. 1998, Astrophys. J., 493, 694
Pohl, M., Englmaier, P., & Bissantz, N. 2008, Astrophys. J., 677, 283
Strong, A. W. & Moskalenko, I. V. 1998, Astrophys. J., 509, 212
Strong, A. W., Moskalenko, I. V., & Ptuskin, V. S. 2007, Annual Review of Nuclear and Particle Science, 57, 285
Weidenspointner, G., Skinner, G. K., Jean, P., et al. 2008, New Astronomy Review, 52, 454

SF2A 2009
M. Heydari-Malayeri, C. Reylé and R. Samadi (eds)

SEARCH FOR MAGNETIC MONOPOLES WITH THE ANTARES DETECTOR

Picot Clémente, N.[1] and Escoffier, S.[1]

Abstract. The ANTARES neutrino telescope is fully operational since May 2008. Located at a depth of 2500 m in the Mediterranean Sea, 40 km off the Provencal coast, it comprises a large three-dimensional array of 885 Optical Modules deployed on 12 vertical lines. The telescope is aimed to observe high energy cosmic neutrinos through the detection of the Cherenkov light produced by up-going induced muons. Besides the detection of high energy neutrinos, the ANTARES telescope offers an opportunity to improve sensitivity to exotic cosmological relics, like magnetic monopoles. Monopoles are hypothetical particles initially predicted by Dirac in 1931, and reintroduced some decades later in a large class of Grand Unified Theories. Relativistic magnetic monopoles can emit a large amount of Cherenkov light when passing through matter, with intensity 8500 times higher than that radiated from a muon. Dedicated trigger algorithms and search strategies have been developed to search for such bright objects with the ANTARES detector. The data filtering, background rejection and final selection criteria will be described, as well as the expected sensitivity of ANTARES to exotic physics.

1 Introduction

The ANTARES neutrino telescope is aimed to observe high energy cosmic neutrinos through the detection of the Cherenkov light produced by up-going induced muons. However, the ANTARES detector is also sensitive to a variety of exotic particles, and can provide an unique facility for the search of magnetic monopoles.

2 The ANTARES detector

The ANTARES detector has reached its nominal size in May 2008. The 885 Optical Modules (OM) are deployed on twelve vertical lines in the Western Mediterranean, at depths between 2050 and 2400 meters. The OMs, consisting of a glass sphere housing a 10" Hamamatsu photomultiplier (PMT) (Aguilar J.A. et al. 2005), are arranged by triplet per storey. Each detector line, made of 25 storeys, is connected via interlinks to a Junction Box, itself connected to the shore station at La Seyne-sur-Mer through a 40 km long electro-optical cable. The strategy of the ANTARES data acquisition is based on the "all-data-to-shore" concept (Aguilar J.A. et al. 2007). This implementation leads to the transmission of all raw data above a given threshold to shore, where different triggers are applied for storage.

For the analysis presented here, only the two most generic triggers are described. Both are based on local coincidences. A local coincidence (L1 hit) is defined either as a combination of two hits on two OMs of the same storey within 20 ns, or as a single hit with a large amplitude, typically 3 pe. The first trigger, a so-called directional trigger, requires five local coincidences anywhere in the detector but causally connected, within a time window of 2.2 μs. The second trigger, a so-called cluster trigger, requires two T3-clusters within 2.2 μs, where a T3-cluster is a combination of two L1 hits in adjacent or next-to-adjacent storeys. When an event is triggered, all PMT pulses are recorded over 2.2 μs.

The ANTARES observatory was built gradually, giving rise to various detector layouts used for physics analysis. The 5-line, 10-line and 12-line detector configurations match with data taken from January 2007, from December 2007 and from May 2008, respectively.

[1] CNRS / Centre de Physique des Particules de Marseille, Marseille, France

3 Introduction to magnetic monopoles

Most of the Grand Unified Theories (GUTs) predict the creation of magnetic monopoles in the early Universe. Indeed, in 1974, 't Hooft (t'Hooft G. 1974) and Polyakov (Polyakov A.M. 1974) showed independently that elements caracterising well a magnetic charge, as introduced by Dirac in 1931 (Dirac P.A.M. 1931), occur as solutions in unified gauge theories, in which $U(1)_{E.M.}$ is embedded in a spontaneously semi-simple gauge group. These particules are topologically stable and carry a magnetic charge defined as a multiple integer of the Dirac charge $g_D = \frac{\hbar c}{2e}$, where e is the elementary electric charge, c the speed of light in vacuum and $\hbar$ the Planck constant. Depending on the group, the masses inferred for magnetic monopoles can take range over many order of magnitudes, from 10^8 to 10^{17} GeV.
As magnetic monopoles are stable, and so would survive until now, they should have been very diluted in the Universe, as predicted by numerous theoritical studies which set stringent limit on their fluxes, like the Parker limit flux. More stringent limits were set recently by different experiments as MACRO (Giacomelli G. & Margiotta A. 2007), and AMANDA (The Icecube Coll. 2007).
The development of the neutrino astronomy in the last decade led to the construction of huge detectors, which allow new hopes in the search for magnetic monopoles. Actually, the ANTARES detector seems to be well designed to detect magnetic monopoles, or at least to improve limits on their fluxes, as described below.

4 Signal and background simulations

Since fast monopoles have a large interaction with matter, they can loose large amounts of energy in the terrestrial environment. The total energy loss of a relativistic monopole with one Dirac charge is of the order of 10^{11} GeV (Derkaoui J. et al. 1998) after having crossed the full diameter of the Earth. Because magnetic monopoles are expected to be accelerated in galactic coherent magnetic field domain to energies of about 10^{15} GeV (Wick S.D. et al. 2003), some could be able to cross the Earth and reach the ANTARES detector as upgoing signals.
The monopole's magnetic charge $g = ng_D$ can be expressed as an equivalent electric charge $g = 68.5ne$, where n is an integer. Thus relativistic monopoles with $\beta \geq 0.74$ carrying one dirac charge will emit a large amount of direct Cherenkov light when traveling through the ANTARES detector, giving rise to ~ 8500 more intense light than a muon. The number of photons per unit length (cm^{-1}) emitted on the path of a monopole is shown in figure 1, as a function of the velocity of the monopole up to $\gamma = 10$ ($\beta = 0.995$).

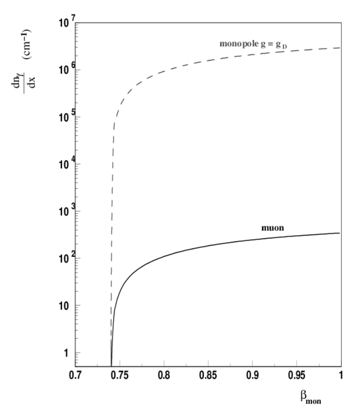

Fig. 1. Number of emitted photons per unit length (cm^{-1}) by a magnetic monopole with a charge $g = g_D$ through direct Cherenkov emission (dashed line) compared to the number of photons emitted by a muon (black line), as a function of their velocities.

For the analysis, monopoles have been simulated inside an optimised volume containing the 12-line detector, for six ranges of velocities between $\beta = 0.74$ and $\beta = 0.995$. In addition, downgoing atmospheric muons have been simulated using the CORSIKA package (Heck D. et al 1998), as well as upgoing and downgoing atmospheric neutrinos according to the Bartol flux (Agrawal V. et al. 1996; Barr G. et al. 1989). Optical background from ^{40}K decay has been added to both magnetic monopole signal and atmospheric background events.

5 Search strategy

The 12-line detector data are triggered by both trigger logics, the directional and the cluster triggers (see section II). A comparison of efficiency was therefore performed on magnetic monopoles and restricted only to upward-going events. As the efficiency of the directional trigger was found to be lower than the cluster trigger, it was decided to perform searches for upgoing magnetic monopoles with the cluster trigger only.
The standard reconstruction algorithm, developped in ANTARES for upward-going neutrino selection, and mainly based on a likelihood maximisation, was applied. In order to select upgoing particules, only reconstructed events with a zenith angle lower than 90° were kept. However, muon bundles are difficult to reconstruct properly and some of them can be reconstructed as upward-going events.
As it is shown in figure 2, a magnetic monopole traversing the detector will emit an impressive quantity of light, compared to atmospheric muons or muons induced by atmospheric neutrinos. The large amount of induced hits

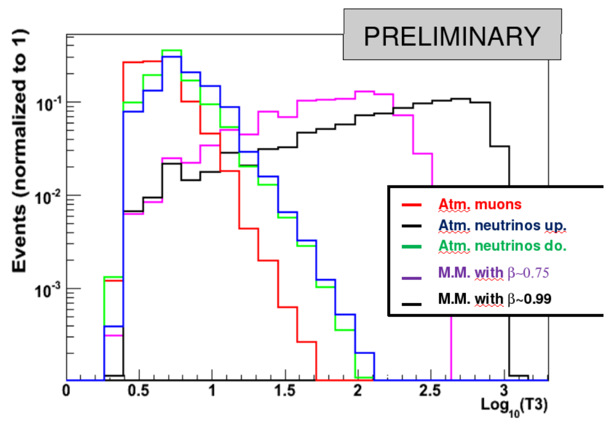

Fig. 2. Normalized events as a function of the number of T3 clusters for downgoing atmospheric muons, upgoing and downgoing atmospheric neutrinos, and upgoing magnetic monopoles with $\beta \sim 0.75$ and $\beta \sim 0.99$.

in the detector, more precisely the number of T3 clusters, is therefore used as a criteria to remove a part of the atmospheric background.
Before to apply supplementary cut to reduce the remaining background, 10 active days of golden[1] data were taken as reference to check the data MonteCarlo agreement. The comparison of T3 distributions between the data and the background simulation for 10 days is shown in figure 3.

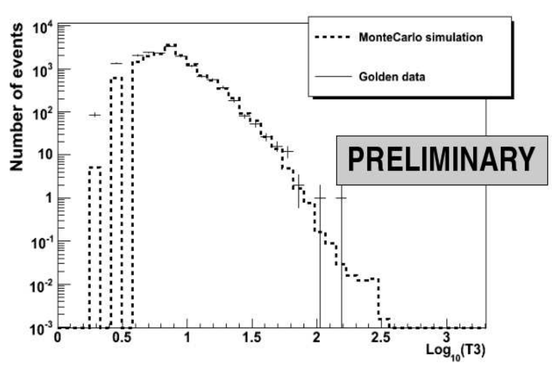

Fig. 3. Comparison of T3 distributions between data and MonteCarlo simulations for 10 days of data taking.

We optimised the cuts on the number of T3 clusters to maximise the 90% C.L. sensitivity, calculated with the

[1]Golden data assumes experimental data complying with certain selection criteria like low baserate and burstfraction.

usual Feldman-Cousins formula (Felman G.J. & Cousins R.D. 1998), for magnetic monopoles after one year of data taking. In the optimisation process the same selection criteria have been applied to calculate the sensitivity to magnetic monopole events over the whole velocity range $0.74 \leq \beta \leq 0.995$.
Finally the 90% C.L. sensitivity for this range was found, for a cut of at least 140 T3 clusters, for which around 1.9 background events are expected. The 90% C.L. sensitivity for ANTARES after one year of data taking is shown in figure 4.

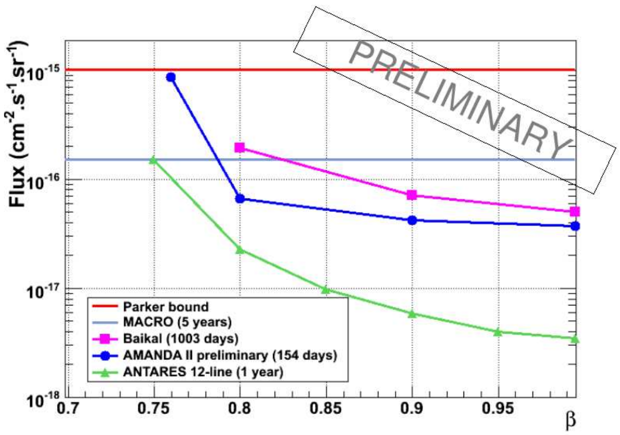

Fig. 4. Preliminary expected sensitivity with 90% C.L. with the 12-line ANTARES detector after one year of data taking, compared to upper limits set by other experiments.

6 Conclusion

The emergence of neutrino astronomy in the last decade gives new opportunities for the search of exotic particles. In this paper was presented the search strategy employed for upgoing relativistic magnetic monopoles with the ANTARES detector in the 12-line configuration. As shown, the signal emitted by a relativistic magnetic monopole in sea water would be easily isolated from the background light coming mainly from atmospheric muons, and neutrinos. This study leads to a sensitivity on magnetic monopoles of the order of $\sim 1.10^{-17} cm^{-2} s^{-1} sr^{-1}$ with 90% C.L. after one year of data taking, competitive with upper limits set by the other experiments over the whole velocity range $0.74 \leq \beta \leq 0.995$.

References

Agrawal, V., & Gaisser, T.K., & Lipari, P., & Stanev, T., 1996, Phys. Rev. D 53, 1314.

Aguilar, J. A. et al. (ANTARES Collaboration), Nuclear Instruments and Methods in Physics Research A 555 (2005) 132-141.

Aguilar, J. A. et al. (ANTARES Collaboration), 2007, Nuclear Instruments and Methods in Physics Research A 570, 107-116.

Barr, G., & Gaisser, T.K., & Stanev, T., 1989, Phys. Rev. D 39, 3532.

Derkaoui, J. et al., 1998, Astroparticle Physics 9, 173.

Dirac, P.A.M., 1931, Proc. R. Soc. A 133, 60.

Feldman, G.J., & Cousins, R.D., 1998, Physical Review D 57, 3873.

Giacomelli, G., & Margiotta A., 2007, arXiv:0707.1691v1 [hep-ex].

Heck, D. et al., 1998, Report FZKA 6019, Forschungszentrum Karlsruhe.

t'Hooft, G., 1974, Nucl. Phys. B 79, 276.

Parker, E.N., 1970, Ap. J. 160, 383.

Polyakov, A.M., 1974, Sov. Phys. JETP Lett. 20, 194.

The Icecube Coll., 2007, arXiv:0711.0353v1 [astro-ph].

Wick, S.D. et al., 2003, Astropart. Phys. 18, 663.

INVESTIGATION OF THE MECHANISM OF SASI IN CORE COLLAPSE SUPERNOVAE USING SIMPLE TOY MODEL SIMULATIONS

Sato, J.[1], Foglizzo, T.[1] and Fromang, S.[1]

Abstract. We perform numerical simulations of a toy model proposed by Foglizzo (2009) to explain the mechanism of the standing accretion shock instability (SASI), and confirm the results of the linear analysis. Three types of simulations have been performed, measuring (i) the acoustic feedback resulting from the advection of entropy/vorticity in a region of deceleration, (ii) the advected wave generated at a shock perturbed by an acoustic wave, and (iii) the growth rate and oscillation frequency of the dominant advective-acoustic cycle in the linear regime. The results of the simulations agree with the linear analysis within 5% when the mesh size is 1% of the distance between the shock and the deceleration region, with a numerical error dominated by the numerical treatment of the shock. This simple toy model can be used as a benchmark test for numerical codes dealing with SASI simulations.

1 Introduction

The standing accretion shock instability (SASI) takes place in the collapsing core of a massive star, when the shock stalls $\sim$ 150 km above the nascent neutron star (Blondin et al. 2003). This $l = 1$ instability may be responsible for the asymmetric character of core-collapse supernova explosions (e.g. Marek & Janka 2009). The physical mechanism of SASI advocated by Foglizzo et al. (2007), Scheck et al. (2008) is an advective-acoustic cycle (AAC). A simple toy model has been proposed by Foglizzo (2009) (hereafter F09) in order to improve our understanding of the AAC. The purpose of this study is to check the results of the perturbative analysis of F09 through numerical experiments, thus providing concrete examples of the coupling processes involved.

2 Setup of the simulations

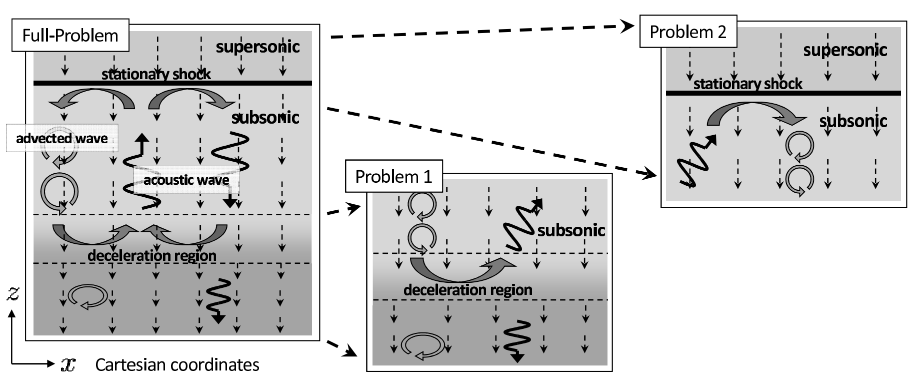

Fig. 1. Schematic view of the toy model of the advective-acoustic cycle, separated into two sub-problems. Advected perturbations are noted as circular arrows, while acoustic waves are noted as wavy arrows.

[1] CEA, Irfu, SAp, Centre de Saclay, F-91191 Gif-sur-Yvette, France and UMR AIM, CEA-CNRS-Univ. Paris VII, Centre de Saclay, F-91191 Gif-sur-Yvette, France

The AAC is due to the interaction of the accretion shock and a deceleration region. The toy model of F09 is studied through three types of simulations in the linear regime, illustrated by Fig. 1. In "Problem 1" , we measure the acoustic feedback δp produced by an entropy/vorticity wave δS advected from the upper boundary to the deceleration region (Fig. 2a). In "Problem 2", we measure the advected entropy/vorticity wave δS generated at the shock by an acoustic wave δp propagating against the flow from the lower boundary (Fig. 2b). The "Full-Problem" involves both the shock and the deceleration region. This flow is linearly unstable. We measure both the growth rate ω_i and the oscillation frequency ω_r of the most unstable mode (Fig. 2c). The details of the simulations are described in Sato et al. (2009).

3 Results

In Fig. 2a and 2b, Problems 1 and 2 are solved for different frequencies ω_0 and mesh sizes (Δx, Δz). The good agreement between the simulations (symbols) and the linear analysis (solid line) confirms the validity of both the linear analysis and the numerical simulation. The convergence to the analytical formula in Problem 2, however, is much slower than in Problem 1 (Sato et al. 2009). The growth rate and oscillation frequency in the Full-Problem are displayed in Fig. 2c for different mesh sizes Δz. An accuracy of 5% is reached for a mesh size of 1% of the distance $r_{\rm sh} - r_\nabla$ between the shock and the deceleration region.

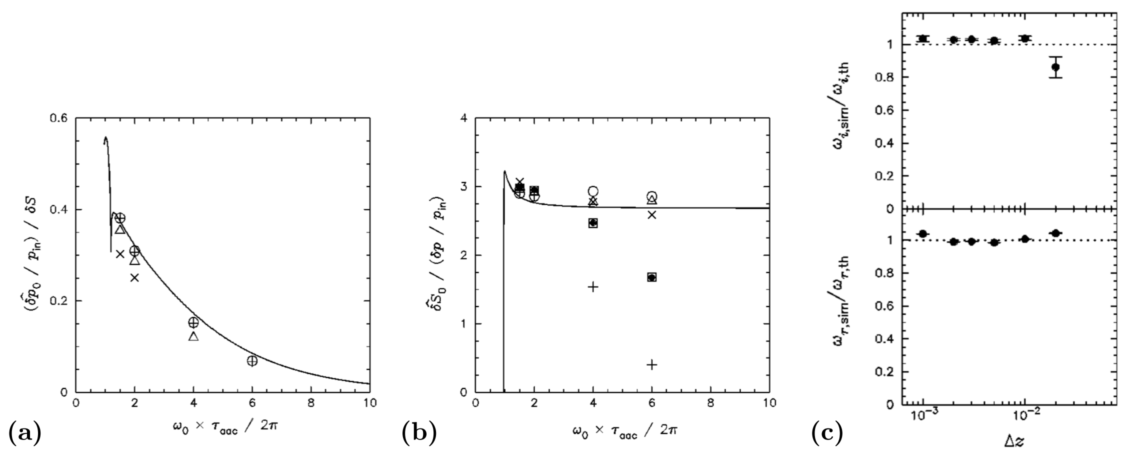

Fig. 2. (a): Efficiency of the production of acoustic waves by the deceleration of advected waves as a function of frequency in Problem 1, deduced from the numerical simulations (symbols) and compared to the perturbative analysis of F09 (solid line). $\tau_{\rm aac}$ is a normalization timescale associated with the AAC in 1D (F09). The different square mesh sizes, measured in units of $r_{\rm sh} - r_\nabla$, are $\Delta x = \Delta z = 5 \times 10^{-2}$ (crosses), 2×10^{-2} (triangles) and 10^{-2} (circles). The results for $\Delta x = 2 \times 10^{-2}$, $\Delta z = 10^{-2}$ are also shown (pluses). **(b)**: Dependence of the entropy production on the frequency in Problem 2. The different mesh sizes are $\Delta z = 2 \times 10^{-2}$ (pluses), 10^{-2} (squares), 5×10^{-3} (crosses), 2×10^{-3} (triangles) and 10^{-3} (circles), with $\Delta x = 2 \times 10^{-2}$, and $\Delta x = \Delta z = 1 \times 10^{-2}$ (filled points). **(c)**: Growth rate $\omega_{i,\rm sim}$ and oscillation frequency $\omega_{r,\rm sim}$ of the most unstable mode ($n_x = 1$) measured in numerical simulations of the Full-Problem, compared to the values $\omega_{i,\rm th}$ and $\omega_{r,\rm th}$ obtained from F09 (dotted line).

This work has been partially funded by the Vortexplosion project ANR-06-JCJC-0119.

References

Blondin, J. M. Mezzacappa, A. and DeMarino, C., 2003, ApJ, 584, 971

Foglizzo, T., Galletti, P., Scheck, L., and Janka, H.-T., 2007, ApJ, 654, 1006

Foglizzo, T., 2009, ApJ, 694, 820 (F09)

Marek, A., and Janka, H.-T. 2009, ApJ, 694, 664

Sato, J., & Foglizzo, T., Fromang, S., 2009, ApJ, 694, 833

Scheck, L., Janka, H.-T., Foglizzo, T., and Kifonidis, K. 2008, A&A, 477, 931

SF2A 2009
M. Heydari-Malayeri, C. Reylé and R. Samadi (eds)

SEARCHES FOR GRAVITATIONAL WAVES BURSTS IN THE FIRST JOINT RUN OF LIGO, GEO600 AND VIRGO

Was, M.[1] and the LIGO Scientific Collaboration and the Virgo Collaboration

Abstract. Gravitational wave burst analysis targets short (< 1 sec), generic or poorly modeled gravitational wave events. Such events could be caused by a wide range of sources like core-collapse of massive stars, neutron star excitations, black-hole mergers or gamma-ray bursts. We present the status of the searches for gravitational wave bursts in the first joint data from the global network of LIGO, GEO600 and Virgo interferometers, and the prospects for the upcoming data taking run.

1 Introduction

A worldwide network of interferometric gravitational wave (GW) detectors is now in operation. These are designed to observe gravitational radiation in a frequency band between a few dozen Hz up to a few kHz from astrophysical sources such as the coalescence of binary systems, core-collapse supernovae, rotating neutron stars as well as a stochastic background. The first Virgo science run (VSR1) took place from May 18^{th} up to October 1^{st} 2007 in coincidence with the end of the fifth LIGO science run (S5) (from November 2005 up to October 2007) (Robinet 2009).

2 Gravitational wave burst source

We consider here gravitational wave sources which may produce transient GW radiation with relativity short duration (< 1 s) or so called "burst". There are a few possible progenitors of such waveforms:

- Black hole (BH) – black hole, or black hole – neutron star (NS) mergers. Such events produce only a few cycles (number depending on mass of the system) in the detector sensitive band, and only in the BH-BH case does numerical relativity give good waveforms of the event. These mergers are the main model to explain the central engine for short gamma-ray bursts (GRBs) (Meszaros 2006), but no such binary has been observed yet. The merger rate is quite uncertain, it is expected to be $10 - 2000$ (including all types of mergers) per year with advanced GW detectors.

- Supernovae. Emission of GW radiation is expected during an asymmetric collapse of the star. The mode through which most of the GWs are radiated is quite uncertain. It could happen during the rebound of the iron core, or at a later stage when the proto neutron star is excited by the infalling matter. There are several instabilities scenarios that could drive this excitation (Ott 2009). Asymmetric supernovae are the main explanation for the origin of long GRB (Meszaros 2006).

- Neutron star oscillations. Relaxation in the crust of the neutron star can produce star-quakes, that results in a non spherically symmetric oscillations, which radiate GWs. This is the main model for Soft Gamma-ray repeaters (SGRs) and NS glitch observations.

- Cosmic string cusps and kinks. are more exotic sources, but are looked for as well (Abbott 2009a).

[1] LAL, Univ Paris-Sud, CNRS/IN2P3, Orsay, France.

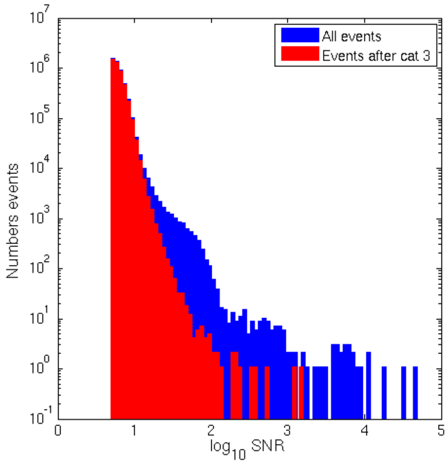

Fig. 1. Effect of data quality on Virgo triggers during VSR1. Histogram of the number of triggers as a function of decimal log of trigger SNR before (in blue) and after (in red) data quality cleaning.

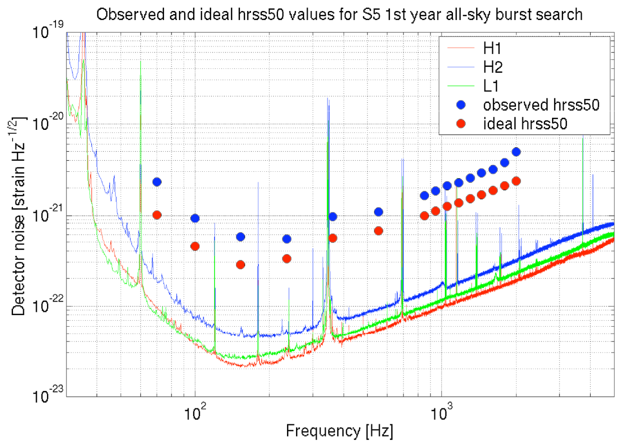

Fig. 2. Plotted are the noise floors of the three LIGO detectors, with overlaid the expected from gaussian noise (in red) and actual 50% sensitivity to GW (in blue).

3 GW bursts search methods

Given that most of the expected GW waveforms are poorly modeled, the search techniques have to be sensitive to a wide variety of waveforms, moreover they need to be robust against detector glitches that are unfortunately present in the data.

The detection algorithms are constructed in three main steps:

1. We make a decomposition of the data onto a time frequency map (using a wavelet transformation for instance), and look for excess power with regard to gaussian noise.

2. We use the information from the environmental channels to discriminate GW events from glitches in the detector.

3. We combine the data from the network of operational GW detectors.

The third step can be done in two different ways. Either after the first two steps, in a coincident analysis; or beforehand by making coherent combination of detector streams and then applying to them step 1 and 2.

The use of a network of detectors is a very powerful tool in GW data analysis. It is used for background estimation and to reduce the background event rate. It also allows a better time and sky coverage, because detectors do not have a 100% duty cycle nor a uniform antenna response. In the case where at least three detectors are operational, one can also reconstruct the source sky position through triangulation methods.

GW detectors have a large contribution of non gaussian noises. Some of those glitches are understood as environmental disturbances or instrumental noises. For others, no obvious explanation is found, and we rely on statistical correlations between auxiliary channels and GW triggers. In both cases triggers happening during noisy times are flagged and removed from the list of potential GW candidates. The result of this data cleaning for Virgo triggers during VSR1 can be seen in Fig. 1. It shows that a large number of glitches has been removed through this process.

Nonetheless a sizable amount of glitches pass these data quality tests and induce a time and frequency dependency of the trigger rate. This forces the detection cuts to be dependent on the frequency of the event. The sensitivities derived from the data are a factor between 2 and 3 (depending on the frequency) worse than what we would expect from a pure gaussian noise as shown on Fig. 2.

4 All sky untriggered search

The baseline search performed on S5/VSR1 data is an all sky untriggered search (Abbott 2009b,2009e). It looks for any kind of burst signal present in the data, using the method described above. In order to tune the search,

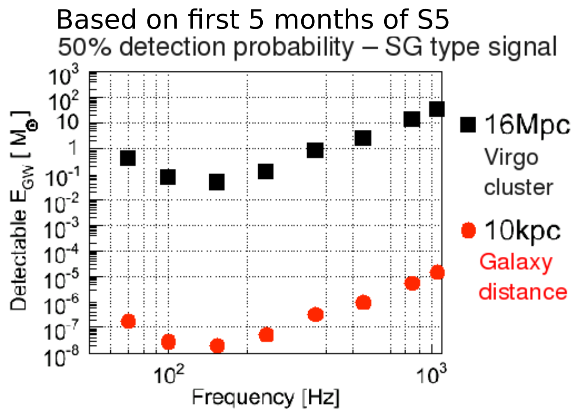

Fig. 3. Sensitivity to isotropically emitted GW energy as a function of signal frequency for two different source distances: 10 kpc and 16 Mpc.

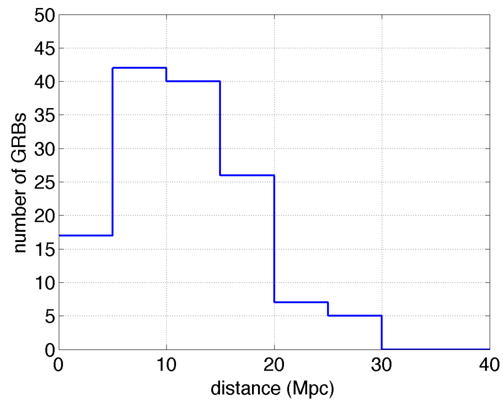

Fig. 4. Distribution of reachable distance for GRBs during S5/VSR1 in Mpc, assuming a standard candle of $0.01\,\mathrm{M_\odot c^2}$ emitted in GWs at 100 Hz.

the network background is estimated using time shifted data of the different detectors; while the detection efficiency is measured by repeatedly injecting simulated signals into the data and measuring the efficiency of retrieving these injections. Then the cuts are tuned to maximize the efficiency over a wide range of waveforms while keeping the background false alarm rate at 0.1 event per year.

The sensitivity estimate (50 % CL) are summarized in Fig. 3. The frequency dependence of these limits is due to the frequency dependence of the gaussian noise floor, and at the most sensitive point (around 150 Hz) the limit is $2 \times 10^{-8}\,\mathrm{M_\odot c^2}$ at 10 kpc, which scales with distance to $0.05\,\mathrm{M_\odot c^2}$ at 16 Mpc (distance to the Virgo cluster).

If we assume some model of emission we can convert this energy sensitivities into detection horizon for a given emission model. For supernovae using the models described in (Ott 2006) for $11\,\mathrm{M_\odot}$ the detection horizon is ~ 0.4 kpc and for $25\,\mathrm{M_\odot}$ it is ~ 16 kpc. This means that depending on the exact supernovae progenitor we can observe a small part or all of the Galaxy. For BH mergers assuming that roughly 3 % of the total mass is radiated into GWs (Pretorius 2009) for two $10\,\mathrm{M_\odot}$ black holes the reach is ~ 3 Mpc and for two $50\,\mathrm{M_\odot}$ it is ~ 100 Mpc, which means that the Virgo cluster is within reach for the merger of heavier black holes.

5 Interaction with electromagnetic observations

GW are not only searched by themselves but also in association of other astrophysical events. There are two ways of interacting with other astrophysical observations: triggering refined GW searches on astrophysical triggers or pointing GW candidates to astronomers for electromagnetic followup. The first way has become a mainstream analysis in the GW community, but the second possibility is currently in active development and should be operational in the near future.

5.1 External triggers

Using external triggers, that is astronomical observation of potential GW sources, provides two important pieces of information: a sky position and a time. The knowledge of the sky position reduces the coincidence time window between detectors, it also greatly simplify coherent analysis. The knowledge of the trigger time reduce the length of data to be analyzed, and thus lower the background level. The overall effect is that the sensitivity to GW is improved by a factor ~ 2. The triggers used so far are those related to GRBs using the GCN alerts, and major SGR outbursts.

In the GRB case, a search for GW counterparts of both long and short GRBs has been performed. During the last data run (S5/VSR1) 212 GRBs have been observed, for 70% of them at least two detectors where operational. The main result of this search is that the reachable distance for observing GW from a GRB is $D \sim 15\,\mathrm{Mpc}\sqrt{E_{\mathrm{GW}}^{\mathrm{iso}}/0.01\,\mathrm{M_\odot c^2}}$ as shown on Fig. 4. This result assumes that most of the GW radiation energy

$E_{\rm GW}^{\rm iso}$ is emitted isotropically and at a frequency around 100 Hz.

The expected number of GRBs within this horizon depends strongly on the population of GRBs that is considered. For long GRBs the expected rate is 10^{-6} evts/yr. Whereas for the under-luminous long GRBs, a subsample of the long GRB, the expected rate is 10^{-3} evts/yr (Abbott 2009c).

Among those GRBs, GRB 070201 has been singled out by a fast track analysis. It is a short GRB whose localization error box overlap the M31 galaxy, which is only 770 kpc away, thus being potentially a very nearby event. Due to its short nature, both an unmodeled and a specific binary coalescence search have been performed. At the time of this GRB only the two Hanford detectors were operational, and the null result exclude the hypothesis of a compact binary merger in M31 with a confidence greater than 99%. However this null result remains compatible with the possibility of an SGR in M31 or a compact merger in a galaxy behind M31 (Abbott 2008).

In the SGR case, the 2006 storm of SGR 1900+14 has been analyzed. The null result constrain the GW emission to $E_{\rm GW} < 10^4 E_{\rm EM}$, assuming an emission at 100 Hz. This limit although high, starts to constrain some theoretical models described in (Abbott 2009d).

5.2 Electromagnetic followup

Exploring GW candidates for further astronomical followup is a crucial issue for GW detection. An electromagnetic afterglow gives an independent confirmation that a real astrophysical event happened, and it also allows a further localization and study of the source of GWs.

Tools to perform these followups are being currently finalized. They require an online analysis at three sites, because interferometers are not pointing instruments and localization with a few degrees precision is obtained through triangulation.

These triggers are expected to be produced with a latency of dozens of minutes and send out to telescopes within a network of collaborators. The collaboration is in contact with robotic optical telescopes with large FOV (several square degrees), that are designed to find optical transients like ROTSE (Kanner 2008); and has also been awarded target of opportunity observation time on the Swift satellite.

6 Conclusions & Prospects

We have presented results from the all sky and externally triggered searches for unmodeled bursts in S5/VSR1 data, the upper limits derived start to be astrophysically relevant. During the next science run S6/VSR2 these analysis will be continued and we will also perform a rapid GW analysis leading to optical followup of candidates. Other multimessenger observations are in discussion with neutrino detectors and radio telescopes.

References

Abbott, B., et al. 2008, Implications for the Origin of GRB 070201 from LIGO. Observations *ApJ*, 681:1419

Abbott, B., et al. 2009, First LIGO search for gravitational wave bursts from cosmic (super)strings. *accepted in Phys. Rev. D*, arXiv/0904.4718

Abbott, B., et al. 2009, Search for gravitational-wave bursts in the first year of the fifth LIGO science run. *submitted to Phys. Rev. D*, arXiv/0905.0020

Abbott, B., et al. 2009, Search for gravitational-wave bursts associated with gamma-ray bursts using data from LIGO Science Run 5 and Virgo Science Run 1. *submitted to Phys. Rev. D*, arXiv/0908.3824

Abbott, B., et al. 2009, Stacked Search for Gravitational Waves from the 2006 SGR 1900+14 Storm. *ApJ*, 701:L68

Abbott, B., et al. 2009, *in preparation.*

Kanner, J., et al. 2008, LOOC UP: locating and observing optical counterparts to gravitational wave bursts. *Class. Quantum Grav.*, 25(18):184034

Meszaros, P. 2006, Gamma-ray bursts. *Rept Prog. Phys.*, 69:2259

Ott, C. D. 2006, A new mechanism for gravitational-wave emission in core-collapse supernovae. *Phys. Rev. Lett.*, 96(20):201102

Ott, C. D. 2009, Probing the core-collapse supernova mechanism with gravitational waves. arxiv/0905.2797

Pretorius, F. 2009, *Physics of Relativistic Objects in Compact Binaries: from Birth to Coalescence*, volume 359 of *Astrophysics and Space Science Library*, chapter Binary Black Hole Coalescence. arxiv/0710.1338

Robinet, F. 2009, *in this volume*

PCMI

Interstellar Medium

SF2A 2009
M. Heydari-Malayeri, C. Reylé and R. Samadi (eds)

ORTHO/PARA SPIN CONVERSION OF D_2 ON A POROUS WATER ICE SURFACE AT 10K IN THE PRESENCE OF O_2 TRACES

Chehrouri, M.[1,2], Dulieu, F.[1], Chaabouni, H.[1], Mokrane, H.[1], Matar, E.[1], Lekic, A.[3], Michault, X.[3], Fillion, J.H.[3] and Lemaire, J.L.[1]

1 Introduction

Molecular hydrogen is the most abundant molecule in the universe. It is at the center of several fundamental questions in astrophysics, and in particular the physics and chemistry of the interstellar medium (ISM). As an example, the relative proportions of ortho- and para-populations of H_2 (Fig. 1 left) are valuable data for establishing the nature of interstellar shocks (Kristensen et al 2007) and may contain information on the history of the grains and the emitting molecular clouds.

We present results on the nuclear spin conversion of D_2 adsorbed on a porous water ice surface at 10 K. Such a surface mimics ice covered interstellar grains as they are assumed to exist in cold dark clouds, H_2O being the main constituent of the ice.

2 Experimental

Experiments have been performed with the FORMOLISM (FORmation of MOLecules in the ISM, Fig. 1 right) setup available at the LAMAp/LERMA laboratory and partly described in Lemaire et al (2007). Main experimental conditions (ultra high vacuum $\sim 10^{-10}$ mbar and very low temperature ~ 8 K) are close to those encountered in some regions of the ISM. Using laser multi-photon ionization (REMPI) and time of flight (TOF) mass spectrometry, it is possible to achieve TPD experiments (Thermally Programmed Desorption) with rovibrational quantum states resolution. REMPI (2+1) ionization is obtained using a laser combination (doubled Nd:YAG + Dye Laser) tuned around 201 nm. As demonstrated previously (Amiaud et al 2008) the E,F (v'=0,J) - X (v " =0,J) transitions can be selected to detect separately the molecules in the ortho state (J=0) or in the para state (J=1). Our results derive from relative population measurements of the molecules during desorption from the cold surface after different latency periods.

3 Preliminary results

According to the Boltzmann statistics, at LTE at 10K, 33% of the molecules are in the para state and 66% in the ortho one (Fig. 1 center). Our results show that a very small amount of molecular oxygen deposited on the ice surface induces a conversion from the para to the ortho state. The conversion times have been measured at several O_2 and D_2 coverage. They are found to exceed few hours in the non oxygen-doped limit, on the contrary to previous study (Hixon et al 992).

4 Discussion

These results can be easily interpreted considering the mobility of the D_2 molecules on the surface at 10K. The conversion is due to the paramagnetic property of the O_2 molecules but, as already demonstrated for D_2

[1] LERMA/LAMAp, UMR 8112 du CNRS, de l'Observatoire de Paris et de l'Université de Cergy-Pontoise, France
[2] L.D.P.C. Université de Saïda, BP138 Enasr, Saïda 20002, Algérie
[3] UPMC Université Paris 06, CNRS, UMR 7092, LPMAA, F-75005, Paris, France

(Motizuki 1957) (and Motizuki & Nagamiya 1956, for H_2), the conversion only occurs if D_2 goes across an O_2 interaction sphere of 3.8 Å in diameter. At 10K O_2 molecules are frozen on the surface or in the pores, the only possibility for D_2 molecules to encounter an O_2 molecule is then residing in their mobility.

5 Conclusions

The general trend of these experimental results can be understood considering the mobility of D_2 molecules on the surface at 10 K together with the catalytic role of paramagnetic O_2, which is well known from cryogenics matrices studies. Such an experimental diagnostic is, at our knowledge, used here for the first time to measure nuclear spin conversion occurring on a surface at very low temperatures. These conditions are particularly relevant to the interstellar medium.

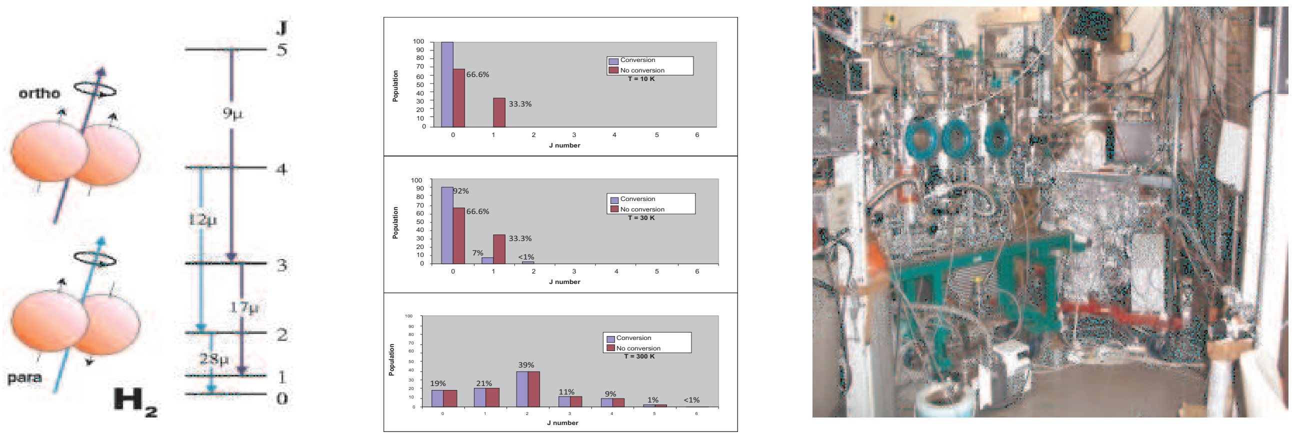

Fig. 1. Left: Ortho and Para states of H_2. Center: Ortho and Para populations ratios of D_2 at 10, 30 and 300K, at LTE. Right: FORMOLISM setup

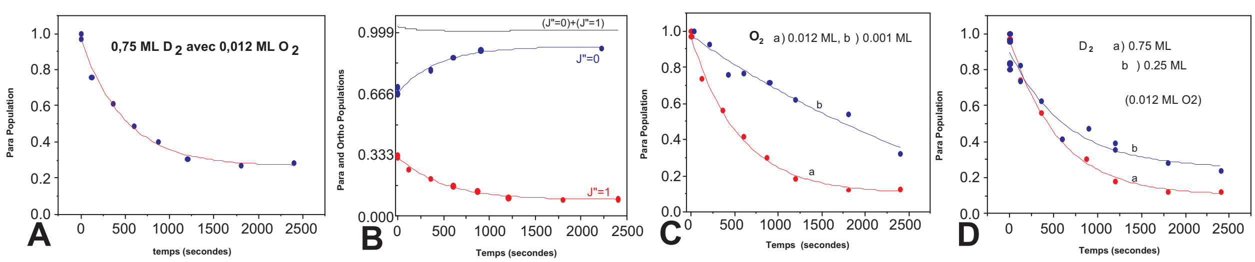

Fig. 2. A: Para population versus delay time after D_2 deposition. B: Para and Ortho populations vs. delay time. C: Para population for different O_2 depositions vs. delay time. D: Para population for different D_2 depositions vs. delay time

References

Amiaud L., Momeni A., Dulieu F., Fillion J.-H., Matar E. and Lemaire J.L., PRL 100, 056101 (2008).

Hixson H.G., Wojcik M.J., Devlin M.S. and Buch V., J.Chem.Phys. 1992, 97, 753

Kristensen L.E., Ravkilde T. L., Field D., Lemaire J. L., Pineau Des Forêts G., A&A,.2007,.469, 561

Lemaire J.L., Fillion J.H., Dulieu F., Momeni A., Amiaud L., Matar E., Chaabouni H., Congiu E. and Pirronello V.. 2007, http://www.u-cergy.fr/Mol_Spa_Lab/php/index_presentation_articles.php

Motizuki K. JPS Japan, 1957, 12, 153

Motizuki K. & Nagamiya T.. JPS Japan. 1956, 11, 93

SF2A 2009
M. Heydari-Malayeri, C. Reylé and R. Samadi (eds)

NEW CO ABSORPTION SPECTROSCOPY DATA WITH THE VUV-FTS ON THE DESIRS BEAM LINE AT SOLEIL

Eidelsberg, M.[1], Lemaire, J.L.[1,2], Federman, S.R.[3], Sheffer, Y.[3], Fillion, J.H.[4] and Rostas, F.[1]

1 Introduction

One of the processes controlling the interstellar CO abundance and the ratio of its isotopologues is photodissociation. Accurate modeling requires basic quantitative spectroscopic data for CO and its isopotologues at wavelengths below the dissociation limit, mainly oscillator strengths and predissociation rates. Absorption spectra of $^{12}C^{16}0$ and its isotopologues $^{13}C^{16}0$ and $^{13}C^{18}0$ have been obtained using the VUV FTS installed on the DESIRS beam line at SOLEIL (de Oliveira et al 2007). Spectra have been recorded between 90-100 nm with a resolution R=350000 (∼12 times better than those obtained in the same wavelength range with the 6.6 m VUV spectrometer on the SU5 beam line at SUPER-ACO in Orsay).

2 Calibration

The four W bands (v=0, v=0-3) at 97.2, 95.6, 94.1 and 92.5 nm resp. for which oscillator strengths have been previously measured at SUPER-ACO (Eidelsberg et al 2004a) for CO and its isotopologues, have been used as calibration bands in order to obtain an accurate determination of the column density (shown here in Fig. 1, the W(0-0) band recorded both at SuperAco and SOLEIL).

3 Experimental

The energy range on the DESIRS beam line at SOLEIL is selected by choosing the appropriate intensity for the undulator installed on the synchrotron e- beam. The CO gas flowing through a 10 cm capillary tube inserted on the light beam path is differentially pumped. The CO absorption spectra are analyzed by a VUV-FT spectrograph. Several pressures are used in order to accurately determine the CO column density and to detect both the lowest absorption features as well as the strongest ones without saturation.

4 Preliminary results

The synthetic spectra have been obtained by using energy levels and mixing coefficients deduced from the interacting coefficients given by Eidelsberg & al (2004) and an approximative value of the line width measured for a rotationally resolved R, P or Q line for each band. The final gamma values are then calculated separately for R,P and Q lines by fitting of the whole band. The predissociation rates are then calculated. Results are presented in Fig. 2.

$^{12}C^{16}0$: a cluster of 6 overlapping bands involving the 4 high Rydberg states 4pσ, 4pπ(v=2), 5pσ, 5pπ(v=0) and $2^1\Pi$ states of mixed Rydberg valence character, assigned by Eidelsberg et al. (2004b) have been successfully disentangled by taking into account energy levels and interaction coefficients given in the reference. Oscillator strengths and line widths are extracted for each band from the recorded spectra by least square fitting of the

[1] LERMA, UMR 8112, Observatoire de Paris-Meudon, France
[2] LERMA/LAMAp, UMR 8112, Université de Cergy-Pontoise, France
[3] University of Toledo, USA
[4] LPMAA, Université UMPC, Paris VI, France

experimental profiles with synthetic spectra. In addition a narrow continuum is observed under the 5pπ(0) band.

^{13}C^{16}0 & ^{13}C^{18}0: the 4p$\sigma^1\Sigma^(+)$(2) band which is Franck-Condon forbidden is not observed or very weak and only a few lines of the perturber II$^1\Pi$(v') appear. With the exception of the very diffuse I$^1\Pi$(v') band towards the long wavelengths, the rotational lines of the 3 strongest bands: 4p$\pi^1\Pi$(2), 5p$\pi^1\Pi$(0) and 5p$\sigma^1\Sigma^+$(0) have smaller predissociation widths than the corresponding bands in ^{12}C^{16}0 and the widths can be measured directly on the spectrum for many lines.

5 Perspectives

A similar work is in progress for new bands recorded in the 91.3-91.7 nm range.

We acknowledge SOLEIL for provision of synchrotron radiation facilities and we would like to thank N. de Oliveira, D. Joyeux and L. Nahon for assistance in using the beamline DESIRS

References

de Oliveira N., Joyeux D., Phalippou D., Rodier J.C., Nahon L., Polack F. & Vervloet M. 2007, AIPC, 879, 447

Eidelsberg et al, 1991 A&AS, 90, 231

Eidelsberg, M., Lemaire, J. L., Fillion, J. H., Rostas, F., Federman, S. R. & Sheffer Y., ., 2004a, A&A, 424, 355

Eidelsberg M., Launay F., Ito K., Matsu T., Hinnen P.C., Rheinhold E., Ubachs W. & Huber K.P., J. Chem. Phys., 2004b, 121, 29

Stark et al, 1991, ApJ, 369,574.

Ubachs et al, 1994, ApJL, 427, 5

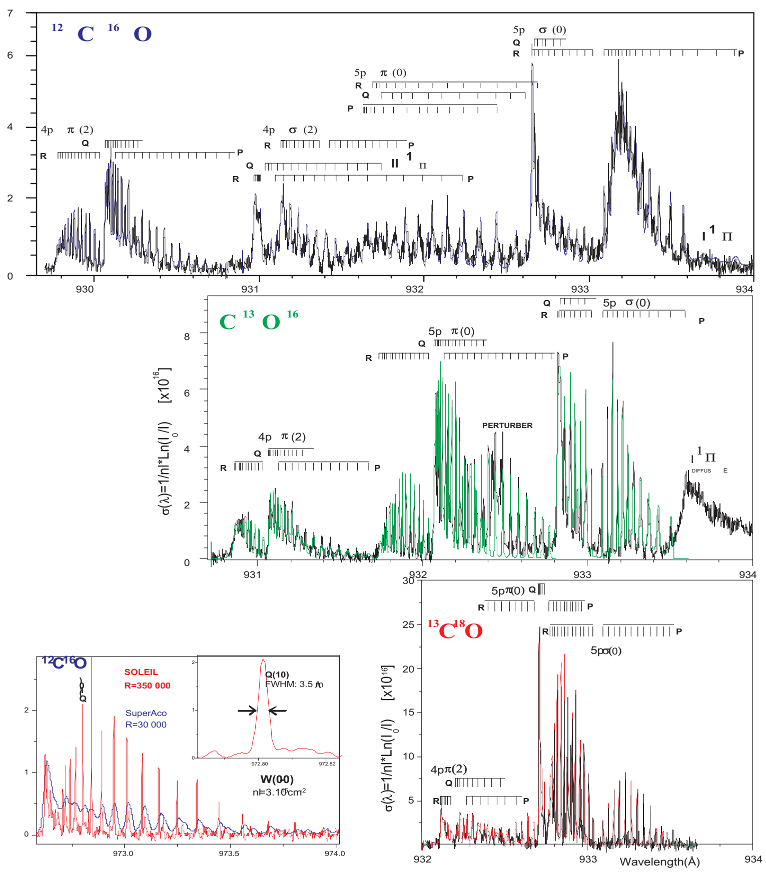

Fig. 1. Right, top to bottom: $^{12}C^{16}0$, $^{13}C^{16}0$ & $^{13}C^{18}0$ spectra (same wavelength scale). Left bottom: Calibration line

	f-values*10^3									Predissociation rates k*10^11 s^-1 k=k0+kR,P*X and X=J*(J+1)			
	$^{12}C^{16}O$				$^{13}C^{16}O$			$^{13}C^{18}O$		$^{12}C^{16}O$		$^{13}C^{16}O$	$^{13}C^{18}O$
Band		Present	E91	S91	?(	Present	E91	?(	Present	Present	U94	Present	Present
4pξ(2)	*930.03*	**7.61(0.47)**	6.3	7.3(0.7)	*931.03*	**7.43**	6.17	*932.17*	**9.98**	kR,P=0.86(0.02) +0.65(0.02)*X kQ=0.86(0.015) +0.65(0.002)*X	-	kR,P=0.76+0.03*X kQ=0.70+0.019*X	kR,P=0.87+0.043*X kQ=1.08+0.0005*X
ξ	*930.99*	**4.96(0.31)**				not observed			not observed	2.2	-	-	-
4pS(2)	*931.36*	**3.03(0.21)**		21.6(2.2)		not observed			not observed	2.2	<3.0	-	-
ξ(0)	*931.64*	**8.65(0.54)** **continuum: 5.5(1.0)**	43.9		*932.04*	**14.47**	33.69	*932.68*	**19.04**	2.2	2.7(0.4)	kR,P=0.95+0.011*X kQ=0.84+0.011*X	kR,P=0.43+0.001*X kQ=0.43+0.01*X
ξ(0)	*933.02*	**15.27(0.95)**		8.40 P branch	*933.03*	**17.13**		*933.04*	**16.33**	kR,P=0.86(0.015) +0.65(0.002) X up to J=7	kR,P=0.34(0.20) +0.65(0.15) X	kR,P=0.76+0.04*X up to J=7	kR,P=0.1 up to J=7
ξ	*933.18*	**5.89(0.56)**		16.5(1.6)	*933.59*	**10.20**	9.98	*935.48*	**5.15**	2.2 to 10.8		Diffuse	Diffuse
ξ		**50.91**	50.2	53.8(5.4)		**49.18**	49.84		**50.50**				

Fig. 2. Oscillator strengths and predissociation rates for the bands appearing in the 92.9-93.5 nm range in $^{12}C^{16}0$, $^{13}C^{16}0$ & $^{13}C^{18}0$. **E91**=Eidelsberg et al (1991). **S91**=Stark et al (1991). **U94**=Ubachs et al (1994).

SF2A 2009
M. Heydari-Malayeri, C. Reylé and R. Samadi (eds)

HYDROGENATED AMORPHOUS CARBONS PHOTOLUMINESCENCE AND ASTROPHYSICAL IMPLICATIONS FOR THE EXTENDED RED EMISSION

Godard, M.[1] and Dartois, E.[1]

Abstract. Hydrogenated amorphous carbons (a-C:H) have proved to be excellent analogs of interstellar dust through IR vibrational absorption bands (3.4 μm, 6.8 μm and 7.2 μm bands (respectively 2960 cm^{-1}, 1460 cm^{-1} and 1380 cm^{-1})) widely observed in galaxies diffuse interstellar medium (ISM). a-C:H are candidates for one of the observed interstellar dust features : a large emission band in the red part of the visible spectrum, attributed to photoluminescence (PL) of interstellar dust, and called the extended red emission (ERE). The PL absolute quantum yield is one of the strongest constraints set by such ERE observations. The PL relative quantum yield is known and measured for many a-C:H at discrete excitation wavelengths. The few absolute efficiencies determined are scattered and sometimes vary by orders of magnitude for supposedly identical a-C:H. We thus produce astrophysical a-C:H and analyze their PL and IR behavior, carefully accounting for thin film optical effects. By properly determining the excitation wavelength dependent PL absolute quantum yields for a wide variety of astrophysically relevant a-C:H, we can constrain these interstellar dust analogs as possible ERE candidates.

1 Introduction

The spaces between stars in galaxies are not empty but are filled with gas and dust which form the interstellar medium (ISM). The ISM permanently interacts with stars from their birth to their death. To understand this dynamical and chemical evolution, it is necessary to identify the ISM components. One of the goals of the interstellar medium research is to attribute the observed spectral features to carriers since most of accessible information about ISM results of its interaction with light. One of the ISM spectral features is the extended red emission (ERE): this is a large (FWHM between 60 and 120 nm) featureless emission band in the red part of the spectrum (between 540 and 950 nm) observed in many interstellar environments, first observed in the Red Rectangle nebulae by Cohen et al. (1975). An example of ERE spectrum, observed in the Red Rectangle nebulae (Schmidt et al. 1980) is represented on figure 3 (left). This spectral feature is probably due to interstellar photoluminescence (PL) initiated by absorption of UV-visible photons, but the identification of the ERE carriers remains an important issue. Many candidates have been proposed over the past decades.

Amorphous hydrogenated carbons (a-C:H or HAC) are one of the ERE carrier candidates. They are organic material of astrophysical interest since they have proved to be analogs of one of the significant interstellar dust components (Sandford et al. 1991; Pendleton & Allamandola 2002; Spoon et al. 2004; Dartois et al. 2005) through IR absorption bands (C-H stretching at 3.4 μm and C-H bending at 6.85 and 7.25 μm) ubiquitously observed in the diffuse interstellar medium of our Galaxy but also of other galaxies.

Amorphous hydrogenated carbons photoluminesce in the visible spectral range. It is thus important to characterize the photoluminescence behavior of this interstellar component that will contribute to the interstellar dust emission and compare the a-C:H PL to the ERE observed properties. In particular, the PL efficiency, which is for the ERE carrier candidates one of the strongest constraints set by the observations, has to be accurately investigated for a-C:H materials : until now, most of the works provided results in terms of relative efficiencies (e.g. Rusli et al. 1996). The results dedicated to astrophysical analogs about absolute a-C:H PL efficiencies (Furton & Witt 1993; Furton et al. 1999) vary by one order of magnitude, although the material is supposed to be similar and are determined with a simple optical description of what happens to the absorbed or emitted light in the sample. It is important to carefully study PL absolute efficiency of amorphous hydrogenated carbons, taking care to account for optical effects occurring in the sample bulk and at the thin film interfaces.

[1] Institut d'Astrophysique Spatiale (IAS), Université Paris-Sud, bâtiment 121, 91405 Orsay cedex, France
marie.godard@ias.u-psud.fr

2 Experimental Methods

We produced interstellar a-C:H analogs, using a plasma-enhanced chemical vapour deposition system with different hydrocarbons precursor gas, as films of few micrometers deposited on a substrate. We record ex-situ their IR and UV-visible transmission spectra allowing us to characterize them and to determine the parameters necessary to a complete description of their PL (optical band gap, absorption coefficient, film thickness).

The photoluminescence of the a-C:H films is recorded between 250 nm and 800 nm with a luminescence spectrometer, while the samples monochromatic excitation scan is selected in the UV-visible wavelengths greater than 250 nm. The intrinsic (internal) photoluminescence quantum yield, defined as the ratio of emitted to absorbed photons numbers, is calculated from the measured external PL by taking into account several effects due to the absorption and the interfaces of the a-C:H film. We developed an optical model based on previous work (Lukosz 1981; Holm et al. 1982; Nollau et al. 2000) that considers the thin film as an absorbing layer located between two different media and viewing the luminescent centers as electric dipole sources. Such an approach is required to determine the a-C:H intrinsic and absolute PL yield. This model includes the effective absorbed excitation quantity, the a-C:H film self-absorption of the PL emitted, the wide-angle and multiple reflections interference effects, the detection solid angle and the transmittance at the film-air interface, ... The PL efficiency determined is the intrinsic absolute PL quantum yield of the a-C:H material. It is important to obtain the intrinsic efficiency and not the external efficiency since the geometry of our samples is different from the interstellar grains one.

3 Results and Discussion

We produced and analyzed many different a-C:H samples covering an optical gap range E_{04} varying typically between 3.0 and 4.2 eV depending on the plasma production conditions. These few micrometers, transparent to yellow orange films are photoluminescent in the visible when illuminated by UV photons (when seen under a UV lamp, the a-C:H PL appears luminescent with a color varying from yellow to red). The wavelength of the photoluminescence maximum varies from about 460 nm to 650 nm as the optical gap energy decreases (see Fig. 1). As observed for the extended red emission (Darbon et al. 1999), the photoluminescence band FWHM is correlated to the variation of the band position : the band width increases with the band central wavelength for both ERE and a-C:H PL (see Fig. 2). However, the ERE width varies from 60 to 120 nm while the a-C:H PL we measured exhibits band widths between 130 and 340 nm, i.e about twice wider than for the ERE observations.

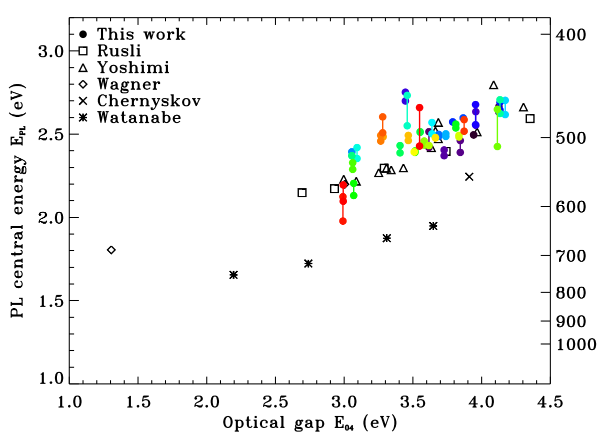

Fig. 1. Variation of the a-C:H photoluminescence color with the optical gap E_{04}. Other results are also plotted (Rusli et al. 1996; Yoshimi et al. 1992; Wagner et al. 1986; Chernyshov et al. 1991; Watanabe et al. 1982).

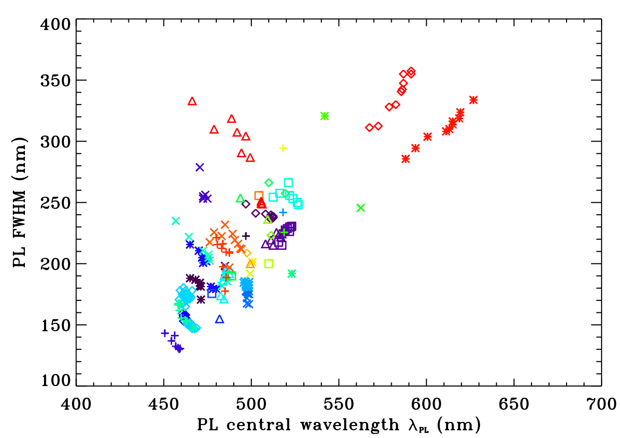

Fig. 2. Correlation of the FWHM with the central wavelength for the a-C:H photoluminescence bands. Different a-C:H samples produced are represented with di?erent symbols and colors.

To better correspond to the ERE spectra, the produced a-C:H should explore slightly lower optical band gaps than those we produce and have lower band width, in order to better overlap with the observational range. The figure 3 shows a comparison between a spectrum of the a-C:H PL and an ERE observation.

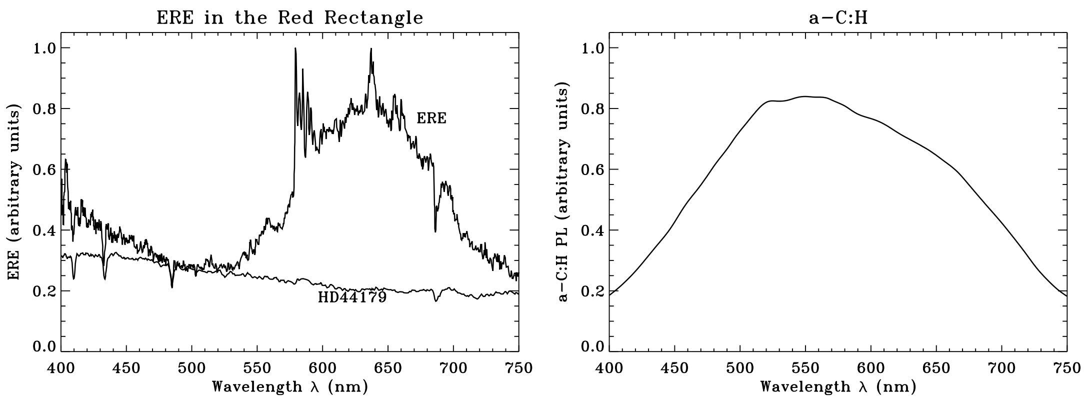

Fig. 3. *Left* : ERE spectrum observed in the Red Rectangle nebulae (and a reference spectrum of the Red Rectangle central star HD 44179) (Schmidt et al. 1980). *Right* : typical a-C:H photoluminescence spectrum.

We studied the influence of the excitation wavelength that gives rise to the photoluminescence : by varying this excitation between 250 and 490 nm, no strong modification of the photoluminescence band (position and width) has been observed and the PL quantum yield does not change by more than a factor of 2-3 (see Fig. 4).

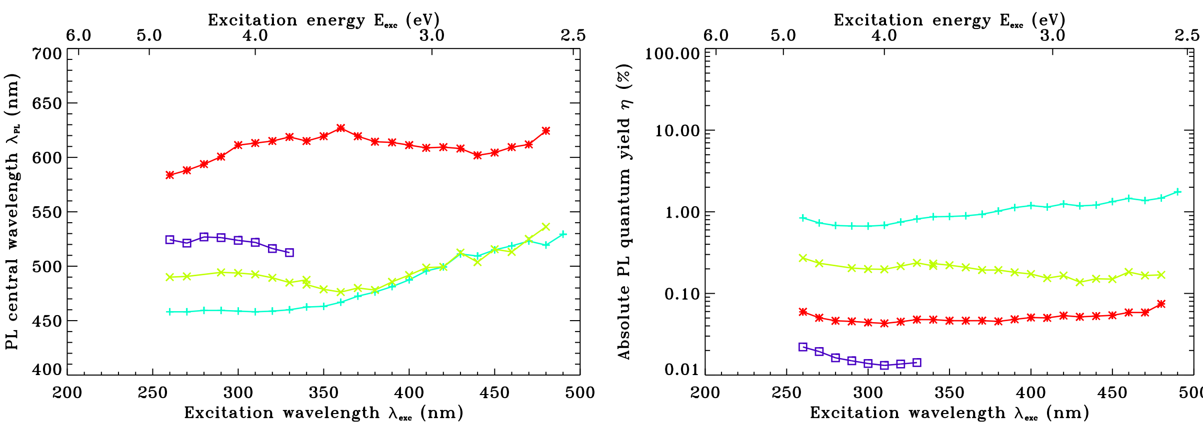

Fig. 4. Influence of the excitation wavelength on the a-C:H photoluminescence central wavelength (left) and efficiency (right) for four different a-C:H samples. By varying this excitation between 250 and 490 nm, no strong modification of the photoluminescence is observed (except the expected increase of the photoluminescence central wavelength when the excitation occurs in the PL band).)

As already shown in previous a-C:H photoluminescence studies (Rusli et al. 1996), we observed that the a-C:H PL yield decreases with the optical gap of the samples (see Fig. 5). Our work provides absolute PL yields ranging from few hundredths of percent to few percents in the optical band gap explored range. The astrophysical extended red emission observations provide lower limits for the carrier quantum yield, varying from one ISM environment to another. Near strong UV-visible stellar sources, the ERE efficiency lower limits are found to be the lowest ones (∼0.01%), and in the diffuse interstellar medium (DISM), high quantum yields lower limits of about 10% are estimated (Smith & Witt 2002). The corresponding yields correlate and increase with the decreasing density of the local radiation field. The quantum yields that we deduce are compatible with most of quantum yield limits set by ERE observations. However, they are not compatible to the highest quantum yield of 10% set by the scarce and difficult observations of the weakly emitting DISM.

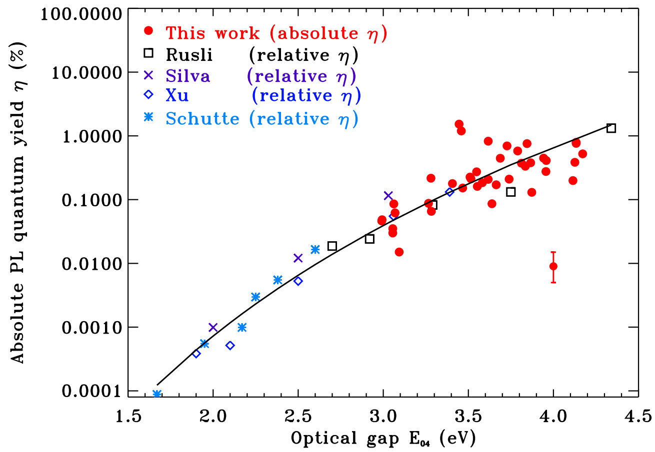

Fig. 5. Variation of the a-C:H photoluminescence quantum yield with the optical gap E_{04}. Typical error bar on the absolute yield including systematic effects are represented. Relative quantum yield results from other photoluminescence studies (Rusli et al. 1996 and references therein) are converted into absolute quantum yield using our absolute results and added to this figure. It allows to see variation of a-C:H PL absolute quantum yield on a larger optical gap range than with only our samples. The line is a fit to the relative efficiency data.

4 Conclusion

The evaluation of the astrophysical ERE efficiency from observations of different ISM environments, and more specifically the diffuse low density medium, is generally not a trivial task. The absolute yield, together with the elemental cosmic abundances requirements, are by far stronger constraints than the profile of astrophysical PL spectrum, as many materials are able to photoluminesce in the visible. Being the strongest astrophysical constraint, the PL efficiency determination need to be improved, in particular by insisting on additional observations of the extended red emission in the diffuse interstellar medium and proper evaluations of the UV-visible photons absorbed by the ISM carriers.

We provide in our study the first measurements of absolute PL yield as a function of excitation wavelength for a-C :H laboratory analogs to interstellar dust and a law linking the a-C:H optical gap to their absolute PL quantum yield comes out.

References

Chernyshov, S., Terukov, E., Vassilyev, V., & Volkov, A. 1991, Journal of Non-Crystalline Solids, 134, 218

Cohen, M., Anderson, C. M., Cowley, A., et al. 1975, ApJ, 196, 179

Darbon, S., Perrin, J.-M., & Sivan, J.-P. 1999, A&A, 348, 990

Dartois, E., Munoz Caro, G. M., Deboffle, D., Montagnac, G., & D'Hendecourt, L. 2005, A&A, 432, 895

Furton, D. G., Laiho, J. W., & Witt, A. N. 1999, The Astrophysical Journal, 526, 752

Furton, D. G. & Witt, A. N. 1993, The Astrophysical Journal, 415, L51

Godard, M. et al., in preparation

Holm, R. T., McKnight, S. W., Palik, E. D., & Lukosz, W. 1982, Appl. Opt., 21, 2512

Lukosz, W. 1981, Journal of the Optical Society of America (1917-1983), 71, 744

Nollau, A., Hoffmann, M., Floreck, K., Fritz, T., & Leo, K. 2000, Journal of Applied Physics, 87, 7802

Pendleton, Y. J. & Allamandola, L. J. 2002, The Astrophysical Journal Supplement Series, 138, 75

Rusli, R., Robertson, J., & Amaratunga, G. A. J. 1996, Journal of Applied Physics, 80, 2998

Sandford, S. A., Allamandola, L. J., Tielens, A. G. G. M., et al. 1991, The Astrophysical Journal, 371, 607

Schmidt, G. D., Cohen, M., & Margon, B. 1980, ApJ, 239, L133

Smith, T. L. & Witt, A. N. 2002, The Astrophysical Journal, 565, 304

Spoon, H. W. W., Armus, L., Cami, J., et al. 2004, The Astrophysical Journal Supplement Series, 154, 184

Yoshimi, M., Shimizu, H., Hattori, K., Okamoto, H., & Hamakawa, Y. 1992, Optoelectronics, 7, 69

SF2A 2009
M. Heydari-Malayeri, C. Reylé and R. Samadi (eds)

EQUILIBRATION OF NUCLEAR SPIN STATES OF CH_4 AT LOW TEMPERATURES

Lekic, A.[1], Michaut, X.[1], Bertin, M.[1], Fillion, J.-H.[1], Pardanaud, C.[2], Martin, C.[2] and Coussan, S.[2]

Abstract. Hydrogenated molecules are observed in astrophysical cold media as interstellar media (ISM) or cometary atmospheres. In many cases, the relative populations of each nuclear spin configuration of these hydrogenated species diverge strongly from their value at thermal equilibrium in the gaseous phase. In order to understand the parameters ruling the nuclear spin states equilibration of these kind of molecules in astrophysical conditions, experimental studies are performed in cold media (solid and at gas-solid interface). We present the latest experimental results of NSC dynamics for methane trapped in argon matrix between 4.3 K and 20 K. Preliminary results concerning nuclear spin states equilibration in a cold closed cell are also presented.

1 Introduction

CH_4 and other hydrogenated molecules of astrophysical interest like H_2, H_2O, H_2CO, NH_3, CH_3OH, or C_2H_4 play an important role for the chemistry in the interstellar medium (ISM) and in the protosolar *nebulae*. Because of the spin 1/2 of the protons, these molecules exist in different nuclear spin configurations. The four protons of methane gives three nuclear spin modifications called *para*, *ortho*, and *meta* depending whether the total nuclear spins are $I = 0$, $I = 1$, or $I = 2$, respectively. Due to the Pauli's exclusion principle and the symmetry properties of the rovibrational molecular wave functions, each species *para*, *ortho*, and *meta* is associated to species E, F, and A of the T_d point group respectively. Each nuclear spin modification can be identified by its rotation-vibration spectrum. In the high temperature limit ($> 50K$) and thermodynamical equilibrium, it is known that 13 % of the molecules are *para*, 56 % are *ortho* while 31 % are *meta*. Below 50 K, the E/A and F/A ratios become strongly temperature dependent. From these ratios of molecules measured in cometary *comae* (Crovisier 2006; Kawakita *et al* 2006) or in dark clouds (Dickens & Irvine 1999), it is expected to determine the formation conditions of molecules in space, and especially the formation temperature. However, very few laboratory studies are available concerning nuclear spin conversion in relevant astrophysical conditions. We present here a study of the nuclear spin equilibration at low temperature using the mid-infrared spectroscopy of CH_4 in argon matrix and at gas-solid interface. The spectra were recorded in the frequency range 400-4000 cm^{-1} with medium resolutions using FTIR spectrometers.

2 Nuclear Spin Conversion in rare gas matrix

First, we have investigated the parameters involved in the nuclear spin conversion of methane isolated in argon matrix at low temperatures (between 4.3 and 20 K). In this kind of environment, the hydrogenated molecules vibrate and rotate almost freely within the cage made of rare gas atoms (Michaut 2004). After a fast cooling from 20 K to 4.3 K, populations of the nuclear spin species do not follow a Boltzmann distribution because of a slow nuclear spin conversion. Following the time evolution of the transitions associated with one or the other species, we have measured characteristic times of nuclear spin conversion in various conditions. We observed that rare gas can be stabilized in Face-Centered Cubic (FCC) or Hexagonal Close-Packed (HCP) crystal structures for which the measured conversion times (450 minutes in FCC and 100 minutes in HCP) are clearly different,

[1] Laboratoire de Physique Moléculaire pour l'Atmosphère et l'Astrophysique-UMR CNRS 7092, Université Paris 6, 4 place Jussieu, 75252 Paris cedex 5
[2] Laboratoire Physique des Interactions Ioniques et Moléculaires - UMR CNRS 6633 - Université de Provence - Centre Saint-Jérôme - 13397 Marseille Cedex 20

despite the fact that both cages have similar dimensions. We observed that the NSC rate constant increases concomitantly with respect to the methane concentration in argon matrix. This phenomenon can be compared to the strong acceleration of the NSC of water in rare gas matrices as the concentration increases (Pardanaud 2008). Numerical calculations showed that the intermolecular magnetic interactions are responsible for this concentration dependence.

3 Nuclear spin equilibration at gas-solide interface

IR-driven experiments have been performed in pure gas or in gas-solid mixture in a closed cell under various pressure and temperature conditions above 55 K . Figure 1 shows that infrared spectrum of gaseous methane in the ν_3 stretching mode region is affected by the presence of solid methane in the cell. This effect is illustrated on Figure 1.b. In case of the R(1) line corresponding to the F species, the relative intensity decreases by 30 % in presence of solid methane. Further experimental developments are in progress to confirm this effect at lower temperature with a better signal-to-noise ratio and a good sensitivity.

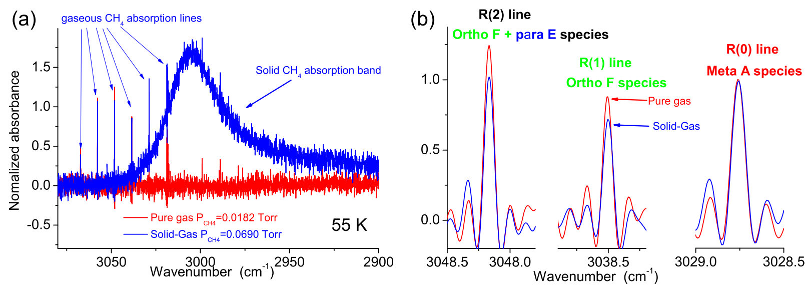

Fig. 1. FTIR spectra in the region of the stretching vibrational mode ν_3 of CH_4 obtained in pure gas and in solid-gas mixture obtained at 55 K. (a) whole spectrum and (b) zoom on the rovibrational lines R(0), R(1) et R(2) of the molecules in the gaseous phase

4 Conclusions

The environment of the molecule seems to play a crucial role on the nuclear spin conversion of hydrogenated molecules as it has already been pointed out for water embedded in different rare gas matrices (Pardanaud 2008, Abouaf-Marguin 2009). Due to the sensitivity of the Nuclear Spin Conversion to the intermolecular magnetic interactions, the decrease of mean distance between methane molecules enhances the NSC of methane trapped in rare gas solid. This process might be faster in solid methane (or solid ice in general). Furthermore, as rotation of molecules in ice is blocked, the mechanism for the dissipation of the rotational energy might be different. Extrapolation to the astrophysical context is not straight forward. In the meanwhile, efforts are made to investigate the possible influence of the solid methane on the equilibration of the nuclear spin states at low temperature.

This work has been performed within the project entitled CoSpiNu which was financially supported by INSU through the national programs 'Planétologie' and 'Physique et Chimie du Milieu Interstellaire'

References

Abouaf-Marguin, L., Vasserot, A.-M., Pardanaud, C.,& Michaut X. 2009, Chem. Phys. Lett. 480, 82

Crovisier, J. 2006, Molecular Physics 104, 2737

Dickens,J. E. & Irvine,W. M. 1999, ApJ 518, 733

Kawakita, H., Dello Russo, N., Furusho, R., *et al* 2006, ApJ 643, 1337

Michaut, X., Vasserot, A.-M., & Abouaf-Marguin, L. 2004, Vib. Spectrosc. 34, 83

Pardanaud, C., Michaut,X., Fillion, J.-H., Vasserot, A.-M., & Abouaf-Marguin, *in* Journées de la SF2A 2008, eds. C. Charbonnel, F. Combes, & R. Samadi (Paris, 2008), 337, 2008

EXPERIMENTAL EVIDENCE FOR WATER FORMATION VIA O_3 HYDROGENATION ON A WATER ICE COVERED SURFACE UNDER INTERSTELLAR CONDITIONS

Mokrane, H.[1], Chaabouni, H.[1], Accola, M.[1,2], Congiu, E.[1], Dulieu, F.[1], Chehrouri, M.[1,3] and Lemaire, J.L.[1]

1 Introduction

In dense cold interstellar clouds, dust grains are covered with an ice mantle mainly composed of water H_2O ice (Gibb et al 2000). Solid water ice has been observed in general on the surface of many different astronomical objects, such as outer planets, satellites, comets and interstellar cloud.

The chemical origin of the water is not well understood. Its formation in the gas phase is not efficient to reproduce the observed abundance. Then water ice in dark clouds is likely to be formed directly on grain surfaces.

Several reaction schemes for water formation on cold grain surfaces, predicted by astrochemical models are likely to occur via the hydrogenation of O, O_2 and O_3 (Tielens & Hagen 1982, Cuppen & Herbst 2007). Although O_3 molecules have not so far been detected on interstellar dust grains, their presence is presumed.

2 Experimental

Experiments are performed with the FORMOLISM setup using the Temperature Programmed Desorption (TPD) diagnostics. Ozone (prepared ex-situ by radio frequency electric discharge in O_2 gas in a glass bottle) is first deposited on a non-porous amorphous solid water ice. Then D-atoms are sent onto the sample held at 10K. HDO molecules are detected during the desorption of the whole substrate where isotope mixing takes place, indicating that water synthesis has occurred. The efficiency of water formation via hydrogenation of ozone is of the same order of magnitude than found for reactions involving O atoms or O_2 molecules and exhibits no apparent activation barrier. These experiments validate the assumption made by models using ozone as one of the precursors of water formation via solid-state chemistry on interstellar dust grains.

3 Discussion

There are several possible chemical pathways (Tielens & Hagen 1982, Miyauchi et al 2008, Ioppolo et al 2008) to form D_2O. At T_s= 10K, formation of D_2O on np-ASW ice from O_3 + D may proceeds through the following steps:

$$O_3 + D \rightarrow OD + O_2$$
$$OD + D \rightarrow D_2O$$

and

$$O_2 + D \rightarrow DO_2$$
$$DO_2 + D \rightarrow D_2O_2$$
$$D_2O_2 + D \rightarrow D_2O + OD$$

At $T_s > 120$K and during the heating, an isotopic exchange is occuring between D_2O formed and the H_2O substrate, leading to HDO formation:

[1] LERMA/LAMAp, UMR 8112 du CNRS, de l'Observatoire de Paris et de l'Université de Cergy-Pontoise, France
[2] Università di Catania, Italy
[3] L.D.P.C. Université de Saïda, BP138 Enasr, Saïda 20002, Algérie

$$D_2O + H_2O \rightarrow 2\ HDO$$

In dense clouds where H_2 and D_2 are abundant, another reaction (Tielens & Hagen 1982) is possible:

$$OD + H_2 \rightarrow HDO + H$$

4 Conclusions

1) The reaction O_3 + D proceeds without activation barrier. **2)** The formation of water from O_3 + D reaction on non-porous ASW is efficient and produces water HDO molecules. **3)** The experimental result confirms the theoretical models considering O_3 as the major actor of water formation in dark clouds (Tielens & Hagen 1982, Cuppen & Herbst 2007).

This work (Mokrane et al 2009) presents the first experimental evidence of water formation from O_3 reaction with D-atoms on non-porous amorphous solid water ice under conditions relevant to interstellar molecular clouds.

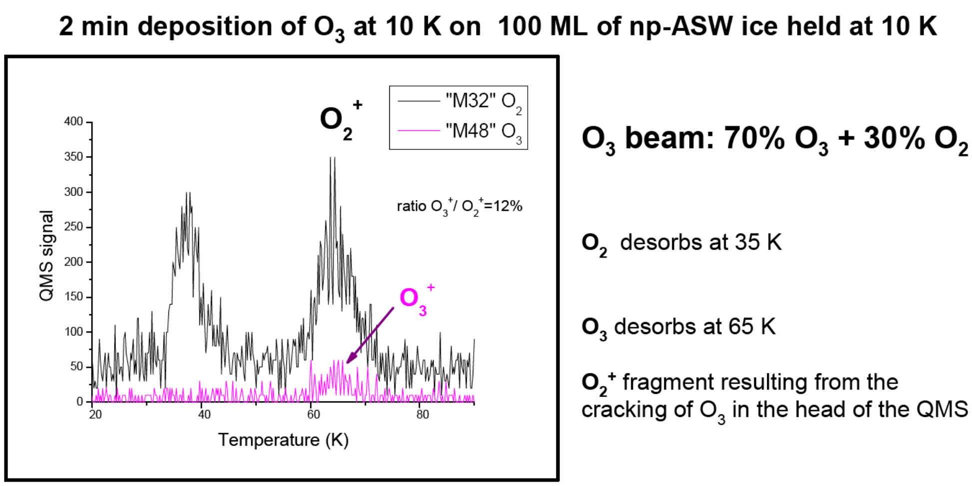

Fig. 1. TPD spectra of O_3 (in red) and O_2 (in black) on np-ASW

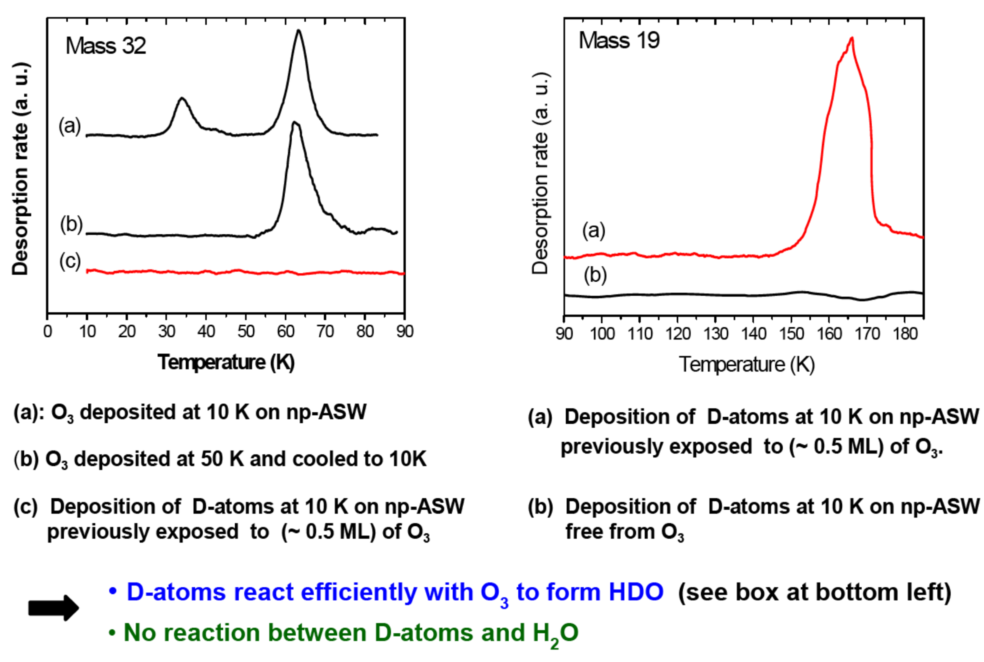

Fig. 2. TPD spectra of O_3 +D on np-ASW, for mass 32 (O_2) and 19 (HDO)

References

Cuppen. H. M., Herbst. E, 2007,ApJ, 668, 294

Gibb, E. L., Whittet, D. C. B., Schutte, W. A., Boogert, A. C. A., Chiar, J. E., Ehrenfreund, P., Gerakines, P. A., Keane, J. V., Tielens, A. G. G. M., van Dishoeck, E. F. & Kerkhof, O. 2000, ApJ, 536, 347

Ioppolo, S., Cuppen, H. M., Romanzin, C., van Dishoeck, E. F., & Linnartz, H. 2008, ApJ, 686, 1474

Miyauchi, N. , Hidaka, H., Chigai, T., Nagaoka, Watanabe, N., & Kouchi, A. 2008, Chemical Physics Letters, 456, 27

Mokrane H., Chaabouni H., Accolla M., Congiu E., Dulieu F., Chehrouri M., Lemaire J.L., 2009, accepted in ApJ Letters

Tielens, A. G. G. M., & Hagen, W. 1982, A&A, 114, 245.

SF2A 2009
M. Heydari-Malayeri, C. Reylé and R. Samadi (eds)

VLT/NACO NEAR-INFRARED IMAGING AND SPECTROSCOPY OF N88A IN THE SMC

Testor, G.[1], Lemaire, J.L.[1,2], Kristensen, L.E.[3], Diana, S.[1], Field, D.[4] and Heydari-Malayeri, M.[1]

1 Introduction

N88A in the Small magellanic Cloud (SMC) is a high excitation 'blob' belonging to a rare class of compact HII regions in the Magellanic Clouds (Mcs). These objects now generically named HEBs are probably the final stages in evolution of the ultra compact HII regions. In contrast to typical HII regions of the MCs greater than 50 pc and powered by a large number of stars, HEBS are dense and smaller in diameter (1-3pc). They are affected by local dust where the ionizing stars are enshrouded. The study of star formation in the Mcs is easier than in our Galaxy because their known and relatively small distance and low interstellar extinction. Their distance also permits to study not only individual stellar objects but also extended ones in a same CCD frame.

Among the HEBs, N88A is the brightest and the most extincted and is part of the large complex N88 located east of the main body of the SMC. Numerous multiwavelengths studies have been made on this peculiar object. Nevertheless, many uncertainties remain, especially due to the strong extinction or the lack of spatial resolution, to understand its true nature. Here we present our results of the first NIR high spatial resolution (0.1-0.2 arcsec) observations (J, H, Ks and L' imaging and Ks-band spectroscopy) of N88A and its environment in the SMC, performed with the adaptative optics camera NAOS/CONICA at the ESO VLT (Fig. 1, central image).

2 Results

Our IR data reveal for the first time a morphology of N88A in unprecedented detail, and using colour-magnitude and color-color diagrams several young sources with infra-red excess are detected.

- NIR high spatial resolution images of N88A have shown that N88A is formed by a tight cluster of diameter 2 .5 arcsecs superposing a circular continuum emission centered on a bright star (Fig. 1-Ks).

- The JHK magnitude and color diagrams have revealed that the resolved stars in N88A could be massive young stellar objects (YSOs) of class II, as well as three stars stars located east of the central bright star along a H_2 filament. They also show that numerous stars in N88 exhibit IR-excess.

- L' band observations have pointed out a bright emission peak in the component L1 without counterpart in JHK (Fig. 1-L'). This peak could be classified as a MYSO of Class I (Lada 2000)

- The central bright star (♯19) is assumed to be an O7V type. As the ionizing source derived by radio observations (Indebetouw et al 2004) is of type O5, several other stars should contribute to the ionization of N88. This is strengthened by the I(He 2.11 m/I(Brγ) ratio (Hanson et al 2002) indicating that the ionizing source of N88A has a spectral type earlier than O7 star.

- The H_2 band image (Fig. 2) shows that N88A is composed of three bright knots where massive star formation should take place . From spectroscopy we show that the excitation mechanism is caused predominantly by PDRs and not by shocks.

[1] LERMA, UMR 8112, Observatoire de Paris-Meudon, France
[2] LERMA/LAMAp, UMR 8112, Université de Cergy-Pontoise, France
[3] University of Leiden, Netherland
[4] University of Aarhus, Denmark

3 Conclusions

The observations of N88A at IR high spatial resolution have shown the stellar complexity of the HEB N88A, as well as its unusual bright dust emission. This object, of dimension similar to the trapezium in Orion in our galaxy, appears a very good candidate for studies of young massive stars in low-metallicity

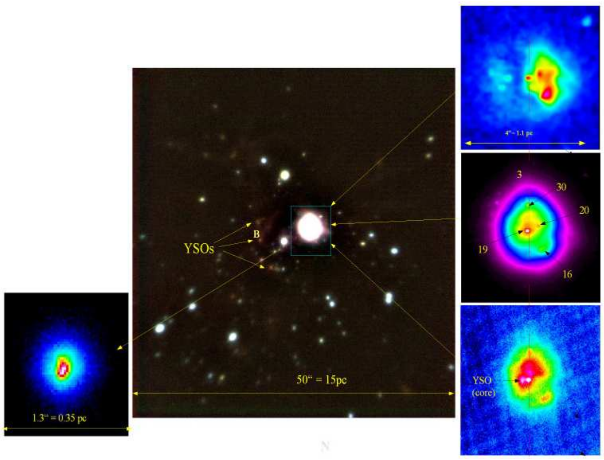

Fig. 1. Central image: False-color image of the N88 region obtained with NACO *(blue is assigned to the J band, green to the H band and red to the Ks band)*. **Right row from top to bottom**: close-up of N88A in the y(547), Ks and L' bands *(in Ks and L' images YSOs candidates are indicated by arrows)*. **1) y(547)-band**: Hubble observations (Heydari et al 1999) have revealed a complex structure consisting of two inhomogeneous wings separated by a north south absorption lane. The bright western wing contains two faints stars corresponding to our stars ♯19 and ♯20 as well as a dark spot to the the south. **2) Ks-band**: Using similar spatial resolution IR observations, the morphology of N88A appears more homogeneous. It consists of a bright continuum centered on a bright star of magnitude Ks = 14.9. A cluster of at least 10 resolved embedded stars is detected. The stars ♯16, ♯19, ♯20 and ♯30 are expected to be YSOs. From color-magnitude diagram they can be classified as massive. (*We consider to be YSOs the objects observed just before a normal OB star emerges from its natal birth environment.*) **3) L'-band**: The bright core of magnitude 14 is classified YSO of class I (K-L .4.5 mag) and coincides with the HST lane. **Left image**: close-up of N88B showing at least three components.

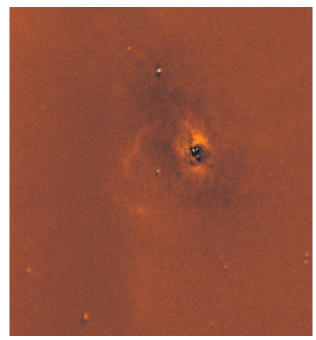

Fig. 2. H_2 2.12 μm emitting region (Size 42"x 40"). Three bubbles are visible around the young bright star of N88A. Around N88B a filament is in interaction with the eastern bubble. This is also noticed in the HST Hα image.

We acknowledge ESO for provision of VLT-UT4 and we would like to thank the instrument manager on duty for assistance in using NACO

References

Hanson, K., Luhman, K.L., Rieke, G.H. 2002 ApJS 138, 35

Heydari-Malayeri, M., Charmandris, V;, Deharveng, L., Rosa, M., Zinnecker, H A&A 347, 841

Indebetouw, R., Johnson, K., Conti, P. 2004, AJ 128, 2206

Lada, J.C and five authors. 2000 ApJ 120, 3162

PNCG-SSAA

High-resolution numerical simulations and complex physical modelisation

SF2A 2009
M. Heydari-Malayeri, C. Reylé and R. Samadi (eds)

HISTORICAL AND NEW SPECTRAL INDICATORS FROM THE NEARBY SUPERNOVA FACTORY

Chotard, N.[1], Gangler, E.[1], Smadja, G.[1] and the SNFactory collaboration

Abstract. From a sample of 58 SNe Ia spectra obtained by the Nearby Supernova Factory with the SuperNovae Integral Field Spectrograph (SNIFS), we present measurements of spectral indicators proposed in the literature. In addition, we probe the direct correlation of spectral indicators to the Hubble diagram residuals and the relevance of such indicators as substitutes to stretch and colour.

1 The SNe Ia sample

The data presented here has been obtained by the Nearby SNF collaboration with SNIFS on the UH 2.2 m (Aldering et al. 2002). The light curves in synthetic BVR filters are reconstructed from the absolute spectra of each SN. The present study is performed on a sample of 58 SNe Ia selected for the quality of their SALT2 (Guy et al. 2007) light-curve fit, the phase coverage, and for which a spectrum in a window of ± 2.5 days around the peak luminosity was obtained. The parameters of the fit (stretch ($x1$), colour (c)) are also used in this analysis.

2 Classical spectral indicators

Two regions of interests between 3500 and 4200 Å and between 5500 and 6500 Å have been shown to exhibit calcium and silicon features correlated to the supernova intrisic parameters (Nugent et al. 1995; Bongard et al. 2005). They defined the following classical spectral indicators :

$$R_{Ca} = \frac{F^{3950}_{max}}{F^{3650}_{max}} \quad RSi = \frac{\mathrm{depth}_{5800}}{\mathrm{depth}_{6200}} \quad RSiSS = \frac{\int_{5500}^{5700} F(\lambda)d\lambda}{\int_{6200}^{6450} F(\lambda)d\lambda}$$

where $F(\lambda)$ is the flux ($[erg/cm^2/s/A]$), F^{λ}_{max} is the flux at the peak position found around the given wavelength, and depth_λ is the difference between the continuum flux and the real minimum flux of the absorption feature. Computing these indicators in an objective way requires an automatic smoothing procedure which preserves spectral extrema, as shown in Fig. 1.

Other spectral indicators such as equivalent widths (EW) (Hachinger et al. 2006; Bronder et al. 2007) were computed in relevant regions of the SN Ia spectrum. In our sample, $EW_{SiII}(4000)$ (shown in Fig. 1 on the top right of the control plot) was found to correlate strongly with the SALT2 $x1$ parameter . The general definition of EW is:

$$EW = \sum_{i=1}^{N} \left(1 - \frac{f_\lambda(\lambda_i)}{f_c(\lambda_i)}\right) \Delta\lambda_i$$

[1] Institut de Physique Nuclaire de Lyon, 4 rue Enrico Fermi, domaine scientifique de la DOUA 69622 Villeurbanne CEDEX, France

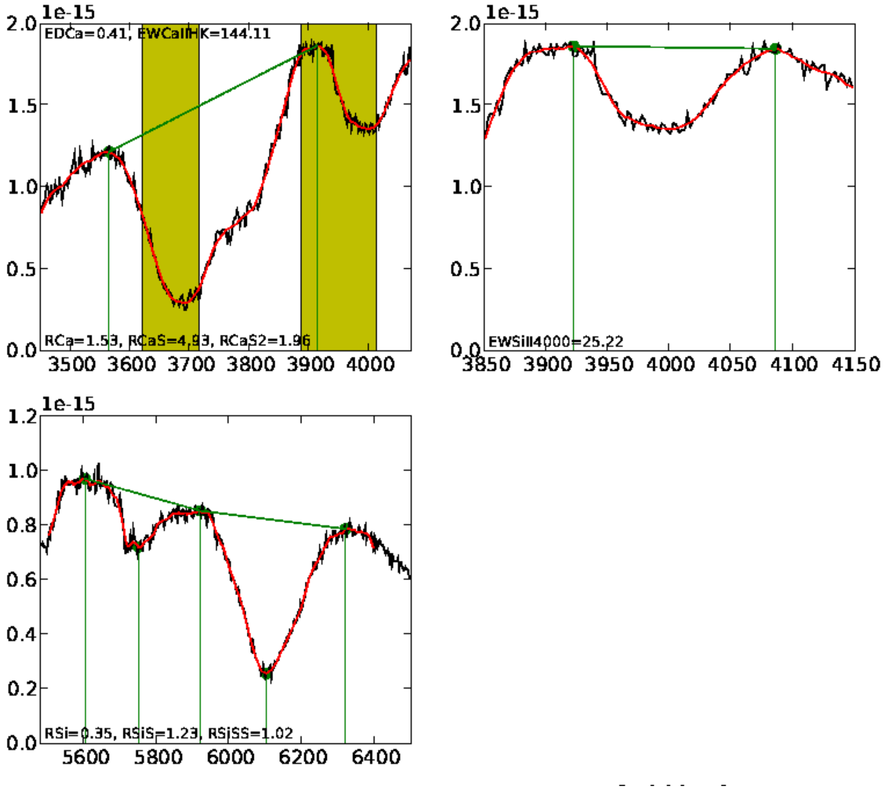

Fig. 1. Automatic control plot for a spetrum of the sample.

3 The correlation of spectral indicators with SNe Ia parameters

The relative standardization power of these indicators were studied with their correlations with $x1$, colour and a proxy to their absolute magnitude, ΔM_B: the latter was derived from the residual of a fit to the Hubble diagram for a flat ΛCDM.

The Table 1 shows the correlation coefficients between parameters and spectral indicators. A SALT2 colour cut is applied on the sample ($c < 0.1$), to study the intrisic part of the SN Ia variability. 44 over our 58 SNe pass the cut. Fig. 2 shows the correlation between $EW_{SiII}(4000)^{cut}$ and ΔM_B after the colour cut.

	ΔM_B	$x1$	colour	ΔM_B^{corr}	phase
R_{Ca}	0.55	-0.45	0.35	0.17	0.05
R_{Si}	0.26	-0.60	0.04	0.00	0.06
R_{SiSS}	-0.77	-0.57	-0.54	-0.16	0.27
$EW_{SiII}(4000)$	0.33	-0.76	-0.01	0.17	0.23
$EW_{SiII}(4000)^{cut}$	**0.80**	**-0.84**	0.01	0.28	0.21

Table 1. Correlation coefficients between spectral indicators and other SN Ia parameters.

The $EW_{SiII}(4000)$'s correlations with Hubble residuals and x1 **increase after the colour cut** (see Table 1 and Fig. 2). $EW_{SiII}(4000)$ is independant of colour (the correlation coefficient is 0.01) and can be a good proxy for x1, it thus proves to be particularly useful for standardizing SNe Ia.

4 Corrected Hubble residuals

In the SALT2 approach, the luminosity is corrected for stretch and colour with α and β tuned to minimize the residuals to the cosmological fit to the data: $\Delta M_B^{corr} = \Delta M_B + \alpha \times x1 - \beta \times c$. The spectral correction can be

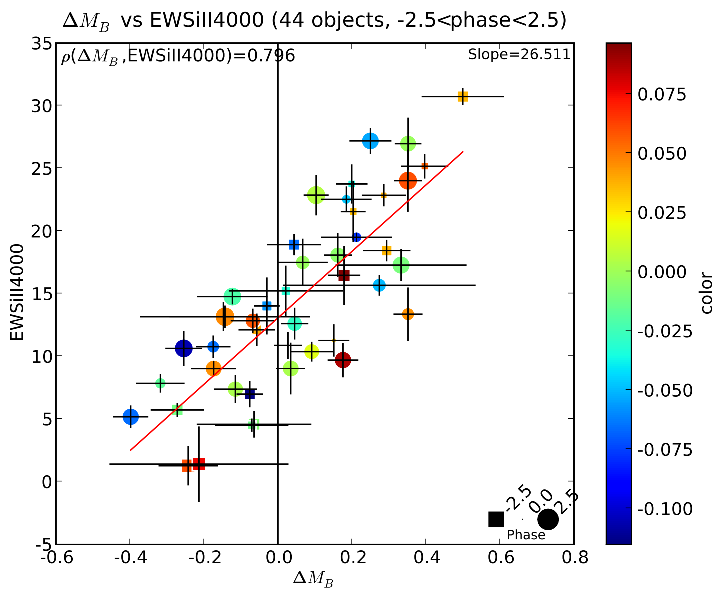

Fig. 2. Correlation between ΔM_B and $EW_{SiII}(4000)^{cut}$, after the colour cut ($c < 0.1$)

used in the similar way. Table 2 gives the RMS of the Hubble diagram residuals uncorrected and corrected with spectral indicators. The Hubble residual with colour and $EW_{SiII}(4000)$ corrections are as effective as colour and $x1$ before the colour cut and perform better after. $EW_{SiII}(4000)$ is then an excellent candidate for the estimate the intrinsic part of the SN Ia variability and replaces or strengthens the $x1$ parameter.

Correction	None	c & x1	c & $EW_{SiII}(4000)$	None	c & x1	c & $EW_{SiII}(4000)$
RMS	0.406	0.161	0.164	0.217	0.153	0.123
nMAD	0.264	0.159	0.177	0.243	0.139	0.148

Table 2. Standard deviation and normalized median absolute deviation of hubble diagram residual without any cut (left values) and with a colour cut (right values).

5 Conclusion

Traditional spectral indicators are correlated to the SNe Ia absolute luminosity, and some of them such as $EW_{SiII}(4000)$ are strongly correlated to the intrinsic variability of SNe Ia. Another spectral indicator presented in (Bailey et al. 2009) using the same sample of SNe Ia from the SNFactory collaboration also shows a very strong correlation (0.95) between the spectral ratio R(642/443) and ΔM_B even without any colour cut. It proves to be a strong competitor of x1 and colour for the luminosity standardization and reaches a final RMS on the hubble diagram of 0.128 ± 0.012.

References

Aldering, G. 2002, Proceedings of the SPIE., vol. 4836 of Presented at SPIE Conference, 61-72

Bongard, S. 2005, arXiv:astro-ph/0512229v1

Bronder, T.J. 2007, arXiv:astro-ph/0709.0859v1

Guy, J., 2007 arXiv:astro-ph/0701828v1

Hachinger, S. 2006, arXiv:astro-ph/0604472v2

Nugent, P. 1995, ApJ, 455, L147

SF2A 2009
M. Heydari-Malayeri, C. Reylé and R. Samadi (eds)

PRIMORDIAL NON-GAUSSIANITY IN THE HALO BIAS

Desjacques, V.[1]

Abstract. Primordial non-Gaussianity of the local type induces a scale-dependent bias in the clustering of rare objects. Calibration with numerical simulations is essential to measurements of galaxy/quasar power spectra that aim to put constraint on the amount of primordial non-Gaussianity. We compare theoretical predictions with the outcome of large N-body simulations evolved from Gaussian and non-Gaussian initial conditions. At low wavenumber $k < 0.03\ h\mathrm{Mpc}^{-1}$, the theory and the simulations agree well with each other for haloes with linear bias $b(M) > 1.5$. Including a scale-independent bias correction improves the comparison between theory and simulations on smaller scales where the k-dependent effect becomes rapidly negligible. We place limits on the size of the cubic order correction using a compilation of large-scale structures data.

1 Introduction

A wide class of inflationary scenarios lead to non-Gaussianity of the local type, i.e. which depends on the local value of the primordial curvature perturbation (Here and henceforth, the usual Bardeen potential in matter-dominated era). In these models, deviation from Gaussianity can be conveniently parametrised by the nonlinear coupling parameters $f_{\rm NL}$ and $g_{\rm NL}$ through the relation

$$\Phi(\mathbf{x}) = \phi(\mathbf{x}) + f_{\rm NL}\phi(\mathbf{x})^2 + g_{\rm NL}\phi(\mathbf{x})^3 \ , \tag{1.1}$$

where $\phi(\mathbf{x})$ is an isotropic Gaussian random field whose power spectrum is a power-law $P_\phi(k) \sim k^{n_s-4}$. Note that the quadratic correction is small since curvature perturbations are typically $\mathcal{O}(10^{-5})$.

The cosmic microwave background (CMB) and large scale structures offer two different routes to test for the presence of primordial non-Gaussianity. The main advantage of the CMB resides in the fact that the observed spherical harmonics coefficient a_l^m are a linear superposition of the primordial curvature perturbations (weighted by the radiation transfer function). Therefore, any non-zero three-point and/or higher correlation function of $\Phi(\mathbf{x})$ is directly mirrored in the corresponding statistics of the primary temperature anisotropies. Thus far, analysis of the CMB three-point function indicates that the data is fully consistent with Gaussianity, with $-9 < f_{\rm NL} < +111$ at 95% C.L. (Komatsu et al. 2009).

Unlike the CMB, nonlinear gravitational evolution of large-scale structures can significantly contaminate the signal due to primordial non-Gaussianity. However, causality implies that this contamination decays rapidly as one goes to large distances. Another important difference with the CMB is that large-scale structures are traced by galaxies etc. which are biased relative to the matter distribution (since these preferentially form in overdense regions). As a consequence of this bias relation, high order statistics of the matter density field (such as the three-point function) can project onto low order statistics of biased tracers (such as the power spectrum). In particular, Dalal et al. (2008), Matarrese & Verde (2008), Slosar et al. (2008), showed that the three-point function for the local quadratic coupling $f_{\rm NL}\phi^2$ induces a scale-dependent bias $\Delta b_\kappa(k, f_{\rm NL})$ in the large-scale power spectrum of biased tracers,

$$\Delta b_\kappa(k, f_{\rm NL}) = 3 f_{\rm NL}\left[b(M) - 1\right]\delta_{\rm c}\frac{\Omega_{\rm m}H_0^2}{k^2 T(k) D(z)} \ , \tag{1.2}$$

[1] Institute for Theoretical Physics, University of Zürich, Winterthurerstrasse 190, CH-8057 Zürich, Switzerland

where $b(M)$ is the linear bias parameter, H_0 is the Hubble parameter, $T(k)$ is the matter transfer function normalised to unity as $k \to 0$, $D(z)$ is the growth factor normalised to $(1+z)^{-1}$ in the matter era and $\delta_c \sim 1.68$ is the present-day (linear) critical density threshold. Slosar et al. (2008) applied this relation to constrain the value of $f_{\rm NL}$ using a compilation of large-scale structures data and found limits comparable to those from WMAP5, $-29 < f_{\rm NL} < +69$. Still, in order to fully exploit the potential of forthcoming galaxy surveys, theoretical predictions for the non-Gaussian bias need to be tested against the outcome of large numerical simulations. Here we study the impact of local non-Gaussianity on the bias of dark matter haloes.

2 N-body simulations

Investigating the scale-dependence of the halo bias requires simulations large enough so that many long wavelength modes are sampled. At the same time, the simulations should resolve the dark matter haloes hosting the surveyed objects, i.e. luminous red galaxies (LRGs) or quasars (QSOs), so that one can construct halo samples whose statistical properties mimic as closely as possible those of the real data.

We utilise a series of large N-body (collisionless) simulations of the ΛCDM cosmology seeded with Gaussian and non-Gaussian initial conditions. We adopt the standard (CMB) convention in which the Bardeen potential $\Phi(\mathbf{x})$ is primordial, and not extrapolated to present epoch. We run five sets of three 1024^3 simulations, each of which has $f_{\rm NL} = 0, \pm 100$, with the N-body code GADGET-2 (Springel 2005). We use the same Gaussian random seed field ϕ in each set of runs so as to minimise the sampling variance. The box size is 1600 h^{-1}Mpc such that the particle mass of these simulations is 3.0×10^{11} M$_\odot/h$, enough to resolve haloes down to 10^{13} M$_\odot/h$. Dark matter haloes are identified using the MPI parallelised version of the AHF halo finder which is based on the spherical overdensity (SO) finder developed by Gill, Knebe & Gibson (2004).

We interpolate the dark matter particles and halo centres onto a regular cubical mesh. The resulting dark matter and halo fluctuation fields were then Fourier transformed to yield the matter-matter, halo-matter and halo-halo power spectra $P_{\rm mm}(k)$, $P_{\rm mh}(k)$ and $P_{\rm hh}(k)$, respectively. These power spectra are measured for various halo masses and redshifts, covering a range of statistical properties corresponding to those of the available galaxy or quasar populations with different luminosities and bias. Note that these quantities are computed on a 512^3 grid, whose Nyquist wavenumber is sufficiently large (≈ 1 hMpc^{-1}) to allow for an accurate measurement of the power in wavemodes of amplitude $k \lesssim 0.1$ hMpc^{-1}. The halo power spectrum is corrected for the shot-noise due to the discrete nature of dark matter haloes, which we assume to be the standard Poisson term $1/\bar{n}$. Yet another important quantity is the linear halo bias $b(M)$ which must be measured accurately from the Gaussian simulations as it controls the magnitude of the scale-dependent shift (see equation 1.2). We use the ratio $P_{\rm mh}(k)/P_{\rm mm}(k)$ as a proxy for the halo bias since it is less sensitive to shot-noise.

In order to quantify the effect of non-Gaussianity on the halo bias, we consider the ratios

$$\begin{aligned} \frac{P_{\rm mh}(k, f_{\rm NL})}{P_{\rm mh}(k,0)} - 1 &= \frac{\Delta b(k, f_{\rm NL})}{b(M)} \\ \frac{P_{\rm hh}(k, f_{\rm NL})}{P_{\rm hh}(k,0)} - 1 &= \left(1 + \frac{\Delta b(k, f_{\rm NL})}{b(M)}\right)^2 - 1 \,. \end{aligned} \tag{2.1}$$

Although $P_{\rm mh}$ is less affected by discreteness, it is important to measure the effect in the auto-power spectrum $P_{\rm hh}$ of dark matter haloes since the latter gives the strongest constraint on $f_{\rm NL}$.

3 Non-Gaussian bias shift

At the lowest order, there are two additional, albeit relatively smaller, corrections to the halo bias which arise from the dependence of both the halo number density $n(M,z)$ and the matter power spectrum $P_{\rm mm}$ on the nonlinear parameter $f_{\rm NL}$. These terms must be included in the comparison with the simulations (Desjacques, Seljak & Iliev 2009).

Firstly, assuming the peak-background split holds, the change in the mean number density of haloes induces a k-independent shift

$$\Delta b_{\rm I}(f_{\rm NL}) = -\frac{1}{\sigma}\frac{\partial}{\partial\nu}\ln\left[R(\nu, f_{\rm NL})\right] \tag{3.1}$$

where $\nu = \delta_c(z)/\sigma(M)$ is the peak height at mass scale M and $R(\nu, f_{\rm NL})$ is the fractional correction to the Gaussian mass function. Notice that $\Delta b_{\rm I}(f_{\rm NL})$ has a sign opposite to that of $f_{\rm NL}$, because the bias decreases when the mass function goes up (cf. left panel of Fig. 1).

Secondly, primordial non-Gaussianity affects the matter power spectrum as positive values of $f_{\rm NL}$ tend to increase the small-scale power. For $f_{\rm NL} \sim \mathcal{O}(10^2)$, the magnitude of this correction is at a per cent level in the weakly nonlinear regime $k \lesssim 0.1$ hMpc^{-1}. We find that leading order perturbation theory (PT) provides an excellent description of the effect over the wavenumbers of interest, $k \lesssim 0.1$ hMpc^{-1} (cf. left panel of Fig. 1).

Summarising, local non-Gaussianity adds a correction $\Delta b(k, f_{\rm NL})$ to the bias $b(k)$ of dark matter haloes that can be written as

$$\Delta b(k, f_{\rm NL}) = \Delta b_\kappa(k, f_{\rm NL}) + \Delta b_{\rm I}(f_{\rm NL}) + b(M)\beta_{\rm m}(k, f_{\rm NL}) \tag{3.2}$$

at first order in $f_{\rm NL}$, where $\beta_{\rm m}(k, f_{\rm NL}) = P_{\rm mm}(k, f_{\rm NL})/P_{\rm mm}(k, 0) - 1$. The right panel of Fig. 1 illustrates the relative contribution of these terms for haloes of mass $M > 2 \times 10^{13}$ M$_\odot/h$ identified at redshift $z = 0.5$. The data points are obtained from measurements of the cross-power spectrum in the N-body simulations. The solid curve shows the total non-Gaussian bias $\Delta b(k, f_{\rm NL})$. Considering only the scale-dependent shift Δb_κ leads to an apparent suppression of the effect in simulations relative to the theory. Including the scale-independent correction $\Delta b_{\rm I}$ considerably improves the agreement at wavenumbers $k \lesssim 0.05$ hMpc^{-1}. Finally, adding the scale-dependent term $b(M)\beta_{\rm m}$ further adjusts the match at small scale $k \gtrsim 0.05$ hMpc^{-1} by making the non-Gaussian bias shift less negative.

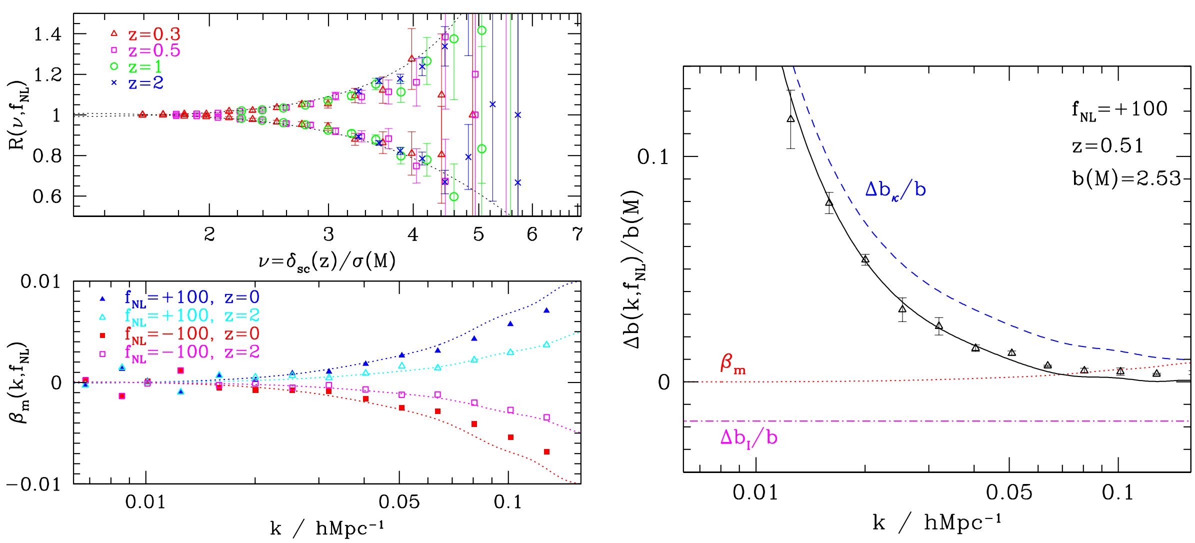

Fig. 1. Upper left: Fractional deviation from the fiducial Gaussian mass function. Different symbols refer to different redshifts as indicated. Error bars denote Poisson errors. **Lower Left**: Non-Gaussian fractional correction to the matter power spectrum, $\beta_{\rm m}(k, f_{\rm NL}) = P_{\rm mm}(k, f_{\rm NL})/P_{\rm mm}(k, 0) - 1$, that originates from primordial non-Gaussianity of the local type. Results are shown at redshift $z = 0$ and 2 for $f_{\rm NL} = \pm 100$. The dotted curves indicate the prediction from a leading-order perturbative expansion. **Right**: Non-Gaussian bias correction for haloes of mass $M > 2 \times 10^{13}$ M$_\odot/h$ extracted from the snapshot at $z = 0.5$ (filled symbols). The solid curve represents our theoretical model eq. (3.2). The dashed, dotted-dashed-dotted and dotted curves show the three separate contributions that arise at first order in $f_{\rm NL}$. Our theoretical scaling agrees very well with the data for $k \lesssim 0.05$ hMpc^{-1}.

If haloes and dark matter do not trace each other on large scales, i.e. if there is stochasticity, then analyses based on the auto- and cross-power spectrum may not agree with each other. While models with Gaussian initial conditions predict little stochasticity on large scales, this has not been shown explicitly for models with non-Gaussianity. We find that measurements of the non-Gaussian bias correction obtained with the halo-halo or the halo-matter power spectrum are in a good agreement with each other, suggesting that non-Gaussianity does not induce stochasticity and the predicted scaling applies equally well for the auto- and cross-power spectrum.

For highly biased haloes ($b(M) \gtrsim 1.5$), our results indicate that the simulated non-Gaussian bias converges towards the theoretical prediction for $k \lesssim 0.03\ h\mathrm{Mpc}^{-1}$. At smaller scales, the effect depends strongly on scale-independent bias. If we include this contribution using analytic calculation (equation 3.1), the suppression relative to theory is much smaller and in some cases goes in the opposite direction. Still, one could argue that scale-independent bias cannot be identified from the data alone, so one should fit for it and include it in the overall bias, as was done in Slosar et al. (2008). In this case the agreement between theory and simulations is improved further. For the halo samples with $b(M) \lesssim 1.5$ there is some evidence that the actual bias exceeds the theory on all scales. Therefore, the proposed eq. (3.2) does not appear to be universal, so care must be exercised when applied to the actual large scale structure data.

4 Constraints on $g_{\rm NL}$ (trispectrum)

Thus far, we have only considered the effect of the quadratic term $f_{\rm NL}\phi^2$ on the clustering of dark matter haloes. However, in inflationary scenarios such as the curvaton model, a large cubic correction $g_{\rm NL}\phi^3$ can be produced while simultaneously keeping the quadratic correction small. Therefore, we have also explored the effect of the cubic term on the halo bias (Desjacques & Seljak 2009). Simulations of non-Gaussian models with $g_{\rm NL} = \pm 10^6$ and with properties similar to those of the aforementioned simulations are used to calibrate the theory. The k-dependence of the bias correction $\Delta b_\kappa(k, g_{\rm NL})$ measured from the auto- and cross-power spectrum of haloes, is similar to that found in $f_{\rm NL}$ models, but the amplitude is lower than theoretical expectations. Using the compilation of large-scale structure data of Slosar et al. (2008), we obtain for the first time a limit on $g_{\rm NL}$ of

$$-3.5 \times 10^5 < g_{\rm NL} < +8.2 \times 10^5 \quad \text{(at 95\% CL)} \tag{4.1}$$

For the limits obtained here, $\Delta b_{\rm I}$ should be much smaller than $b(M)$ and can thus be ignored. Note also that, whereas the non-Gaussian bias scales as $D(z)^{-1}$ in $f_{\rm NL}$ models, the redshift dependence is stronger for $g_{\rm NL}$ non-Gaussianity, $\Delta b(k, g_{\rm NL}) \propto D(z)^{-2}$, so one can achieve relatively larger gains from measurements of high redshift tracers. We expect our limit to improve by 1-2 orders of magnitude with future large-scale structures data. In fact, the extent to which one can tighten the observational bounds will mainly depend on our ability to minimise the impact of sampling variance caused by the random nature of the wavemodes, and the shot-noise caused by the discrete nature of the tracers. By comparing differently biased tracers of the same surveyed volume (Seljak 2009) and suitably weighting galaxies (Seljak, Hamaus, & Desjacques 2009), it should be possible to circumvent these problems and considerably improve the detection level.

References

Dalal, N., Doré, O., Huterer, D., & Shirokov, A., 2008, Phys. Rev. D, 77, 123514

Desjacques, V., Seljak, U., & Iliev, I.T., 2009, MNRAS, 396, 85

Desjacques, V., & Seljak, U., 2009, arXiv:0907.2257

Gill, S.P.D., Knebe, A., & Gibson, B.K., 2004, MNRAS, 351, 399

Komatsu, E., et al., 2009, ApJS, 180, 330

Matarrese, S., & Verde, L., 2008, ApJ, 677, L77

Seljak, U., 2009, Phys. Rev. Lett., 102, 021302

Seljak, U., Hamaus, N., & Desjacques, V., 2009, arXiv:0904.2963

Slosar, A., Hirata, C., Seljak, U., Ho, S., & Padmanabhan, N., 2008, JCAP, 8, 31

Springel, V., 2005, MNRAS, 364, 1105

SF2A 2009
M. Heydari-Malayeri, C. Reylé and R. Samadi (eds)

BIMODAL GAS ACCRETION IN THE HORIZON-MARENOSTRUM GALAXY FORMATION SIMULATION

Ocvirk, P.[1], Pichon, C.[2] and Teyssier, R.[3]

Abstract. This proceedings summarizes some of the findings of Ocvirk et al. 2008. The physics of diffuse gas accretion and the properties of the cold and hot modes of accretion onto proto-galaxies between z=2 and z=5.4 is investigated using the large cosmological simulation performed with the RAMSES code on the MareNostrum supercomputing facility. Galactic winds, chemical enrichment, UV background heating and radiative cooling are taken into account in this very high resolution simulation. Using *accretion–weighted temperature histograms*, we have measured the transition halo masses characterizing the existence of stabel hot shocks $\mathrm{M_{shock}}$ and filamentary gas accretion $\mathrm{M_{stream}}$.

We find a hot shock transition mass of $\mathrm{M_{shock}} = 10^{11.6}\mathrm{M_\odot}$, with no significant evolution with redshift. Conversely, we find that $\mathrm{M_{stream}}$ increases sharply with z. This is in striking agreement with the analytical predictions of Birnboim & Dekel 2003 and Dekel & Birnboim 2006, *if we correct their metallicity assumptions to those we measure when computing radiative cooling rates*. We therefore find that metal enrichment of the intergalactic medium is a key ingredient in determining the transition mass from cold to hot dominated diffuse gas accretion.

1 Introduction

It is currently accepted that the ΛCDM theory provides a framework with which a large number of observed galaxy properties can be interpreted. This framework is referred to as the "hierarchical scenario of galaxy formation". Most importantly, this framework explains why many of these properties (physical sizes, black hole mass, bulge mass...) are found to correlate simply with galaxy mass. Amidst this apparently simple scaling of galaxy properties with mass, the discovery of a bimodality in the colour distribution of Sloan Digital Sky Survey (SDSS) galaxies Kauffmann et al. 2003 stood unexpected and at odds with the predictions of hierarchical galaxy formation. Indeed, in the simplest flavours of the hierarchical buildup of galaxies, massive ellipticals would still be blue and forming stars at $z = 0$. The fact that observed elliptical galaxies do not obey this fundamental prediction is the origin of the so-called "anti-hierarchical" behaviour of massive red galaxies (Rasera & Teyssier 2006). This observation is further supported by the analysis of spectroscopic data, using star formation history reconstruction methods (Panter et al. 2003, Ocvirk et al. 2006a,b). Since these giant galaxies are in the form of apparently "dead" (i.e. no ongoing star formation) red elliptical galaxies, the quest has been ongoing for several years to find the origin of this halt in the star formation process (also refered to as "star formation quenching").

In this respect, the detailed analysis of diffuse gas accretion around star forming galaxies is of great interest because it can provide a form of self-regulation. The seminal paper of Birnboim & Dekel 2003 (hereinafter BD03) investigates the stability of hot accretion shocks around disc galaxies, showing that such shocks can exist only for haloes more massive than $\approx 10^{11.5}\mathrm{M_\odot}$. In an ideal spherical flow, this hot shock would prevent cold gas from reaching the disc (or at least slow it down) and thus is likely to affect star formation. Dekel & Birnboim 2006 (hereinafter DB06) extended this approach to the study of the stability of cold streams ("filaments") within the shock–heated halo gas. They showed that the observed transition mass from blue to red galaxies at $z \simeq 0$ could be matched to the critical mass at which a stable accretion shock can exist and that stable filaments would disappear around z=1.5. These findings were also driven and further confirmed by numerical simulations

[1] Astrophysikalisches Institut Potsdam, an der Sternwarte 16, D-14482 Potsdam, Germany
[2] Institut d'Astrophysique de Paris, 98bis boulevard Arago, 75014 Paris, France
[3] Service d'Astrophysique, CEA Saclay, Bâtiment 709, 91191 Gif-sur-Yvette Cedex

of high redshift galaxy formation based on smoothed particle hydrodynamics (SPH), as in Kereš et al. 2005. DB06 actually presented the rise of stable hot shocks not as the origin of the quenching but only as a necessary condition for an efficient AGN feedback.

The stability of accretion shocks and filaments is driven by the competition between compressive heating and radiative cooling. The latter is itself set by the metallicity of the gas, which is thus a crucial parameter. However self-consistent modelling of the chemical enrichment in cosmological simulation is a notoriously difficult problem. In this paper, we propose to use the HORIZON-MareNostrum galaxy formation simulation, which includes a treatment of chemical enrichment, to analyse the accretion of diffuse gas on forming galaxies and revisit the accretion shocks and filamentary accretion scenarios proposed in earlier studies.

The outline of this paper is as follows: first we describe in Sec. 2 our methodology, in terms of numerical techniques and statistical measurements. We then present in Sec. 3 our main results concerning the physical properties of the accreted gas. Our findings are then discussed in the framework of earlier theoretical modelling in Sec. 4.

2 Methodology

2.1 The MareNostrum simulation

We have used the adaptive mesh refinement code RAMSES (Teyssier 2002) implementing metal-dependent cooling and UV heating using the Hardt and Madau background model. We have incorporated a simple model of supernovae feedback and metal enrichment using the implementation decribed in Dubois & Teyssier 2008. For high–density regions, we have considered a polytropic equation of state with a 5/3 index to model the complex, multi-phase and turbulent structure of the ISM in a simplified form (see Dubois & Teyssier 2008): the ISM is defined as gas with a density greater than $n_0 \simeq 0.1$ H/cm^3. Star formation has also been included, for ISM gas only ($n_{\mathrm{H}} > n_0$), by spawning star particles at a rate consistent with the Kennicutt law derived from local observations of star forming galaxies. The simulation was started with a base grid of 1024^3 cells and the same number of dark matter particles. The simulation was ran for a ΛCDM universe with $\Omega_M = 0.3$, $\Omega_\Lambda = 0.7$, $\Omega_B = 0.045$, $H_0 = 70$ km/s/Mpc, $\sigma_8 = 0.9$ in a periodic box of 50 h^{-1}Mpc. Our dark matter particle mass is $m_{\mathrm{part.}} \simeq 8 \times 10^6\ M_\odot$, and our spatial resolution 1 kpc *physical.* The simulation was run for 4 weeks dispatched over a full year, reaching a final redshift $z = 1.5$, where the total number of star particles at the was more than 2×10^5, and the total number of AMR cells was larger than 5×10^9.

2.2 Mass-accretion-weighted histograms

We have built from our simulation data a Friend–Of–Friend (FOF) halo catalogue. We put each analysed halo at rest by subtracting the mass-weighted gas velocity in a 0.5R$_{\mathrm{vir}}$ sphere. We use temperature and density probability distribution functions, and we weight the contribution to each temperature and density bin by the local accretion rate. In this way, static regions will be discarded from the analysis, while large radial velocity regions will dominate the signal, emphasizing the properties of the material being accreted. In order to explore the radial dependence of the properties of the accreted gas, we perform our measurements on a number of concentric shells spanning $[0.2-1]$R$_{\mathrm{vir}}$. In our model, the star–forming dense ISM is defined as $n_{\mathrm{H}} \geq 0.1$H/cm^3. In order to focus on smooth gas accretion rather than merging, we remove from our spherical analysis all pixels whose density exceeds this theshold.

3 Properties of diffuse gas accretion

We computed the accretion-weighted PDFs for several hundred haloes spanning dark matter masses between 10^{10}M$_\odot$ and 10^{13}M$_\odot$ between $2 \leq z \leq 5$. We then co-added (stacked) these distributions for haloes of the same mass range in order to produce an "average" PDF for a given mass scale, which we use to discuss the physical properties of the accretion flow.

3.1 Bimodality in the temperature distribution

Fig. 1 shows several radially–averaged accretion–weighted stacked histograms for haloes from 10^{10} to 10^{13}M$_\odot$ taken from the $z = 4$ snapshot of the simulation. We see that the accretion pattern involves two main distinct

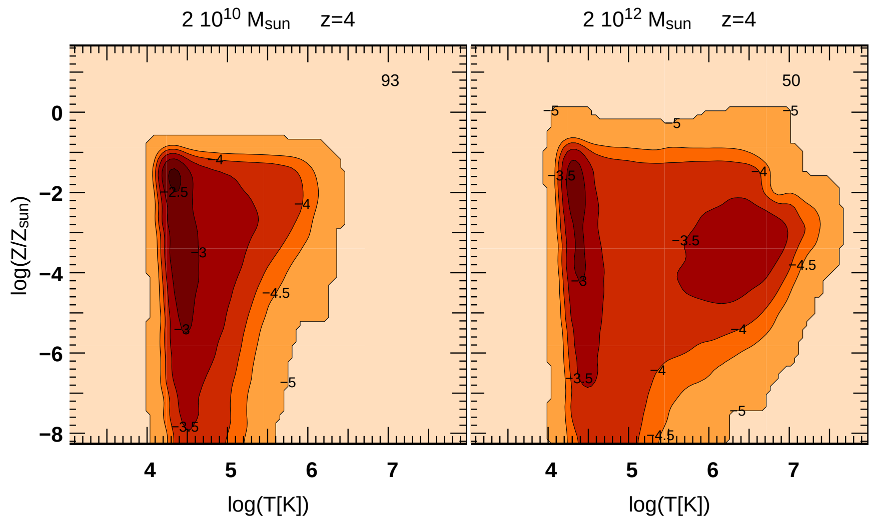

Fig. 1. Radially averaged Accretion–weighted PDFs for 2 mass bins centered on 2×10^{10} (*left*) to $2 \times 10^{12} \mathrm{M}_\odot$ (*right*). The numbered labels on the contours give the logarithm of the PDF. When the hot phase is well developed, there is a clear bimodality in temperature.

components:

1. A cold component spanning a large range in metallicity, associated with filaments (metal-poor) as well as the close vicinity of galaxy satellites (metal-rich).

2. A hot, metal-poor component, the temperature and contribution of which increases sharply with halo mass.

3.2 Two critical masses and 3 regimes of diffuse gas accretion

Marginalizing the accretion rate over metallicity and integrating over temperature on the hot and cold temperature domains yields the hot and cold accretion rate respectively. Dividing by the total accretion rate at the chosen radius gives the contributions of the hot and cold mode to the total accretion rate.

The top left panel of Fig. 2 displays the fractions computed from the accretion-weighted histograms averaged over the entire halo (between $0.2\mathrm{R}_{\mathrm{vir}}$ and $\mathrm{R}_{\mathrm{vir}}$). The bottom left panel of Fig. 2 shows these fractions measured at radius $0.2R_{\mathrm{vir}}$ (galaxy vicinity) as a function of mass for various redshifts. A common feature of these plots is the increasing importance of the hot accretion mode with increasing mass, and the corresponding decreasing contribution of the cold mode, as could be foreseen from Fig. 1. The mass at which hot and cold contributions are equal defines a critical mass marking the transition between two accretion regimes.

This critical mass increases sharply with redshift, if the entire halo is considered. This evolution is the signature of a gradual disappearance of cold radially extended features, like filaments, in the massive haloes between $z = 5.4$ and $z = 2$. Therefore we note $\mathrm{M}_{\mathrm{stream}}$ this transition mass. On the contrary, the corresponding critical mass defined using the $0.2\mathrm{R}_{\mathrm{vir}}$ measurements shows only a slow variation with redshift, if any. It indicates that there is a stable hot shock in the inner parts of the halo as soon as $\mathrm{M}_{\mathrm{DM}} \geq 10^{11.5-12}\mathrm{M}_\odot$, while the outer part of the halo can still be dominated by cold accretion. We note $\mathrm{M}_{\mathrm{shock}}$ the transition mass where hot and cold fractions of the accreted gas are equal at $0.2\mathrm{R}_{\mathrm{vir}}$. The right panel of Fig. 2 summarizes the evolution of these transition masses. The latter define 3 different regimes for diffuse gas accretion: a low mass cold accretion mode for $M < \mathrm{M}_{\mathrm{shock}}$, a purely hot mode for $M > \max(\mathrm{M}_{\mathrm{shock}}, \mathrm{M}_{\mathrm{stream}})$, and a mode featuring cold streams flowing through hot shocked gas for $\mathrm{M}_{\mathrm{shock}} < M < \mathrm{M}_{\mathrm{stream}}$. The latter mode exists in our simulation only for $z > 2.5$. These regimes and transitions agree with those found by DB06 provided that one tunes their metallicity assumption for the filaments to almost zero, as measured in the simulation.

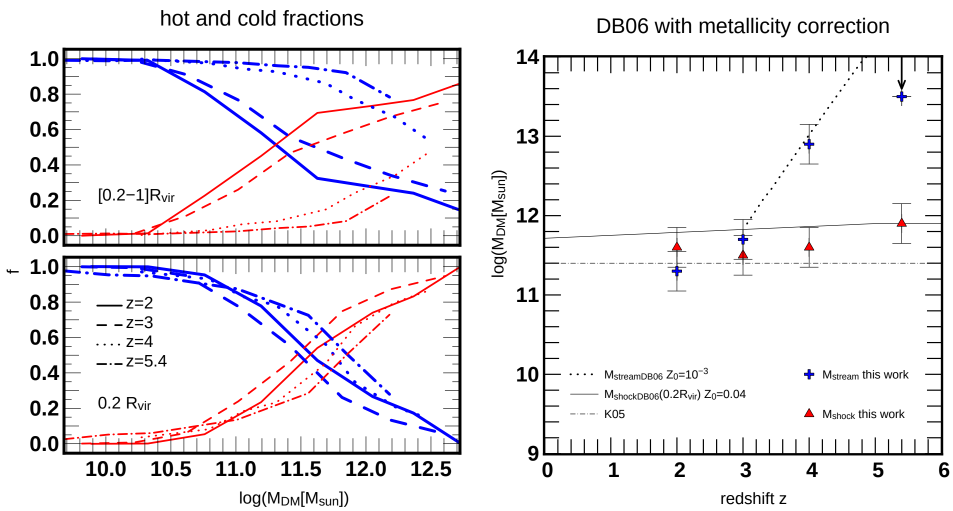

Fig. 2. *Left:* Evolution of the hot (thin line) and cold (thick lines) accreted gas mass fractions versus M_{DM} with redshift. Top: (integrated inwards down to $0.2R_{vir}$). Bottom: f_{cold} and f_{hot} on the $0.2R_{vir}$ sphere. Right: evolution of M_{shock} and M_{stream} with redshift, from our measurements and comparison to analytical modelling. The solid line shows DB06 prediction for $M_{shock}(0.2R_{vir})$ with a metallicity assumption $Z_0 = 0.02$, while the dotted line shows their prediction for M_{stream} with a metallicity assumption $Z_0 = 0.0003$. The dash dotted line shows the constant transition mass reported by Kereš et al. 2005.

4 Conclusions

We used the MareNostrum galaxy formation simulation to study the processes involved in gas accretion on galaxies. In agreement with DB06, we find that accretion proceeds in 3 different regimes: a cold accretion mode, prevailing at $M < M_{shock}$, a mode with a stable hot shock at low redshift and $M > M_{shock}$, and at high redshift, a regime where hot shocks and cold streams cohabit. However, at variance with DB06, the low metallicity of these cold streams results in their earlier disappearance, thereby showing the importance of taking chemical enrichment into account in cosmological simulations of galaxy formation.

References

Ocvirk, P., Pichon, C., Teyssier, R., 2008, MNRAS, 390, 1326

Kauffmann, G. et al., 2003, MNRAS, 346, 1055

Rasera, Y., Teyssier, R., 2006, A&A, 445, 1

Panter, B., Heavens, A. F., Jimenez, R., 2003, MNRAS, 343, 1145

Ocvirk, P., Pichon, C., Lançon, A., Thiébaut, E., 2006a, MNRAS, 365, 46

Ocvirk, P., Pichon, C., Lançon, A., Thiébaut, E., 2006b, MNRAS, 365, 74

Birnboim, Y., Dekel, A., 2003, MNRAS, 345, 349 (BD03)

Dekel, A., Birnboim, Y., 2006, MNRAS, 368, 2 (DB06)

Kereš D., Katz N., Weinberg D. H., Davé R., 2005, MNRAS, 363, 2

Teyssier R., 2002, A&A, 385, 337

Dubois Y., Teyssier R., 2008, A&A, 477, 79

SF2A 2009
M. Heydari-Malayeri, C. Reylé and R. Samadi (eds)

COSMOLOGICAL SIMULATIONS AND GRAVITATIONAL LENSING: STATISTICAL SIGNATURES OF SUBSTRUCTURES

Peirani, S.[1], Alard, C.[1], Pichon, C.[1], Gavazzi, R.[1] and Aubert, D.[2]

Abstract. The popular model of hierarchical structure formation in a universe dominated by cold dark matter, while quite successful in matching the observed large-scale density distribution, is currently facing a "small-scale crisis". For instance, the predicted abundance of satellites (or substructures) is more than an order of magnitude larger than the number of dwarf galaxies with comparable mass within the local group. This "missing satellite problem" represents then an ideal framework in order to test theoretical models. We present a new approach, based on numerical modelling and a perturbative theory, to study and characterize statistical signatures of substructures in the strong lensing regime.

1 Introduction

The cold dark matter (CDM) paradigm (Cole et al. 2005 and references therein) has led to a successful explanation of the large-scale structure in the galaxy distribution on scales $0.02 \leq k \leq 0.15$h Mpc^{-1}. In spite of these impressive successes, there are still discrepancies between simulations and observations on scales ≤ 1 Mpc, extensively discussed in the recent literature. For instance, one problem that requires closer examination concerns the large number of sub-L_* subhalos present in simulations but not observed (Kauffmann, White & Guiderdoni 1993; Moore et al. 1999; Klypin et al. 1999).

This "missing satellite problem" remains an ideal framework to test cosmological models. During the past years, different methods have been employed in order to study the gravitational potential of groups or clusters of galaxies, for instance through their X-ray lines emission of hot gas in the intra-cluster medium or through lensing considerations. However, while lensing directly probes the mass distribution in those objects, the other methods rely more often than not on strong hypotheses on the dynamical state of the gas and interactions between baryons and dark matter. For example, the gas is supposed to be in hydrostatical equilibrium in the gravitational potential well created by dark matter halo, while spherical symmetry is assumed.

In Peirani et al. (2008), we have studied the effects induced by substructures on the deflection potential of dark matter halos in the strong lensing regime. The presence of substructures follows from the capture of small satellites which have not yet been disrupted by tidal forces and/or suggests that the relaxation of halos is not totally finished. One interesting alternative approach is to treat all deviations from a circularly symmetrical potential as small perturbations (Alard 2007, 2008) defining the location where multiple extended images will form (see Fig. 1).

This paper is organized as follows: section 2 first sketches the pertubative lens solution while section 3 presents our main results on the statistics of perturbations.

2 A perturbative theory

The general lens equation, relating the position of an image on the lens plane to that of the source on the source plane can be written in polar coordinates as

$$\mathbf{r_s} = \Big(r - \frac{\partial\phi}{\partial r}\Big)\mathbf{u_r} - \Big(\frac{1}{r}\frac{\partial\phi}{\partial\theta}\Big)\mathbf{u}_\theta\,, \tag{2.1}$$

[1] Institut d'Astrophysique de Paris, 98 bis Bd Arago, 75014 Paris, France -
Unité mixte de recherche 7095 CNRS - Université Pierre et Marie Curie.
[2] Observatoire Astronomique de Strasbourg, 11 Rue de l'Université, 67000 Strasbourg, France.

where $\mathbf{r}_s$ is the source position, and r, $\mathbf{u}_r$ and $\mathbf{u}_\theta$ are the radial distance, radial direction and orthoradial direction respectively. Here $\phi(r,\theta)$ is the projected potential. The basics ideas of the perturbative approach is to expand equation (2.1) by introducing i) small displacements of the source from the origin and ii) non-circular perturbation of the potential, ψ which can be described by:

$$r_s = \epsilon r_s\,, \quad \text{and} \quad \phi = \phi_0 + \epsilon\psi\,, \tag{2.2}$$

where ϵ is small number: $\epsilon \ll 1$. To obtain image positions (r,θ) by solving equation (2.1) directly, may prove to be analyically impossible in the general case. It is then easier to find perturbative solution by inserting equation (2.2) into equation (2.1). And using the Taylor expansion of ϕ:

$$\phi = \phi_0 + \epsilon\psi = \sum_{n=0}^{\infty}[C_n + \epsilon f_n(\theta)](r-1)^n \quad \textit{where} \quad C_n \equiv \frac{1}{n!}\Big[\frac{d^n\phi_0}{dr^n}\Big]_{r=1} \; \textit{and} \quad f_n(\theta) \equiv \frac{1}{n!}\Big[\frac{\partial^n\psi}{\partial r^n}\Big]_{r=1}, \tag{2.3}$$

one can finally obtain the general perturbative response (Alard 2007):

$$\mathbf{r_s} = (\kappa_2\delta r - f_1)\mathbf{u}_r - \frac{\mathrm{d}f_0}{\mathrm{d}\theta}\mathbf{u}_\theta \quad \textit{with} \quad \kappa_2 = 1 - 2C_2. \tag{2.4}$$

In the perturbative theory, all deviations from the perfect ring configuration is in two fields, f_1 and $\frac{\mathrm{d}f_0}{\mathrm{d}\theta}$: f_1 gives informations of the mean position of the contour lines whereas $\frac{\mathrm{d}f_0}{\mathrm{d}\theta}$ gives informations about the image width along the radial direction (see Fig 2).

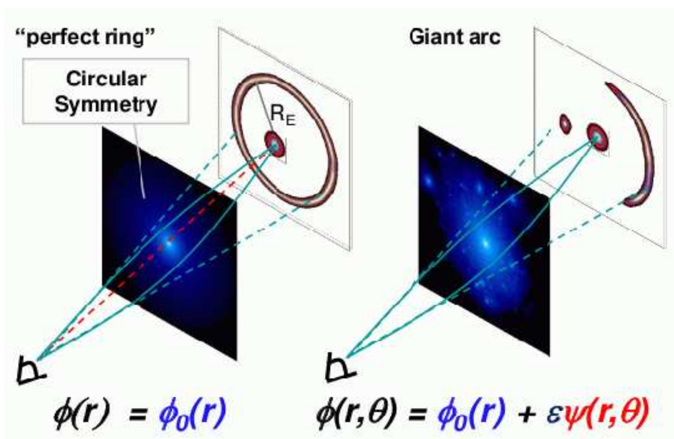

Fig. 1. Sketch about the Einstein ring (left part) and the giant arc (right part) configurations.

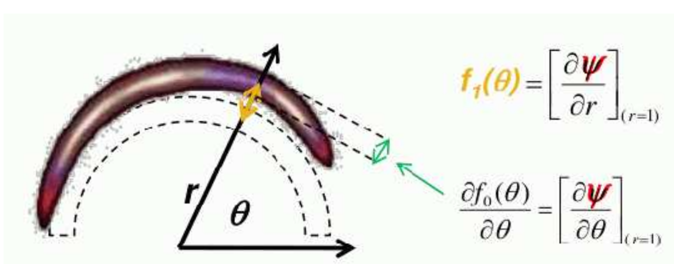

Fig. 2. Sketch about the interpretation of f_1 and $\frac{\mathrm{d}f_0}{\mathrm{d}\theta}$ in term of deviations from the perfect ring.

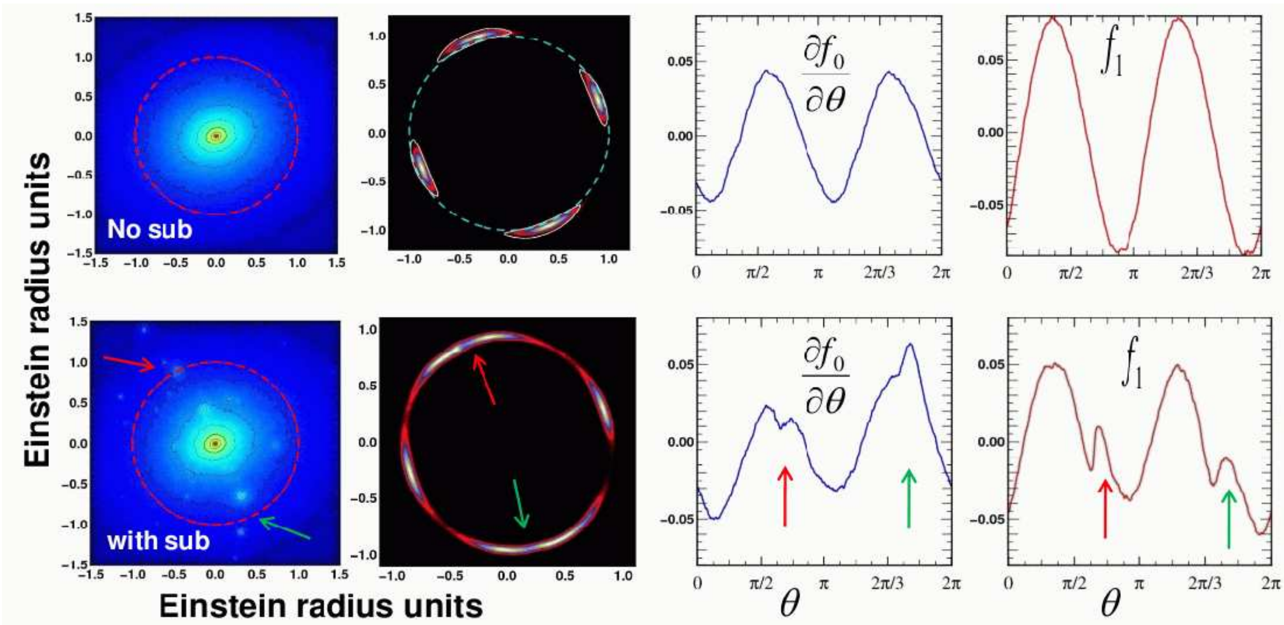

Fig. 3. Projected density map of a lens modelled by a dark matter halo with and without substructures. The respective solutions from ray-tracing simulations are plotted in the second column. Finally, columns 3 and 4 show the evolution of f_1 and $\frac{\mathrm{d}f_0}{\mathrm{d}\theta}$for each associated lens.

3 Numerical modelling and statistical effects of substructures

Lenses are modelled either by dark matter halos extracted from cosmological simulations or via toy models. The advantage of toy models is to reach a higher resolution and to allow us to study the influence of free parameters such as the inner profiles of substructures which are expected to play a central role here. For instance, the sample A represents our reference catalogue in which all halos have no substructure. For each of them, we introduce a fraction of subtructures. These halos are classified in catalogues B and C according the definition of inner density profile of clumps. For example, each halo from samples B1 and B2 have 15% of substructures with an inner profile represented by a cusp whereas lenses catalogues C1 and C2 have substructures represented by a core profile with $C_{sub} = 5$ and $C_{sub} = 8$ respectively.

In Figure (3), we show the projected mass density of the same lens with and without substructures near the Einstein radius, the image's solution obtained from ray-tracing (when an elliptical source is placed at the origin) and the evolutions of f_1 and $\frac{\mathrm{d}f_0}{\mathrm{d}\theta}$. As expected, when no substructure are considered, we obtain four distinct arcs in a cross configuration. From a theoretical point of view, it is easy to show that the functions $f_1$and $\frac{\mathrm{d}f_0}{\mathrm{d}\theta}$are proportional to $\propto \cos(2\theta + \psi)$ and $\propto \sin(2\theta + \psi)$ respectively. These functionnal form are recovered in our experiment and shown in Figure (3).

When substructures are present, the shape of images is significantly altered. First, we notice that the positions of substructure tend to break the ellipticity of the halo center. Thus, it is not surprising that the shape of the image is approaching a ring in that case. Moreover, it is interesting to see that the position of one substructure (at the top left of the figure) is exactly at the Einstein radius. This produces an alteration of the luminosity. This effect can be clearly seen when comparing the perturbative fields $f_1$and $\frac{\mathrm{d}f_0}{\mathrm{d}\theta}$relative to the lens L_1 in Figure (3). For instance, we can see two clear bumps in the evolution of $\frac{\mathrm{d}f_0}{\mathrm{d}\theta}$. The second one ($\theta > 2\pi/3$) is produced by substructures in the lower right part and induced an alteration of the luminosity again.

The angular functions $f_1$and $\frac{\mathrm{d}f_0}{\mathrm{d}\theta}$can be characterized by their Fourier expansion:

$$\frac{df_0(\theta)}{\mathrm{d}\theta} = \sum_n \langle a_n^0 \rangle \cos\left(n\theta + \phi_n^0\right) , \tag{3.1}$$

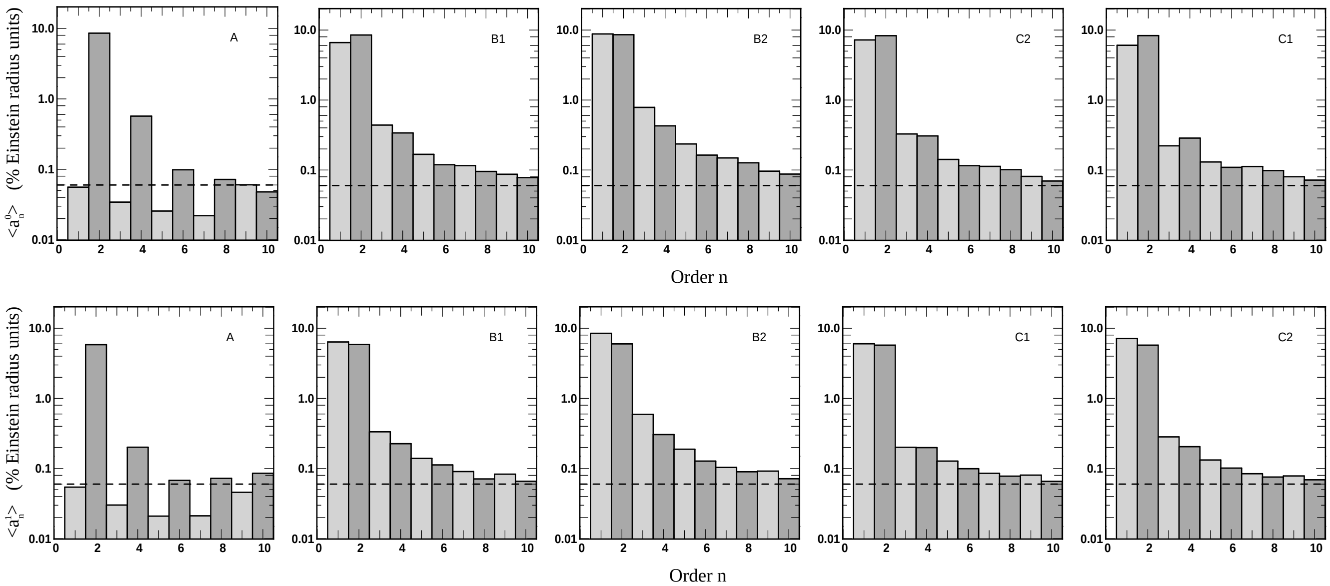

Fig. 4. Variation of mean amplitudes $\langle a_n^0 \rangle$ (first line) and $\langle a_n^1 \rangle$ (second line) derived from multipole expansions of $\frac{\mathrm{d}f_0}{\mathrm{d}\theta}$ and f_1 respectively for lenses catalogue A, B_1, B_2, C_1 et C_2. The dashed lines represent limits at 1σ.

$$f_1(\theta) \quad = \quad \sum_n \langle a_n^1 \rangle \cos\left(n\theta + \phi_n^1\right) \ , \tag{3.2}$$

where $P_i(n)$, $i = 1, 2$ correspond to associated power spectra. We have derived the multipole expansion of $f_1$and $\frac{\mathrm{d}f_0}{\mathrm{d}\theta}$for each halo of the different catalogues and we focus in the following on the mean amplitudes $\langle a_n^0 \rangle$ and $\langle a_n^1 \rangle$ obtained (see Fig. 4). When substructures are absent, both harmonic power spectra of $f_1$and $\frac{\mathrm{d}f_0}{\mathrm{d}\theta}$are dominated by the second order mode, which is characteristic of a projected elliptical potential. The situation is totally different when substructures are taken into account. First, we notice that first mode ($n = 1$) increase for lenses L_1 and L_2. This is due to the fact that we kept the same definition of the mass center between the three lenses. The random position of subtructures generates a non zero impact parameter which affect the first order mode. Moreover, since substructures tend to break the ellipticity of the halo center in the present case, one expects that the second mode decreases. However, the most interesting feature is that modes corresponding to $n \geq 3$ increase when substructures are present.

4 Conclusions and perspectives

The upcoming generation of high spatial resolution instruments dedicated to cosmology (*e.g.* JWST, DUNE, SNAP, ALMA) will provide us with an unprecedented number of giant arcs at all scales. The large samples expected will make standard lens modellings untractable and require the development of new methods able to capture the most relevant source of constraints for cosmology. In this respect, the perturbative method we present here may turn out to be a promising research line.

References

Alard, C. 2007, MNRAS, 382, L58

Alard, C. 2008, MNRAS, 388, 375

Cole, S., et al. 2005, MNRAS, 362, 505

Kauffmann G., White S. D. M. & Guiderdoni B., 1993, MNRAS 264, 201

Klypin A., Kravtsov A. V., Valenzuela O. & Prada F., 1999, ApJ 522, 82

Moore B., Ghigna S., Governato F., Lake G., Quinn T., Stadel J. & Tozzi P., 1999, ApJ 524, L19

Peirani, S., Alard, C., Pichon, C., Gavazzi, R., & Aubert, D. 2008, MNRAS, 390, 945

SF2A 2009
M. Heydari-Malayeri, C. Reylé and R. Samadi (eds)

COSMOLOGICAL SIMULATIONS AND GALAXY FORMATION: APPLICATIONS TO GIRAFFE

Peirani, S.[1], Hammer, F.[2], Flores, H.[2], Yang, Y.[2] and Athanassoula, E.[3]

Abstract. We compare the morphological and kinematic properties of massive galaxies at z=0.4-0.75 obtained by the GIRAFFE spectrograph, to those derived from the merger of two spiral galaxies described by N-body simulations, including a star formation prescription. The study of these systems is particularly interesting to the understanding of the connection between mergers and bars, as well as the properties and fate of this system in relation to disk galaxy formation.

1 Observations

The VLT large program entitled IMAGES ("Intermediate-Mass Galaxy Evolution Sequence", Yang et al. 2008) is gathering high quality kinematics for a representative sample of ~ 100 massive galaxies at $z = 0.4 - 0.75$ and with $MJ(AB) \leq -20.3$. Using the GIRAFFE spectrograph at the VLT, the kinematic properties of 65 of these galaxies, for instance J033239.72-275154.7, a galaxy we study here, have been derived.

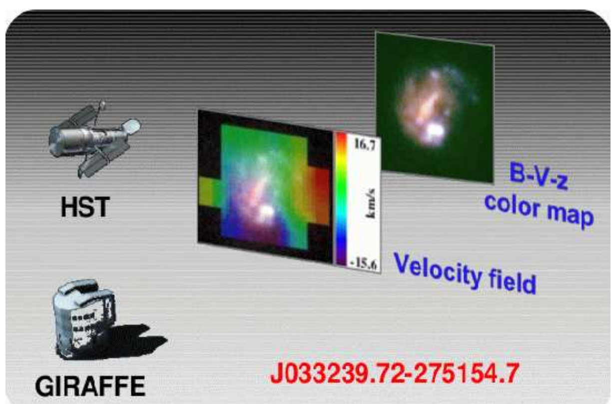

Fig. 1. Sketch of the observations of J033239.72-275154.7 through The HST and the GIRAFFE spectrograph.

This galaxy lies at $z = 0.41$, has a stellar mass of $2.0 \times 10^{10} M_{\odot}$, a K-band magnitude of $M_K = -20.94$ and its center is dominated by an elongated structure, most likely a giant thin bar of semi-major axis 6 kpc. This bar is embedded within a diffuse region, which is probably a disk. At the bottom of the galaxy, there are two bright adjacent knots, which dominate the rest-frame UV light. And have the color of a pure starburst. The velocity field (VF) is obviously complex since the kinematical major axis is almost parallel to the bar and it is offset by more than one GIRAFFE pixel from the bulge, towards the prominent blue knots (in the bottom).

Could merging of the two bright knots with J033239.72-275154.7 be compatible with the formation of a giant bar with a relatively blue color? It's what we propose to investigate with a numerical study.

[1] Institut d'Astrophysique de Paris, 98 bis Bd Arago, 75014 Paris, France -
Unité mixte de recherche 7095 CNRS - Université Pierre et Marie Curie.
[2] GEPI, Observatoire de Paris, CNRS, University Paris Diderot, 5 place Jules Janssen, 92190 Meudon, France
[3] LAM, UMR6110, CNRS/Université de Provence, Technopôle de Marseille-Etoile, 38 rue Frédéric Joliot Curie, 13388 Marseille Cédex 20, France

2 Numerical Simulations and results

We use idealized hydrodynamical N-body simulations of the merger of two spiral galaxies using the code GADGET2 (Springel et al. 2005) with added prescriptions for cooling, star formation and feedback from Type Ia and II supernovae.

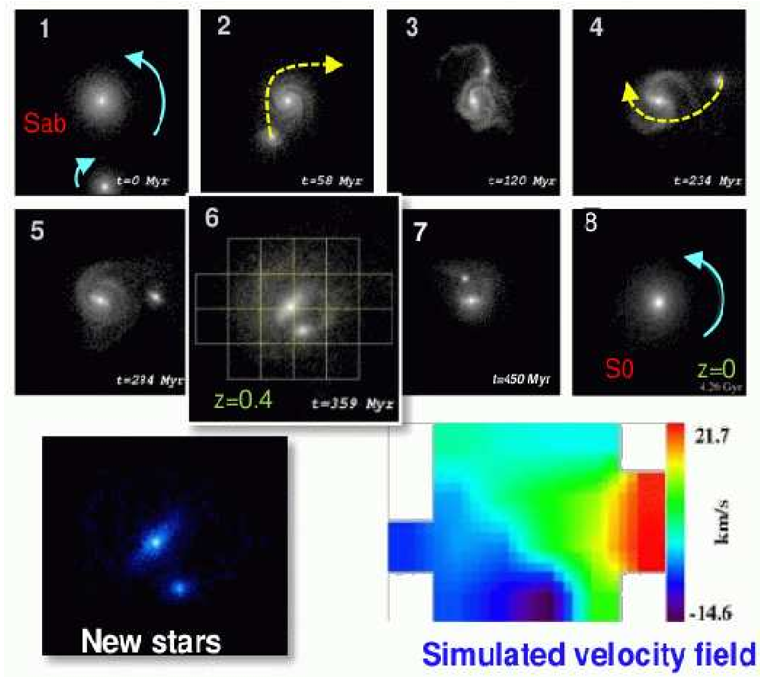

Fig. 2. Time evolution of the projected star number density. The light blue arrows indicate the specific rotation of each galaxy, while the yellow dashed lines show the motion of the satellite. In panel 6, we superposed the GIRAFFE grid. Each frame is 40 kpc × 40 kpc in size. The lower left panel shows the projected distribution of newly formed stars at $t = 0.36$ Gyr whereas the lower right panel shows the simulated velocity field.

In Peirani et al. 2008, we found that the general morphological shape and most of the dynamical properties of the object can be well reproduced by a model in which the satellite is initially put in a retrograde orbit and the mass ratio of the system is 1:3. In such a scenario, a bar forms in the host galaxy after the first passage of the satellite where an important fraction of available gas is consumed in an induced burst. In its later evolution, however, we find that J033239.72-275154.7, whose major progenitor was an Sab galaxy, will probably become a S0 galaxy. This is mainly due to the violent relaxation and the angular momentum loss experienced by the host galaxy during the merger process, which is caused by the adopted orbital parameters.

This result suggests that the building of the Hubble sequence is significantly influenced by the last major collision. In the present case, the merger leads to a severe damage of the disk of the progenitor, leading to an evolution towards a more bulge dominated galaxy. The main objective is now to extend this kind of analysis to the whole sample of galaxies observed in order to compare with closer galaxies and draw a complete picture of the evolution of galaxies over the past six to eight billions years, that is, over half the age of the Universe.

References

Peirani, S., Hammer, F., Flores, H., Yang, Y., & Athanassoula, E. 2009, A&A, 496, 51

Springel, V. 2005, MNRAS, 364, 1105

Yang, Y., et al. 2008, A&A, 477, 789

SF2A 2009
M. Heydari-Malayeri, C. Reylé and R. Samadi (eds)

INSIGHT INTO GALACTIC STRUCTURE AND EVOLUTION FROM THE POPULATION SYNTHESIS APPROACH

Robin, A.C.[1], Marshall, D.J.[2], Reylé, C.[1] and Schultheis, M.[1]

Abstract. The population synthesis approach aims at understanding Galactic structure and evolution, and testing formation scenarios. Applied to the Milky Way, this approach allows the interpretation of large scale surveys and is able to place constrains on our knowledge of the Galaxy. Detailed comparisons between large scale surveys and model predictions have led to new constraints on Galactic structure and evolution of the stellar populations. Recent results concerning the Galactic warp and the study of the Galactic central region have been obtained by adjusting model parameters to the 2MASS point source catalogue. The stellar warp is found to be asymmetric and different from the HI warp. We emphasize the existence of two structures in the Galactic central region: a triaxial outer bulge coexisting with a narrow boxy bar.

1 Introduction

Stellar populations are good tracers of Galactic structure; they are numerous, nearly everywhere in the Galaxy and they furnish a number of important indices for the understanding of Galactic structure and evolution history, particularly distance indicators, age estimates and kinematical tracers. However these indices are very difficult to calibrate. The synthesis approach can be used to assert the validity of these calibrations and the consistency of the overall scheme. When scenarios of Galaxy formation and evolution are inferred from suitable constraints, tests of these scenarios can be done using population synthesis models whose predictions can be directly compared with observations. This synthetic approach ensures that biases have been correctly taken into account and that the scenario is compatible with many kinds of constraints.

In recent years wide surveys have been obtained from optical and near-infrared photometry thanks to wide mosaic camera of CCDs, from spectroscopy, and helped by the availability of dedicated telescopes and multi-object spectrometers, both from the ground and from space. All these data sets benefit Galactic evolution studies and provide constraints on the population synthesis approach. Among them, the 2MASS survey (Skrutskie et al. 2006) has provided one of these rich data sets from which substantial results have been obtained.

Here we report on two analysis of Galactic structure features which have been done applying the population synthesis approach onto the 2MASS data. In Sect. 2 we present the model and the population synthesis approach. In Sect. 3 we describe the data used and the method used to compute the extinction. In Sect. 4 we present our results concerning the external stellar disc of the Galaxy as well as its central regions. Conclusions and perspectives are given in Sect. 5.

2 The population synthesis approach

The population synthesis approach aims at assembling scenarios of galaxy formation and evolution, theories of stellar formation and evolution, models of stellar atmospheres and dynamical constraints, in order to make a consistent picture explaining currently available observations of different types (photometry, astrometry, spectroscopy) at different wavelengths. The validity of any Galactic model is always questionable, as it describes a smooth Galaxy, while inhomogeneities exist, either in the disc or the halo. The issue is not to make a perfect

[1] Institut Utinam, Observatoire de Besançon, BP1615, F-25010 Besançon cedex
[2] Département de physique, de génie physique et doptique et Centre de recherche en astrophysique du Québec, Université Laval, Quebec, QC, G1V 0A6, Canada

model that reproduces the known Galaxy at any scale. Rather one aims to produce a useful tool to compute the probable stellar content of large data sets and therefore to test the usefulness of such data to answer a given question in relation to Galactic structure and evolution. Modelling is also an effective way to test alternative scenarios of galaxy formation and evolution.

The main scheme of the model is to reproduce the stellar content of the Galaxy, using some physical assumptions and a scenario of formation and evolution. We essentially assume that stars belong to four main populations : the thin disc, the thick disc, the stellar halo (or spheroid), and the outer bulge. The modelling of each population is based on a set of evolutionary tracks, assumptions on density distributions, constrained either by dynamical considerations or by empirical data, and guided by a scenario of formation and evolution, that is to say assumptions on the initial mass function (IMF) and the star formation rate (SFR) history for each population. The originality of the Besançon model, as compared to a few other population synthesis models presently available for the Galaxy, is the dynamical self-consistency. The Boltzmann equation allows the scale height of an isothermal and relaxed population to be constrained by its velocity dispersion and the Galactic potential (Bienaymé et al.1987). The use of this dynamical constraint avoids a set of free parameters and gives the model an improved physical credibility. More detailed descriptions on these constraints can be found in Robin et al. (2003).

3 2MASS survey and extinction distribution

The 2MASS survey Skrutskie et al. (2006) is a powerful tool to study large scale structure in the Galaxy, particularly in the Galactic plane because NIR data are well suitable to study stellar population in regions of medium to high extinction. The first effect visible in the star density distribution close to the Galactic plane is due to the dust, even at near-infrared wavelengths. Without a good estimate of the extinction and of its distance it is nearly impossible to understand the structure in the thin disc. Hence it is essential to start by constructing a three dimensional extinction map of the Galaxy.

Extinction is so clumpy in the Galactic plane that it determines for a great part the number density of stars, more than any other large scale stellar structure. So, it is possible to extract information about the distribution of the extinction from photometry and star counts. Marshall et al. (2006) have shown that the 3D extinction distribution can be inferred from the stellar colour distributions from the 2MASS survey. Using stellar colours in J-K as extinction indicators and assuming that most of the model prediction deviations on small scales from observed colours arises from the variation of extinction along the line of sight, we built a 3D extinction map of the galactic plane ($-10 < b < 10$ and $-100 < l < 100$). The final resolution in longitude and latitude is 15 arcmin and the resolution in distance varies between 100 pc to 1 kpc, depending on stellar density and on the dust distribution along the line of sight. The resulting 3D extinction map furnishes an accurate description of the large scale structure of the disc of dust. These maps show clearly the warp in the dust distribution in the external disc. The method has now been extended to external regions (Marshall et al, in preparation).

4 Constraining Galactic structure and formation

Using this extinction map, a comparison between simulations from the Besançon Galaxy model and 2MASS star counts shows that the model reproduces the data with a high degree of realism in the plane, even without modelling the spiral arms Robin et al. (2008). It means that either the spiral structure does not have a high contrast or that 2MASS data are not a good tracer for these arms. This is expected as the model estimates that 2MASS counts are dominated by red clump giants which are rather old stars (90% have ages larger than 1 Gyr, having made at least 4 revolutions around the Galaxy) and have mainly lost the memory of their birth place (although suitable colour selections would probably place more constraints on spiral arms).

4.1 The stellar warp

Looking at 2MASS star counts in external regions, the warp is easily visible on both sides of the Galaxy. Thus we expect to be able to constrain a model of the stellar warp using this data set. In Reylé et al. (2009) we investigate the shape of the warp as seen from stellar populations. We first attempted to model the warp as a simple S-shape symmetrical warp with a slope taken from the literature Gyuk et al. (1999) (0.18), a line of node being the sun-Galactic center direction (as seen in HI). This investigation showed that the simulated warp departs too quickly from the plane (the slope value of the default model is too high). Further, it shows that the warp is not symmetrical. A simple S-shape warp reproduces well the northern side of the warp (positive longitudes) with a slope of 0.09, but not the southern side. On the southern side no simple S-shape warp reproduce the data. We also attempted to fit star counts with alternative warp models, in particular non-axisymmetric ones, like the Levine et al. (2006) model which represents in detail the HI asymmetric warp. The results how that the stellar warp is not similar to the HI warp. The agreement is not satisfactory on the southern part of the warp (negative longitudes).

The dust warp have been detected and measured by Marshall et al. (2006) in their study of the 3D extinction distribution. A comparison of the warp slope as measured in dust, HI gas and stars shows that the stellar warp slope is significantly smaller than the HI gas warp, by a factor of about 2. There is an indication that the HI gas is the strongest, the dust warp seems a bit smaller and the stellar warp is significantly smaller. However if we limit the investigation to short distances (R<12 kpc) the differences between various warp models are less important. Our result is well in agreement with studies in external galaxies, where Van der Kruit (2007) noted that stellar discs look flatter than gas layers. This is understandable in a scheme where the HI warps start close to the truncation radius (truncation seen in the exponential distribution of stars which may be due to a threshold effect in the star formation efficiency).

4.2 The central region of the Galaxy : bar and/or bulge ?

Since the discovery of a triaxial structure in the Galactic central regions from COBE, numerous attempts have been done in order to characterize this structure and to investigate its origin. It is still unclear whether this structure, often called the outer bulge but sometimes named the bar, had its origin from the early formation of the spheroid (as a typical bulge, similar to ellipsoidal galaxies) or was formed by a bar instability later in the disc. The question of formation history is crucial and necessary to investigate, as our Galaxy is a benchmark for understanding formation of disc galaxies. Thanks to the ability of the model to simulate the stellar populations as they are seen in surveys, we compared model simulations with 2MASS star counts in all the region covered by the outer bulge. As in Picaud & Robin (2004) we first attempted to fit a unique old bulge population and characterized the shape of the structure which maximizes the likelihood, but in a much larger region covering $-20 < l < 20$ and $-10 < b < 10$. We investigated several shapes, using gaussian, exponential or sech^2 shapes, and adjusting angles, 3 axis scale lengths, 3 boxiness parameters, as well as the disc scale length and central hole. It results that the best fit bulge structure has a small angle of about 10deg with regards to the sun-Galactic center axis. However the result is unsatisfactory: this structure leaves significant residuals when we subtract the resulting simulation from the data, and the fit depends on the choice of the region fitted. In particular, when one selects regions at low latitudes and high longitudes, the fitted structure gets a higher angle, while the selection concerns regions at high latitudes and low longitudes, on the contrary the angle is found to be close to 0. It seems that we are seeing two distinct populations, the ratio of which change with longitude and latitude. Hence, we investigated this possibility and attempted to fit two populations of similar triaxial shapes. The likelihood of this two-population model is larger than the one-population model and no systematical residuals appear when looking at relative difference between model and data. We conclude that in the bulge region cohabit two different structures, a triaxial bulge with an angle of about 20deg and a narrow bar nearly aligned with the x axis. The comparison of 2MASS star counts with the 1-structure and 2-structure models is shown in figure 1. The 2-structure solution gives a very good agreement with the data, hence it appears to be a good explanation. We also explored alternative models, like a spiral arm between the sun and the Galactic center, but none gave satisfactory results.

5 Conclusions and perspectives

From the comparison of 2MASS star counts with a model of population synthesis in the outer regions of the Galaxy we investigate the warp feature followed by stars. We obtain a good fit of one side of the warp with a simple warp model but we fail to find a satisfactory fit on the other side, at negative longitudes, even with a 3 Fourier mode model like the Levine et al. (2006) gaseous warp model. Despite the uncertainties, it is clear from our study of the 2MASS star counts that the warp is less marked in stars than in the gas and it also shows different shapes at negative and positive longitudes. There is also a slight tendancy for the dust warp to be intermediate between the HI and the stars. In the central regions, we show evidence for two independent

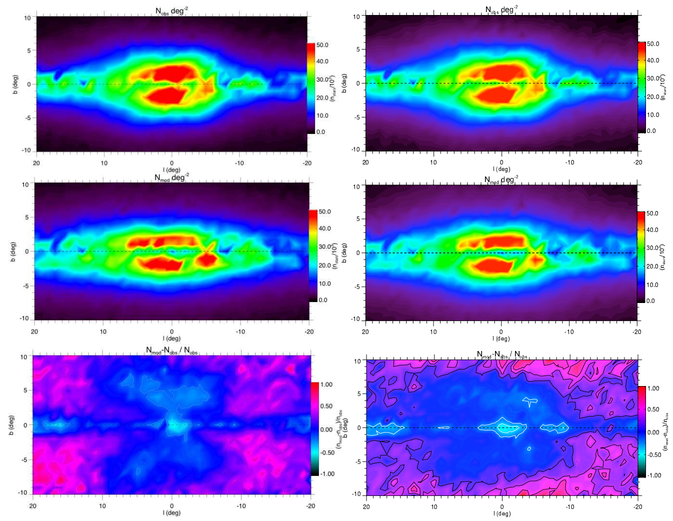

Fig. 1. Star counts up to magnitude K=12 from 2MASS data (top) compared with 2 models (middle panels) and residuals (Nmod-Nobs)/Nobs (bottom). Left pannel: model with 1 bulge population. Right: model with 2 bulge populations : a triaxial bulge and a bar. In pink the excess in the model is at the level of 70% on the left pannel. The light blue corresponds to a lack in the model at the level of 50%. The 2-population model allows to nicely reproduce the boxy shape of the outer bulge region, while the 1-population model leaves significant X-shaped residuals. Near the Galactic center the nuclear bar population is missing in the model. The residuals in the outer region are not much significant due to the small number of stars in each bin.

structures, a triaxial bulge and a long and narrow bar which angles are different. This long bar is different from recent studies (Hammersley et al, 2000, Benjamin et al., 2005) which have an angle of about 43-45deg. Further studies are needed to confirm these preliminary conclusions, in particular kinematical data, helpful in understanding the dynamics, especially to measure the rotation and velocity dispersions of these populations.

References

Benjamin, R.A., et al. 2006, ApJ 630, L149.

Bienaymé, O., Robin, A. C., & Crézé, M. 1987, A&A, 180, 94

Gyuk, G., Flynn, C., and Evans, N. W. 1999, ApJ, 521, 190

Hammersley, P. L., Garzón, F., Mahoney, T. J., López-Corredoira, M., Torres, M. A. 2000, MNRAS 317, L45

Levine, E. S., Blitz, L., & Heiles, C. 2006, ApJ, 643, 881

Marshall, D. J., Robin, A. C., Reylé, C., Schultheis, M., Picaud, S. 2006. A&A 453, 635-651.

Picaud, S., & Robin, A. C. 2004, A&A, 428, 891

Reylé, C., Marshall, D.J., Robin A.C. and Schultheis, M. . 2009. A&A 495, 819.

Robin, A. C., Reylé, C., Derrière, S., & Picaud, S. 2003. A&A, 409, 523 -540

Robin, A. C., Reylé, C., & Marshall, D. 2008, IAU Symposium, 248, 443

Skrutskie, M. F., et al. 2006, AJ, 131, 1163

van der Kruit, P.C., 2008, in "Formation and Evolution of Galaxy Disks", ASP Conference Series, 2008, Eds. Jose G. Funes, S.J. and Enrico M. Corsini

SF2A 2009
M. Heydari-Malayeri, C. Reylé and R. Samadi (eds)

LYMAN-ALPHA RADIATION TRANSFER IN SIMULATED GALAXIES : VARIATION OF LYA ESCAPE FRACTION, SPECTRA, AND IMAGES WITH VIEWING ANGLE, FOR DIFFERENT GALAXY FORMATION SCENARIOS

Verhamme, A.[1,2], Dubois, Y.[1], Slyz, A.[1] and Devriendt, J.[1]

Abstract. We present our first results from a study of Lyman-alpha (hereafter Lyα) radiation transfer calculations in a simulated dwarf galaxy (M$_{halo}$ = 10^{10} M$_{\odot}$) isolated in its dark matter halo. For two different galaxy formation senarios, we discuss the variation of the Lyα spectra, images and escape fractions with the line of sight. In the case of star-formation with supernova feedback, the Lyα emergent spectra are different edge-on and face-on, whereas they are identical in all directions in the simulation without supernova feedback. In particular, the Lyα beam is collimated along the rotation axis in the case with feedback, leading to double the Lyα equivalent width compared to the intrinsic emission. The Lyα escape fraction depends more strongly on the assumptions concerning the star formation (feedback or not), than on the different lines of sight for one given simulation.

1 Introduction

One of the most efficient methods to discover distant galaxies has been so far the "narrow band" imaging technique, selecting galaxies with a very bright emission line falling onto the detector, followed by spectroscopic confirmations that this line is indeed Lyα at high redshift. However, because of complex radiation transfer effects in this resonant line, the escape of the Lyα radiation from star-forming galaxies is not ubiquitous : there are exemples of galaxies at low redshift presenting a very strong burst of star-formation, but Lyα in absorption (Kunth et al. 1998; Atek et al. 2008); and at high redshift, 25% of the star-forming galaxies detected by the "Lyman break" technique (Steidel et al. 1996) also present a Lyα spectrum in absorption. The physical parameters which govern Lyα escape from starbursting galaxies is still unclear. Is it a question of orientation? As seems to be observed at $z \sim 0.3$ (Mallery et al. 2009), face-on galaxies might show more Lyα emission than galaxies seen edge-on. How does the geometry and the kinematics of the interstellar gas influence the ability of Lyα to escape, and in what proportion (Verhamme et al. 2006,2008)? Is there a mass sequence? Massive galaxies might have a mean Lyα escape fraction lower than less massive ones, given their stronger gravitational potential well, and higher dust content (Laursen et al. 2009). Is there a time sequence? with successive Lyα-loud and Lyα-quiet phases, as proposed by several semi-analytic models trying to reproduce observed Lyα luminosity functions (Nagamine et al. 2008; Mori et al. 2009; Dayal et al. 2009). Carrying out detailed Lyα radiation transfer on the various redshifts outputs of high resolution hydrodynamical simulations allows us to test these assumptions.

2 Description of the simulations

Simulations of galaxy formation were run using the Adaptive Mesh Refinement code called RAMSES (Teyssier 2002), allowing to describe the evolution of a gas component in presence of massive particles. It solves the Euler equations using a second order Godunov scheme. The gravitational potential given by the Poisson equation for a self-gravitating gas is added as a source term in the momentum equation. Initial conditions are generated as in Dubois & Teyssier (2008). Dark matter is a static gravitational potential (any back reaction of the baryons

[1] Oxford Astrophysics, Denys Wilkinson Building, Keble Road, OX1 3RH Oxford, UK
[2] Observatoire de Genève, Université de Genève, 51 chemin des Maillettes, CH-1290 Versoix, Switzerland

on the dark matter distribution is neglected) with a spherical NFW (Navarro, Frenk & White 1996) profile. The gas is distributed with the same profile assuming a baryon fraction $f_b = 0.15$ and an hydrostatic equilibrium to compute its temperature distribution. Radiative losses are accounted for a monoatomic primordial H/He abundance as given by the cooling function of Sutherland & Dopita 1993. We also account for a metal cooling function given by the abondancy of a mean (but not necessarily homogenous) metal component in the gas, that could enhance the cooling rate down to the minimum temperature floor T_0. No UV heating background source term is taken into account. In order to mimic the observational law (Kennicutt 1998), star formation process is computed in a heuristic way following a simple Schmidt law. We ensure that no more than 90% of the gas in the cell is depleted in one time step. The complex multiphase ISM is simulated by a polytropic equation of state (EOS) (Springel & Hernquist 2003). The supernovae feedback is treated using the same recipe than in Dubois & Teyssier (2009) : each supernovae inflates a bubble within which we deposit the energy in a full kinetic form.

We ran two sets of simulations. In the first case, the temperature floor is set to $T_0 = 300$ K and the supernovae feedback is turned off. As a consequence, the galaxy disk is thin (0.1 kpc) and starformation takes place in clumpy dense cores, the halo gas is symetrically infalling onto the disk. We call this run GALAXYCLUMPS. In the second case, the temperature floor is set to $T_0 = 10^4$ K and the supernovae feedback is turned on. The galaxy disk is thick (1 kpc) and starformation takes place homogeneously. A bipolar galactic wind develops from the disk into the halo after 2 Gyrs. This run is called GALAXYWIND.

To compute the Lyα radiation transfer in the snapshots described above, we use MCLya (Verhamme et al. 2006). This 3D Monte Carlo code includes the treatment of interstellar dust (and Deuterium). The Lyα emissivity is assumed to be located around the youngest stars of the simulations (< 200 Myrs), and proportional to the stellar mass in each emitting cell. We derive Lyα spectra, images and escape fraction along any given line of sight.

3 Results of the Lyα radiation transfer

First, we tested the effect of inclination for one given configuration: the Lyα escape fraction is indeed higher when the galaxy is seen face-on rather than edge-on for GALAXYWIND, even if the relative difference is only a factor of two. We expected a big difference: strong winds escape the galaxy along the rotation axis,whereas the gas remains neutral and almost static in the perpendicular direction. The emergent Lyα spectral shape is also very different along different lines of sight, as expected. In particular, double-peaked profiles are observed when the galaxy is seen edge-on, signature of mostly static gas along the line of sight. On the contrary, an interesting effect is seen face-on: the Lyα beam can be collimated by tunnels of ionised gas, ending with twice as more photons emerging in the direction along the rotation axis than the number of photons originaly produced in this direction (see Fig. 1).

Then, by varing the quantity of energy injected in the surrounding gas when a star dies and explodes, we investigated the influence of the supernova feedback efficiency on Lyα escape fraction, spectral shape and image (see Fig. 2). Supernova feedback efficiency has an influence on the kinematics of the interstellar gas. Indeed, the global Lyα escape is two times higher in the simulation with supernova feedback, GALAXYWIND, than in the simulation without, GALAXYCLUMPS.

Furthermore, we studied the effect of the floor of the cooling function. This influences the clumpiness of the interstellar gas, and allows us to test the effects of the interstellar medium geometry on the Lyα line. However, no straightforward conclusion could be derived from our calculations so far, as we were confronted to a numerical issue: a lack of resolution in the McLya code may erase the clumpiness effect, making the emergent spectra from GALAXYCLUMPS being the same in all directions. A new version of MCLya working on Adaptive Mesh Refinement grids in under developpement, to carry out the Lyα radiation transfer using all the detailed information contained in the hydrodynamical simulations.

Finally, radiation transfer calculations will be performed in isolated galaxies with different halo masses, to test the influence of mass on the Lyα escape fraction.

4 Perspectives

We will then test the influence of the environment on the Lyα escape from distant galaxies. Instead of considering a single galaxy isolated in its dark mater halo, we will perform Lyα radiation transfer in very-high resolution resimulations of a forming galaxy, embedded in its cosmological environment: filled with cooling flows, and undergoing mergers. This step needs the technical improvement described above, as well as the addition of another Lyα emission process: Lyα production by gravitational cooling of pristine gas onto the galaxy. Among other results, we are particularly interested in testing what "Lyα signature" cold flows imprint, as they have recently been proposed as an explanation for the mysterious observed Lyα-blobs (Dekel et al. 2009; Dijkstra et al. 2009).

The final step of this collaboration will be to post-process a cosmological volume, using these data to pin down the statistics, compute the spatial, physical and spectral properties of the sources, compare them to existing data up to $z = 5 - 6$ and make predictions for Lyα Emitters number counts for future instruments (especially MUSE and JWST).

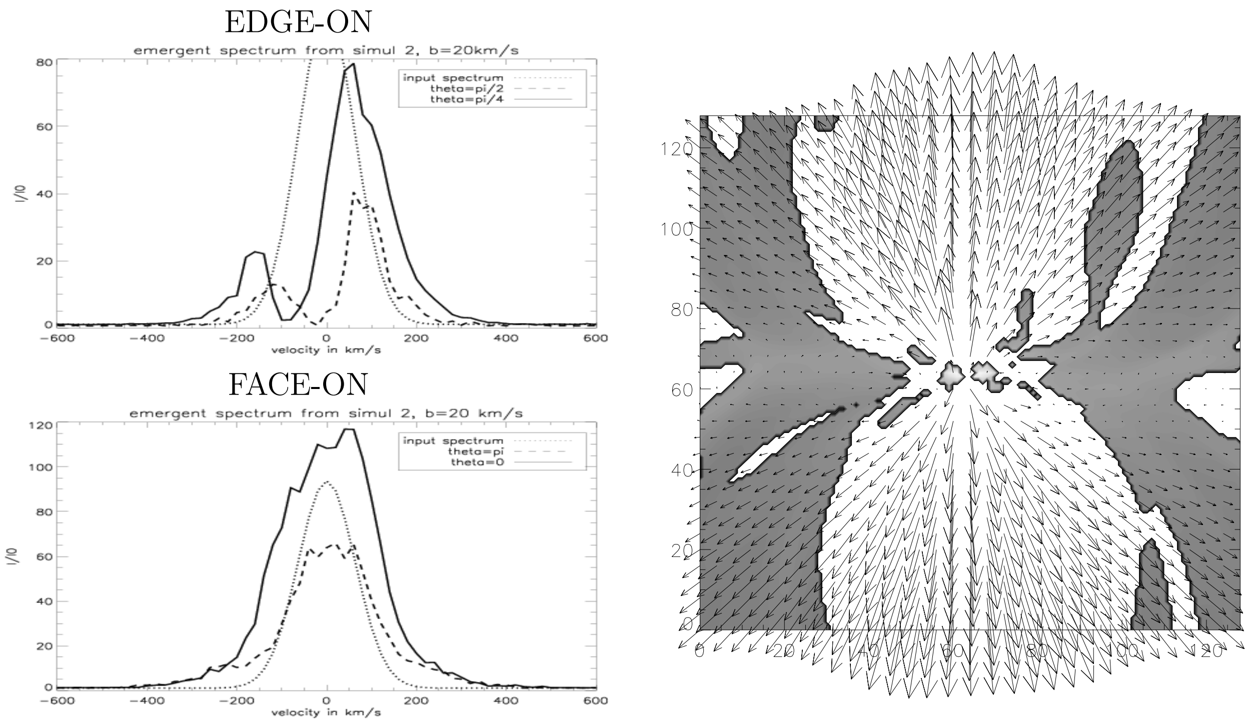

Fig. 1. Left: Emergent spectra from the galaxy along different lines of sight, for GALAXYWIND. Top panel: the emergent spectrum along the rotation axis (solid line) is boosted compared to the input spectrum (dotted line), the Lyα beam has been collimated by the neutral gas tunnel. Lower panel: the emergent spectrum along the x axis is double-peaked (solid line), with the red peak slightly higher than the blue peak, meaning that the gas is almost static in this direction. Looking at this galaxy in a direction $\theta = pi/4$, the emergent spectrum is double-peaked (dashed line), but shifted compared to the spectrum along x axis. In particular, the minimum is reached at the abscissa ~ -100 km/s, which means that most of the gas in this direction is expanding at this velocity. **Right:** Snapshot of the galaxy in which McLya was processed. In grey scale is the density distribution of the neutral gas. The velocity field is overlayed.

References

Atek, H., Schaerer, D., Kunth, D. 2009, A&A, 502, 791

Dayal, P., Ferrara, A., Saro, A., et al. 2009, MNRASsubmitted, astroph/0907.0337

Dekel, A., Birnboim, Y., Engel, G., et al. 2009, Nature, 457, 451

Dijkstra, M., Loeb, A. 2009, MNRASsubmitted, astroph/0902.2999

Dubois, Y., & Teyssier, R. 2009, A&Asubmitted, astroph/0908.3862

Dubois, Y., & Teyssier, R. 2008, A&A, 477, 79

Kennicutt, R. 1998, ApJ, 498, 541

Kunth, D., Mas-Hesse, J.M., Terlevich, E. et al. 1998, A&A, 334, 11

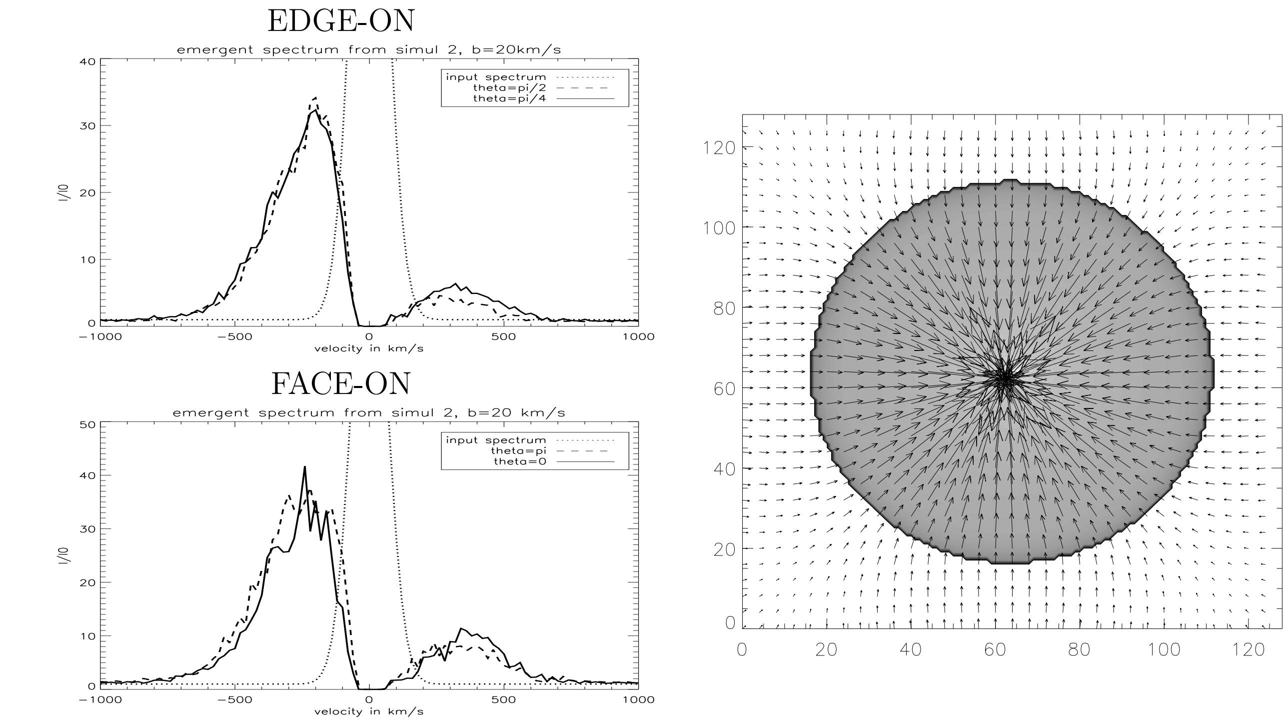

Fig. 2. Left: Emergent spectra from the galaxy along different lines of sight, for GALAXYCLUMPS. All emergent spectra show a similar shape : an asymetric blue peak, as expected for Lyα radiation transfer through an infalling halo. **Right:** Snapshot of the galaxy in which McLya was processed. In grey scale is the density distribution of the neutral gas. The velocity field is overlayed.

Laursen, P., Sommer-Larsen, J., Andersen, A. 2009, ApJ, submitted, astroph/0907.2698

Mallery, R., et al. 2009, ApJ, in prep

Mori, M., & Umemura, M. 2007, Astrophysics and Space Science, Volume 311, Issue 1-3, pp. 111-115

Nagamine, K., Ouchi, M., Springel, V., et al. 2008, astroph/0802.0228

Navarro, J., Frenk, C., White, S. 1996, ApJ, 462, 563

Springel, V., & Hernquist, L. 2003, MNRAS, 339, 289

Steidel, C., Giavalisco, M., Pettini, M., et al. 1996, ApJ, 462, 17

Sutherland, R., & Dopita, M. 1993, ApJS, 88, 253

Teyssier, R. 2002, A&A, 385, 337

Verhamme, A., Schaerer, D., Atek, H., et al. 2008, A&A, 491, 89

Verhamme, A., Schaerer, D., Maselli, A. 2006, A&A, 460, 397

PNP

Planets

CONNECTING THE CDPP/AMDA SERVICE TO PLANETARY PLASMA DATA: VENUS, EARTH, MARS, SATURN (JUPITER AND COMETS)

André, N.[1], Cecconi, B.[2], Budnik, E.[3], Jacquey, C.[1], Génot, V.[1], Fedorov, A.[4], Gangloff, M.[1], Pallier, E.[4], Bouchemit, M.[1], Hitier, R.[5], Dériot, F.[6], Heulet, D.[7] and Topf, F.[8]

Abstract. These last years, CDPP has developed a new service, AMDA (Automated Multi-Dataset Analysis), which is a web-based facility for on line analysis of space physics data (magnetospheric, heliospheric, planetary plasmas) coming from either its local database or distant ones. This tool allows the user to perform on line classical manipulations such as data visualization, parameter computation or data extraction. AMDA also offers innovative functionalities such as event search on the content of the data in either visual or automated way. AMDA has been recently integrated as a service to the scientific community for the Plasma Physics thematic node of the EuroPlaNet IDIS (Integrated and Distributed Information Service) activities. We will present the service AMDA and the planetary plasma data accessible via the service. We will then illustrate some of its applications (boundary identification and planetary space weather) for the comparative analysis of the planetary ionized environments. We will finally discuss future developments under study at CDPP to integrate with AMDA new datasets (Jupiter, comets) and new (astronomical) tools.

1 Introduction

The field of planetary sciences has greatly expanded in recent years with missions orbiting around most of the planets of our Solar System. The growing amount and wealth of data available to researchers makes it clear that our understanding of the planetary objects and of their space environments 1) requires multi-disciplinary studies and 2) should greatly benefit from comparative studies. However, until now, the number of such comparative studies has been quite limited, each planets being studied to a large extent as unique objects. One of the main difficulties to do such comparative studies is that scientists have to exploit together data coming from many sources which can initially be heterogeneous in their organization, description and format. To overcome this difficulty and makes this task easier to all scientists, innovative tools taking advantage of mass storage, computer power and web technologies have to be developed and offered to the community. This is the general idea behind the Virtual Observatory paradigm.

2 The CDPP and its AMDA service

The CDPP (Centre de Données de Physique des Plasmas) is the French national centre for space physics data. Recently, the CDPP has opened a new web-based service, AMDA (Automated Multi-Dataset Analysis, http://cdpp-amda.cesr.fr/), which is a web-based facility for on line analysis of space physics data coming from either its local database or distant ones. AMDA allows the user to perform on line classical manipulations such as

[1] CDPP & CESR, CNRS/Université Paul Sabatier, 9, avenue du colonel Roche, 31028 Toulouse, France
[2] LESIA, Observatoire Paris-Meudon, 92195 Meudon, France
[3] NOVELTIS, 2 Avenue Europe, 31520 Ramonville Saint Agne, France
[4] CESR, CNRS/Université Paul Sabatier, 9, avenue du colonel Roche, 31028 Toulouse, France
[5] Co-Libri, Cremefer 11290 Montréal, France
[6] CNES, 18 avenue Edouard Belin, 31400 Toulouse, France
[7] CNES, 18 avenue Edouard Belin, 31400 Toulouse, France
[8] Space Research Institute, Austrian Academy of Sciences, Graz, Austria

data visualization, parameter computation or data extraction. AMDA also offers innovative functionalities such as event search on the content of the data in either visual or automated way. These functionalities extendable for automated recognition of specific signatures can be used for performing classification of events and for generating time-tables and catalogues (Jacquey et al., 2009; Génot et al., 2009; André et al., 2009). AMDA is also evolving in the Virtual Observatory paradigm. It gives a direct access to data from distant databases and includes a data access layer compliant with the SPASE (http://www.spase-group.org/) standards. Finally, the time tables produced and used by AMDA can be seen as one of the primary brick to be used for the interoperable exchanges in space physics. Whereas the AMDA service was primarily designed for heliospheric and magnetospheric science at Earth, where in-depth studies generally request the analysis of multi-point and multi-instruments data, it has been recently extended to planetary plasma science for the same reasons.

3 Planetary Plasma Data Accessible via AMDA

In the context of its EuroPlaNet-RI IDIS activities, the CDPP has recently included Mars and Venus Express ASPERA data in the local database of AMDA, and set up an interoperable connection between AMDA and the VEX/MAG database hosted by IWF Graz. This service will be publicly opened to the planetary community in December 2009; this will add to the already remotely connected Cassini MAPSKP (from CESR, http://mapskp.cesr.fr) and SKR (from LESIA) data at Saturn. In addition, various electromagnetic field and particle data on the Earth's magnetosphere have been obtained by numerous instruments on board a variety of spacecraft and CDPP has a long heritage in archiving many of these data sets. Widely-used data from spacecraft like THEMIS, Cluster, DoubleStar, IMP-8, Geotail, ISEE-1 and 2, ACE, WIND , as well as a variety of geomagnetic indices that diagnose the state of the terrestrial magnetosphere, have therefore been made accessible via AMDA. To register to AMDA, a user just needs to send an email to amda@cesr.fr.

4 Example science cases: Planetary boundary identification and planetary space weather

Planetary environments contain plasma of various origins, hence, with various composition and energy. These different plasma populations structure the environment and their identification can be used to define magnetospheric regions and boundaries, where exchanges of mass, momentum and energy take place. The magnetospheres of Mars, the Earth and Venus share common features such as a bow shock, magnetopause (Earth, Saturn and other magnetized planets) or ion composition boundary (Mars, Venus), and magnetotails. From the definitions of these boundaries, it may be possible to identify automatically a bow shock by looking at the flow deceleration and/or plasma heating, a magnetopause or ion composition boundary layer by looking at magnetic field increases and/or changing plasma composition, and a current sheet crossings in planetary magnetotails by searching for changes of the polarity of the Sun-planet magnetic field component which occur when the spacecraft effectively crosses the neutral sheet. Figure 1 illustrates the AMDA-based identification of 1) a current sheet in the magnetotail of Venus and of 2) multiple magnetopause crossings at Saturn.

These years, the Solar System plasma environment is currently explored by an exceptional set of observatories providing continuous observations of the Sun and its corona, in situ plasma and field measurements obtained in the vicinity of various planets, and inside the heliosphere. This wealth of data will offer previously unequalled opportunities to study global and multi-scale phenomena of the inner heliosphere, the propagation of the solar perturbations and space meteorology, local interplanetary conditions around planets and the comparison of the ionised environments of various planets. We consider the case of a user who is interested to study the response of the Martian, Terrestrial and Venusian magnetospheres during the passage of solar wind disturbances. Whereas the lack of solar wind monitor in the vicinity of Mars and Venus makes this kind of study more challenging, the solar wind properties at Earth are continuously and routinely monitored by various spacecraft (SOHO, ACE, WIND). We take advantage of a particularly favorable configuration of the planets and satellites in the inner heliosphere in November 2007 when Venus, ACE (orbiting the Earth) and Mars were more or less radially aligned. We focus our attention on the last ICME reported during the year 2007, and we used AMDA to time-shift ACE solar wind observations at Earth by the appropriate time delay to reach Mars and superpose the time-shifted ACE observations on top of MEX ASPERA ELS observations, in order to look if and how this ICME may have impacted the Martian environment (André et al., 2009). Figure 2 displays the end results. Modifications of the response of the Martian environment appear clearly in the MEX/ASPERA ELS observations, with enhanced electron fluxes at all energies (especially for low-energy and suprathermal electrons) observed at the time of the

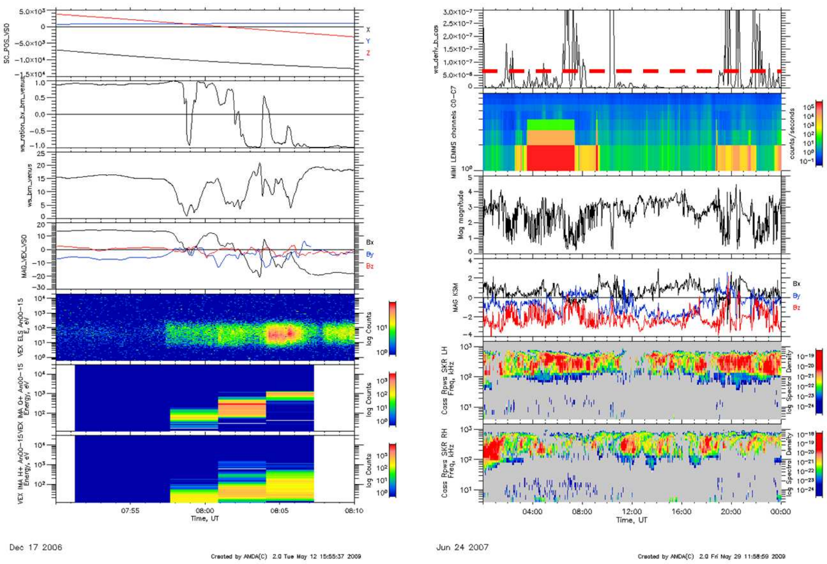

Fig. 1. Let: Crossing of a magnetotail current sheet at Venus. From top to bottom: Time series of VEX trajectory, ratio B_x/B_m, VEX/MAG magnetic field intensity B_m, (VSO) magnetic field components, VEX/ASPERA electron, oxygen and proton counts. Right: Magnetopause crossings at Saturn. From top to bottom: Time series of (squared and normalized) time-derivative of Cassini MAG magnetic field intensity, MIMI-LEMMS electron counts, MAG (KSM) magnetic field intensity and components, RPWS left- and right-handed polarized Saturn Kilometric Radiation emissions.

arrival of the solar wind perturbation.

5 Perspectives: Giant planet auroral emissions and Jupiter Science Archive

AMDA is in continuous development and user feedback is welcome (amda@cesr.fr). Future developments under study at CDPP to exploit planetary plasma data concern 1) the connection to other generic (analysis and simulation) tools in space physics or in astronomy, as well as 2) the accessibility of new datasets in AMDA (Jupiter and comets) thanks to a potential collaboration with other data centers (e.g., ESA PSA and NASA PDS). Multi-wavelength remote sensing of giant planet auroral emissions provide a unique tool for the global understanding of the large-scale coupling between the planetary ionosphere, the magnetosphere and the solar wind. In the context of our EuroPlaNet-RI activities, the CDPP aims to connect its AMDA service together with VO interoperable tools like Aladin. The extension of our AMDA service to the relevant astronomical data (e.g., HST) and IVOA tools will open a new window in our understanding of comparative auroral and magnetospheric physics of giant planets. This will consist of one of the first experiment to combine tools at the interface of the plasma (SPASE) and astronomy (IVOA) communities. Support from Euro-VO has been requested to follow this development. Finally, in the context of the preparation of the NASA/ESA Europa Jupiter System Mission (EJSM), the CDPP aims to develop a service to connect AMDA with magnetospheric and plasma observations obtained by previous missions having flown by or orbited Jupiter. Indeed, the preparation of EJSM will stimulate new scientific, instrumental, and engineering studies that will rely on a deep re-analysis of the existing datasets. Support from CNES has been requested to integrate locally plasma observations (not raw data but physical parameters) at CDPP, for the benefit of a broad science community.

References

André, N., & al., 2009, Planetary and Space Sscience, submitted

Génot, V., & al., 2009, Advances in Space Research, in press

Jacquey, C., & al., 2009, Astrophysics and Space Science Proceedings, in press

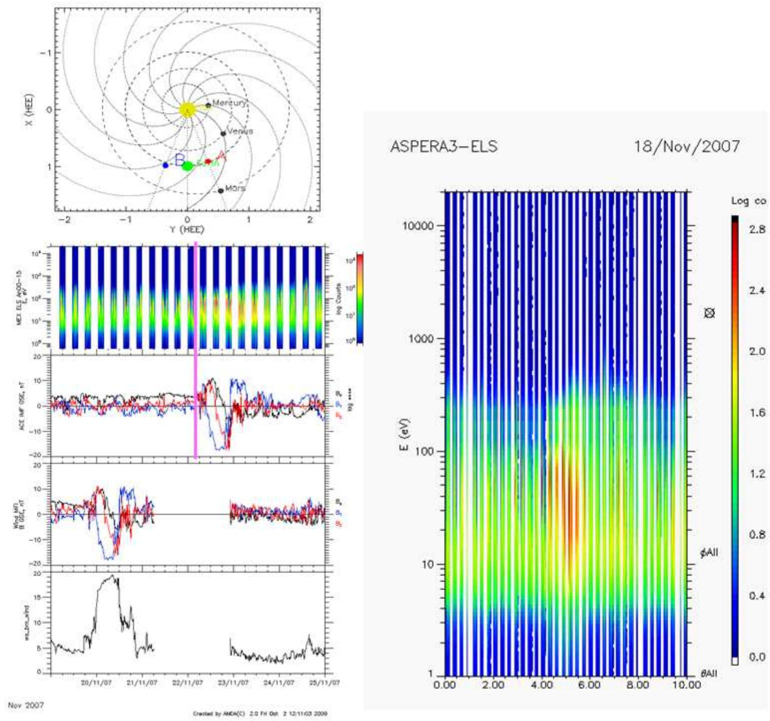

Fig. 2. Top left: position of the planets in the heliosphere on 14/11/2007. Bottom left: AMDA plot showing (from top to bottom): Time series of MEX ASPERA/ELS electron counts, time-shifted ACE/MAG (GSE) magnetic field components, WIND (GSE) magnetic field components and intensity (without time-shift), from 19/11 to 25/11/2007. Right: Zoom in on MEX/ASPERA ELS counts.

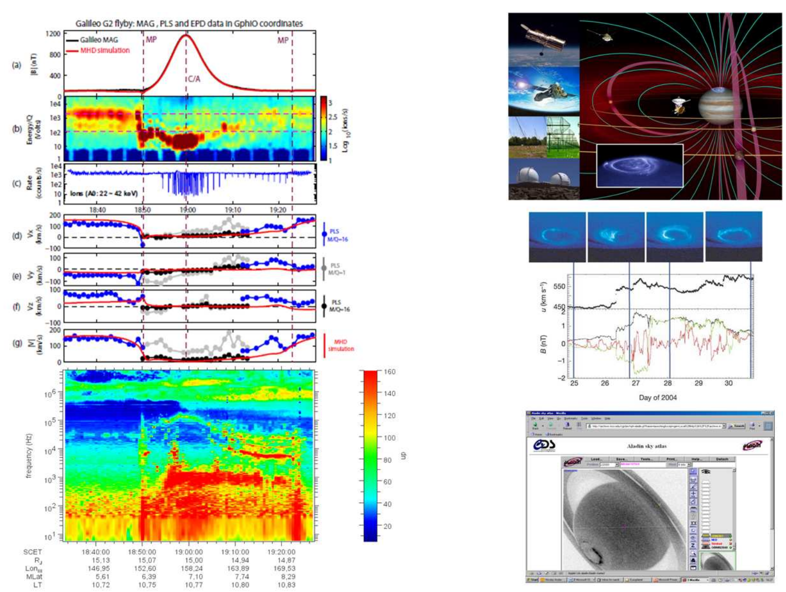

Fig. 3. Left: Multi-instrumental view of the G2 Gallileo Ganymede flyby. From top to bottom: Time series of magnetic field, low-energy ion plasma, energetic particle, plasma bulk velocity and frequency-time spectrogram of radio emissions (data obtained from NASA PDS). Right: Schematic illustrating potential applications of VO tools to couple in situ plasma (Cassini data) and remote multi-wavelength auroral observations (HST data at Saturn previewed with Aladin).

HOW TO BRING TWO NEPTUNE MASS PLANETS ON THE SAME ORBIT

Crida, A. [1,2]

Abstract. We perform numerical simulations of Uranus and Neptune migrating in a dense protoplanetary disk, in the presence of a non migrating Saturn. Due to the high density of the gaseous disk, the two 15 Earth mass planets are caught in the same resonance by Saturn. Different kinds of configuration are observed: planets in opposition, at 30 degree from each other, or satellite of each other. This would lead to horseshoe, tadpole, or satellite orbits after dissipation of the gas disk. This appears to be a new way of making double planets or pairs of planets on the same orbit (Crida, 2009).

1 Introduction

Planets form in protoplanetary gaseous disks, in which they also migrate. If several planets migrate together in a same disk, the ratio of their semi-major-axes (and of their orbital periods) varies. It is then possible that they enter in a Mean Motion Resonance (MMR). If the disk torques are stronger than the MMR, the planets cross the MMR and go on migrating at different speeds. If the MMR is stronger than the torques from the disk, the planets stay locked in resonance and migrate together.

In this work, we consider the migration of the giant planets of the Solar system in a disk about ten times denser as the standard Minimum Mass Solar Nebula. In this case, resonances between two Neptune mass planet are not strong enough to hold them away from each other against migration, which leads Uranus and Neptune to end on the same orbit.

2 Results

We present the results of three simulations performed using the code FARGO-2D1D (code publicly available at `http://fargo.in2p3.fr/`). The initial density profile of the disk is: $\Sigma_0 = 3430(r/10\mathrm{AU})^{-2.168}$ kg.m^{-2}. Jupiter, Saturn, Neptune and Uranus start on circular orbits at 5.45, 8.18, 11.5 and 14.2 AU respectively, and are released after 1250 years. Jupiter's fast inwards migration stops when Jupiter encounters the inner edge of the 2D grid. Then, Jupiter catches Saturn in MMR, which stops Saturn's migration. Then, Neptune is caught in MMR by Saturn. Because the disk is too massive for Neptune to hold Uranus, Uranus ends in the same MMR with Saturn as Neptune, as can be seen in Figs. 1 and 2.

Opposition In the first case, the equation of state of the gas is radiative, and the grid resolution is $\delta r/r = \delta\theta = 0.01$. After 12000 years, Uranus and Neptune have close encounters, and after 15000 years, the distance between them stays equal to two times their common semi-major-axis (see red crosses in the left panel of Fig. 1): they are in opposition. One can expect that once the disk disappears, the two planets should have mutual horseshoe orbits.

30° **angle** In the second case, the equation of state is locally isothermal, and the resolution is $10^{-2.5}$. After Uranus and Neptune end on the same orbit, the angle between them as seen from the Sun stays constant to $\sim 30^\circ$. This is not a stable configuration in the 3-bodies problem (Sun, Uranus, Neptune). Once the disk disappears, these two planets should librate around their mutual L_4 L_5 points, in tadpole orbits.

[1] CpT-TAT, Universität Tübingen – where this work was done, until december 2008.
[2] D.A.M.T.P., University of Cambridge – since january 2009.
contact: `crida@oca.eu`

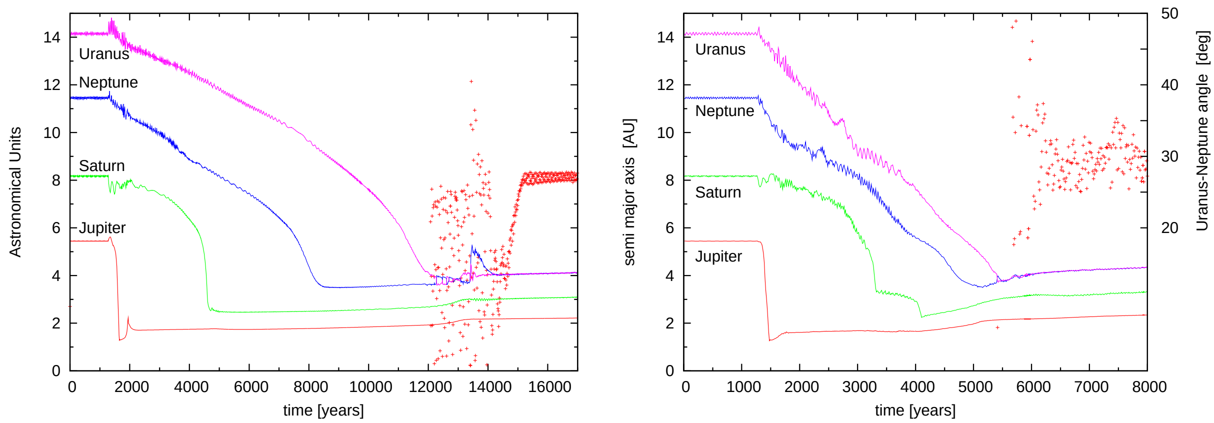

Fig. 1. Migration paths of Jupiter, Saturn, Neptune and Uranus (from bottom to top) in a dense disk. Left: radiative equation of state and grid resolution 0.01. Right: locally isothermal equation of state, $\delta r/r = \delta\theta = 10^{-2.5}$.

Satellite motion In the last case, the equation of state is still locally isothermal and the grid resolution is 0.01. When Neptune joins Uranus, their distance shrinks below the Hill radius of the latter (see crosses in right panel of Fig. 2), betraying a satellite motion. This capture is enabled by the high density of the gas that provides dissipation. To our knowledge, this is the first time that a satellite capture is observed in numerical simulations between two bodies of the mass of Neptune in the frame of planetary migration. This satellite configuration is stable over the disk dissipation.

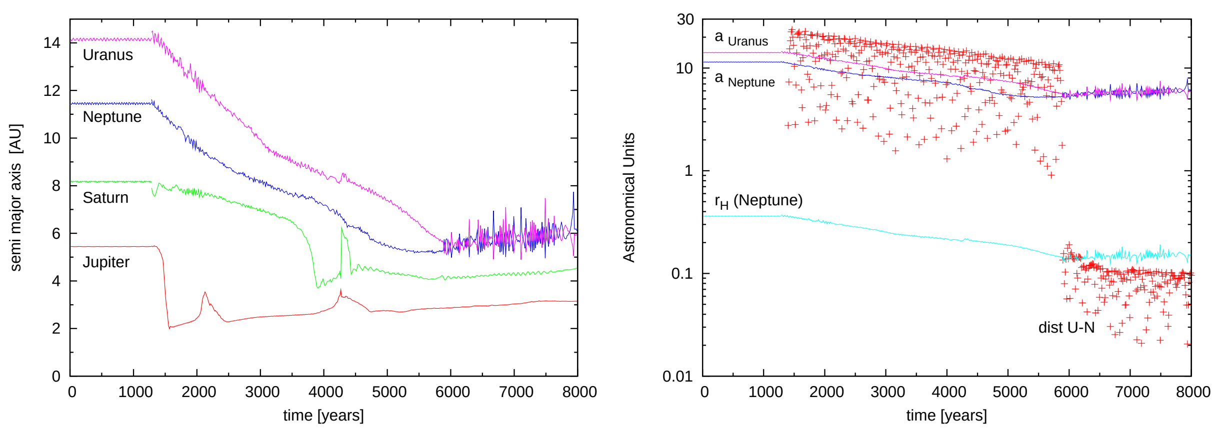

Fig. 2. Right : Migration paths of Jupiter, Saturn, Neptune and Uranus (from bottom to top). Left : Uranus and Neptune semi-major-axes (top curves), distance (crosses), and Hill radius (bottom curve).

3 Conclusion

Migration in dense disks can be a way of forming pairs of Neptune-mass planets on the same orbits. If for some reason their migration is halted at some point in the disk (like a resonance with an other, more massive planet), they will both end on the same orbit. This can lead to configurations like tadpole orbits, mutual horseshoe orbits, or double planets, one being satellite of the other. More detail on this work can be found in section 5.2 of Crida (2009).

References

Crida, A. 2009, ApJ, 698, 606

CLATHRATE HYDRATES FORMATION IN COMETARY NUCLEI

Marboeuf, U.[1], Mousis, O.[1], Petit, J.-M.[1] and Schmitt, B.[2]

Abstract. The initial composition of current models of cometary nuclei is only based on two forms of ice: crystalline ice for long period comets and amorphous ice for short period comets. A third form of ice, i.e. clathrate hydrate, could exist within the shord period cometary nuclei, but the area of formation of this crystalline structure in these objects has never been studied. Here, we show that the thermodynamic conditions in the interior of short period comets allow the existence of clathrate hydrates in Halley Type Comets. We show that their existence is viable in the Jupiter Family Comets only when the equilibrium pressure of CO clathrate hydrate is at least one order of magnitude lower than the usually assumed theoretical value. The amount of volatiles that could be trapped in the clathrate hydrate layer may be orders of magnitude greater that the daily amount of gas released at the surface of the nucleus at perihelion. The formation and the destruction of the clathrate hydrate cages could then explain the diversity of composition of volatiles observed in comets.

1 Introduction

Cometary nuclei are now regarded as the most primitive objects in the solar system. However, their physical characteristics remain unknown. Models of cometary nuclei (e.g. Espinasse et al. 1991; Enzian et al. 1997; Orosei et al. 1999; Capria et al. 2003; Prialnik et al. 2004; Mousis et al. 2005; Huebner et al. 2006) consider only two types of ice structure in these objects: crystalline when the nucleus was formed in the protoplanetary disk (long-period comet), amorphous when it comes from the transneptunian region (short period comet). A third structure of ice, called clathrate hydrates (hereafter "clathrate"), could exist within the cometary nuclei (Delsemme and Swings 1952; Schmitt and Klinger 1987; Smoluchowski 1988; Prialnik et al. 2004; Huebner et al. 2008). The formation of such structures within the cometary nuclei may change their physical behavior and contribute to the physical diversity observed in the comets in the same way as their orbital and collisionnal history and their formation location.

A model of comet nucleus with such a structure of ice has already been developed (Flammer et al., 1998), but the physics on which it is based is incorrect: this model considers that the icy matrix of cometary nucleus was entirely composed of clathrates and that their dissociation occured only during the sublimation of H_2O ice. The possible formation of clathrates and their location inside the short period comets has been discussed by Schmitt and Klinger (1987) but has never been studied, certainly because they are initially completely composed of amorphous ice. However, experiments by Bar-Nun et al. (1988), Blake et al. (1991) and Schmitt et al. (1992) showed that the crystallization of amorphous ice with volatile molecules trapped inside creates clathrates.

In the present work, we demonstrate that thermodynamic conditions for the formation of clathrates are met within the short period comets. The short-period comets are divided into two categories which we studied separately: the Halley Type Comets (periods between 20 and 200 years; hereafter HTCs) and the Jupiter Family Comets (period less than 20 years; hereafter JFCs) represented in this work by the orbits of comets 1P/Halley and 67P/Churyumov-Gerasimenko respectively. We discuss the implication of the presence of clathrates in the physics of cometary nuclei. Their formation could explain the diversity of composition of volatiles observed in comets and outbursts that take place before the perihelion passage of some nuclei. Note that the model presented here does not form clathrates within the porous network. The following study is based on a comparison between the equilibrium pressure of clathrate and that of the gaseous phase in the porous network.

[1] Institut UTINAM, CNRS-UMR 6213, Observatoire de Besançon, BP 1615, 25010 Besançon Cedex, France.
[2] Université Joseph Fourier, Laboratoire de Planétologie de Grenoble, CNRS INSU, France.

2 Nucleus model

The nucleus model employed in this work is based on the one-dimensional model developed by Marboeuf et al. (2009a,b). The model considers an initially homogeneous sphere composed of a predefined porous mixture of ices (essentially water ice) and dust in specified proportions. It describes heat transmission, gas diffusion, sublimation/recondensation of volatiles within the nucleus, dust release and mantle formation. Water ice is initially amorphous. A fraction of the volatiles can be trapped in the water ice matrix, while the remaining form pure condensates in the pores. When heated, the fraction of volatiles condensed in the pores sublimates first, and then the other fraction trapped within the matrix is released during the transition from amorphous to crystalline water ice.

3 Thermodynamic parameters and initial composition

We assume that all the objects share a similar composition and have identical thermodynamic parameters at the beginning of the computation, regardless their formation location. The initial ice phase of our models is assumed to be composed of a mixture of amorphous water ice (Taylor 1992; Kouchi et al. 1994) with CO and CO_2, which are the most abundant volatile species observed in cometary nuclei (Bockelée-Morvan et al. 2004). The amorphous to crystalline ice phase transition is exothermic and irreversible[1].

The parameters adopted for our study are the mole fractions CO/H_2O and CO_2/H_2O respectively equal at 15% and 5%. The nucleus porosity is assumed to be equal at 50% and we adopt 770 $J.kg^{-1}.K^{-1}$ and 4 $W.m^{-1}.K^{-1}$ for the Heat Capacity and heat conductivity of dust's grains.

The presence of several volatile compounds in the gas phase of the porous network could generate the formation of a multiple guest clathrate (hereafter MG clathrate) whose equilibrium pressure varies as a fonction of the gas phase composition and the temperature. The equilibrium pressure of the MG clathrate P_c is given by (Hand et al. 2006):

$$P_c = (\sum \frac{y_i}{P_i^c})^{-1} \tag{3.1}$$

where y_i is the mole fraction of the volatile i in the gas phase and P_i^c the equilibrium pressure of the corresponding clathrate. The equilibrium pressure curves of CO and CO_2 are derived from Lunine & Stevenson (1985) (Hersant et al. 2004). When the gas pressure is higher than the equilibrium pressure of the MG clathrate, the clathration of the volatiles in the pores becomes possible.

4 Results

4.1 Halley Type Comets

Figure 1 represents the evolution of the stratigraphy of a HTC over a 300 yr period. It shows that the stability zone of the MG clathrate can extend from the amorphous-to-crystalline water ice zone to the surface of the nucleus, the size of this zone depending on the location of the comet on its orbit. When the comet approaches perihelion, the amorphous layers crystallize and the CO and CO_2 released in the pores can be enclathrated by crystalline water ice available on their surface. However, at perihelion, due to the increase of temperature, the MG clathrate equilibrium pressure increases faster than the gas pressure and exceeds it, then leading eventually to the dissociation of the clathrates. Because the dissociation kinetics of clathrates is poorly known, it is indeed impossible to determine whether the dissociation is effective or not in comets. On the other hand, when the comet moves away from perihelion, approaches aphelion and then comes back toward the Sun during a timespan of $\sim$ 70 yr, the equilibrium pressure of the MG clathrate becomes lower than the gas pressure in the pores, favoring again its formation in the porous network, provided that there is free crystalline water ice.

When the comet approaches perihelion, the clathration of volatiles is kinetically favorable because H_2O molecules are highly mobile, due to the crystallization of amorphous water ice (Blake et al. 1991; Schmitt et al. 1992). Hence, if a clathrate layer succeeded to form in the pores during the nuclei crystallization, the formation

[1]Note that Kouchi & Sirono (2001) have shown that crystallization of amorphous mixtures of water ice and some other molecules can become endothermic.

of additional layers of clathrates should be favored at later times on the orbit because the nucleation process eases the formation of new cages. If the formation of clathrates is effective in HTCs along their orbits, then the amount of volatiles trapped and released during their formation/dissociation in the porous network may represent up to 2,400 times the masses of CO and CO2 and 60 times that of H_2O produced daily at perihelion, assuming a full conversion of H_2O ice into clathrate in the stability zone and complete cage filling.

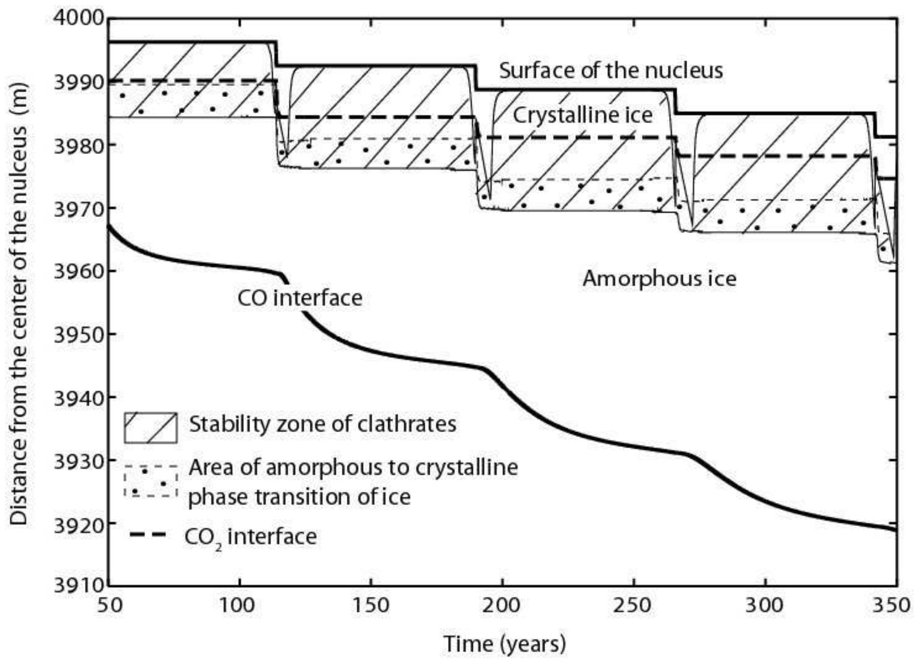

Fig. 1. Stratigraphy of a HTC nucleus as a function of time. The lines represent the surface and the minimum depths at which solid CO_2 (dashed line) and CO (bold solid line) exist. The dotted area corresponds to the zone where the amorphous-to-crystalline water ice phase transition occurs and the dashed area to the zone of the MG clathrate stability.

4.2 Jupiter family comets

We have first found that the clathration of volatiles in the porous network occurs only sporadically in a small area of the nucleus. Lunine & Stevenson (1985) acknowledge that their formula for the equilibrium pressure of CO clathrate is not very well constrained, and Fig. 6 of that paper shows that adding the dipole-dipole interaction in the model lowers the equilibrium pressure by as much as a factor of five. So we have conducted a second test for a JFC over a 60 yr timespan with an equilibrium pressure of CO clathrate which has been divided by 10 with respect to the value given in Hersant et al. (2004). The results have shown that the clathration and crystallization zones are almost superimposed and are located within the stability area of solid CO_2 condensed in the pores. For this family of comets, this implies that the formed clathrate only incorporates CO because CO_2 remains condensed in solid phase in the porous network. The thickness of the clathration zone slightly oscillates with time as a function of the Sun distance and never vanishes. When approaching the Sun, the clathration zone decreases, and inversely, it increases as the nucleus cools. The maximum amount of volatiles trapped or released during the formation or dissociation of CO clathrate in the porous network may represent up to 8,600 times the mass of CO and 2,900 times that of H_2O produced daily at perihelion.

5 Discussion and Conclusions

We have shown that, provided the kinetics of clathrate formation is fast enough, HTCs incorporate a clathrate layer in their interiors most of the time during their orbital evolution around the Sun. The formation of clathrates in JFCs is also possible but we had to assume an equilibrium pressure of CO clathrate that is one magnitude order lower than usually estimated to get a persistent stability zone in the nuclei. On the other hand, molecules such as methane or ethane that exist in lower abundances in coma can also form clathrates in cometary nuclei and their respective equilibrium curves are closer to that of the modified equilibrium curve of CO clathrate. This implies that, in any case, a clathrate layer is likely to exist in JFCs. If a deep clathrate layer does exist, our results suggest that the composition of the coma could be different from that of the gas released in the pores during the crystallization of the amorphous matrix. The formation of a CO-rich clathrate layer in the nucleus could imply the decrease of the outgassing rate of this species and lead to a higher CO_2/CO ratio in the coma than in the gas released in the nucleus itself.

The kinetic of clathrates formation or dissociation is still poorly constrained. The physical parameters that may affect kinetic are multiple (activity of the ice, temperature, difference between the gas pressure and the equilibrium pressure of the clathrate, ...). At low temperature, the formation rate of clathrates must be relatively slow but could anyway take place because the pressure and temperature conditions are favorable and stable over long time periods for both families of comets. Moreover, the formation of clathrates during crystallization of amorphous ice could ease the formation of new cages thereafter, due to the high mobility of water molecules. However, in the absence of more detailled knowledge of the kinetics, it is difficult to assess the relative amount of volatile molecules outgassing and trapped on the long term even during perihelion approach.

References

Bar-Nun, A., Kleinfeld, I., & Kochavi, E. 1988, Phys. Rev. B, 38, 7749

Blake, D., Allamandola, L., Sandford, S. et al. 1991, Science, 254, 548

Bockelée-Morvan, D., Crovisier, J., Mumma, M. J., & Weaver, H. A. 2004, Comets II, 391

Capria, M. T., Coradini, A., & de Sanctis, M. C. 2003, Advances in Space Research, 31, 2543

Coradini, A., Capria, M. T., de Sanctis, M. C., & McKinnon, W. B. 2008, The Solar System Beyond Neptune, 243

Enzian, A., Cabot, H., & Klinger, J. 1997, A&A, 319, 995

Espinasse, S., Klinger, J., Ritz, C., & Schmitt, B. 1991, Icarus, 92, 350

Flammer, K. R., Mendis, D. A., & Houpis, H. L. F. 1998, ApJ, 494, 822

Hand, D. P., Chyba, C. F., Carison, R. W. & Cooper, J. F. 2006, AstroBiology, 6, 463

Huebner, W. F. 2008, Space Science Reviews, 138, 5

Huebner, W. F., et al. 2006, Heat and Gas Diffusion in Comet Nuclei. SR-004, June, 2006. ISBN 1608-280X. ISSI, Bern, Switzerland, ESA Publications Division.

Kouchi, A., Yamamoto, T., Kozasa, T., Kuroda, T., & Greenberg, J. M. 1994, A&A, 290, 1009

Kouchi, A., & Sirono, S.-i. 2001, Geophys. Res. Lett., 28, 827

Lunine, J. I., & Stevenson, D. J. 1985, ApJs, 58, 493

Marboeuf, U., Mousis, O., Ehrenreich, D. et al. 2008, ApJ, 681, 1624

Marboeuf U., 2009a, PhD Thesis, Univ. de Franche-Comté

Marboeuf, U., Petit, J.-M., & Mousis, O. 2009b, MNRAS, 397, L74

Mousis, O., et al. 2009a, ApJ, 691, 1780

Mousis, O., Marboeuf, U., Lunine, J. I., et al. 2009b, ApJ, 696, 1348

Mousis, O., Marboeuf, U., Petit, J.-M., & Klinger, J. 2005, MNRAS, 362, L40

Orosei, R., Capaccioni, F., Capria, M. T. et al. 1999, Planetary and Space Science, 47, 839

Prialnik, D., Benkhoff, J., & Podolak, M. 2004, Comets II, 359

Schmitt, B., Grim, S.R.J.A., Greenberg, J.M. & Klinger, J. 1992. Crystallization of water rich amorphous mixtures. Physics and Chemistry of Ice. Hokkaido U. Press, Sapporo, 344-348

Schmitt, B., & Klinger, J. 1987, Proc. Symposium on the Diversity and Similarity of Comets. ESA Spec. Publ., 278, 613

Smoluchowski, R. 1988, MNRAS, 235, 343

Tancredi, G., Rickman, H., & Greenberg, J. M. 1994, A&A, 286, 659

Taylor, S. R. 1992, Cambridge, New York: Cambridge University Press, —c1992

SF2A 2009
M. Heydari-Malayeri, C. Reylé and R. Samadi (eds)

FORMATION CONDITIONS OF ENCELADUS AND ORIGIN OF ITS METHANE RESERVOIR

Mousis, O.[1], Lunine, J. I.[2] and Waite, J. H.[3]

Abstract. We describe a formation scenario of Enceladus constrained by the deuterium-to-hydrogen ratio in the gas plumes as measured by the Cassini Ion and Neutral Mass Spectrometer (INMS). We propose that, similarly to Titan, Enceladus formed from icy planetesimals that were partly devolatilized during their migration within the Kronian subnebula. In our scenario, at least primordial Ar, CO and N_2 were devolatilized from planetesimals during their drift within the subnebula, due to the increasing temperature and pressure conditions of the gas phase. The origin of methane is still uncertain since it might have been either trapped in the planetesimals of Enceladus during their formation in the solar nebula or produced via serpentinization reactions in the satellite's interior. If the methane of Enceladus originates from the solar nebula, then its D/H ratio should range between $\sim 4.7 \times 10^{-5}$ and 1.5×10^{-4}. On the other hand, if the methane of Enceladus results from serpentinization reactions, then its D/H ratio should range between $\sim 2.1 \times 10^{-4}$ and 4.5×10^{-4}.

1 Introduction

The composition of the gas plume emanating from Enceladus' southern pole has been measured five times by the INMS instrument aboard the *Cassini* spacecraft. From these data, Waite et al. (2009) inferred that the composition of the plume is dominated by H_2O vapor, a few percent of CO_2, CH_4, NH_3, H_2S, and organic compounds ranging from C_2H_2 to C_6H_6. Signatures of possible CO, N_2, and H_2 are seen but the presence of such species cannot be confirmed from the data alone. ^{40}Ar has also been detected and is probably the decay product of ^{40}K (Waite et al. 2009).

Among the compounds observed by the INMS instrument, at least H_2O, NH_3, H_2S and CO_2 are expected to be primordial (Waite et al. 2009). Indeed, the possible presence of N_2 can be explained as a result from the thermal decomposition of NH_3 in the interior of Enceladus (Matson et al. 2007). The measured CO is likely the product of fragmentation of primordial CO_2 during collection by the INMS (Waite et al. 2009). Moreover, the origin of CH_4 and high order hydrocarbons is uncertain because these compounds might have been trapped by the planetesimals of Enceladus at the time of their formation (Waite et al. 2009) or might also result from hydrothermal reactions in the interior of the satellite (Matson et al. 2007).

In the present work, we propose that Enceladus formed from icy planetesimals initially produced in the solar nebula that, once embedded in the subnebula of Saturn, have been partly devolatilized due to the increasing gas temperature and pressure conditions during their migration inwards within the subdisk. The idea of a solar nebula origin for the planetesimals of Enceladus is supported by the recent D/H measurement in H_2O in the satellite's plume (D/H = $2.9^{+1.5}_{-0.7} \times 10^{-4}$), which is close to the cometary value (Waite et al. 2009). Here, we aim at providing observational tests that may allow characterization of the importance of the devolatilization undergone by the planetesimals of Enceladus during their migration within Saturn's subnebula. Our attention is focused on the origin of CH_4, which is directly tied to the magnitude of this devolatilization. We show that the resulting D/H ratio in CH_4 differs as a function of its source.

[1] Université de Franche-Comté, Institut UTINAM, CNRS/INSU, UMR 6213, 25030 Besançon Cedex, France
[2] Lunar and Planetary Laboratory, University of Arizona, Tucson, AZ, USA
[3] Center for Excellence in Analytical Mass Spectroscopy, Southwest Research Institute, San Antonio, Texas, USA

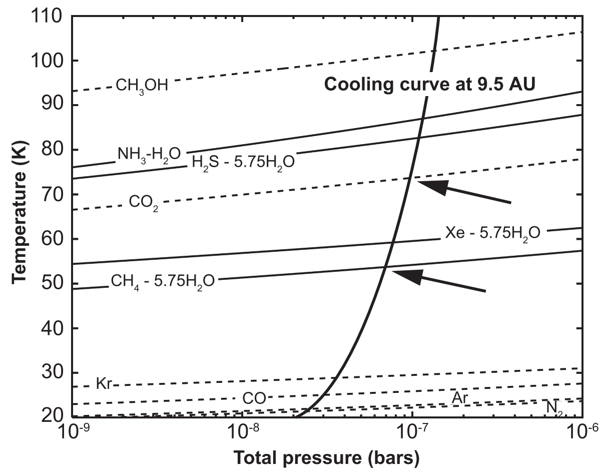

Fig. 1. *Formation sequence of the different ices in Saturn's feeding zone.* Equilibrium curves of ammonia monohydrate, clathrates (solid lines), and pure condensates (dotted lines), and cooling curve of the solar nebula at the heliocentric distance of 9.5 AU, assuming a clathration efficiency of 25%. The bottom and top arrow designate respectively the maximum temperatures at which the planetesimals of Enceladus can be heated during their migration within the Saturn's subnebula if methane observed in the plumes is primordial or if it is produced in the satellite.

2 Formation of Enceladus' planetesimals

The process by which volatiles are trapped in icy planetesimals, illustrated in Fig. 1, is calculated using the stability curves of hydrates, clathrates and pure condensates, and the thermodynamic path detailing the evolution of temperature and pressure at 9.5 AU in the solar nebula, corresponding to the position of Saturn. The cooling curve intercepts the equilibrium curves of the different ices at particular temperatures and pressures. For each ice considered, the domain of stability is the region located below its corresponding equilibrium curve. The clathration process stops when no more crystalline water ice is available to trap the volatile species. As a result of the assumed solar gas phase abundance for oxygen, ices formed in the outer solar nebula are composed of a mix of clathrates, hydrates and pure condensates which are, except for CO_2 and CH_3OH[1], produced at temperatures ranging between 20 and 50 K. Once formed, the different ices agglomerated and incorporated into the growing planetesimals. Figure 1 illustrates the case where the efficiency of clathration is only of $\sim$ 25%. Here, either only a part of the clathrates cages have been filled by guest molecules, either the diffusion of clathrated layers through the planetesimals was too slow to enclathrate most of the ice, or the poor trapping efficiency was the combination of these two processes. In this case, only NH_3, H_2S, Xe and CH_4 form NH_3-H_2O hydrate and H_2S-5.75H_2O, Xe-5.75H_2O and CH_4-5.75H_2O clathrates. Due to the deficiency in accessible water in icy planetesimals, all CO, Ar, Kr and N_2 form pure condensates in the feeding zone of Saturn.

3 What if serpentinization were the source of methane observed in Enceladus?

Two different maximum devolatilization temperatures can be envisaged for the planetesimals of Enceladus. In the first case, similarly to Titan we assume that the methane detected in the plumes is primordial. This corresponds to the hypothesis that the devolatilization temperature of planetesimals never exceeded $\sim$ 50 K during their drift within the subdisk. In the second case, we assume that methane is not primordial and has

[1]CO_2 is the only species that crystallizes at a higher temperature than its associated clathrate in the solar nebula. Moreover, we consider only the formation of CH_3OH pure ice because no experimental data concerning the equilibrium curve of its associated clathrate have been reported in the literature.

been produced in the interior of the satellite. Here, the maximum devolatilization temperature is then of ~ 75 K because a higher value would not be compatible with the presence of primordial CO_2 in Enceladus (see Fig. 2). In the framework of the second case, we examine the possibility that CH_4 is the result of serpentinization reactions, as proposed by Atreya et al. (2006) in the case of Titan. We first estimate the D/H value in the methane of Enceladus, assuming it was produced in its interior from the association of CO_2 or carbon grains with the H_2 formed during the hydrothermal alteration of peridotite (Moody 1976; Atreya et al. 2006; Oze & Charma 2007), and we compare this value to the one acquired by methane had if it originated from the solar nebula.

In terrestrial oceans, hydrothermal fluids and seawater interact with peridotite via the following summary reaction (Moody 1976; Atreya et al. 2006):

$$\begin{aligned}&\text{peridotite (olivine/pyroxene)} + \text{water} \rightarrow\\ &\text{serpentine} + \text{brucite} + \text{magnetite} + \text{hydrogen}.\end{aligned} \tag{3.1}$$

With a bulk density of 1,610 kg m^{-3}, thermal evolution models suggest that Enceladus is most likely a differentiated body with a large rocky core surrounded by a water ice shell that may be liquid at depth (Schubert et al. 2007). In our calculations, we assume that this liquid layer constitutes the water reservoir that is in contact with peridotite during serpentinization reactions. Under these conditions, residual water is deuterium-enriched at the expense of the initial reservoir of free-water and the fractionation factor, α, between OH-bearing minerals and water is then (Lécuyer et al. 2000):

$$\alpha_{r-w} = \frac{R_r^f}{R_w^f}. \tag{3.2}$$

The effect on the D/H ratio of the residual water of a D/H fractionation between the initial water and hydrated peridotite can be readily tested with the following mass balance equation that describes a batch equilibrium mechanism of both hydration and isotopic fractionation between given masses of rock and water (Lécuyer et al. 2000):

$$M_w^i X_w^i R_w^i + M_r^i X_r^i R_r^i = M_w^f X_w^f R_w^f + M_r^f X_r^f R_r^f, \tag{3.3}$$

where M is the mass, X the mass fractions of hydrogen in water ($X_w^i = X_w^f = 1/9$) or rock ($X_r^f = 4/277$), R the D/H ratios before hydratation reactions (i) and at batch equilibrium (f). If we neglect the amount of water incorporated in primordial peridotites of Enceladus ($X_r^i = 0$) and postulate that $M_w^i \simeq M_w^f$ and $M_w^f.X_w^f \gg M_r^f.X_r^f$, which is a reasonable assumption[2], then Eq. 3.3 can be expressed as:

$$R_r^f \simeq \alpha_{r-w} R_w^i. \tag{3.4}$$

We consider two extreme values, 0.95 and 1.03, of the hydrogen fractionation α_{r-w} between serpentine and the free-water reservoir in the literature based on laboratory and field data made at temperatures ranging between 298 and 773 K (Vennemann et al. 1996). We also postulate that the D/H ratio in the methane initially released from the interior is that acquired by hydrated rocks once equilibrium is reached during serpentinization reactions. Hence, the D/H ratio acquired by hydrated rocks would be preserved in the H_2 produced from the alteration of peridotite and used in the recombination of CH_4. Table 1 summarizes the range of predicted values for D/H in CH_4 produced within Enceladus, assuming that D/H ratio in the primordial water reservoir is the value measured by *Cassini* (Waite et al. 2009). This value is compared to the one acquired by methane if it was initially incorporated by the planetesimals of Enceladus during their formation in the nebula. In this case, since it was established that the methane of Titan originates from the solar nebula (Mousis et al. 2009) and since the buiding blocks of the two satellites share a common origin, the D/H ratio in Enceladus' methane should range between the minimum D/H ratio initially acquired by Titan if a significant photochemical enrichment of

[2]The CH_4/H_2O volume ratio observed in the plumes is $\sim$0.5% during the E2 encounter (Waite et al. 2006) and is representative of the value existing in the hypothetical internal ocean (Waite et al. 2009). Assuming that all H_2 involved in the formation of CH_4 results from the reaction of peridotite and water, the fraction of used water is only of $\sim$1 % and the term $M_w^f.X_w^f$ is more than 11 times greater than the term $M_r^f.X_r^f$.

Table 1. D/H ratio in methane as a function of its postulated origin.

Origin	Range of D/H values
Serpentinization reactions	2.1×10^{-4}–4.5×10^{-4}
Solar nebula	$4.7 \times 10^{-5*}$–1.5×10^{-4}

*Minimum D/H ratio acquired by the primordial methane of Titan in case of strong photochemical enrichment in the atmosphere (see text).

deuterium occurred during the evolution of its atmosphere (Cordier et al. 2008) and the value observed today in Titan by *Cassini* (Bézard et al. 2007). From these values, we infer that the D/H ratio in CH_4 produced by serpentinization should be enriched by a factor of 1.9–6.8 relative to D/H in methane originating from the nebula.

4 Discussion

A word of caution must be given about our estimate of the D/H ratio in CH_4 produced via serpentinization. It is based on the idea that no D-fractionation occurred between the produced H_2 and serpentine, and between the produced CH_4 and H_2. Unfortunately, these points are still not well established in the literature and future laboratory work is required to assess their validity. As noted in Waite et al. (2009), the measured H_2 in recent encounters is most likely a product of H_2O interactions with the instrument's antechamber walls due to the high spacecraft velocity relative to the plume. Therefore the amount of endogenous H_2 and its D/H ratio remains undetermined. Future *Cassini* encounters are currently planned at slower spacecraft speed that may allow separate assessments of H_2 in the plume from that synthesized inside the INMS instrument. In this case determinations of D/H in H_2 during the Cassini mission remain a remote possibility that could tell if this species is produced by serpentinization reactions. Measurement of D/H in CH_4 cannot be made with INMS due to overlapping signals of several species in this portion of the mass spectrum. This measurement requires an instrument with mass resolution ($M/\Delta M$) greater than 6000 and thus must wait for a future spacecraft mission, such as TSSM actually studied by NASA and ESA.

Support from the *Cassini* project is gratefully acknowledged.

References

Atreya, S. K., Adams, E. Y., Niemann, H. B., Demick-Montelara, J. E., Owen, T. C., Fulchignoni, M., Ferri, F., & Wilson, E. H. 2006, PSS, 54, 1177

Bézard, B., Nixon, C. A., Kleiner, I., & Jennings, D. E. 2007, Icarus, 191, 397

Cordier, D., Mousis, O., Lunine, J. I., Moudens, A., & Vuitton, V. 2008, ApJL, 689, L61

Lécuyer, C., Simon, L., & Guy, F. 2000, Earth and Planetary Science Letters, 181, 33

Matson, D. L., Castillo, J. C., Lunine, J., & Johnson, T. V. 2007, Icarus, 187, 56

Moody, J. 1976, Lithos, 9, 125

Mousis, O., Lunine, J. I., Pasek, M., Cordier, D., Waite, J. H., Mandt, K. E., Lewis, W. S. & Nguyen, M.-J. 2009, Icarus, in press

Oze, C., & Sharma, M. 2007, Icarus, 186, 557

Schubert, G., Anderson, J. D., Travis, B. J., & Palguta, J. 2007, Icarus, 188, 345

Vennemann, T. W., & O'Neil, J. R. 1996, GCA, 60, 2437

Waite, J. H., et al. 2006, Science, 311, 1419

Waite, J. H., et al. 2009, Nature, 460, 487

COMPOSITION OF THE LAKES OF TITAN

Mousis, O.[1], Cordier, D.[2], Lunine, J. I.[3], Lavvas, P.[3] and Vuitton, V.[4]

Abstract. Hundreds of radar-dark patches interpreted as lakes have been discovered in the north and south polar regions of Titan. We have estimated the composition of these lakes by using the direct abundance measurements from the Gas Chromatograph Mass Spectrometer (GCMS) aboard the Huygens probe and recent photochemical models based on the vertical temperature profile derived by the Huygens Atmospheric Structure Instrument (HASI). Thermodynamic equilibrium is assumed between the atmosphere and the lakes, which are also considered as nonideal solutions. We find that the main constituents of the lakes are ethane (C_2H_6) ($\sim$ 76–79%), propane (C_3H_8) ($\sim$ 7–8%), methane (CH_4) ($\sim$ 5–10%), hydrogen cyanide (HCN) ($\sim$ 2–3%), butene (C_4H_8) ($\sim$ 1%), butane (C_4H_{10}) ($\sim$ 1%) and acetylene (C_2H_2) ($\sim$ 1%). The calculated composition of lakes is then substantially different from what has been expected from models elaborated prior to the exploration of Titan by the Cassini-Huygens spacecraft.

1 Introduction

The surface of Saturn's haze-shrouded moon Titan had long been proposed to have oceans or seas, on the basis of the stability of liquid methane and ethane at the ground level (Flasar 1983; Lunine et al. 1983; Lorenz et al. 2003). Ground-based radar observations ruled out the presence of a global ocean in the 1990s (Muhleman et al. 1995), but the presence of isolated lakes was not precluded (Campbell et al. 2003). A large, dark, lake-like feature subsequently named Ontario Lacus was detected at Titan's south polar region by the Cassini ISS system in 2005 (McEwen et al. 2005) and hundreds of radar dark features with a variety of properties consistent with liquid-filled lakes were found in the northern hemisphere by the Cassini RADAR system (Stofan et al. 2007).

The chemical composition of the lakes of Titan is still not well determined. Good quality spectral data of the Ontario Lacus have been obtained by the Visual and Infrared Mapping Spectrometer (VIMS) aboard Cassini but the only species that seems firmly identified is C_2H_6 (Brown et al. 2008); the atmosphere contains so much CH_4 that it is very difficult to detect the surface liquid phase of this molecule even if it is dominant in the lakes. Because the detection of other compounds in the lakes of Titan remains challenging in the absence of in situ measurements, the only way to get a good estimate of the chemical composition of these lakes is to elaborate a thermodynamic model based on theoretical calculations and laboratory data. Several models, that investigate the influence of photochemistry and the atmospheric composition on the chemical composition of liquids formed on the surface of Titan, have been elaborated in the pre-Cassini years (Lunine et al. 1983; Dubouloz et al. 1989; McKay et al. 1993; Tokano 2005). Based on atmospheric observations these models assumed surface bodies of liquid on Titan to contain a mixture of C_2H_6, CH_4 and N_2 and a large number of dissolved minor species.

However, Cassini-Huygens measurements have improved our knowledge of the structure and composition of Titan's atmosphere, requiring the solubilities to be recomputed under actual Titan conditions. In particular, the Gas Chromatograph Mass Spectrometer (GCMS) aboard Huygens and the Cassini Composite Infrared Spectrometer (CIRS) provided new atmospheric mole fraction data (see Niemann et al. 2005). Moreover, near-surface brightness temperatures at the high latitudes where the lakes exist have now been determined (Jennings

[1] Université de Franche-Comté, Institut UTINAM, CNRS/INSU, UMR 6213, 25030 Besançon Cedex, France
[2] Ecole Nationale Supérieure de Chimie de Rennes, CNRS, UMR 6226, Avenue du Général Leclerc, CS 50837, 35708 Rennes Cedex 7, France; Université européenne de Bretagne; Institut de Physique de Rennes, CNRS, UMR 6251, Université de Rennes 1, Campus de Beaulieu, 35042 Rennes, France
[3] Lunar and Planetary Laboratory, University of Arizona, Tucson, AZ, USA
[4] Université Joseph Fourier, Laboratoire de Planétologie de Grenoble, CNRS/INSU, France

et al. 2009). Here, we propose a model that takes into account these recent advances and thus provides the most up-to-date chemical composition of Titan's lakes as a function of their location on the satellite's surface. Our model considers the same assumptions as those made by Dubouloz et al. (1989) (hereafter D89) when they calculated the composition of the hypothetical ocean proposed to exist on Titan in the years prior the Cassini-Huygens exploration. The lakes are then considered as nonideal solutions in thermodynamic equilibrium with the atmosphere.

2 The model of lake-atmosphere equilibrium

Our model is based on the regular solution theory and the thermodynamic equilibrium is assumed between the liquid and the atmosphere. This thermodynamic equilibrium, which is expressed by the equality of chemical potentials, can be written (Eq. 1 of D89):

$$Y_i\,P = \Gamma_i\,X_i\,P_{vp,i}, \tag{2.1}$$

where P is the total Titan's surface pressure, Y_i and X_i are respectively the mole fractions of the i compound in the atmosphere and the liquid, $P_{vp,i}$ its vapor pressure, and Γ_i its activity coefficient in the liquid given by Eq. 2 of D89. Because the system of involved equations is non-linear, it is solved with the use of the Newton Raphson's method.

Our model also allows us to estimate the fractions of solid precipitates that can be dissolved in the lakes of Titan. To this end, we calculate the *saturation* mole fraction $X_{i,sat}$[1] of the i compound, which is given by (Eq. 7 of D89):

$$\ln(\Gamma_i\,X_{i,sat}) = (\Delta H_m/RT_m)(1 - T_m/T), \tag{2.2}$$

where T_m is the component's melting temperature and ΔH_m its enthalpy of fusion. Our calculation procedure is then conducted as follows:

1. The unknown X_i's and Y_i's are computed via the Newton-Raphson method.

2. Once the X_i's have been determined, the $X_{i,sat}$'s are in turn calculated and compared to the X_i's for each species. If for compound i we get $X_{i,sat} < X_i$, then we fix $X_i = X_{i,sat}$.

3. We get new values of X_i's and $X_{i,sat}$'s via the resolution of the nonlinear system.

4. The iterations are continued until we get a difference between $X_{i,sat}$ and X_i lower than 10^{-6}, value for which the numerical inaccuracy is clearly negligible compared to other sources of uncertainties.

The known Y_i's are derived from Niemann et al. (2005). The precipitation rates used here derive from the photochemical models of Lavvas et al. (2008a,b) and Vuitton et al. (2008) and correspond to the main products of CH_4 and N_2 photolysis. These rates allow to express each i compound that precipitates in the form $X_i = \frac{\tau_i}{\tau_{C_2H_6}} \times X_{C_2H_6}$. We also ensure that $\sum_{i=1}^{n} X_i = 1$ and $\sum_{i=1}^{n} Y_i = 1$. The thermodynamic data used in our calculations derive from the NIST database[2] when they are available and the remaining ones have been taken from D89. Note that H_2 is the only compound whose mole fraction in the liquid is not determined with the aforementioned procedure. Instead, we calculate the amount of dissolved H_2 in the liquid via Henry's law (D89).

3 Results

Our calculations have been performed for two different zones of Titan's surface. The first zone corresponds to the vicinity of the landing site of the Huygens probe, where the surface temperature was measured to be 93.65 K (Niemann et al. 2005). The Huygens probe detected drainage-like features and a high surface relative

[1] The saturation mole fraction of the i compound corresponds to the maximum mole fraction of i in the liquid form. Above this value, the i material in excess remains in solid form.

[2] `http://webbook.nist.gov`

Table 1. Chemical composition of lakes at the poles and the equator.

	Equator (93.65 K)	Poles (90 K)
Main composition (lake mole fraction)		
N_2	2.95×10^{-3}	4.90×10^{-3}
CH_4	5.55×10^{-2}	9.69×10^{-2}
Ar	2.88×10^{-6}	5.01×10^{-6}
CO	2.05×10^{-7}	4.21×10^{-7}
C_2H_6	7.95×10^{-1}	7.64×10^{-1}
C_3H_8	7.71×10^{-2}	7.42×10^{-2}
C_4H_8	1.45×10^{-2}	1.39×10^{-2}
H_2	5.09×10^{-11}	3.99×10^{-11}
Solutes (lake mole fraction)		
HCN	2.89×10^{-2} (s)	2.09×10^{-2} (s)
C_4H_{10}	1.26×10^{-2} (ns)	1.21×10^{-2} (ns)
C_2H_2	1.19×10^{-2} (ns)	1.15×10^{-2} (ns)
C_6H_6	2.34×10^{-3} (ns)	2.25×10^{-3} (ns)
CH_3CN	1.03×10^{-3} (ns)	9.89×10^{-4} (ns)
CO_2	3.04×10^{-4} (ns)	2.92×10^{-4} (ns)

(s): saturated; (ns) non saturated.

humidity, so the presence of liquids cannot be excluded in this area (Tomasko et al. 2005; Niemann et al. 2005). The second zone corresponds to the north pole of Titan where the surface temperature is around ~ 90 K based on near-surface brightness temperature measurements (Jennings et al. 2009). In both cases, the atmospheric pressure is assumed to be identical and corresponds to that (1.46 bar) measured by Huygens at the ground level (Niemann et al. 2005).

Table 1 gives the mole fractions of the main compounds in lakes formed on the surface of Titan and calculated for the two different zones. It shows that, whatever the considered site, their composition is dominated by C_2H_6, C_3H_8, CH_4, HCN, C_4H_8, C_4H_{10} and C_2H_2. On the other hand, with mole fractions much lower than 1%, N_2, C_6H_6, CH_3CN, CO_2, Ar, CO and H_2 are found to be minor compounds in the lakes.

4 Discussion

Our solubility calculations imply that a number of species produced by methane photolysis and energetic particle chemistry in Titan's upper atmosphere should be readily detectable with a mass spectrometer carried to the surface of a liquid-filled lake by a Huygens-like entry probe (Coustenis et al. 2009). The measured abundances of multiple minor constituents in the lake, coupled to measurements and models of stratospheric abundances and production rates, and direct temperature measurements of the lake surface, will constrain lake properties that are of interest in understanding the methane hydrologic cycle. For example, at the winter pole a seasonally deposited upper-layer of liquid methane might exist on top of a longer-lived ethane-methane liquid reservoir by virtue of methane's lower density and limited vertical mixing in the cold lakes (Stevenson and Potter 1986). Such a transient layer would be bereft of minor components compared with our values thanks to the slow sedimentation rate of the high altitude aerosols compared to the seasonal (meteorological) methane deposition rate; our solubility values provide a means of calculating the extent to which the longer-lived liquid reservoir below has mixed into the methane meteorological layer. (The extreme cold of the tropopause of Titan prevents the hydrocarbon constituents other than methane and possibly ethane from passing directly to the lower atmosphere in the gas phase; thus the lakes must be seeded by stratospheric aerosol sedimentation).

This work was supported in part by the CNES. Support from the PID program "Origines des Planètes et de la Vie" of the CNRS, and the *Cassini* project, are also gratefully acknowledged.

References

Brown, R. H., et al. 2008, Nature, 454, 607

Campbell, D. B., Black, G. J., Carter, L. M., & Ostro, S. J. 2003, Science, 302, 431

Coustenis, A., Lunine, J., Matson, D. L., Hansen, C., Reh, K., Beauchamp, P., Lebreton, J.-P., and Erd, C. 2009, LPSC, 40, 1060.

Dubouloz, N., Raulin, F., Lellouch, E., & Gautier, D. 1989, Icarus, 82, 81

Flasar, F. M. 1983, Science, 221, 55

Jennings, D.E., et al. 2009, ApJ, 691, L103

Lavvas, P. P., Coustenis, A., & Vardavas, I. M. 2008b, PSS, 56, 67

Lavvas, P. P., Coustenis, A., & Vardavas, I. M. 2008a, PSS, 56, 27

Lorenz, R. D., Biolluz, G., Encrenaz, P., Janssen, M. A., West, R. D., & Muhleman, D. O. 2003, PSS, 51, 353

Lunine, J. I., Stevenson, D. J., & Yung, Y. L. 1983, Science, 222, 1229

McEwen, A., Turtle, E., Perry, J., Dawson,D., Fussner, S., Collins, G., Porco, C., Johnson, T., &Soderblom, L. 2005, B.A.A.S., 37, 739

McKay, C. P., Pollack, J. B., Lunine, J. I., & Courtin, R. 1993, Icarus, 102, 88

Muhleman, D. O., Grossman, A. W., & Butler, B. J. 1995, Annual Review of Earth and Planetary Sciences, 23, 337

Niemann, H. B., et al. 2005, Nature, 438, 779

Stofan, E. R., et al. 2007, Nature, 445, 61

Tomasko, M. G., et al. 2005, Nature, 438, 765

Tokano, T. 2005, Advances in Space Research, 36, 286

Vuitton, V., Yelle, R. V., & Cui, J. 2008, JGR, 113, 5007

SF2A 2009
M. Heydari-Malayeri, C. Reylé and R. Samadi (eds)

LONG-TERM & LARGE-SCALE SIMULATIONS OF SATURN'S RINGS : VARIABLE VISCOSITY & SATELLITE INTERACTIONS

Salmon, J.[1], Charnoz, S.[1], Crida, A.[2] and Brahic, A.[1]

Abstract. We use a 1-dimensional hydrodynamic code to simulate the global evolution of Saturn's Rings through viscous spreading, including satellites torques. While previous studies, using constant viscosities, suggest a rapid spread out of the ring system in a few hundred million years (Esposito 1986), we show that new viscosity prescriptions derived from N-body simulations such as the one of Daisaka et al. (2001) would dramatically affect the large scale evolution of the ring system, allowing for a survival of the rings over 5 billion years. We show also that transitions form self-gravitating to non self-gravitating regions would produce large scale structures. Surprisingly the final state of the ring system seems somewhat independent of the initial mass using the viscosity of Daisaka et al. (2001). The possibility of confinement by nearby satellites is still under investigation but first results suggest that they could significantly lengthen the rings viscous age.

1 Introduction

Saturn's rings have been studied for more than 400 years and still remain a puzzling object of our Solar System. While most popular scenarios for their formation are based on phenomena occurring in the early ages of our Solar System (Pollack et al. 1973; Dones 1991; Charnoz et al. 2009), several recent observations come to the conclusion that the rings must be quite young (Esposito 1986; Cuzzi & Estrada 1998).

The evolution of Saturn's rings share a lot of similarities with other disks in the universe, e.g. protoplanetary discs or accretion discs. They evolve through 3 main physical processes : viscous spreading, resonant interactions with nearby satellites, and meteoritic bombardment. In the present study we investigate the effects of non-constant viscosity that has been quantified recently in small scale N-body simulations.

The viscous spreading is responsible for the flattening and the widening of the rings (Linden-Bell & Pringle 1974). During this process, mass is lost when material falls onto the planet, or crosses the Roche limit and accretes in satellites. Constraining the timescales for this physical process is thus fundamental to determine the age of Saturn's rings.

2 Viscous spreading with variable viscosity

2.1 Our model

We study the evolution of the surface density of the disk Σ, considering only the radial component of the evolution. Using the formalism of Pringle (1981) we combine the equations of mass and angular momentum conservation to obtain the single equation

$$\frac{\partial \Sigma}{\partial t} = \frac{3}{R}\frac{\partial}{\partial R}\left[\sqrt{R}\frac{\partial}{\partial R}\left(\nu\Sigma\sqrt{R}\right)\right] \tag{2.1}$$

where R is the distance to Saturn, and ν is the kinematic viscosity.

[1] UMR AIM, Université Paris Diderot/CEA/CNRS, CEA/SAp, Centre de l'Orme des Merisiers, 91191, Gif-sur-Yvette Cedex, FRANCE
[2] Department of Applied Mathematics and Theoretical Physics, University of Cambridge, UK

Several N-body simulations have been performed to determine the expression for the viscosity of a disk of particles (Salo 1992; Richardson 1994; Daisaka & Ida 1999; Ohtsuki & Emori 2000). In this work we use the results of Daisaka et al. (2001). They propose a 3-component model for the viscosity : 1) the translational (or "local") viscosity that accounts for the direct collisions between particles, 2) the collisional (or "non-local") viscosity that accounts for the finite size of particles, and 3) the gravitational viscosity that accounts for the self-gravitational torque between particles. This third component is the main improvement of this work. We use the analytical fit to their numerical results in our simulations.

We have developed a 1D hydrodynamical code to compute the variation of the surface density through time by numerically solving equation 2.1. We evaluate the variation of the surface density at each point of a grid by computing the material fluxes through the limits of each bin of the grid. Because of this approach we lose every perturbation smaller than the grid resolution, but it allows us to perform simulations over the age of the Solar System.

2.2 Viscous spreading over 5 billion years

We study the evolution of the disk considering only the viscous torque, using the variable viscosity model described in section 2. Our initial ring is a Gaussian distribution centred on R = 110000 km and 3000 km wide. The initial mass of the rings is about the mass of the satellite Mimas, which is the estimated value of today's rings' mass (Tiscareno et al. 2007). We use particles with $r_p = 1$ m, as suggested by Goldreich & Tremaine (1982).

The first hundred thousand years of evolution are plotted on the left graph of Fig. 1.

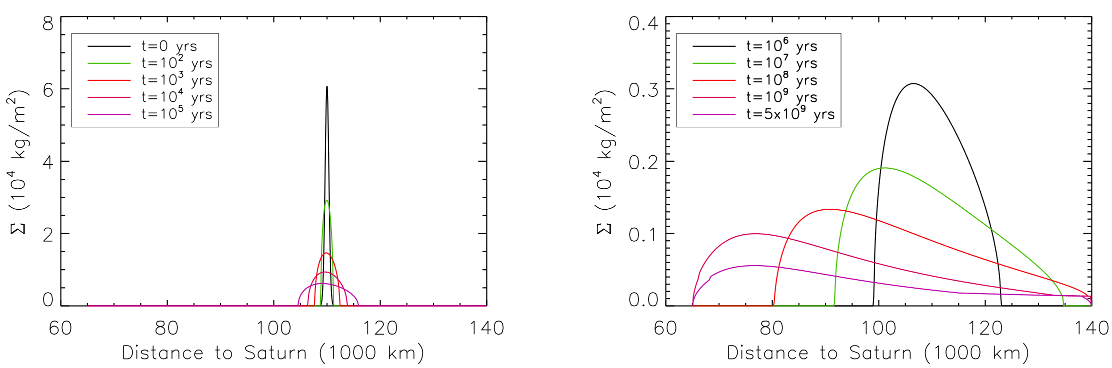

Fig. 1. Viscous evolution of the surface density over 10^5 years (left) and 5×10^9 years (right)

The first comment we can make is that the disk spreads with very stiff edges. This is very different from the spreading with constant viscosity (e.g. (Pringle 1981)) where the progressive edges of the gaussian are conserved through the spreading. This is due to the fact that the edges of the rings have very low surface density and so their viscosity is very low. Therefore, they spread less rapidly than the more dense and viscous core of the rings. Once the edges have been overwhelmed by the material from the core, their viscosity raises and the whole disk spreads.

The evolution up to 5 billion years is plotted on the right graph of Fig. 1. One can see that the spreading rate is quite slow, particularly for the inner edge. The disk is fully spread only after 1 billion years. It is also noticeable that after 5 billion years of evolution, the disk has not disappeared, its average surface density being of the order of 10^2kg/m^2 which is close to the surface density of the middle of today's A ring (Tiscareno et al. 2007).

With variable viscosity, the survival of a disk of dense planetary rings in the dynamical environment of Saturn over the age of the Solar System seems then possible.

2.3 Evolution of the disk's mass

We have plotted in Fig. 2 the evolution of the mass of the disk, for different initial masses ranging from 1 to 10 Mimas' masses.

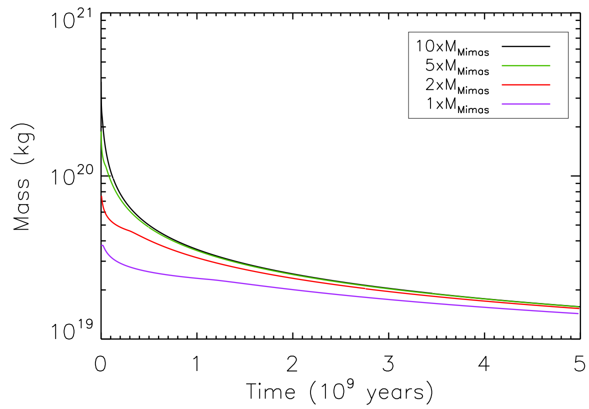

Fig. 2. Evolution of the disk's mass over 5 billion years.

Starting with 1 Mimas' mass (violet curve), the disk's mass is still about 10^{19} kg after 5 billion years of viscous evolution. To study the influence of the initial mass on this result, we performed the same simulations starting with different masses. It appears that whatever the initial disk's mass, the final mass is always about 1×10^{19}. Using the condition of self-gravity of the disk (Toomre 1964; Salo 1995), we computed that this mass corresponds to the maximal mass of a fully non self-gravitating disk. This disk evolves very slowly because in the viscosity model we use the viscosity drops importantly when the disk becomes non self-gravitating.

3 Satellite interactions

We now include in our simulations a satellite with a mass close to Janus' mass. We consider only the first order Lindblad resonances of the disk, and use the formalism of Takeuchi et al. (1996) to compute the evolution of the disk and the migration of the satellite. We plot our results on Fig. 3.

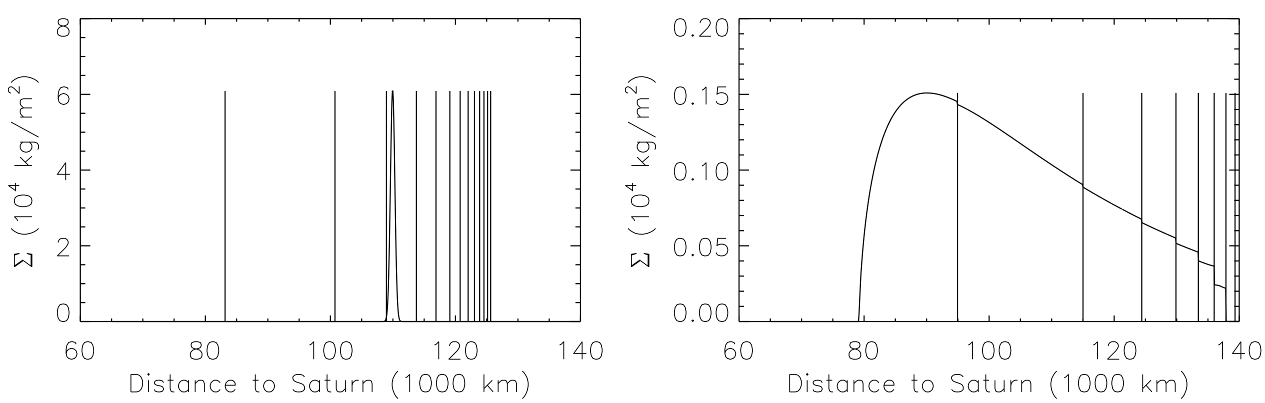

Fig. 3. Initial disk's surface density (left) and after 100 million years of evolution (right). The vertical lines correspond to the Lindblad resonances' locations.

The vertical lines on the graph are the positions of the 15 first first-order Inner Lindblad Resonances. At this locations, the satellite exerts a negative torque that flushes the material inward. The disk itself exerts a retroactive torque on the satellite that starts to migrate outward. The initial configuration is plotted on the left graph of Fig. 3. The satellite's initial position is 132000 km.

The situation of the simulation after 100 million years of evolution is plotted on the right part of Fig. 3. The disk has spread because of the viscosity, but the shape of the surface density is altered at resonances positions : while the viscous torque tends to send material outward, the negative torques at resonances positions prevents the material from doing so. The material is then stuck at the resonance, and so the surface density increases locally, leading to this stairs-like shape.

It is also noticeable that the resonances have moved toward the right. This is due to the retroactive torque from the disk that makes the satellite migrate outward, which moves the resonances positions. After 100 million years of evolution, the satellite's semi-major axis is 169000 km.

Just like the surface density, the mass lost by the disk is also altered by the presence of the satellite. First it is significantly reduced, about two times less than without the satellite. Second, as material is stuck at resonances positions, there are abrupt releases of material when a resonance leaves the disk. The loss of mass by the disk in this configuration is then very "bumpy" and not continuous like in Fig. 2.

4 Conclusions

Using a model of variable viscosity we showed in our simulations that Saturn's rings may have survive against viscous spreading over 5 billion years. We found that the final mass of the disk seems somewhat independent of the initial mass, and that the disk seems to evolve toward a more stable state which is a situation where it becomes entirely non self-gravitating.

Contrarily to the spreading with constant viscosity, the shape of the disk's surface mass density is significantly modified, in particular in the formation of very stiff edges because of the viscosity dropping due to the low surface density values.

While only an early result, we showed that resonant interactions with outer satellites can significantly reduce the outward spreading of the rings, which would increases their survival time. Adding several other satellites is needed to constrain more precisely the effect of the resonant interactions on the spreading time scale of the rings.

References

Charnoz, S., Morbidelli, A., Dones, L. & Salmon, J. 2009, Icarus, 199, 413.

Cuzzi, J. N. & Estrada, P. R. 1998, Icarus, 132, 1.

Daisaka, H. & Ida, S. 1999, Earth, Planet Space, 51, 1195.

Daisaka, H., Tanaka, H. & Ida, S. 2001, Icarus, 154, 296.

Dones, L. 1991, Icarus, 92, 194.

Esposito, L. W. 1986, Icarus, 67, 345.

Goldreich, P. & Tremaine, S. 1982, An. Rev. of Astron. & Astrop, 20, 249.

Linden-Bell, D. & Pringle, J. E. 1974, Mon. Not. of the Roy. Astr. Soc., 168, 603.

Ohtsuki, K. & Emori, H. 2000, Astronomical Journal, 119, 403.

Pollack, J. B., Summers, A. & Baldwin, B., 1973, Icarus, 20, 263.

Pringle, J. E. 1981, An. Rev. of Astron. & Astrop, 19, 137.

Richardson, D. C. 1994, Mon. Not. of the Roy. Astr. Soc., 269, 493.

Roche, E. A. 1847, Académie des Sciences et lettres de Montpellier, Mem. Sect. Sci., 1, 243.

Salo, H. 1992, Nature, 395, 619.

Salo, H. 1995, Icarus, 117, 287.

Takeuchi, T., Miyama, S. M. & Lin, D. N. C. 1996, Astrophysical Journal, 460, 832.

Tiscareno, M. S., Burns, J. A., Nicholson, P. D., Hedman, M. M. & Porco, C. C. 2007, Icarus, 189, 14.

Toomre, A. 1964, Astronomical Journal, 139, 1217.

PNPS

Stellar Physics

SF2A 2009
M. Heydari-Malayeri, C. Reylé and R. Samadi (eds)

SELF-SIMILAR EXPANSION OF POLYTROPIC GAS: APPLICATION TO THE SUPERNOVAE PHOTOSPHERE DYNAMICS

Busschaert, C.[1], Falize, E.[2] and Drouin, M.[2]

Abstract. In this paper we analyze the self-similar expansion of polytropic gas in order to predict the evolution of the supernovae photosphere. We consider a specific solution that we obtained thanks to similarity considerations and which permits to extract an explicit expression of the photosphere dynamics. The latter is compared to silicium line dynamics of 25 SN Ia.

1 Introduction

Similarity analysis and self-similar solutions play an important role in many fields of physics and astrophysics. They give basic information about physical studied systems and are a crucial complement to numerical simulations. In most cases, these specific solutions describe the asymptotic dynamics of systems when a part of boundary and/or initial conditions are lost (Barenblatt & Zeldovich 1972) but in many situations they present important attractor properties. Different methods (dimension analysis (Sedov 1959), Lie group symmetries or Burgan-Feix-Munier transformation (Burgan et al. 1978, Falize et al. 2008) exist in order to obtain them. These methods are based on the invariance properties of equations or on the quasi-invariance principle (Burgan-Feix-Munier transformation),which allows to construct general solutions including those obtained by the standard invariance of equations.

In this paper we consider the dynamics of collisional plasma where the two-temperature effects, viscosity, radiative transfert and thermal conductivity are negligible. As a consequence, the polytropic gas dynamics allows to quantify the hydrodynamic response of matter when submited to high-density energy (Zeldovich & Raizer 1967). Thus, this regime allows to describe detonation, cylindrical and spherical implosion, foil explosion by laser, meteorit explosion, blast wave dynamics or first phase of supernova remnants. Different initial and/or boundary conditions entail various applications. Several analysis have been realized and different self-similar solutions were obtained (see for example Coggeshall 1991, Falize 2008, Falize et al. 2008, Sedov 1959, Simonsen & Meyer-ter-Vehn 1997) in order to describe the following physical systems. In this paper we consider the photosphere dynamics of type Ia supernovae in the vicinity of maximal luminosity. The main motivation of this paper is to use the standard self-similar solution on 25 type Ia supernovae (SN Ia) and find out the exponant dependance of density spatial, which appears as a free parameter depending on the past history of the supernova and particularly the explosion mechanism.

Firstly, we recall the main self-similar solutions and the link between them. Secondly, we apply these considerations to the supernovae photosphere dynamics. Finally we conclude on the main results of this study.

2 Self-similar polytropic gas dynamics

The dynamics of polytropic gas is given by the mass, momentum and energy conservation laws which are given respectively by (Sedov 1959):

$$\frac{\partial \rho}{\partial t} + \frac{1}{r^N}\frac{\partial}{\partial r}\left[r^N \rho v\right] = 0, \quad \left[\frac{\partial}{\partial t} + v\frac{\partial}{\partial r}\right] v = -\frac{1}{\rho}\frac{\partial P}{\partial r}, \quad \left[\frac{\partial}{\partial t} + v\frac{\partial}{\partial r}\right] P - \gamma \frac{P}{\rho}\left[\frac{\partial}{\partial t} + v\frac{\partial}{\partial r}\right]\rho = 0, \tag{2.1}$$

[1] UFR Science - Magistère de Physique Fondamentale - Bat 470 - 91405 Orsay Cedex, France
[2] CEA-DAM-DIF F-91297 Arpajon Cedex, France

where N, ρ, P, v and γ are respectively the dimensionality (N=0, 1, 2 in plane, cylindrical and spherical geometry, respectively) of the problem, the density, the pressure, the velocity and the polytropic index. When, initially or asymptotically, kinetic energy is more important than internal energy, the pressure gradient becomes negligible and the evolution of the different physical quantities is given by the following general solutions:

$$\rho(r,t) = \frac{1}{r^{N+1}} f\left(\frac{r}{t}\right), \quad v = \frac{r}{t}, \tag{2.2}$$

The generality of the function f is very interesting since it is possible to introduce the structure of initial and/or boundary conditions in the form of solutions. For example we can introduce the rarefaction wave solution described by Falize et al. (2008):

$$f\left(\frac{r}{t}\right) = \rho_0 \left(\frac{r}{t}\right)^{N+1} \times \left(1 - \left[\frac{\gamma-1}{2c_s}\sqrt{N+1}\frac{r}{t}\right]^2\right)^{2/(\gamma-1)}, \tag{2.3}$$

but we can also introduce the Stanyukovich (Stanyukovich 1960) or Coggeshall (Coggeshall 1991) solutions. Among those, a very interesting one is a consequence of the similarity properties of polytropic gas. This is the case introduced by Chevalier (Chevalier 1982), particularly valuable within the context of our study, where the function f is given by:

$$f\left(\frac{r}{t}\right) = \left(\frac{r}{t}\right)^{-\alpha}. \tag{2.4}$$

With such a form of f we can deduce the evolution of the photosphere since it is defined by:

$$\frac{2}{3} = \int_{R_{ph}}^{\infty} \kappa(\rho, T)\rho.dr, \tag{2.5}$$

where κ and R_{ph} are respectively the opacity and the position of photosphere. Furthermore, we suppose that opacity is given by a power law, *i.e.* $\kappa(\rho, T) = \kappa_0 \rho^m T^n$. Consequently, we can explicitly derive the expression of the photosphere position which is given by:

$$R_{ph}(t) \propto t^{-\alpha[1+m+n(\gamma-1)]/[1-(N+1+\alpha)(1+m+n(\gamma-1))]}. \tag{2.6}$$

When the opacity is determined by Thomson scattering we find the classic result (Branch et al. 1988, Pearce et al. 1988) in spherical case:

$$R_{ph}(t) \propto R_0 \left[\frac{t}{t_0}\right]^{\alpha/(\alpha+2)}. \tag{2.7}$$

In the following, we will deduce values of alpha fitting with formula (2.7) from SN Ia spectra.

3 Application to supernovae photosphere

We measured the photospheric velocity of 25 SN Ia using the blueshift of the silicium line SiIIλ λ 6347Å 6371Å in their spectra[1]. On the whole, we notice that all the photospheric velocities have the same evolution and, more precisely, the dispersion of velocity drops from 5 690 km/s before the peak brightness to 3 590 km/s a few days later (see Fig 1). This can be explained by a decreasing influence of the initial conditions set by the explosion mechanism. We found that the model of homologous expansion with $f(r/t) \propto v^{-\alpha}$ fits well with the measures. Indeed, by derivating the expression of the photospheric radius (2.7), we can easily devise a linear relation between the logarithm of the photospheric velocity and the logarithm of the time which is observed in the data. It gives us the free parameter for each supernovae (Table 1) and the median for this parameter in our sample is around 8, which is slightly higher than those found in previous work (Chevalier 1982).

[1] The spectra were extracted from the database SUSPECT (*http://bruford.nhn.ou.edu/~suspect/index.html*)

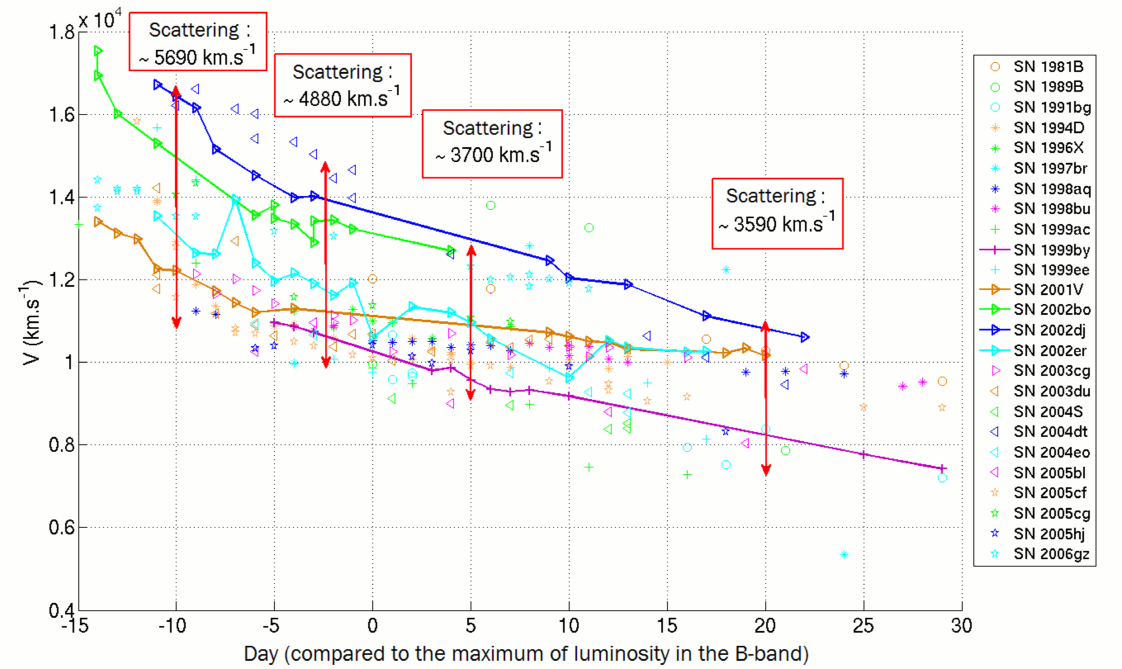

Fig. 1. Evolution of photospheric velocities of 25 SNIa with the time. We estimate the uncertity of the measurement around 200km/s.

4 Conclusion

In this paper we present a self-similar analysis of polytropic gas dynamics. We construct a self-similar solution which describes the asymptotic behavior of this gas. Thanks to a very simple homologous expansion model, we can determine the free parameter which governs the evolution of photospheric velocities of 25 SN Ia. The value of this parameter depends on the past history of the supernova, this may help us to further constrain the current theoretical model based on self-similar solutions.

References

Barenblatt, G. I. & Zeldovich, Y. A., 1972, Ann. Rev. Fluid Mech., 4, 285

Branch, D., Drucker, W. & Jeffery, D. J., 1988, ApJ, 330, L117

Burgan, J. R., Gutierrez, J., Munier, A., Fijalkow, E. & Feix, M. R., 1978, Strongly coupled plasmas, B36, 597

Chevalier, R. A., 1982, ApJ, 258, 790

Coggeshall, S. V., 1991, Phys. Fluids A, 3, 757

Falize, E., 2008, PhD thesis, Observatoire de Paris, France

Falize, E., et al., 2008, J. Phys. Conf. Series, 112, 042015

Pearce, E. C., Colgate, S. A. & Petschek, G., 1988, ApJ, 325, L33

Sedov, L. I., 1959, Mir Edition

Simonsen, V. & Meyer-ter-Vehn, J., 1997, Phys. Fluids, 9, 1462

Stanyukovich, K. P., 1960, Pergamon press

Zeldovich, Y. B. & Raizer, Y. P., 1967, Academic Press (London)

Table 1. References used to get the data concerning the photospheric velocities along with the value of the free parameter α for each SN Ia

Supernovae	Reference / Source	Redshift	Δm_{15}	α
SN 1981B	Branch D. et al., ApJ, 270:123 (1983)	0,00601		6,04
SN 1989B	Barbon R. et al., A&A, 237:79 (1990)	0,00213		4,52
SN 1991bg	Turatto M. et al., MNRAS, 283:1 (1996)	0,00312	1,95	3,60
SN1994D	Patat F. et al., MNRAS, 278:111 (1996)		1,26	8,22
SN 1996X	Salvo M. E. et al., MNRAS, 321:254 (2001)	0,00691	1,31	23,93
SN 1997br	Li W. D. et al., A. J., 117:2709 (1999)	0,0069	1,00	4,31
SN 1998aq	Branch D. et al., Astron. J., 126:1489 (2003)	0,003699	1,12	18,87
SN 1998bu	Spyromilio J. et al., A&A, 426:547 (2004)	0,003	1,01	15,72
SN 1999ac	Garavini G. et al., A. J., 130:2278 (2005)	0,00949	1,30	6,01
SN 1999ee	Hamuy M. et al., A. J., 124:417 (2002)	0,0117	0,94	3,80
SN 1999by	Peter Garnavich / Höflich P. et al., ApJ, 568:791 (2002)	0,00271	1,87	4,68
SN 2001V	Matheson T. et al., A. J., 135:1598 (2008)	0,015	0,99	14,90
SN 2002dj	Pignata G. et al., ArXiv 0805.1089P (2008)	0,00939	1,08	6,04
SN 2002bo	Benetti S. et al., MNRAS, 348:261 (2004)	0,00468	1,13	8,90
SN 2002er	Kotak R. et al., A&A, 436:1021 (2005)	0,00856	1,33	8,21
SN 2003cg	Elias-Rosa N. et al., MNRAS, 369:1880 (2006)	0,004	1,25	12,12
SN 2003du	Stanishev V. et al., A&A, 469:645 (2007) Anupama G. C. et al., A&A, 429:667 (2005)	0,0073	1,02	12,03
SN 2004eo	Pastorello A. et al., MNRAS, 377:1531 (2007)	0,016	1,46	7,77
SN 2004dt	Altavilla G. et al., A&A, 475:585 (2007)	0,01973	1,21	3,41
SN 2004S	Kriscuinas K. et al., A. J., 133:58 (2007)	0,0094	1,14	9,69
SN 2005bl	Taubenberger S. et al., MNRAS, 385:75 (2008)	0,024	1,93	10,90
SN 2005cf	Garavini G. et al., A&A, 427:535 (2007)	0,0065	1,12	8,09
SN 2005hj	Quimby R. et al., ApJ, 660:1083 (2007)	0,0574		10,97
SN 2005cg	Quimby R. et al., ApJ, 636:400 (2006)	0,0313		6,25
SN 2006gz	Hicken M. et al., ApJ, 669:17 (2007)	0,028	0,69	18,78

SF2A 2009
M. Heydari-Malayeri, C. Reylé and R. Samadi (eds)

FROM SOLAR TO STELLAR OBLATENESS

Damiani, C.[1], Tayoglu, M.B.[2], Lefebvre, S.[3] and Rozelot, J.P.[4]

Abstract. Rotation, and more precisely differential rotation, have a major impact on the internal dynamics of stars (and the Sun) and induce many instabilities driving the transport of angular momentum. In the present paper we shall consider the effects on the shape of shellular layers, and to first order, these concerning the apparent oblateness. The first case concerns the Sun, for which accurate limb fluctuations permit to ascertain not only the oblateness, but also its shape, that it to say the determination of the radius with latitude. Thanks to the advent of interferometry techniques, stellar shapes can be now measured with a great accuracy. We will review here the main results obtained so far on different stars and we will give their physical parameters derived from a model fitting procedure. It will be shown how the core density can be reached.

1 Introduction

The non homogeneous mass and velocity rate distributions of stars, including the Sun, modifies their outer shape. Up to a recent date, this departure to sphericity has been considered only as a second order effect on theories of stellar structure. However, discrepancies between models and observations have been noticed, so that the study of stellar shapes cannot be bypassed anymore (Meynet, 2009).

With the advent of more and more precise observations through dedicated techniques such as interferometry, the signature of stellar oblateness, that is to say the difference between the equatorial and polar radius Δr, is now acknowledged. The question is to incorporate this parameter in the equations presently used in stellar interior models to compute the effects on central density.

We will first recalled the solar case, in order to see to what extent the physical basis reached for the internal solar structure can be applied to stars.

2 What can be learned from solar oblateness?

One of the puzzling features of the solar fundamental parameters is its oblateness, as the way to estimate it strongly depends on the variation of both the velocity rate of the rotation, non uniform in latitude and depth, and the distribution of mass inside the Sun. If we look at the Sun as a succession of shellular layers, they all have a different density $\rho(r)$ and they all rotate with a different angular velocity. It is known today that the solar core ($0 < r < 0.2 \ \ R_\odot$) is rigidly rotating faster than the surface, maybe nearly twice (Sturrock, 2009). The tachocline $0.713 < r < 0.718 \ \ R_\odot$) plays a key role in differentiating the rotation up to the near surface. The thin width of this layer is not supposed to be independent of latitude. In the case of a slowly rotating star (like the Sun), it has been shown that hydrostatic background acquires a small ellipticity (as the angular velocity profile is viscously dominated). Charbonneau et al. (1999) found that the mean position of the tachocline moves upwards with latitude. They found a shift of $(0.024 \pm 0.004)R_\odot$ in tachocline position between the latitudes of 0° and 60°, a result found again by Basu & Antia (2006). At the top of the convective zone, the leptocline ($0.975 < r < 0.995 \ \ R_\odot$) will change the shape of the outer surface, mainly due to a reversal

[1] INAF-Osservatorio Astronomico di Roma, via Frascati 33, I-00040 Monteporzio
[2] Kandili Observatory, Turkey
[3] UVSQ; UPMC Univ. Paris 06; CNRS/INSU, LATMOS-IPSL, Tour 45-46, 4 place Jussieu, 75252 PARIS cedex 05, France
[4] Nice University, Fizeau/OCA Dpt, CNRS–UMR6525, Av. Copernic, 06130 Grasse (F)

	Spectral Type	Mass ($M_\odot$)	b ($R_\odot$)	a ($R_\odot$)	T_{eff} (K)	References
Alderamin	A7 IV-V	2.0	2.823	2.175	4750	van Belle et al., 2006
Achernar	B3 Vpe	6.07	12.0	8.3	15000	de Souza et al., 2008
Altair	A7 IV-V	1.8	1.915	1.681	7680	van Belle et al., 2001
Vega	A0 V	2.303	2.873	2.306	9306	Peterson et al., 2006
Regulus	B7 V	3.4	4.16	3.14	12901	McAlister et al., 2005
υ **Cygni**	B2 Ve	6.81	4.62	3.93	19600	Neiner et al., 2005
Rasalhague	A5 III	3.0	2.871	2.390	8250	Zhao et al., 2007

Table 1. Fundamental parameters as deduced from literature, for the seven stars for which an oblateness was observed (up to 2008).

	Alderamin HD 203280	**Achernar** HD 10144	**Altair** HD 187642	**Vega** HD 172167	**Regulus** HD 87901	υ**Cygni** HD 202904	**Rasalhague** HD 159561
$\omega(\mu rad/s)\sin i$	157	36	196	153	118	112	161)
$T_c(K)$	8.2310^6	2.6010^7	1.3210^7	1.6310^7	2.2610^7	3.4410^7	1.4510^7
$P_c(Pa)$	2.0110^{15}	6.5510^{13}	6.4710^{15}	2.3510^{15}	1.2610^{15}	2.8610^{15}	3.8110^{15}
$\rho_c(g/cm^3)$	11.87	0.52	30.04	12.45	6.44	8.35	15.67
J_2	-8.1310^{-3}	-0.1010^{-2}	-4.5910^{-2}	-7.1110^{-2}	-8.6110^{-2}	-5.5210^{-2}	-6.1410^{-2}
Oblateness	0.229	0.308	0.122	0.197	0.245	0.149	0.167
A(gr/cm^2)	4.8810^{55}	2.4810^{57}	2.2410^{55}	6.0110^{55}	1.7710^{56}	4.8210^{56}	8.0510^{55}
C(gr/cm^2)	6.1310^{55}	3.3610^{57}	2.5410^{55}	7.3110^{55}	2.2510^{56}	5.5910^{56}	9.5110^{53}

Table 2. Derived Stellar Parameters from our study.

of the gradient of the radial velocity rate : $\partial\Omega/\partial r$ being < 0 from the equator to around 60°, then canceling and becoming > 0 beyond. The whole shape remains oblate, varying in phase with solar activity, albeit the different layers radius just beneath the surface shows a non monotonic expansion with time (in antiphase with solar activity, the strongest variations of the stratification located at around 0.995 $R_\odot$) (Lefebvre and Kosovichev, 2005). Lefebvre et al. (2009) have studied the behavior of key physical parameters in this layer, for instance opacities changes, super-adiabatic stratification, hydrogen and helium ionisation processes. Probably this layer is the cradle of in-situ changes of magnetic fields, which will need further studies.

From such physical grounds, it can be easily understood that the limb fluctuations reflects the properties of all the physical mechanisms from the core to the surface. If we are able to quantify the chain, it would be possible, from accurate measurements of the outer shape, to go down to the core. For the Sun, we are progressively paving the way, and we are just touching the point to understand how the different mechanisms are articulated all together (Turck-Chièze and Mathis, 2009). Obviously dedicated astrometric space missions (i.e. experiments working at the mas level of accuracy) already scheduled to be launched in a near future (such as SDO –Solar Dynamics Observatory–), will help in a need future to solve such question.

3 Modeling star oblateness

The first approach was made by Chandrasekhar (1933) who was able to compute oblateness of stars under the assumption of a non differential rotation and a power density law with the radius r of the Star. The problem was taken again, mainly by Tassoul (2000). It is shown that rotation flattens the star and produce non uniform temperature and density distributions (i.e. gravitational darkening, De Souza et al, 2002). While the flattening mostly increases the absolute flux level of the energy distribution, gravitational darkening makes an equatorial viewed star apparently cooler than a star seen through the pole.

We will assume here a Clayton's model (Clayton, 1986) for which developments are given elsewhere (Damiani et al., 2010). The main point is the introduction of a scale-length parameter a in the behavior a the pressure gradient with the radius variation r from the core to the surface. a vanishes at the center to increases rapidly in absolute magnitude, until reaching the radius where the density $\rho(r)$ begins to decline where it flattens out, to latter on asymptotically decline toward 0. Thus a has a physical meaning and becomes a key parameter to determine the pressure variation with r, and then the central density. This model must be used cautiously but it can be refined a little bit more by taking into account the oblateness. If we look at the inverse problem, the observed oblateness will permit to derive central density and also the moment of inertia C and A on the z and x axis respectively, and from them, the gravitational moment J_2 which is directly linked.

4 Results

An observed oblateness of seven stars have been reported in the literature. Table 1 gives their spectral type, mass M, effective temperature T_{eff}, as well as their polar b and equatorial a measured radius. From these data, calculated parameters are listed in Table 2: central temperature T_c, central pressure P_c and central density ρ_c, and certainly for the first time the A and C moments of inertia and the gravitational second order moment J_2. This last one seems to be faint, in absolute value, four to five orders of magnitude less than the solar estimate (which is $\approx -2 \times 10^{-7}$).

5 Conclusion

Crucial new insight into the stellar properties is gained from the observations of oblate stars indicating a clear need for more sophisticated stellar structure models than current "standard" models. We encourage observations of oblate stars in order to determine their equatorial and polar radius, through existing facilities such as the CHARA array, the Keck interferometer, the Navy prototype Interferometer (NPOI) or the Palomar Testbed Interferometer PTI). A catalogue of 67 prospective rotationally distorted stars has been given by Van Belle et al (2004) who gave a rough estimate of the ratio R_b/R_a based upon a simplification of an expression describing self-gravitating rotationally distorted gaseous masses: $vsini \approx (2GM/R_b \times (1 - R_b/R_a))^{0.5}$. In the case of Altair, the approximation gives 1.14 instead of 1.16 observed.

References

Basu S., Antia, H.M. and Bogart, R. 2006, ApJ, 654, 1146

Chandrasekhar, S. 1933, MNRAS, 93, 539.

Charbonneau, P., Christensen-Dalsgaard, J., Henning, R., Larsen, R. M., Schou, J., Thompson, M. J., Tomczyk, S. 1999, ApJ, 527, 445

Clayton, D.D. 1986, American Journal of Physics, 54, 354

Damiani, C., Tayoglu, M.B., Lefebvre, S. and Rozelot, J.P. 2010, "Unveiling stellar cores via their flattening", in Synergies between solar and stellar modelling, ROMA (I), 22-26 June 2009, to be published in JASTP

Domiciano de Souza, A., Vakili, F., Jankov, S., Janot-Pacheco, E. and Abe, L. 2002, A & A 393, 345

Lefebvre, S. & Kosovichev, A. G. 2005, ApJ, 633, L149

Lefebvre, S., Nghiem, P. A. P. and Turck-Chièze, S. 2009, ApJ, 660, 1272

Meynet, A. 2009, Physics of rotation in stellar models, in "The Rotation of Sun and Stars", ed. J.P. Rozelot & C. Neiner (Heidelberg: Springer), 765, 139

Sturrock, P.A. 2009, Solar Physics, 254, 227

Tassoul J.L.: 2000, Stellar rotation, Cambridge Astrophysical series, 36, 251p.

Van Belle, G.T., Ciardi, D.R., Thompson, R.R. and Akeson, R.L. 2004, in "Stellar rotation", IAU symposium 215, 177.

Turck-Chièze, S. and Mathis, S. 2009, Earth, Moon, and Planets, 104, 11

SF2A 2009
M. Heydari-Malayeri, C. Reylé and R. Samadi (eds)

PLANE-PARALLEL NUMERICAL STUDY OF THE VISHNIAC INSTABILITY IN SUPERNOVA REMNANTS

Cavet, C.[1], Michaut, C.[1], Nguyen, H. C.[1,2], Bouquet, S.[1,3] and Sauty, C.[1]

Abstract. In this work we study the Vishniac instability with the HYDRO-MUSCL2D code. In the framework of supernova remnants, we realize numerical simulations of a shock front perturbed by a sinusoidal disturbance in the plane-parallel geometry. We vary the wavenumber of the perturbation to understand its effect on the evolution of the instability. For the perturbative wavenumber range of this geometry, we observe an oscillation of increasing amplitude like the Vishniac overstability. Furthermore we obtain the similar dependence of the numerical and theoretical models between the growth rate of the instability and the wavenumber.

1 Introduction

The Vishniac instability discovered analytically in the context of radiative shocks is not well known nowadays. With numerical simulations, we want to explore the parameters allowing the triggering and the growth of the instability and we finally want to go deeper in the understanding of this process. In the astrophysical context, the Vishniac instability is invoked to explain the fragmentation of the shock front of supernova remnants (SNRs) when the blast wave resulting from a star explosion evolves in the radiative phase and particularly in the Pressure Driven Thin Shell (PDTS) stage. The linear regime of the instability was theoretically studied by Vishniac in 1983 (see also Cavet et al. 2008) and was continued to a less constraining approximation by Ryu & Vishniac (1987) and Vishniac & Ryu (1989). In SNRs, the action of instabilities on the resulting morphology of these objects is confirmed by observations (Mac Low & Norman 1999; Raymond 2003). But the role of the Vishniac instability is not yet proved in these astrophysical objects. In laboratory astrophysics, several experiments based on laser facilities have been achieved on this subject (Grun et al. 1991; Edens et al. 2007) and they have enabled to produce a hydrodynamic instability on the radiative shock front. But the discrepancy between the experimental and the analytical growth rate of the instability does not allow the probate of the existence of the instability in the laboratory. To improve the understanding of the Vishniac instability, we perform a numerical study of a perturbed thin shell of shocked matter propagating under the strong shock regime in plane-parallel geometry ((y, x) inverse coordinates). The instability starts when a small perturbation appears on the thin shell creating a mismatch between the ram pressure and the thermal pressure which push on both sides of the thin shell. The consequence of this mismatch is the establishment of opposite matter flows along the thin shell *i.e.* in the transverse direction of the shock front propagation. A crucial point of numerical simulations of the instability is to correctly introduce the perturbation on thin shell. In a previous paper (Cavet et al. 2009) we have introduced perturbative spots on the density to trigger the instability but this method does not allow to easily control the wavenumber of the perturbation. In the present approach, we introduce a sinusoidal perturbation on the thin shell defined by a wavenumber l and an amplitude A. To explore a part of the parameters leading the instability, we set the shock front velocity V_s (along the x axis) and A and we vary l to analyze the effect of the perturbative wavenumbers on the growth of the instability. Furthermore, we study the Vishniac overstability on short time evolution of the simulations. The overstability, predicted by Vishniac (1983), consists in obtaining an oscillation of increasing amplitude on the fluid parameters (density ρ, velocity

[1] LUTH, Observatoire de Paris, CNRS, Université Paris-Diderot, place Jules Janssen, 92190 Meudon, France
[2] Laboratoire de Mathématiques, Université Paris-Sud, 91400 Orsay, France
[3] Département de Physique Théorique et Appliquée, CEA-DIF, 91297 Arpajon, France

v, and pressure p) and on the spatial parameter x. We observe this process on the thin shell displacement until unfortunately the numerical carbuncle instability (Quirk 1994) perturbs the system. Finally, we present the numerical results of the growth of the shock front density and we compare the growth rate of the instability to the analytical one.

2 Numerical simulations

To realize numerical simulations of a perturbed shock front we use the HYDRO-MUSCL2D code developed by our team (Cavet et al. 2009). We realize the simulations of the instability in two steps. Firstly we create an unperturbed isothermal (radiative approximation) shock provided by the strong explosion model adapted to the plane-parallel geometry. In order to simulate the strong and punctual explosion, we introduce an energy $E_1 = 10^{44}$ J in a strip of cells. The simulation produces three different media: the internal region included between the cell strip of the explosion and the internal side of the evolving thin shell (medium 1), the thin shell itself included between its internal side and the shock front (medium 2), and finally the region representing the interstellar medium (medium 3) where the density is $\rho_3 = 10^{-20}$ kg.m^{-3}. The adiabatic indices are set for the three media at $\gamma_1 = \gamma_3 = 5/3$ and $\gamma_2 = 1.1$ where the value of γ_2 reports the energy loss by radiation in an optically thin radiative approximation. We let evolve the self-similar shock front until it reaches a preselected shock front velocity V_s. This settled parameter have an effect on the growth of the instability but its effect is not predicted by the theory and then V_s can take values on a large domain. The only constraint is that the velocity has to be sufficient to preserve the strong shock regime (*i.e.* the shock front compression equal to $(\gamma_2 + 1)/(\gamma_2 - 1)$). Nevertheless the choice of the value of V_s is not easy. The self-similar law for the PDTS phase gives a velocity range $V_s \sim 150 - 200$ km s^{-1}. But observations of the radiative Crab Nebula SNR give a higher velocity $V_s \sim 300$ km.s^{-1} (Sankrit & Hester 1997). Considering different reasons, we have chosen in this study $V_s = 470$ km.s^{-1}.
Secondly we introduce a sinusoidal perturbation on the previous unperturbed thin shell to trigger the instability as Blondin & Marks (1996) in their study of the Non linear Thin Shell Instability. We chose to perturb the shape of the shock front and not the fluid parameters differently of Mac Low & Norman (1993). The interest of our approach is its linkage property with the analytical model of Ryu & Vishniac (1987), thus we can retrieve the same optimal wavenumber. We can directly control the sinusoidal perturbation by two parameters: the wavenumber l and the amplitude A. In this study, we vary only l. The theoretical analysis gives the instable wavenumber range for the plane-parallel case (Ryu & Vishniac 1987): $l = [4 - 26]$ with a maximal growth rate for $l = 14$. Then we set the amplitude $A \sim 8\%$ of the wavelength λ (where $\lambda = 2\pi x_s/l$) to initialize the linear regime of the instability but in a future work we will study the forced nonlinear regime where $A > 10\%$ of λ. The results of simulation shown in Fig. 1 are realized with the more perturbative wavenumber $l = 14$ (*i.e.* the

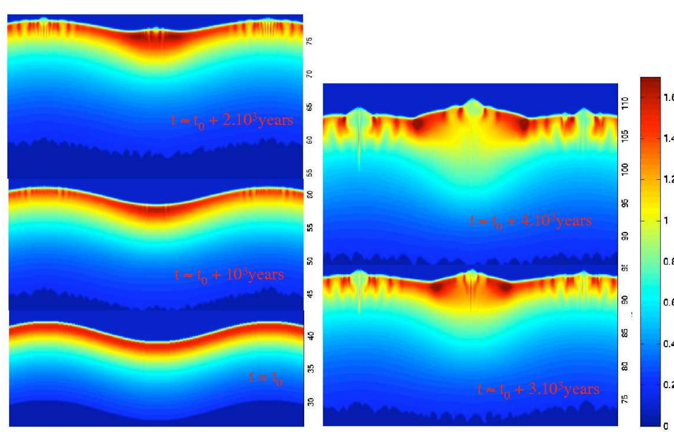

Fig. 1. Evolution of the Vishniac instability in plane-parallel geometry for $l = 14$, $A = 8\%$ of λ and $V_s = 470$ km.s^{-1}: snapshots of a zoom of the density map in 10^{-19} kg.m^{-3}. The shock front propagates according to the x axis (vertical direction) and the origin of this axis corresponds to $x_0 = 42 \times 10^{15}$ m. On the zoom, the evolution of one valley and two hills is observable. The shock front matter moves from the hills to the valley and *vice-versa*. The empty bubble appearing at $t = t_0 + 10^3$ years are due to the numerical carbuncle instability.

optimal wavenumber). In this simulation we have introduced the perturbation at the SNR age $t_0 \sim 4 \times 10^3$ years and we have let evolve the instability during $\Delta t = 10^4$ years. At the first step of the evolution ($t = t_0 + 10^3$ years), the process predicted by the theoretical model is acting on the thin shell: diminution of the density on the hills (orange in the density scale) and growth of density in the valleys (dark red) due to the action of a transversal flow moving the matter from the hills to the valleys. This flow of shoked gaz is the strongest at the maximum deflection point *i.e.* the middle point between a hill and a valley. At this moment, the maximum of density in the valley is $\rho_{valley} = 1.08\,\rho_{s,init}$ where $\rho_{s,init}$ is the initial density on the shock front *i.e.* the unperturbed shock front density. The spatial perturbation triggers the density variation. Then at $t = t_0 + 2 \times 10^3$ years, we already observe the deformation of the valley structure on the x axis indicating a change of the matter motion in the thin shell. At this time we remark a second linked effect which is the taking up of the lagging of the valleys. Indeed the positions of the valleys are close to the position of the hill. This evolution of the initial sinusoidal perturbation of the thin shell is the Vishniac instability. We understand better this phenomenon at $t = t_0 + 3 \times 10^3$ years when the transversal flow changes of direction. Indeed the valley matter is divided in two clumps, then the valleys lose their matter and become hills and *vice-versa*. This oscillating process of the thin shell displacement and the fluid parameters is the overstability predicted by Vishniac (1983). More latter and until the end of the simulation, we observe a numerically perturbed phase with transformation of numerical oscillations in empty bubbles with triangular structures due to the numerical carbuncle instability acting on perturbed shock front in this geometry (Quirk 1994).

3 Discussion of the results

After this first morphological study, we focus ourselves on the first phase of the instability where we have only small numerical problems. We let evolve the perturbed shock front during $\Delta t = 2 \times 10^3$ years. During this period, we want to understand how the wavenumber l acts on the evolution of the fluid parameters by calculating the growth rate s of the instability and by comparing the numerical growth rate law $s(l)$ with the analytical one. First, we make a cut on the map density following the shock front to see the parameter evolution. We

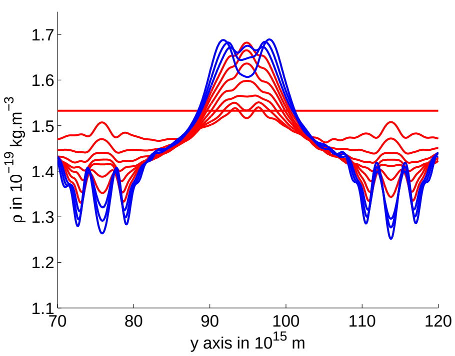

Fig. 2. Evolution of a density cut following the shock front (cut alongt the y axis, density in 10^{-19} kg.m^{-3}). Each curves correspond to one time and the time step is $dt = 0.2 \times 10^3$ years . The density is smoothed to remove the numerical oscillations present on hills and valleys.

visualize in Fig. 2 one part of this cut (two hills and one valley) to study the density variation at the center of the valley (at $y = 95 \times 10^{15} m$ in Fig. 2). At this position, we see the growth (in red) and the decrease (in blue) of the density due to the transversal motion of the matter in the thin shell and we can calculate the density perturbation $\delta\rho = |\rho_{pert} - \rho_{s,init}|$ where we choose $\rho_{s,init}$ constant and given by the straight line at $t = 0$, $\rho_{s,init} = 1.54 \times 10^{-19}$ kg.m^{-3}. The theoretical analysis gives the variation of the density perturbation with time t: $\delta\rho \propto K t^s$ where $s = s_r + i\, s_i$ is the complex growth rate and K a constant including the self-similar profile of the unperturbed density. With a χ^2 fitting, we find the growth rate of the instability for several wavenumbers visualized in Fig. 3. Comparing with the analytical model, we do not find the same value of the growth rate but we observe the same dependence between the growth rate and the wavenumber: the optimal wavenumber is $l = 14$. But we have large error bars in our data due to the small size of the sample and due to the numerical noise created by the carbuncle instability. We note that not all our simulations realized with a

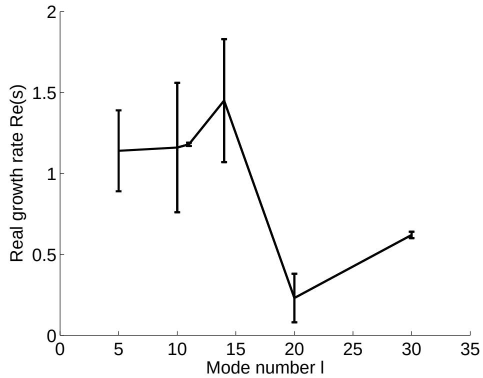

Fig. 3. Real part of the growth rate s_r versus the wavenumber of the perturbation l. We observe a similar law with the analytical model.

specific wavenumber are included in this plot due to some initialization problems in these simulations preventing a normal evolution of the density variation in our measurement point, the valley center. This fact points out that the measure of the density in only one point is not the better parameter to determine the growth rate. In future works we will use the mass of a hill and a valley, *i.e.* the density integrated over a half period of the wavelength λ, to find s.

4 Conclusion

In this numerical study, we have obtained the Vishniac overstability. We have observed the oscillation of the thin shell displacement and we have found numerically the same theoretical law between the growth rate and the wavenumber of the perturbation. But in this work we have tested only one part of the instable parameters and we need to purchase this study to understand the effect of the other variables on the growth of the instability, specially in cylindrical and spherical geometries where the action of the carbuncle instability is reduced on the axis of the thin shell. In an other domain, we have two experimental projects at short and long terms. In a close future, we propose in collaboration with Edens et al. on the Z-Beamlet laser of Sandia laboratory to prove the existence of the Vishniac instability in laboratory. In a later future, we want to explore the instability parameters on the LIL facility (high-power laser, 60 kJ) in Bordeaux. Then, by two different approaches, namely numerical analysis and laboratory experiments, we tend to a complete overview of the Vishniac instability.

Thank to PNPS for financial support allowing us to realize experiments on plasma jets on LULI2000 (Ecole Polytechnique).

References

Blondin, J. M., Marks, B. S. 1996, New Astronomy, 1, 235
Cavet, C., Michaut, C., Falize, E. 2008, SF2A-2007: Semaine de l'Astrophysique Française, meeting held in Grenoble, France, July 2-6, 2007. (Eds.: J. Bouvier, A. Chalabaev, C. Charbonnel) EDP-Sciences, Conference Series, p.443
Cavet, C., Nguyen, H. C., Michaut, C. , Falize, E., Bouquet, S., Di Menza, L. 2009, Astrophys. Space Sci., 322, 91
Edens, A. D., et al. 2007, Astrophys. Space Sci., 307, 127
Grun, J., et al. 1991, Phys. Rev. Lett., 66, 2738
Mac Low, M-M., Norman, M. L. 1993, Astrophys. J., 407, 207
Mac Low, M-M., & Norman, M. L.1999, Lect. Notes in Physics, 523, 391
Quirk, J. J. 1994, Int. J. Num. Meth. Fluids, 18, 555
Raymond, J. C. 2003, RevMexAA, Conference Series, 15, 258
Ryu, D., & Vishniac, E. T. 1987, Astrophys. J., 313, 820
Sankrit, R.; Hester, J. J. 1997, Astrophys. J., 491, 796
Vishniac, E. T. 1983, Astrophys. J., 274, 152
Vishniac, E. T., & Ryu, D. 1989, Astrophys. J., 337, 917

SF2A 2009
M. Heydari-Malayeri, C. Reylé and R. Samadi (eds)

THE GAIA-RVS STANDARDS: A NEW FULL-SKY LIST OF 1420 STARS WITH RELIABLE RADIAL VELOCITIES

Crifo, F.[1], Jasniewicz, G.[2], Soubiran, C.[3], Veltz, L.[4], Hestroffer, D.[5], Katz, D.[1], Siebert, A.[6] and Udry, S.[7]

Abstract. The Gaia-RVS is a integral-field spectrograph with no calibration device onboard. The instrument will be self-calibrated through the reduction procedure; but it needs a list of well-know stars to define the zero-point and to initiate the iterative reduction process. The IAU RV-standards are not numerous enough (some 140 objects; whereas some 1500 are needed), and many are too bright for the RVS. A new list has been defined, with criteria adapted to the RVS capabilities: magnitude and spectral range, no double stars, no variables, "clean" environment up to 80 arcsec, uniform sky coverage. The stars were taken from a few existing good lists, and each one needs to be reobserved at least 2 times before launch (2012), and also during the mission (end 2018). The list is now ready, and the reobservations are going on at high rate. This list should be released in a near future, so that everyone can use it, and eventually improve it.

1 The need for ground-based standards, and reference star selection

The RVS is designed mainly for measuring radial velocities of the brightest Gaia targets. Such a device had been missing on HIPPARCOS; however, due mainly to weight problems, it must be extremely light, and hence contains NO onboard calibration device for this slitless spectrograph. The wavelength calibration has to come from target stars for which the radial velocity is already known from ground- based measurements with a much higher accuracy. The expected final accuracy on the RVS stars is 1 to 15 km/s, depending on magnitude and spectral type.

Bright asteroids are the best references, as their velocity can be calculated theoretically with great accuracy; but they are not numerous enough and not well distributed on the sky; therefore stars have to be used too. These reference stars must be selected with care and verify a list of requirements, among them RV-stability within 100 m/s at the end, non-multiplicity, and lack of disturbing neighbours within the selection window (80 arc-sec), FGKM non-variable stars, etc. All these stars must have already several measurements available in the literature, and are all taken from the Hipparcos Catalogue for homogeneity reason. They are selected within the three following published lists: Nidever et al. (2002); Nordström et al. (2004; mostly CORAVEL data); Famaey et al. (2005; CORAVEL data). A list of 1420 stars (hereafter g8 list) well distributed over the sky is now defined, and each star must be reobserved at least two times before launch, and then during the mission, in order to insure that they are stable.

2 Status of ground observations

Three spectrographs are used: Sophie at OHP and Narval at Pic du Midi for the northern stars; and Coralie at La Silla (swiss Euler Telescope) for the southern ones. In addition, most spectra contained at OHP in the

[1] GEPI (UMR 811 du CNRS; Université Paris 7), Observatoire de Paris, 92195 MEUDON Cedex, France
[2] UMR CNRS/UM2 GRAAL, CC 72, Université Montpellier2, 34095 MONTPELLIER Cedex 05, France
[3] Université Bordeaux 1, CNRS, LAB, F-33270 FLOIRAC, France
[4] Astrophysikalisches Institut Potsdam, POTSDAM, Germ any
[5] IMCCE (UMR 8028 du CNRS),Observatoire de Paris , 77 av. Denfert-Rocherau, 75014 PARIS, France
[6] Observatoire de Strasbourg (Université Louis Pasteur et CNRS), 11 rue de l'Université, 67000 STRASBOURG, France
[7] Observatoire de Genève, 51 Ch. des Maillettes, 1290 SAUVERNY, Switzerland

Elodie archive are also available. Figure 1 left shows the sharing between the spectrographs. Some stars are in common between the various spectrographs. Bright asteroids are systematically observed during each observing run. The Narval spectrograph is of special interest, as it is the only one covering the RVS spectral interval (847 - 874 nm): a same spectrum over the total available interval is reduced with 2 different procedures, the first using the Elodie-Sophie spectral interval (390 - 690 nm), and the second one over the RVS interval (see figure 2, right). As the spectral lines included are not the same, a small difference is expected, and is presently investigated.

In conclusion, the observations are going well, but need to be continuated at the present rate.

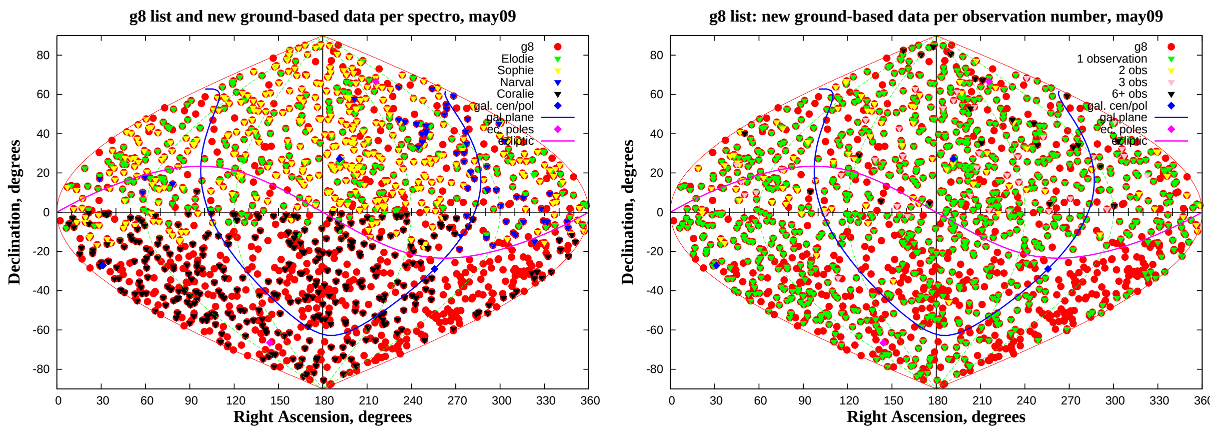

Fig. 1. Maps of reobservations. Left : Share-out of the stars between the spectrographs. **Right**: Number of reobervations per star with a SAME spectrograph. Red dots indicate stars not yet reobserved in May 2009.

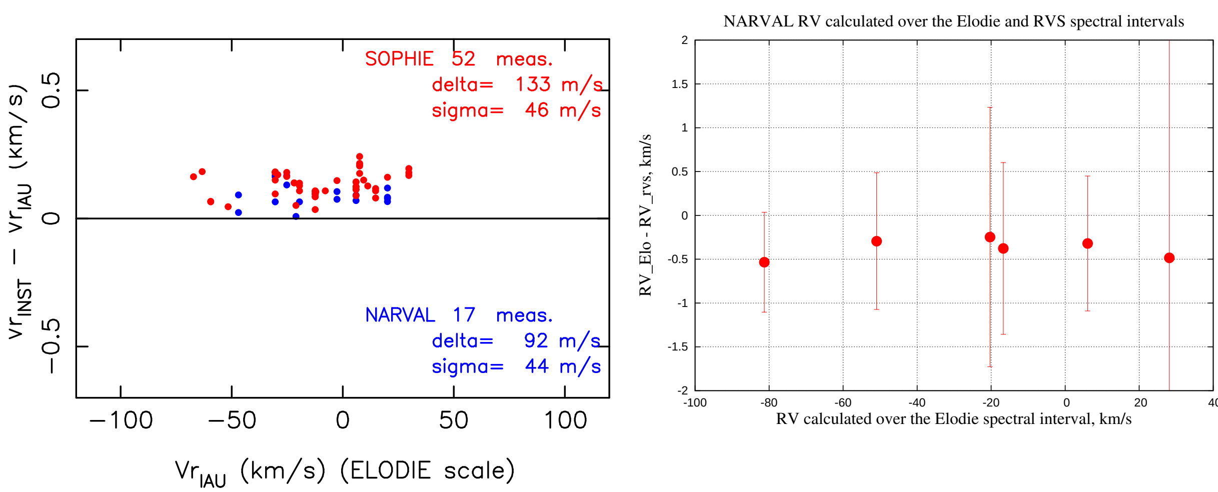

Fig. 2. Left : Comparison of RVs obtained by SOPHIE and NARVAL for several IAU standards, with the IAU value. **Right**: RV derived from the same NARVAL spectra over the Elodie and RVS spectral intervals; very preliminary values.

References

Famaey, B., Jorissen, A., Luri, X., et al., 2005, A&A, 430, 165

Nidever, D. L., Marcy, G. W., Butler, R.P., et al., 2002, ApJS, 141, 503

Nordström, B., Mayor, M., Andersen, J., et al., 2004, A&A, 418, 989

SF2A 2009
M. Heydari-Malayeri, C. Reylé and R. Samadi (eds)

PRELIMINARY RESULTS ON A SAMPLE OF BE STARS OBSERVED WITH THE VEGA/CHARA INTERFEROMETER

Delaa, O.[1], Stee, P.[1], Zorec, J.[2] and Mourard, D.[1]

Abstract.
It is well known that the Be phenomenon, i.e. presence of Balmer lines emission and infrared excess in the spectrum of Be stars, takes its origin in a rotating disk-like circumstellar environment. On the other hand, the origin, kinematics and geometry of those circumstellar environments are still hardly debated. In this contribution, we present the first results from the VEGA/CHARA interferometer observations of the classical Be star Ψ Per. We have extracted the visibilities and differential phases from these interferometric data, mainly around the Balmer H_α and H_β emission lines, and tried to determine the geometry and kinematics of the concerned emitting regions.

1 Introduction

Classical Be stars are Main Sequence B-type stars with high rotational velocities, which are surrounded by a rotating flattened circumstellar environment, which produces the emission lines in spectrum of these objects. This circumstellar environment is also responsible for the measured infrared excess, due mainly to the free-free and free-bound transitions (Gehrz et al. 1974). These two most outstanding characteristics define what has been called the "Be phenomenon". The geometry and structure of these envelopes were intensively studied since Struve's scenario proposed in 1931, where the rapid rotation is responsible for a lens-shaped stellar photosphere and an equatorial ejection of matter that leads to the formation of a nebulous ring. There is now clear evidence for the geometry of these circumstellar envelopes being mostly flattened and axisymmetric (Dougherty & Taylor 1992; Hanuschik 1996; Quirrenbach 1997; Stee 2003). From the study of accretion disks it follows that disks in hydrodynamical equilibrium and in Keplerian rotation are very thin, since their vertical scale height is governed by the gas pressure only. For a disk to be thicker, either additional mechanisms have to be assumed, or the disk might not be in equilibrium (Bjorkman & Carciofi 2004). Be stars have "excretion" disks rather than "accretion" ones. The hydrostatic equilibrium might not only be determined by the gas pressure but also by magnetic fields (Arias et al. 2006, Zorec et al. 2007), so that their vertical scale height can increase. Another important property of "classical" Be disks is that their equatorial region must be characterized by a very low radial expansion velocity (Poeckert & Marlborough 1978; Waters et al. 1986, 1987, 1992). In a recent paper, Meilland et al. (2007) have confirmed that the equatorial disk around the Be star α *Area* is in Keplerian rotation with a disk radial velocity of only few kms^{-1}. In addition to this rotating equatorial disk-like region, Be stars seem to have a much more rarefied region above and below the equatorial plan where the velocities may reach up to 1000 km/s, often called "polar winds". Evidence for such high velocity regions are found in the strong asymmetry of far-UV lines, which are formed in these regions (e. g. Marlborough 1987), and from the recent interferometric observations that put forward evidence for a polar wind along the rotational axis of Achernar (Kervella & Domiciano de Souza 2006).

Differential spectro-interferometry is a powerful tool to study the kinematics within the circumstellar environments. The shape of the differential phase of fringes across the Brγ line profile is related to the photocenter

[1] Lab. H. Fizeau, CNRS UMR 6525, Univ. de Nice-Sophia Antipolis,Observatoire de la Cote d'Azur, Avenue Nicolas Copernic, 06130 Grasse, France. email: Omar.delaa@obs-azur.fr
[2] Institut dAstrophysique de Paris, UMR 7095 du CNRS, Universite Pierre & Marie Curie, 98bis bd. Arago, 75014 Paris, France

displacement as a function of the wavelength and is very sensitive to the β exponent of the rotation power law used in the modeling of disks (Stee 1996). As already mentioned, by using a Keplerian rotation within the disk, Meilland et al. (2007) were able to obtain a very good agreement between the VLTI/AMBER data and the theoretically predicted visibilities and phases of the Brγ emission line as a function of wavelength, for four VLTI baselines.
Nevertheless, many questions regarding the origin of the Be phenomenon remain still unsolved and are source of intense debated. For instance, why some hot stars are able to form disks, but not others ? Why some disks appear and disappear quasi-cyclically ? What are the final geometry and kinematics of Be stars disks ? What is the incidence of these disks on the underlying star evolution ? Is the Be phenomenon due to binarity ?

The following paper deals with the study of the geometry and kinematics of the circumstellar disk around the Be star Ψ Per. It is structured as follows: In section 2, the VEGA/CHARA instrument and the observations of the classical Be stars Ψ Per are presented. In section 3, we summarize our main results. Some prospectives regarding the study of this star are drawn in section 4.

2 Observations

2.1 The VEGA/CHARA instrument

The Visible spEctroGraph and polArimeter (VEGA) instrument (Mourard et al. 2009) operates in the visible domain and combines a spectrograph with a polarimeter. The spectrograph is designed to sample data in the visible wavelengths from 0.45 to 0.85 μm. Two photon counting detectors in the blue and red spectral domains can record the dispersed fringes. The main characteristics of this spectrograph are summarized in Table 1.

Grating	R	$\delta\lambda$(blue)	$\delta\lambda$(Red)	$\lambda_R - \lambda_B$
R1: 1800 gr/mm	30000	5 nm	8 nm	25 nm
R2: 300 gr/mm	5000	30 nm	45 nm	170 nm
R3: 100 gr/mm	1700	100 nm	150 nm	not possible

Table 1. Spectral resolutions (Rx) and bandwidths ($\delta\lambda$) of the VEGA spectrograph, and the spectral separation between the two detectors.

Simultaneous observations with the two detectors are possible only in the high and medium spectral resolution modes. Thus, it is possible to record simultaneously data in the medium resolution mode around Hα with the red detector and around Hβ with the blue detector. Nevertheless, the observations with the blue detector require good seeing conditions, which is the main reason that our results obtained with the blue detector are not as good as those with the red one. The medium (6000) and high (30000) spectral resolutions are well suited for studies of disk kinematics. They provide velocity resolutions of 60 and 10 kms^{-1}, respectively. The low (1700) and medium resolution powers are useful for absolute visibility measurements and for the study of binaries or multiple systems.

The polarimeter has a Wollaston prism to separate two orthogonal polarization states, and a movable quarter wave plate. A fixed quarter wave plate is placed after the Wollaston prism to transform the two linearly polarized output beams into two circularly polarized beams. This is done to avoid unbalanced transmissions by the grating. After being spectrally dispersed, the two beams carry each both the interference pattern and the polarization information. These are focused on the photon-counting detectors, which produce two (x, λ) images, one per polarization state, referred as "High" and "Low" polarizations with respect to their position on the detector. As previously detailed by Rousselet-Perraut et al. (2006), this polarimeter can measure three (I, Q, and V) over four Stokes parameters.

2.2 VEGA/CHARA observations

ψ Per was observed with VEGA using the CHARA array facilities located at the Mount Wilson Observatory (LA, California, USA). The Observations were carried out on 7, 8 and 9 October 2008. ψ Per was observed with the Red and Blue detectors, centered around 656 nm and 486 nm, respectively. We used the medium (R = 5000) spectral resolution, but no polarimetric mode observation was carried out for this star. For each observation, two over six 1 meter telescopes available within the CHARA array were used. Thus, no closure phase (which requires at least 3 telescopes) was available. Details on the observing run can be found in Table 2.

Object	date	Telescopes	baseline (m)	Orientation (deg)
ψ Per	07/10/2008 11h33	S1S2	32.35	-20.92
	08/10/2008 06h52	S1S2	32,54	18,38

Table 2. Observing logs

3 Results

The extensions of the emitting regions in the Hα and Hβ lines are determined from the modulus of the visibility. Figure 1 presents the evolution of the visibility modulus as a function of wavelength:

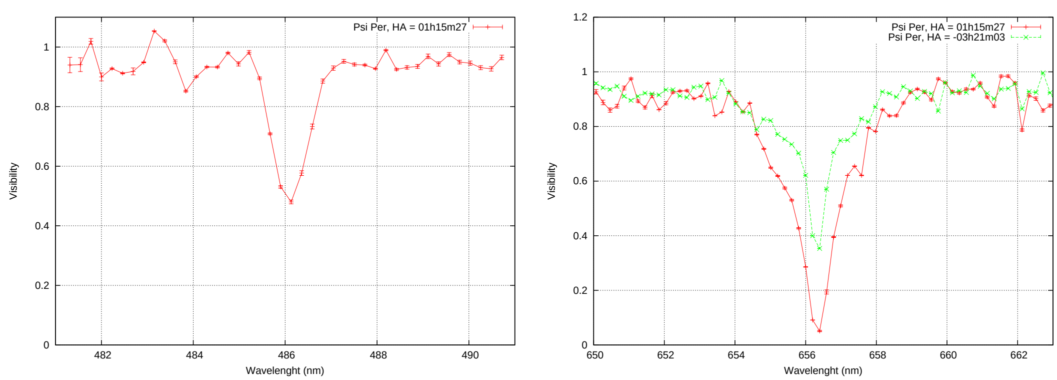

Fig. 1. Differential visibility across the Hβ(left) and Hα (right) lines for ψ Per, at HA indicated on the figure, for the S1S2.

The visibilities in the continuum nearby Hα and Hβ are close to one, which implies that the observed object is a point-like source in these two spectral domains, i.e. remains unresolved. Within the Hα and Hβ lines, we have a strong decrease of the visibility (stronger in Hα than in the Hβ line), which clearly indicates that the object extension in these two emission lines is larger than in the nearby continuum. The corresponding emitting regions can reach 10 $R_\star$ (Tycner et al. 2008; Grundstrom & Gies 2006).

In Fig. 1 we can see that the Hα visibilities (red and green) are different, which correspond to different baseline orientations into the sky-plane. This is a direct evidence for the shape of the Hα emitting region being not spherical, but that it depends on the baseline orientation. According to Marlborough's (1997) measurements, ψ per is supposed to have an inclination angle of about 80 deg. Thus, its circumstellar disk could exhibit an elliptical elongation. This is also confirmed by our measurements. Unfortunately, due to a poor seeing during our observing run, we only have one measurement in the Hβ line that impedes us to detect any departure from spherical symmetry.

In order to estimate the size of the Hα and Hβ emitting regions, we used an uniform disk to model the visibility measurement at the center of each emission line. To estimate properly the envelope sizes in Hα and Hβ, we need to take into account also the effect of stellar continuum emission within each line. The visibility $V_{H\alpha}$ can be written as:

$$V_{H\alpha} = \frac{V_{line}F_{line} - V_{cont}F_{cont}}{F_{line} - F_{cont}} \tag{3.1}$$

where $F_{H\alpha}= F_{line} - F_{cont}$

Following this equation, the corresponding Hα emitting region has 4.04 mas as from the red curve and 3.21 mas from the green one, respectively when the sky-plane orientation are -20.92 and 18.38 degrees. The error bars, about 10 %, were estimated from the visibility fluctuations in the continuum. For the Hβ emitting region, we have obtain a diameter of about 1.66 $\pm$ 0.1 mas.

The kinematics within the disk is related to the differential phase of fringes. With a small spectral resolution (smaller than the line width), we have only information on the global size of the emitting region at the studied wavelength. With a high spectral resolution, as the one available with VEGA (up to 30000), it is possible to study the kinematics within the line, since each spectral channel isolates one iso-velocity region with its own phase shift. Thus, following the phase shift as a function of wavelength, this is equivalent to follow the displacement of the photocenter of each iso-velocity curve, which reflects the velocity law within the disk, projected onto the line of sight. This technique, called "spectro-interferometry, is a very powerful tool to study in depth the kinematics in the Be star disks. Figure 2. shows the evolution of the phase of the visibility as a function of wavelength, called "differential phase:

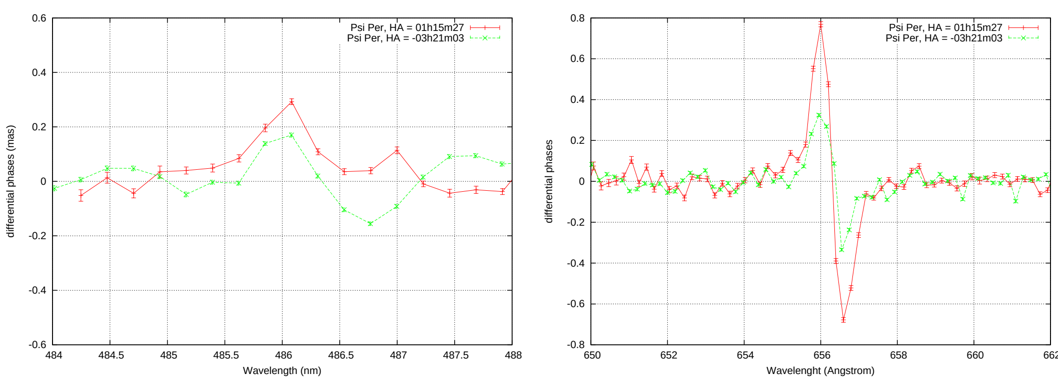

Fig. 2. Differential phase across the Hβ(left) and Hα (right) lines for ψ Per, at indicated HA for the S1S2 baseline.

The observed "S" shape is a clear signature indicating a rotating disk. The Keplerian rotation of the disk in α Arae was recently discovered by Meilland et al. (2007a), whereas in κ CMa such a disk rotation is not so clear, it could also be non-Keplerian (Meilland et al. 2007b). The differences between the amplitudes of the two "S", observed in Fig. 2, are due to the fact that the baseline orientations are different and thus, the projected photocenter displacement (or phase shift) are not the same (see Table 2). In practice, for a purely rotating disk the photocenter displacement is larger when the baseline is oriented along the major-axis of the disk.

4 Conclusions and prospectives

In this paper we present the study of the geometry of the ψ Per circumstellar environment, performed with the CHARA array and the VEGA focal instrument. Using a uniform disk model to interpret the interferometric observations, we have obtained two different diameters for the Hα emitting region: 4.04 $\pm$ 0.4 mas and 3.21 $\pm$ 0.32 mas for baseline orientations respectively of -20.92 deg and 18.38 deg. These quantities carry evidence for the non-spherical nature of the circumstellar environment around this star. We have obtained only one diameter measurement of the Hβ emitting region: 1.66 $\pm$ 0.1 mas for a baseline orientation of -20.92 deg, but cannot conclude on the spherical or non-spherical nature of the circumstellar environment at this wavelength. In a next step we shall try to fit our measurements using empirical kinematic models. The aim is to determine the rotation law within the disk of ψ Per and the main parameters constraining the star + disk system, with the help of a global simulation of data with the SIMECA code (Stee & Araújo 1994; Stee & Bittar 2001).

References

Arias, M.L., Zorec, J., Cidale, L. et al. 2006, A&A, 460, 821

Bjorkman, J. E., & Carciofi, A. C. 2004, A&A, 204, 6206

Dougherty, S. M., and Taylor A. R. 1992, Nature, 359, 808

Hanuschik, R. W., 1996, A&A, 308, 170

Kervella, P. & Domiciano de Souza, A. 2006, A&A, **453**, 1059

Marlborough, J. M., 1987, IAU Colloquium 92, ed. Sletterbak A., and Snow T. P., Cambridge, Cambridge University Press

Marlborough, J. M., Zijlstra, J.-W., Waters, L. B. F. M., 1997, ApJ, 321, 867

Poeckert, R., and Marlborough, J. M., 1978, ApJ, 220, 940

Quirrenbach, A., Bjorkman, K.S., Bjorkman, J.E., et al. 1997, ApJ, 479, 477

Stee, Ph., 1996, A&A, 311, 945

Stee, Ph., 2003, A&A, 403, 1023

Stee, Ph., Araújo, F. X., 1994, A&A, 292, 221

Stee, Ph., Bittar, J. 2001, SB, A &A, 367, 532

Struve, O., 1931, ApJ, 73, 94

Tycner, C., Jones, C. E., Sigut, T. A. A. et al., 2008, ApJ, 189, 461

Waters, L.B.F.M., 1986, A&A, 162, 121
Stee, P., Bittar, J.

Waters, L.B.F.M., Cot, J., Lamers, H.G.J.L.M., 1987, A&A, 185, 206

Waters, L.B.F.M., Marlborough, J. M., 1992, A&A, 253, L25

Zorec, J., Arias, M.L., Cidale, L. et al. 2007, A&A, 470, 239

SF2A 2009
M. Heydari-Malayeri, C. Reylé and R. Samadi (eds)

SIMILARITY CONCEPTS AND SCALING LAWS OF THE ACCRETED COLUMN IN MAGNETIC CATACLYSMIC VARIABLES: THE POLAR PROJECT

Falize, E.[1,3], Loupias, B.[1], Dizière, A.[2], Ravasio, A.[2], Gregory, C.D.[2], Cavet, C.[3], Michaut, C.[3], Koenig, M.[2], Leidinger, J.P.[2], Ribeyre, X.[4], Nazarov, W.[5], Barroso, P.[3], Millerioux, M.[1], Chevrot, M.[2] and Leconte, L.[2]

Abstract. In this paper we present the similarity properties and scaling laws of the accreted column in magnetic cataclysmic variables. To model this astrophysical object, two radiating regimes have been explored and different classes of scaling laws have been obtained.

1 Introduction

Magnetic cataclysmic variables (mCVs) are close binary systems containing an accreting magnetic white dwarf which accretes matter from a late type Roche-lobe filling secondary star (Warner 1995). The presence of intense magnetic field, radiation and hydrodynamics imply a rich range of behavior at different spatial and time scales. Moreover it leads to a variation of observable quantities and a variety of observed optical, X-ray and radio phenomena. These astrophysical objets class provides an excellent probe of the magnetic accretion processes under extreme conditions. More generally, the cataclysmic variables constitute an important class of low-luminosity, compact galactic X-ray sources. This radiation mainly comes from an area near the white dwarf surface: the accreted column (Kylafis & Lamb 1982; Chevalier & Imamura 1982; Cropper 1990; Wu 2000) which has a thousand kilometers spatial extension (Wu et al. 1994; Falize et al. 2009b). It is currently admitted that mCVs is divided in two sub-classes according to the intensity of magnetic field: the intermediate polar or DQ Her star which has $B < 10$ MG, and the polar ($B > 10$ MG) or Am Her star. In the last sub-class the Alfven radius is greater than the L1 Lagrange point; consequently the magnetic field is enough strong to prevent the formation of an accretion disc which is present in non magnetic or weakly magnetic cataclysmic variables. It imposes the white dwarf to rotate synchronously, to guide the flows and it could also dictate the radiative loss processes (Warner 1995). Having a correct model of the radiating region allows to determine fundamental properties of the mCVs (Suleimanov et al. 2005). The possibility to study the dynamics of the accreted column by a new way is very important in order to test the theoretical model. The intense development of laser facilities, which allows to bring up matter to extreme states of density and temperature in laboratory, is a very promising way for astrophysicists to explore the coupling between radiation and matter (Remington et al. 2006). In this paper we present recent results which show that we can reproduce *exactly* the accreted column in laboratory (Falize et al. 2008; Falize et al. 2009b). In the first part, we present an extended classification of similarity concepts that we use in laboratory astrophysics. In the second part we remind the accreted column standard model, we analyze the similarity properties and establish the scaling laws of the accreted column in different radiating regimes. Finally we conclude on the results.

[1] CEA-DAM-DIF, F-91297 Arpajon, France
[2] LULI Ecole Polytechnique, CNRS, CEA, UPMC, Route de Saclay, 91128 Palaiseau, France
[3] LUTH, Observatoire de Paris, CNRS, Universit Paris-Diderot, 92190 Meudon, France
[4] Centre Lasers Intenses et Applications (CELIA), UMR 5107 Université Bordeaux 1, 351, cours de la Liberation, 33405 Talence Cedex FRANCE
[5] School of Chemistry, University St Andrews, Purdie Blg, St Andrews KY16 9ST, United Kingdom

2 Symmetry and Invariance concepts

Symmetry provides tools to analyze the solutions of a problem without needing to solve the problem explicitly (Olver 1995) or it can also suggest methods to simplify it. In order to assure the link between the experimental and astrophysical systems we must elaborate scaling laws which will allow us to characterize the astrophysical character of experimental plasma. Although the time and spatial scales are very different between the astrophysical phenomena and the laboratory plasma, we can exhibit a theoretical connexion (scaling laws) which assures equivalent physics. Consequently scaling laws play a major role in laboratory astrophysics in order to connect the astrophysical phenomena or object to laboratory plasmas but also in order to connect the laboratory plasmas created with different powerful facilities. Laboratory astrophysics experiments can be divided into several fundamental classes which are connected to the type of similarity used as can be seen on the following diagram 1b.

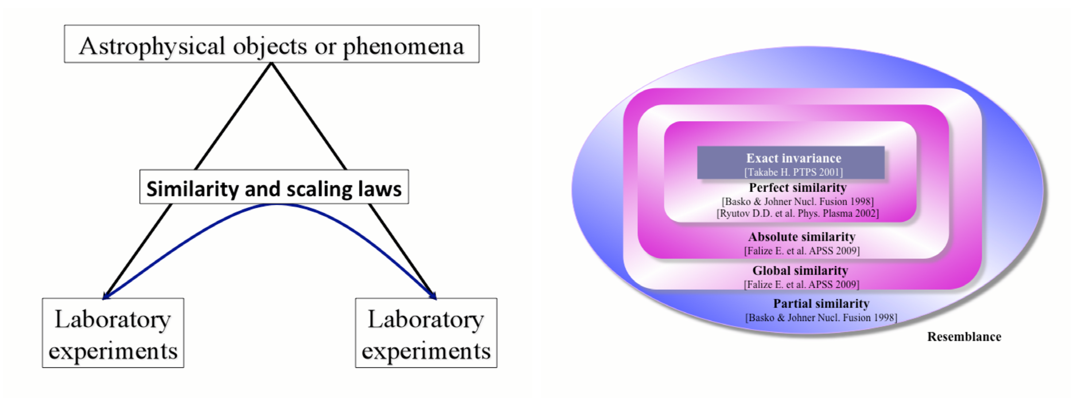

Fig. 1. a. Not only are the scaling laws fundamental in order to connect the astrophysical phenomena to laboratory plasmas but also in order to connect the laboratory plasmas themselves. b. The diagram of experiments classification.

These classes are:

1. **Exact invariance**: also called sameness (Takabe 2001), includes the experiments which consist in reproducing thermodynamical conditions identical to those of the astrophysical objects. More generally these experiments do not introduce the notions of time and space and allow to determine the input data of hydrodynamic models such as the opacity or equations of state of matter in extreme conditions.

2. **Similarity**: Although the spatial and temporal scales are very different, the astrophysical relevance of these experiments can be checked thanks to scaling laws to assure that the physical system under study satisfies similarity properties. This type of experiments gathers, for instance, high Mach numbers plasmas (Loupias et al. 2007; Gregory et al. 2008). This specific class can be decomposed in four sub-classes:

   (a) *Perfect similarity*: It is a concept introduced by Ryutov & Remington (2003) and this type of scaling laws are firstly identified in hydrodynamics by Basko & Jonher (1998). This type of scaling laws consists in rescaling the time and spatial variables only.

   (b) *Absolute similarity*: This scaling law class is very interesting in order to adapt a target design to powerful facilities or to rescale a system with the same composition (Falize et al. 2009a).

   (c) *Global similarity*: Based on the Lie symmetry invariance, the global scaled invariance only needs the invariance of the equation form. It is less constraining that the absolute similarity and introduces additional free parameters in order to rescale astrophysical experiments (Falize et al. 2009a) as we will see in the next section.

   (d) *Partial similarity*: The principle of this last scaling law category is to conserve only a part of equation and examine the effect of other physical phenomena on different quantity evolutions. This principle has been used by Basko & Jonher (1998) in the context of inertial fusion.

3. **Resemblance**: This last category gathers all laboratory astrophysics experiments which allow to verify a physical model or astrophysical numerical simulations. In other words, this category joins the experiments which depend greatly on microscopic physics.

3 Similarity properties and scaling laws of the accreted column

3.1 Accreted column: the standard model

When the supersonic in-falling matter, which is canalized by the magnetic field, impacts the white dwarf photosphere, a shock front is created. The kinetic energy of the material in the accretion stream, acquired from the Roche lobe, is converted into radiation. The equilibrium height x_s of the shock is determined by the requirement that the post-shock flow must have enough time to cool in order to match the conditions in the stellar photosphere. Consequently x_s is determined by the efficiency of cooling processes (bremsstrahlung, cyclotron and compton cooling) which act in the accreted column. The relative importance of these cooling processes depends mainly of the magnetic field B and accreted the mass rate $\dot{m}_a$. In order to model this specific zone of in-falling matter, we consider a plane-parallel, collisional shock with a post-shock medium where the local gravitational field does not modify its structure and which can be described successively by a one (Kylafis & Lamb 1982; Falize et al. 2009b) and two temperature regimes (Saxton & Wu 1999).

3.2 One-temperature radiating plasmas scaling laws

In the one-temperature approximation, the dynamics of the accreted column is given by:

$$\frac{d\rho}{dt} + \rho\frac{\partial v}{\partial x} = 0, \quad \frac{dv}{dt} + \frac{1}{\rho}\frac{\partial P}{\partial x} = 0, \quad \frac{dP}{dt} - \gamma\frac{P}{\rho}\frac{d\rho}{dt} = -(\gamma - 1)\mathcal{L}(\rho, P) \tag{3.1}$$

where we have respectively the mass conservation, the impulsion conservation and the equation of energy. The quantities x, t, ρ, v, P, T, γ, $\mathcal{L}$ are respectively the spatial and temporal coordinate, the density, the velocity, the pressure, the temperature, the adiabatic index and the cooling function. In this model we suppose a cooling function in the form[1] $\mathcal{L}(\rho, P) = \mathcal{L}_0\rho^{\epsilon}P^{\zeta}$, and we consider the plasma as a perfect gas, *i.e.* $P = \varepsilon_0\rho T$. Using the homothetic group we build the scaling laws which are given by:

$$\rho = a\tilde{\rho}, \quad x = b\tilde{x}, \quad P = c\tilde{P}, \quad \varepsilon_0 = d\tilde{\varepsilon}_0 \tag{3.2}$$

$$t = b\sqrt{\frac{a}{c}}\tilde{t}, \quad v = \sqrt{\frac{c}{a}}\tilde{v}, \quad T = a^{-1}cd^{-1}\tilde{T}, \quad \mathcal{L}_0 = a^{-(\epsilon+1/2)}b^{-1}c^{3/2-\zeta}\tilde{\mathcal{L}}_0 \tag{3.3}$$

where the quantities with the tilde correspond to the laboratory quantities. We see that we have four free parameters in the global similarity case (a, b, c, d) and only two in the absolute similarity case (a,b) with $\mathcal{L}_0 = \tilde{\mathcal{L}}_0$ and $\varepsilon_0 = \tilde{\varepsilon}_0$ (Falize et al. 2009a). To both similarity results, we add the analytical solution which describes the structure of the cooling layer in a stationary regime (Falize et al. 2009b). It allows to determine the spatial extension of the cooling layer corresponding to 100 μm in the laboratory field if the cooling time is 1 ns and the shock velocity is 100 km/s. Consequently the structure of the cooling layer and its dynamics can be diagnosed allowing potentially to analyze the quasi-periodic oscillation phenomena in laboratory. This result has given birth to the POLAR experiment which has been recently realized with LULI2000 facility. The goal of this first experiment was to determine the similarity properties of laboratory plasmas and the measurements are still being analyzed. To go deeper in the similarity analysis we have been examining the two-temperature regime presented below. In order to complete the scaled analysis we examined the two temperature regime that we present now.

[1] Let's note that in the bremsstrahlung case $\epsilon = 3/2$ and $\zeta = 1/2$.

3.3 Two-temperature radiating plasmas scaling laws

When $t_{ei} > t_{cool}$ where t_{ei} and t_{cool} are respectively the characteristic time of energy exchanged by Coulombian collision and the cooling time, the temperature of the electron decreases faster more rapidly than the collisions heat the electron (Kylafis & Lamb 1982; Wu 2000). Thus it is necessary to include the two-temperature effects and in order to describe its evolution we use the standard model described by Saxton & Wu (1999) and we add the energy equation:

$$\frac{dP_e}{dt} - \gamma \frac{P_e}{\rho} \frac{d\rho}{dt} = (\gamma - 1)[\Gamma(\rho_i, \rho_e, T_e, T_i) - \Lambda(\rho_e, T_e)] \tag{3.4}$$

where P_e, T_e, T_i and ρ_e are respectively the electron pressure, the electronic and ionic temperature and the electronic density. The heating due to the difference of temperature is given by:

$$\Gamma(\rho_i, \rho_e, T_e, T_i) = \Gamma_0 \rho^2 \left[\frac{T_i - T_e}{(T_e + m_e T_i / m_i)^{3/2}} \right] \tag{3.5}$$

where m_e and m_i are respectively the electron mass and the ion mass. We suppose a cooling function in the form $\Lambda(\rho_e, P_e) = \Lambda_0 \rho_e^{\alpha} P_e^{\beta}$. By using the same theoretical formalism as in the one-temperature case, we construct the scaling laws of two-temperature plasmas:

$$\rho = a\tilde{\rho}, \quad \Lambda_0 = b\tilde{\Lambda}_0, \quad \Gamma_0 = c\tilde{\Gamma}_0, \tag{3.6}$$

$$x = a^{(7-6\beta-4\alpha)/(2\beta+1)} b^{-4/(2\beta+1)} c^{(3-2\beta)/(2\beta+1)} \tilde{x}, \quad t = a^{(5[1-\beta]-3\alpha)/(2\beta+1)} b^{-3/(2\beta+1)} c^{2(1-\beta)/(2\beta+1)} \tilde{t},$$

$$v = a^{(2-[\alpha+\beta])/(1+2\beta)} b^{-1/(1+2\beta)} c^{1/(1+2\beta)} \tilde{v}, \quad P = a^{(5-2\alpha)/(1+2\beta)} b^{-2/(1+2\beta)} c^{2/(1+2\beta)} \tilde{P},$$

The important result is the existence of one free parameter in absolute similarity (b=c=1) which allows to scale such plasmas in laboratory. Although we consider here the regime in the accreted column context, the applicability of these results is fundamental to several astrophysical environments.

4 Conclusion

In this paper we presented different results on the similarity properties of the accreted column in magnetic cataclysmic variables. We have seen that reproducing exactly the astrophysical phenomena and examining its behaviors and its dynamics in details is theoretically possible. It is the aim of the POLAR experiment project. The possibility to reproduce these phenomena is a real opportunity to increase our understanding of the physics of accreted processes.

References

Basko, M. M. & Johner, J. 1998, Nucl. Fusion, 38, 1779

Chevalier, R. A., & Imamura, J. N. 1982, ApJ, 261, 543

Cropper, M. 1990, Space Sci. Rev., 93, 611

Falize, E., et al. 2009a, ApSS, 322, 107

Falize, E., et al. 2009b, ApSS, 322, 71

Falize, E., et al. 2008, J. Conf. Phys. Ser., 112, 042016

Gregory, C. D., et al. 2008, ApJ, 676, 420

Kylafis, N. D., & Lamb, D. Q. 1982, ApJS, 48, 239

Loupias, B., et al. 2007, Phys. Rev. Lett., 99, 265001

Olver, P. J. 1995, Equivalence, Invariants, and Symmetry, Cambridge

Remington, B. A., Drake, R. P. & Ryutov, D. 2006, Rev. Modern Phys. 78, 755

Ryutov, D. D., & Remington, B. A. 2003, Phys. Plasma, 10, 2629

Saxton, C. J., & Wu, K. 1999, MNRAS, 310, 677

Suleimanov, V., Revnivtsev, M., & Ritter, H. 2005, A&A, 435, 191

Takabe, H. 2001, Progress of Theoretical Phys. Suppl., 143, 202

Warner, B. 1995, Cataclysmic variable stars, Cambridge Univ. Press, Cambridge

Wu, K. 2000, Space Sci. Rev., 93, 611

Wu, K., Chanmugam, G., & Shaviv G. 1994, ApJ, 426, 664

SF2A 2009
M. Heydari-Malayeri, C. Reylé and R. Samadi (eds)

THERMOHALINE INSTABILITY AND ROTATION-INDUCED MIXING IN LOW AND INTERMEDIATE-MASS STARS.

Lagarde, N.[1] and Charbonnel, C.[1,2]

Abstract. The classical theory of stellar evolution predicts that low-mass stars are strong producers of ^3He, in contradiction with abundance observations of this element in Galactic HII regions and in the protosolar nebula. However in 2007, Charbonnel & Zahn showed that thermohaline mixing drastically reduces the yields of ^3He producted by low-mass red giants. Simultaneously this mechanism changes the surface of carbon isotopic ratio as well as the abundances of lithium, carbon and nitrogen. In this paper, we present and discuss models computed with the code STAREVOL that include the transport of chemical species in the radiative regions due to thermohaline instability and to rotational mixing. We compare our theorical predictions with recent observations.

1 Introduction

During the first dredge-up, the standard theory predicts that the convective envelope deepens in mass, and engulfes hydrogen-processed material. This induces a decrease of the surface $^{12}C/^{13}C$, Li, or ^{12}C abundances, while ^{14}N and ^3He abundances increase. After the first dredge-up, the convective envelope retracts and the hydrogen burning shell moves outward (in mass). The standard theory predicts ^3He is present and does not change further. The observations in open clusters and in galactic field are agree with standard theory at the first dredge-up. However, a second change in the surface abundance is observed latter, on RGB, more precisely at the BUMP luminosity. Eggleton et al. (2006) have proposed that the inversion of molecular weight created by $^3He(^3He,2p)^4He$ reaction may be at the origin of mixing on the red giant branch, for low-mass stars. Charbonnel & Zahn showed that this inversion sets of the so-called thermohaline mixing. Which is a double diffusive instability. In following sections, we present some results obtained with the code STAREVOL, including thermohaline mixing and rotation-induced mixing, at solar metallicity.

2 Models and results

We discuss in this section the effects of rotation-induced mixing and thermohaline mixing in a low-mass star ($M = 1.25M_{\odot}$) and in a intermediate-mass star ($M = 2.0M_{\odot}$).

2.1 *Low-mass star,* $M = 1.25M_{\odot}$

In figure 1, we present a Kippenhahn diagram for a $M = 1.25M_{\odot}$ star, with thermohaline mixing and rotation with $V_{ZAMS} = 110km/s$. We note that the thermohaline zone (blue) extends between the convective envelope (CE, in black hatching) and the external wing of the hydrogen burning shell (HBS) at the luminosity near the BUMP luminosity. In figure 1, we present also the evolution of surface carbon isotopic ratio for the same star. Due to thermohaline mixing, $^{12}C/^{13}C$ decreases at the BUMP luminosity contrary to the standard theory. We note that the value after the first dredge-up is lower with rotation. Due to rotation-induced mixing on the main sequence (see Palacios, A. et al. 2003, 2006). We note that the luminosity where thermohaline mixing connect the CE and HBS is the same in both cases. In addition, the value of $^{12}C/^{13}C$ at the end of RGB is also very similar in all cases.

[1] Geneva Observatory, 51 chemin des Maillettes, 1290 Sauverny, Switzerland
[2] LATT, CNRS UMR 5572, Universite de Toulouse, 14 avenue Edouard Belin, F-31400 Toulouse Cedex 04, France

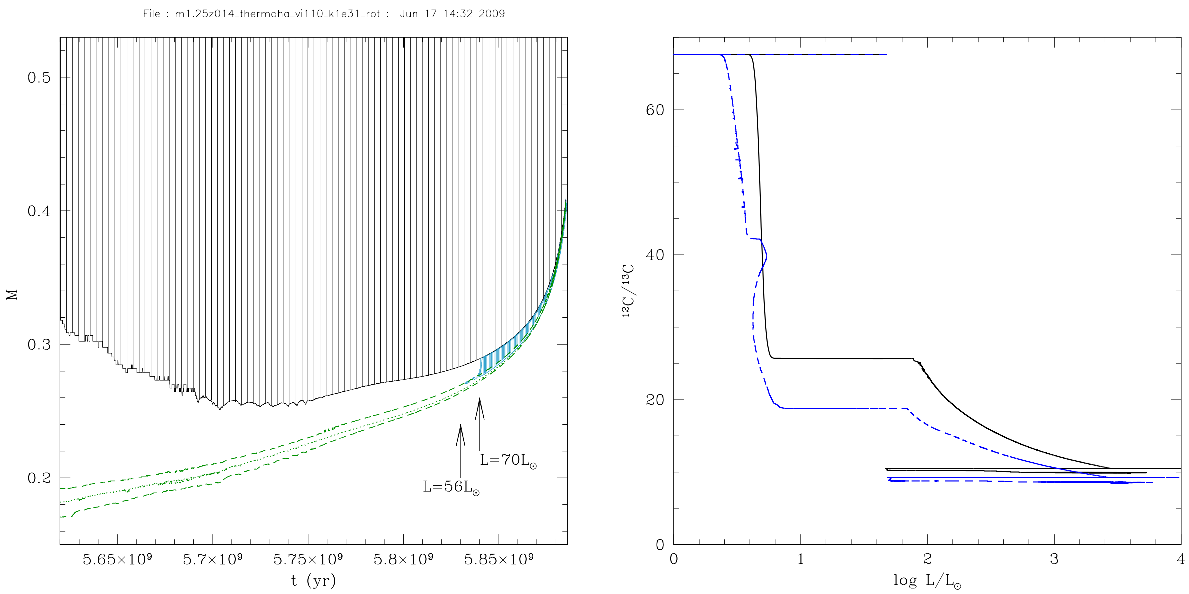

Fig. 1. Left : Kippenhahn diagram for a $M = 1.25M\odot$, $Z_\odot$ star, computed with thermohaline mixing and rotation-induced mixing ($V_{ZAMS} = 110km/s$). Thermohaline zone (between HBS and CE) is shown as blue hatching zone. **Right**: The evolution of surface carbon isotopic ratio as a function of luminosity. The solid line represents the standard model, and the dashed line represents the model computed with rotation $V_{ZAMS} = 110km/s$. Thermohaline mixing is present in both cases.

2.2 *Intermediate-mass star :* $M = 2.0M_\odot$

In figure 2, we present a Kippenhahn diagram for $M = 2.0M_\odot$, $Z_\odot$ star, with and without rotation. When the rotation is not included (left pannel), the thermohaline zone connects the CE with HBS at the end of RGB. So, it has not an effect on the surface abundance, as shown in figure 3. However, when the rotation is included (right pannel, fig 2), the thermohaline zone connects CE and HBS earlier in luminosity than in the model without rotation. In fact, the rotation changes the stellar structure on the main sequence, and favors the thermohaline mixing, in intermediate-mass stars. So, the evolution of $^{12}C/^{13}C$ for this star changes on the RGB. As can be seen in fig 3, the value of $^{12}C/^{13}C$ after the first drege-up decreases when the initial rotation velocity increases. Otherwise, the value of $^{12}C/^{13}C$ at the end of RGB decreases when the initial velocity increases. So the rotation favors the effect of thermohaline mixing on the RGB in the intermediate-mass star.

2.3 *Comparison with observations*

We compare our predictions with the observations in M67 by Gilroy & Brown (1991), and in 10 open clusters by Smiljanic et al. (2008) (see Smiljanic et al. 2009 (in press) for other comparisons). The standard theory does not explain the lower value of $^{12}C/^{13}C$ observed in the open clusters. For low-mass stars ($M \leq 1.7M_\odot$), thermohaline mixing explains well the observed carbon isotopic ratio, and the value of $^{12}C/^{13}C$ with rotation is approximatly the same, as discussed above. However, for interdiate-mass stars ($M \geq 1.7M_\odot$), rotation-induced mixing favors the effect of thermoaline mixing on the RGB.

3 Conclusion

An inversion of molecular weight created by the $^3He(^3He, 2p)^4He$ reaction is at the origin of thermohaline mixing in RGB stars brighter than the BUMP luminosity. This mixing connects the convective envelope with the external wing of hydrogen burning shell and induces surface abundance modifications. The introduction of this process in models of rotating stars allows us to explain the carbon isotopic ratio anomalies in giant stars

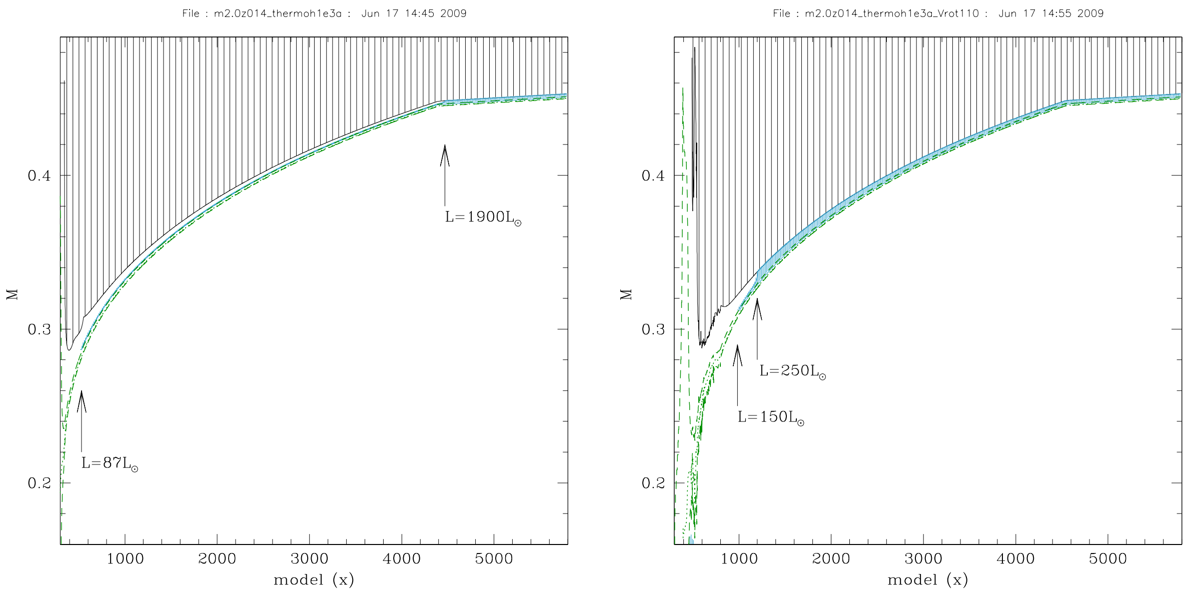

Fig. 2. Kippenhahn diagram for $M = 2.0M_{\odot}$, $Z_{\odot}$ star computed without rotation (**Left**), and with rotation (**Right**). In both cases, thermohaline mixing is included, and the region where it developsis represented with blue hatching between CE (black hachting) and HBS (green zone). The luminosity of BUMP and the luminosity when the thermohaline mixing connects CE and HBS are indicated.

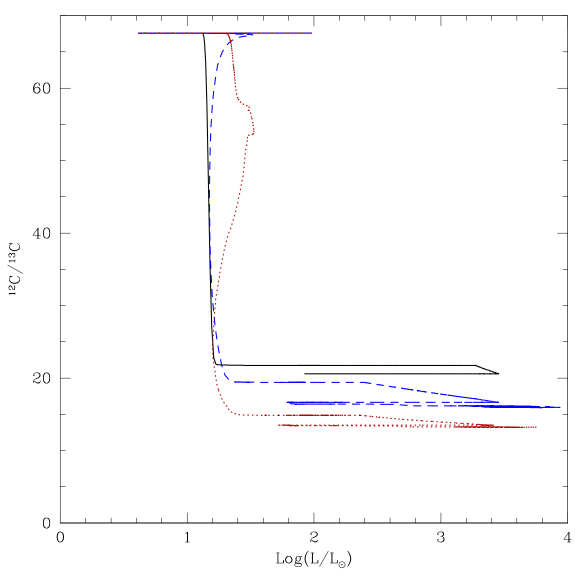

Fig. 3. The evolution of surface carbon isotopic ratio as a function of luminosity for a $M = 2.0M_{\odot}$, $Z_{\odot}$ star. Thermohaline mixing is present in all cases. The solid line is for the model without rotation, the dashed line for the model with $V_{ZAMS} = 110km/s$, and the dotted line for the model with $V_{ZAMS} = 180km/s$.

of open clusters over a broad range of turn-off.

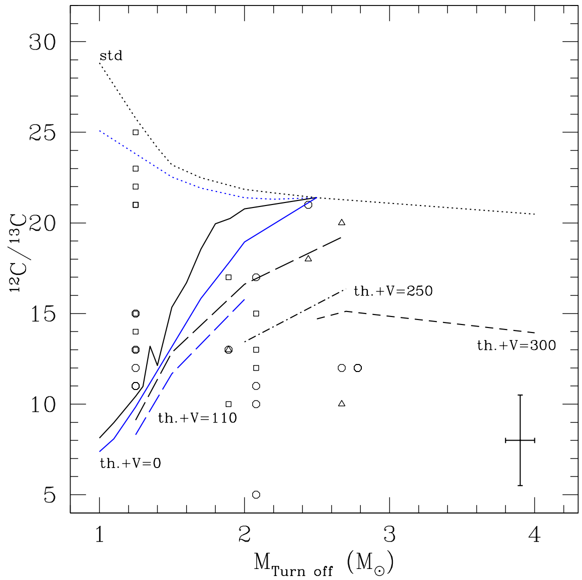

Fig. 4. Theorical predictions compared with observations of the carbon isotopic ratio, $^{12}C/^{13}C$, as a function of the open cluster turn-off mass. Our theorical values of $^{12}C/^{13}C$ as a function of the initial stellar mass : the standard models is shown as dotted lines ; the thermohaline models is shown as a solid line ; and the rotational models are shown as a long dashed lines for $V_{ZAMS} = 110km/s$; as a dot-dashed lines for $V_{ZAMS} = 250km/s$; and as a short dashed lines for $V_{ZAMS} = 300km/s$. For all theoricals models, values at the tip-RGB are shown in black and values at the tip-AGB are shown in blue. Observations of $^{12}C/^{13}C$ in open cluster by Smiljanic et al. (2008) and Gilroy & Brown (1991) : possible RGB stars are shown as open square, clump giants as open triangle, and possible early-AGB as open circle. For observations a typical error bar is shown.

References

Charbonnel, C., & Zahn, J.P., 2007, A&A, 467, L15-L18.

Eggleton, P.P., Dearborn, D.S.P., Lattanzio, J.C., 2006, Science, 314, 1580

Gilroy, K.K., Brown, J.A., 1991, ApJ, 371, 578-583

Palacios, A., Talon, S., Charbonnel, C., Forestini, M., 2003, A&A, 399, 603-616

Palacios, A., Charbonnel, C., Talon, S., Siess, L., 2006, A&A, 453, 261-278

Smiljanic, R., Gauderon, R., North, P., Barbuy, B., Charbonnel, C., Mowlavi, N, 2008, A&A, 502, 267-282

Smiljanic, R., Pasquini, L., Charbonnel C., Lagarde,N. , 2009, in press

SF2A 2009
M. Heydari-Malayeri, C. Reylé and R. Samadi (eds)

B[E] STARS AT THE HIGHEST ANGULAR RESOLUTION: THE CASE OF HD87643

Millour, F.[1], Chesneau, O.[2], Borges Fernandes, M.[2] and Meilland, A.[1]

Abstract. New results on the B[e] star HD87643 are presented here. They were obtained with a wide range of different instruments, from wide-field imaging with the WFI camera, high resolution spectroscopy with the FEROS instrument, high angular resolution imaging with the adaptive optics camera NACO, to the highest angular resolution available with AMBER on the VLTI. We report the detection of a companion to HD87643 with AMBER, subsequently confirmed in the NACO data. Implications of that discovery to some of the previously difficult-to-understand data-sets are then presented.

1 Introduction

B[e] stars (or "stars with the B[e] phenomenon") have little similarities with the classical Be stars. They do show permitted emission lines from Hydrogen and metallic elements, and they have an infrared excess. However, they also exhibit forbidden emission lines, and their infrared excess is due to hot dust ($T \approx 1300-1500$K) instead of heated plasma. Another difference is that the evolutionary status of B[e] stars is unclear. Some of them show characteristics typical of evolved objects (e.g. supergiant B[e] stars or SgB[e]), while others show characteristics of young stellar objects (Herbig B[e] stars are an example). Hence, "stars with the B[e] phenomenon" do not form a homogeneous class of objects. They have sometimes a poorly known distance, making their evolutionary status highly controversial. As a consequence, many B[e] stars are "classified" as "unclassified B[e] stars" (or UnclB[e]). One example is the star HD87643, located in the direction of the Carina arm, which has been classified as SgB[e] due to its putative distance ≥ 1 kpc, and which, at the same time, shows variability typical of a young stellar object. It shows one of the most extreme infrared excess of all B[e] stars and, hence, needs to be further investigated. We have observed this star with a variety of techniques to try to fix its properties and evolutionary status. These techniques range from high-resolution spectroscopy to high angular resolution imaging. We present here the high angular resolution discovery images of a companion to HD87643, as well as a larger scale image of arcs in its surrounding nebula, that might be related to the binary star. These results were presented in details in Millour et al. (2009). We will also present a tentative new interpretation of previously published spectro-astrometric measurements (from Baines et al. 2006, that failed to detect the binary), having in mind, now, that HD87643 is indeed a binary system.

2 A companion star detected with the highest angular resolution.

2.1 AMBER + NACO: detection of a companion star

We observed HD87643 using AMBER (Petrov et al. 2007), the near-infrared instrument of the VLTI in 2006 and in 2008. The AMBER data-sets were recorded in the K-band in medium spectral resolution ($R = 1500$) in 2006 and at low spectral resolution ($R = 35$) in 2008. We were able to perform an image reconstruction analysis with various image reconstruction software: MIRA, BSMEM, and BBM. All gave the same result, i.e. the clear separation of the source into two components and the partial resolution of the southern component (see Fig. 1, top-left). A subsequent test using a home-made model-fitting tool gave basically the same result. This probably means that a companion star has been detected around HD87643 with AMBER.

[1] Max-Planck Institut für Radioastronomie, Auf dem Hügel 69, 53121, Bonn, Germany
[2] UMR 6525 H. Fizeau, Univ. Nice Sophia Antipolis, CNRS, Observatoire de la Côte d'Azur, F-06108 Nice cedex 2, France

To check this discovery, we got additional observing time with the adaptive optics camera NACO (Rousset et al. 2003) of the VLT. We found that the L-band images did not show any elongation, as the angular resolution of NACO at that wavelength does not allow the partial resolution of the binary. On the contrary, the K-band de-convolved image was barely elongated in the same direction as the binary star detected with AMBER (see Fig. 1, top-right). Therefore, the NACO observation fully supports the AMBER observation, which detected a companion star for HD87643.

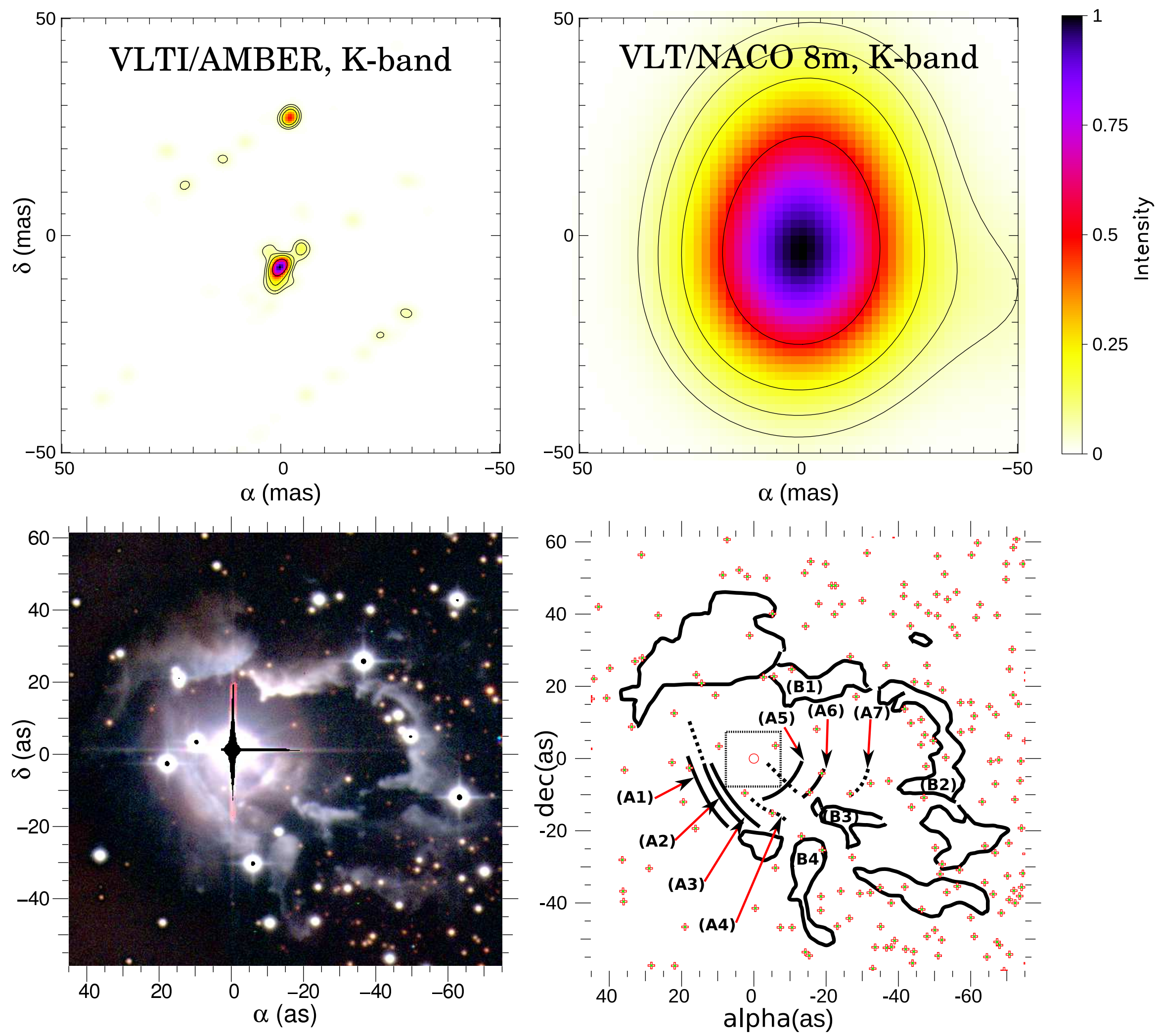

Fig. 1. Top: High angular resolution images of HD87643: Left: AMBER image giving a typical resolution of 2 mas; Right: De-convolved NACO image with a resolution of ≈ 50 mas. **Bottom:** The reflection nebula around HD 87643: Left: WFI image (composite of R, V and B filter); Right: Sketch presenting the main structures. Saturated regions are masked by black zones. The sketch shows HD 87643 as a red circle and other stars as red crosses. The nebular contours are drawn as black lines, and the prominent features are labelled (A1) to (A7) for arc-like structures and (B1) to (B4) for knots. Faint or uncertain structures are marked as dotted lines.

2.2 *MIDI+AMBER: characterizing the system*

In addition, we observed HD87643 in 2006 in low spectral resolution ($R = 30$) using MIDI (Leinert et al. 2004), the mid-infrared instrument of the VLTI. Since MIDI only provides visibilities and differential phases, it is virtually impossible to recover an image from its data. Thanks to the same model-fitting software as described before, we could indeed fit the MIDI data-sets with a binary star model, whereas previous attempts using a 2D radiative-transfer dusty disk model completely failed to do so.

We separated the spectra of all components of the system, composed of a binary system, whose southern component is partly resolved in the H and K bands, plus an extended envelope, clearly detected both in MIDI and L-band NACO data. We found that, while the extended envelope contains most of the silicate (warm dust) emission at 10μm, the southern component can be well-described by a black-body emission at 1300 K. The temperature (1300 K) and size (6 AU at 1.5 kpc) of this southern component is compatible with the inner-rim emission of a circumstellar disk around a hot (B-type) star. On the other hand, the northern component keeps its secrets by exhibiting an unresolved shape with a variety of dust temperatures (from 1300 K to 300 K). It could be, for example, a T-Tauri star still deeply embedded in its dust cocoon.

3 Wide-field imaging: binarity at work?

We also retrieved and reduced unpublished data of HD87643 from the WFI camera in 2001. The image is shown in the bottom of Fig. 1, together with a sketch of all the features detected. In comparison with previous works (van den Bergh 1972; Surdej et al. 1981; Surdej & Swings 1983), the image presented here has a larger dynamic range.

It appears that the nebula around HD87643 is made of three components: filamentary structures, composing the main nebula in the north-west quadrant (thick black line in the sketch); apparently blown-up structures appearing as " knots" (labelled (B1) to (B4)), connected to the previous filaments; and finally, arc-like structures (labelled (A1) to (A7)), grouped in two sets south-east and south-west of the star, respectively.

The nebular filamentary structures can be explained by a past outburst that took place ≈355 yrs ago, given an expansion velocity of $\approx 1000\,\mathrm{km\,s^{-1}}$ and a distance of 1.5 kpc. The knots seen in our image would correspond to denser interstellar clouds or clumps that would offer more resistance to the nebular ejecta.

The arc-like structures appear regularly spaced in our image. At the same adopted distance, they would correspond to regular ejections every ≈14 yrs to ≈50 yrs, depending on the arc. These broken structures suggest short, localised ejection that might coincide with short periastron passages of the previously detected companion, triggering violent mass-transfer between the components.

4 Comparison with previous works

Previous observations of HD87643 did not detect the companion star. Spectro-polarimetric (Oudmaijer et al. 1998) and spectro-astrometric observations (Baines et al. 2006) had the highest spatial resolution at that time. Both techniques provided evidence for a significant north-south asymmetry of the system, but the complexity of the signal prevented a direct interpretation, and especially the detection of the binary star.

The Hα P-Cygni profiles of HD87643 (between -1000 and -2000$\mathrm{km\,s^{-1}}$) show a flat-bottomed shape, seen in both of the Baines et al. (2006) and Oudmaijer et al. (1998) spectra, as well as in spectra we acquired with the FEROS instrument in 1999 and 2000 (see Fig. 2). It could mean that in that spectral region, *one* source of continuum is strongly absorbed, while other emission sources are not. This (variable) absorption represents 50% to 60% of the continuum.

The spectro-astrometric results from Baines et al. (2006) can be summarized as follows. The photo-centre of the Hα emission and of the P Cygni absorption is shifted toward the north compared to the continuum photo-center. The PSF FWHM is increased by 40mas both in the EW and NS directions in the P Cygni absorption, but not in other parts of the Hα line. This FWHM increase is larger than our inferred binary separation (34.5 mas). This implies that the remaining continuum originates from an extended component, unaffected by the P Cygni absorption. This component contributes *at most* (i.e. considering a fully saturated P Cygni absorption) 40-50% of the total visible continuum. We can tentatively attribute most of this contribution to the scattered light from the circumbinary envelope, detected by MIDI and NACO in the mid-infrared.

The photo-centre shifts may be understood as follows. The P-Cygni absorption hides the southern component; hence, a northern photo-centre shift is observed. Both stars emit Hα, but the northern star emits more; so again, a northern photo-centre shift in the Hα emission is observed. In the P-Cygni absorption, the large envelope surrounding the system appears larger as a consequence of, e.g., increase of optical depth, leading to the PSF FWHM increase. Therefore, in this frame, the spectro-astrometric observations of Baines et al. (2006) strongly support a multiple-component origin for the Hα emission. This also suggests that the northern companion is also a hot source able to ionize circumstellar hydrogen.

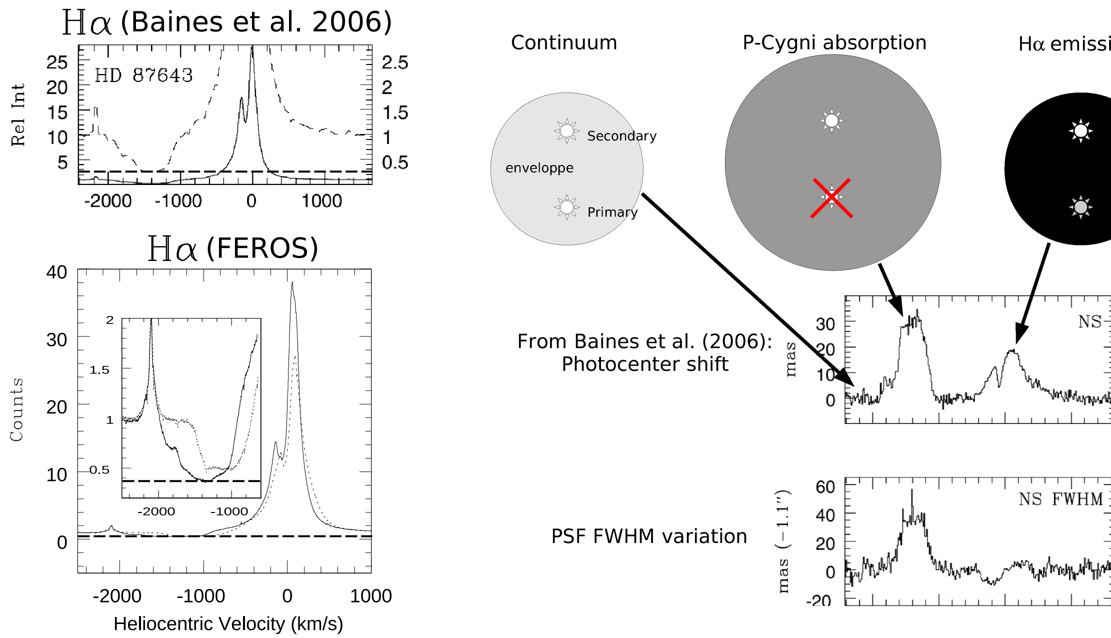

Fig. 2. Left: Hα line as seen by Baines et al. (2006, top) and FEROS (1999, solid line and 2000, dotted line). Dashed lines indicate the flat-bottomed shape of the P Cygni absorption. **Right:** A tentative new interpretation of the Baines et al. (2006) spectro-astrometric measurements: Both stars emits Hα, while only one is absorbed in the P Cygni absorption. Note the change in flux-balance of the two components between the continuum and both Hα emission and P Cygni absorption.

5 Discussion and conclusion

We presented high angular resolution AMBER and NACO images as well as a high dynamic range WFI image of HD87643. AMBER and NACO images undoubtedly reveal a binary companion to the main star, while the WFI one suggest a high-eccentricity orbit for the binary. Separating the spectra of the different components in the system using the AMBER and MIDI data, it was possible to infer that the main source is likely a hot star encircled by a 6 AU hot dust envelope, that the secondary is embedded in a compact cocoon of dust, and that a circumbinary envelope holds most of the dust silicate emission in the system. Finally, we propose a new interpretation of literature spectro-astrometric data, in which both stellar components emit Hα.

The global view of the system has been completely changed by our discovery of a companion to HD87643. The system might resemble in fact the following: a hot star encircled by a dusty disk, whose inner rim is seen in the AMBER image (a Herbig star?), a T Tauri companion star, and a dusty circumbinary envelope. All this suggests a much younger evolutionary status of HD87643 and, hence, a much closer distance than previously thought. A monitoring campaing of the binary throughtout its orbit would enable us to set accurately and definitively the distance of the system and, hence, its evolutionary status.

References

Baines, D., Oudmaijer, R. D., Porter, J. M., & Pozzo, M. 2006, MNRAS, 367, 737
Leinert, C., van Boekel, R., Waters, L. B. F. M., et al. 2004, A&A, 423, 537
Millour, F., Chesneau, O., Borges Fernandes, M., et al. 2009, A&A, accepted.
Oudmaijer, R. D., Proga, D., Drew, J. E., & de Winter, D. 1998, MNRAS, 300, 170
Petrov, R. G., Malbet, F., Weigelt, G., et al. 2007, A&A, 464, 1
Rousset, G., Lacombe, F., Puget, P., et al. 2003, in SPIE Conf., Vol. 4839, 140
Surdej, A., Surdej, J., Swings, J. P., & Wamsteker, W. 1981, A&A, 93, 285
Surdej, J. & Swings, J. P. 1983, A&A, 117, 359
van den Bergh, S. 1972, PASP, 84, 594

SF2A 2009
M. Heydari-Malayeri, C. Reylé and R. Samadi (eds)

IS THE PERIOD-LUMINOSITY RELATION OF AGB STARS UNIVERSAL?

Schultheis, M.[1]

Abstract. One characteristic of AGB stars is their large amplitude variation due to pulsation. I studied the behaviour of the pulsational properties of Long Period Variables (LPVs) in different galactic environments such as the galactic Bulge, the LMC and SMC. I have shown that the Bulge LPVs follow nearly the same Period-luminosity relation in these three different environments. In the infrared, the PL relation of AGB stars is *universal*. Therefore AGB stars can be seen as excellent extraglactic distance indicators.

1 Introduction

AGB stars are dominated by dynamical phenomena like pulsation and shock waves. They are long-period variables (up to $\sim 2000^d$) with large amplitude variation (Mira Variables have amplitudes in the Visual greater than 2.5 mag). Therefore only hydrodynamical model atmospheres can reproduce the observed molecular features (see e. g. Aringer et al. 1999; Alvarez et al. 2000). The study of molecular features covering a whole pulsational cycle are essential to understand the interaction between pulsation, the resulting propagation of shock waves, dust formation and mass loss.

Based on the regularity of the lightcurve, one distinguishes between Mira-type variables (regular pulsational behaviour), semiregular Variables (SRVs) and irregular variables (no periodicity in the light variation). Recently, thanks to the microlensing searches, such as MACHO, EROS and OGLE, high quality light curves were obtained for the galactic Bulge, LMC and SMC which allows to study the pulsational properties of AGB stars. PL relations of AGB stars show four parralel sequences (A-D). Large-amplitude Mira variables are located at the top of sequence C are are fundamental pulsators. On the other hand, semiregular variables are located on sequences A and B and pulsate in first, second or third overtone mode. Stars located on sequence D are multi-periodic and their origin is still unknown.

2 Long-period Variables in different galactic environments

Do different galactic environments influence the fundamental physical parameters of pulsating AGB stars?

The Spitzer infrared satellite has now surveyed the LMC (SAGE; Meixner et al. 2006) and the NGC 6522 field (Baade's window) at mid-IR wavelengths with sensitivities unobtainable from the ground. Each of these surveys used the IRAC camera at 3.6, 4.5, 5.8 and 8 m and the MIPS camera at 24 m. The SAGE data have been publicly released; the NGC 6522 data were reduced by M. Stute (Uttenthaler et al., 2009, submitted). Cross-correlating the known AGB variables with the SPITZER data I found that they obey period-luminosity relations in the mid-infrared (mid-IR) similar to those seen at K_S (2.14 μm), even at 24 μm where emission from circumstellar dust is expected to be dominant. Their loci in the M, log P diagrams are essentially the same for the Large Magellanic Cloud (LMC) and for NGC 6522 in spite of different ages and metallicities. I have included a number of AGB stars from the solar neighbourhood for comparison using synthetic IRAC photometry. Fig. 1 contains the five M vs log$P$ diagrams for the GC field and the LMC, superimposed to show their similarity. Dots correspond to the dominant period of each star. Miras, defined here to have MACHO amplitudes > 1.5 have the symbol ($\times$). The very long periods associated with many SRVs are given the colour magenta for the LMC and green for NGC 6522. The scatter due to depth effects is much greater in the NGC 6522 than in the LMC field.

[1] Observatoire de Besançon, 41bis avenue de l'Observatoire, 25000 Besançon

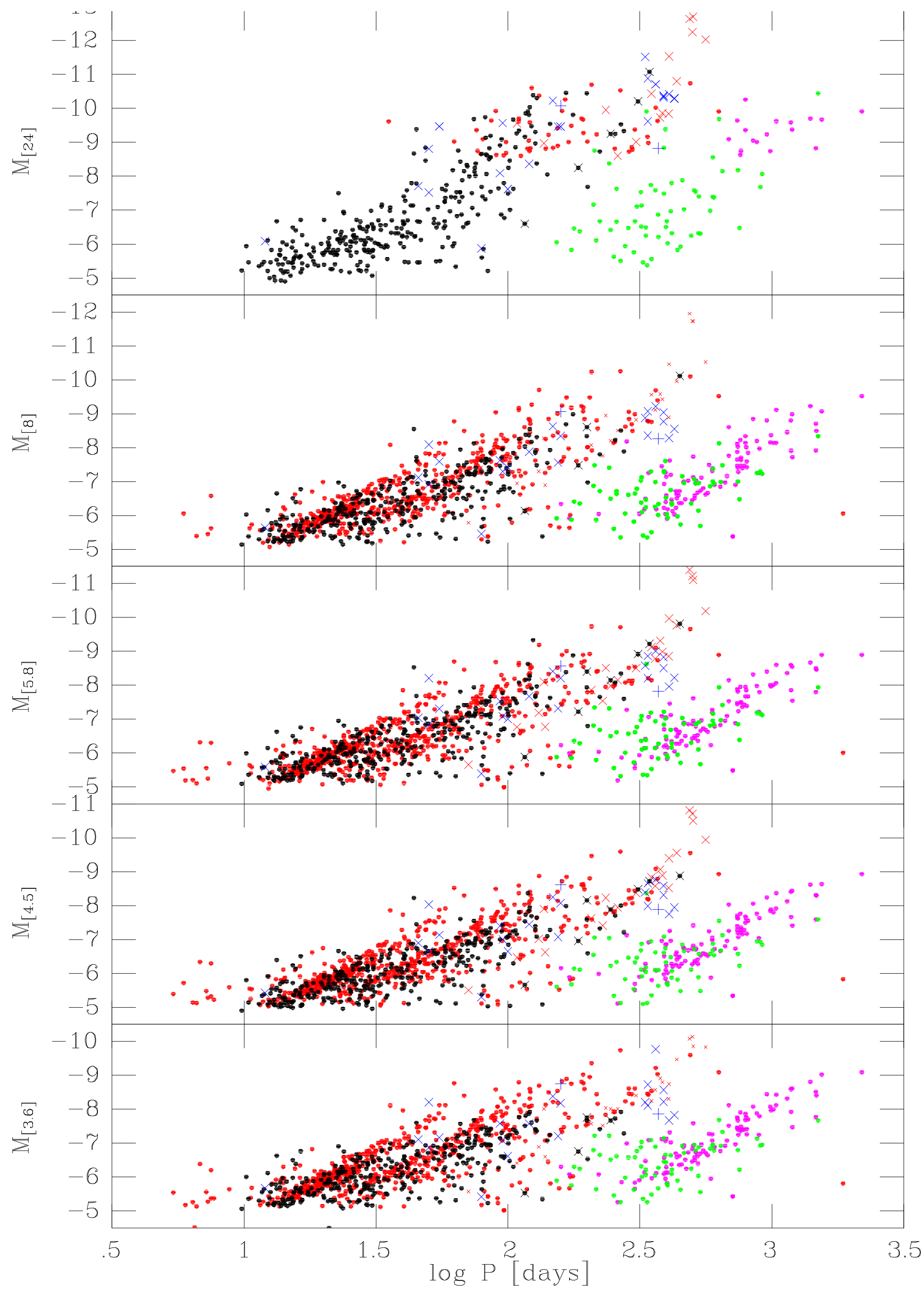

Fig. 1. log P vs Spitzer magnitudes. Red dots are the LMC SRVs (principal periods), red ×s the LMC Miras, magenta dots the LMC subsidiary long periods and black and green the same respectively for NGC 6522. The principal M, $\log P$ sequences are clearly visible. Note that the LMC data are limited in sensitivity at 24μm (from Glass et al. 2009)

3 Long-period Variables in the Galactic Center

In order to investigate more the universality of the PL relations, I studied the probably most metal-rich field in our Galaxy, the Galactic Center region. Glass et al. (2001) conducted a K-band (2.2 μm) survey for variable stars covering 24×24 arcmin^2 (56×56 pc at a distance of 8 kpc) and centred on the GC in a study spanning 4 years. The majority of the variable sources they found were, as expected, Miras and OH/IR stars with periods ranging from 150 d to about 800 d. Uncertainty as to the foreground extinction unfortunately precluded any detailed comparison of their luminosities with similar populations in other well-studied areas, such as the solar neighbourhood, Baade's window, and the Magellanic Clouds, where period-luminosity relations have been determined.

The central $2.0^o \times 1.4^o$ of the GC have been mapped with Spitzer/IRAC between 3.6 and 8.0 μm. Ramírez et al. (2008) performed point-source extraction on the IRAC data and published a confusion-limited catalogue of point sources that also included photometry from 2MASS. Schultheis et al. (2009) obtained based on these data a high resolution interstellar extinction map of the Galactic Center. It combines observations of the RGB/AGB population with the newest isochrones (Marigo et al. 2008). I used this map to deredden the LPVs in the GC region.

Fig. 1 shows clearly that the slopes of the period-magnitude relations at the IRAC wavelengths for the Glass-LPVs are similar to those of the LMC. This suggests that any dependence of the log P vs. $IRAC$ relations on abundance, if present at all, must be small. Within the uncertainties, there is no evidence for a significant difference between the period-magnitude relations in the LMC and in the GC. This is in agreement with Whitelock et al. (2008) who found, after reanalyzing published lightcurves of AGB variables in the LMC, similar zero points in the period-M_K relations for systems with different metallicities. They did not, however, include in their analysis the variables towards the GC, which is thought to be the most metal-rich environment.

I conclude that the period-luminosity relations of LPVs in the Infrared seem to be universal in the wavelength range between 2.2 and 24 μm. Therefore AGB stars can be seen as excellent extragalactic distance indicators

4 Perspectives

While much progress has been obtained in the Long-period Variables study in the galactic Bulge, the LMC and SMC (due to the microlensing surveys), the knowledge of LPVs in the solar neighbourhood is still poorly limited. The current picture of LPVs in the solar neighbourhood remains sketchy because of the small sample sizes.

The ESA mission GAIA will provide in the next decade besides precises parallaxes also light curve information due to repeated observations. With GAIA we should get a complete census of Long-period Variables inside the solar neighbourhood as well as inside our Galaxy.

Projects like super-MACHO, OGLE-IV continue to observe the Magellanic Clouds and Galactic Bulge region and will provide us with even more and better sampled light curves.

References

Alvarez R., Lançon A., Plez B., Wood P. R., 2000, A&A 353, 322

Aringer B., Höfner S., Wiedemann G., Hron J., Jørgensen U. G., Käufl U. U., Windsteig W., 1999, A&A 342, 799

Glass I.S.,Matsumoto, S., Carter, B. S., & Sekiguchi, K. 2001, MNRAS, 321, 77

Glass I.S., Schultheis M., Blommaert J.A.D.L., et al., 2009, MNRAS 395L, L11

Jura M., Kleinmann S. G., 1992, ApJS 79, 105

Kerschbaum F., Hron J., 1994, A&AS 106,397

Marigo P., Girardi L., Bessan A., et al., 2008, A&A 482, 883

Meixner M. et al., 2006, AJ 132, 2268

Ramírez S.V., Arendt R.G., Sellgren K., et al., 2008, ApJS 175, 147

Schultheis M., Sellgren K., Ramirez S., et al., 2009, A&A 495, 157

Whitelock P.A., Feast M.W, van Leeuwen F., 2008, MNRAS 386, 313

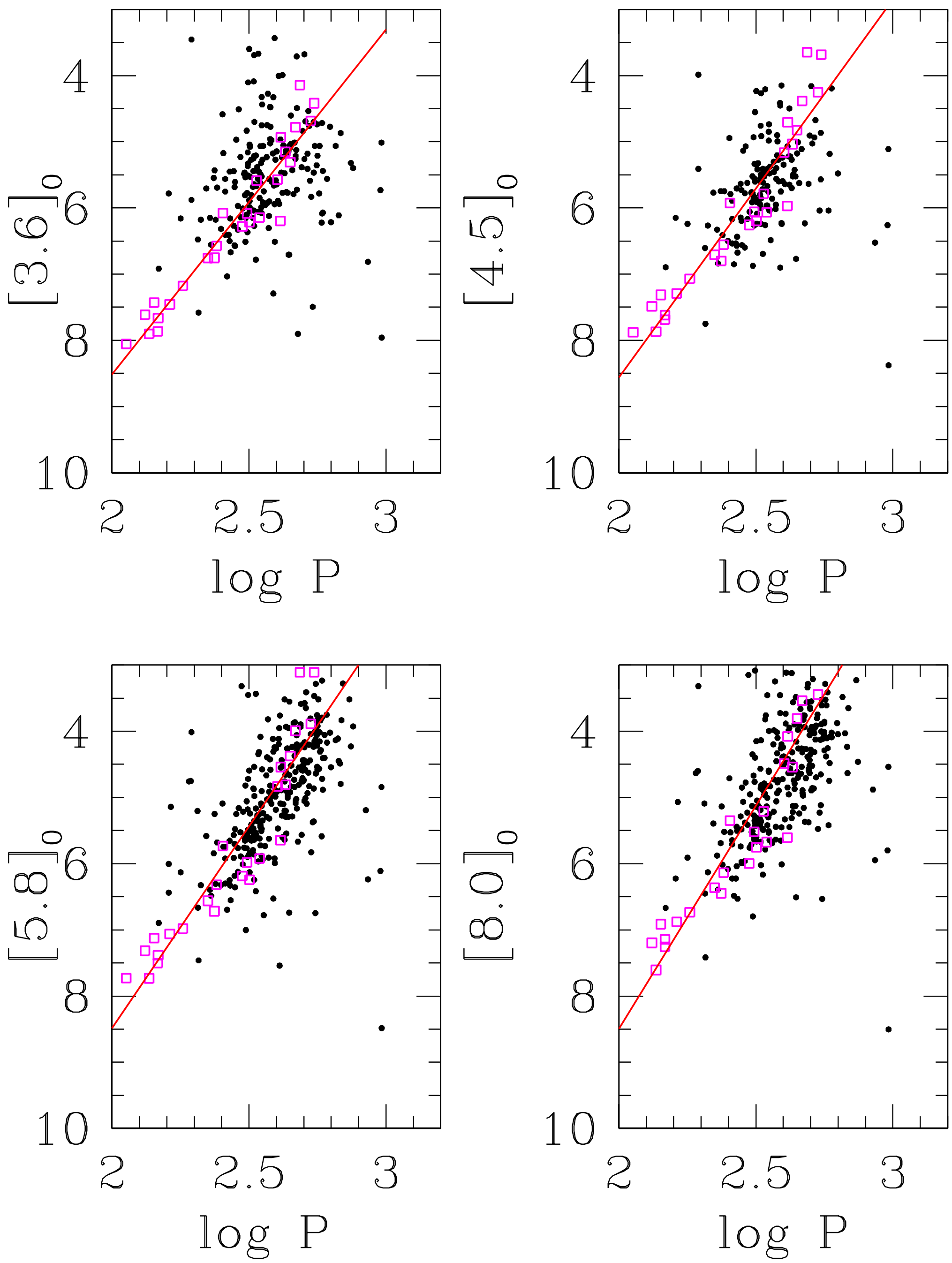

Fig. 2. Dereddened IRAC magnitudes (using the extinction map as described in Sect. 3) vs. log P for LPVs in the Glass et al. (2001) GC field (Glass-LPVs; black dots), where P is the period. Open magenta squares are LMC-AGB stars (oxygen-rich Mira variables). The straight red line is a least-squares fit to the LMC-AGB data set (from Schultheis et al. 2009)

SF2A 2009
M. Heydari-Malayeri, C. Reylé and R. Samadi (eds)

GIRAFFE OBSERVATIONS OF COROT VARIABLE STARS

Semaan, T.[1], Neiner, C.[1], Martayan, C.[2], Debosscher, J.[3] and Sarro, L. M.[4]

Abstract. We present preliminary results from the ground-based ESO/GIRAFFE observational program set up for the spectroscopic study of variable stars observed in the CoRoT exoplanet fields. About 3000 variable stars have been identified in each CoRoT field by the CVC (CoRoT Variable Classifier). The multi-object GIRAFFE medium resolution spectroscopic observation of these fields allows us to accurately classify the variable stars in various types of pulsators, binaries, etc. In addition, our team identifies the Be stars to determine their fundamental parameters thanks to synthetic spectral fitting taking NLTE and rapid rotation effects into account. We will then test for correlations between the stellar parameters and pulsation properties of Be stars in a statistical way and study their instability strip. Moreover, knowing the fundamental parameters of the stars is necessary to perform seismic modeling.

1 Scientific Context

Stellar oscillations have been observed at almost all phases of stellar evolution. However, there exists a particular region in the HR diagram in which the density of pulsating stars is higher than elsewhere, called the classical instability strip. This strip includes classical Cepheids, RR Lyrae stars, δ Scuti stars and DB white dwarfs. On the blue hot side of the strip one can find high-mass pulsators such as β Cephei, Slowly Pulsating B (SPB) and Be stars. The goal of our program is to obtain one spectrum of each variable star detected by CoRoT (Auvergne et al. 2009) in its exo fields, in order to classify each star into a variable class according to its spectrum and determine its fundamental parameters. This information is needed for all the pulsating stars observed by CoRoT in order to perform their seismic modeling.

2 Spectral classification and fundamental parameters determination with GIRAFFE

We use the multi-object spectrograph FLAMES/GIRAFFE (Pasquini et al. 2004) mounted at UT2 to observe the variable stars detected in the exofields of CoRoT by the CVC (Debosscher et al. 2007). Data have already been acquired for parts of the IR1 and LRA1 fields and the whole LRC1 field. Observing time has been requested for further CoRoT runs. GIRAFFE allows the simultaneous observation of up to 132 targets (in a field of $25'$ in diameter). We use two setups: one at λ=4272 Å and R=6400 (LR2) and one at λ=6438 Å and R=8600 (LR6). Thanks to the GIRAFFE LR6 spectra, we are able to discriminate between the various pulsators observed by CoRoT. The LR2 spectra allow each team to determine the parameters of their class of stars. The LR2 domain contains important lines for all types of stars, in particular two H lines (H_γ and H_δ) and 6 HeI lines at 4009, 4026, 4144, 4388, 4438 and 4471, as well as the SiIII 4552 line. It also contains NII 3995, CII 4267, TiII 4501, FeII 4508 … The reduced LR6+LR2 GIRAFFE data are then distributed to the various CoRoT teams according to the classification.

[1] GEPI/UMR 8111 du CNRS, Observatoire de Paris-Meudon, 5 place Jules Janssen, 92195 Meudon, France
[2] ESO, Alonso de Cordova, 3107, Vitacura, Santiago, Chile & GEPI, Observatoire de Paris
[3] Instituut voor sterrenkunde, Catholic university of Leuven, Belgium
[4] Dpt. De Inteligentia Artificial, UNED, Juan del Rosal, 16, 28040 Madrid, Spain

3 Need for GIRAFFE spectroscopy

After each CoRoT run, the CoRoT Variable Classifier (CVC) identifies variable stars among all observed stars of the EXO program and tries to roughly classify them into categories of variables. However, the CVC cannot discriminate certain types of variables from photometry alone. For example there is strong confusion between SPB and Be stars (same pulsations but Be stars rotate faster and have a disk). To perform a seismic modeling of the variable stars and derive their internal structure, the fundamental parameters (temperature, gravity, vsini) as well as the abundances of the stars are needed. Only a spectrum allows to obtain a reliable classification and to perform an accurate determination of the parameters.

4 Discovery and confirmation of Be Stars

Be stars are defined as B stars that show or have shown at least once emission in their Balmer lines. This emission is due to the presence of a circumstellar disk built from matter ejected from the star through outbursts. For a complete review, see Porter & Rivinius (2003). We confirm the detection of 3 Be stars (CoRoT ID : 102766835, 102725623, 102719279), candidates according to their CoRoT lightcurves, and found 3 other Be stars (CoRoT ID : 102686433, 102672979, 102847615) thanks to the GIRAFFE spectra. Fig. 1 shows the easily recognizable H_α emission of the Be stars and the corresponding CoRoT lightcurve. Our team will determine the fundamental parameters of all Be stars observed by CoRoT thanks to the FASTROT/GIRFIT code (Frémat et al. 2005), which takes into account the effects of rapid rotation.

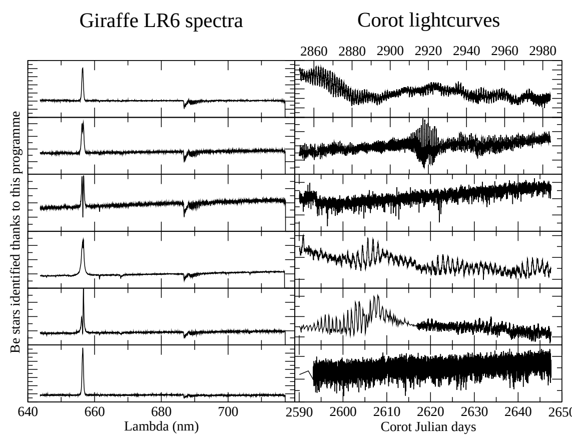

Fig. 1. Spectra and light curves of the confirmed and new Be stars

5 Conclusion

The spectroscopic GIRAFFE data allow us to improve the CVC classification of the variable stars detected in the exofields of CoRoT and distribute the CoRoT and GIRAFFE data to the appropriate thematic teams of CoRoT. They will then be able to determine the fundamental parameters of each variable star and use those to perform seismic modeling. In the case of Be stars our team will search for the possible correlation between these fundamental parameters, the pulsational properties and the outbursts of Be stars.

References

Auvergne, M., Bodin, P., Boisnard, L., et al. A&A, 2009 in press

Debosscher, J., Sarro, L. M., Aerts, C., et al. E. 2007, A&A, 475, 1159

Pasquini, L., Castillo, R., Dekker, H., et al. 2004, Procspie, 5492, 136

Porter, J. M., & Rivinius, T. 2003, PASP, 115, 1153

Frémat, Y., Zorec, J., Hubert, A.-M., et al. 2005, A&A, 440, 305

SF2A 2009
M. Heydari-Malayeri, C. Reylé and R. Samadi (eds)

SEARCHING FOR MOLECULAR HYDROGEN MID-INFRARED EMISSION IN THE CIRCUMSTELLAR ENVIRONMENTS OF HERBIG STARS.

Martin-Zaïdi, C.[1], Augereau, J.-C.[1], Ménard, F.[1], van Dishoeck, E.F.[2,3], Habart, E.[4], Lagage, P.-O.[5], Pantin, E.[5] and Olofsson, J.[1]

Abstract. We present a review of high-resolution spectroscopic mid-infrared observations of the pure rotational S(1) line of H_2 at 17.035 μm, as a tracer of warm gas in the surface layers of circumstellar (CS) disks around Herbig Ae/Be stars with the VLT Imager and Spectrometer for the mid-InfraRed (*VISIR*).

1 Introduction

The detection of H_2 provides the most direct information about the gaseous content of disks, setting limits on the timescales for the dissipation of CS matter and possibly planet building. The pure rotational mid-infrared H_2 lines are useful probes because the level populations are expected to be in local thermodynamic equilibrium (LTE) at the local gas temperature, and so line ratios allow the determination of the excitation temperature and mass of the warm gas. Using the high spectral resolution long slit mode of *VISIR*, we observed 10 Herbig Ae/Be stars (HAeBes) with well known disks, and/or whose CS environments are rich in gas (Martin-Zaïdi et al. 2008a). We focussed the observations on the S(1) pure rotational line of H_2 at 17.0348 μm since it is the most intense mid-IR H_2 line that could be detected from the ground. For details on the observation and data reduction techniques, we refer the reader to papers by Martin-Zaïdi et al. (2007, 2008b, 2009a).

2 Numerous non-detections

All but one, namely HD 97048, of the target's spectra show no evidence for H_2 emission near 17.035 μm. By integrating over a Gaussian of full width at half maximum (FWHM) equal to a spectral resolution element, and an amplitude of about $3\sigma \times (flux)$, centered on the expected wavelength for the S(1) line, we derived 3σ upper limits on the integrated line fluxes and upper limits on the total column densities and masses of H_2 as a function of adopted temperatures (Table 1). For this purpose, we used the method detailed in Martin-Zaïdi et al. (2008b, 2009a), by assuming that the line is optically thin at LTE and that the radiation is isotropic.

3 Only one detection

We have detected the H_2 pure rotational S(1) line in the spectrum of the Herbig Ae star HD 97048. We deduced a 6σ detection in amplitude for the line. The line is not spectrally resolved as we can fit it with a Gaussian with a FWHM equal to a spectral resolution element. From our fit, we derived the integrated flux in the line (see Table 1). From the wavelength position of the Gaussian peak, we considered that the radial velocity of the H_2 is compatible with zero (at the *VISIR* resolution) and therefore similar to that of the star, implying that the emitting gas is gravitationally bound to the star, and likely arising from the disk and not from an outflow.

[1] Laboratoire d'Astrophysique de Grenoble, CNRS, Université Joseph-Fourier, UMR 5571, Grenoble, France
[2] Leiden Observatory, Leiden University, P.O. Box 9513, 2300 RA Leiden, the Netherlands
[3] Max Planck Institut für Extraterrestrische Physik, Giessenbachstrasse 1, 85748 Garching, Germany
[4] Institut d'Astrophysique Spatiale, 91405 Orsay, France
[5] Laboratoire AIM, CEA/DSM - DAPNIA/Service d'Astrophysique, Bat. 709, CEA/Saclay, 91191 Gif-sur-Yvette Cedex, France

Table 1. Integrated fluxes F_{ul} ($\mathrm{ergs\,s^{-1}\,cm^{-2}}$) and intensities I_{ul} ($\mathrm{ergs\,cm^{-2}\,s^{-1}\,sr^{-1}}$) of the S(1) line, and total column densities and masses of H_2 as a function of the adopted temperature. (a) The line is not spatially resolved, we calculated a lower limit on the intensity, and thus obtained lower limits on the total column densities.

Star	F_{ul}	I_{ul}	$N(H_2)$ upper limits ($\mathrm{cm^{-2}}$)			H_2 mass upper limits ($M_{\mathrm{Jup}}\sim10^{-3}\ M_\odot$)		
HD	($\times10^{-14}$)	($\times10^{-3}$)	150K	300K	1000K	150 K	300 K	1000 K
Non detections at 17.035μm								
142527	<1.0	<2.5	9.4×10^{22}	6.1×10^{21}	1.4×10^{21}	1.9×10^{-1}	1.2×10^{-2}	3.3×10^{-3}
169142	<1.8	<4.2	1.6×10^{23}	1.0×10^{22}	2.4×10^{21}	3.5×10^{-1}	2.1×10^{-2}	6.1×10^{-3}
150193A	<2.1	<5.0	1.9×10^{23}	1.2×10^{22}	2.8×10^{21}	4.5×10^{-1}	2.7×10^{-2}	7.7×10^{-3}
163296	<2.8	<6.7	2.5×10^{23}	1.6×10^{22}	3.8×10^{21}	3.9×10^{-1}	2.4×10^{-2}	6.9×10^{-3}
100546	<14	<33	1.2×10^{24}	7.9×10^{22}	1.9×10^{22}	1.4	8.4×10^{-2}	2.4×10^{-2}
98922	<1.2	<1.2	1.1×10^{23}	6.9×10^{21}	1.6×10^{21}	3.3	2.0×10^{-1}	5.9×10^{-2}
250550	<1.6	<3.8	1.5×10^{23}	9.3×10^{21}	2.2×10^{21}	$5.5^{+8.8}_{-4.7}$	$3.4^{+5.4}_{-2.9}\times10^{-1}$	$1.0^{+1.6}_{-0.8}\times10^{-1}$
259431	<1.8	<4.2	1.6×10^{23}	1.0×10^{22}	2.4×10^{21}	$1.4^{+0.9}_{-0.7}$	$8.6^{+5.7}_{-4.3}\times10^{-2}$	$2.5^{+1.7}_{-1.3}\times10^{-2}$
45677	<1.6	<3.7	1.4×10^{23}	9.1×10^{21}	2.1×10^{21}	3.7	2.3×10^{-1}	6.7×10^{-2}
The only one detection at 17.035μm								
			(a)	(a)	(a)			
97048	2.4	5.7	$>2.2\times10^{23}$	$>1.4\times10^{22}$	$>3.3\times10^{21}$	7.4×10^{-1}	4.5×10^{-2}	1.3×10^{-2}

The H_2 line is not resolved spatially either. Given the *VISIR* spatial resolution, and the star distance, we can assess that the emitting H_2 is located within the inner 35 AU of the disk. Assuming that the H_2 gas follows the same (Keplerian) kinematics as the disk, the emitting gas observed with *VISIR* is likely not concentrated significantly in the innermost AU of the disk (< 5 AU) otherwise rotational broadening would be observed. The emitting H_2 is thus more likely distributed in an extended region within the inner disk, between 5 AU and 35 AU of the disk. Assuming the emission arises from an isothermal mass of optically thin H_2, we estimated the corresponding column densities and masses of H_2 as a function of prescribed temperatures (Table 1).

HD 97048 spectra showed no evidence for H_2 emission neither at 12.278 μm nor at 8.025 μm. From the derived upper limits on the column densities of the rotational levels of H_2, and assuming that all three levels are populated by thermal collisions (LTE), we estimated the excitation temperature of the observed gas to be lower than 570 K, and re-evaluated the mass of gas to be lower than 0.1 M_{Jup} in the inner 35 AU of the disk.

4 Discussion

In our sample of 10 stars, only one spectrum present H_2 emission at 17.035 μm. We stress that in their sample of 6 Herbig Ae stars, Carmona et al. (2008) have not detected any S(1) line of H_2 with *VISIR*. Those authors demonstrated that in LTE conditions, mid-IR H_2 lines could not be detected with the existing instruments. However, the S(1) line of H_2 has been already detected in the disk of another Herbig star, namely AB Aur (Bitner et al. 2007; with *TEXES*). The main goal now, is to explain these detections. Why HD 97048 and AB Aur seem to be peculiar stars? Are the physical conditions of the gas typical of a particular stage of evolution of the disk ? At the present time, a detailed model (of gas and dust) of the disk of HD 97048 is in progress, using the McFOST code (Pinte et al. 2006), in order to answer these questions.

Work based on observations obtained at ESO/VLT with VISIR, programs 076.C-0299, 077.C-0309, 079.C-0839, 083.C-0910. CMZ. warmly thanks A. Smette (ESO) for fruitful discussions about the observations. CMZ was supported by a CNES fellowship.

References

Bitner, M. A., Richter, M. J., Lacy, J. H., et al. 2007, ApJ, 661, L69

Carmona, A., et al. 2008, A&A, 477, 839

Martin-Zaïdi, C., et al. 2007, ApJ, 666, L117

Martin-Zaïdi, C., et al. 2008a, A&A, 484, 225

Martin-Zaïdi, C., et al. 2008b, A&A, 489, 601

Martin-Zaïdi, C., et al. 2009a, ApJ, 695, 1302

Martin-Zaïdi, C., et al. 2009b, A&A to be submitted

Pinte, C., Ménard, F., Duchêne, G., & Bastien, P. 2006, A&A, 459, 797

SF2A 2009
M. Heydari-Malayeri, C. Reylé and R. Samadi (eds)

PROBING THE CHEMISTRY AND THE EVOLUTION OF THE CIRCUMSTELLAR ENVIRONMENT OF HERBIG Ae/Be STARS

Martin-Zaïdi, C.[1], Le Bourlot, J.[2], Roueff, E.[2], Hily-Blant, P.[1] and Gry, C.[3]

Abstract. We present *UVES* (*Ultraviolet and Visual Echelle Spectrograph*) observations of a sample of Herbig Ae/Be stars for which we had already measured the amount of circumstellar molecular hydrogen (H_2) using the *FUSE* (*Far Ultraviolet Spectroscopic Explorer*) satellite. The preliminary analysis of these spectra confirms the well known problem of the formation and excitation of the molecules in the circumstellar environments of our sources, especially those of CH and CH^+. In the future, combined to our H_2 data, these new observations should allow us to constrain the chemical mechanisms of formation/destruction and excitation of these different molecules.

1 Introduction

Molecular hydrogen, from which giant planets are believed primarily to form, is the most abundant molecule in the circumstellar (CS) environment of young stars. The detection of H_2 provides the most direct information about the gaseous content in the CS environment of HAeBes and allows limits to be set on the timescale for the dissipation of the circumstellar matter and the possible planet building. The analysis of far ultraviolet (FUV) spectra of a sample of Herbig Ae/Be stars (HAeBes) demonstrated that the excitation of H_2 is clearly different around most of the HAeBes compared to the interstellar (IS) medium (Martin-Zaïdi et al. 2008, hereafter CMZ08). Moreover, the characteristics of H_2 around Herbig Ae and Be stars give evidence for different excitation mechanisms. In addition, no clear correlation has been found between the ages of the stars and the amount of circumstellar H_2. From this analysis, CMZ08 suggest structural differences between Herbig Ae and Be star environments. This analysis also points to the need for complementary observations to better understand the physical conditions of formation and excitation of H_2 and the origin of the gas.

We thus observed spectral lines of the CH and CH^+ molecules in the optical range at high spectral resolution using the VLT/*UVES* spectrograph of the same sample of HAeBes as previously observed by *FUSE*. These molecules are linked to the formation and excitation of H_2 (Federman 1982, Mattila 1986, Somerville & Smith 1989). The formation of CH is predicted to be controlled by gas-phase reactions with H_2. CH is thus a good tracer of H_2 and their abundances are generally strongly correlated. The formation of the CH^+ molecule through the chemical reaction $C^+ + H_2$ needs a temperature of about 4500 K to occur. Thus, the CH^+ molecule is a probe of hot and excited media, which could be interpreted for our targets as material close to the star, and this would allow us to better constrain the excitation of H_2. The observation of CH and CH^+, if present, could provide direct evidence of warm/hot CS gas close to the star. Combined with the H_2 data, this should allow us to explain the chemical mechanisms of formation/destruction and excitation of the different molecules in the CS environment of HAeBes and to better evaluate the velocity dispersion along the line of sight.

In this paper, we first recall the results obtained about H_2 in the *FUSE* spectra of a sample of 18 Herbig stars (for a detailed analysis, see CMZ08), and present the preliminary results on the CH and CH^+ molecules in the *UVES* spectra.

[1] Laboratoire d'Astrophysique de Grenoble, CNRS, Université Joseph-Fourier, UMR 5571, Grenoble, France
[2] LUTH, UMR 8102 CNRS, Université Paris 7 and Observatoire de Paris, Place J. Janssen, 92195 Meudon, France
[3] Laboratoire d'Astrophysique de Marseille (UMR 6110), Technopôle de Marseille-Etoile, F-13388 Marseille cedex 13, France

2 Molecular hydrogen in the circumstellar environments of Herbig Ae/Be stars probed by FUSE.

FUSE is a spectrograph which covers the spectral range from 905Å to 1187Å with a resolution of R∼15,000 (30"×30" LWRS aperture), which offers acces to the Werner and Lyman electronic bands of H_2. Especially, one would expect to observe H_2 lines if HAeBe stars have greatly extended CS disks and if the lines of sight to the stars pass through the disks. In that case, the H_2 lines may be observable in absorption between 950 Å and 1150 Å, projected against the UV continua of the stars. Alla

CMZ08 have studied the characteristics and excitation conditions of molecular hydrogen in the CS environment of a sample of 18 HAeBes observed with *FUSE*. The *FUSE* data do not enable to constrain the spatial distribution of the detected gas, but allow to set new constraints on the nature and evolution of the CS environment of HAeBes. From the excitation diagram of the H_2 molecule towards each star, those authors showed marked differences between the Herbig Ae/B9 stars on the one hand, and the Herbig Be stars on the other hand. They distinguished two groups of stars: the stars known to possess CS disks (Ae/B9 stars) and the stars with no evidence of disks (Be stars). They interpreted the different excitation characteristics of H_2 as direct probes of the origin of the observed gas: interstellar, circumstellar disk, or circumstellar envelopes.

For most of the Herbig Ae/B9 stars, the inclination angles of the CS disks from the lines of sight are quite high and not favorable to probe the disks using absorption spectroscopy. When molecular hydrogen gas is observed in the *FUSE* spectra of the Herbig Ae/B9 stars, their analysis shows several kinds of excitation, implying different origins and different physical processes.

In one case, namely HD 141569, the origin of the detected gas is clearly interstellar. For AB Aur there is also some evidence for an IS gas origin, but there is a lack of spectral resolution that could allow to probe the velocity distribution along the line of sight and definitively disentangle between a CS or IS origin for the gas. In spite of its relatively high inclination away from edge-on, it is not geometrically impossible for the gas to originate in the upper layers of the outer disk regions at about 800 AU, but the excitation conditions of H_2 towards AB Aur are fairly typical of what is generally observed in the diffuse interstellar medium. However, CMZ08 showed that the excitation diagram could not be reproduced well by a single gaseous component along the line of sight by using the Meudon PDR Code (Le Petit et al. 2006). The large line width value favors the presence of two components along the line of sight, which are not resolved in the spectrum. In that case, one of these components could correspond to the remnant of the molecular cloud in which the star formed, as suggested by (Roberge et al. 2001). The high J-levels absorption could be interpreted as due to a hotter component, probably close to the star, with negligible contribution to the low J-levels.

For HD 100546, HD 163296, and HD 104237, CMZ08 observed excited and probably warm/hot, circumstellar H_2 that has excitation conditions clearly different from those observed in the diffuse interstellar medium. Such excitation conditions for H_2 give evidence of collisionally excited media close to the stars. The measured radial velocities favor a CS origin for the H_2. However, assuming that the gas and dust are coupled, the lines of sight towards these three stars do not pass through their disks, and thus the observed H_2 is not located in the disks. This raises questions about the origin of the detected gas. One interesting possibility could be that the H_2 gas is a FUV-driven photoevaporative wind from the outer parts of the disk, but clues are still missing for a firm conclusion. The Meudon PDR Code did not allow to reproduce the excitation of the observed H_2 gas. This implies that peculiar excitation processes such as shocks or X-Rays, not taken into account in the Meudon PDR Code, may play a role in the environment of these stars.

The excitation conditions of circumstellar H_2 around the stars of the second group (Be stars) are clearly different from those of the first group. CMZ08 found similar excitation conditions for the H_2 from one star to the next. They present similarities to the conditions found in the IS medium. The analysis of the *FUSE* spectra favors an interpretation in terms of spherically symmetric media, not affected by inclination effects. The excitation diagrams are reproduced nicely by PDR models, at least for the cold component that includes more than 90% of the gas. On the other hand, these models systematically underpredicts the high J-levels column densities. The observed environments are very likely complex environments, such as large CS envelopes, remnants of the original clouds in which the stars formed. However, other excitation processes, in addition to those taken into account in the Meudon PDR Code, are probably necessary to fully explain the observed excitation diagrams.

This FUV analysis reinforces the differences between the two subclasses of stars (Ae and Be) already highlighted by different authors (e.g. Natta et al. 2000). It also points to the need for complementary observations to better understand the physical conditions of formation and excitation of H_2 and the origin of the gas.

Table 1. Measured radial velocities of the CH and H_2 molecules to be compared to that of the star (all given in the heliocentric rest frame). Measured column densities of CH, CH^+ and H_2, and ratio CH/H_2.

Star	Sp. Type	$v_{\rm rad}$ star km s^{-1}	$v_{\rm rad}$(CH) km s^{-1}	$v_{\rm rad}(H_2)$ km s^{-1}	log N(CH) cm^{-2}	log N(CH^+) cm^{-2}	log N(H_2) cm^{-2}	log(N(CH)/N(H_2))
HD135344	F4V	-3	–	–	$\leq$12.5	$\leq$12.7	$\leq$15	–
HD36112	A5	+17.6	+19.0±0.6	–	12.53±1.2	$\leq$12.9	$\leq$15.78	–
NX Pup	A0	?	+14.2±1.0	–	12.68±3.27	12.97±0.65	–	–
AB Aur	A0V	+21	+15.0±0.1	+23±3	12.28±1.40	13.08±0.11	$20.03^{+0.15}_{-0.19}$	$-7.75^{+1.25}_{-1.21}$
HD163296	A1V	+4	–	+4±2	$\leq$12.1	$\leq$12.3	$18.16^{+0.27}_{-0.40}$	–
HD141569	B9V	-6.4	-13.0±0.02	-14.0	12.14±1.27	12.56±0.56	$20.32^{+0.20}_{-0.22}$	$-8.18^{+1.07}_{-1.05}$
HD100546	B9V	+17	–	+17±2	$\leq$12.0	$\leq$12.3	$16.46^{+0.24}_{-0.14}$	–
HD176386	B9/B8	+7.3	-5.0±0.2	0	12.61±0.65	12.84±0.14	$20.80^{+0.18}_{-0.26}$	$-8.19^{+0.47}_{-0.39}$
HD250550	B7	+31	–	$+30^{+1.7}_{-2.0}$	$\leq$12.0	$\leq$12.6	$19.26^{+0.17}_{-0.40}$	–
HD85567	B5V	(-5 / 0)	–	$(-1.5\ /\ 4.5)^{+0.3}_{-0.2}$	$\leq$12.3	$\leq$12.6	$19.33^{+0.20}_{-0.17}$	–
HD259431	B5	+43	–	$+56^{+2.2}_{-1.8}$	$\leq$12.0	$\leq$12.4	$20.64^{+0.11}_{-0.19}$	–
HD38087	B5V	+33	+26.0±0.2	$+35.4^{+1.2}_{-2.1}$	12.93±0.47	13.57±0.05	$20.43^{+0.15}_{-0.08}$	$-7.50^{+0.32}_{-0.49}$
HD76534	B2	+17	+20.4±0.2	$+17^{+0.3}_{-1.3}$	12.89±0.46	13.46±0.07	$20.64^{+0.16}_{-0.16}$	$-7.75^{+0.30}_{-0.30}$

3 UVES observations

Nearly the same sample of stars have been observed with VLT/*UVES* to detect lines of the CH and CH^+ molecules, which are linked to the formation and excitation of H_2. We observed 13 HAeBes between ∼3700 Å and 5000 Å in the blue arm of *UVES* in order to observe simultaneously CH and CH^+ lines as well as atomic lines such as Ca II. We used no image slicer, low gain with a 1×1 binning of the CCDs and a slit width of 0.4 arcsec providing the maximum resolution of ∼80,000. This maximum spectral resolution of *UVES* was required to separate the different gaseous components along the line of sight. For each target, the signal-to-noise ratio is higher than 100 in the whole spectrum.

For 6 out of our 13 targets, both lines of CH and CH^+ are detected. For one target, only CH is detected while CH^+ is not. The 6 other spectra do not present any features of CH and/or CH^+. When observed, we derived the column densities of CH and CH^+ using the Owens line fitting procedure (Lemoine et al. 2002). For most stars of the sample, the mean projected velocity of CH is very close to that of the star and to that of H_2, whithin the resolution of the spectra. This is a clue that the detected CH and H_2 are produced in the same region of the environments of our targets. When H_2 and CH are both observed, their column densities are correlated (Fig. 1) in proportions consistent with those observed in the diffuse interstellar medium (e.g. Welty et al. 2006, Sheffer et al. 2008). It is important to note here that for these stars, the H_2 data implied an IS origin for the gas or a remnant of the parent molecular cloud (close to IS excitation conditions). The present results are thus fully consistent with the H_2 data. On the other hand, Lambert & Danks (1986) presented correlations between N(CH^+) and N(H_2^*), i.e., column densities of excited states of H_2 involving the $J \geq 5$ levels. We do not find obvious correlation between N(CH^+) and N(H_2^*) (see Fig. 1). However, excluding HD 141569 for which the observed gas is clearly IS in origin, a weak correlation N(CH^+)$\propto$N(H_2^*)$^{-3.5}$ may be seen. Our results are summarized in Table 1. In addition, for the Be stars for which CH and CH^+ are observed (3 out the 13 in our sample), we stress that the best-fit model for H_2 obtained by CMZ08 with the Meudon PDR Code, do not reproduce the present CH and CH^+ data. The observed column densities of CH are at least a factor 3 higher than those given by the model, while the observed column densities of CH^+ are more than 100 times higher that those given by the model. This confirms the well known problem of CH and CH^+ formation (see Sect. 4). It is known that CH^+ is likely formed in shocked regions, and the Meudon PDR Code is stationary, thus it cannot explain the observed CH^+. One way to solve this problem is to use non-stationary codes such as shocks or turbulent dissipation region (TDR) models. At the present time, this work is in progress.

4 Discussion

We presented here our preliminary results about the observation of the CH and CH^+ molecules with *UVES* in the circumstellar environments of Herbig Ae/Be stars, in relation with previous *FUSE* observations of H_2. We

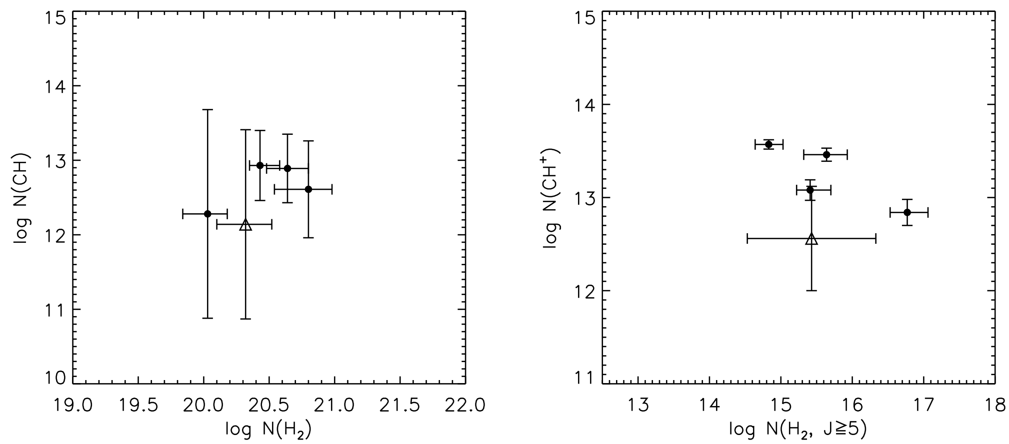

Fig. 1. *Left:* Total column density of H_2 versus column density of CH. *Right:* Column densities of excited levels of H_2 (J$\geq$5) versus column density of CH^+ (see text). The triangles distinguish HD 141569 since the observed gas is clearly IS in origin (see CMZ08).

showed that there is a clear correlation between the column densties of CH and H_2 as observed in the interstellar medium and that these two molecules are likely produced in the same region of the CS environment of our target stars. No correlation has been found between CH^+ and excited levels of H_2. Althought the Meudon PDR Code reproduces well the H_2 data, it fails to reproduce the CH and CH^+ observations. This raises the well known problem of the formation of these molecules.

It is generally agreed that non-equilibrium chemistry is the key to solve the CH^+ abundance problem in diffuse clouds. However, the exact physical mechanism producing CH^+ is still unclear. Formation of CH^+ have been quantitatively investigated in the specific cases where dissipation occurs within MHD shocks (e.g. Flower & Pineau des Forets 1998) or coherent vortices in MHD turbulence (Godard et al. 2009). In such models the temperature of the warm gas and the ratio between CH^+ and warm H_2 column densities depends strongly on local physical conditions (e.g. shock velocity, gas density, magnetic field value). However, the lack of velocity differences between CH and CH^+ (e.g. Gredel et al. 1993) argues against shocks. Recently, Lesaffre et al. (2007) modeled the effects of turbulent diffusion on diffuse cloud chemistry, determining that this mechanism can increase the CH^+ abundance by up to an order of magnitude, which is still lower than observed.

Work based on observations obtained at ESO/VLT with UVES, programs 075.C-0637 and 078.C-0774. CMZ was supported by a CNES fellowship.

References

Federman, S. R. 1982, ApJ, 257, 125
Flower, D. R., & Pineau des Forets, G. 1998, MNRAS, 297, 1182
Godard, B., Falgarone, E., & Pineau Des Forêts, G. 2009, A&A, 495, 847
Gredel, R., van Dishoeck, E. F., & Black, J. H. 1993, A&A, 269, 477
Lambert, D. L., & Danks, A. C. 1986, ApJ, 303, 401
Lemoine, M., et al. 2002, ApJs, 140, 67
Le Petit, F., Nehmé, C., Le Bourlot, J., & Roueff, E. 2006, ApJs, 164, 506
Lesaffre, P., Gerin, M., & Hennebelle, P. 2007, A&A, 469, 949
Martin-Zaïdi, C., et al. 2008, A&A, 484, 225 (CMZ08)
Mattila, K. 1986, A&A, 160, 157
Natta, A., Grinin, V., & Mannings, V. 2000, Protostars and Planets IV, 559
Roberge, A., et al. 2001, ApJ, 551, L97
Sheffer, Y., Rogers, M., Federman, S. R., Abel, N. P., Gredel, R., Lambert, D. L., & Shaw, G. 2008, ApJ, 687, 1075
Somerville, W. B., & Smith, C. A. 1989, MNRAS, 238, 559
Welty, D. E., Federman, S. R., Gredel, R., Thorburn, J. A., & Lambert, D. L. 2006, ApJs, 165, 138

PNPS-PNP-SSAA

Connecting our understanding of star and planet formation and physics

SF2A 2009
M. Heydari-Malayeri, C. Reylé and R. Samadi (eds)

EXOZODIACAL DUST DISKS

Augereau, J.-C.[1]

Abstract. The zodiacal cloud has long been suspected to have extrasolar analogs, exozodiacal, debris clouds that remained elusive until very recently. Over the last decade, the presence of exozodiacal dust in the habitable zone around nearby stars, has essentially been discussed as a potential noise source that may compromise the ability of future exo-Earth finding missions to reach their goals. Our pioneering detection of exozodiacal dust around Vega in 2006 using near-IR interferometry shows that exozodiacal disks are by themself very interesting astrophysical objects. In these proceedings, I review the current observations of exozodiacal dust disks around nearby main sequence stars using near-infrared interferometry, and show that, as a rule of thumb, the detected exozodiacal dust disks differ from the zodiacal cloud. I then consider possible dynamical scenarios that may give rise to an abundant production of exozodiacal dust. I emphasize a promising scenario involving the outward migration of a planet toward a planetesimal belt similar to the Kuiper belt, and responsible for a cometary bombardment.

1 Introduction

Within about 2 AU, the inner solar system is filled with dust near the ecliptic plane that originates from tails of comets, or produced when asteroids collide. This dust forms the zodiacal cloud that, despites its tiny total mass equivalent to a medium-sized asteroid ($\sim 10^{-8}\mathrm{M}_\oplus$, vertical optical thickness of $\sim 10^{-7}$ at 1 AU), is the most luminous extended circumsolar component. The zodiacal cloud is furthemore not smooth but structured. Dust bands discovered by IRAS would trace back recent (5–8 Myr ago) breakups of members of known asteroids families (e.g. Nesvorný et al. 2008 and ref. therein), while some dust trails may be associated to short period comets. A noticeable feature of the zodiacal cloud is its resonant 1:1 ring caused by grains migrating inward due to Poynting-Robertson (P-R) and solar wind drag, and trapped in mean motion resonance with the Earth. This leads to a brightness enhancement in the Earth trailing direction, and a dust cavity at the Earth location. All these features make the zodiacal cloud asymmetric and probably variable in time.

To feed the future exo-Earths finders design studies with realistic numbers, and to improve their detection strategy, it appears crucial to better assess the brightness level and structure of exozodiacal clouds around potential targets, namely nearby Main Sequence stars. Our pioneering detection of exozodiacal dust around Vega in 2006 with the CHARA/FLUOR interferometric instrument in the K-band (Absil et al. 2006), soon followed by more detections using the same technique, have shown that exozodiacal disks (henceforth exozodis) are by themself very interesting astrophysical objects that deserve detailled studies. In this paper, I briefly review the current observations of exozodis around nearby main sequence stars using near-IR interferometry, and show that the detected exozodis differ from the zodiacal cloud. I then discuss possible dynamical scenarios that may give rise to an abundant production of exozodiacal dust, with emphasis on a promising scenario involving the outward migration of a planet toward a Kuiper belt and initiating a cometary bombardment.

2 Near-IR interferometry of exozodiacal dust disks

Only very recently, hot dust has been unambiguously resolved for the first time around several stars (Vega, τ Ceti, ζ Aql, β Leo, ζ Lep, Fomalhaut) using high-precision near-infrared interferometry at the CHARA Array and at the VLTI (Absil et al. 2006, di Folco et al. 2007, Absil et al. 2008, Akeson et al. 2009, Absil et al.

[1] Université Joseph Fourier/CNRS, Laboratoire d'Astrophysique de Grenoble, UMR 5571, Grenoble, France

2009). The detection principle is based on the small decrease of visibility produced by the resolved circumstellar structure with respect to the expected photospheric visibility. This departure from the stellar size can best be detected at short baselines (∼30–50 m), while the long baseline measurements determine the stellar parameters. An example data set on the debris disk system Fomalhaut is shown in Figure 1 (from Absil et al. 2009). The

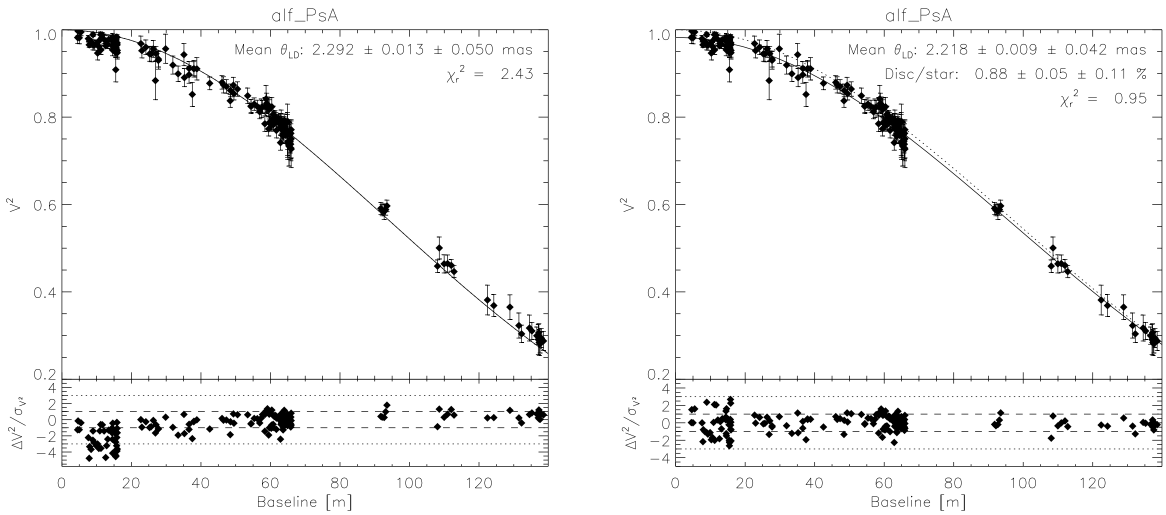

Fig. 1. Left : result of the fit of an oblate limb-darkened stellar photosphere to the full VLTI/VINCI data set (top panel). The dashed and dotted lines in the bottom panel represent respectively a 1σ and a 3σ deviation with respect to the best-fit model. **Right**: Result of the fit of a star-disk model. The solid line represents the best fit star-disk model, while the dotted line represents the best-fit result with a single star for comparison. From Absil et al. (2009).

VLTI/VINCI measurements are inconsistent with a naked star within the field of view of the interferometer as can be seen in the left panel of Figure 1, while the visibility deficit for Fomalhaut is evidenced when the stellar size is extrapolated to small spatial frequencies (shorter baselines), revealing an extended (over-resolved) emission (right panel). In fact, the restricted field of view of the interferometer ensures that any detected emission comes from much smaller spatial scales than the cooler material, which produces the previously known mid- to far-infrared excess toward these stars. The main outcomes of these observations are therefore a maximum radius where the dust must be confined, and an accurate estimate of the K-band ($2.2\,\mu$m) flux excess, which was not known through broadband spectral modeling, since the interferometrically detected near- infrared excesses are within the photometric uncertainties (e.g. $1.29 \pm 0.19\%$ excess for Vega, 0.98 ± 0.21 for τ Ceti). More and more similar cases are found with the CHARA Array suggesting that about 20% of the stars may have an exozodiacal dust disk, depending on spectral type.

3 Nature of the exozodiacal dust

The fit to the $2.2\,\mu$m excess with the solar system zodiacal model (using for example the Zodipic package developped by M. Kuchner), indicates densities a few thousand times larger than the zodiacal density (about 3000 zodis for Vega, 5000 zodis for Fomalhaut). This model nevertheless predicts much too large flux (by about an order of magnitude) in the mid-IR compared to the observations, indicating that the solar system zodiacal spectrum does not match the spectral energy distributions (SEDs) of detected exozodiacal disks. Dust much closer to the star is required to shift the spectrum to shorter wavelengths.

Based on the sole photometric and spatial information derived from the CHARA or VINCI measurements, complemented by (much less accurate) archival photometric data at other infrared wavelengths, it has become possible to put useful constraints on the disk morphology, composition and dynamics by using the radiative transfer code of Augereau et al. (1999) and dust optical constants from laboratory measurements to reproduce the disk SEDs. An example fit to the SED of ζ Aql is displayed in Figure 2 (top panel), where the derived total mass and fractional luminosity of these exozodiacal grains are documented in the upper right corner (from

Absil et al. 2008). While the case of a binary low-mass companion, or of a background star, can generally be safely excluded to explain the observed near-IR excesses, a 0.6–0.65 $M_\odot$ object at 5.5–8 AU remains compatible with all observational constraints, including direct imaging and astrometric measurements in the case of ζ Aql (bottom panel of Figure 2).

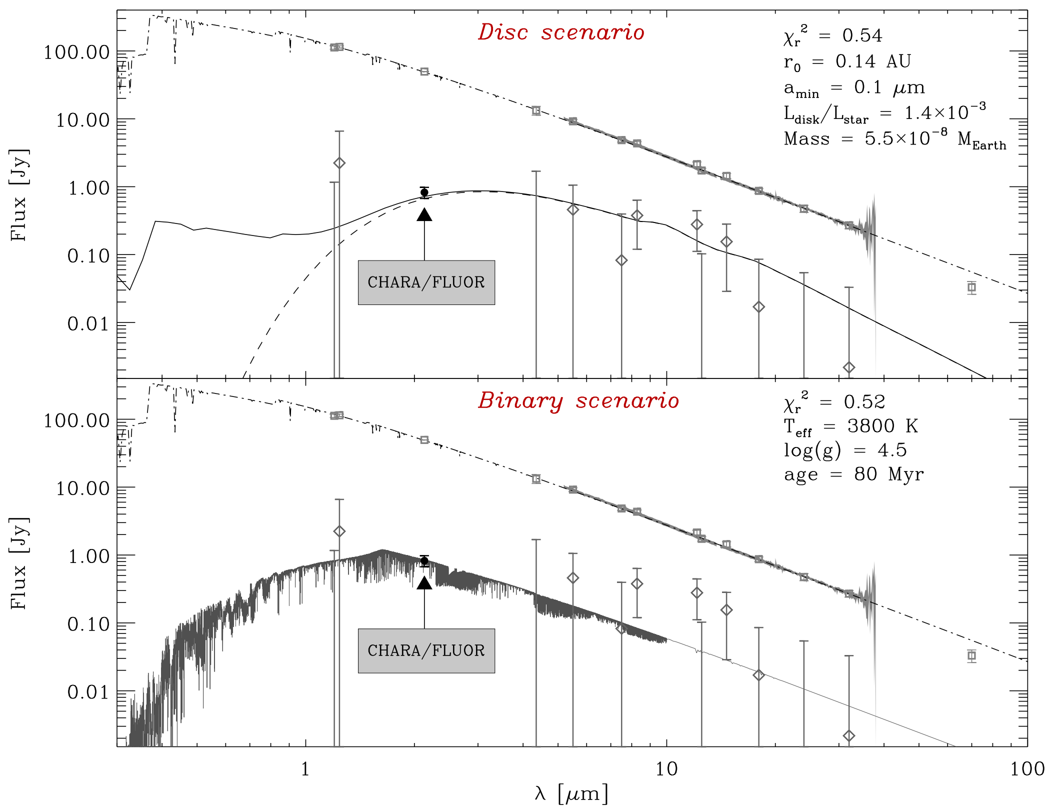

Fig. 2. Top: a possible fit of our debris disk model to the photometric and interferometric constraints (excesses represented with diamonds). Dashed line: thermal emission from the disk, solid line: includes the scattered light contribution. **Bottom**: case of a low-mass companion ($T_{\rm eff} = 3800$ K, $\log(g) = 4.5$). From Absil et al. (2008).

In the case of Vega, the modeling shows that the resolved emission emanates mostly from hot sub-μm carbonaceous grains located within 1 AU from the photosphere, close to their sublimation limit (~0.5 AU for the sub μm-sized grains, ~0.15 AU for the few > μm-sized grains). The dust mass, $\sim 8 \times 10^{-8} M_\oplus$, is equivalent to the mass of a 70 km diameter asteroid. Because of the high temperature of the grains, the luminosity of the exozodiacal dust disk ($L_{\rm exozodi}/L_\star \sim 5 \times 10^{-4}$) is more than one order of magnitude larger than the luminosity of the outer, Kuiper Belt-like, disk, even though it is almost 105 times less massive than the outer ring. Due to radiation pressure, small grains cannot survive in the Vega exozodiacal disk more than a few years before being ejected toward cooler regions (e.g. Krivov et al. 2006). Larger grains would survive somewhat longer, but not more than a few tens of years due to the high collision rate. This implies a large dust production rate ($\sim 10^{-8} M_\oplus$) to explain the interferometric observations, a conclusion valid for all systems with detected exozodiacal dust.

4 Origin of the exozodiacal dust

In fact, all detected exozodiacal disks have luminosities orders of magnitudes larger than those expected for a steady state collisionally-dominated belt of planetesimals. This suggests that dynamical perturbations are currently ongoing in these systems. As discussed in Absil et al. (2006), a scenario involving the presence of star-grazing comets, injected into the inner planetary system by dynamical perturbations caused by migrating planets, has been proposed, inspired by the most recent models for the Late Heavy Bombardment (LHB) that happened in the early solar system (Gomes et al. 2005). A similar, catastrophic scenario is also proposed by Wyatt et al. (2007) to explain the presence of warm dust ($\sim$300 K) detected by the Spitzer Space Telescope around a few solar-type stars.

The problem of the huge mass of the exozodiacal disks can therefore be mitigated by an assumption that they are fed from outside. While standard dust transport mechanisms such as P-R drag are two slow compared to other dynamical timescales (i.p. collision timescales) to do the job, possible planets in the region between the exozodiacal disk and a Kuiper belt could assist transporting the planetesimals. For Vega, our team is currently building on the planet migrating scenario published in Wyatt (2003) and Reche et al. (2008) to explore the fraction of Kuiper-Belt objects penetrating the inner Vega system to compare with the near-IR observations. Assuming a two planet system composed of a Neptune-mass planet migrating outward from 40 to 60 AU on a low eccentric orbit, and a Jupiter-mass at 20–25 AU, we estimate that this configuration can sustain over 40 Myr the transportation of 10^{-3} the mass of the Vega Kuiper Belt within 1 AU every million of year, a rate which is consistent with the $10^{-8}\,M_{\oplus}.yr^{-1}$ derived from the SED modeling (Vandeportal et al., in prep.).

5 Conclusion

The mechanisms for the exozodiacal dust production are still largely unclear despites some first attempts to link the exozodiacal disk properties to those of the outer regions of planetary systems. It is in particular not known whether or not the dust production mechanisms are similar to those operating in the solar system. It is not known how different they are in different systems and what is the role of transient events.

To address some of these issues, an ISSI international team (http://www.issibern.ch/teams/exodust) has been assembled. The working group, leads by J.-C. Augereau and A. Krivov, gathers scientists with vast, and mutually complementary expertise in modeling, observations, laboratory experiments, and instrumentation. It includes both specialists in extrasolar dust disks and experts in the Solar System's zodiacal cloud, thus bringing together two communities that use various approaches. Two one-week meetings were held in August 2007 and April 2009, with the concluding meeting planned in 2010. A significant effort is invested into intensive modeling and characterisation of the detected exozodiacal clouds, in an attempt to uncover possible commonalities and diversities between them and the zodiacal cloud in our Solar System. This expertise shall be very beneficial to prepare future space missions, such as the Fourier-Kelvin Stellar Interferometer (FKSI, Danchi et al., these proceedings) that aims at detecting exozodiacal emission levels to that of our solar system around nearby solar-type stars, and characterizing the atmospheres of exoplanets.

This work is supported by the ISSI (Bern, Switzerland), the Programme National de Planétologie (PNP) and the Programme National de Physique Stellaire (PNPS) in France, and EGIDE/DAAD (PROCOPE programme).

References

Absil, O., et al. 2006, A&A, 452, 237

Absil, O., et al. 2008, A&A, 487, 1041

Absil, O., Mennesson, B., Le Bouquin, J.-B., Di Folco, E., Kervella, P., & Augereau, J.-C. 2009, ApJ, 704, 150

Akeson, R. L., et al. 2009, ApJ, 691, 1896

Augereau, J. C., Lagrange, A. M., Mouillet, D., Papaloizou, J. C. B., & Grorod, P. A. 1999, A&A, 348, 557

di Folco, E., et al. 2007, A&A, 475, 243

Gomes, R., Levison, H. F., Tsiganis, K., & Morbidelli, A. 2005, Nature, 435, 466

Krivov, A. V., Löhne, T., & Sremčević, M. 2006, A&A, 455, 509

Nesvorný, D., Bottke, W. F., Vokrouhlický, D., Sykes, M., Lien, D. J., & Stansberry, J. 2008, ApJL, 679, L143

Reche, R., Beust, H., Augereau, J.-C., & Absil, O. 2008, A&A, 480, 551

Wyatt, M. C. 2003, ApJ, 598, 1321

Wyatt, M. C., Smith, R., Greaves, J. S., Beichman, C. A., Bryden, G., & Lisse, C. M. 2007, ApJ, 658, 569

SF2A 2009
M. Heydari-Malayeri, C. Reylé and R. Samadi (eds)

YOUNG STARS IN TAURUS: A SEARCH FOR GAS TRACERS IN PROTOPLANETARY DISKS WITH SPITZER IRS SPECTRA.

Baldovin-Saavedra, C.[1], Audard, M. [1], Güdel, M.[2], Padgett, D., Rebull, L.[3], Glauser, A. [2,4], Skinner, S.[5], McCabe, C. [3], Briggs, K. [2], Fajardo-Acosta, S.[6] and Wolf, S.[7]

Abstract. In order to understand the structure and evolution of proto-planetary disks is fundamental to study the gas, which represents the $\sim$ 99% of their mass. But its properties are not yet well constrained because its detection is a difficult task. Dust, although a minor constituent of disks dominates the opacity, therefore it is much easy to observe. Our current knowledge of disks is largely based on the study of the emission from the dust. In the last few years, several detections of gas tracers in the mid-infrared have been reported, in particular [Ne II] (12.81 μm) whose origin is somehow controversial.

We have started a search for gas tracers in a sample of low-mass pre-main sequence stars in the Taurus Molecular Cloud. This study is based on archival observations of young stellar objects done by the *Spitzer Space Telescope* with the IRS high-resolution module spectrometer (R=600). Our sample contains 70 objects, we have detected emission lines from ionized gas and molecular rotational lines in 23 of them. We have fitted the line profiles and obtained line fluxes, with the aim to look for correlations with stellar parameters such as L_X or mass accretion rate in order to test the mechanism at the origin of the lines (irradiation, shocks, thermal, etc.). We present a review on our current understanding of gas in young stars and present the results from our study of the Taurus Molecular Cloud through *Spitzer* spectra.

1 Introduction

To understand the formation of planetary systems it is crucial to start by studying the processes leading to the formation of stars, such as the initial conditions of pre-stellar cores, the chemistry, composition and evolution of proto-planetary disks, etc. Although gas is the main component of disks (99%), the dust dominates the opacity becoming much easier to observe. Nevertheless, gas can be probed through rotational lines of CO and H_2 at near-IR, mid-IR and mm wavelengths. Theoretical studies suggest that irradiation of the circumstellar disks from high-energy photons can heat up the circumstellar material, heating and ionizing the gas and forming emission lines, mainly [Ne II] (12.8 μm), [Ne III] (15.6 μm), [Fe I] (24.0 μm) and [Fe II] (17.9 μm). Additional rotational molecular gas lines of H_2 (12.3, 17.0 μm) may also be detected. Although the origin of the lines is not yet clear, the absorption of stellar X-rays is an obvious candidate (Glassgold et al. 2007), but alternative models include the ionization by extreme UV photons, strong shocks, or cosmic rays.

In the last few years there has been an increasing number of studies reporting the detection of gas tracers in the mid-infrared. Pascucci et al. (2007) have observed six low-mass pre-main sequence stars with optically thick disks using the *Spitzer Space Telescope*. They have detected emission of [Ne II] in four of them. Lahuis et al. (2007) have also used *Spitzer* to obtain spectra for a sample of 76 low-mass pre-main sequence stars detecting emission from [Ne II] in $\sim$ 20% of the sample, and [Fe I] in $\sim$ 9% of them, but also [Fe II], [S III], and H_2 in a smaller number. Bitner et al. (2008) have detected H_2 emission in 6 out of 29 young stars observed in the

[1] ISDC & Observatoire de Geneve
[2] ETH Zürich
[3] SSC/Caltech
[4] UK Astronomy Technology Centre
[5] CASA, U. of Colorado
[6] IPAC/Caltech
[7] U. of Kiel

near-infrared. Güdel et al. (2009) have detected [Ne II] in *Spitzer* spectra of 59 out 93 young stars. Flaccomio et al. (2009) have sampled the ρ Ophiuchi cluster in both X-rays (XMM-Newton) and mid-infrared (*Spitzer*), among the 28 observed young stars, [Ne II] emission has been detected in 10 sources, while [Ne III] has been detected in one case.

2 Sample

We have focused our study on the Taurus Molecular Cloud (TMC). This nearby star-forming region is indeed the ideal laboratory to study the low-mass star formation process; its distance (137 pc, Torres et al. 2007) allows us to observe fainter sources with no influence of high-mass young stars. The TMC has been observed in the X-rays with *XMM-Newton* (the XEST survey has covered ∼5 square degrees of the TMC, Güdel et al. 2007), and in the infrared with *Spitzer* (Spitzer Taurus Project covering ∼43 square degrees, Padgett et al. 2007).

This study is based on archived observations from the *Spitzer Space Telescope* using the Infrared Spectrograph (IRS) and its high resolution module (SH), with a resolving power of R∼ 600 for a wavelength coverage between ∼ 9 and ∼ 20 μm. Observations are mainly part of GTO programs (Guaranteed Time Observations).

Our sample accounts for 70 low and intermediate mass pre-main sequence stars; 8 Class I objects, 36 Class II, 4 Class III, 4 intermediate-mass Herbig stars. 7 objects are classified in the literature as both Class I and Class II. Furthermore, 11 objects have no classification in the literature.

3 Method

3.1 Data analysis

We have retrieved the data from the Spitzer Science Center. We have started our analysis from the post-BCD data, i.e.; spectra extracted automatically by the pipeline as they arrive from the spacecraft. The main problem encountered has been the lack of dedicated background observations for the main part of the sources in our sample, probably because it was thought that the background emission in Taurus was not contributing significantly. But the mid-infrared background comes predominantly from zodiacal light at IRS wavelengths and it can contribute significantly. Sky observations also help to alleviate the effects of rogue pixels (pixels with abnormally high dark current and/or photon responsivity).

In a first step we have used the interactive tool IRSCLEAN_MASK in order to create masks for the rogue pixels from the BCD images. Once the images are free from obvious rogue pixels we have re-extracted the spectra using SPICE (Spitzer IRS Custom Extraction).

In order to be sure that the lines detected were emitted from the source and they were not coming from the background or a nearby contaminating source, we have carefully examined the echellogram for each spectrum. In Fig.1 we present an example for the [Ne II] line. The echellogram displays in a 2D image the spectral order (10 for the SH module) and the wavelength. We have considered two regions with no emission lines adjacent to the position of the line studied. These two regions were used as local background plus stellar continuum; they were averaged and then subtracted to the region were the line is located. If after this procedure the line was still present, we considered that the emission was coming from the star.

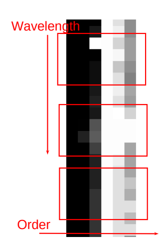

Fig. 1. Example of the echellogram image showing the [Ne II] line (12.8μm) in the 15$^{\rm th}$ order. The middle box shows the position of the line, the upper and lower boxes show the regions used as local background plus stellar continuum. Wavelengths are represented in the vertical direction and the spectral order in the horizontal direction.

3.2 Line Fitting

Once we solved the problem of lack of background measurements using the procedure described in 3.1, we fitted the line profiles in order to obtain their luminosity. We have focused our search in the emission lines from H_2 (12.3, 17.0 μm), [Ne II] (12.8 μm), [Ne III] (15.6 μm), [Fe II] (17.9 μm), and [S III] (18.7 μm). The lines have been fitted with a function including a gaussian component plus a linear polynomial component to account for the adjacent continuum. All the parameters of the function were left free to vary. A detection is claimed when the peak of the line is three times higher than the continuum standard deviation in the wavelength range of interest (the range typically used was 0.6 μm). The FWHM obtained from our fits were consistent with the FWHM expected for the IRS spectral resolution.

4 Results

4.1 Detections

We have detected the [Ne II] line in 13 objects representing the 18% of the sample. This detection rate is consistent with the result from Lahuis et al. (2007) where [Ne II] has been detected in a 20% of the sample. The main difference between Lahuis et al. (2007) and this work is that our sample is based only in the TMC. In contrast Lahuis et al. (2007) have used a mixed sample with stars from different star-forming regions; Chamaeleon, Lupus, Serpens, Perseus, and Ophiuchius. Flaccomio et al. (2009) have detected [Ne II] in 10 sources out of a sample of 29 young stars in Ophiuchius.

Among the objects in our sample with [Ne II] detections there is one class I, seven class II, four sources with ambiguous classification class I/II and one Herbig star. The [Ne III] line was detected in 1 class II source with no detection of [Ne II]. H_2 (12.3 μm) is detected in 4 sources; one class II, two class III, and one with unknown classification. H_2 (17.0 μm) is detected in 5 sources; two class II, one class III, and two sources with unknown classification. Only in 2 sources there is the detection of H_2 at both wavelengths. [Fe II] is detected in 4 sources; two class II, one class I/II, and one class III. Finally, [S III] is not detected in any star of our sample. Figure 2 shows some of the lines detected in our sample; Tau-2 is a class I object; Tau-4, is a class II, Tau-6 and Tau-8 are class III, Tau-7 and Tau-9 are class I/II, Tau-5 has unknown classification.

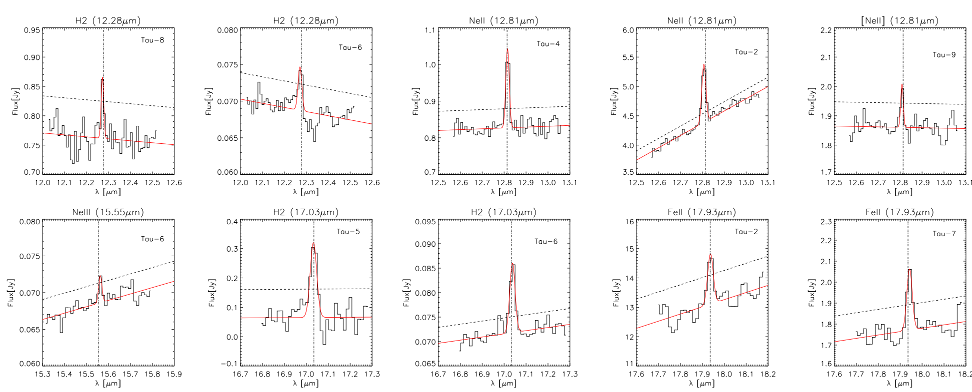

Fig. 2. Examples of detected lines from gas tracers in our sample of young stars in Taurus. The spectra are plotted as histogram in solid black line, the red solid line shows the fitted continuum plus line profile, and the black dashed line shows the 3-sigma continuum level.

4.2 Correlations

The high level of detection of the [Ne II] line has prompted us to search for possible correlations between the luminosity of the line, and different stellar parameters such as mass, mass accretion rate, X-ray luminosity (L_X), and Hα equivalent width (Figure 3). The equivalent width of the Hα line (seen usually in emission in young stars) is commonly used to differentiate between accreting and non-accreting stars; Hα(EW) > 20 Å accreting stars, and Hα(EW) < 20 Å non-accreting stars (Martin 1997).

For each parameter we have performed a Spearman's statistical test to probe the level of correlation. A significant correlation is found between the [Ne II] line luminosity and the mass accretion rate (significance of 0.10, where small values in the range [0,1] indicate a significant correlation), a weaker correlation is found with the equivalent width of the Hα line (significance of 0.35). No correlation is found with L_X and stellar mass (significance higher than 0.54).

Previous works have also explored the possibility of these correlations. The main drawback of early studies has been the reduced size of the samples. The first study of Pascucci et al. (2007) suggested a correlation with X-ray luminosity based on four detections. Espaillat et al. (2007) increased the sample to seven objects and did not find any evident correlation between $L_{[NeII]}$ and L_X, but they did find a correlation with mass accretion rate. Flaccomio et al. (2009) have found no correlation with L_X based on 10 detections. A correlation is found instead with disk mass accretion rate. In the sample of Güdel et al. (2009) based on 93 sources and 59 detections, there is a trend between $L_{[NeII]}$ and L_X and mass accretion rate, although with a large scatter. A correlation is found instead with jet/outflow parameters; $L_X \cdot L$[O I] at 6300 Å.

The lack of correlation between $L_{[NeII]}$ and L_X in our sample goes in the same direction than previous studies and would indicate that the ionization of Ne is not directly related to the X-ray irradiation from the central star, as predicted by the X-ray heating model of Glassgold et al. (2007). In our sample, the ionization of Ne appears to be related with accretion.

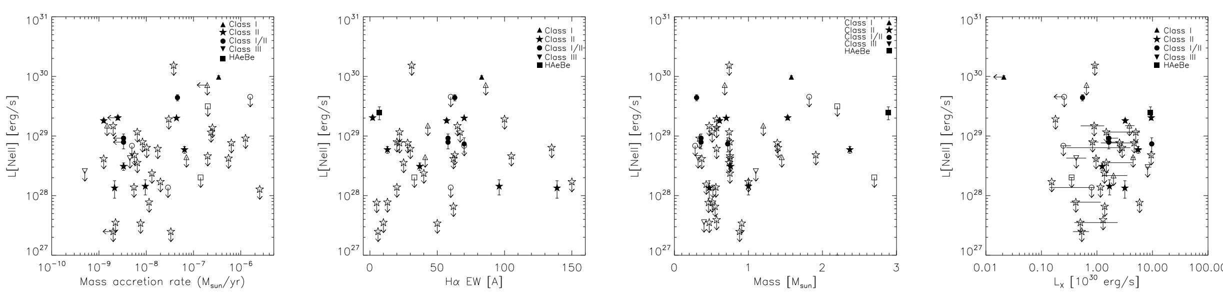

Fig. 3. Attempted correlations between the luminosity of the [Ne II] line and the stellar parameters; mass accretion rate, Hα equivalent width, stellar mass, and X-ray luminosity. These values were taken from the literature. Each symbol represent a different class of object: class I objects are represented by upwards triangle, class II objects by stars, class I/II objects by circles, class III by downward triangles, and herbig stars are represented by squares. The filled symbols indicate the [Ne II] detection, while empty symbols indicate upper limits.

C. B-S. acknowledges the SF2A for the possibility of presenting this work at the atelier of the SF2A/SSAA/PNPS/PNP: Connecting our understanding of star and planet formation and physics. M. A. and C. B.S. acknowledge the support of the Swiss National Science Foundation grant PP002-110504.

References

Bitner, M. A., Richter, M. J., Lacy, J. H., Herczeg, G. J., Greathouse, T. K. et al. 2008, ApJ, 688, 1326

Espaillat, C., Calvet, N., D'Alessio, P., Bergin, E., Hartmann, L., et al. 2007, ApJ. 664, L111

Flaccomio, E., Stelzer, B., Sciortino, S., Micela, G., Pilliteri, I., Test, L. 2009, 2009arXiv0906.4700F

Glassgold, A. E., Najita, J. R., Igea, J. 2007, ApJ, 656, 515

Güdel, M., Briggs, K. R., Arzner, K., Audard, M., Bouvier, J., et al. 2007, A&A, 468, 353

Güdel, M., Lahuis, F., Henning, T., et al. 2009 in prep. http://www.ipac.caltech.edu/spitzer2008/talks/ManuelGuedel.html

Herczeg, G. J., Najita, J. R., Hillenbrand, L. A., Pascucci, I. 2007, ApJ, 670, 509

Lahuis, F., van Dishoeck, E. F., Blake, G. A., Evans, N. J. II. 2007, ApJ, 665, 49

Martin, E. L., 1997, A&A, 321, 492

Padgett, D., McCabe, C., Rebull, L., Noriega-Crespo, A., Carey, S., et al. 2007, AAS, 211.2904P

Pascucci, I., Hollenbach, D., Najita, J., Muzerolle, J., Gorti, U., et al. 2007, ApJ, 663, 383

Torres, R. M., Loinard, L., Mioduszewski, A. J., Rodriguez, L. F., 2007, ApJ, 671, 1813

SF2A 2009
M. Heydari-Malayeri, C. Reylé and R. Samadi (eds)

NEAR-INFRARED INTEGRAL FIELD SPECTROSCOPY OF YOUNG LATE-M AND EARLY-L DWARFS CLOSE TO THE DEUTERIUM-BURNING BOUNDARY

Bonnefoy, M.[1], Chauvin, G.[1], Rojo, P.[2], Dumas, C.[3], Allard, F.[4], Lagrange, A-M.[1] and Beuzit, J-L.[1]

Abstract. We report the first results of a uniform high-quality spectral characterization of 8 young late-M and early-L dwarfs in the near-infrared (1.1-2.45 μm) with the integral field medium-resolution (R=1500-2000) spectrograph SINFONI. Our targets are companions to stars, or free-floating objects members of young (< 100 Myrs) associations. The sample noticeably includes the companion to AB Pic, which is known to lie at the deuterium-burning boundary (13.6 M_{Jup}). A comparison of the spectrum of AB Pic b with empirical libraries of young late dwarfs spectral standards and to synthetic atmosphere spectra yielded the spectral type, the surface gravities ($log(g)$) and the effective temperature (T_{eff}) of the source. By combining T_{eff}, $log(g)$, the observed photometry, the surface fluxes from atmosphere models and the known distance of AB Pic A, we derived new masses, luminosities and radii estimates that were carefully compared to evolutionary models predictions.

1 Introduction

Since the discovery of the first brown dwarfs (BD) companions to GD165 B (Becklin & Zuckerman 1988), and Gl 229 B (Nakajima et al. 1995), more than 600 low-mass stars and BDs (also named ultracool dwarfs) have been discovered, isolated in the field, or as companion to stars. The spectra of many of these sources (Geballe et al. 2002; McLean et al. 2003, Cushing et al. 2005) revealed a mélange of narrow atomic features and broad absorptions produced by molecules and condensates from refractory elements. Two new spectral classes "L" and "T" were then added to distinguish these objects from "normal" M dwarfs. A spectral classification scheme is now well establish at visible and near-infrared wavelengths (see the review of Kirkpatrick 2005).

The observational programs to find substellar objects (M < 0.078 M_{Jup}) members of young nearby associations and in star forming regions brought a new sample of young very low mass objects. They are companions to stars, free-floating objects, or binaries with masses close or below the deuterium-burning boundary (M < 13.6 M_{Jup}, currently used to distinguish planets from brown dwarfs). The great diversity of these systems rises questions on their formation mechanisms.

Our knowledge of their chemical and physical properties is currently very limited and even inexistent for young T dwarfs. Their larger radii (still contracting) and very lower masses than their same spectral type counterparts in the field made them less dense. Together with the effective temperature (T_{eff}), the surface gravity $log(g)$ plays an important role, modifying the pressure and the composition of cloudy emissions layers. In the near-infrared (NIR), spectra of young M and of the known early-L dwarfs show a weakening of alkali lines and the appearance of a triangular-shape in the H band (McGovern et al. 2004; Kirkpatrick et al. 2006, hereafter K06). So far, only one study aimed at characterizing the impact of surface gravity on their spectral classification (Lodieu et al. 2008).

We present the first results of a uniform high-quality spectral characterization of late-M and early-L dwarfs in the NIR (1.1-2.45 μm) with the integral field medium-resolution (R=1500-2000) spectrograph SINFONI. Our spectral library is described in Sec. 2. We then focus on the study of the young very low mass companion AB Pic b in Sec. 3.

[1] Laboratoire d'Astrophysique, Observatoire de Grenoble, 414, Rue de la piscine, Saint-Martin d'Hères, France
[2] Departamento de Astronomia, Universidad de Chile, Casilla 36-D, Santiago, Chile
[3] European Southern Observatory. Alonso de Cordova 3107, Vitacura. Casilla 19001. Santiago 19, Chile
[4] CRAL-ENS. , 46, Allée d'Italie , 69364 Lyon Cedex 07

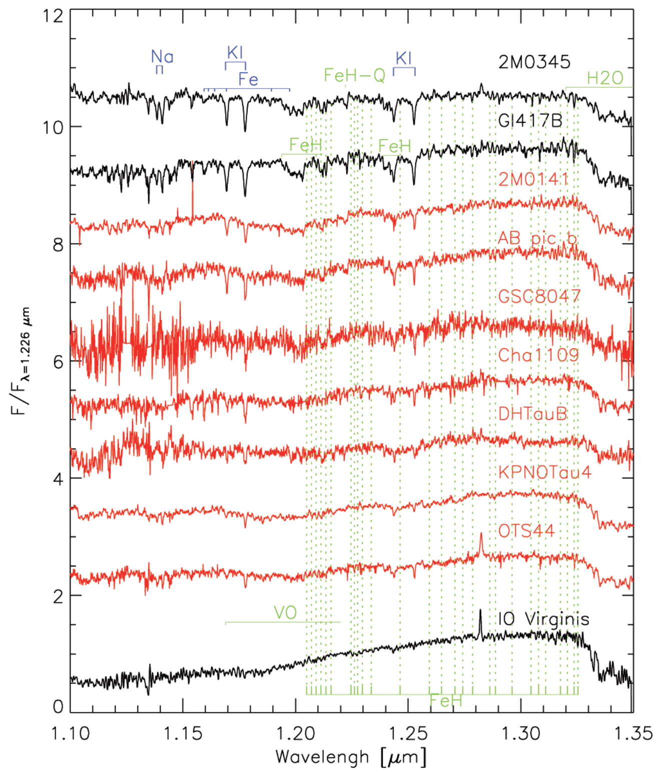

Fig. 1. The SINFONI J-band normalized spectra of our sources. Spectra of young sources are plotted in red. The spectra of the L0 dwarf 2M0345, the L4 companion Gl 417 B (black line) and of the M giant IO Virginis are reported in black for comparison. Molecular lines are flagged in green. Atomic lines are identified in blue. The young M and L dwarfs spectra appear intermediate between those of field dwarfs and of the giant.

2 The library

2.1 Observations and source sample

Our sample is composed of 8 ultracool dwarfs with estimated spectral types ranging from M8 and L0. It includes the companions to TWA5 A, AB Pic, GSC 8047-0232, DH Tau and to the young field dwarf star Gl417. Because of the limited number of young late-M and early-L companions, we also observed the isolated objects KPNO Tau 4, OTS44 and Cha1109-7734. TWA5 B, AB Pic and GSC 8047-0232 are members of the young (age 8–40 Myrs) nearby associations TW Hydrae and Tucana-Horologium. DH Tau and KPNO Tau are associated with the Taurus (age∼1–2 Myrs) molecular cloud. OTS44 and Cha1109-7734 belong to the Chameleon molecular cloud (age∼2 Myrs). Finally, the L0 field dwarf 2MASS J03454316+2540233 (hereafter 2M0345) and the late M giant IO Virginis were also observed. They serve as reference for high and very low surface gravity object spectra.

Our sources were observed with the integral field NIR (1.1–2.45 μm) spectrometer SINFONI (Eisenhauer et al. 2003; Bonnet et al. 2004), installed on the Very Large Telescope UT4 (Yepun). The instrument benefits from the high angular resolution provided by a modified version of the Multi-Applications Curvature Adaptive Optic (AO) system MACAO and of the integral field spectroscopy offered by SPIFFI (SPectrograph for Infrared Faint Field Imaging). All the sources were observed with the J (1.1–1.4 μm) and $H + K$ (1.45–2.45 μm) gratings at resolving powers of 2000 and 1500 respectively. The adaptive optics system was used for TWA5B, GSC8047-0232 B, AB Pic B and DH Tau B to limit the contamination of their primary star in the field of view of the instrument.

2.2 Data reduction

The reduction of SINFONI data is a long and complex task. We used the SINFONI data reduction pipeline (Modigliani et al. 2007) and custom *IDL* routines. Our routines correct raw images from negatives rows created during the bias subtraction (see *The ESO data reduction cookbook*; version 1.0, ESO, 2007) and from correlated noises that affect a part of the dataset. The pipeline then carries out the flagging of hot and non-linear pixels, the distortion, and the wavelength calibration of the detector. When a sky frame had been acquired, it is subtracted to the object frame. Otherwise, the sky is estimated from the median of a series of dithered exposures and subtracted to the object frame. The resulting frame is then flat fielded and corrected from bad pixels and distortions. Datacubes are finally reconstructed and are merged into a master cube. A telluric standard star observed the same night is used to correct the spectra from telluric absorption lines.

2.3 Preliminar spectral analysis

The SINFONI J-band normalized spectra are presented in Fig 1. Young sources spectra show atomic and molecular features intermediate between those of the L0 dwarf 2M0345 and of the M giant IO Virginis. The reduced K I absorption depth at 1.169 μm, 1.177 μm, 1.243 μm and 1.253 μm, together with the reduced FeH absorption at 1.2 μm, are characteristic of intermediate surface gravity objects. In the H band, our spectra present a triangular shape typical of young M and L dwarfs (K06). Finally, our K band spectra present CO overtones longward 2.9 μm. In the following section, we present a complete spectral analysis of the AB Pic b companion.

3 The case of AB Pic b

AB Pic b was detected by Chauvin et al. 2005 at 5.5” from the young (~30 Myrs) K2V star AB Pic A. Evolutionary models predict a companion mass of 13–14 M_{Jup} in agreement with the L0–L3 spectral type derived from NACO K-band spectroscopy. Additional SINFONI spectra with SNR ranging from 40 in the J band to 50 in the H+K band were necessary to complete its characterization.

3.1 A new spectral type determination

Our spectra were normalized and compared to young M8–L4 spectral standards (Lodieu et al. 2008, Lafrenière et al. 2008) members of Upper Sco (~5 Myrs). A χ^2 minimization was obtained for young L1 and L2 dwarfs in the J band, L0 dwarf in the H band and, L0 and L2 dwarfs in the K band. L2 and L4 were excluded from the visual comparison in the H band. We confirmed this preliminary spectral type determination using spectral indexes designed to measure the depth of water absorptions at 1.34 μm, 1.5 μm, and 2.04 μm (Allers et al. 2007; Slesnick et al. 2004). Finally, the good match of our J-band spectrum with that of the young isolated dwarf 2MASS J01415823-4633574 (see Fig. 1) classified as L0 in the optical (K06) confirms that AB Pic b is a L0–L1 dwarf.

3.2 Effective temperature and surface gravity

We compared our spectra to models generated spectra of the AMES–Dusty00 library (Allard et al. 2001). AMES–Dusty00 incorporates formation of dust in the atmosphere below 2600 K. During the comparison, we masked H_2O absorptions from 1.32 to 1.60 μm and from 1.75 to 2.20 μm that are known to be overestimated in the models (see K06).

The J band was fitted for $T_{\rm eff}$ = 2000 ± 100 K and log(g) = 4.0 ± 0.5 dex. The fit was still visually acceptable for $T_{\rm eff}$ down to 1700 K and up to 2100 K. The observed depth of CO overtones at $\lambda \geqslant 2.3\mu$m and the shape of the pseudo-continuum in the K-band are better reproduced at $T_{\rm eff}$ = 2500 K. However, this band is dominated by H_2O absorptions. A better match is achieved at $T_{\rm eff}$ = 2000 K and log(g) = 4.0 dex using the most recent SETTL08 library (D. Homeier, Priv. com.).

In conclusion, both AMES–Dusty00 and SETTL08 libraries yield $T_{eff} = 2000^{+100}_{-300}$ K and log(g) = 4.0 ± 0.5 dex for AB Pic b.

3.3 Mass estimations

We infer a mass of 11 $M_{\rm Jup} \leq M \leq 14 M_{\rm Jup}$ from the estimated $T_{\rm eff}$ of part 3.2 and evolutionary tracks (Chabrier et al. 2000). However, tracks remain to be calibrated at young ages and very low masses down to the planetary mass regime where the formation mechanisms could actually play a key role (Marley et al. 2007). We then tried to use alternative methods to estimate the mass of AB Pic b.

Using the empirical relations between BC_K and spectral types for *field dwarfs*, we derived a bolometric correction $BC_K=3.24^{+0.18}_{-0.19}$ mag and a luminosity of −3.7 ± 0.2 $L/L_\odot$ for our source. Combining the luminosity with the T_{eff} and the *log(g)* derived in part 3.2, we estimate a radius of $1.22^{+0.70}_{-0.25}$ R_{Jup} and the mass of 1 to 45 M_{Jup} in agreement with evolutionary model predictions. However, the assumption of a similar BC_K-SpT relation between young and field dwarfs has never been established. It could therefore add systematic errors that are difficult to quantify.

A second alternative approach described by Mohanty et al. 2004, use the photometry and the surface fluxes provided by atmospheric models to estimate the mass of the companion. The absolute K-band magnitude is combined to the surface flux of the AMES–Dusty00 spectra at $T_{\rm eff} = 2000$ K and $\log(g) = 4.0$ to determine a radius of $0.81^{+0.83}_{-0.2}$ R_{Jup}. From the radius and the log(g), we deduce a mass of 2 to 24 M_{Jup}. Finally, the $T_{\rm eff}$ and the radius allows a new determination of the luminosity ($-3.72^{+0.15}_{-0.20}$ $L/L_{\odot}$). Using J-band fluxes leads to slightly different values. This was explained by a non-simultaneous reproducibility of the J and K_s-band surface fluxes at $T_{\rm eff} = 2000$ K. In both case, estimated masses of AB Pic b are still in agreement with evolutionary model predictions within uncertainties. Similar results are derived from the SETTL08 surface fluxes. However, one could note that these results strongly rely on the ability of atmospheric models to reproduce the *absolute* NIR fluxes of young L dwarfs.

4 Conclusions

We presented the first results of a program to build a library of near-infrared (1.1–2.5 μm) spectra of young late-M and early L dwarfs using the integral field spectrograph SINFONI. A preliminary analysis already confirmed the youth of our sources. AB Pic b is confirmed to be a L0–L1 dwarf. The comparison of its spectra to synthetic spectral grids enabled the estimation of $T_{eff} = 2000^{+100}_{-300}$ K and $\log(g) = 4.0 \pm 0.5$ dex. Our analysis highlights the difficulties of the models to successfully match the near-infrared spectra of young L dwarfs. We used two methods to derive masses estimations independent from evolutionary models predictions non-calibrated at young ages. They both confirm the predicted mass. However, even if they have been used in the literature (see Mohanty et al. 2004; Luhman et al. 2006; Seifahrt et al 2007) for young late M dwarfs, they could introduce systematic errors difficult to quantify. To solve the problem, simultaneous visible and infrared spectro-photometry of luminous young dwarfs could enable the direct determination of empirical luminosities and masses.

We would like to thanks the *ESO* staff for performing the observations. We also acknowledge financial support from the Agence National de la Recherche, the *PNP* and the *PNPS*. We are grateful to Andreas Seifahrt, David Lafrenière and Nicolas Lodieu for providing their spectra.

References

Allard et al. 2001, ApJ, 556, 357
Allers et al. 2007, ApJ, 657, 511
Becklin & Zuckerman 1988, Nature, 336, 656
Bonnet et al. 2004, Msngr, 117, 17
Chabrier et al. 2000, ApJ, 542, 464
Chauvin et al. 2005, A&A, 438, 29
Cushing et al. 2005, ApJ, 523, 1115
Eisenhauer, F. et al. 2003, SPIE 4841, 1548
Geballe et al. 2002, ApJ, 564, 466
Kirkpatrick 2005, ARA&A, 43, 195
Kirkpatrick et al. 2006, ApJ, 639, 1120
Lafrenière et al. 2008, ApJ, 689, 153
Lodieu et al. 2008, MNRAS, 383, 1385
Luhman et al. 2006, ApJ, 659, 894
McGovern et al. 2004, ApJ, 600, 1020
McLean et al. 2003, ApJ, 596, 561
Marley et al. 2007, ApJ, 655, 541
Modigliani et al. 2007, astro-ph/0701297
Mohanty et al. 2004, ApJ, 609, 885
Nakajima et al. 1995, Nature, 378, 463
Seifahrt et al. 2007, A&A, 463, 309
Slesnick et al. 2004, ApJ, 610, 1045

SF2A 2009
M. Heydari-Malayeri, C. Reylé and R. Samadi (eds)

MINIMUM MASS SOLAR NEBULÆ AND PLANETARY MIGRATION

Crida, A. [1,2]

Abstract. The Minimum Mass Solar Nebula (MMSN) is a protoplanetary disk that contains the minimum amount of solids necessary to build the planets of the Solar System at the desired location. Assuming that the giant planets formed in the compact configuration they have at the beginning of the "Nice model" (Tsiganis et al, 2005; Gomes et al, 2005), Desch (2007) built a new MMSN, about ten times denser than the standard MMSN by Hayashi (1981).

However, a planet in a protoplanetary disk migrates. With numerical simulations, we show that the four giant planets of the solar system could not survive in Desch's dense disk. In contrast, in a low density disk, planetary migration smoothly brings the planets closer to each other ; then planet-planet interactions may stop migration, in a configuration compatible with the "Nice model" (Crida, 2009).

In fact, planetary migration makes the concept of MMSN irrelevant : planet formation is not a local process. Migration and radial drift of solids should be taken into account when reconstructing the proto-solar nebula.

1 Introduction

The Minimum Mass Solar Nebula (hereafter MMSN) is the protoplanetary disk of solar composition that has the amount of metals necessary to build the eight planets of the Solar System (and the asteroid belts). From the masses and compositions of the planets, a density of solids is derived at several locations of the disk. Then, the solar composition is restored by adding gas, and a smooth protoplanetary disk density profile is derived. The most famous version of the MMSN was provided by Weidenschilling (1977) and Hayashi (1981). Of course, the density profile obtained depends crucially on the position of the planets. They assumed that the planets formed where they presently orbit.

A recent model explains several features of the Solar System (the Late Heavy Bombardment, the orbital distribution of the Trojans of Jupiter, the orbital elements of the giant planets. . .), based on the assumption that the four giant planets were in a compact configuration just after the Solar nebula dissipation (Tsiganis et al., 2005 ; Gomes et al., 2005 ; Morbidelli et al., 2005). If one assumes that this so called "Nice model" is true, then the above nebula is out of date because the planets didn't form where they are now observed. In a recent article, Desch (2007) constructed a new MMSN, assuming that the planets were formed in the disk at their starting position in the Nice model.

However, planets in protoplanetary disks migrate. Here, we study the migration in the dense disk proposed by Desch (2007) and in the older one given by Hayashi (1981). We show that in a dense solar nebula, Jupiter can't avoid migration all the way to the Sun, and that all the giant planets are lost in a short time. In contrast, interactions between the planets enable to save them in a lighter disk.

2 Migration in Desch (2007)'s dense disk

Figure 1 shows the semi-major-axes of the four giant planets as a function of time in a disk of initial surface density profile the one given by Desch (2007) : $\Sigma_0 = 3430 \times (r/10\mathrm{AU})^{-2.168}$ kg.m^{-2}. The temperature is $150 \times (r/1\mathrm{AU})^{-0.429}\,K$, which corresponds to an aspect ratio of $(H/r)_0 = 0.05 \times (r/1\mathrm{AU})^{0.2855}$. The viscosity

[1] CpT-TAT, Universität Tübingen – where this work was done, until december 2008.
[2] D.A.M.T.P., University of Cambridge – since january 2009.
contact: `crida@oca.eu`

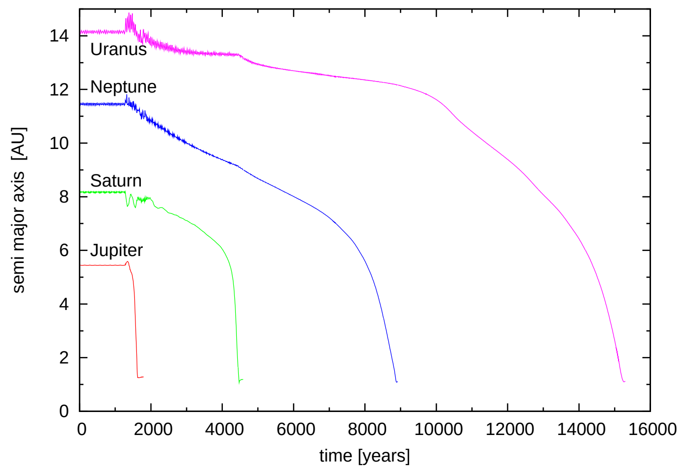

Fig. 1. Migration paths of Jupiter, Saturn, Neptune and Uranus (from bottom to top) in a dense Solar nebula.

is given by an α prescription (Shakura & Sunyaev, 1973), with $\alpha = 4 \times 10^{-4}$. We use the code FARGO-2D1D (Crida et al. 2007, and `http://fargo.in2p3.fr/`), which enables to simulate accurately simultaneously the planet-disk interactions and the global evolution of the disk. For more details on the set-up of the simulations, the reader is refereed to Section 2 of Crida (2009), the paper relative to this work.

As soon as Jupiter is released, it enters in fast, runaway, type III migration inwards. This migration regime can be achieved only if the mass of the gas in the disk in the neighborhood of the planet is larger than the planet mass. It drives Jupiter to 1.5 AU in a few hundred years only, where Jupiter hits the inner edge of the 2D-grid and is removed from the simulation. Then, Saturn migrates to the Sun too, and Neptune and Uranus as well, in type I migration. In 16000 years, the four giants are lost.

In the case presented in Fig. 1, the resolution of the grid is $\delta r/r = \delta\theta = 10^{-2.5}$. The energy equation of the gas is computed, with viscous heating and vertical radiative cooling. Other simulations with locally isothermal equation of state, or different resolution, give similar results.

Changing the aspect ratio and the viscosity, or releasing Jupiter later than Saturn, doesn't change the conclusion that the four planets can not survive in Desch (2007)'s nebula.

3 Migration in a moderate density disk

Figure 2 shows the result of a similar experiment as in previous section, but performed in Hayashi (1981)'s disk, of surface density $\Sigma(r) = 538 \times (r/10\,\mathrm{AU})^{-3/2}$ kg.m^{-2}. This disk is not massive enough for Jupiter to enter in the type III, runaway regime of migration. Consequently, Jupiter is caught up by Saturn and the two planets enter in mean motion resonance after about 10^4 years. This almost stops their migration, as can be seen in the figure and is explained by Masset & Snellgrove (2001) and Morbidelli & Crida (2007). In contrast, Jupiter alone in the same disk would go on migrating inwards in a slow, type II regime, shown by the long dashed, orange curve in the figure, reaching 3 AU in 40 000 years.

Then, Uranus and Neptune, migrating inwards in type I migration are caught in mean motion resonance by Saturn, and stop as well. In the end, we have the four giant planets in a compact configuration, that prevents their migration. This enables to save the giant planets, but this configuration is not similar to the present one, neither to the one required in the original "Nice model" published in 2005. However, such a compact, fully resonant configuration has been proven compatible with the "Nice model" by Morbidelli et al. (2007).

4 Conclusion

Preventing the migration of the giant planets requires interactions between the planets. In the massive disk proposed by Desch (2007), this is impossible. Shortly said, we conclude that this nebula is incompatible with our present knowledge of planetary migration (in particular because of the unavoidable type III migration of Jupiter).

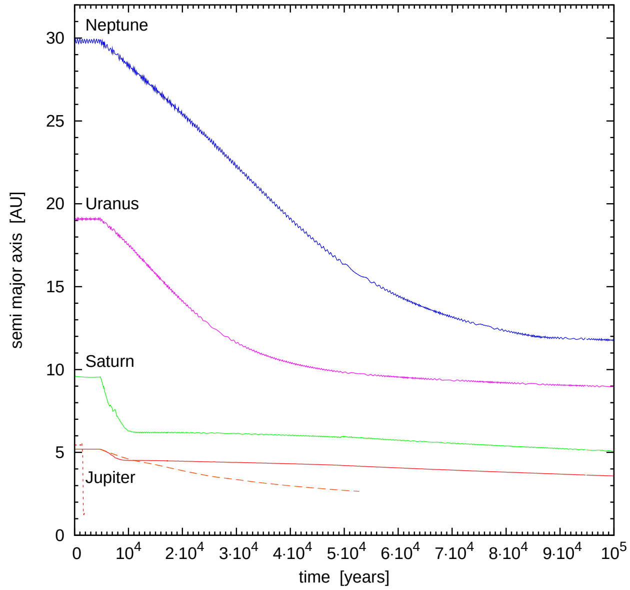

Fig. 2. Migration paths of Jupiter, Saturn, Neptune and Uranus (from bottom to top) in a light Solar nebula. Red dotted curve on the bottom left : migration of Jupiter in Fig. 1, for comparison. Orange, long dashed curve : migration of Jupiter alone, without Saturn.

However, migration can account for planetary formation on a large radial range, followed by a compaction of the configuration of the giant planets, like in Fig. 2. In addition, the solid material that built the giant planets may come not only from the region around their respective orbits : dust drifts inwards in a protoplanetary disk (Weidenschilling 1977), and small bodies migrate as well, so that the giant planets region may be replenished in solids by the outer parts of the disk. This enables the following scenario : (i) formation of Jupiter, Saturn, Uranus and Neptune in a relatively light disk on a large radial range, (ii) migration of the planets to a compact, resonant configuration, (iii) global instability after the gas disk has dissipated, to drive the planets to their presently observed positions (Nice model, see Morbidelli et al. 2007).

In fact, planetary migration makes the concept of the Minimum Mass Solar Nebula irrelevant, because the latter is based on the assumption that planets form locally, from local material, and stay on constant orbits in the disk. Planetary migration has to be taken into account in the reconstruction of the proto-solar nebula. Our result advocates for the density in the solar nebula to be moderate at the time where the giant planets formed, possibly close to Hayashi (1981)'s one. But neither Desch (2007) nor Hayashi (1981) should be considered as the disk out of which the solar system was born.

References

Crida, A., Morbidelli, A., & Masset, F. 2007, A&A, 461, 1173

Crida, A. 2009, ApJ, 698, 606

Desch S. J. 2007, ApJ, 671, 878

Gomes, R., Levison, H. F., Tsiganis, K, & Morbidelli, A. 2005, Nature, 435, 466

Hayashi, C. 1981, Progress of Theoretical Physics Supplement, 70, 35

Masset, F., & Snellgrove, M. 2001, MNRAS, 320, L55

Morbidelli, A., Levison, H. F., Tsiganis, K, & Gomes, R. 2005, Nature, 435, 462

Morbidelli, A., & Crida, A. 2007, Icarus, 191, 158

Morbidelli, A., Tsiganis, K, Crida, A., Levison, H. F., & Gomes, R. 2007, AJ, 134, 1790

Shakura, N. I., & Sunyaev, R. A. 1973, A&A, 24, 337

Tsiganis, K, Gomes, R., Morbidelli, A., & Levison, H. F. 2005, Nature, 435, 459

Weidenschilling, S. J. 1977, MNRAS, 180, 57

THE FOURIER-KELVIN STELLAR INTERFEROMETER: EXPLORING EXOPLANETARY SYSTEMS WITH AN INFRARED SPACE MISSION

Danchi, W. C.[1], Barry, R. K. [1], Lopez, B.[2], Augereau, J. C.[3], Ollivier, M.[4], Leger, A.[4], Petrov, R.[2], Kern, P.[3], Borde, P.[4], Monin, J.-L.[3], Jacquinod, S.[4], Beust, H.[3] and Bonfils, X.[3]

Abstract. The Fourier-Kelvin Stellar Interferometer (FKSI) is a mission concept for a nulling interferometer for the near-to-mid-infrared spectral region. FKSI is conceived as a mid-sized strategic or Probe class mission. FKSI has been endorsed by the Exoplanet Community Forum 2008 as such a mission and has been costed to be within the expected budget. The current design of FKSI is a two-element nulling interferometer. The two telescopes, separated by 12.5m, are precisely pointed (by small steering mirrors) on the target star. The two path lengths are accurately controlled to within a few nanometers to be precisely the same. A phase shifter/beam combiner (via Mach-Zender interferometer) produces an output beam consisting of the nulled sum of the planets light and the stars light. When properly oriented, the starlight is nulled by a factor of 10^{-4}, and the planet light is undimmed. Accurate modeling of the signal is used to subtract this residual starlight, permitting the detection of planets much fainter than the host star. The current version of FKSI with 0.5 m apertures and waveband 3-8 μm has the following main capabilities: (1) detect exozodiacal emission levels to that of our own solar system (1 Solar System Zodi) around nearby F, G, and K, stars; (2) characterize spectroscopically the atmospheres of a large number of known non-transiting planets; (3) survey and characterize nearby stars for planets down to 2 Earth-radii from just inside the habitable zone and inward. An enhanced version of FKSI with 1-m apertures separated by 20-m and cooled to 40 K, with science waveband 5-15 μm, allows for the detection and characterization of 2 Earth-radius and smaller super-Earths in the habitable zone around nearby stars.

1 Discussion

The FKSI mission concept has been under development for a number of years at NASA's Goddard Space Flight Center (Danchi et al. 2003, 2007) and it has a budget that fits into the strategic mission or Probe-class category with a lifecycle cost of around $600-800 million US dollars. During the last few years technology development funded by NASA and ESA for TPF-I, Darwin, and JWST have retired most of the major risks. Most of the key technologies are at a Technical Readiness Level (TRL) of 6 or greater, which means that, if funded, FKSI could entire into Phase A within the next two years (Danchi et al. 2008). The FKSI mission is designed to answer major scientific questions on the pathway to the discovery and characterization of Earth-twins around nearby F, G, and K main sequence stars.

One of the most vexing questions is the location and amount of emission of warm dust in the habitable zone of these stars, analogous to the zodiacal light in our own Solar System. This emission around nearby stars is called exozodi emission and is measured in units relative to that of our own Solar System (SSZs). Figure 1(Left) is a comparison of the ability of ground- and space- based concepts to measure this emission for nearby solar type stars.

Another major scientific area is characterizing the atmospheres of exoplanets discovered through radial velocity and other techniques. Currently only a small fraction of exoplanet atmospheres can be studied spectroscopically using transit methods, and these exoplanets are largely the ones with short periods that are very

[1] NASA Goddard Space Flight Center, USA
[2] Observatoire de la Côte d'Azur, France
[3] Laboratoire d'Astrophysique de Grenoble, France
[4] Insitut d'Astrophysique Spatiale, France

close to their stars. Not being limited to transiting planets, FKSI will greatly extend the size of the sample, which will have a major impact on models of planet formation and evolution. A third area is the search for rocky planets of size 2 Earth radii or smaller in the habitable zone of nearby stars. Figure 1 (Right) displays the FKSI's capability for super-Earth detection and Figure 2 (Left) displays results for an upgraded FKSI with waveband centered at 10 μm. Figure 2 (Right) displays the discovery space of FKSI for exoplanets as a function of semi-major axis and compares it to other missions. During the coming year, it is planned to validate the capability of an enhanced version of FKSI (1-m apertures, 40 K telescope temperature, 20-m separation), which would increase the efficiency of super-Earth detection down possibly to Earth-size planets.

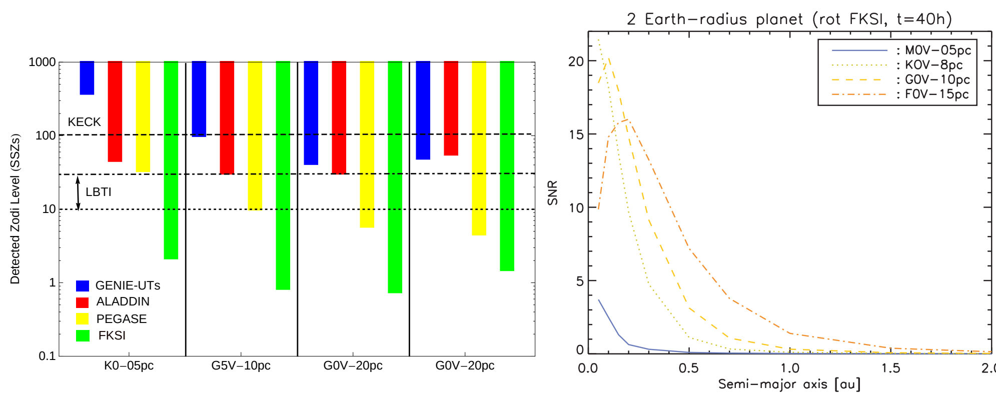

Fig. 1. Left : Comparison of exozodiacal detection limits for two ground-based concepts (GENIE with UTs on the VLTI and ALADDIN), and two space mission concepts (PEGASE and FKSI) (Defrère et al. 2008, A&A, 490, 435). **Right** : Result of a simulation for 2 Earth-radius super-Earth detection for FKSI showing that for SNR > 5, FKSI can detect many such rocky planets around nearby F, G, K, and M stars (Defrère et al. 2009, private communication).

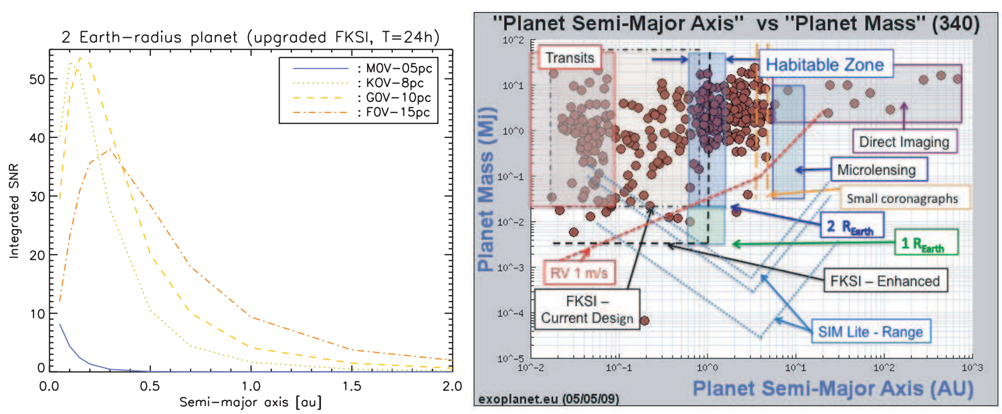

Fig. 2. Left : Result of a simulation for 2 Earth-radius super-Earth detection for the enhanced FKSI (1-m apertures, 40 K telescope temperature, 20-m separation) showing that for SNR > 5, FKSI can detect many such rocky planets *in the habitable zone* around nearby F, G, K, and M stars (Defrère et al. 2009, private communication). **Right**: Discovery space for exoplanets for FKSI compared with other mission concepts and techniques.

References

Danchi, W. C., et al., 2003, ApJ, 597L, 570.

Danchi, W. C., and Lopez, B. 2007, Compte Rendu Physique, 8, 396.

Danchi, W. C., et al. 2008, Proc. SPIE, vol. 7013.

SF2A 2009
M. Heydari-Malayeri, C. Reylé and R. Samadi (eds)

PROBING EXTREME ATMOSPHERE PHYSICS: T DWARFS AND BEYOND

Delorme, P.[1], Delfosse, X.[2], Forveille, T.[3], Albert, L.[4], Artigau, E.[5] and Reylé, C.[6]

Abstract. We present the latest results from the Canada-France Brown Dwarf Survey (hereafter CF-BDS), which identified about 70 T dwarfs and more than 300 L dwarfs. It particularly discovered CFBDS J005910.90011401.3 (Delorme et al. 2008a, hereafter CFBDS0059), the coolest brown dwarf known (Albert et al, in prep.). This lead to the discovery of a probable ammonia absorption band in the near infrared spectra of CFBDS0059 and ULAS J003402.77005206.7 (Warren et al. 2007, hereafter ULAS0034). These objects, along with the recently identified ULAS1335 (Burningham et al. 2008) are the coolest known brown dwarfs and their spectra probe a hitherto unobserved effective temperature range.

The spectra of both CFBDS0059 and ULAS J0034 show absorption by a wide band on the blue side of the *H* band flux peak, which we attribute to ammonia. If, as we expect, that feature deepens further for still lower effective temperatures, its appearance would become a natural breakpoint for the transition between the T spectral class and the new Y spectral type.

1 Introduction

Current atmosphere models are rather uncertain in the unexplored temperature range between the the 500-700 K coolest known brown dwarfs and the ∼100 K giant planets of the Solar System. Two major physical transitions are expected to occur between ∼ 700 K and ∼ 400 K and strongly alter the emergent near-infrared spectra (Burrows et al. 2003): NH_3 becomes an abundant atmospheric constituent and its near-infrared bands become major spectral features, and water clouds form and deplete H_2O from the gas phase. The corresponding near-infrared spectral changes are likely to be sufficiently drastic that the creation of a new spectral type will be warranted (Kirkpatrick et al. 2000).

However no ammonia absorption have been identfied in brown dwarfs spectra until recently, the discovery of ultracool brown dwarfs being challenging due to their very faint absolute magnitudes (J∼19). Two major wide field surveys, UKIDSS, Lawrence et al. (2007) and CFBDS Delorme et al. (2008b) have succeded into discovering a handful of these elusive objects. CFBDS singles-out brown dwarfs in the far-red, taking advantage of their very red $i' - z'$ colors while UKIDSS relies on near infrared identification. Their recent discoveries allowed to have a first look at cool atmospheres, below 600-700K.

We examine here the new spectral features, most notably a broad ammonia absorption band, which appears below 600K. Note that the absolute temperature estimates derived from models are still very uncertain, with mid-infrared estimations being in average 100K cooler than near infrared ones. this as been highlighted for differents objects by Leggett et al. (2009); Burningham et al. (2009) and Albert et al, in preparation. This latter paper also shows mid-infrared evidence that CFBDS0059 is the coolest brown dwarf known, with a temperature estimated at 525K.

[1] School of Physics and Astronomy, University of St Andrews, North Haugh, St Andrews KY16 9SS, United Kingdom
[2] Laboratoire d'Astrophysique de Grenoble,Université J.Fourier, CNRS, UMR5571, Grenoble, France
[3] Laboratoire d'Astrophysique de Grenoble,Université J.Fourier, CNRS, UMR5571, Grenoble, France
[4] Canada-France-Hawaii Telescope Corporation, 65-1238 Mamalahoa Highway, Kamuela, HI96743, USA
[5] Observatoire du Mont Mégantic, Université de Montréal, C.P. 6128, Succursale Centre-Ville, Montréal, QC H3C 3J7, Canada
[6] Observatoire de Besançon, Institut Utinam, UMR CNRS 6213, BP 1615, 25010 Besançon Cedex, France

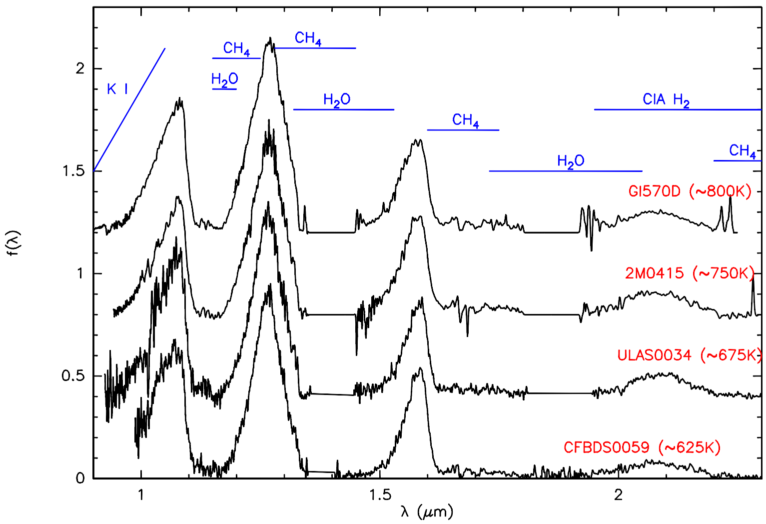

Fig. 1. 0.9 μm - 2.3 μm spectra of CFBDS0059 and the three other coolest brown dwarfs.The main T-dwarf spectral features are labeled. From Delorme et al. (2008a).

2 A new absorption feature in the H photometric band

Fig 1 presents spectrum of CFBDS0059, together with those of ULAS0034, >T8 (Warren et al. 2007), 2M0415, T8 (Burgasser et al. 2003) and Gl570, T7.5 (Burgasser et al. 2000), which successively were the coolest known brown dwarfs. Direct comparison of the four spectra can be used to shed light on incipient new features and atmospheric chemistry. Features which are seen in both CFBDS0059 and ULAS0034 are likely to be real even when their significance is modest in each object, and those which are absent or weaker in the two hotter brown dwarfs, can reasonably be assigned to low temperature molecules. Together with a significantly decreased K-band flux for CFBDS0059, one can notice in Fig 1 a narrowing of the H-band peak, particularly on its blue slope, that increases when temperature decreases.

To visually emphasize this broad feature, we bin the spectra to R=$\sim$100 and overlay the four H-band spectra (Fig. 2, left panel). The new wide-absorption feature is conspicuous in CFBDS0059 and well detected in ULAS0034, and with hindsight is weakly visible in the 2M0415 spectrum. It is however clearly stronger at $T_{\rm eff} < 700$K. Absorption sets in at $\sim 1.585\mu m$ and becomes deeper for $\lambda < 1.565\mu m$. These wavelengths overlap with strong H_2O and NH_3 bands. Either molecule could, a priori, be responsible for this new feature.

Is this new absorption due to ammonia?

Leggett et al. (2007) compare synthetic spectra computed with and without NH_3 opacity, and find that ammonia absorption in cold brown dwarfs strongly depletes the blue wing of the H band. Similarly, Saumon et al. (2000) plots synthetic H-band spectra with and without NH_3 opacity, and find differences for $\lambda < 1.565\mu$m.

Fig 2 right panel plots two BT-Settl models (Allard et al., in prep) for [$T_{\rm eff} = 600$K; $\log g = 4.75$], with and without near-infrared NH_3 opacity. As discussed in Delorme et al. (2008a) the models do not reproduce the observed H-peak shape very well, and a quantitative comparison is thus difficult. The comparison of the two models nonetheless confirms the Saumon et al. (2000) conclusion that ammonia produces strong absorption below $\sim 1.57\mu$m and weaker residual out to 1.595μm. These model predictions qualitatively match the behaviour seen in Fig 2, left panel.

To emphasize the changes in brown dwarfs spectra when their effective temperature decreases from $\sim$800 to $\sim$600 K, we plot in Fig 3,left panel, the ratio of the spectra of CFBDS0059 and Gl570. Right panel shows the equivalent plot for ULAS0034, which is very similar. The signal to noise ratio of the resulting K-band spectrum is too low for detailed analysis, and we therefore focus on the Y, J and H flux peaks. To avoid confusion from

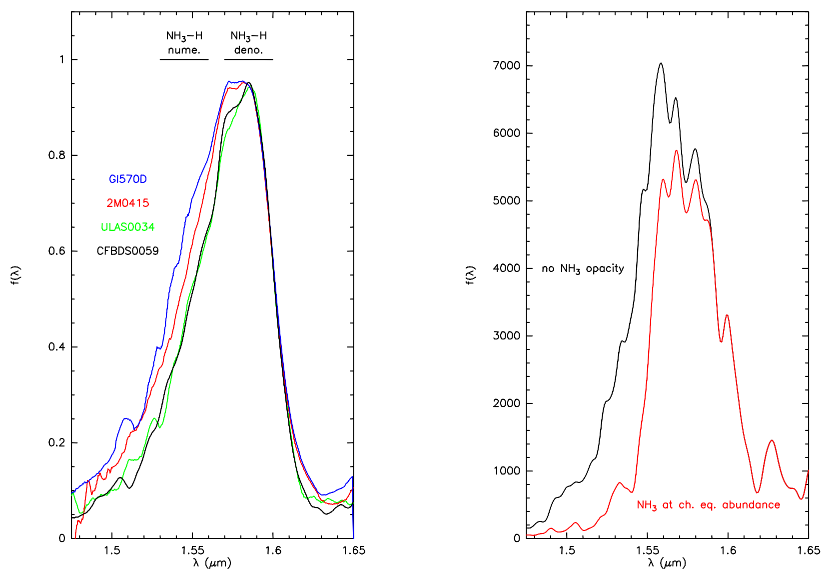

Fig. 2. Left: H-band spectrum of the four cool brown dwarfs binned to R∼100. **Right**: BT-Settl synthetic spectra for $[T_{\rm eff} = 600{\rm K}; \log g = 4.75]$ with and without near-infrared NH_3 opacity; the NH_3 abundance is at its chemical equilibrium value. From Delorme et al. (2008a).

changes in the temperature-sensitive methane bands, we mostly ignore the parts of the spectrum affected by CH_4 absorption bands. The H-band spectrum ratio prominently shows the new absorption band, which sits outside the CH_4 bands and closely matches the 300 K NH_3 transmission spectrum of Irwin et al. (1999). Both spectra are strongly absorbed between 1.49 and 1.52 μm and rebound from 1.52 to 1.57μm. Water absorption, by contrast, is a poor match to the features of spectrum ratio. The strongest water absorption (as computed from the HITRAN molecular database for a 600 K temperature) occurs below 1.49μm, at significantly bluer wavelengths than the CFBDS0059 absorption feature.

3 Conclusion

Ammonia absorption thus seems by far the best explanation for the flux decrease observed in the blue wing of the H-band peaks of both ULAS 0034 and CFBDS 0059. If that association with a NH_3 band is confirmed, and if, as we expect, the band deepens at still lower effective temperatures, its development would naturally define the scale of the proposed Y spectral class. ULAS 0034 and CFBDS 0059 could then become the prototypes of the Y class. Weak near-infrared absorption by ammonia has been tentatively detected by Saumon et al. (2000) in the T7 dwarf Gl 229B, but this analysis of CFBDS0059 and ULAS0034 provides the first robust evidence of a strong near-infrared NH_3 band in brown dwarf spectra.

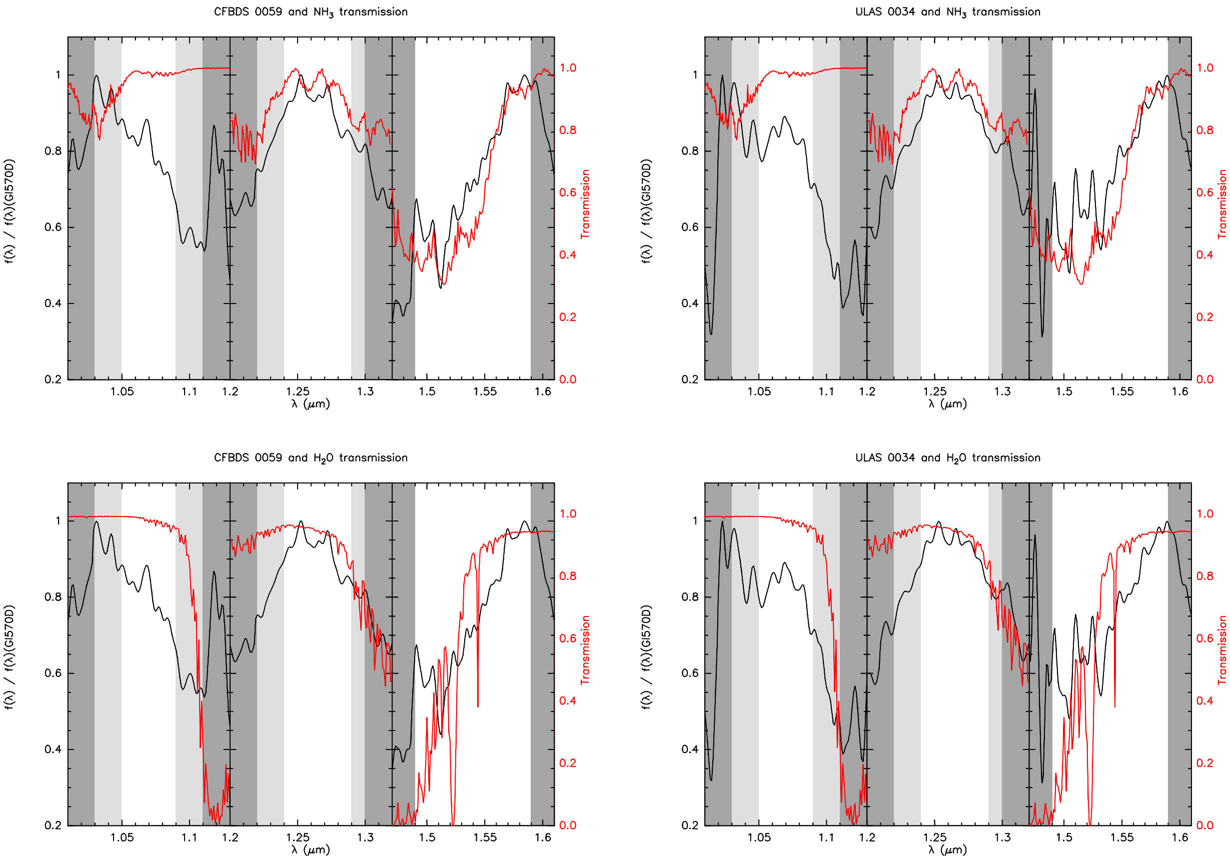

Fig. 3. Left panel: Flux ratio between CFBDS0059 and Gl570 (black), together with the 300K transmission spectrum of NH_3 (Irwin et al. 1999) (red, top panel) and the 600 K H_2O transmission spectrum (red, bottom panel). Grey bands mark the parts of the spectrum affected by strong (dark grey) or moderate (light grey) CH_4 absorption. Right panel: same overlays for the flux ratio between ULAS0034 and Gl 570D (black). From Delorme et al. (2008a).

References

A. J. Burgasser, J. D. Kirkpatrick, R. M. Cutri, et al. 2000, ApJl 531, L57

A. J. Burgasser, J. D. Kirkpatrick, A. Burrows, et al. 2003, ApJ 592, 1186

B. Burningham, D. J. Pinfield, S. K. Leggett, et al. 2008, MNRAS, 391, 320

B. Burningham, et al. 2009, MNRAS, 395, 1237

A. Burrows, D. Sudarsky, J. I. Lunine, et al. 2003, ApJ 596, 587

P. Delorme, X. Delfosse, L. Albert, et al. 2008a, A&A 482, 961

P. Delorme, C.J. Willott, T. Forveille, et al. 2008b, A&A 484, 469

A. Lawrence et al. 2007, MNRAS, 379, 1599

P. G. J. Irwin, S. B. Calcutt, K. Sihra, et al. 1999, Journal of Quantitative Spectroscopy and Radiative Transfer 62, 193

J. D. Kirkpatrick, I. N. Reid, J. Liebert, et al. 2000, AJ 120, 447

S. K. Leggett, D. Saumon, M. S. Marley, et al. 2007, ApJ 655, 1079

S. Leggett, et al. 2009, ApJ, 695, 1517

D. Saumon, T. R. Geballe, S. K. Leggett, et al. 2000, ApJ 541, 374

S. J. Warren, D. J. Mortlock, S. K. Leggett, et al. 2007, MNRAS 381, 1400

SPITZER AND HST TRANSIT SPECTROPHOTOMETRY OF THE EXOPLANET HD189733B

Désert, J.-M.[1], Sing, D. K.[1], Vidal-Madjar, A.[1], Lecavelier des Etangs, A.[1], Hébrard, G.[1], Ehrenreich, D.[2], Ferlet, R.[1], Parmentier, V.[1] and Henry, G.[3]

Abstract.
Transit observations in the infrared allow the atmospheric content of exoplanets to be determined. Here we present new primary transit observations of the hot-jupiter HD 189733b, obtained in the near and mid-IR with Hubble and Spitzer Space Telescopes. The high-S/N photometric transit light curves allow us to improve the precision of the near infrared planet radius. We are able to derive accurate system parameters, including planet-to-star radius ratios, impact parameter, scale of the system, and central time of the transit from fits to the transit light curves. We compare the results obtained here with transmission spectroscopic models and with results from various other observations of this planet. These new observations show that water vapour bandheads are not detected using transmission photometry observations at either 1.6 μm or 3.6 μm. Our results further support that another species must absorb at these wavelengths, at high altitudes, and could be attributed to Rayleigh scattering by haze. Observations at 4.5 μm can also be interpreted as due to the presence of CO and would lead to a large CO/H2O ratio estimated to be between 1 and 60.

1 Introduction

Two hot-Jupiters in particular, HD 189733b and HD 209458b, currently offer the very best laboratories in which to study exoplanet atmospheres and have formed the prototype hot-Jupiter planets. These two planets have the brightest parent stars among transiting planets and contain large transit depths, making precise transmission studies at high signal-to-noise ratios possible. The first transiting planet discovered, HD209458b, holds the distinction of the first detection of an extrasolar planetary atmosphere (Charbonneau et al. 2002) and escaping atmosphere (Vidal-Madjar et al. 2003, 2004, 2008). The optical transmission spectra of this planet shows evidence for several different layers of Na (Sing et al. 2008a,b) as well as Rayleigh scattering by molecular hydrogen (Lecavelier et al. 2008) and the presence of TiO/VO (Désert et al. 2008). The atmospheric Na signature has also been confirmed by ground based observations (Snellen et al. 2008).

HD189733b (Bouchy et al. 2005) is among the closest known transiting planets with a K V type parent star, giving it one of the largest transit and anti-transit signals known. The *Spitzer Space Telescope* (Werner et al. 2004) has revealed its potential to probe exoplanetary atmospheres through emission and transmission spectra. Spitzer anti-transit measurements have shown efficient heat-redistribution, measuring the planets temperature profile from orbital phase curves (Knutson et al. 2007; Knutson et al.2009) and a definitive detection of atmospheric water from emission spectra (Grillmair et al. 2008) and the likely presence of carbon monoxide (CO; Charbonneau et al. 2008). In primary transit, Pont et al. (2008) used the HST/ACS grism to provide the first transmission spectra from 0.6 to 1.0 μm. This spectrum is seen to be almost featureless likely indicating the presence of high altitude haze, with a λ^{-4} wavelength dependence of the spectra likely due to Rayleigh scattering by sub-micron $MgSiO_3$ molecules (Lecavelier et al. 2008). From the ground, Redfield et al. (2008 detected strong Na absorption in the core of the doublet. In the infrared, Swain et al. (2008) used *Near*

[1] UPMC Univ Paris 06, UMR7095, Institut d'Astrophysique de Paris, F-75014, Paris, France
[2] Laboratoire d'Astrophysique, Observatoire de Grenoble, UJF,CNRS;BP 53, F-38041 GRENOBLE Cedex 9 (France)
[3] Center of Excellence in Information Systems, Tennessee State University,3500 John A. Merritt Blvd., Box 9501, Nashville, TN 37209, USA

Infrared Camera and Multi-Object Spectrometer (NICMOS) aboard *HST* and showed evidence for absorption of atmospheric water and methane using spectroscopic observations between 1.5 and 2.5 μm.

Knutson et al. (2007) obtained the first accurate near infrared (NIR) transit measurements for this planet using the Infrared Array Camera (IRAC; Fazio et al. 2004) aboard *Spitzer* at 8.0 μm. The search for molecular spectroscopic signatures by comparing two photometric bands with *Spitzer* has been attempted by Ehrenreich et al. (2007). This study concluded that uncertainties on the measurements were too large to draw firm conclusions on the detection of water at high altitudes. Yet, using the same data set, but a different analysis (Beaulieu et al. 2008), Tinetti et al. (2007) claimed to detect the presence of atmospheric water vapour from comparison of the absorptions at 3.6 μm and 5.8 μm. We recently performed a consistent and complete study of the stellar mode observations obtained with the four IRAC channels (Désert et al. 2009), with a detailed assessment of systematics. We concluded that there is no excess absorption at 5.8 μm compared to 3.6 μm. Moreover, we found that water absorption alone cannot explain the radius at 3.6 μm. Therefore, other species must be present in the atmosphere of the planet and absorb at this wavelength, such as Rayleigh scattering by haze as found by Pont et al. (2008). We also derived a slightly larger radius at 4.5 μm that cannot be explained by H_2O nor Rayleigh scattering. We interpreted this hint of absorption excess as due to the possible presence of CO molecules (Désert et al. 2009) which could be in agreement with the small emission seen with secondary eclipse measurement at the same wavelength (Charbonneau et al. 2008).

Here, we present a joint analysis of our *Spitzer*/IRAC and HST/NICMOS observations of primary transits of HD 189733b. This work is our ongoing efforts to charaterize the transit spectra of HD 189733b using space-based observatories (Désert et al. 2009a,b; Sing et al. 2009). The data consists of high-cadence time series. The photometric precision achieved allows us to derive accurate measurements of the radius used to probe the planet's atmospheric composition. Our results together with a comparison with previous studies and theoretical predictions are given below.

2 Observations and analysis

2.1 Spitzer transit lightcurves

First observations (visit 1 hereafter) of the system were performed on 2006 October 31 simultaneously at 3.6 and 5.8 μm (channels 1 and 3). The second part of the program was completed on November 23, 2007 using the 4.5 and 8 μm channels (channels 2 and 4) following the same methods (visit 2 hereafter). In both visits, the system was observed using IRAC's stellar mode during 4.5 hours for each visit, upon which 1.8h was spent in planetary transit. A third primary transit (visit 3 hereafter) was obtained on 25 November 2007 at 3.6 μm (Channel 1). In that specific case, the system was observed using IRAC's 32×32 pixel subarray mode during 4.5 hours, upon which 1.8h was spent in planetary transit. The details of the analysis of these three visits can be found in Désert et al. (2009a,b).

We used aperture photometry to extract the transit lightcurves in each channel from the *Spitzer*/IRAC Basic Calibrated Data (BCD) frames. These frames are produced by the standard IRAC calibration pipeline and include corrections for dark current, flat-fielding, detector nonlinearity, and conversion to flux units.

After producing a time series, we iteratively select and trim outliers greater than 4 σ by comparing the photometric measurements to the best fit of a transit light curve model. Doing so, we removed any remaining points affected by transient hot pixels. We discarded frames, which represent 0.1% of the total number of photometric data points.

We finally modeled the transit light curve with 4 parameters: the planet-star radius ratio $R_p/R_\star$, the orbital distance to stellar radius ratio (system scale) $a/R_\star$, the impact parameter b, and the time of mid-transit T_c. We used the IDL transit routine `OCCULTNL` developed by Mandel & Agol (2002) for the transit light curve model. We took into account limb darkening correction using a three non-linear limb-darkening coefficients. We performed a least-squares fit to our transit light curves simultaneously over the whole parameter space ($R_p/R_\star$, $a/R_\star$, b, T_c). We used the Prayer Bead method (Moutou et al. 2004; Gillon et al. 2007) to determine the mean value as well as the statistical and systematical errors for the measured parameters.

Nevertheless, the transit lightcurves are affected by systematical effects that have to be taken into account and properly corrected to determine the correct parameters. The pixel phase effect is predominant at shorter wavelength whereas the ramp effect affected longer wavelength. These effects and their corrections are described below.

2.1.1 Pixel phase effect decorrelation

Because of instrumental effects, the measured stellar flux out-of-transit is not constant, but is seen to vary in time. Telescope jitter and intra-pixel sensitivity variations are responsible for fluctuations seen in the centroid and in the raw light curves. A description of this effect, known as the pixel-phase effect, is given in the *Spitzer*/IRAC data handbook (Reach et al. 2006, p. 50; see also Charbonneau et al. 2005) and affect mainly Channels 1 and 2. To correct for this instrumental effect, we defined a baseline function which is a quadratic function of X and Y target positions, with five parameters K_i, as described in Désert et al. (2009). This function is more robust against systematics compared to a function with one parameter used by the previous analyses (Ehrenreich et al. 2007; Beaulieu et al. 2008).

2.1.2 Baseline

The baselines are known to be inherently linear for channel 1 and 2 and logarithmic for channel 3 and 4 (Knutson et al. 2008). However, we tested three different baselines functions: polynomial of one, two and three degrees, an exponential with a polynomial, and logarithmic with a linear function. We tested the robustness of each of these different baselines by dropping the first exposures from the beginning of the observations (exposure with a phase smaller than -0.03). We found that for channels 3 and 4, the best fits are obtained when using a logarithmic baseline (see lower panel in Fig. 2). In the case of a linear, polynomial or exponential baseline, the fitted parameters show large residuals and large scatter with the number of data point removed. The radius dramatically changes according to the number of points removed when using a linear or a third degree polynomial baseline functions indicating that systematics errors remain in the corrected data. In the case of a logarithmic baseline, the radius extracted does not depend on the number of removed points. The logarithmic function is the only one which allows the observable parameters to oscillate around the same value independently of removed exposures. Only small systematics still remain and they are included in the final error bar.

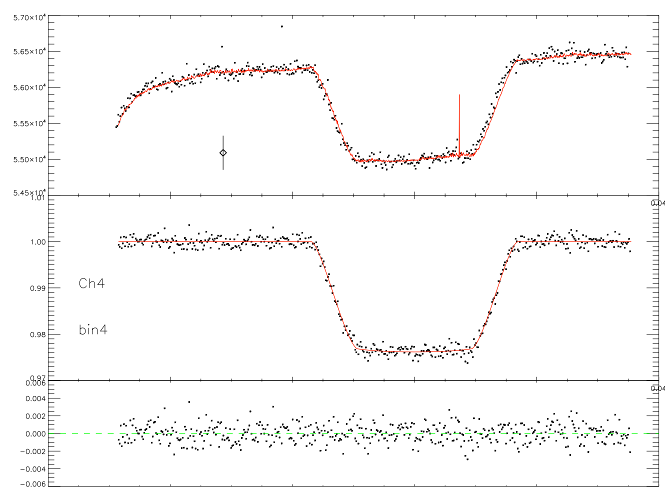

Fig. 1. Channel 4. Top panel: The full raw transit light curve (TLC) with its best fit model (red line). The ramp effect can be easelly seen at the begining of the TLC. Middle panel: Normalized TLC corrected for the ramp and pixel phase effect. Bottom panel: Root-mean-square (RMS) resulting from the best fit model. The fit is always better when using the logarithmic function. This is particularly true at the beginning of the time series, where the ramp effect is the strongest.

2.2 HST transit lightcurves

We observed HD189733 during five transits using the Near Infrared Camera and Multi Object Spectrometer (NICMOS) aboard the Hubble Space Telescope during Cycle 16. Each transit observation consisted of four consecutive spacecraft orbits, each roughly centered on a transit event. For each transit event, we obtained

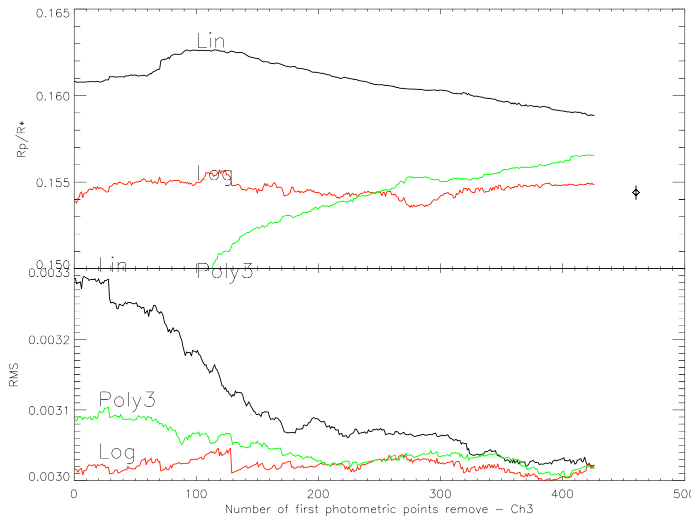

Fig. 2. Channel 3. Top panel: $R_p/R_\star$ ratios extracted when using linear, polynomial of a 3rd degree, and logarithmic baselines as function of the number of first photometric points removed from which the transit light curve is fitted. In the abscisse, 0 point removed correspond to the full transit light curve (TLC). The left over TLC when padded at a phase of -0.03 correspond to the removal of nearly ~ 430 measured points. The diamond point on the right hand side with its error bar, indicates the mean value with its error bar obtained by bootstrap when using a logarithmic baseline. Bottom panel: Root-mean-square (RMS) resulting from the fit using the three different baselines describe above as function of first exposures removed. The fit is always better when using the logarithmic function. This is particularly true at the beginning of the time series, where the ramp effect is the strongest.

images using the high resolution NIC1 camera with only a single narrowband filter, using either the F166N filter centered at 1.6607 μm ($\Delta\lambda = 0.0170\mu$m) or the F187N filter centered at 1.8748 μm ($\Delta\lambda = 0.0191\mu$m).

We performed aperture photometry on the calibrated STScI pipeline reduced images. The pipeline includes corrections for bias subtraction, dark current, detector non-linearities, and applies a flat field calibration. The aperture location for each image was determined using a two dimensional Gaussian fit of the point spread function (PSF) for each image. We found apertures with a radii of 15.2 pixels for the F187N filter and 14.7 pixels for the F166N filter minimized the standard deviation of the out-of-transit light curves. The background in our short exposures was found to be negligible, typically accounting for only $\sim$50 total counts per image.

2.3 Three parameter non-linear limb-darkening law

For solar-type stars at near-infrared and infrared wavelengths, the strength of stellar limb-darkening is weaker compared to optical wavelengths. However, the intensity distribution is increasingly non-linear at these longer wavelengths, which require adopting non-linear limb-darkening laws that we took into account when fitting high S/N transit light curves.

2.4 Monitoring the stellar activity

We monitored the stellar activity of HD189733 using both ground-based data as well as the absolute flux level from the NICMOS instrument itself. The ground-based coverage was provided by the T10 0.8 m Automated Photoelectric Telescope (APT) at Fairborn Observatory in southern Arizona (Henry et al. 2008). The near-IR flux levels for HD189733, during our five visits, are based on the baseline flux level from each transit light-curve as well as the first 50 exposures obtained in the filter opposite to that of the transit (ie. F166N or F187N).

Finally, we followed the same methodology as the one described above for the *Spitzer*lightcurves and both results are presented below.

3 Results

As seen here, IRAC (Désert et al. 2009a,b) and NIMCOS (Sing et al. 2009) photometry can provide robust methods for obtaining precision near and mid-infrared transit radii. With carefully selected band filters, we are able to provide stringent constraints on the presence of H_2O absorption features, finding instead upper-atmospheric haze provides sufficient opacity in slant transit geometry to obscure the near and mid-IR molecular signatures. While absorption due to H_2O were reported by Tinetti et al. (2007) and Swain et al. (2008), our both independant observation with IRAC and NICMOS rule out any such feature at 5σ and find their observed feature is likely artifacts of residual systematic errors in both cases. The planetary radii values from Pont et al. (2008) and this work indicate that Rayleigh scattering dominates the broadband transmission spectrum from at least 0.5-2 μm, with sub-micron $MgSiO_3$ haze particles a probable candidate (Lecavelier et al. 2008). The transition wavelength between the transmission spectra being dominated by haze particles and molecular features would seem to be between 2 and 3 μm, as the IRAC spitzer photometry between 3 and 8 microns all show planet radii in excess of those predicted by Rayleigh scattering (Désert et al. 2009a,b).

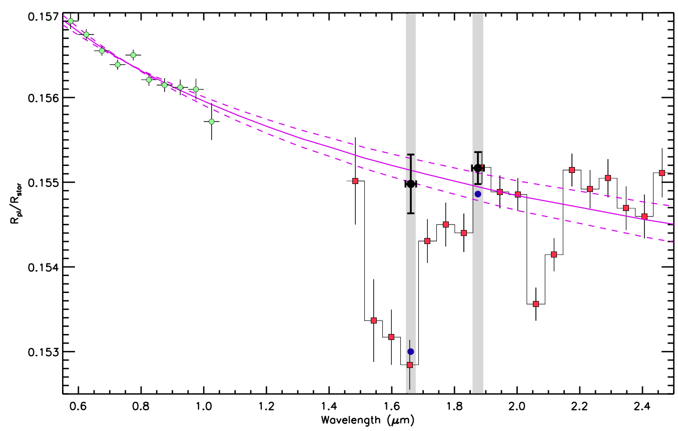

Fig. 3. Measured planetary radii for HD189733b at optical and near-infrared wavelengths. Plotted are the results from our NICMOS narrowband photometry (black dots), along with the NICMOS grism spectrum (red squares) from Swain et al. (2008), and ACS grism spectrum (green dots) from Pont et al. (2008). The 1-σ error bars on the fit radii are indicated (y-axis error bars), along with the wavelength range of each observation (x-axis error bars, grey vertical bars). Also plotted (purple) is the prediction by Rayleigh scattering due to haze from Lecavelier et al. (2008), projected here into the near-infrared along with the 1-σ error on the predicted slope (purple, dashed lines). The NICMOS spectrum from Swain et al. (2008) is quoted as being uncertain in its absolute flux level by $\pm 2\times10^{-4}$ (± 0.00064 $R_{pl}/R_\star$), an offset of -0.00042 $R_{pl}/R_\star$ was applied here for comparison reasons such that the values at 1.87 μm match. Our 1.66μm results are in disagreement with the both the Swain et al. spectra and the expected H_2O atmospheric signature (blue dots), but are in excellent agreement with the predicted planetary radii values from atmospheric haze.

References

Beaulieu, J. P., Carey, S., Ribas, I., & Tinetti, G. 2008, ApJ, 677, 1343

Bouchy, F., et al. 2005, AA, 444, L15

Charbonneau, D., Brown, T. M., Noyes, R. W., & Gilliland, R. L. 2002, ApJ, 568, 377

Charbonneau, D., et al. 2005, ApJ, 626, 523

Charbonneau, D., Knutson, H. A., Barman, T., Allen, et al., & Udry, S. 2008, ApJ, 686, 1341

Désert, J.-M., Vidal-Madjar, A., Lecavelier Des Etangs, A., Sing, et al., R. 2008, AA, 492, 585

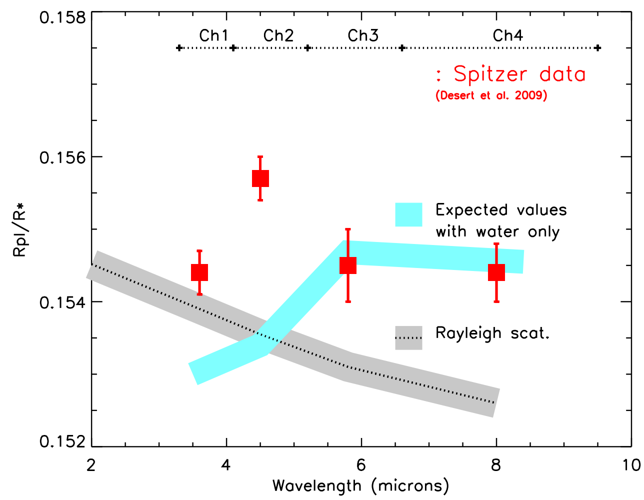

Fig. 4. Census of the measured values of $R_p/R_\star$ ratios in the four *Spitzer*/IRAC channels for HD 189733b obtained from the observations of three transits. Results from our previous analysis of stellar mode observations are plotted with red squares and are shown with their 1 σ errorbars.(Désert et al. 2009). The IRAC bandpasses for each channel are shown with dotted line. The $R_p/R_\star$ ratio obtained at 3.6 μm in subarray mode is 10 σ larger than expected with water absorption only (light blue line) and is consistent with what is expected with Rayleigh scattering by small particles (grey dotted line). The $R_p/R_\star$ obtained at 4.5 μm is larger (4 σ) than expected with either water absorption only or with Rayleigh scattering by small particles. This supplementary absorption could be due to the presence of CO molecules in the planetary atmosphere. The $R_p/R_\star$ obtained at 5.8 μm and at 8.0 μm are consistent with absorption by water vapour.

Désert, J.-M., Lecavelier des Etangs, A., Hébrard, G., Sing, D. K., Ehrenreich, et al., A. 2009, ApJ, 699, 478

Désert, J.-M. et al. submitted

Ehrenreich, D., Hébrard, G., Lecavelier des Etangs, A., Sing, D. K., Désert, J.-M., et al., A. 2007, ApJL, 668, L179

Fazio, G. G., et al. 2004, ApJS, 154, 10

Gillon, M., et al. 2007, AA, 471, L51

Grillmair, C. J., et al. 2008, Nature, 456, 767

Henry, G. W., & Winn, J. N. 2008, AJ, 135, 68

Knutson, H. A., et al. 2009, ApJ, 690, 822

Knutson, H. A., Charbonneau, D., Allen, L. E., Burrows, A., & Megeath, S. T. 2008, ApJ, 673, 526

Knutson, H. A., et al. 2007, Nature, 447, 183

Lecavelier Des Etangs, A., Vidal-Madjar, A., Désert, J.-M., & Sing, D. 2008, AA, 485, 865

Mandel, K., & Agol, E. 2002, ApJL, 580, L171

Moutou, C., Pont, F., Bouchy, F., & Mayor, M. 2004, AA, 424, L31

Pont, F., et al. 2007, AA, 476, 1347

Pont, F., Knutson, H., Gilliland, R. L., Moutou, C., & Charbonneau, D. 2008, MNRAS, 385, 109

Redfield, S., Endl, M., Cochran, W. D., & Koesterke, L. 2008, ApJL, 673, L87

Sing, D. K., Vidal-Madjar, A., Désert, J.-M., Lecavelier des Etangs, A., & Ballester, G. 2008, ApJ, 686, 658

Sing, D. K., Vidal-Madjar, A., Lecavelier des Etangs, A., Désert, J.-M., et al., D. 2008, ApJ, 686, 667

Sing, D. K., Désert, J.-M., Lecavelier Des Etangs, A., Ballester, et al. 2009, AA, 505, 891

Snellen, I. A. G., Albrecht, S., de Mooij, E. J. W., & Le Poole, R. S. 2008, AA, 487, 357

Swain, M. R., Vasisht, G., & Tinetti, G. 2008, Nature, 452, 329

Tinetti, G., et al. 2007, Nature, 448, 169

Vidal-Madjar, A., et al. 2004, ApJL, 604, L69

Vidal-Madjar, A., Lecavelier des Etangs, A., Désert, J.-M., et al. 2008, ApJL, 676, L57

Vidal-Madjar, A., Lecavelier des Etangs, A., Désert, J.-M., Ballester, et al. 2003, Nature, 422, 143

Werner, M. W., et al. 2004, ApJS, 154, 1

THE INITIAL CONDITIONS OF STAR FORMATION IN INTERMEDIATE- TO HIGH-MASS PROTOCLUSTERS

Fontani, F.[1], Zhang, Q.[2], Caselli, P.[3] and Bourke, T.L.[2]

Abstract. To better understand how the initial conditions of the highly complex star formation process depend on environmental conditions, it is crucial to study at high-angular resolution the morphology, the kinematics, and eventually the interactions of pre–stellar core candidates associated with intermediate-/high-mass star formation. In this work, we study the cold condensations in the intermediate-/high-mass proto-cluster IRAS 05345+3157, focusing on the interaction with the other objects in the cluster. We have performed millimeter high-angular resolution observations, both in the continuum and several molecular lines, with the PdBI and the SMA. The main results of this work are the following: the observations reveal the presence of 3 warm cores identified in the millimeter continuum, called C1-a, C1-b and C2, and of two very cold and dense cores, called N and S, identified by observations of N_2D^+, a molecular species eminently suitable to trace pre–stellar gas. None of the millimeter cores are associated with cores N and S. C1-b is likely a massive young stellar object driving a powerful ouflow. The study of the gas kinematics across the source indicates a tight interaction between the deuterated condensations and the sources embedded in the millimeter cores. For the nature of N and S, we propose two scenarios: they can be either low-mass pre–stellar condensations in which turbulent motions are dominant, or 'seeds' of future high-mass star(s).

1 Introduction

The physical and chemical properties of pre-stellar cores, i.e. cores on the verge of the gravitational collapse, were extensively investigated in the last decade in nearby low-mass star forming regions. Studies demonstrate that *isolated low-mass pre–stellar cores* have dense ($n \sim 10^5 - 10^6$ cm^{-3}) and cold ($T \sim 10$ K) nuclei, in which C-bearing molecular species such as CO and CS are strongly depleted, while N-bearing species such as N_2H^+ and NH_3 maintain large abundances in the gas phase (see Bergin & Tafalla 2007 for a review). The combination of low temperatures and CO depletion originates high values of *Deuterium fractionation* ($D_{\rm frac}$), defined as the column density ratio between one species containing deuterium and its counterpart containing hydrogen. The production of deuterated species starts from the exothermic proton-deuteron exchange reactions of the simplest molecular ions (e.g. $H_3^+ + HD \rightarrow H_2D^+ + H_2 + 270$ K, Millar et al. 1989): at temperatures lower than $\sim 20-30$ K, the inverse reactions are inhibited, so that the abundance of the deuterated ions (and hence of their daughter species) increases. In addition, these deuterated molecules are mainly destroyed by CO, but in environments where CO is depleted they can survive and give rise to strong lines. Actually the $D_{\rm frac}$ in pre–stellar cores, measured through non-depleted molecules, e.g. NH_2D/NH_3 and N_2D^+/N_2H^+, is orders of magnitude larger than the [D/H] interstellar abundance (Tiné et al. 2000; Crapsi et al. 2005). Can the properties of isolated pre-stellar cores be extended to clustered cores surrounding high mass (proto)stars? In crowded environments, turbulence, relative motions, and interactions with nearby forming (high-mass) protostars can affect the less evolved condensations (Ward-Thompson et al. 2007). To understand if, and how, crowded pre–stellar cores close to intermediate-/high-mass star formation are different from isolated ones, high-angular resolutions studies of the cold and dense gas that surrounds massive (proto-)stellar objects are necessary.

The object of the present work is an intermediate- to high-mass proto-cluster located nearby the luminous IRAS point source 05345+3157 ($\sim 60''$ to the N-E). The region is located at a distance of 1.8 kpc (Zhang et

[1] ISDC, Ch. d'Ecogia 16, 1290 Versoix, Switzerland
[2] Harvard-Smithsonian Center for Astrophysics, 60 Garden Street, Cambridge, MA 02138, USA
[3] School of Physics and Astronomy, University of Leeds, Leeds, LS2 9JT, UK

al. 2005), and its surface density (~ 1.3 gr cm^{-2}) and mass-to-luminosity ratio ($\sim 8L_{\odot}/M_{\odot}$) indicate that it is potentially a site of massive star formation (see Fig. 1 of Chakrabarti & McKee 2005). Hereafter, we will call our target I05345. From IRAM-30m data, Fontani et al. (2006) have measured an average CO depletion factor of ~ 3 and an average deuterium fractionation from the column density ratio $N(N_2D^+)/N(N_2H^+)$ of ~ 0.01, three orders of magnitude higher than the cosmic [D/H] abundance. These findings would indicate the possible presence of pre–stellar cores analogous to those detected in several low-mass star forming regions. However, the angular resolution was insufficient to determine whether we are dealing with a single high-mass core or instead with several low-mass ones. Therefore, we have recently mapped I05345 at high-angular resolution in the N_2H^+ (1–0) line with the IRAM Plateau de Bure Interferometer (PdBI), and in the N_2H^+ and N_2D^+ (3–2) lines with the Submillimeter Array (SMA), in order to derive a detailed map of the deuterium fractionation in the source. Simultaneously, we have obtained observations in the continuum at ~ 96, ~ 225 and ~ 284 GHz with the two interferometers, as well as in several lines of other molecules. We present here the main results of these observations.

2 N_2D^+ and N_2H^+ emission and deuterium fractionation

In left panel of Fig. 1 we summarise the main observational results of the observations of N_2H^+, N_2D^+ and of the 96 GHz continuum: (i) the 96 GHz continuum observed with PdBI (grey-scale in left panel of Fig. 1) reveals the presence of 4 cores; two of these are inside the interferometer primary beam (C1 and C2 in left panel of Fig. 1), while the other two are outside and at the edge of it (C3 and C4, respectively, in left panel of Fig. 1). When observed at a resolution of $\sim 1''$ at 286 GHz, core C1 is resolved in two sources, C1-a and C1-b (see the grey-scale in right panel of Fig. 1). Core C1-b is a hot core and thus likely harbors an early-B ZAMS star; (ii) the distribution of the intensity of the N_2H^+ (1–0) line (green contours in left panel of Fig. 1) is extended and with a complex structure; (iii) the distribution of the N_2D^+ (3–2) line integrated emission (red contours in left panel of Fig. 1) is concentrated in two condensations, called N and S. The integrated emission of the N_2H^+ (3–2) line (not shown in Fig. 1) is compact, and detected towards the strongest continuum peak only. We have derived the masses of N and S, which are ~ 9 and ~ 2.5 M$_{\odot}$, respectively. Also, from the N_2D^+ /N_2H^+ column density ratio we have obtained a $D_{\rm frac}$ of ~ 0.1 in both condensations, which are the typical values derived in low-mass pre–stellar cores. For more details, see Fontani et al. (2008).

3 Interaction between the deuterated condensations and a powerful CO outflow

In this section we concentrate on the interaction between the deuterated condensations N and S and a powerful outflow, revealed by CO observations obtained at the SMA simultaneously to the N_2D^+ maps. In right panel of Fig. 1, we show the map of the integrated intensity in the ^{12}CO (2–1) line wings, derived from channel maps obtained combining SMA and NRAO data. The blue- and red-shifted emissions have been averaged in the velocity intervals (–46.4, –26) km s^{-1} and (–9.2, 6.4) km s^{-1}, respectively. The outflow axis is predominantly oriented in the WE direction, with redshifted gas in the east and blueshifted gas in the west. The lobes are clearly separated and have approximately a biconical shape. The outflow center is near the position of the continuum source C1, and the exciting source can be either C1-a and C1-b. The blueshifted gas shows a fainter secondary peak to the north of the map. From geometrical considerations, this northern blue-shifted emission might be driven by a source within N, rather than C1-a or C1-b. However, as we will further discuss later, the sources eventually embedded within N are probably in the pre–stellar phase, i.e. prior to the main accretion phase in which the outflow is expected to form, so that this solution seems to us very unlikely. The outflow length, from end-to-end, is approximately $35''$ (if we do not consider the secondary peaks of the blueshifted emission), corresponding to ~ 0.28 pc at a distance of 1.8 kpc. The semi-opening angle is between about 30 and 40^o, and the spatial separation of the lobes suggests that the inclination angle with respect to the line of sight is likely to be very close to the plane of the sky (see also Cabrit & Bertout 1986).

4 Nature of the deuterated condensations

To better understand the nature of the two condensations, a detailed analysis of the gas kinematics is certainly very helpful. For this reason, here we investigate in more detail the gas kinematics in N and S by using as diagnostics the peak velocity and widths of the N_2H^+ (1–0) and N_2D^+ (3–2) lines. In the two left panels of

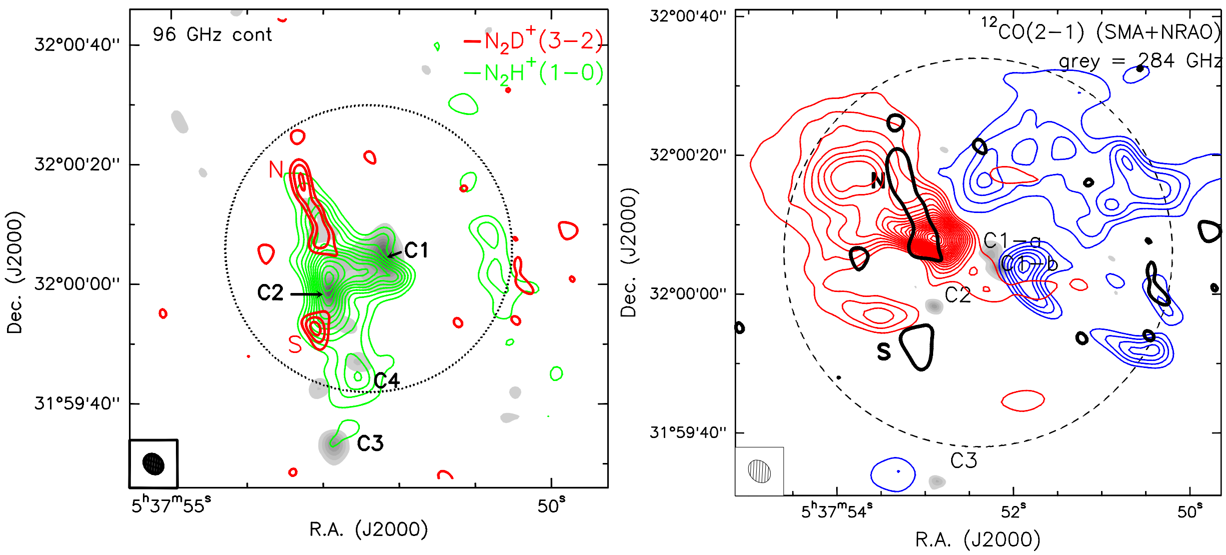

Fig. 1. Left panel: Interferometric maps obtained towards I05345 and published by Fontani et al. (2008). The green contours represent the intensity of the N_2H^+ (1–0) line, integrated in the velocity range corresponding to the main group of the hyperfine components of this line, observed with the PdBI. Levels are in steps of 3σ rms. The red contours represent the N_2D^+ (3–2) line emission integrated over the total velocity range with emission, obtained with the SMA. The two main condensations are indicated as N and S. The grey scale shows the 96 GHz continuum, in steps of 3σ. The grey scale image indicates 4 millimeter continuum peaks, called C1, C2, C3 and C4. Note that peaks C3 and C4 areoutside and at the edge, respectively, of the PdBI primary beam at 96 GHz ($\sim$48″, dotted circle). The ellipse in the bottom left corner shows the synthesised beam of the N_2D^+ image, comparable to that of the PdBI data at 96 GHz.
Right panel: red- and blue-shifted integrated emission of the ^{12}CO (2-1) line (combined SMA + NRAO data), superimposed on the 96 GHz continuum map observed with the PdBI (grey-scale). The solid black contours represent the 3σ level of the N_2D^+ (3-2) line integrated emission, and indicate the location of the deuterated cores N and S. ¿From geometric considerations, the outflow driving source may be either C1-a or C1-b, or another source undetected in the continuum at the centre of the lobes. The dashed circle represents the SMA primary beam at the frequency of the ^{12}CO (2-1) line.

Fig. 2 we show the maps of $V_{\rm LSR}$ and ΔV, respectively, obtained for N from the N_2H^+ (1–0) line. The same plots derived from N_2D^+ (3–2) are shown in the two right panels. Both quantities are derived by fitting the hyperfine structure of the N_2H^+ (1-0) and the N_2D^+ (3-2) lines. For both tracers, the line widths are larger where the red lobe of the ^{12}CO outflow impinges core N (Fig. 1, right panel). At the same position, the gas emission is clearly red-shifted. The line broadening is $\sim$ 3 times larger than the expected thermal broadening, indicating internal motions dominated by turbulence. For S, we find similar results. This indicates that both cores are characterised by a probable interaction with the red lobe of the ^{12}CO outflow, which can trigger turbulence in the cores themselves and can influence their evolution. Unlike the pre-stellar cores studied here, those studied in low-mass star forming regions (both isolated and clustered) have close-to-thermal line widths (see e.g. Foster et al. 2009).

In theoretical models of clustered star formation, turbulence (which in this case is generated by already formed protostars) can create density modifications across the cloud, originating several dense and cold 'seeds', which subsequently can accrete backgound gas that was initially not associated with the 'accretion domain' of the seed itself (see e.g. Bonnell et al. 2004, and McKee & Tan 2003). In this scenario, the two condensations can become more massive and form pre–stellar cores of higher mass. Alternatively, the interaction with the other cluster members, in particular with the powerful ^{12}CO outflow, could also cause the fragmentation of the condensations. For more details, see Fontani et al. (2009).

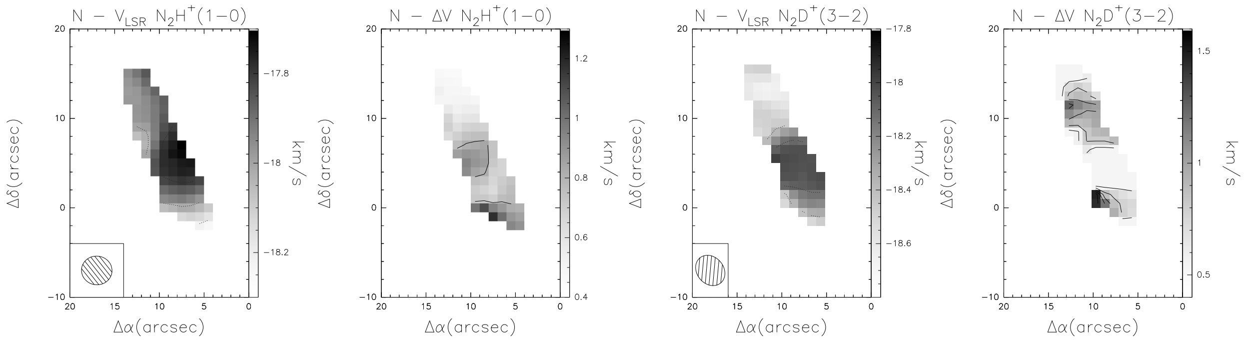

Fig. 2. Left panels: map of the peak velocity ($V_{\rm LSR}$) and line width (ΔV) derived from the N_2H^+ (1–0) line inside the 3σ level of the N_2D^+ (3–2) emission of core N. The vertical grey-scale on the right side of the two plots indicates the intensity, in km s^{-1}, of $V_{\rm LSR}$ and ΔV, respectively. In the bottom left corner, the synthesised beam of the channel maps are shown. Right panels: same as left panel for the N_2D^+ (3–2) line.

5 Summary

We have presented a millimeter high-angular resolution study of the intermediate-/high-mass star forming region IRAS 05345+3157. The main findings of this work are the following: (i) detection of two molecular condensations (called N and S) showing high values of deuterium fractionation (~ 0.1), derived from the column density ratio $N(N_2D^+)/N(N_2H^+)$; (ii) detection of three millimeter warm cores, among which one likely harbors a massive (proto-)stellar object driving a powerful CO outflow; (iii) the line widths in the pre-stellar cores indicate internal motions dominated by turbulence: this latter is likely triggered by the CO outflow, and this indicates that the kinematics of the pre–stellar core candidates in I05345 is affected by the environment; (iv) on the other hand, the deuterium fractionation is comparable to the values measured in isolated starless cores, implying that some aspects of the chemistry do not appear to be affected by the environment.

Can the results obtained for IRAS 05345+3157 be considered typical in intermediate-/high-mass protoclusters? Namely: how do the presence of intermediate-/high-mass protostars generally affect the physical/chemical properties of cores on the verge of forming stars? To answer these questions, more studies of intermediate-/high-mass protoclusters like the one presented here need to be performed.

It is a pleasure to thank the staff of the Smithsonian Astrophysical Observatory for the SMA observations. We also thank the IRAM staff and Riccardo Cesaroni for their help in the calibration of the PdBI data. FF acknowledges support by Swiss National Science Foundation grant (PP002 – 110504). TB acknowledges support from US National Science Foundation grant (0708158).

References

Bergin, E.A., & Tafalla, M., 2007, ARA&A, 45, 339

Bonnell, I.A., Vine, S.G., Bate, M.R. 2004, MNRAS, 349, 735

Cabrit, S. & Bertout, C. 1986, ApJ, 307, 313

Chakrabarti, S. & McKee, C.F. 2005, 631, 792

Crapsi, A., Caselli, P., Walmsley, C.M., et al. 2005, ApJ, 619, 379

Fontani, F., Caselli, P., Crapsi, A., et al. 2006, A&A, 460, 709

Fontani, F., Caselli, P., Bourke, T.L., Cesaroni, R., Brand, J. 2008, A&A, 477, L45

Fontani, F., Zhang, Q., Caselli, P., Bourke, T.L. 2009, A&A, 499, 233

Foster, J.B., Rosolowsky, E.W., Kauffmann, J. et al. 2009, ApJ, 696, 298

McKee, C.F. & Tan J.C. 2002, Nature, 416, 59

Millar, T.J., Bennett, A., Herbst, E. 1989, ApJ, 340, 906

Tiné, S., Roueff, E., Falgarone, E., Gerin, M., Pineau des Forets 2000, A&A, 356, 1039

Ward-Thompson, D., André, P., Crutcher, R. 2007, PPV conference, 951, p. 33

Zhang, Q., Hunter, T.R., Brand, J. et al. 2005, ApJ, 625, 864

SF2A 2009
M. Heydari-Malayeri, C. Reylé and R. Samadi (eds)

PROTOPLANETARY DISKS AND PLANET FORMATION

Fouchet, L.[1]

Abstract. With more than 300 exoplanets discovered, the understanding of their formation has become central. But this formation is tightly linked to their environment, the protoplanetary disk which, itself, is a byproduct of stellar formation. I will thus quickly present the stellar formation scenarii (observational constraints, turbulence versus ambipolar diffusion). Then, I will come to our knowledge of disks (observations, models of irradiated disks, passive/active, flat/flared). I will describe the evolution of solids which are the building blocks for protoplanetary cores (radial migration, vertical settling and growth). I will then show synthetic images that can be produced with a self consistent treatment of dust in order to prepare for the ALMA observations. I will mention the Heidelberg scenario for rapid planetesimals formation. I will then sum up the state of our knowledge on planet migration which is an essential process to form giant planets before the disk has disappeared in the frame of the core accretion scenario. This will lead me to the actual models for core accretion and the central role of the disk on those and I'll finally quickly mention the other giant planet formation scenario: the gravitational instability.

1 Introduction

Protoplanetary disks are the birthplaces for planets, and as such, their physical properties must be understood in order to build a consistent scenario for planet formation. Disks mass amount to 1 to 10% of the mass of the central star. They are made of gas and dust with the dust component representing 1 to 2% of the disk mass. The dust phase is made of silicates, ices and PAHs (Polycyclic Aromatic Hydrocarbons). In simple models, the temperature profile goes as $T \sim r^{-q}$ with $1/2 < q < 3/4$ and the surface density profile as $\Sigma \sim r^{-p}$ with $1/2 < p < 2$ where r is the distance to the star.

Disks harbor a wealth of physical processes. In the gas phase, temperature is defined by viscous heating and irradiation while the velocity field is set by gravity and some turbulence. In the dust phase, we want to understand how dust grows or gets shattered during collisions. Gas-dust interactions occur through aerodynamic drag leading to vertical settling and radial migration (Weidenschilling 1977). Finally, disk-planet interactions are characterized by core formation from planetesimals, then runaway gas accretion and together with planet migration under the effect of disk gravitational torques.

2 Disk structure

2.1 Temperature structure in the disk

Disks can be flat or flared or, even, self-shadowed (Dullemond & Dominic 2004). If they are flat, it means that H, the vertical scaleheight goes as $H \sim r$. In that case as in the self-shadowed one (where $H \sim r^{\sigma}$ with $\sigma < 1$), the outer disk doesn't get direct stellar light and is cooler than in the flared case (where $\sigma > 1$) where the outer disk can get direct stellar light. These issues were recognized a long time ago (Kenyon & Hartmann 1987) and the flared structure helped explain observed SEDs (Spectral Energy Distribution). Another level of refinement was to add a puffed up inner rim (because the inner part of the disk is directly heated by the star) and help reproduce SEDs even better (Dullemond et al. 2001). Now, different methods are used to provide a reasonable temperature structure for the disk: 3D codes with full radiative transfer (see the benchmark for a few of them done by Pinte et al. 2009) or 1+1D axisymmetric approximations where the vertical structure is computed independently of the radial one. The choice depends on the the level of accuracy needed and on the time available for computation.

[1] Physikalisches Institut, Universitaet Bern, Sidlerstrasse 5, CH-3012 Bern, Switzerland

2.2 Turbulence

The best candidate as source for turbulence is the MRI (Magneto-Rotational Instability) as was shown by Balbus & Hawley (1991), although it is not clear that the ionization fraction in the midplane is high enough for MRI to be sustained there. Only full 3D, local or global, simulations can allow to characterize this kind of turbulence and they are tremendously numerically demanding. Therefore, when the characterization of turbulence is not the main topic, people often revert to the ”alpha” formalism (Shakura & Sunyaev 1973) where turbulence is described as some sort of viscosity with $\nu = \alpha c_s H$ where c_s is the soundspeed.

3 Dust phase

3.1 Dynamics

Dust dynamics is influenced by the disk structure and, reversely, dust acts on the temperature structure of the disk. The opacity is dominated by small grains and will vary according to the spatial and size distribution of the grains. In the disk, gas is supported against gravity by a pressure gradient. Therefore, its velocity field is slightly subkeplerian. On the opposite, the dust phase has no internal pressure and needs to flow at a keplerian speed in order to compensate for the stellar gravity. As a result, dust feels a headwind and looses angular momentum. This is why it settles to the midplane of the disk and spirals inward towards the star. To be more precise, dust will always accumulate in pressure maxima (Haghighipour & Boss 2003). The pace at which these movements occur depend on the the grain size. Small grains are strongly coupled to the gas and will follow its motion, intermediate size grains are partly decoupled and will settle and migrate most efficiently, large grains will almost not feel the gas and follow perturbed keplerian orbits. In a MMSN (minimum mass solar nebula, see Hayashi 1981), the faster radial migration occurs for 1 m size boulders, while in a CTTS (Classical T Tauri Star) it will rather be 1 cm.

3.2 Observations

In the Infrared, observations can be analyzed with models where gas and dust is well mixed, because we observe grains that are small enough to be strongly coupled to the gas. But, in the case of ALMA observations, the problem is different. Disks will be observed in the millimeter wavelength, i.e., we will observe mm size pebbles. Their dynamics and subsequent spatial distribution is substantially different to that of the gas. Grains have to be self-consistently followed together with the gaseous evolution.

Especially, we investigate the visibility of a gap in the dust layer of a CTTS disk created by a 5 Jupiter mass planet at 40 AU from its parent star (Fouchet et al. 2009a,b). We first ran SPH (Smooth Particle Hydrodynamics) 2-fluid simulations in order to derive the spatial distribution of dust in the case where a planet is embedded in the disk. Then we fed these results into the radiative transfer code MCFost and show that the appearance of the disk is substantially different if we consider dust as well mixed or if we self-consistently compute its spatial distribution (see Fig. 1).

3.3 Growth

Beside dynamics, growth and shattering of dust will also affect the disk structure. Growth occurs upon collisions until 1 to 10 cm through Van Der Waals forces. Collisions occur because of the existence of velocity dispersion due to brownian motion for the smaller particles, gas drag for the slightly larger ones and turbulence for all of them. This initial phase of dust growth has been investigated by Laibe et al. (2008) while neglecting shattering. They show that growth occurs without migration during the settling phase, then migration occurs faster than growth, and then, once grains are large enough to decouple from the gas, they grow without migrating. As a result, a plateau appears in the size distribution at the level of the faster migrating grains. Beyond the 10 cm size, collisions become rather destructive. It is yet unclear how to go from 10 cm boulders to 1 km size planetesimals for which gravity will take over and growth will proceed.

Johansen et al. (2007) then propose a scenario to jump directly from 10 cm rocks to planetesimals. They run simulations where self-gravity and magnetic fields are included. They have two fluids, gas and dust and they also include the back-reaction of dust on gas (often neglected). They can show how streaming instability first, then MRI and/or Kelvin-Helmholz instability can concentrate dust into transient vortices. These vortices

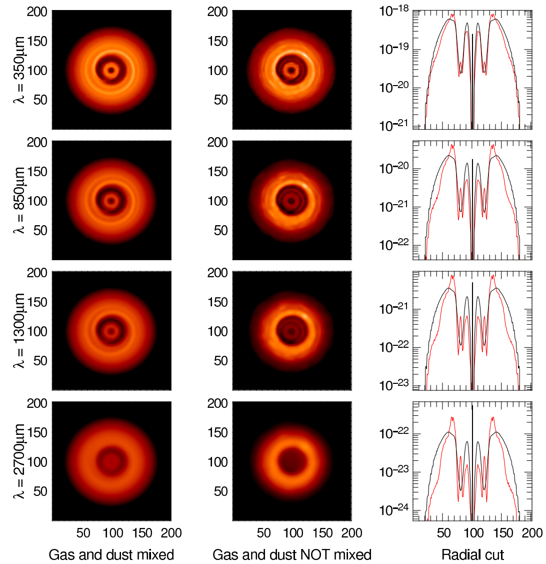

Fig. 1. Synthetic images of the disk at different wavelengths in the well mixed (left) and non well mixed (center) cases. Brightness profiles (right)

leave long enough for dust to accumulate up to a mass where self-gravity will take over and keep the structure together.

3.4 Open questions

A lot of questions remain concerning dust. How is crystalline dust transported to large radii where it is observed? Is it simply due to the viscous spreading of the disk (Dullemond et al. 2006; Ciesla 2009). What is the timescale for grains growth? Millimeter grains are observed in class 0 stars, but, at the same time, smaller grains are observed in older disks. What is the timescale for planetesimals formation? How do planetesimals form? Through coagulation? Is it a global instability in the dust layer? Is it local fragmentation in density enhancements in the dust phase due to turbulence (c.f. Johansen et al. 2007)?

4 Planet migration

While the planet forms, it migrated already. There are different regimes of migration but they share the same issue that they are all too fast for planets to survive without being eaten by the star. Fortunately, potential solutions are under study to slow down migration. Type I migration: Small planets (less than a few Earth Masses) do not strongly affect the disk (they do not create a gap). The linear theory (Goldreich & Tremaine 1980) is often used but insufficient. Yet recent works show that it is sensitively dependent on thermodynamics and that migration happens at a slower pace if we better model the radiative transfer (Paardekooper & Mellema 2006, 2008). Type I migration may also be slower when turbulence is included because the planets achieve a random walk through the disk (Nelson 2005). Type II migration: Large planets (more than a Jupiter mass) open a gap in the disk. Here, the linear theory is inadequate. If the gap is very deep and clean, migration will occur on the viscous timescale. Otherwise, it will depend on thermodynamics (Fouchet & Mayer 2009c), viscosity etc... Type III migration: Intermediate planets can enter a runaway migration which is very fast but can be directed outwards for a small period (Masset & Papaloizou 2003).

In all cases, physical ingredients are often neglected because of the difficulty to evolve the simulations if they are properly included. This is the case for self-gravity, thermodynamics and turbulence. Also, the importance of corotation torques and of the circumplanetary material get recognized (Crida et al. 2009). At the moment, there is no general picture and it is becoming very challenging numerically but a huge effort is invested in solving this problem and answers are coming.

5 Core accretion and gravitational instability

All the previous ingredients are included in a single model, the core accretion model. This was devised by Pollack et al. (1996). They had a steady disk, a model for core formation from a subearth core and planetesimals getting accreted and a detailed model for the planet envelop and the gas accretion. But the timescale to build a Jupiter was longer than the lifetime of a disk (less than 10 millions of years from observations). Alibert et al. (2005) found a solution to this issue by accounting for the migration of the forming core. This allowed the core to meet more planetesimals in its feeding zone and to grow faster. Such a model relies on a prescription for the migration rate of the planet and progress in this domain will improve this model. Mordasini et al. (2009a,b) then produced a giant planet population synthesis which reproduces well the planet observations.

Now, in the Bern group, we improve the disk structure in order to match observations. Namely, we now include irradiation, making the outer parts of the disk warmer than in the previous models. As a result, the transition from type I to type II migration is delayed because the gap is more difficult to open in the warmer outer disk.

The other process to form planets is the gravitational instability. There, a direct collapse of a gaseous clump can lead to a giant planet without a core if the disk is massive and cold enough (Mayer et al. 2002). There is no need for a core and no problem with the too fast type I migration. The formation of a Jupiter mass planet is very rapid removing the issue of the short disk lifetime. Yet, this scenario is highly debated because there are uncertainties concerning the survival of clumps because of the shear in the disk. The simulations are very demanding and cannot follow hundredth of orbits. The thermodynamics is, here again, very important. It is not clear that the disk cools fast enough for the clump to collapse. The perspective at the moment is rather a hybrid model between core accretion and gravitational instability given that giant planets have been observed at such a large distance in the disk that they could never be formed in situ by core accretion (Boley 2009).

References

Alibert, Y., Mordasini, C., Benz, W., Winisdoerffer, C., 2005. A&A, 434, 343.

Balbus, S. A.; Hawley, J. F., 1991, ApJ, 376, 214.

Boley, A. C., 2009, ApJ, 695, 53

Ciesla, F. J., 2009, Icarus, 200, 655.

Dullemond, C. P., Apai, D., Walch, S., 2006, ApJ, 640, 67.

Crida, A., Baruteau, C., Kley, W., Masset, F., 2009, A&A, 502, 679

Dullemond, C. P., Dominik, C., 2004, A&A, 417, 159.

Dullemond, C. P., Dominik, C., Natta, A., 2001, ApJ, 560, 957.

Fouchet, L., Gonzalez, J.-F., Maddison, S., in prep.

Fouchet, L., Pinte, C., Gonzalez, J.-F., Ménard, F., Maddison, S., in prep.

Fouchet, L., Mayer, L., 2009, submitted to Icarus.

Goldreich, P., Tremaine, S., 1980, ApJ, 241, 425.

Haghighipour, N., Boss, A. P., 2003, ApJ, 583, 996.

Hayashi, C. 1981, Prog. Theor. Phys., 70, 35

Johansen, A., Oishi, J. S., Mac Low, M., Klahr, H., Henning, T., Youdin, A., 2007, Nature, 448, 1022.

Kenyon, S. J., Hartmann, L., 1987, ApJ, 323, 714.

Masset, F. S., Papaloizou, J. C. B., 2003, ApJ, 588, 494.

Mayer, L.; Quinn, T.; Wadsley, J.; Stadel, J., 2002, Science, 298, 1756.

Mordasini, C., Alibert, Y., Benz, W., 2009, A&A, 501, 1139.

Mordasini, C., Alibert, Y., Benz, W., Naef, D., 2009, A&A, 501, 1161.

Nelson, R. P., 2005, A&A, 443, 1067.

Paardekooper, S.-J., Mellema, G.,2006. A&A, 459, 17

Paardekooper, S.-J., Mellema, G.,2008. A&A, 478, 245

Pinte, C., Harries, T. J., Min, M., Watson, A. M., Dullemond, C. P., Woitke, P., Mnard, F., Durn-Rojas, M. C. 2009, A&A, 498, 967.

Pollack, J. B., Hubickyj, O., Bodenheimer, P., Lissauer, J. J., Podolak, M., Greenzweig, Y., 1996, Icarus, 124, 62.

Shakura, N. I., Sunyaev, R. A., 1973, A&A, 24, 337.

Weidenschilling, S. J., 1977, MNRAS, 180, 57.

SF2A 2009
M. Heydari-Malayeri, C. Reylé and R. Samadi (eds)

PHOTOPHORETIC TRANSPORT OF HOT MINERALS IN THE SOLAR NEBULA

Moudens, A.[1], Mousis, O.[2], Petit, J.-M.[2] and Alibert, Y.[2]

Abstract. A grid of protoplanetary disk models is used to study the outward transport of hot minerals in the form of aggregates from the warm inner regions of the solar nebula under the influence of photophoresis. We compute the distance range at which these aggregates migrate and we show that this mechanism can lead to an influx of hot minerals in the formation regions of the main cometary reservoirs. Moreover, we calculate the size distribution of dust within the disks and we show that small particles evolve outwards to greater heliocentric distances than larger particles in more evolved disks. Future measurements of the size distribution of dust could then place important constraints on the physical properties of disks.

1 Introduction

Hot temperature minerals (crystalline silicates, CAIs) have been detected in several comets and also identified in the samples returned by the Stardust mission (Brownlee et al. 2006). Because these minerals are expected to be formed at high temperatures in the inner regions of the Solar Nebula, a mechanism of transport towards the outer parts of the disk is required to explain their presence in cometary bodies. Here we use a time-dependent model of the solar nebula using the alpha prescription (Alibert et al. 2005) to explore the photophoretic transport of aggregates formed in the inner part of the disk towards its outer regions.

2 Model

The solid particles embedded in the gas are heated heterogeneously by light. Gas molecules adsorbed and rejected at their surface will carry different momentum and a net force on the particle results (photophoresis effect), which is strongly pressure dependent and can be stronger than radiation pressure and Sun's gravity. The dust particles migrate in the nebula under the combined action of three forces: the residual gravity force, the radiation pressure and the photophoretic force. The dust particles are pushed away via photophoresis and at the same time, being dragged back towards the Sun by the infalling nebula flow (Mousis et al 2007). An inner gap is also postulated, corresponding to a dust-free zone due to material clearing by the young star radiative forces. Aggregates considered in our simulations have sizes ranging between 10^{-5} and 10^{-1}m and are assumed to be spherical and composed of olivine, with a variable porosity. We also consider a density of aggregates of 500 kg.m^{-3}, value holding within the range of densities measured by the Stardust mission in the Wild 2 cometary samples. All the disks used in our calculations extend up to 50 AU and their viscosity parameter is fixed to 7x10^{-3}. The mass of the disks is varied between 1 and 10 times that of the Minimum Mass Solar Nebula (MMSN) and their considered lifetimes range between 1 and 6 Myr.

3 Outward transport of hot temperature aggregates

In all cases shown in Fig.1, the trajectories of 10^{-2} and 10^{-1} m aggregates are almost similar within the disk. These aggregates migrate faster than the smaller ones at the beginning of the disk evolution and are pushed far away in the nebula, at distances that can exceed 30 AU when an inner gap of 2 AU is postulated. Note that all

[1] Institut de Physique de Rennes, Equipe Astrochimie Experimentale, Universite de Rennes 1, Bat.11C, Campus de Beaulieu, 35042 Rennes Cedex
[2] Laboratoire UTINAM, UMR-CNRS 6213, Observatoire de Besancon, 41 bis avenue de lobservatoire, 25010 Besancon France

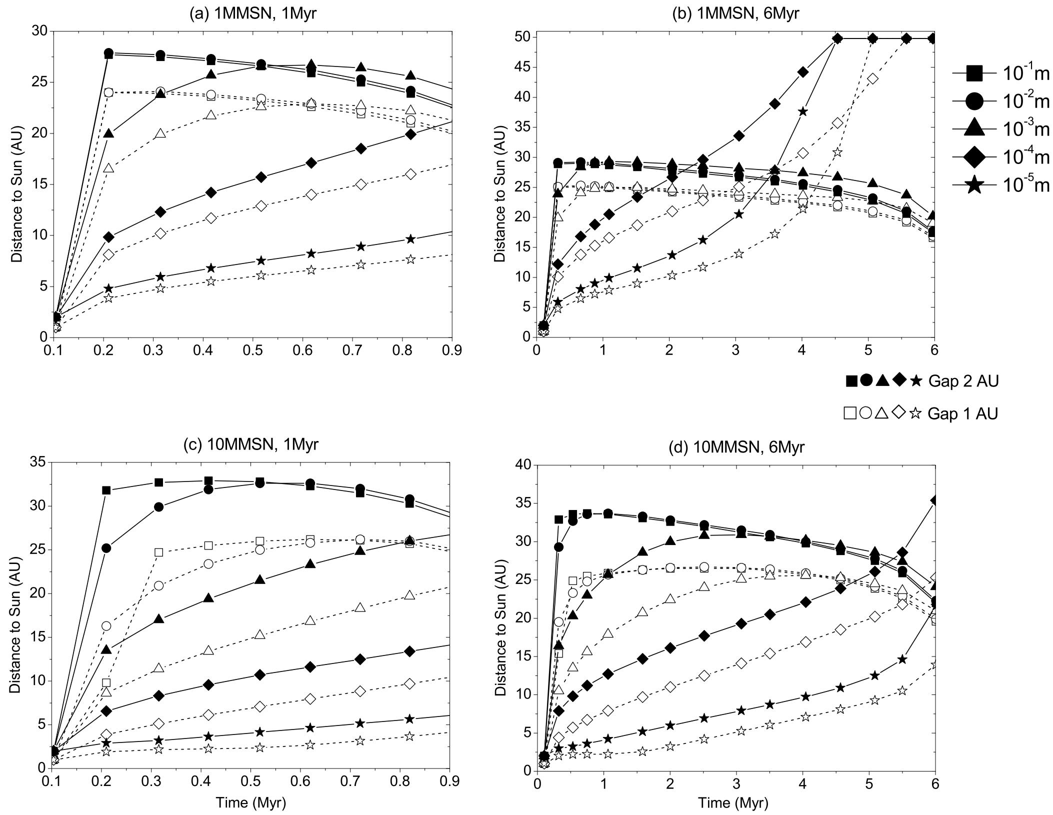

Fig. 1. *Panels (a), (b), (c) and (d) describe the pathway followed by aggregates owning a density of 500 kg.m*$^{-3}$ *as a function of their size and time in the Solar Nebula. Two sizes of inner gaps are considered : 1AU and 2AU. Each plot corresponds to a model of nebula (1MMSN and 10MMSN, with lifetimes of 1Myr or 6Myr).*

our calculations are based on the assumption that the disk opacity is dominated by the Rayleigh scattering and not by that of dust. Moreover, the figures show that 10^{-3}–10^{-1} m aggregates reach an equilibrium where the outward drift just balances the accretion flow, and hence rebound slightly toward the Sun during the late stages of evolution of the disk. Interestingly enough, smaller aggregates (10^{-5}–10^{-4} m) migrate at higher heliocentric distances than the bigger ones (10^{-3}–10^{-1} m) within disks with longer lifetimes. This is due to the progressive decrease of the gas density and opacity that enable the radiation pressure to push the particles beyond the outer edge of our disk models (50 AU).

References

Alibert, Y., Mousis, O. and Benz, W., 2005, ApJ, 622, L145

Augereau, J.-C., Lagrange, A.-M., Mouillet, D., Papaloizou, J.C.B. and Grorod, P.-A., 1999, A&A, 348, 557

Brownlee et al., 2006, Science, 314, 1711

Krauss, O., Wurm, G., Mousis, O., Petit, J.-M., Horner, J. and Alibert, Y., 2007, A&A, 462, 977

Mousis, O., Petit, J.-M., Wurm, G., Krauss, O., Alibert, Y. and Horner J., 2007, A&A, 466, L9

Schneider, G., Smith, B.A., Becklin, E.E., Koerner, D.W., Meier, R., Hines, D.C., Lowrance, P.J., Terrile, R.J., Thompson, R.I. and Rieke, M., 1999, ApJ, 513, L127

Telesco, C. M., Fisher, R. S., Pia, R. K., Knacke, R. F., Dermott, S. F., Wyatt, M. C., Grogan, K., Holmes, E. K., Ghez, A. M., Prato, L., Hartmann, L. W. and Jayawardhana, R., 2000, ApJ, 530, 329

Wahhaj, Z. et al., 2005, ApJ, 618, 385

SF2A 2009
M. Heydari-Malayeri, C. Reylé and R. Samadi (eds)

THE FIELD BROWN DWARFS LUMINOSITY FUNCTION AND SPACE DENSITY FROM THE CANADA-FRANCE BROWN DWARF SURVEY

Reylé, C.[1], Delorme, P.[2], Delfosse, X.[3], Forveille, T.[4], Albert, L.[5], Willott, C.[6] and Artigau, E.[7]

Abstract. Since the first discoveries in 1995, hundreds of field brown dwarfs have been found in DENIS, 2MASS and SDSS. The new generation of large-area surveys uses deeper images and probes a larger volume in the Galaxy, increasing the number of known brown dwarfs. Such surveys are the UKIRT Infrared Deep Sky Survey (UKIDSS) and the one we undertook, the Canada-France-Brown-Dwarf Survey (CFBDS). We expect that complete characterization of all our candidates will yield about 100 T and 400 L or very late-M dwarfs, approximately doubling the number of known brown dwarfs. At mid-course of the CFBDS survey, we are able to define an homogeneous sample of 67 brown dwarfs, from the mid-L dwarfs to the far end of the brown dwarfs observed sequence at the T/Y transition, and to derive a luminosity function.

1 Introduction

Thanks to recent and ongoing large scale surveys, hundreds of brown dwarfs have been discovered. Still the luminosity function of field brown dwarfs is poorly constrained. Recently, Cruz et al. (2007) and Metchev et al. (2008) obtained homogeneous sample to study the space density of cool dwarfs (46 L dwarfs and 15 T dwarfs, respectively). In this work we attempt to compute the luminosity function for dwarfs from L5 to the latest T dwarfs, using a sample of 60 objects in this spectral type range, drawn from the Canada-France Brown Dwarf Survey (hereafter CFBDS). We describe the sample including the determination of completeness and contamination, and photometric classification. The luminosity function is given in the last section.

2 Observations and sample

The CFBDS is fully described in Delorme et al. (2008). The i' and z' imaging part of the survey (900 deg^2) is nearing completion to typical limit of $z' = 22.5$. The reddest sources are then followed-up with pointed J-band imaging to distinguish brown dwarfs from other astronomical sources and spectra are obtained for the latest type dwarfs. As the priority was given for the reddest candidates for J-band follow-up, we can now built a complete sample of late L and T dwarf candidates over 16 patches with total area of 520 deg^2. The sample contain all candidates with $z' < 22.5$ and $i' - z' > 2.0$ detected in this area, that is 191 objects that are candidates cooler than L5 on the basis of their $i' - z'$ colour. A classification is made on the basis of the position in the $i' - z'/z' - J$ diagram (Fig. 1, left panel). Based upon this classification, 81 over the 191 objects remain L5 and later dwarf candidates, the others being dwarfs earlier than M8, artefacts or quasars. Still, M8 and early L dwarfs contaminate the sample as their $z' - J$ colours are similar to those of late L dwarfs.

To estimate the completness of the sample, 1 500 000 fake cool dwarfs built on the observed local PSF are added to the original frames. The resulting images go through the analysis and selection pipelines used to

[1] Observatoire de Besançon, Institut Utinam, UMR CNRS 6213, BP 1615, 25010 Besançon Cedex, France
[2] School of Physics and Astronomy, University of St Andrews, North Haugh, St Andrews KY16 9SS, United Kingdom
[3] Laboratoire d'Astrophysique de Grenoble,Université J.Fourier, CNRS, UMR5571, Grenoble, France
[4] Laboratoire d'Astrophysique de Grenoble,Université J.Fourier, CNRS, UMR5571, Grenoble, France
[5] Canada-France-Hawaii Telescope Corporation, 65-1238 Mamalahoa Highway, Kamuela, HI96743, USA
[6] Herzberg Institute of Astrophysics, National Research Council, 5071 West Saanich Rd, Victoria, BC V9E 2E7, Canada
[7] Observatoire du Mont Mégantic, Université de Montréal, C.P. 6128, Succursale Centre-Ville, Montréal, QC H3C 3J7, Canada

select true candidates. The completeness is given by the fraction of recovered fake objects at the end of the analysis process. The average completness of the sample is 85%. As shown in Fig. 1 (left panel), our sample selects L5 and cooler dwarfs. However, due to photometric errors, part of these <L5 dwarfs are spread within the $i' - z' > 2.0$ sample. All objects with $z' - J < 2.5$ are removed from the sample. They are artifacts with obviously no J-band detection, quasars and dwarfs with true $i' - z'$ colour lower than 1.3, corresponding to M8 and earlier type dwarfs. The measured magnitudes of fake stars compared to the injected magnitudes is used to compute the contamination by >M8 dwarfs. The total number of contaminants is 30.

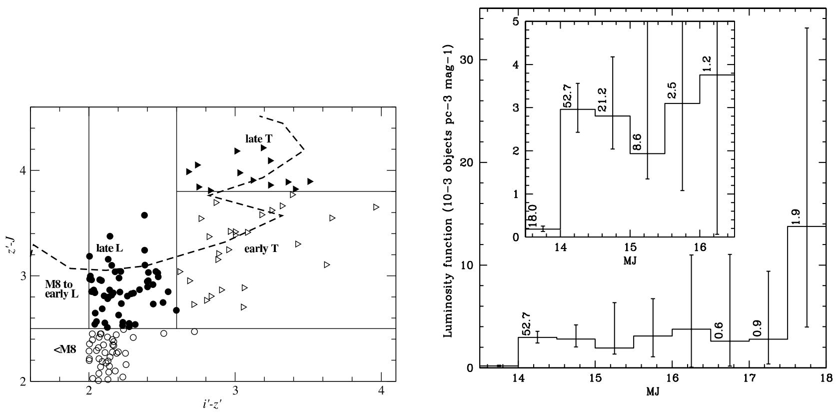

Fig. 1. Left: $z' - J$ versus $i' - z'$ diagram of the brown dwarf candidates in our sample with complete J-band follow-up. Open circles: dwarfs earlier than M8. Filled circles: M8 to L dwarfs. Open triangles: early T dwarfs. Filled triangles: late T dwarfs. The solid lines show the different spectral type regions. Right: Luminosity function in the J band. The number of objects in magnitude bins are also indicated, taking into account completness and contamination

3 Luminosity function

Among the publicly available spectra found in the L and T dwarf data archive, 32 have also measured parallax. They allow us to derive absolute magnitude-colour relations. It appears that the $i' - z'$ colour is a good luminosity estimator for late M and L dwarfs whereas $z' - J$ is better for late T dwarfs. These relations are used to derive photometric distances and a preliminary luminosity function in the z' band, shown in Fig. 1 (right panel). The absolute magnitude of early T dwarfs being nearly constant, this causes a bump in the luminosity function around $Mz' = 17.5$. This corresponds to roughly $M_J = 14$ where such a bump is already known to exist. These results suggest that 6±1 T0.5 to T5.5 dwarfs and 22^{+13}_{-9} T6 to T8 dwarfs are expected in a 10 pc radius sphere around the Sun. To date, 8 T6 to T8 but only two T1 and T2 are found within 10 pc, suggesting that early T-dwarfs are missing in the solar neighbourhood census. The increase of the luminosity function at the faintest absolute M_J is due to 3 T8.5 and cooler dwarfs. This either suggests that many of these extreme objects remain to be discovered in the solar neighbourhood, or that we were lucky finding them. At least 3 additional dwarfs close to the T-Y transition have been discovered in UKIDSS (Burningham et al. 2008, 2009). This could indicate that the strickingly high density of ultracool brown dwarfs found by the CFBDS is not entirely due to a fluke of statistics.

References

Burningham, B., et al. 2008, MNRAS, 391, 320
Burningham, B., et al. 2009, MNRAS, 395, 1237
Cruz, K. L., et al. 2007, AJ, 133, 439
Delorme, P., et al. 2008, A&A, 484, 469
Metchev, S. A., et al. 2008, ApJ, 676, 1281

HERITAGE

Heritage

PROPERTY AND INSTRUMENTAL HERITAGE OF THE BORDEAUX ASTRONOMICAL OBSERVATORY; WHAT FUTURE?

de La Noë, J.[1], Charlot, P.[1] and Grousset, F.[1]

Abstract. In the years 1870, the Government of the Third Republic decided to develop scientific and technical research. Such an effort contributed to supporting and creating universities and other institutes such as astronomical observatories. The dual wish of the Bordeaux council and professors at the Faculté des Sciences de Bordeaux led to the foundation of the astronomical Observatory of Bordeaux. It was set up by Georges Rayet in the years 1880's. The observatory owns a property of 12 hectares with a dozen of buildings, five domes housing an instrument, a Würzburg radiotelescope, a 2.5 meter radiotelescope, and a large collection of about 250 instruments, 4 500 photographic plates, drawings, slides for teaching astronomy, maps of the Carte du Ciel and 200 files of archives. In addition, the library contains about a thousand books for the period 1600-1950. The future of the observatory is not clear at the present time, when the Laboratoire d'Astrophysique will leave to the campus in a few years.

1 Introduction

At the end of the Franco-Prussian war, the defeat of Sedan (September 1870) and the surrender of the Emperor Napoléon III lead to the advent of the Third Republic. After some turbulent years, the new Government decided to develop universities which had been given up during the last two decades. In this framework, some decrees were taken by the Government, in particular about astronomical observatories, under the impetus given by Jules Simon (1814-1896), Minister of Public Education of the Provisional Government and then as Prime Minister. A first decree was signed in 1873 about astronomical observatories, in 1875 about the Bureau des Longitudes. In 1878, several decrees were taken about the foundation of the Besançon, Bordeaux and Lyon observatories. In the meanwhile, Georges Rayet (1839-1906) is appointed lecturer to the chair of astronomy newly created at the Faculté des Sciences de Bordeaux, then given a permanent appointment as professor in 1876. As soon as Georges Rayet settles in Bordeaux, he works for the foundation of the Bordeaux Observatory. In 1877, a property is purchased at Floirac, on the hills of the right bank of the Garonne river by Maréchal de Mac-Mahon, Minister of Public Education, Worships and Beaux-Arts. On 16 January 1879, Georges Rayet is nominated Director of the Bordeaux Observatory and works on the definition of the instruments to be built for astronomical works. He was helped in his task by trips to Italy in 1875 and to Germany in 1879 where he visited a large number of observatories, taking numerous hand-written notes in small notebooks kept in the archives of the observatory.

2 Collection of buildings and instruments

The observatory was constructed in an ancient property successively own by various middle-class persons of Bordeaux growing woods and vineyard. The sixteenth century house, rebuilt and extended in 1839, is used as housing of the director. Georges Rayet supervised the construction of four buildings: the main building housing the meridian circle, two towers for equatorial telescopes and a small building with two separated wings for measuring magnetic field and telluric currents. In addition a meteorology station with various instruments was also installed, since G. Rayet was previously in charge of meteorology measurements at the Paris Observatory and meteorology was also a motivation for the new Bordeaux Observatory (Fig. 1). Three instruments were installed in the 1880's. All details of negotiations between Georges Rayet, the Minister of Public Education, the

[1] Observatoire Aquitain des Sciences de l'Univers, Laboratoire d'Astrophysique de Bordeaux, BP 89, 33270 Floirac, France

Fig. 1. The Rayet building with central part housing the meridian telescope, Cliché Rose©INSU.

city of Bordeaux, and the instruments makers are found in Maison (2004). They were ordered to the instrument maker William Eichens (1818-1884) in Paris. The first one is the meridian telescope with an aperture of 18,95 cm, installed in 1880, in the central part of the building now called the "Rayet building". The meridian circle successively went through different technical modifications to improve the quality of measurements, the last one in the 1980's, when it was completely renewed, automated and controlled by a computer and the installation of a CCD camera. The internationally known instrument participated to the preparation of the input catalogue of the HIPPARCOS space mission. It is still in operation and several observation programmes are going on (Fig. 2).

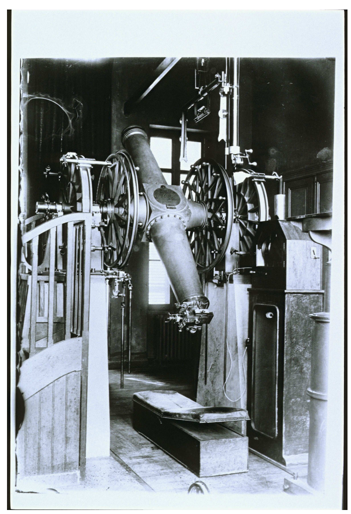

Fig. 2. The meridian telescope around 1890, Cliché M. Dubau©inventaire général ADAGP.

In 1880 a small equatorial telescope with an aperture of 18 cm was ordered, to be built by W. Eichens while the optic was made by Paul (1848-1905) and Prosper Henry (1849-1903) at the Paris Observatory. When Eichens was seriously ill and unable to go on with the construction of the some other ordered telescopes, different negotiations were undertaken between the directors of observatories and the Minister of Public Education to nominate Paul Gautier (1842-1909) in charge of the construction of instruments instead of Eichens' son. Finally the instrument was installed in 1881 (Fig. 3).

A large equatorial telescope with an objective of 38 cm was also ordered to W. Eichens and finalized by P. Gautier. The objective was ordered by G. Rayet during his trip in Germany in 1879 to the lens maker Merz. The instrument was operational in 1883. It served to observe comets and multiple stars thanks to its high

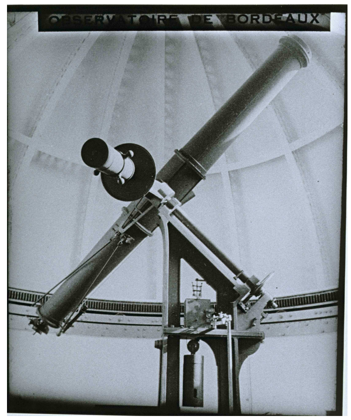

Fig. 3. The small equatorial telescope around 1890, Cliché M. Dubau©inventaire général ADAGP.

resolution power (Fig. 4).

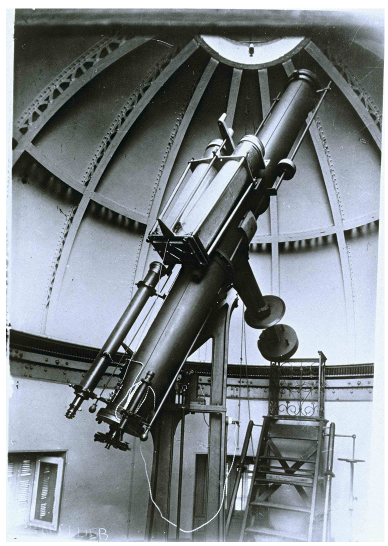

Fig. 4. The large equatorial telescope around 1890, Cliché M. Dubau©inventaire général ADAGP.

In the framework of the first large international project " Carte du Ciel " decided in Paris in 1887 and for Bordeaux described by Le Guet-Tully et al. (2008), an equatorial photographic telescope was built from the model of the prototype instrument designed and built by the Henry brothers at the Paris Observatory. Three such instruments were financed and ordered in 1889 by the Ministry and installed in Bordeaux, Toulouse and Alger. The astro-graphic telescope made by P. Gautier was inaugurated in 1891, the first plates being obtained in 1892. It is composed of two parallel telescopes with objectives of 33 cm, one being dedicated to observations to the eye, the second one to photography with photographic plates of 16 x 16 cm. A specific tower was built associated to a photographic laboratory and to a room for storing and measuring the plates (Fig. 5). After the death of Georges Rayet, Luc Picart (1867-1956) was nominated director from 1906 to 1937. Then Gilbert Rougier (1886-1947), from the Strasbourg Observatory, took the direction and was in charge of the construction of a large building (now named "Bouguer") in the years 1942-1943, as well as the tower containing an equatorial table, now holding up a mirror telescope of 60 cm diameter, equipped with a new CCD camera. Pierre Sémirot (1907-1972) succeeded G. Rougier and developed the observatory by introducing radioastronomy techniques et observations in the years 1960's, with the installation of a radiotelescope using a Würzburg parabolic radar mirror of 7.5 m diameter, from the Second World War. P. Sémirot also constructed a new building (now named " Sémirot " building) in 1968, which was extended in 1986. Thus the Bordeaux observatory displays a panorama

Fig. 5. The photographic equatorial telescope around 1892, Cliché M. Dubau©inventaire général ADAGP.

of more than a hundred years of architecture. Recently, the "Commission régionale de protection des sites" of the Direction régionale des Affaires culturelles decided to protect nine of the twelve buildings (and instruments) of the observatory.

3 Collection of small instruments and other pieces

In addition to these observation instruments, the observatory owns a collection of about 250 smaller instruments: 150 instruments used in astronomy, 25 clocks and apparatus for time measuring, 15 instruments for meteorology and Earth physics measurements, 12 apparatus for geodesy, 7 instruments used for telegraphy, 5 photographical cameras, about 15 instruments for various uses. There are also 15 pieces of furniture as the director's desk and six associated arm chairs (end nineteenth century), leather beds and stepladders associated with the telescopes (Fig. 6) and (Fig. 7).

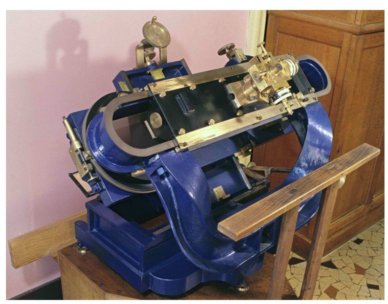

Fig. 6. Blink microscope built by P. Gautier in 1908, Cliché M. Dubau©inventaire général ADAGP.

For the period 1891-1996, the equatorial photographic telescope produced more than 5 000 photographic plates of which 4 322 are perfectly identified and well preserved at constant temperature and hygrometry. 500 of them were digitized (Ducourant et al. 2006; Rapaport et al. 2006). In 1890's, in order that astronomers be acquainted with photographical techniques, about 50 plates were taken of the buildings, instruments and persons of the observatory. Later on in the 1940's, Dubois (1950) took several hundreths photographical plates and spectra either at Floirac or at the Pic du Midi Observatory to study the Earth's shadow. There is also a large collection of glass slides used for teaching astronomy at the university.

A few drawings and watercolours complete the collection of observations made at the end of the nineteenth century. A very large number of printed maps either of the " Carte du Ciel " or of the Schmidt telescope of the European Southern Observatory is also kept in specific drawer furnitures. Finally, the observatory owns a very large of ancient and more recent documents of astronomy: a thousand books from 1605 to now, notices, periodic journals, etc. 200 files contain scientific, administrative and historical archives since the foundation of the observatory.

Fig. 7. Heliostat of Silbermann type, built by Duboscq in 1883, Cliché M. Dubau©inventaire général ADAGP.

4 Conclusions

The important collection of the Bordeaux astronomical Observatory belongs to the Université Bordeaux 1 as one of the nine scientific collections: Prehistory, Anthropology, Geology, Mineralogy, Palaeontology and micro-Palaeontology, oceanic cores, animal Biology and the collection of ancient books of the university library. All collections are presented in a brochure (Collective team 2006). At the present time, all collections are scattered in different places and buildings, sometimes in very bad conditions of preservation. Scientits in charge of the various collections are working together to speak in favour of getting a position of curator, to make known the great variety and the importance of university collections by publishing papers and preparing an exhibition to be presented in Bordeaux in 2010.

Therefore, there is a threat of danger for the astronomy collection since, in October 2006, the Direction of Research of the Ministry of National Education has scheduled that astronomers and technicians of the Laboratoire d'Astrophysique de Bordeaux should move to the Université Bordeaux 1 campus in Talence, as soon as possible. The desertion of the historic site of the observatory hangs over the future of the site threats of housing estate if the university, in the framework of its autonomy, does not decide to build a project of science animation site, as it could be possible in the framework of plans of a green belt of parks on the hills Hauts de Garonne, made by the urban community of Bordeaux.

References

Armand, D., de La Noë, J., Bessou, M., Boutin, A., Cahuzac, B., Courtaud, P., Gauvain C.-L., Lachaud, L., Londeix, L., Mémoire, N., Pape, J.-R., Pubert, é., Rousseau, J.-M., Surville, M. and Turon, J.-L. 2009, Proceedings of the General Assembly of CTHS, in press.

Collective team 2006, Les collections de l'Université Bordeaux 1, ed. Université Bordeaux 1(Talence: Université Bordeaux 1), 26 p.

Ducourant, C., Le Campion, J.-F., Rapaport, M., Camargo, J. I. B., Soubiran, C., Perié, J.-P., Daigne, G., Triaud, A., Requième, Y., Fresneau, A. and Colin, J. 2006, A &A 448, 1235.

Le Guet-Tully F., de La Noë, J. and Sadsaoud, H. 2008, La Carte du Ciel, histoire et actualité dun projet scientifique international, ed. J. Lamy (Paris: EDP Sciences), 69.

Maison, L. 2004, La fondation et les premiers travaux de lobservatoire astronomique de Bordeaux (1871-1906) : Histoire dune réorientation scientifique, Ph. D. Thesis, ed. L. Maison, (Talence: Université Bordeaux 1), 431 p.

Rapaport, M., Ducourant, C., Le Campion, J.-F., Fresneau, A., Argyle, R. N., Soubiran, C., Teixeira, R., Camargo, J. I. B., Colin, Daigne, G., J., Perié, J.-P. and Requième, Y. 2006, A &A 449, 435.

SF2A 2009
M. Heydari-Malayeri, C. Reylé and R. Samadi (eds)

THE HERITAGE OF THE STRASBOURG ASTRONOMICAL OBSERVATORY

Issenmann D.[1] and Dubois P.[2]

Abstract. The history of the Strasbourg astronomical Observatory is an illustration of the political, cultural and scientific history of the country.

1 Introduction

The present Observatory is the third one in Strasbourg. The first one was erected in 1673 on a tower of the outer walls of the town. The second one was installed in 1828 on a building of the Academie. When Alsace was transfered to Germany in 1872, Emperor William 1st decided to use Strasbourg to promote its empire by including a prestigious university, with an astronomical observatory.

2 The heritage

This architectural set, built in the 1880s, occupies a strategic place in the new district built by the Germans. Alternately German or french, this observatory, which is still a place for university research, has been a witness of scientific and technical developments in astronomy since the late 19th century, and of the political history of Alsace as well. The richness of the architectural and instrumental heritage bears evidence of this prestigious past. This heritage, because it is probably less conventional and more unusual, is sometimes misunderstood by the public and especially astronomers themselves. To strengthen the knowledge and accessibility of such wealth, the instruments of observatories have been for a few years identified and studied by the Inventaire (Inventory Department of the French Ministry of Culture) in a partnership between French Ministry of Culture and Ministry of Research. The inventory work on the ancient instruments of the Strasbourg Observatory is part of this national program. But it is also based at the local level on a convention between the University of Strasbourg and the regional service of the Inventory of cultural heritage (Alsace). The aim is to study and document the scientific heritage of the University and then to identify its specificities. This allows the implementation of a appropriate policy to safeguard and promote both buildings and instruments, notably through a database accessible to all.

3 The database

The database is presently open at
`http://www.hp-physique.org/sdx/sriaulp/main.xsp?form=disc_query_form`

[1] Université de Strasbourg, 4 rue Blaise Pascal, 67000 Strasbourg, France
[2] Observatoire astronomique de Strasbourg, 11 rue de l'Université, 67000 Strasbourg, France

SF2A 2009
M. Heydari-Malayeri, C. Reylé and R. Samadi (eds)

LE PATRIMOINE DE L'OBSERVATOIRE DE LYON: ETAT DES LIEUX

Rutily, B.[1]

Abstract. This Note describes the heritage of the Observatory of Lyon. After drawing up a short inventory, we summarize the policy to safeguard this heritage and evoke its current physical status. We then move to the future, which is uncertain in Lyon as in other provincial observatories.

1 Introduction

L'Observatoire de Lyon, créé en 1878 en même temps que les observatoires de Bordeaux et Besançon, regroupe l'essentiel du patrimoine astronomique de la région lyonnaise. En effet, il a hérité des instruments qui équipaient l'observatoire municipal l'ayant précédé au 19ème siècle, et à la fin des années 1980, il a reçu en dépôt les principaux instruments d'un site astronomique lyonnais contemporain du sien: l'observatoire religieux de Fourvière. Aujourd'hui le sort de ce patrimoine est incertain, à cause d'un projet de migration des astronomes lyonnais sur le campus universitaire de la Doua. À Lyon comme à Toulouse, Marseille et Bordeaux, se pose la question du devenir d'un patrimoine resté sur son site d'origine, une fois que les astronomes l'auront quitté. Le problème est d'importance, il mérite sûrement une réflexion au niveau national.

2 Le patrimoine de l'Observatoire de Lyon

L'Observatoire de Lyon a été construit entre 1879 et 1887 au sommet d'une colline de 300 m d'altitude située sur la commune de Saint-Genis-Laval, à une dizaine de kilomètres du centre de Lyon. Dans son parc de 4 ha, magnifiquement arboré, ont été édifiés une vingtaine de bâtiments, dont la moitié datent de la fin du 19ème siècle. Les pavillons anciens se divisent en trois catégories:
- ceux qui abritaient des instruments d'observation (les deux salles méridiennes, la coupole de la lunette de Brunner, le pavillon de la lunette équatoriale coudée) ou des appareils de mesure (le pavillon météorologique, le pavillon magnétique),
- le pavillon administratif, dit aujourd'hui pavillon Lagrange, qui contenait les bureaux des astronomes et leur bibliothèque,
- les bâtiments à vocation non scientifique: le château d'eau et les trois logements de fonction, dont la très belle maison du directeur.

Le patrimoine instrumental et mobilier de l'observatoire comprend:
- de gros instruments: lunettes anciennes, méridiennes ou équatoriales (cercle méridien d'Eichens de 15 cm d'ouverture, lunette équatoriale coudée de 35 cm, lunette de 32 cm du sidérostat, deux lunettes de 16 cm d'ouverture) et deux télescopes datant des années soixante (60 cm et 1 m d'ouverture),
- des petits instruments astronomiques: trois quarts de cercle du 18ème siècle (1 mural, deux sur pieds), un petit cercle méridien portatif de 6 cm d'ouverture, 4 lunettes astronomiques sur pieds, des instruments d'astronomie de position (théodolites, ...), des instruments de mesure du temps (6 régulateurs, dont un électrique),
- des petits instruments de météorologie, de géophysique (magnétisme terrestre) et de physique,
- des objets décoratifs divers (globes terrestre et céleste, bustes, ...) ou illustrant la vie scientifique du laboratoire (machines à calculer ou à écrire, récepteurs télégraphiques,...).

Ne pouvant illustrer cet inventaire par des images par manque de place, nous renvoyons le lecteur au diaporama qui termine l'article "L'Observatoire de Lyon" de notre site WEB (http://www-obs.univ-lyon1.fr), rubrique "Patrimoine".

[1] Observatoire de Lyon, 9 avenue Charles André, Saint-Genis-Laval, F-69230, France

3 Gestion du patrimoine lyonnais

Cette gestion est confiée à un groupe particulièrement actif et idéalement constitué, puisqu'il comprend:
- le directeur de l'observatoire,
- les responsables de quatre services: Mécanique, Optique, Diffusion des Connaissances et Parc, ainsi que leurs collaborateurs directs: 6 personnes au total,
- 5 astronomes, dont deux déjà comptés,
- un historien des sciences et astronome amateur de haut niveau,
- le responsable du groupe de travail "Patrimoine scientifique et technique" de l'Université Lyon 1.

Les 12 membres de ce groupe se réunissent en moyenne deux fois par an, et invitent régulièrement Françoise Le Guet Tully (astronome à l'Observatoire de la Côte d'Azur) et Jean Davoigneau (Ministère de la Culture et de Communication, Direction de l'Architecture), qui apportent aux débats leur vision globale du patrimoine astronomique national.

Voici un résumé succint des principales actions entreprises depuis 2001:

1) *Achèvement de l'inventaire commencé en décembre 2001*:

L'inventaire du patrimoine astronomique français est une opération nationale lancée au début des années 1990 conjointement par les ministères de la Culture et de la Recherche. Elle a été supervisée par Jean Davoigneau et Françoise Le Guet Tully, dont il vient d'être question. Leur passage à Lyon en décembre 2001, accompagnés de deux experts en instruments scientifiques anciens, a permis de dresser une première liste des instruments les plus intéressants de l'observatoire, avec leur photographie. Ces éléments ont été complétés jusqu'à l'achèvement de l'inventaire en novembre 2007. Ce travail de longue haleine a permis le stockage rationnel, dans un lieu sain, des petits instruments et objets qui se trouvaient disséminés aux quatre coins de l'observatoire. L'inventaire actuel comprend 654 "petits" objets, 13 "grands instruments", 30 ouvrages et documents (inventaire très incomplet sur ce point), 31 éléments immobiliers (salles, coupoles, bâtiments) et 8 films, photographies ou séries de photographies.

2) *Protection du site au titre des monuments historiques*:

Cette action a également été initiée par Jean Davoigneau et Francoise Le Guet Tully, en décembre 2002. Elle a abouti, cinq ans plus tard, aux mesures de protection suivantes:
- janvier 2007: inscription, au titre des Monuments Historiques, de l'ensemble du site: bâtiments et parc,
- juin 2007: inscription de 43 instruments et objets anciens,
- juin 2007: classement de la lunette équatoriale coudée, de ses accessoires (micromètres et chronographe) et de son pavillon, classement de la lunette méridienne et de ses piliers et accessoires, classement des trois quarts de cercle du 18ème siècle, d'un régulateur Hipp et d'un anémomètre Neumann.

3) *Dépôt des archives aux Archives Départementales*:

Une première vague d'archives a été déposée en septembre 2005, une deuxième vague en juin 2007. Il est également prévu de déposer nos clichés. Nous participons au tri des archives, qui n'est pas encore terminé.

4) *Restauration de la lunette équatoriale coudée*:

Suite au classement de cette lunette et du bâtiment qui l'abrite, un dossier a été constitué pour obtenir le financement de leur restauration. En même temps, nous avons proposé de créer un petit espace muséal au rez-de-chaussée du pavillon du Coudé, et un lieu d'expériences dans la grande galerie qui parvient au sous sol de ce bâtiment. Notre demande, adressée au Ministère de la Recherche et de l'Enseignement Supérieur, a reçu un accueil favorable puisqu'une subvention de 230 k€ nous a été accordée en octobre 2008. Les travaux devraient commencer courant 2010.

5) *Autres actions*:

Réfection de la coupole abritant à l'origine la lunette de Brunner (16 cm), remise en station de cet instrument, consultation d'archives et autres recherches en histoire des sciences, recherches archéologiques même, puisque le groupe vient de retrouver la mire sud lointaine de notre lunette méridienne...

Cette liste non exhaustive illustre le degré de motivation et le dynamisme des membres d'un groupe qui se passionne de plus en plus pour le site qu'il fréquente, et qui continue à accréter régulièrement parmi le personnel de l'observatoire. Nous estimons à environ 15% la fraction de ce personnel qui s'intéresse aujourd'hui au patrimoine de l'observatoire.

4 Aspect humain: un faisceau de circonstances favorables

Nous venons d'évoquer la première circonstance favorable au développement des activités patrimoniales de l'observatoire: le nombre et le dynamisme des membres du groupe "Patrimoine". Parmi ces membres figure Bruno Guiderdoni, l'actuel directeur de l'observatoire, qui soutient sans réserve nos actions et y joue même un rôle moteur. Un autre membre important, extérieur à l'observatoire, est Jean-Francois Jal, l'actuel responsable du groupe de travail "Patrimoine scientifique et technique" de l'Université Claude Bernard Lyon 1. Physicien de formation, passionné d'astronomie, J.F. Jal est un adepte inconditionnel de notre site, qu'il fréquente régulièrement. Le président actuel de l'Université Lyon 1 est également intéressé par la valorisation du patrimoine de son établissement et la soutient, dans des limites budgétaires strictes comme on l'imagine.

Les relations avec l'Université sont donc bonnes, ce qui ne signifie pas qu'elles sont toujours faciles. En effet les universitaires ont leur propre politique patrimoniale, par essence pluridisciplinaire, et les astronomes ont tendance à se consulter et à développer leur propre politique, une attitude que nous encourageons pour des raisons historiques évidentes. Il est parfois difficile de concilier ces deux lignes de conduite orthogonales, même à Lyon.

Enfin mentionnons l'excellence de nos relations avec la ville de Saint-Genis-Laval, qui est omniprésente dans nos actions grand public: soutien logistique et financier, collaboration avec le service Communication de la mairie et avec le CADEC (Conseil d'Animation et de Développement Culturel), qui fédère les activités des associations Saint-genoises. Cette structure nous a permis de travailler avec l'une de ces associations lors des dernières journées du patrimoine.

5 Les points négatifs

Le principal d'entre eux est l'état de vétusté dans lequel se trouve la quasi-totalité des bâtiments de l'observatoire, et aussi ses instruments anciens. La plupart des bâtiments n'ont pas été entretenus depuis plus de 15 ans et doivent être révisés. Il n'y a pas de problème majeur, mais les travaux à effectuer sont nombreux. Nous avons grossièrement estimé le coût d'une remise à niveau du parc immobilier, qui est de l'ordre de 1 M€.

Les instruments anciens sont pour la plupart dans un triste état. Les instruments métalliques sont fortement corrodés, ce qui nécessite un traitement d'urgence. Quelques objets ont pu (ou vont) être restaurés aux frais des musées auxquels nous les avons prêtés. C'est le cas de notre cercle méridien et de notre quart de cercle mural, qui doivent être exposés au musée des Confluences de Lyon. Pour les autres instruments, nous espérons un retour favorable à une demande de crédits adressée au Ministère de l'Enseignement Supérieur et de la Recherche pour le quadriennal 2011-2014. Rappelons que ce ministère a déja financé, fin 2008, la restauration de la lunette équatoriale coudée et de son bâtiment.

Un autre point négatif concernant notre parc instrumental est l'absence de lieu de présentation au public de nos petits instruments. La lunette coudée est le seul instrument ancien que nous montrons à nos visiteurs, ce qui est paradoxal dans un observatoire largement ouvert au public: nous recevons de l'ordre de 5000 visiteurs par an, dont une forte proportion de scolaires.

6 Perspectives d'avenir

La plupart des observatoires de province ont été implantés au 19ème siècle sur des sites isolés plus ou moins excentrés de leur ville de rattachement. Aujourd'hui l'isolement de ces sites n'est plus justifié par des considérations scientifiques, ce qui explique le déplacement passé ou à venir de certains observatoires (Toulouse, Marseille, Bordeaux et peut-être Lyon).

Le plan Campus présenté par l'Université de Lyon, et accepté en mai 2008, prévoit que les astronomes lyonnais rejoignent le campus de la Doua dans les années 2013-2015. Ce déplacement est encore incertain, il devrait être confirmé ou infirmé à la fin de l'année 2009. S'il est confirmé, le problème de la sauvegarde du patrimoine astronomique lyonnais, resté sur un site déserté des astronomes, se pose. Une solution est en cours de discussion, elle consiste à transformer le site en un lieu d'accueil massif du public ayant la triple vocation suivante:

- présenter le patrimoine astronomique lyonnais, en essayant de le faire revivre,
- poursuivre et étendre les activités de diffusion des connaissances mises en place depuis plus d'un quart de siècle. L'accueil du public est pour l'instant centré sur l'astronomie et l'observation du ciel, mais nous souhaitons l'étendre aux sciences physiques, en proposant au public des expériences de laboratoire réalisées avec les instru-

ments anciens de nos collègues physiciens de l'université, ainsi que ceux de l'observatoire,
- promouvoir les sciences de la matière et de l'univers en évoquant les progrès récents de la science et de l'instrumentation. Grâce à la construction d'une salle de conférences (120 places) et celle en cours d'une cafétéria (80 places), il est possible d'organiser sur place des cycles de conférences, des journées scientifiques à thème, d'accueillir dans d'excellentes conditions le public des opérations médiatiques nationales : nuit des étoiles, journées du patrimoine, Fête de la Science, etc.
Ce projet est en état de gestation seulement, la première version d'un texte le décrivant vient d'être rédigée.

7 Conclusion

Nous traversons une période de grande incertitude sur l'avenir du site de l'Observatoire de Lyon. Nous avons souligné la volonté d'une fraction importante du personnel de sauvegarder et de valoriser ce site. Notre projet "Musée" concrétise cette volonté. Dans le climat actuel, il devrait recevoir un accueil de principe favorable des dirigeants de l'Université de Lyon. Il n'en reste pas moins vrai que cette dernière fonctionne désormais comme une entreprise, et que l'aspect comptable va être prépondérant dans sa décision d'accepter ou non le transfert de propriété de l'observatoire dans le cadre des responsabilités et compétences élargies prévues par la loi LRU. Nous avons souligné la vétusté de nos bâtiments, ce qui est un point négatif important. Les frais d'infrastructure de l'observatoire ont également la réputation d'être élevés auprès des gestionnaires de l'université. La recherche de fonds privés (mécénat) n'est pas favorisée par la crise économique que nous traversons.
Ces préoccupations ne sont pas sans rappeler celles d'autres observatoires ayant été délocalisés ou sur le point de l'être (Toulouse, Marseille et Bordeaux). La priorité est de sauver le parc instrumental des quatre observatoires. Les informations dont nous disposons sur les trois autres sont partielles et plutôt pessimistes, aussi proposons-nous d'améliorer la communication entre ces observatoires, par exemple en suggérant aux responsables du patrimoine de dresser un état des lieux similaire à celui de cet article et de le diffuser. Il est souhaitable que chaque site puisse continuer à faire vivre son patrimoine et évite la dispersion de ses instruments, de sorte que la belle unité de nos observatoires de province soit préservée. À défaut de solution locale acceptable, nous sommes favorables à une solution globale du problème posé, c'est-à-dire au regroupement des instruments en un lieu unique. Ce dernier pourrait devenir, à terme, ce musée national de l'astronomie qui fait défaut à notre pays. [1]

Je remercie mes collègues du groupe "Patrimoine" de l'Observatoire de Lyon (Gilles Adam, Christian Blanc, Alain Brémond, Jean-Pierre Dubois, Bruno Guiderdoni, Jean-Francois Jal, Johan Kosmalski, Emmanuel Pécontal, Edgard Renault, Isabelle Vauglin, Emilie Wernli) pour leur relecture critique de cet article.

[1]Nous rejoignons ainsi le point de vue de Françoise Le Guet Tully, que résument ces lignes tirées d'une communication privée: "L'opération d'inventaire du patrimoine astronomique français a permis de constater la richesse de celui-ci en terme de patrimoine matériel (sites, architecture, grands instruments, petits instruments, archives, fonds de bibliothèque) et immatériel (histoire institutionnelle croisée, acteurs scientifiques et non scientifiques, savoir-faire, etc.). Elle a aussi permis de mettre en évidence similitudes et complémentarités instrumentales entre les observatoires de province et l'observatoire de Paris. Elle a enfin souligné l'absence en France de musée thématique sur l'astronomie et sur son patrimoine, alors même que celui-ci est d'une richesse exceptionnelle sur un plan international".

SF2A 2009
M. Heydari-Malayeri, C. Reylé and R. Samadi (eds)

LILLE OBSERVATORY: A UNIVERSITY HERITAGE

Vienne, A.[2]

Abstract. Lille observatory was a private research structure from 1909 to 1933, but it was declared "Observatory of Lille University" in 1912. So from the beginning, the actions of the observatory were linked to research observations (measurements of double stars) and to pedagogic activities with students. In 1933, all the astronomical instruments (including the 32.5 cm telescope with a focal length of 6 m) were transfered in Lille and the new observatory became a public structure incorporated into the university. Nowadays, the scientists of Lille observatory are a team of the CNRS/UMR8028 (IMCCE, Paris Observatory, Lille 1, Paris 6), and still use the telescope for science and teaching purposes. In 2009, within the framework of the centenary of the telescope, Lille university leads several actions to promote its heritage (including restorations of the dome and the offices).

1 Introduction

The Observatory of Lille university houses a group of lecturers and researchers in celestial mechanics. They take part in computing the national ephemerids which, according to the law of *7 messidor an III* (25th June 1795), are the liability of the "Bureau des Longitudes". The history of this observatory is complex but strongly related to that of Lille university. The observatory exists since 1909, and has been declared *Observatoire de l'Université de Lille* according to the ministerial decree of the 6th July 1912, but the scientific instruments has been owned by the university in 1933 when it has been transfered from Hem to Lille. I present here its history since its foundation until its present activities in order to understand its place in the regional and university scene.

2 The foundation of the Observatory

One hundred years ago, Robert Jonckheere, the son of a rich manufacturer in Roubaix built an astronomical observatory to satisfy his passion. The building, set in a small hill of Hem, was worthy of national observatories at this epoch: a refracting telescope of 325 mm of aperture and of 6 m of focal. We could find there a library, some offices, a meteorologic station and a house.

Rapidly, contacts are established between Hem observatory, the North department and Lille university. Daily meteorologic bulletins were established there. The observatory took part also into the times service and gave some lectures (including the use of the refractor) for students of the university. Then, the 26th June 1912, the council of the university voted that the observatory of Hem is an attached unit. In July, from a ministerial decree, it was the "Observatory of the Lille university". Robert Jonckheere lived in his observatory where four persons were working. He continued to measure the double stars (Jonckheere 1911). With these studies, R. Jonckheere became internationally famous (Jonckheere 1962).

Nevertheless, after the first world war and the following economic difficulties, Robert Jonckheere was not able to finance the running and the maintenance of his observatory. After several years of negotiations, he sold his scientific instruments to Lille university in 1929.

Fig. 1. Observatory of Lille university (photo: Obs. Lille)

3 The Observatory of Lille university ... in Lille

Around 1930, under the influence of Roger Salengro, the Mayor of Lille, the district *Lille-Moulins* had been restored. The project corresponded to a social politic and a scientific orientation. Hence, the fluid mechanics institute, the Denis Diderot institute, the open-air school, the botanical garden and the Lille Observatory were built. The latest received all the instruments of the Hem observatory, including the telescope. Lille observatory was inaugurated the 8th December 1934.

Despite his requests, Robert Jonckheere could not access to a research position in this new institution because of a lack of university degree. Then he left Lille and lived in Marseille where he had several jobs. During the second world war he made him know at Marseille observatory where he became a professional astronomer in CNRS (*Centre National de la Recherche Scientifique*). He kept on with his studies and his discovers of double stars. He became editor-in-chief of the *Journal des Observateurs*. At the end of his career, he had obtained several important scientific prizes. He retired in 1962 and died the 27th June 1974.

So, the existence of an astronomical observatory at the north of Paris is due to the will of both the city council and the university of Lille. It is due also to the opportunity to obtain a scientific material built at the beginning of the century by an enthusiast astronomer. At the university, this will was carried in particular by mathematicians: Albert Châtelet, Joseph Kampé de Fériet and the first director of Lille observatory, Charles Galissot (from 1934 to 1951). We know very few about him and even about this epoch. The group *Association Jonckheere Les Amis de l'Observatoire de Lille* leads research in this way. Later, from 1952 to 1962, the director was Vladimir Kourganoff. He was born in Moscow in 1912, he had brilliant studies in France and abroad (Berkeley, Oslo, ...). His research concerned as well the study of the interior of stars and cosmological theories. Then Pierre Bacchus has been the director from 1962 to 1986. Before arriving in Lille, he was professor at Strasbourg observatory where, with the professor Lacroute, he had the idea to use a satellite in space in order to measure precisely the positions and the motions of stars (Bacchus & Lacroute 1974). This idea was at the origin of the international astrometric project Hipparcos. He handed, by its personality and its very clear pedagogy, the taste of astronomical computations. The reader can see on the website of the "association Jonckheere", the homage paid by his former student Luc Duriez who was in charge of the Observatory between 1986 to 1989. Irne Stellmacher took then the direction until 2003. Coming from the Computations Department of the Bureau des Longitudes , known nowadays as IMCCE (*Institut de Mécanique Céleste et de Calcul des Ephémérides*), she has worked on the administrative link between Lille observatory to this department. This link has been made very naturally because the astronomers of the observatory already worked to make ephemeris (Duriez 1982; Vienne & Duriez 1992).

[1] Université Lille 1, LAL-IMCCE, 1 impasse de l'Observatoire, F-59000 Lille, France

[2] Institut de mécanique céleste et de calcul des éphémérides-Observatoire de Paris, UMR 8028 du CNRS, 77 avenue Denfert-Rochereau, F-75014 Paris, France

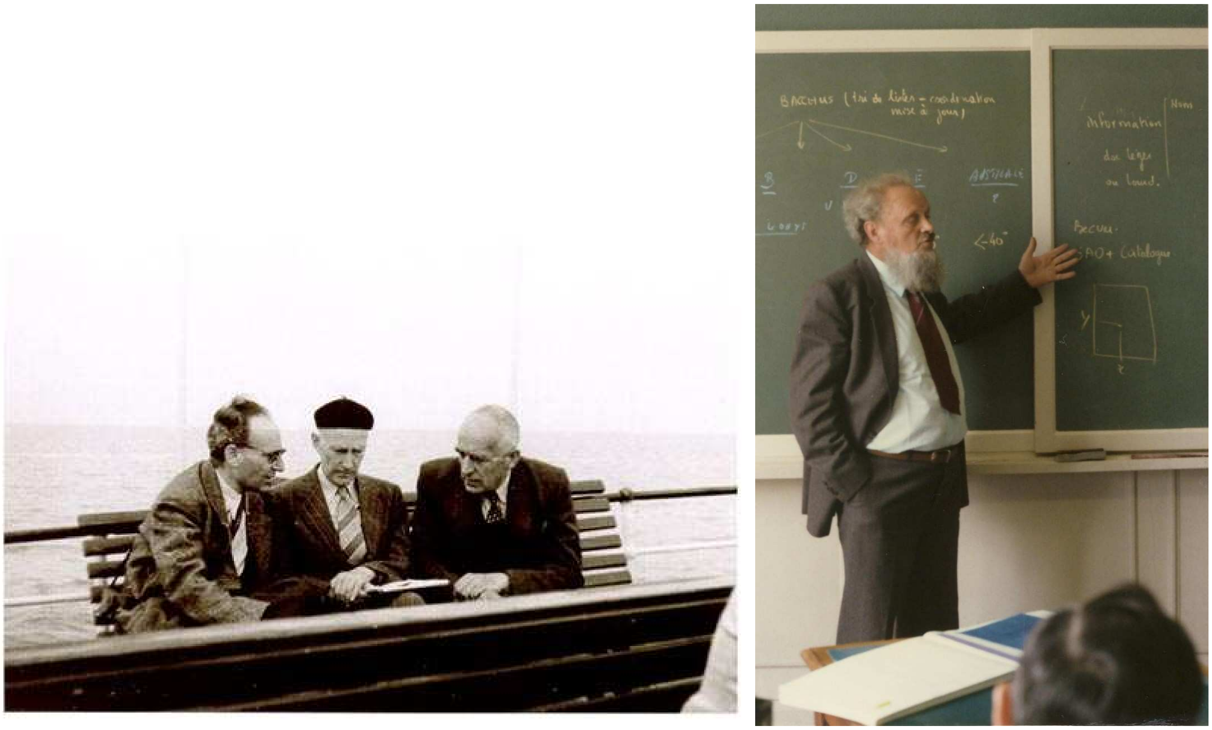

Fig. 2. Left : V. Kourganoff, J.H. Oort and H. Spencer in 1953 (photo: ESO). **Right**: Pierre Bacchus in 1986 (Photo: SAF).

4 Science, students and observations

Then, the astronomers of Lille observatory built general theories of motion of the planets of the solar system (that is, theories with a lower precision than the ones published but, on the other hand, valid over several million years), theories of motion of natural satellites which orbit around Jupiter and Saturn. More generally, their research concerns dynamics of the gravitational systems and dynamical planetology : search for scenario of formation of resonance, study of tides in the considered bodies (and then linked with their internal structure such as the possibility of an ocean inside Enceladus), long term dynamics of comets, capture of satellites ...

The refractor of 35 cm is sometimes used for scientific purposes but it is especially used for pedagogical activities. Astronomical lectures are given to students preparing their License in mathematics or physics. When the sky is clear, practical works are organized in order to familiarize these students to observe stars with the telescope. Since 1999, an agreement between the planetarium of Villeneuve d'Ascq (near the campus) and Lille 1, allows amateur astronomers to use the refractor for their own observations. At last, the group Jonckheere association follows a scientific program of observations of double stars, just as Robert Jonckheere began one hundred years ago!

5 Conclusion

We can summarize the hundred years of Lille by these main following points:

- It has been a private structure from 1909 to 1933.
- But it was named "Observatory of Lille university" since 1912.
- It was transfered to Lille city and managed by the university in 1933.
- Since, it is a university laboratory with about 3 or 4 lecturers researchers.

Fig. 3. The 32.5cm telescope with a focal length of 6 m of Lille observatory (photo: Asso. Jonckheere).

- It is a team of the IMCCE (a laboratory labeled by CNRS) since 1998. IMCCE is managed by Paris observatory and secondary by the university of Paris 6 and the university of Lille 1. 20 researchers and 20 technicians or engineer work there.

In 2009, for the centenary, of the telescope, the new presidency of Lille university undertakes to restore the dome, the offices, the patrimonial space, ... Then it is show that Lille university want to take advantage of the existence of an instrument liked by students and, more generally, by many people.

References

Bacchus, P., & Lacroute, P. 1974, Prospects of Space Astrometry, in New Problems in Astrometry; Proceedings of the Symposium, Perth, Australia, August 13-17, 1973. Edited by W. Gliese, C. A. Murray, and R. H. Tucker.

Duriez, L. 1982, General planetary theory extended to the case of resonance and application to the Galilean satellite system of Jupiter, Celestial Mechanics, vol. 26, Mar. 1982, p. 231-255.

Jonckheere, R. 1911, Stars, double and multiple, Cent nouvelles étoiles doubles, Monthly Notices of the Royal Astronomical Society, Vol. 71, p.750

Jonckheere, R. 1962, Catalogue général de 3 350 étoiles doubles de faible éclat observées de 1906 a 1962, ed. Observatoire de Marseille

Vienne, A., & Duriez, L. 1992, A general theory of motion for the eight major satellites of Saturn. III - Long-period perturbations, A& A., 257, 331-352

Archives of Lille Observatory

http://asso.jonckheere.free.fr/

http://asa3.univ-lille1.fr/

Author Index